Theory of Chemical Reaction Dynamics

Edited by

Antonio Lagana and György Lendvay

Theory of Chemical Reaction Dynamics

NATO Science Series

A Series presenting the results of scientific meetings supported under the NATO Science Programme.

The Series is published by IOS Press, Amsterdam, and Kluwer Academic Publishers in conjunction with the NATO Scientific Affairs Division

Sub-Series

I. **Life and Behavioural Sciences**	IOS Press
II. **Mathematics, Physics and Chemistry**	Kluwer Academic Publishers
III. **Computer and Systems Science**	IOS Press
IV. **Earth and Environmental Sciences**	Kluwer Academic Publishers
V. **Science and Technology Policy**	IOS Press

The NATO Science Series continues the series of books published formerly as the NATO ASI Series.

The NATO Science Programme offers support for collaboration in civil science between scientists of countries of the Euro-Atlantic Partnership Council. The types of scientific meeting generally supported are "Advanced Study Institutes" and "Advanced Research Workshops", although other types of meeting are supported from time to time. The NATO Science Series collects together the results of these meetings. The meetings are co-organized bij scientists from NATO countries and scientists from NATO's Partner countries – countries of the CIS and Central and Eastern Europe.

Advanced Study Institutes are high-level tutorial courses offering in-depth study of latest advances in a field.
Advanced Research Workshops are expert meetings aimed at critical assessment of a field, and identification of directions for future action.

As a consequence of the restructuring of the NATO Science Programme in 1999, the NATO Science Series has been re-organised and there are currently Five Sub-series as noted above. Please consult the following web sites for information on previous volumes published in the Series, as well as details of earlier Sub-series.

http://www.nato.int/science
http://www.wkap.nl
http://www.iospress.nl
http://www.wtv-books.de/nato-pco.htm

Theory of Chemical Reaction Dynamics

edited by

Antonio Lagana

Department of Chemistry,
University of Perugia, Perugia, Italy

and

György Lendvay

Institute of Chemistry,
Chemical Research Center, Budapest, Hungary

Created in the United States of America

Visit Springer's eBookstore at: http://ebooks.kluweronline.com
and the Springer Global Website Online at: http://www.springeronline.com

PREFACE

Theoretical treatment of the dynamics of chemical reactions has undergone a spectacular development during the last few years, prompted by the progress in experiments. Beam production, spectroscopic detection using high resolution, polarized lasers allowing energy and angular momentum selection, etc. have advanced so much that the experiments now offer detailed scattering information for theory to explain and rationalize. At the same time advances in computing and networking technologies for heteregeneous and grid environments are giving new possibilities for theoretical studies of chemical reactivity. As a consequence, by now calculation of atom+diatom reactions has become routine, accurate methods have been developed to describe reactions in tetraatomic systems, nonadiabatic reactions are being studied in simultaneous experimental and theoretical efforts, and statistical theories of unimolecular reaction dynamics are applied to systems that were a mystery a few years ago.

The increased interest in the field is testified by an intense activity of conferences, schools and collaborative networks. The NATO scientific division has traditionally contributed to this field through supporting workshops and schools. Along this line we organized the NATO Advanced Research Workshop on the Theory of the Dynamics of Chemical Reactions in Balatonföldvár, Hungary in June, 2003. The workshop has given a snapshot of the current status of research in reaction dynamics. At the meeting 36 papers were presented followed by enlightening discussions. Accurate time-dependent and time-independent methods of quantum scattering, treatment of non-adiabatic processes, studies of associative and inelastic collisions, calculation of potential surfaces received increased attention.

This book summarizes the proceedings of the Workshop, and is dedicated to Professor E.E. Nikitin on the occasion of his 70th birthday. Authors of 21 papers of the meeting agreed to make a written contribution aimed at giving a review of their recent work instead of just summarizing the brand new results, with the hope of providing researchers in the field with a useful reference.

We thank all the authors for their helpful collaboration. The grant from the NATO Science Program, without which the meeting could not have been organized, is gratefully acknowledged, as well as support from the Hungarian Ministry of Education. We thank Dr. Ákos Bencsura, Erika Bene and Tamás Vértesi for their participation in organizing the meeting. The efficient help of Dr. Andrea Hamza in editing the book is highly appreciated.

Antonio Laganà
Department of Chemistry,
University of Perugia, Italy

György Lendvay
Institute of Chemistry,
Hungarian Academy of Sciences
Budapest, Hungary

CONTENTS

It is our pleasure to dedicate this volume to Professor Evgueni Nikitin on the occasion of his 70th birthday. Evgueni has been an active contributor to the field of reaction dynamics for more than forty years and has become a leader in theoretical methodology of elementary processes, including uni- and bimolecular reactions, especially in the aspects related to nonadiabatic processes. His deep insight and original ideas led to completely new approaches and opened new areas of research.

In his postdoctoral study he got interested in non-equilibrium effects in thermal decomposition of diatomic molecules. In his paper on thermal unimolecular reactions in 1959 [P11][*] he provided a description for thermal activation by weak collisions. His earlier work on this subject is summarized in a book [B1].

Later on he moved to the theory of non-adiabatic transitions. He extended the Landau-Zener model to low energies which was important for application of this model to atomic and molecular collisions in the thermal energy range [P77], and suggested a more general model with non-linear crossing or non-crossing diabatic potentials [P89] concisely described in his recent review articles [P251,P271].

He applied the theory of nonadiabatic transitions to numerous specific systems. For atom-atom and ion-atom collisions, the one-dimensional models can be easily incorporated into a semiclassical scattering matrix [B10], which provides an easy interpretation of inelastic differential cross sections [P262]. Generalization of one-dimensional models for atom-molecule and molecule-molecule collisions required passing a conceptual threshold which was done in 1967 [P62] when a semiclassical procedure was suggested to combine a one-dimensional transition probability with a trajectory in multidimensional space. He is, therefore, considered to be one of the founders of the so-called trajectory surface hopping method. His ensuing work in the theory of non-adiabatic transitions is related to the generalization of the Landau method of estimating transition probabilities under near-adiabatic conditions beyond the correspondence principle [P220,P233] and the application of this approach to vibrational predissociation and vibrational-to-translational energy transfer [P221,P257].

In parallel to the study of dynamics of molecular collisions, he was working on a more accurate statistical description of unimolecular reactions and complex formation compared to the standard RRKM approach. He suggested a statistical theory which explicitly accounts for the conservation of the total angular momentum of a decomposing system, and laid down the foundations – simultaneously with John Light – of what is called the phase-space theory of chemical reactions [P51,P52]. This approach is described in detail in his books [B1,B8,B13]. Later Evgueni started [P198] and actively participated in the application of an advanced version of the statistical description (known as the statistical adiabatic channel model, SACM, by Quack and Troe) to particular processes (reviewed in [P259]). Now and again attempts were made to go beyond the adiabatic approximation without the need of being engaged in heavy numerical computations [P239]

Evgueni's current interests lie in the theoretical study of vibrational relaxation at ultra-low energies where quantum suppression and resonance enhancement are

---

[*] The numbers Bxx and Pxx refere to the corresponding line in the "Books" and "Papers" sections, respectively, of the ensuing List of Publications o Evgueni Nikitin.

important [P276], classical chaotic dynamics and its relation to quantum resonances [P273,P277,P278], threshold effects in low-energy complex formation [P282] and vibrational predissociation [P285], molecular wavepacket dynamics on atto-second timescales [P286]. Some of these points are illustrated also by his contributions to this volume.

Besides active research he very much enjoys teaching. In the Physical-Technical Institute of Moscow he taught (1966-1992) general courses on Molecular Dynamics and Chemical Kinetics. In the Technion (since 1992) he has taught and still teaches graduate courses on different subjects: Advanced Quantum Chemistry, Theory of Molecular Collisions, Kinetic Processes in Gases and Plasma, Theory of Fluctuations, Density Matrix Formalisms in Chemical Physics etc.

In addition to many people who enjoyed his teaching, Evgueni has a number of collaborators, including his former students and fellow researchers. The most notable among the latter is Prof. J. Troe of Göttingen. In addition, Evgueni always expressed his appreciation of his tight contacts with famous Russian kineticists like Prof. V. Kondratiev. The picture would not be complete without mentioning yet another of his long-term collaborators, his wife Dr. Elena Dashevskaya.

Graduated from Saratov University in 1955, Evgueni joint the Institute of Chemical Physics, Academy of Sciences in Moscow, first as a graduate student, then a researcher and as a head of a research group. Since 1966 he also held a position of Professor of Chemical Physics at the Physical-Technical Institute of Moscow. Starting from 1992 he has been a Professor of Chemistry at the Department of Chemistry, Technion, Haifa and a Guest Professor at the Institut für Physikalische Chemie, Universität Göttingen, and the Max-Planck Institut für Biophysikalische Chemie. During the years, he was an invited professor in many institutions through the world and got several research awards, among them, the Alexander von Humboldt award and the Gauss Professorship of the Göttingen Academy of Science. He enjoys being a member of three renown Academies: the International Academy of Quantum Molecular Sciences, the Deutsche Akademie der Naturforscher Leopoldina, and the European Academy of Arts, Sciences and Humanities.

Evgueni is a person whose activity follows the motto "Der Zeit ihre Kunst, der Kunst ihre Freiheit", the more so as he considers research and teaching as a kind of art.

We wish a lot of energy and health to Evgueni for the coming years and hope to see him at many more meetings.

The Editors

E. E. NIKITIN
LIST OF PUBLICATIONS (1955-2003)

BOOKS

1. E.E. Nikitin, *Current Theories of Thermal Decomposition and Isomerisation of Molecules in Gas Phase*. Moscow: Nauka, 1964, 106p. (in Russian). English Edition: *Theory of Thermally Induced Gas Phase Reactions.* Bloomington & London, Indiana University, Press 1966, 156p.
2. E.E. Nikitin, *Theory of Elementary Atom-Molecule Processes in Gases.* Moscow: Khimiya, 1970, 435p. (in Russian); English Edition: *Theory of Elementary Atomic and Molecular Processes in Gases.* Oxford, Clarendon Press, 1974, 472p.
3. E.E. Nikitin, *Theory of Elementary Atom-Molecule Reactions*. *Part 1. Methods*. Novosibirsk, Novosibirsk University Press, 1971, 190p. (in Russian).
4. E.E. Nikitin, *Theory of Elementary Atom-Molecule Reactions*. *Part 2. Processes*. Novosibirsk, Novosibirsk University Press, 1974, 220p. (in Russian).
5. V.N. Kondratiev and E.E. Nikitin, *Kinetics and Mechanisms of Gas-Phase Reactions*.Moscow, Nauka, 1974, 558p. (in Russian).
6. E.E. Nikitin and L.Zuelicke, *Theory of Chemical Elementary Processes*. Berlin, Central Institute of Physical Chemistry, 1976, 168p.
7. V.N. Kondratiev, E.E. Nikitin, A.I.Reznikov, and S.Ya.Umanskii, *Thermal Bimolecular Reactions in Gases*. Moscow, Nauka, 1976, 192p. (in Russian).
8. E.E. Nikitin and L. Zuelicke, *Selected Topics of the Theory of Chemical Elementary Processes*. Lecture Notes in Chemistry. Berlin-Heidelberg, Springer, 1978, 176p.
9. E.E. Nikitin and A.I. Osipov, *Vibrational Relaxation in Gases.* Moscow, VINITI, 1977, 180p. (in Russian).
10. E.E. Nikitin and S.Ya. Umanskii, *Nonadiabatic Transitions in Slow Atomic Collisions*. Moscow, Atomizdat, 1979, 272p. (in Russian). Revised English Edition: *Theory of Slow Atomic Collisions*, Berlin- Heidelberg, Springer, 1984, 432p.
11. E.E. Nikitin and S.Ya. Umanskii, *Semiempirical Methods of Calculation of Interatomic Interaction*. Moscow, VINITI, 1980, 250p. (in Russian).
12. V.M.Galitski, E.E. Nikitin, and B.M. Smirnov, *Collision Theory of Atomic Particles.* Moscow, Nauka, 1981, 255p (in Russian).
13. V.N.Kondratiev and E.E. Nikitin, *Chemical Processes in Gases*. Moscow, Nauka, 1981, 262p. (in Russian). Revised English Edition: *Gas-Phase Reactions. Kinetics and Mechanisms*. Berlin-Heidelberg, Springer, 1981, 240p.
14. E.E. Nikitin, *Dynamics of Molecular Collisions*. Moscow, VINITI, 1983, 240p. (in Russian).
15. E.E. Nikitin, *Elementary Events of Energy Transfer in Three-Atom Systems*, Moscow, VINITI, 1985, 198p. (in Russian).
16. E.E. Nikitin and L. Zuelicke, *Theorie Chemicher Elementarprozesse.* Berlin, Akademie Verlag, 1981. 230p.
17. E.E. Nikitin and B.M. Smirnov, *Atomic and Molecular Processes. Problems and Solutions*. Moscow, Nauka, 1989. 303p. (in Russian).

18. E.E. Nikitin and B.M. Smirnov, *Slow Atomic Collisions*, Moscow, Energoatomizdat, 1990, 250p. (in Russian).

PAPERS:

1. A.D.Stepukhovich and E.E.Nikitin, Inhibition and initiation of paraffin cracking, Doklady Akad.Nauk SSSR, **105**, 997 (1955)
2. A.D.Stepukhovich and E.E.Nikitin, Kinetics and mechnism of hydrocarbon decomposition; initiation of the butane cracking by traces of azomethane, Zhurn.Fiz.Khim. **30**, 1291 (1956)
3. A.D.Stepukhovich, I.G.Kaplan and E.E.Nikitin, Tetramethylethylene as a new inhibitor of cracking. Zhurn.Fiz.Khim. **31**, 1437 (1957)
4. A.D.Stepukhovich and E.E.Nikitin, Theory of inhibition of hydrocarbon cracking by tetramethylethylene, Zurn.Fiz.Khim. **31**, 1677 (1957)
5. A.D.Stepukhovich and E.E.Nikitin, On kinetics and mechanism of tetramethylethylene decomposition, Zhurn.Fiz.Khim. **31**, 2400 (1957)
6. E.E.Nikitin, On deviations from the Boltzmann distribution in decomposition of diatomic molecules, Doklady Akad.Nauk SSSR, **116**, 584 (1957)
7. E.E.Nikitin, Calculation of the rate constant for decomposition of diatomic molecules, Doklady Akad.Nauk SSSR, **119**, 526 (1958)
8. E.E.Nikitin, On a perturbation of the thermal equilibrium in thermal dissociation of diatomic molecules, Zhurn.Fiz.Khim. **33**, 519 (1959)
9. E.E.Nikitin, On the calculation of the rate constant for a bimolecular decomposition of molecules, Zhurn.Fiz.Khim. **33**, 1893 (1959)
10. E.E.Nikitin and N.D.Sokolov, On the relation between rate constants of thermal decomposition of diatomic molecules in the presence and absence of equilibrium, Doklady Akad.Nauk.SSSR, **124**, 366 (1959)
11. E.E.Nikitin and N.D.Sokolov, Theory of thermal second-order decomposition of molecules, J. Chem. Phys. **11**, 1371 (1959)
12. E.E.Nikitin, Theory of thermal decomposition of nitrous oxide at low pressures, Doklady Akad.Nauk.SSSR, **129**, 157 (1959)
13. E.E.Nikitin, Calculation of vibrational excitation probabilities of molecules in collisions. Optika i Spektr. **6**, 141 (1959)
14. E.E.Nikitin, Band shapes of pressure-induced vibrational and rotational spectra of diatomic molecules, Optika i Spektr. **7**, 744 (1959)
15. E.E.Nikitin, Vibrational relaxation of diatomic molecules, Doklady Akad. Nauk SSSR, **124**, 1084 (1959)
16. E.E.Nikitin, On a mechanism of the intermolecular energy exchange in dissociation reaction, Doklady Akad.Nauk SSSR, **132**, 395 (1960)
17. E.E.Nikitin and N.D.Sokolov, Theory of thermal decomposition of diatomic molecules, Izvestiya AN SSSR, **24**, 996 (1960)
18. E.E.Nikitin, Vibrational distribution functions of polyatomic molecules in thermal decomposition, Doklady Akad.Nauk SSSR, **135**, 1442 (1960)
19. E.E.Nikitin, Nonadiabatic vibrational excitation of molecules, Optika i Spektr. **9**, 16 (1960)

20. E.E.Nikitin, On the interpretation of spectra of compressed gases, Optika i Spektr. **8**, 264 (1960)
21. E.E.Nikitin, On a possible mechanism of electronic excitatation in slow collisions, Optika i Spektr. **8**, 157 (1960)
22. E.E.Nikitin, Wave functions of diatomic molecules at strong spin-orbit interaction, Optika i Spektr. **10**, 443 (1961)
23. E.E.Nikitin, Nonadiabatic transitions near the turning point in atomic collisions, Optika i Spektr. **11**, 452 (1961).
24. E.E.Nikitin, Intermolecular energy transfer in collisions of chemically active molecules, Doklady Akad. Nauk SSSR, **136**, 1376 (1961)
25. E.E.Nikitin, On the interelectron interaction in large molecules, Optika i Spektr. **12**, 691 (1962)
26. E.E.Nikitin, Effect of the vibrational-rotational interaction in vibrational relaxation of diatomic molecules, Kinetika i Kataliz, **3**, 332 (1962)
27. E.E.Nikitin, On the mechanism of nonadiabatic relaxation of NO molecules. Eight Int. Symposium on Combustion, Baltimore, p. 319, 1962
28. E.E.Nikitin, Band shapes of induced rotational and vibrational spectra of diatomic molecules, in: Adv. Molec. Spectroscopy, Pergamon Press, p.298 (1962)
29. E.E.Nikitin, Resonance and nonresonance intermolecular energy exchange in molecular collisions, Disc.Faraday Soc. **33**, 14 (1962)
30. E.E.Nikitin, Resonance vibrational relaxation in a system of harmonic oscillators, Doklady Akad. Nauk SSSR, **148**, 298 (1962)
31. E.E.Nikitin, The probability of nonadiabatic transitions in the case of nondivergent terms, Optika i Spectr. **13**, 761 (1962)
32. E.E.Nikitin, On the relation between rate constants for dissociation and recombination, Kinetika i Kataliz, **3**, 380 (1962)
33. E.E.Nikitin, Bimolecular preassociation of polyatomic molecules, Doklady Akad. Nauk. SSSR,.**152**, 1395 (1963)
34. E.E.Nikitin, On the interelectronic and nonadiabatic interactions in long-chain molecules, in: *Voprosy Kvantovoy Khimii*, Leningrad, University Press, 1963, p.100.
35. E.E.Nikitin, Charge exchange in the accidental resonance case, Izvesiya AN SSSR, **27**, 996 (1963)
36. V.K.Bykhovski and E.E.Nikitin, Nonadiabatic transitions in atomic collisions. Quenching of sodium resonance fluorescence by argon, Optika i Spektr. **17**, 815 (1964)
37. V.K.Bykhovski and E.E.Nikitin, Nonadiabatic transitions in atom-molecule collisions. Quenching of mercury resonance fluorescenc Optika.i Spektr. **16**, 202 (1964)
38. E.E.Nikitin, Theory of nonadiabatic vibrational relaxation in atom-molecular collisions, Mol. Phys. **7**, 389 (1964)
39. E.E.Nikitin, Mean lifetimes of active molecules and oscillator models of unimolecular reactions, Mol. Phys. **8**, 65 (1964)
40. E.E.Nikitin, The compound-molecule model in the theory of chemical reactions, Mol. Phys. **8**, 473 (1964)

41. V.K.Bykhovski, E.E.Nikitin, and M.Ya.Ovchinnikova, Probability of a nonadiabatic transition near the turning point, Zh.Eksp.Teor. Fiz. **47**, 750 (1964)

42. E.E.Nikitin, Methods for the calculation of nonadiabatic transition probabilities, Optika i Spekt. **18** 763 (1964)

43. E.E.Nikitin, Mechanism of atomic fluorescence quenching in collisions with diatomic molecules, J.Quant.Spectr.Rad.Transfer, **5**, 435 (1965)

44. E.E.Nikitin, Rotational relaxation of diatomic molecules, Doklady Akad.Nauk SSSR, **161**, 637 (1965)

45. V.K.Bykhovski and E.E.Nikitin, Charge exchange in collisions of multiply charged ions, Zhurn. Eksp. Teor. Fiz. **48**, 1944 (1965)

46. E.E.Nikitin, Nonadiabatic transitions between fine-structure components of alkalies in atomic collisions, Optika i Spektr. **19**,161 (1965)

47. E.E.Nikitin, Nonadiabatic transitions between fine-structure components of alkali atoms upon collision with inert-gas atoms, J. Chem. Phys. **43**, 744 (1965)

48. E.E.Nikitin, Average lifetime of activated molecules, Kinetika i Kataliz, **6**, 17 (1965)

49. E.E.Nikitin, Intermediate complex model in the theory of chemical reactions, Kinetika i Kataliz, **6**, 337 (1965)

50. E.E.Nikitin, On the statistical theory of endothermic reactions. I. Bimolecular reactions, Teor. Eksp. Khim. **1**, 135 (1965)

51. E.E.Nikitin, On the statistical theory of endothermic reactions. II. Unimolecular reactions, Teor. Eksp. Khim. **1**, 144 (1965)

52. E.E.Nikitin, On the statistical theory of exothermal unimolecular reactions, Teor.Eksp.Khim. **1**, 428 (1965)

53. E.E.Nikitin and N.N.Korst, Relaxation in a double potential well, Teor. Eksp. Khim. **1**, 11 (1965)

54. E.E.Nikitin, Activation mechanisms and nonequilibrium distribution functions in unimolecular reactions, Teor.Eksp.Khim. **2**, 19 (1966)

55. V.N.Kondratiev and E.E.Nikitin, Rate constants for the processes O_2 + Ar$\rightarrow$ $\rightarrow$O+O+Ar, J. Chem. Phys. **45**, 1078 (1966)

56. V.N.Kondratiev, E.E.Nikitin, and V.L.Tal'rose, Problems connected with the investigation of elementary processes in low-temperature plasma, Pure and Applied Chemistry, **13**, 367 (1966)

57. E.E.Nikitin, Theory of thermal excitation and de-excitation of alkali atoms in an inert gas heat bath, Comb.and Flame, **10**, 381 (1966)

58. E.E.Nikitin, Inelastic transitions between fine-structure components of alkalies in adiabatic collisions. I.General theory, Optika i Spektr. **22**, 689 (1967)

59. E.E.Nikitin, Theory of thermal excitation and deexcitation of alkali atoms in a noble gas heat bath, Teplofiz. Vysokich Temperatur, **2**, 224 (1967)

60. E.I.Dashevskaya and E.E.Nikitin, Inelastic transitions between fine-structure components of alkalies in adiabatic cillisions. II.Calculation of cross sections, Optika i Spektr. **22**, 866-875 (1967)

61. E.E.Nikitin, Effect of rotation on vibrational relaxation of molecules, Teor. Eksp. Khim. **3**, 185 (1967)

62. A. Bjerre and E.E.Nikitin, Energy transfer in collisions of excited sodium atom with nitrogen molecule, Chem. Phys. Lett. **1**, 179 (1967)

63. V.N.Kondratiev and E.E.Nikitin, Temperature dependence of the rate constants of gas phase reactions, Uspekhi khimii, **11**, 36 (1967)

64. E.E.Nikitin, Optical model for spectator-stripping reaction, Chem.Phys.Lett. **1**, 266 (1967)

65. E.E.Nikitin, Nonadiabatic energy transfer in gases, in: *Nobel Symposium 5. Fast Reactions and Primary Processes in Chemical Kinetics*, ed. S.Claesson, Stockholm, Almqvist & Wiksell, 1967, p.165

66. E.E.Nikitin, Charge-exchange induced reactions, Teor.Eksp.Khim. **4**, 593 (1968)

67. E.E.Nikitin, Quantum effects in electron-harpoon reactions, Teor. Eksp. Khim. **4**, 751 (1968)

68. E.E.Nikitin, Der gegenwaertige Stand der Theorien bimolekularer Reaktionen, Ber. Bunsenges. phys.Chem. **72**, 949 (1968)

69. A.I.Burshtein and E.E.Nikitin, Line shape of transition between lambda-doublet components, Zhurn.Eksp.Teor.Fiz. **55**, 1401 (1968)

70. E.E.Nikitin, The current status of the theory of bimolecular reactions, Uspekhi Khimii, **38**, 1153 (1968)

71. E.E.Nikitin, Quasistationary states in a conical potential well, Doklady Akad.Nauk SSSR, **183**, 319 (1968)

72. E.E.Nikitin, Nonadiabatic processes in energy transfer in gases, Uspekhi Khimii, **37**, 1669 (1968)

73. E.E.Nikitin, Relaxation of vibrational energy in collisions of polyatomic molecules, Teor. Eksp. Khim. **4**, 305 (1968)

74. G.A.Kapralova, E.E.Nikitin, and A.M.Chaikin, Nonempirical calculations of the probabilities of vibrational transitions in hydrogen halide molecules, Chem. Phys. Lett. **2**, 581 (1968)

75. E.E.Nikitin and G.H.Kohlmaier, Energieuebertragung mehratomigen Molekuelen mit hohen Energieniveaudichten, Ber. Bunsenges. Phys.Chem. **72**, 1021 (1968)

76. E.E.Nikitin, Quasistationare Zustaende in der konischen Potentialmulde. Teoret.chim. Acta, **13**, 308 (1968)

77. E.E.Nikitin, Theory of nonadiabatic transitions. Recent development of Landau-Zener model, in: *Chemische Elementarprozesse*, ed. H.Hartmann, Berlin-Heidelberg, Springer, 1968, p.43

78. A.I.Voronin and E.E.Nikitin, Intramultiplet mixing cross sections for atoms of second column, Optika i Spektr. **25**, 803 (1968)

79. E.E.Nikitin, Nonresonance excitation transfer in atomic collisions induced by dipole-dipole interaction, Chem.Phys.Lett. **2**, 402 (1968)

80. E.I.Dashevskaya, A.I.Voronin, and E.E.Nikitin, Theory of excitation transfer in collisions between alkali atoms. I. Identical partners, Canad.J.Phys. **47**, 1237 (1969)

81. E.E.Nikitin and S.Ya.Umanski, Electronenwellenfunktionen und Terme zweiatomiger Molekuele bei grossen Atomabstaenden, Theoret.chim.Acta, **13**, 91 (1969)

82. G.A.Kapralova, E.E.Nikitin, and A.M.Chaikin, Vibrational transition probabilities in hydrogen halides, Kinetika i Kataliz, **10**, 974 (1969)

83. E.E.Nikitin, Resonance and nonresonance excitation transfer in collisions of excited and ground-state alkali atoms, Comm. At. Mol. Phys. **1**, 111 (1969)

84. E.P.Gordeev, E.E.Nikitin, and M.Ya.Ovchinnikova, Calculation of cross sections for the depolarization of ^{2}P states in alkali atoms, Canad. J. Phys. **47**, 1819 (1969)

85. E.E.Nikitin, Mixing and depolarisation of $P_{1/2}$ and $P_{3/2}$ states of excited alkali atoms. Comm. At. Mol. Phys. **1**, 122 (1969)

86. E.I.Dashevskaya, E.E.Nikitin, and A.I.Reznikov, Theory of intramul tiplet mixing in alkali atoms in collisions, Optika i Spektr. **29**, 1016 (1970)

87. E.I.Dashevskaya, E.E.Nikitin, and A.I.Resnikov, Theory of collisionally induced intramultiplet mixing in excited alkali atoms, J. Chem. Phys. **53**, 1175 (1970)

88. E.I.Dashevskaya, E.E.Nikitin, A.I.Voronin, and A.A.Zembekov, Theory of excitation transfer in collisions between alkali atoms. II. Dissimilar partners. Canad.J.Phys. **48**, 981 (1970)

89. E.E.Nikitin, The theory of nonadiabaic transitions. Recent development with the exponential model. Adv. Quant. Chem. **5**, 135 (1970)

90. E.E.Nikitin, The Landau-Zener model and its region of applicability, Comm. At. Mol. Phys. **1**, 166 (1970)

91. E.E.Nikitin, Gyroscopic interpretation of two-state hypergeometric models of nonadiabatic coupling, Comm. At. Mol. Phys. **2**, 4 (1970)

92. E.E.Nikitin and E.A.Andreev, Nicht-adiabatische Uebergaenge bei Stoessen zwischen Atomen und Molekuelen. Desaktivierung von Br und I-Atomen durch zweiatomige Molekuele, Theoret.chim.Acta **17**, 171 (1970)

93. E.E.Nikitin, VT versus VR energy transfer in molecular collision, Comm. At. Mol. Phys. **2**, 166 (1970)

94. E.I.Dashevskaya, E.E.Nikitin, and A.I.Reznikov, Mechanisms of intramultiplet mixing in alkalies, in: *Sensitized fluorescence of matal vapours*, Riga, University Publishing, 1971, p.91

95. E.P.Gordeev, E.E.Nikitin, and M.Ya.Ovchinnikova, Depolarization of the P-state of alkalies in collisions with noble gas atoms, Optika i Spektr. **30**, 189 (1971)

96. E.E.Nikitin and A.I.Reznikov, Excitation transfer in highly excited alkali atoms.I. Cs + noble gases, Chem. Phys. Lett. **8**, 1, (1971)

97. E.E.Nikitin, Remarks on different theoretical approaches to the collisionally induced depolarization, Comm. At. Mol. Phys. **3**, 7 (1971)

98. A.A.Zembekov and E.E.Nikitin, Excitation transfer in highly excited alkali atoms. II.Cs + Cs, Chem. Phys. Lett. **9**, 213 (1971)

99. E.I.Dashevskaya, E.E.Nikitin, and A.I.Reznikov, Theory of intramultiplet mixing in alkali atoms in collisions, Optika i Spektr. **21**, 108 (1971)

100. E.E.Nikitin and S.Ya.Umanski, Effect of electronic-vibrational interaction on vibrational relaxation of O_2 and N_2 in collisions with O atoms, Doklady Akad. Nauk SSSR **145**, 196 (1971)

101. A.I.Voronin, E.E.Nikitin, and A Steinman, On the mechnism of the singlet-triplet transition in methylene, Doklady Akad. Nauk SSSR **196**, 852 (1971)

102. E.E.Nikitin and L.Yu.Rusin, Angular distrubution of reaction products in decomposition of a long-lived complex. Doklady Akad. Nauk SSSR, **198**, 330 (1971)

103. A.A.Zembekov and E.E.Nikitin, On dynamics of harpoon reactions, Doklady Akad. Nauk SSSR **205**, 1392 (1972)

104. E.E.Nikitin and S.Ya.Umanski, Effect of vibronic interaction upon the vibrational relaxation of diatomic molecules, Faraday Disc.Chem.Soc. No.**53**, 7 (1972)

105. E.E.Nikitin and A.I.Reznikov, Calculation of transition probabilities using the Landau-Zener model, Phys. Rev. **A6**, 522 (1972)

106. E.E.Nikitin and S.Ya.Umanski, Vibrational to translational vs vibronic to translational energy transfer in molecular collisions, Comm. At. Mol. Phys. **3**, 195 (1972)

107. E.E.Nikitin, The Landau-Zener model in the theory of atomic collisions, in: *Physics of Ionized Gases*, ed. M.V.Kurepa, Belgrade, Institute of Physics, 1972, p.117

108. E.E.Nikitin and M.Ya. Ovchinnikova, Interference phenomena in atomic scattering, Uspekhi Fiz. Nauk **104**, 2 (1972)

109. E.E.Nikitin, Transfer of vibrational energy in collision of diatomic molecules, Proceedings of Institute of Mechanics, Moscow State University **24**, 44 (1973)

110. J.E.Bayfield, E.E.Nikitin, and A.I.Reznikov, Semiclassical scattering matrix for the two-state exponential model, Chem.Phys. Lett. **19**, 471 (1973)

111. E.E.Nikitin and V.N.Kondratiev, On a nonadiabatic mechanism of reactions O + HX -> OH + X (X=F,Cl,Br,J), Doklady Akad.Nauk SSSR, **212**, 159 (1973)

112. E.E.Nikitin, Nonequilibrium chemical reactions, in: *Kinetics of elementary chemical reactions*, Moscow, Nauka 1973, p.51

113. E.E.Nikitin, The Landau-Teller model in the theory of collisional excitation of molecules, Proceedings of second USSR summer school on physics of electronic and atomic collisions. Leningrad Physico-Technical Institute, 1973, p.14

114. E.E.Nikitin and S.Ja.Umanskij, Wellenfunktionen und terme des Systems atom-Zweiatomigen Molekuele bei grossen intermolekularen Abstaenden, Theoret.chim.Acta **28**, 121 (1973)

115. E.I.Dashevskaya, R.McCarroll, F.Masnou, and E.E.Nikitin, Approximation of sudden switching of couplings for intramultiplet transitions, Optika i Spektr. **37**, 209 (1974)

116. E.E.Nikitin, Theory of energy transfer in molecular collisions, in: *Physical Chemistry. An Advanced Treatise* v. 6A, ed. W. Jost, New-York, Academic Press, 1974, p. 167

117. E.E.Nikitin, Dymanics of nonadiabatic bimolecular reactions, Uspekhy khimii **43**, 1905 (1974)

118. E.E.Nikitin and S.Ya. Umanski, Statistical theory of bimolecular reactions, in: *Khimiya Plasmy*, ed. B.M.Smirnov, Moscow, Atomizdat, 1974, p. 8

119. U.Havemann, L.Zuelicke, E.E.Nikitin, and A.A.Zembekov, Model calculation of harpooning elementary process in the system $K + Br_2$, Chem.Phys.Lett. **25**, 487 (1974)

120. U.Havemann, L.Zuelicke, E.E.Nikitin, and A.A.Zembekov, Zur Theorie elektronisch nichtadiabatischer Elementarprozesse, Z. phys. Chem. Leipzig **255**, 1179 (1974)

121. E.E.Nikitin and L.Yu.Rusin, Statistical distribution functions of products of exoergic reactions, Khimiya Vysokhikh Energii **2**, 124 (1975)

122. E.E.Nikitin, Theory of nonadiabatic collision processes including excited alkali atoms, Adv. Chem. Phys. **75**, 317 (1975)

123. E.E.Nikitin, Intramultiplet mixing and depolarization in atomic collisions, in: *Atomic physics IV*, ed. G. zu Putlitz, New York, Plenum Press 1975, p.529

124. E.E.Nikitin, M.Ya.Ovchinnikova, and A.I.Shushin, Excitation mechanism in the Na -Ne system, Pis'ma v Zhurn.Eksp.Teor.Fiz. **21** 633 (1975)

125. I.V.Lebed' and E.E.Nikitin, Deactivation of rotationally excited hydrogen halide molecules, Doklady Akad.Nauk SSSR **224**, 373 (1975)

126. E.E.Nikitin, Non-adiabatic effects in collisional vibrational relaxation of diatomic molecules, in *The Physics of Electronic and Atomic Collisions*, ed. J.S.Risley, R.Geball, University of Washington Press, Seattle and London, 1975

127. E.E.Nikitin, M.Ya.Ovchinnikova, and A.I. Shushin, Collisional excitation in systems Na-Ne and O-Ne, Zhurn.Eksp.Teor.Fiz. **70**, 1243 (1976)

128. E.I.Dashevskaya and E.E.Nikitin, Polarization transfer and relaxation in collisions of excited alkali atoms, Canad.J.Phys. **54**, 709 (1976)

129. E.E.Nikitin, M.Ya.Ovchinnikova, B.Andresen, and A.E. de-Vries, Semiclassical calculation of charge transfer: tunneling at large angular momentum, Chem.Phys. **14**, 121 (1976)

130. E.E.Nikitin, The Landau-Zener theory in atomic collision theory, in: *Proceedings of the Third USSR summer school on physics of elecronic and atomic collisions*, Leningrad, Physical-Technical Institute, 1976, p.131

131. E.E.Nikitin, Nonadiabatic effects in collisional vibrational relaxation of diatomic molecules, in: *Physics of electronic and atomic collisions*, ed. J. Risley, University of Washington Press, 1976, p.275

132. E.E.Nikitin, Nonadiabatic molecular collisions, in: *Proceedings of VI USSR Conference on Physics of Electronic and Atomic Collisions*. Leningrad, Physical-Technical Institute, 1976, p.218

133. E.A.Andreev and E.E. Nikitin, Translational-vibrational energy transfer in atom-molecule collisions, in: *Khimiya Plazmy* **3**, ed. B.M.Smirnov, Moscow, Atomizdat, 1976, p. 28

134. I.V.Lebed', E.E.Nikitin, and S.Ya.Umanski, Collision-induced transitions between rotational levels of diatomic molecules in Pi-states, Optika i Spektr. **43**, 636 (1977)

135. A.I.Burshtein and E.E.Nikitin, Relaxation and depolatization of atomic states in collisions, in: *Gas Lasers*, Novosibirsk, Nauka,1977, p. 7

136. E.E.Nikitin and A.I.Shushin, Excitation paths of alkali atoms in collisions, Optika i Spektr. **43**, 399 (1977)

137. E.A.Gordeev, E.E.Nikitin, and A.I.Shushin, Nonadiabatic coupling between three states: application to alkali diatoms, Mol. Phys. **33**, 1611 (1977)

138. Yu.M.Gershenson, E.E.Nikitin, V.B.Rosenshtein, and S.Ya.Umanski, Interaction of vibrationally excited molecules with chemically active atoms, in: *Khimiya plazmy* **5**, ed. B.M.Smirnov, Moscow, Atomizdat, 1978, p. 3

139. E.E.Nikitin and M.Ya.Ovchinnikova, On the magnetic field effect in collisional depolarization of the $P_{1/2}$ state of alkalies, J.Phys.B. **11**, 465 (1978)

140. E.E.Nikitin and B.M.Smirnov, Quasiresonance processes at slow atomic collisions, Uspekhi Fiz. Nauk **124**, 201 (1978)

141. E.E.Nikitin and A.I.Reznikov, Stueckelberg phase calculations for the two-state exponential model, J.Phys.B. **11**, 695 (1978)

142. E.E.Nikitin, Vibrational relaxation of highly-excited polyatomic molecules, Doklady Akad.Nauk SSSR, **239**, 380 (1978)

143. E.E.Nikitin, Vibrational relaxation of diatomic molecules on potentially reactive atoms, in: *Gas-dynamics lasers and laser photochemistry*. Moscow, University Press, 1978, p.136

144. E.E.Nikitin and B.M.Smirnov, Quasiresonance processes in atomic collisions, in: *Atomic Physics VI*, Riga-New York, Zinantne-Plenum Press, 1979, p. 267

145. E.E.Nikitin, Adiabatische Naeherung und nichtadiabatische Wechselwirkung in der Elementarprozessen, Nova Acta Leopoldina **9**, 49 (1979)

146. U.Havemann, L.Zuelicke, A.A.Zembekov, and E.E.Nikitin, Simple semiclassical optical model of harpooning elementary process K + Br$_2$, Chem.Phys. **41**, 285 (1979)

147. A.A.Zembekov, E.E.Nikitin, U.Havemann, and L.Zuelicke, Dynamics of harpoon reactions as a prototype of chemiionization; in: *Khimiya Plazmy* **6**, ed. B. M. Smirnov, Moscow, Atomizdat, 1979, p.3

148. E.E.Nikitin, Potential energy surfaces and nonadiabatic elementary processes, in: *Problemy Khimicheskoi Kinetiki*, Moscow, Nauka, 1979, p.66

149. E.E.Nikitin and L.Yu.Rusin, Statistical models in dynamics of elementary chemical reactions, in: *Physical Chemistry. Current problems*, ed. Ya.M. Kolotyrkin, Moscow, Khimiya, 1980, p.49

150. E.E.Nikitin, Kinetik chemicher Elementarreactionen, Nova Acta Leopoldina, NF **51**, 153 (1980)

151. V.M.Akimov, E.E.Nikitin, L.Yu Rusin, and A.Stelmakh, Dissociative ionization of molecules in collisions with Xe atoms in crossed molecular beams, Doklady Akad.Nauk SSSR **233**, 633 (1980)

152. E.E.Nikitin and A.I.Resnikov, Simple semiclassical calculations of fine-structure transition probability, J.Phys.B **13**, L57 (1980).

153. E.E.Nikitin and M.Ya.Ovchinnikova, Role of anharmonic dynamics in vibrational relaxation of impurity molecules in solids, Zhurn.Eksp. Teor.Fiz. **78**, 1551 (1980)

154. A.A.Zembekov and E.E.Nikitin, Correlation diagrams of electronic states of triatomic systems and the interpretation of reaction dynamics, *Khimiya plazmy* **7,** ed. B.M. Smirnov, Moscow, Atomizdat, 1980, p. 4

155. J.Grosser, E.E.Nikitin, A.Shushin, and A.E.de Vries, Ion pair formation by spin-orbit interaction in collisions between fluorine atoms and zinc, cadmium and mercury atoms, Chem. Phys. **56**, 21 (1981).

156. A.A.Zembekov, A.I.Maergoiz, E.E.Nikitin, and L.Yu.Rusin, Impulsive model of dissociative ionisation of molecules in collisions, Teor. Eksp. Khim. **17**, 579 (1981)

157. E.E.Nikitin, Asymmetry of inelastic scattering of atoms im magnetic field, Optika i Spectr. **53**, 619 (1982)

158. E.E.Nikitin, Nonadiabatic elementary chemical reactions, in: *Advances in Theoretical Chemical Physics*, Mocow, Nauka, 1982, p.11

159. E.E.Nikitin, Many-trajectory semiclassical approximation in the theory of inelastic scattering of slow heavy particles, Khim. Fiz. **1**, 867 (1982)

160. E.E.Nikitin, A.I.Shushin, J.Grosser, and A.E.de Vries, Study on the mechanism of chemi-ionisation in collisions of IIb-group atoms with fluorine atoms, Khim. Fiz. **1**, 457 (1982).

161. E.E.Nikitin, Nonadiabatic transitions between merging potential curves, Khim. Fiz. **1**, 721 (1982).

162. E.E.Nikitin, Nonadiabatic effects in slow atomic collisions: Many-trajectory semiclassical approximation, in: *New Horizons in Quantum Chemistry*, ed. P-O Löwdin and B.Pullman, Dordrecht, Reidel, 1983, p. 117

163. E.I.Dashevskaya, E.E.Nikitin, and S.Ya.Umanskii, Asymmetry in the cross sections for transitions between magnetic sublevels in atomic collisions, Opt. i Spectr. **55**, 1092 (1983)

164. E.I.Dashevskaya, E.E.Nikitin, and S.Ya.Umanskii, Asymmetry in the cross sections for transitions between magnetic sublevels of the state j = 1 in atomic collisions, Khim. Fiz. **3**, 627 (1984)

165. E.E.Nikitin, Depolarization interferential structure of differential cross sections for scattering of atoms in degenerate state, Khim. Fiz. **3**, 1219 (1984).

166. E.E.Nikitin, Comparison problem for depolarization of atoms with the intrinsic angular momentum j = 1 upon scattering through small angles, Khim. Fiz. **3**, 792 (1984)

167. E.E.Nikitin, Azimuthal asymmetry in scattering of polarized atoms in the P-state, Khim. Fiz. **4**, 310 (1985)

168. A.I.Maergoiz, E.E.Nikitin and L.Yu.Rusin, Dynamics of ion formation in collision-induced dissociation of diatomic molecules, in: *Khimiya Plasmy* **11**, ed. B. M. Smirnov, Moscow, Atomizdat, 1985, p. 3

169. E.E.Nikitin, On a mechanism of collision-induced polarization transfer in atoms, Optika i Spectr. 58, 964 (1985)

170. E.I.Dashevskaya and E.E.Nikitin, Creation of polarization in atoms with j = 1 upon collisions in beams, Khim. Fiz. **4**, 1174 (1985)

171. E.I.Dashevskaya and E.E.Nikitin, Classical dynamics of atomic magnetic moment for quadratic interaction with an external magnetic field, Khim. Fiz. **5**, 457 (1986)

172. B.Friedrich, S.Pick, L.Hladek, Z.Herman, E.E.Nikitin, A.I.Reznikov, and S.Ya.Umanskii, Dynamics of charge transfer Ar^{++} + He -> Ar^+ +He^+ at low collision energies: Comparison of experimental results with quasiclassical calculations of the differential cross sections, J. Chem. Phys. **84**, 807 (1986)

173. E.E.Nikitin, A.I.Reznikov, and S.Ya.Umanskii, Two-level model of charge exchange with Coulomb interaction in one of the channels: Quantum and quasiclassical cross sections in the weak-coupling limit, Zh.Eksp.Teor.Fiz. **91**, 1590 (1986)

174. E.E.Nikitin, Quasimolecular description of polarization transfer of atoms in scattering through classical angles, Khim. Fiz. **5**, 1592 (1986)

175. E.E.Nikitin and M.Ya.Ovchinnikova, An analytical model of vibrational-to-rotational energy transfer for highly anisotropic interaction between an atom and a diatomic molecule, Khim. Fiz. **5**, 291 (1986)

176. E.E.Nikitin, Sterical factor for the rate constant of a VR-process involving 2D-rotor, Khim. Fiz. **5**, 1155 (1986)

177. D.V.Shalashilin, M.Ya.Ovchinnikova, and E.E.Nikitin, Vibronic description of atom-molecule charge-transfer in $[N_2 -Ar]^+$ system, Khim. Fiz. **5**, 750 (1986)

178. E.E.Nikitin, Dynamics of elementary chemical processes, Khim. Fiz. **6**, 1603 (1987)

179. E.E.Nikitin and L.Yu.Rusin, Dynamics of exchange and abstraction reactions in hydrogen-halide systems, Khim. Fiz. **6**, 1643 (1987)

180. E.E.Nikitin, M.Ya.Ovchinnikova, and D.V.Shalashilin, Study on the charge transfer dynamics of $Ar^+ -N_2$ by surface hopping in the vibronic representation, Khim. Fiz. **6**, 573 (1987)

181. E.E.Nikitin, M.Ya.Ovchinnikova, and D.V Shalashilin, Vibronic approach to dynamics of charge transfer in the $[Ar-N_2]$ system, Chem. Phys. **111**, 313 (1987)

182. E.E.Nikitin, Generalized Landau-Zener and Landau-Teller models in theory of molecular collisions, In: *Chemistry Reviews, Soviet Scientific Reviews*, Section B **9**, ed. M. E. Vol'pin, New York, Harwood Academic 1987, p.187

183. E.I.Dashevskaya and E.E.Nikitin, Polarization transfer cross sections in the random phase approximation, Khim. Fiz. **6**, 3 (1987)

184. E.I.Dashevskaya and E.E.Nikitin, Quasiclassical integral polarisation tranfer and relaxation cross sections in atomic collisions, Optika i Spektr. **62**, 742 (1987)

185. E.E.Nikitin, A.I.Reznikov, and S.Ya.Umanskii, Quasiclassical interpretation of the charge transfer of Ar on He at low energies, Khim. Fiz. **6**, 721 (1987)

186. E.E.Nikitin, Effect of rotation of homonuclear diatomic molecules on the efficiency of VT-processes, Khim. Fiz. **7**, 867 (1988)

187. E.E.Nikitin and A.I.Reznikov, Theoretical total cross section and branching ratio for Kr ions produced in low-energy charge-exchange collisions of Kr with He^+, Chem.Phys.Lett. **149**, 212 (1988)

188. E.E.Nikitin, A.I.Reznikov, and S.Ya.Umanskii, Cross sections for charge exchange of atoms on multiple-charged ions: A comparative study of processes Ar,Kr + He -> Ar, Kr + He in eV energy range, Mol. Phys. **65**, 1301 (1988)

189. E.I.Dashevskaya, E.E.Nikitin, Line shape of the magnetic resonance signal for a nonequidistant structure of Zeeman levels, Optika i Spectr. **64**, 732 (1988)

190. E.E.Nikitin, Correlation diagrams of roronic states of diatoms, Khim. Fiz. **8**, 1155 (1989)

191. E.E.Nikitin and A.I.Reznikov, Intramultiplet population of Kr ion in charge transfer of Kr on He at low energies, Khim. Fiz. **8**, 38 (1989)

192. E.E.Nikitin, S.Ya.Umanskii, and D.V.Shalashilin, Vibration-to-rotation energy transfer in collisions of hydrogen halide molecules with noble gas atoms, Khim. Fiz. **8**, 1011 (1989).

193. E.E.Nikitin, A.I.Osipov, and S.Ya.Umanskii, Vibration-to- translation energy exchange in collisions of homonuclear diatomic molecules, in: *Khimiya Plasmy* **15**, ed. B.M.Smirnov, Moscow, Atomizdat, 1989, p.3

194. E.E.Nikitin and M.Ya.Ovchinnikova, Asymmetric rotor model in the description of rotational structure of overtones bands in NH_3 spectrum, Optika i Spekt. **67**, 47 (1989)

195. E.E.Nikitin and M.Ya.Ovchinnikova, Optimal trajectory approach in the theory of photodissociation of thermally excited molecules. Chem. Phys. **138**, 45 (1989)

196. E.I.Dashevskaya and E.E.Nikitin, Scattering asymmetry for atoms of helicopter polarization: manifestation of slipping, Optika i Spectr. **68**, 1006 (1990)

197. E.E.Nikitin, Parity conservation and statistical theories of unimolecular reactions, Khim. Fiz. **9**, 723 (1990)

198. E.E.Nikitin and J.Troe, Correlation diagrams for accurate adiabatic channel potentials of atom+linear molecule reaction system, J. Chem. Phys. **92**, 6594 (1990)

199. E.E.Nikitin and J.Troe, Correlation diagrams of adiabatic channel potentials for a system atom + linear molecule, Khim. Fiz. **9**, 1171 (1990)

200. E.E.Nikitin and M.Ya.Ovchinnikova, Quasiclassical theory of photodissociation of thermally excited molecules, Khim. Fiz. **9**, 1486, (1990)

201. E.I.Dashevskaya, E.E.Nikitin, and J.Troe, Long-range nonadiabatic effects in statistical adiabatic channel models: dynamic orientation of fragments formed in the decompositi of long-lived triatomic compexes, J. Chem. Phys. **93**, 7803 (1990)

202. E.E.Nikitin, Chemische Elementarreaktionen - Static und Dynamik, Nova Acta Leopoldina NF **63**, 145 (1990)

203. A.I.Maergoiz, E.E.Nikitin, and J.Troe, Adiabatic channel potential curves for two linear dipole rotors: I. Classification of states and numerical calculations for identical rotors, J. Chem. Phys. **9**, 5117 (1991)

204. E.I.Dashevskaya, E.E.Nikitin, and J.Troe, Dynamic rotational polarization of diatomic fragments in the decomposition of triatomic complexes, Khim. Fizika **10**, 9 (1991)

205. A.I.Maergoiz, E.E.Nikitin, and J.Troe, Adiabatic channel potential curves for two linear dipole rotors: II. Analytic representation of channel potentials and rate expressions, Z. phys. Chem. **172**, 129 (1991)

206. E.I.Dashevskaya, R.Dueren, and E.E.Nikitin, Semiclassical roronic description of right-left scattering asymmetry of helicopter-oriented atoms, Chem.Phys. **149**, 341 (1991)

207. E.E.Nikitin, On the Landau method of calculating quasiclassical matrix elements, in: *Mode Selective Chemistry, Proceedings of the 24 Jerusalem Symposium on Quantum Chemistry and Biochemistry*, Eds. J.Jortner et al, Dordrecht, Kluwer Academic Publishers, 1991, p. 401

208. E.E. Nikitin and D.V.Shalashilin, Quasiclassical model of vibrational-rotational energy exchange, Khim. Fiz. **11**, 1471 (1992)

209. Y.Rudich, R.J.Gordon, E.E.Nikitin, and R.Naaman, Rotational relaxation in a free expansion of HCl, J. Chem. Phys. **96**, 4423 (1992)

210. E.I.Dashevskaya and E.E.Nikitin, Hard sphere model for two-state differential inelastic scattering, Chem.Phys. **163**, 75 (1992)

211. E.E.Nikitin, Resonance excitation transfer between two dipole rotors for high rotational quantum numbers, Chem.Phys.Lett. **196**, 37 (1992)

212. E.I.Dashevskaya, E.E.Nikitin and J.Troe, Nonadiabatic effects in the statistical adiabatic channel model: the atom + diatom case, J. Chem. Phys. **97**, 3318 (1992)

213. E.E.Nikitin and A.I.Reznikov, Charge transfer in $N^{++}(2P)$-$He(1s^2)$ at low energies, Khim. Fiz. **11**, 163 (1992)

214. A.I.Maergoiz, E.E.Nikitin, and J.Troe, Correlation diagrams and symmetry properties of adiabatic states of a system composed of two linear dipole molecules, Khim. Fizika **11**, 814 (1992)

215. A.I.Maergoiz, E.E.Nikitin, and J.Troe, Calculation of cross sections and rate constants for capture of two identical linear dipole molecules, Khim. Fiz. **12**, 841 (1992)

216. A.I.Maergoiz, E.E.Nikitin, and J.Troe, Diabatic/adiabatic channel correlation diagrams for two linear rotors with long-range dipole-dipole interaction. Z Phys.Chem. **176**, 1 (1992)

217. E.E.Nikitin and A.I.Reznikov, Cross sections for charge exchange of atoms on miltiple-charged ions: charge exchange of N on He in eV energy range. Mol. Phys. **77**, 563 (1992)

218. E.E. Nikitin, Resonance excitation transfer between two dipole rotors with high rotation al quantum numbers, Khim. Fiz. **11**, 1463 (1992)

219. E.I.Dashevskaya and E.E.Nikitin, Two-state differential inelastic scattering of hard spheres, Khim. Fiz. **11**, 1603 (1992)

220. E.E.Nikitin, C.Noda, and R.N.Zare, On the quasiclassical calculation of fundamental and overtone intensities. J. Chem. Phys. **89**, 46 (1993)

221. M.Willberg, M.Gutmann, E.E.Nikitin, and A.H.Zewail, A simple description of vibrational predissociation by a full-collision approach, Chem.Phys Lett. **201**, 506 (1993)

222. E.I.Dashevskaya and E.E.Nikitin, Comparison equation approach to the locking of electronic angular momentum to the molecular axis in atomic collisions, J.Chem.Soc.Faraday Trans. **89**, 1567 (1993)

223. E.E.Nikitin, Optimal trajectory approach in the theory of collisional vibrational relaxation of diatomic molecules, in: *Dynamical Processes in Molecular Physics, First EPS Southern European School of Physics*, ed. G. Delgado-Barrio, Bristol and Philadelphia, Institute of Physics Publishing Ltd, 1993, p. 55

224. E.E.Nikitin, Manifestation of the non-sudden locking in the differential scattering of polarized atoms, in: *European Workshop on Collisions involving Laser Excited Atoms*, Kopenhavn , H.C.O.Tryk, 1993, p.113

225. E.I.Dashevskaya, E.E.Nikitin, and I.Oref, On the adiabaticity restrictions in the collisional energy transfer from highly excited polyatomic molecules, J. Phys. Chem. **97**, 9397 (1993)

226. A.Berengolts, E.I.Dashevskaya, and E.E.Nikitin, Computational study of the locking of electronic angular momentum in diatomic quasimolecules, J. Phys. B **26**, 3847 (1993)

227. E.E.Nikitin and L.P.Pitaevskii, Imaginary time and the Landau method of calculating of the quasiclassical matrix elements, Uspekhi Fizicheskikh Nauk **163**, 101 (1993).

228. E.E.Nikitin, Vibrational relaxation and vibrational predissociation as dynamical tunneling processes, Uspekhi Khimii **62**, 3 (1993)

229. A.I.Maergoiz, E.E.Nikitin, and J.Troe, Diagrams of diabatic/adiabatic channels for two linear rotors coupled by long-range dipole-dipole interaction. Khim. Fiz. **12**, 3 (1993)

230. E.E.Nikitin, On the accuracy of IOSA in calculation of vibrational relaxation rates, Khim. Fiz. **12**, 187 (1993)

231. Y.Karni and E.E.Nikitin, Recovery of the Landau matrix elements from the classical Fourier components:one-dimensional dissociating oscillator, J. Chem. Phys. **100**, 2027 (1994)

232. Y.Karni and E.E.Nikitin. Vibrational predissociation rate from dynamics of the full collision: a test of the Landau method against the exact results, J. Chem. Phys. **100**, 8065 (1994)

233. E.E.Nikitin and L.Pitaevski, Calculation of the Landau quasi-classical exponent from the Fourier components of classical functions, Phys .Rev. A **49**, 695 (1994)

234. E.E.Nikitin, J.Troe, and V.G.Ushakov, Classical simulation of the near-resonance rotational energy transfer between two dipole rotors, J.Phys.Chem **98**, 3257 (1994)

235. E.E.Nikitin and R.N.Zare, Correlation diagrams for Hund's coupling cases in diatomic molecules with high rotational angular momentum, Mol. Phys. **82**, 85 (1994)

236. E.E.Nikitin and K.Taulbjerg, Effect of the rotational coupling on charge transfer into Coulomb channels, J. Phys. B **27**, 2259 (1994)

237. Y.Karni and E.E.Nikitin, Adiabatically corrected quasiclassical model for the vibrational predissociation of van der Waals complexes, Chem.Phys. **191**, 235 (1995)

238. E.E.Nikitin, J.Troe, and V.G.Ushakov, Adiabatic and post-adiabatic channel description of atom-diatom long-range half-collision dynamics: interchannel radial coupling for low-rank anisotropy. J. Chem. Phys. **102**, 4101 (1995)

239. A.Berengolts, E.I.Dashevskaya, E.E.Nikitin, and J.Troe, Dynamic polarization of diatomic fragments formed in decomposition of statistical triatomic complexes. I. Semiclassical study, Chem. Phys. **195**, 271 (1995)

240. A.Berengolts, E.I.Dashevskaya, E.E.Nikitin, and J.Troe, Dynamic polarization of diatomic fragments formed in decomposition of statistical triatomic complexes. II. Classical simulation, Chem. Phys. **195**, 283 (1995)

241. K.Ohmori, T.Kurosawa, H.Chiba, M.Okunishi, K.Ueda, Y.Sato, and E.E.Nikitin, Far-wing excitation study on the transit region of Hg intra-multiplet process in collisions with N_2 and CO, J. Chem. Phys. **102**, 7341 (1995)

242. A.I. Maergoiz, E.E. Nikitin, and J. Troe, Statistical adiabatic channel calculation of accurate low-temperature rate constant for the recombination of OH radicals in their ground rovibronic state. J. Chem. Phys. **103**, 2083 (1995)

243. E.I.Dashevskaya, E.E.Nikitin, and I.Oref, The mean energy transfer within the sequential direct encounter model: the temperature dependence of $<\Delta E>$, J. Phys. Chem. **99**, 10797 (1995)

244. I.Koifman, E.I.Dashevskaya, E.E.Nikitin, and J.Troe, Rotational gateway for the vibrational energy transfer from excited nonlinear triatomic molecules, J. Phys. Chem. **99**, 15348 (1995)

245. E.I.Dashevskaya, F.Masnou-Seeuws, and E.E.Nikitin, The locking phenomenon in scattering of P-state atoms: I. Quasiclassical theory of interference effects for waves scattered by two different potentials, J. Phys. B. **29**, 395 (1996)

246. E.I.Dashevskaya, F.Masnou-Seeuws, and E.E.Nikitin, The locking phenomenon in scattering of P-state atoms: II. Quasiclassical interpretation of high-frequency

interference pattern in the differential scattering of Na* on Ne, J. Phys. B. **29**, 415 (1996)

247. E.E.Nikitin, Ch.Ottinger, and D.V.Shalashilin, Test of the asymptotic method as applied to atom-diatom interaction potentials, Z. Phys. D -Atoms, Molecules and Clusters **36**, 257 (1996)

248. A.I.Maergoiz, E.E.Nikitin, and J.Troe, Adiabatic channel study of the capture of nitrogen and oxygen molecules by an ion: Effect of nuclear symmetry and spin-spin interaction. Z. Phys D- Atoms, Molecules and Clusters, **36**, 339 (1996)

249. Ch. Zhu, H. Nakamura, and E.E.Nikitin, Semiclassaical analysys of resonance states induced by conical intersection, J. Chem. Phys. **104**, 7059 (1996)

250. R.D.Brown, J.E.Boggs, R.L. Hilderbrandt, K.F.Lim, I.M. Mills, E.E.Nikitin, M.H.Palmer, and A.F.McNaught, *Acronyms used in Theoretical Chemistry*, Pure and Appl.Chem. **68**, 387 (1996)

251. E.E.Nikitin, Adiabatic and diabatic collision processes at low energies, in: *Atomic, Molecular & Optical Physics Handbook*, ed. G.W.F.Drake, Woodbury, New York, American Institute of Physics, 1996, p.561

252. A.I.Maergoiz, E.E.Nikitin, J.Troe, and V.G.Ushakov, Classical trajectory and adiabatic channel study of the transition from adiabatic to sudden capture dynamics. I. Ion-dipole capture, J. Chem. Phys. **105,** 6263 (1996)

253. **A**.I.Maergoiz, E.E.Nikitin, J.Troe, and V.G.Ushakov, Classical trajectory and adiabatic channel study of the transition from adiabatic to sudden capture dynamics. II. Ion-quadrupole capture, J. Chem. Phys. **105,** 6270 (1996)

254. A.I.Maergoiz, E.E.Nikitin, J.Troe, and V.G.Ushakov, Classical trajectory and adiabatic channel study of the transition from adiabatic to sudden capture dynamics. III Dipole-dipole capture, J. Chem. Phys. **105,** 6277 (1996)

255. I.Rosenblum, E.I.Dashevskaya, E.E.Nikitin, and I.Oref, On the sampling of microcanonical distributions for rotating harmonic triatomic molecules, Chem. Phys. **213**, 243 (1996)

256. Y. Karni and E.E.Nikitin, Vibrational predissociation: quasiclassical tunneling and classical diffusion, Mol. Phys. **89**, 1327 (1996)

257. E. E. Nikitin, Pathways of vibrational relaxation of diatoms in collisions with atoms: Manifestation of the Ehrenfest adiabatic principle, in: *Gas Phase Chemical Reaction Systems*, Eds. J.Wolfrum et al, Berlin-Heidelberg, Springer, 1996, p 231

258. E.I.Dashevskaya, E.E.Nikitin, F.Perales, and J.Baudon, Qualitative analysis of the right-left scattering asymmetry in Ne*+Ar low-energy collisions, J. Phys. B **30**, 703 (1997)

259. E.E. Nikitin and J.Troe, Quantum and classical calculations of adiabatic and nonadiabatic captrure rates for anisotropic interactions, Ber. Bunsenges. Phys. Chem. **101**, 445 (1997)

260. E.E.Nikitin, Double cone problem revisited: Effect of the geometric phase on the broad semiclassical resonances, J. Chem. Phys. **107,** 6748 (1997)

261. I.Rosenblum, E.I.Dashevskaya, E.E.Nikitin, and I.Oref, Effect of the vibrational-rotational energy partitioning on the energy transfer in atom-triatomic molecule collisions, Molec. Eng. **7**, 169 (1997).

262. E.I.Dashevskaya and E.E.Nikitin, Quasiclassical approximation in the theory of scattering of polarized atoms, in: *Atomic Physics Methods in Modern Research*, Lecture Notes in Physics, v. 499, eds: K. Jungmann et al., Heidelberg, Springer 1997, p.185

263. T.Kurosawa, K.Ohmori, H.Chiba, M.Okunishi, K.Ueda, Y.Sato, A.Z. Devdariani, and E.E.Nikitin, Collision-induced absorption in mercury rare-gas collisions, J. Chem. Phys. **108,** 8101 (1998)

264. K. Amano, K.Ohmori, T.Kurosawa, H.Chiba, M.Okunishi, K.Ueda, Y.Sato, A.Z. Devdariani, and E.E.Nikitin, c-X laser excitation spectrum of the Hg-Ar vdW complex, J. Chem. Phys. **108** 8110 (1998)

265. A.I.Maergoiz, E.E.Nikitin, J.Troe, and V.G.Ushakov, Classical trajectory and adiabatic channel study of the dynamics of capture and unimolecular bond fission. IV. Valence interaction between atoms and linear rotors. J. Chem. Phys. **108,** 5265 (1998)

266. A.I.Maergoiz, E.E.Nikitin, J.Troe, and V.G.Ushakov, Classical trajectory and adiabatic channel study of the dynamics of capture and unimolecular bond fission. V. Valence interaction between two linear rotors. J. Chem. Phys. **108,** 9987 (1998)

267. A. Devdariani, E. Tchesnokov, E.I. Dashevskaya, and E.E. Nikitin, Quasiclassical study of differential inelastic scattering of oriented Ca(4s5p, $^1P_1$) atoms on He, Phys. Rev. A **57**, 4472 (1998)

268. A. Alijah and E.E.Nikitin, Fast quantum, semiclassical and classical dynamics near the conical intersection, Mol. Phys. **96**, 1399 (1999)

269. D.Schroeder, I.Oref, J. Hrusak, T.Weiske, E.E.Nikitin, W. Zummack, and H.Schwarz, Revisiting the mechanism of the unimolecular fragmentation of protonated fluorobenzene. J. Phys .Chem. A **103**, 4609 (1999)

270. F.Di Giacomo, F.A.Gianturco, E.E.Nikitin, and F.Schneider, On the proton-water charge transfer processes: a follow-up study using CI calculations, J. Phys. Chem. **103,** 7116 (1999)

271. E.E.Nikitin, Nonadiabatic transitions: What we learned from old masters and how much we owe them. Ann. Rev. Phys. Chem. **50**, 1 (1999)

272. K.Ohmori, T.Kurosawa, H.Chiba, M.Okunishi, K.Ueda, Y.Sato, A. Devdariani, and E.E.Nikitin, Far-wing excitation study on the transition region of the metastable mercury atom collisions: Hg(6^3P_2)+N_2 and CO, Chem. Phys. Lett. **315**, 411 (1999)

273. E.I. Dashevskaya, I.Litvin, E.E.Nikitin, I.Oref, and J.Troe, Classical diffusion model of vibrational predissociation of van der Waals complexes: truncated mean first passage time approximation, Phys. Chem. Chem. Phys. **2**, 2251 (2000)

274. E.I.Dashevskaya and E.E.Nikitin, Correlation of adiabatic states between perturbed rotor and Renner-Teller limits for a closed-shell ion + open shell diatom system, Z. phys. Chem. **214**, 1001 (2000)

275. E.I.Dashevskaya and E.E.Nikitin, On the relation between elastic and inelastic scattering lengths for vibrational relaxation in atom-diatom collisions, Chem.Phys.Lett. **328**, 119 (2000)

276. E.I. Dashevskaya and E.E. Nikitin, Quantum suppression and enhancement of the quasiclassical Landau-Lifshitz matrix elements. Application to the inelastic H_2-He scattering at ultra-low energies, Phys .Rev. A, **63**, 012711 (2000)

277. E.I. Dashevskaya, I.Litvin, E.E. Nikitin, and J.Troe, Classical diffusion model of vibrational predissociation of van der Waals complexes: II. Comparison with trajectory calculations and analytical approximations, Phys. Chem. Chem. Phys. **3**, 2315 (2001)

278. E.I. Dashevskaya, I.Litvin, E.E. Nikitin, I.Oref, and J.Troe, Classical diffusion model of vibrational predissociation of van der Waals complexes: III. Comparison with quantum calculations, Phys. Chem. Chem. Phys. **4**, 3330 (2002)

279. A.I.Maergoiz, E.E.Nikitin, J.Troe, and V.G.Ushakov, Classical trajectory and adiabatic channel study of the dynamics of capture and unimolecular bond fission. VI. Properties of the transitional modes and specific rate constants k(E,J), J. Chem. Phys. **117**, 4201 (2002)

280. E. I. Dashevskaya, J. A. Kunc, E. E. Nikitin, and I. Oref, Two-channel vibrational relaxation of H_2 by He: a bridge between the Landau-Teller and Bethe-Wigner limits, J. Chem. Phys. **118**, 3141 (2003)

281. E.I.Dashevskaya, E.E.Nikitin, K.Ohmori, M.Okunishi, I.Oref, and Y.Sato, Energy dependence of the intramultiplet mixing cross section in Hg $-N_2$ collisions: conical intersection mechanism, indication at tunneling and interference, Phys. Chem. Chem. Phys. **5**, 1198 (2003)

282. E. I. Dashevskaya, I. Litvin, A.I.Maergoiz, E.E.Nikitin, and J. Troe, Low-temperature behavior of capture rate constants for inverse power potentials, J. Chem. Phys. **118**, 7313 (2003)

283. F.Di Giacomo, F.Schneider, and E.E.Nikitin, Conical intersections between three lowest adiabatic potential energy surfaces of the oxonium ion, Chem. Phys. Lett. **373**, 258 (2003)

284. E.E. Nikitin, E.I.Dashevskaya, J.Alnis, M.Auzinsh, E.Abraham, B.R.Furneaux, M.Keil, Ch.McRaven, N.Shafer-Ray, R.Waskowsky, Prediction and measurements of the speed-dependent throughput of a magnetic octupole velocity filter including nonadiabatic effects, Phys.Rev.A **68**, 023403 (2003)

285. R. Côté, E. I. Dashevskaya, E. E. Nikitin, and J.Troe, Quantum enhancement of vibratonal predissociation near the dissociation threshold, Phys.Rev.A **68**, 06327xx (2003)

286. K. Ohmori, Y. Sato, E E. Nikitin, and S A. Rice, High-precision molecular wave-packet interferometry with Hg-Ar dimers, Phys.Rev.Lett. **91**, 243003-1 (2003).

287. E. I. Dashevskaya E. Nikitin, I. Oref, and J. Troe, Vibrational relaxation of diatoms in collisions with atoms at very low energies, this volume

288. E. Nikitin and J. Troe, Vibrational predissociation: quasiclassical tunneling through classical chaotic sea, this volume

289. A.I.Maergoiz, E.E. Nikitin, J. Troe, and V.G.Ushakov, Asymptotic interaction between open shell partners in low-temperature complex formation, this volume

290. E.I.Dashevskaya, E.E.Nikitin, M.Okunishi , K.Ohmori, and Y.Sato, Nonadiabatic transitions in the conical intersection in the Hg $-N_2$ collisions, Khim.Fiz. (submitted)

291. E. I. Dashevskaya, I. Litvin, E. E. Nikitin, and J. Troe, Quantum scattering and adiabatic channel treatment of the low-energy and low-temperature capture of a rotating quadrupolar molecule by an ion, J.Chem.Phys (submitted)

ASYMPTOTIC INTERACTIONS BETWEEN OPEN SHELL PARTNERS IN LOW TEMPERATURE COMPLEX FORMATION: THE $H\left(X^2S_{1/2}\right)+O_2\left(X^3\Sigma_g^-\right)$ AND $O\left({}^3P_{J_O}\right)+OH\left(X^2\Pi_{\hat{\Omega}}\right)$ SYSTEMS

A.I.MAERGOIZ*, E.E.NIKITIN, J.TROE, and V.G.USHAKOV
*Institut fuer Physikalische Chemie, Universitaet Goettingen,
Tammannstr. 6, D-37077 Goettingen, Germany*

Abstract The asymptotic interactions at large intermolecular distances are determined for two open-shell systems, $H\left(X^2S_{1/2}\right)+O_2\left(X^3\Sigma_g^-\right)$ and $O\left({}^3P_{J_O}\right)+OH\left(X^2\Pi_{\hat{\Omega}}\right)$ for fixed values of intramolecular distances r. The electronic diabatic Hamiltonians are set up for two purposes: i) the direct diagonalization of the electronic Hamiltonian yielding two-dimensional potential energy surfaces (PES) which depend on the intermolecular distance R and the angle γ between R and r, and ii) the incorporation of the diabatic electronic basis into the diabatic roronic basis which can be used in the construction of the roronic Hamiltonian in the total angular momentum representation. The former procedure allows one to compare the asymptotic PES with their *ab initio* counterparts, while the latter provides the input data for the calculation of low temperature capture rate constants within the statistical adiabatic channel model (SACM).

1. Introduction

Rate constants for complex formation in collisions of two partners at low temperatures depend mainly on the long-range part of the interaction. If the partners are in open electronic states, this interaction is given by a set of electronic potential energy surfaces (PES) which depend on the coordinates of the nuclei and which are coupled by the nuclear motion. The complicated dynamical problem of calculating the capture cross section is considerably simplified within the adiabatic channel approximation [1]. The adiabatic channel potentials, or their generalisation, called the axially-nonadiabatic channel potentials [1g] can be constructed from the electronic adiabatic PES and the coupling between them provided that the electronic adiabatic basis is complemented by wave functions of nuclei for all the degrees of freedom except the interfragment distance R. The diagonalization of the full Hamiltonian in this extended basis yields the adiabatic channel potentials that depend on a single coordinate R. However, there exist an alternative way for the construction of adiabatic channel potentials which circumvents the unpleasant problem of calculating inter-PES nonadiabatic interactions. This is based on calculating first the matrix representation of the electronic Hamiltonian in the basis of pre-selected diabatic electronic states, then on supplementing this

electronic basis with the nuclear diabatic basis and, finally on the diagonalization of a diabatic electronic-nuclear Hamiltonian.

For an atom-diatom system, the adiabatic electronic PES depend on three coordinates, the interfragment distance R, the intramolecular distance r, and the angle γ between the vectors $\mathbf{R}$ and $\mathbf{r}$. A useful insight into the structure of adiabatic PES can be gained by fixing r to be through the ground vibrational state averaged distance of the isolated diatom r_0, that is by considering two-dimensional (2D) PES, that depend on R and γ. Within the same approximation, the nuclear wave functions to be used in constructing the electronic-nuclear diabatic Hamiltonian matrix are just the roronic functions of the isolated diatom in its ground vibrational state. An implicit assumption in this approach is that on the stage of the complex-formation at large enough R (low collision energies), the collision-induced adiabatic change of the ground state vibrational wave function of a diatom is insignificant. It was shown in [2] by classical trajectory calculations on 2D and 3D *ab initio* PES for $\mathbf{H+O_2}$ system that capture rate constants practically are not influenced by this limitation to a 2D PES.

With these remarks in mind, we set up the diabatic Hamiltonians for two systems of practical interest, $\mathbf{H}\left(X^2S_{1/2}\right)+\mathbf{O_2}\left(X^3\Sigma_g^-\right)$ and $\mathbf{O}\left(^3P_{j_0}\right)+\mathbf{OH}\left(X^2\Pi_{\hat{\Omega}}\right)$. The former is relevant to the low temperature behavior of high pressure rate constants for the $\mathbf{H/Mu}\left(X^2S_{1/2}\right)+\mathbf{O_2}\left(X^3\Sigma_g^-\right)$ addition reactions [2], while the temperature dependence of the capture rate constant in the latter system (see e.g. [3]) is relevant for O_2 formation in interstellar chemistry.

2. The $\mathbf{H}\left(X^2S_{1/2}\right)+\mathbf{O_2}\left(X^3\Sigma_g^-\right)$ system

We begin our discussion by representing the asymptotic 2D PES of the lowest $^2A''$ and $^4A''$ electronic states to the sum of the exchange and dispersion interactions (a weak induction interaction in the system is neglected).

By writing the exchange Hamiltonian in Heitler-London approximation as

$$V_{(12,i)}^{\text{HL}} = -\sum_{k=2}^{n_{2,i}+1} \frac{1}{2}\left(1+4\mathbf{s}_1 \cdot \mathbf{s}_k\right)\ V_{1k}P_{1k}^x , \qquad (1)$$

we take into account the doublet $1s$ atomic shell of the fragment 1 (atom H) and the outer triplet $1\pi_g^2$ (i=1) and two inner singlet $1\pi_u^4$ (i=2) and $3\sigma_g^2$ (i=3) molecular shells of the fragment 2 (molecule O_2).

The atomic orbital (AO) of H needs no comment. The spatial molecular orbital (MO) functions of O_2 are linear combinations of the one-electron functions with leading one-center Coulomb asymptotics that correspond to the lowest angular momenta, l_1=2, l_2=1, l_3=0

$$\varphi_{\lambda_i}^{(i)} \to C_i r^{1/\gamma_i-1}\exp\left(-\gamma_i r\right)Y_{l_i}^{\lambda_i}\left(\theta,\phi\right),\ \gamma_i^2/2 = -\mathbf{e}_i,\ \lambda_1,\lambda_2 = \pm 1,\ \lambda_3 = 0 \qquad (2)$$

where ε_i are the binding energies of the MOs (in atomic units unless stated otherwise). The transformation of these functions, referred initially to the vector $\mathbf{r}$, to the quantization axis directed along $\mathbf{R}$, expresses the exchange integrals $J^{(i)}$ to the linear combinations of the asymptotic integrals $I(00,l_im_i|00,l_im_i)$ with coefficients depending

on the angle γ between molecular axis $\mathbf{r}$ and axis $\mathbf{R}$. The asymptotic coefficient C_1 and asymptotic integrals can be found in [4] and in ref. 16 therein. The asymptotic coefficients C_2 and C_3 were evaluated by using available Hartree-Fock results for the corresponding MO functions [5].

Expansion coefficients of the anisotropic dispersion interaction $\sim R^{-6}$ in the series of Legendre polynomials $P_l(\cos\gamma)$ were evaluated using the method of Reduced Spectra of Oscillator Forces (RSOF) by Meyer et al [6] and the relevant calculations of the dynamic fragment polarizabilities [7]

$$C_6^{(l)} = -\binom{4}{2}\left(\sum_{m=-1}^{1} C_{1-m\,1m}^{20} C_{1m\,1-m}^{20} C_{1-m\,1m}^{00} C_{1m\,1-m}^{l0}\right) \sum_{m_1=-1}^{1}\sum_{m_2=-1}^{1}(-1)^{m_1+m_2} C_{1m_1\,1-m_1}^{00} C_{1m_2\,1-m_2}^{l0} \sum_{j_1,j_2\neq 0}\frac{f_{11\,m_1}^{(j_1)} f_{11\,m_2}^{(j_2)}}{4e^{(j_1)}e^{(j_2)}\left(e^{(j_1)}+e^{(j_2)}\right)} \quad (3)$$

where j_1 and j_2 specify energies and oscillator forces of the reduced spectra of fragments.

Expansion coefficients for the PES of the lowest electronic states $^2A''$ and $^4A''$

$$V^{(S)}(R,\gamma) = \sum_{i=0}^{3}\left\{W_{2i}(R) + \left(\frac{11}{4}-S^2\right)J_{2i}^{1\pi_g^2}(R)\right\}P_{2i}(\cos\gamma) \quad (4)$$

are represented by the sums of spin-independent and spin-dependent terms. In the spin-dependent part, the σ, π, and δ components contribute:

$$J_0^{1\pi_g^2}(R) = \left\{J^{1\pi_g^2,\sigma}(R) + 2J^{1\pi_g^2,\pi}(R) + 2J^{1\pi_g^2,\delta}(R)\right\}\big/10,$$

$$J_2^{1\pi_g^2}(R) = \left\{J^{1\pi_g^2,\sigma}(R) + J^{1\pi_g^2,\pi}(R) - 2J^{1\pi_g^2,\delta}(R)\right\}\big/14, \quad (5)$$

$$J_4^{1\pi_g^2}(R) = 2\left\{-3J^{1\pi_g^2,\sigma}(R) + 4J^{1\pi_g^2,\pi}(R) - J^{1\pi_g^2,\delta}(R)\right\}\big/35,$$

$$J^{1\pi_g^2,\sigma}(R) = \exp[2.814-1.571R],$$

$$J^{1\pi_g^2,\pi}(R) = -\exp[2.401-1.733R],$$

$$J^{1\pi_g^2,\delta}(R) = -\exp[1.375-1.899R].$$

Besides the dispersion interaction in the spin-independent part contribute σ and π integrals of the exchange interaction with completely filled inner MOs

$$W_0(R) = V_{disp,0}(R) + J^{3\sigma_g^2}(R) + 2\left(J^{1\pi_u^4,\sigma}(R) + 2J^{1\pi_u^4,\pi}(R)\right)\big/3,$$

$$W_2(R) = V_{disp,2}(R) + 2\left(J^{1\pi_u^4,\pi}(R) - J^{1\pi_u^4,\sigma}(R)\right)\big/3,$$

$$J^{3\sigma_g^2}(R) = 4.36\exp[-1.748R], \quad (6)$$

$$J^{1\pi_u^4,\sigma}(R) = 8.721\exp[-1.748R],$$

$$J^{1\pi_u^4,\pi}(R) = -1.784\exp[-1.857R],$$

$$V_{disp,0}(R) = -18.89R^{-6},$$

$$V_{disp,2}(R) = -3.25R^{-6}.$$

For the asymptotic exchange integrals we use simple exponential representations such as given in Eqs. 5 and 6.

In order to fit the constructed PES to the local *ab initio* data [8] (data for quartet state and for T-shaped configuration are taken from [9]) we introduce the spin-dependent contribution of the $P_6(\cos\gamma)$ polynomial

$$J_6^{1\pi_g^2}(R) = -0.004444\exp[-1.03746R]\{1+\exp[4.371-0.5868R-0.00001019R^6]\}. \tag{7}$$

For the spin-dependent contributions (see *Fig. 1*) of the lower polynomials we assume cut-off factors of the form:

$$c_{00}^{corr}(R)=1+\exp[2.445-0.3191R-0.00004149R^6],$$
$$c_{02}^{corr}(R)=1+\exp[1.728-0.0715R-0.0007877R^4], \tag{8}$$
$$c_{04}^{corr}(R)=1+\exp[-0.0998-0.4343R-0.00007025R^6].$$

Figure 1. Spin-dependent terms $c_{0l}=J_l^{1\pi_g^2}$ in Legendre expansion coefficients as functions of the interfragment distance R: dashed curves from Asymptotic Theory (AT); solid curves from AT corrected to fit ab initio data.

Corrections to the spin-independent parts of coefficients are noticeable already at large distances *R* (see *Fig. 2*). Thus we introduce contribution of the $P_6(\cos\gamma)$ polynomial and replace the lower coefficients by

$$W_0(R) = \left\{ 24.8\exp[-1.661R] - 19.75R^{-6} - 1245R^{-8} \right\}\left\{ 1 + \exp\left[9.442 - 6.922R + 1.391R^2 - 0.09321R^3 \right] \right\},$$

$$W_2(R) = \left\{ 20.33\exp[-1.62R] - 3.531R^{-6} - 1176R^{-8} \right\}\left\{ 1 - \exp\left[-117.9 + 81.8R - 16.74R^2 + 0.3225R^4 - 0.02444R^5 \right] \right\}, \quad (9)$$

$$W_4(R) = \left\{ 30.41\exp[-2.043R] - 1.055R^{-6} - 53.87R^{-8} \right\}\left\{ 1 - \exp\left[28.02 - 16.84R + 3.342R^2 - 0.2294R^3 \right] \right\},$$

$$W_6(R) = \left\{ -3.586\exp[-1.829R] - 0.1655R^{-6} + 8.286R^{-8} \right\}\left\{ 1 - \exp\left[1.05 - 0.5363R + 0.0008951R^5 - 0.0001325R^6 \right] \right\}.$$
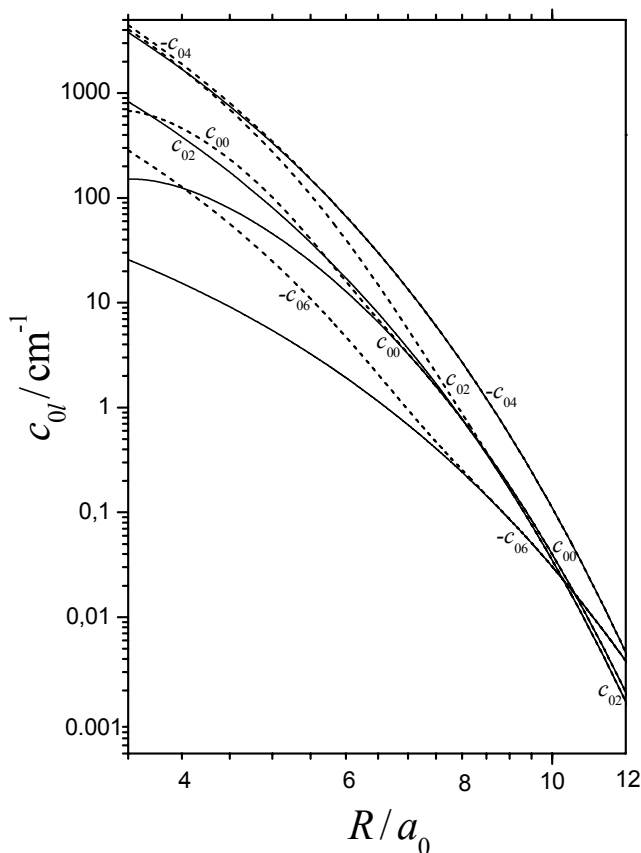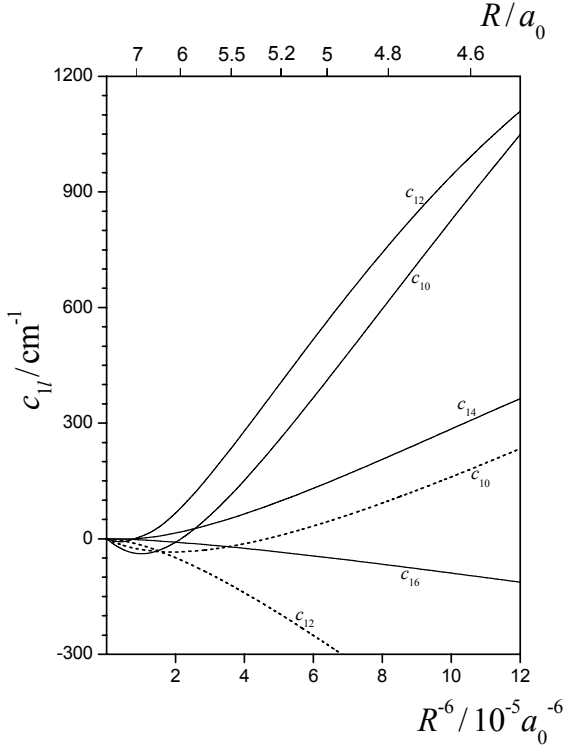

Figure 2. Spin-independent contributions $c_{1l} = W_l$ in Legendre expansion coefficients as functions of the interfragment distance R: dashed curves with l=0,2 from AT; solid curves with l=0,2,4,6 from AT corrected to fit ab initio data.

For a number of the interfragment distances R in Tabs. I-III we demonstrate the fitting quality of energies and bending frequencies in doublet (left side) and quartet (right side) states. One can see that our fitting reproduces sufficiently good local *ab initio* data along the linear Minimum Energy Path (MEP, Tab. I), in T-configuration of γ=90° (Tab. II), in non-linear MEP and saddle path configurations (Tab. III).

The contour plots of the lowest doublet and quartet PES are shown in *Fig. 3* and *Fig. 4* (negative (attraction) and positive (repulsion) energies are shown by the dashed and solid curves respectively). Two dotted curves show the intersections of the PES differing in their energies by not more than spin-spin S-S fine structure (FS)

TABLE I. Fitting quality of Asymptotic Theory after the correction: linear configuration

R/a_0	$^2A''$				$^4A''$			
	$\omega(0°)$/cm^{-1}		$V(0°)$/cm^{-1}		$\omega(0°)$/cm^{-1}		$V(0°)$/cm^{-1}	
	ab initio	corr. AT	*ab initio*	corr. AT	*ab initio*	corr. AT	*ab initio*	corr. AT
3.5		898.5i		2793		822.3		2838
4		645.2i		3880		325.6		4332
4.5		411.8i		2282		151.0		2487
5		256.9i		1060	**92.4**	90.2	**1086.3**	1078.4
5.5		158.9i		411.8	**66.8**	66.77	**361.1**	365.0
6		97.4i		117.1	**51.4**	53.01	**75.6**	69.64
6.5		59.1i		4.03	**41.3**	41.31	**-21.0**	-26.76
7		35.7i		-27.7	**33.5**	30.84	**-43.9**	-44.32
7.5		20.02i		-34.4	**26.6**	23.82	**-41.7**	-42.68
8	**8.7i**	9.15i	**-27.7**	-30.6	**20.3**	18.57	**-33.3**	-34.49
9	**6.4**	6.87	**-17.0**	-18.3	**10.8**	11.68	**-17.9**	-19.16
10	**6**	6.26	**-9.4**	-9.92	**7**	7.71	**-9.5**	-10.12
11	**5.1**	4.81	**-5.5**	-5.38	**5.3**	5.31	**-5.5**	-5.43
12	**4.1**	3.62	**-3.2**	-3.02	**4.1**	3.80	**-3.2**	-3.04
15	**1.6**	1.65	**-0.7**	-0.68	**1.7**	1.67	**-0.7**	-0.68

TABLE II. Fitting quality of Asymptotic Theory after the correction: T-configuration of $\gamma=90°$

R/a_0	$^2A''$				$^4A''$			
	$\omega(90°)$/cm^{-1}		$V(90°)$/cm^{-1}		$\omega(90°)$/cm^{-1}		$V(90°)$/cm^{-1}	
	ab initio	corr. AT	*ab initio*	corr. AT	*ab initio*	corr. AT	*ab initio*	corr. AT
3.5		1002i		6607		788		-2202
4		641.8i		3738		383.1		563.1
4.5		374.6i		1466		241.3		271.6
5		220.7i		517.0	**155.3**	154.7	**40.2**	40.4
5.5		134.5i		156.4	**96**	96.3	**-41.8**	-42.6
6		85.1i		24.40	**57.5**	58.1	**-54.4**	-58.7
6.5		55.0i		-19.66	**33.7**	34.48	**-47.3**	-52.9
7		35.50i		-29.62	**19.3**	20.89	**-37.4**	-42.3
7.5		24.11i		-25.14	**9.7**	10.48	**-28.4**	-29.92
8	**14.7i**	16.94i	**-18.8**	-19.04	**2.3i**	2.25i	**-20.7**	-20.84
9	**9.4i**	9.23i	**-10.3**	-10.12	**7.4i**	6.27i	**-10.6**	-10.38
10	**5.6i**	5.63i	**-5.5**	-5.36	**5.2i**	5.00i	**-5.5**	-5.39
11	**4.0i**	3.73i	**-3.0**	-2.94	**3.8i**	3.65i	**-3.0**	-2.94
12	**2.8i**	2.61i	**-1.7**	-1.69	**2.9i**	2.64i	**-1.7**	-1.69
15	**1.1i**	1.09i	**-0.4**	-0.41	**1i**	1.10i	**-0.4**	-0.41

TABLE III. Fitting quality of Asymptotic Theory after the correction: non-linear Minimal Energy and Saddle Path configurations

R/a_0	$^2A''$						$^4A''$					
	γ		$\omega(\gamma)/cm^{-1}$		$V(\gamma)/cm^{-1}$		γ		$\omega(\gamma)/cm^{-1}$		$V(\gamma)/cm^{-1}$	
	ab initio	corr. AT	ab initio	corr. AT	ab initio	corr. AT	ab initio	corr. AT	ab initio	corr. AT	ab initio	corr. AT
3.5	**42.0°**	41.9°	**749**	991	**-4777**	-4155		36.5°		619.5i		7196
4	**44.7°**	45.2°	**663**	653.1	**-1133**	-1086		26.3°		363.9		4800
4.5	**47.7°**	47.7°	**388**	397.1	**-280.0**	-307.1		19.9°		194.8i		2558
5	**49.5°**	49.2°	**230**	237.9	**-133.0**	-149.8	**18.3°**	19.0°	**118.1i**	116.5i	**1112.4**	1105
5.5	**49.8°**	49.7°	**134**	145.2	**-108.5**	-116.2	**21.9°**	22.5°	**82.5i**	83.75i	**382.6**	387.7
6	**48.9°**	49.1°	**91**	92.49	**-91.0**	-98.56	**27.2°**	28.5°	**58.8i**	62.17i	**96.3**	93.74
6.5		47.6°		58.92		-78.62	**33.7°**	35.2°	**40.8i**	43.31i	**-0.6**	-4.11
7	**44.4°**	45.6°	**39**	37.55	**-52.5**	-58.07	**41.0°**	41.2°	**25.7i**	29.75i	**-25.4**	-26.94
7.5		39.4°		27.27		-42.37	**52.9°**	52.7°	**11i**	21.40i	**-26.9**	-27.45
8	**32.5°**	26.7°	**12.8**	18.08	**-29.1**	-31.44						

parameter (see below in Eq.10 for the roronic Hamiltonian) in the whole asymptotic region limited by the dot-dashed curves. *Fig. 3* demonstrates the characteristic switching between the linear van der Waals and the non-linear valence MEP in the lowest doublet state. The lowest quartet state showing similar van-der-Waals behaviour is fully repulsive at the shorter interfragment distances R (see *Fig. 4*).
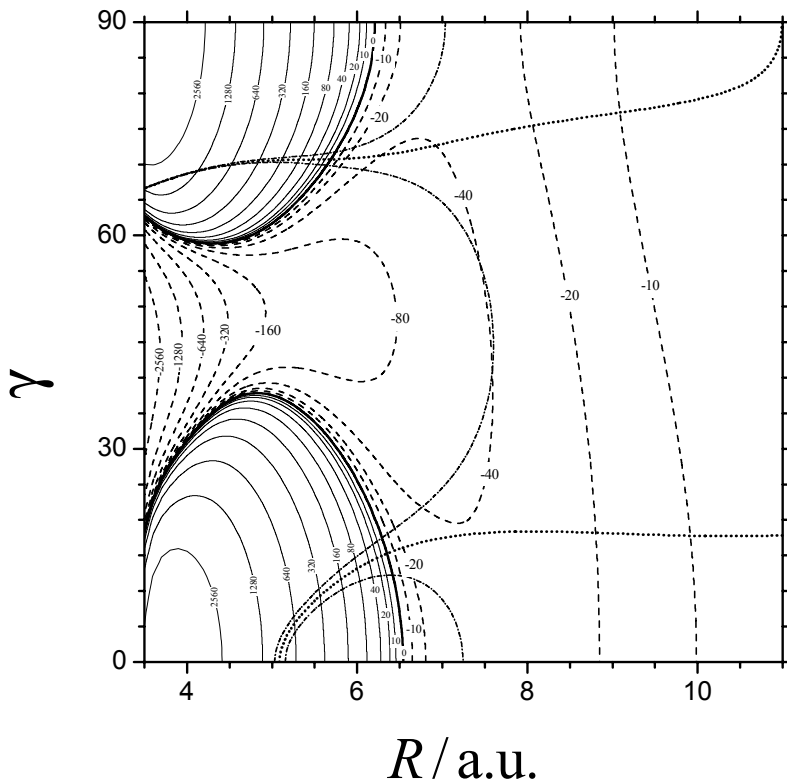

Figure 3. 2D asymptotic PES for the lowest $^2A''$ electronic state of the H+O$_2$ system: for solid, dashed, dotted, and dot-dashed curves see text above; contour energies in units of cm^{-1}.

We now consider adiabatic channel potentials. As indicated in the introduction, for this system with rapid rotation of the collision axis **R**, we develop here the Axially Nonadiabatic version of the SACM [1g]. In order to take into account the quantum character of the also rapid radial motion we plan to provide a generalisation of the approach [10] developed for low-energy capture in systems with isotropic interaction. For open-shell systems, this SACM version is based on the diabatic matrix representation of the roronic Hamiltonian supplemented by the S-S FS interaction (see e.g. [11]). Thus the total Hamiltonian reads:

$$\hat{H} = c(R)\hat{J}^2 - 2c(R)\hat{\mathbf{J}}\cdot\hat{\mathbf{j}} + \left\{B_0 + c(R)\right\}\hat{j}^2 + B_0\hat{S}^2 - 2B_0\hat{\mathbf{j}}\cdot\hat{\mathbf{S}} + \sqrt{2/3}\,a\left(\hat{s}_2\otimes\hat{s}_2\right)_{20} +$$

$$+ \sum_{i=0}^{3}\left\{W_{2i}(R) + \left(11/4 - \hat{S}^2\right)J_{2i}^{1\pi_g^2}(R)\right\}P_{2i}(\cos\gamma);\ c(R) = \left(2\mu R^2\right)^{-1} \tag{10}$$
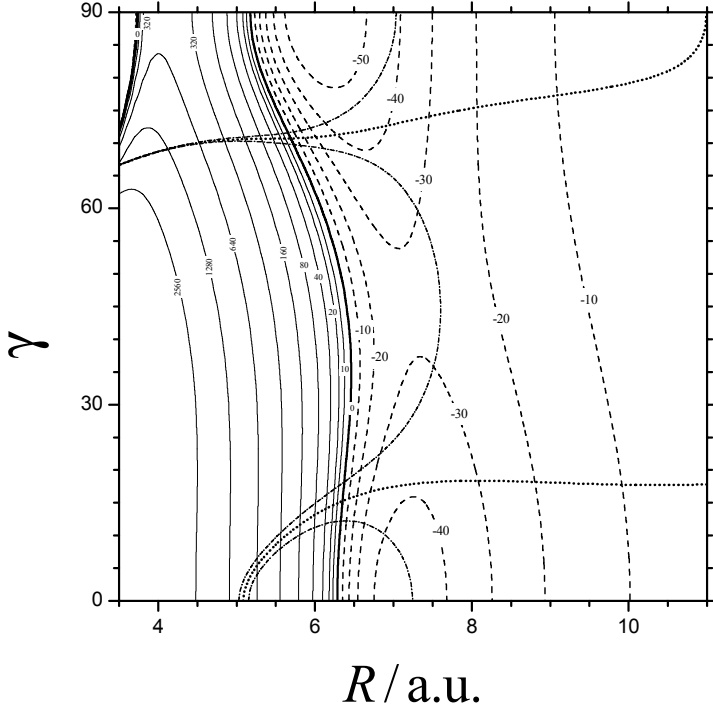

Figure 4. 2D asymptotic PES for the lowest $^4A''$ electronic state of the H+O$_2$ system: for solid, dashed, dotted, and dot-dashed curves see text above; contour energies in units of cm^{-1}.

where the vectors **J** and **S** are the total angular and spin momenta of the system respectively; $\mathbf{s}_k$ is the spin of a fragment k, vector **j** is the sum of $\mathbf{s}_1$ and total angular momentum of the molecular fragment, and B_0 is the rotational constant of O$_2$ in its ground vibrational state. The representation is done in the basis of the parity-adapted functions of the total angular momentum (for the symmetry of these functions see [12] and [13])

$$\psi_{S,\Sigma,j,\Omega,J,\varepsilon} = 2^{-1/2}\left(\left|s_1,s_2,S,\Sigma,j,\Omega,J,M\right\rangle + \varepsilon(-1)^{S+J}\left|s_1,s_2,S,-\Sigma,j,-\Omega,J,M\right\rangle\right);$$

$$\left|s_1,s_2,S,\Sigma,j,\Omega,J,M\right\rangle = D_{\Omega M}^{J}D_{\Sigma\Omega}^{j}\sum_{\sigma_1,\sigma_2}C_{s_1\sigma_1\,s_2\sigma_2}^{S\Sigma}\chi_{s_1\sigma_1}(1)\chi_{s_2,\sigma_2}(2);\quad \varepsilon = \pm 1, \tag{11}$$

where M, Ω, and Σ are the projections of **J**, **J** or **j**, and **j** or **S** onto the space-fixed, onto the intermolecular (**R**), and onto the molecular (z) axes respectively, and ε is the parity.

Non-zero matrix elements in this representation originate from the diagonal

matrix elements

$$\langle s_1,s_2,S,\Sigma,j,\Omega,J,M|\hat{J}^2|s_1,s_2,S,\Sigma,j,\Omega,J,M\rangle = J(J+1);$$

$$\langle s_1,s_2,S,\Sigma,j,\Omega,J,M|\hat{j}^2|s_1,s_2,S,\Sigma,j,\Omega,J,M\rangle = j(j+1);$$

$$\langle s_1,s_2,S,\Sigma,j,\Omega,J,M|\hat{S}^2|s_1,s_2,S,\Sigma,j,\Omega,J,M\rangle = S(S+1); \tag{12}$$

$$\langle s_1,s_2,S,\Sigma,j,\Omega,J,M|\hat{\mathbf{J}}\cdot\hat{\mathbf{j}}|s_1,s_2,S,\Sigma,j,\Omega,J,M\rangle = \Omega^2;$$

$$\langle s_1,s_2,S,\Sigma,j,\Omega,J,M|\hat{\mathbf{j}}\cdot\hat{\mathbf{S}}|s_1,s_2,S,\Sigma,j,\Omega,J,M\rangle = \Sigma^2,$$

and from the non-diagonal Coriolis-type matrix elements

$$\langle s_1,s_2,S,\Sigma,j,\Omega,J,M|2\hat{\mathbf{J}}\cdot\hat{\mathbf{j}}|s_1,s_2,S,\Sigma,j,\Omega\pm 1,J,M\rangle =$$

$$= \sqrt{\{J(J+1)-\Omega(\Omega\pm 1)\}\{j(j+1)-\Omega(\Omega\pm 1)\}}; \tag{13}$$

$$\langle s_1,s_2,S,\Sigma,j,\Omega,J,M|2\hat{\mathbf{j}}\cdot\hat{\mathbf{S}}|s_1,s_2,S,\Sigma\pm 1,j,\Omega,J,M\rangle =$$

$$= \sqrt{\{j(j+1)-\Sigma(\Sigma\pm 1)\}\{S(S+1)-\Sigma(\Sigma\pm 1)\}}.$$

They originate also from the matrix elements

$$\langle s_1,s_2,S,\Sigma,j,\Omega,J,M|(\hat{s}_2\otimes\hat{s}_2)_{20}|s_1,s_2,S',\Sigma,j,\Omega,J,M\rangle =$$

$$= (-1)^{S+s_1+s_2} s_2(1+s_2)(2s_2+1)\sqrt{5(2S+1)} C^{S'\Sigma}_{S\Sigma 20} \begin{Bmatrix} s_2 & s_1 & S \\ S' & 2 & s_2 \end{Bmatrix} \begin{Bmatrix} 1 & 1 & 2 \\ s_2 & s_2 & s_2 \end{Bmatrix} \tag{14}$$

indicating the coupling of the states with $S'\neq S$, and from the "geometrical" matrix elements of elementary anisotropies

$$\langle \psi_{S,\Sigma,j,\Omega,J,\varepsilon}|P_l(\cos\theta)|\psi_{S,\Sigma,j',\Omega,J,\varepsilon}\rangle = \sqrt{\frac{2j+1}{2j'+1}} C^{j'\Omega}_{j\Omega l0} C^{j'\Sigma}_{j\Sigma l0}. \tag{15}$$

It is easy to prove that there is no coupling between states of different parity.

In order to account for the nuclear spin statistics of O_2, the representation just defined should be thinned out by the extraction of spectroscopically relevant matrix from the matrix turned to eigenvectors of the representation at $R\rightarrow\infty$ (in the limit of a free O_2, see e.g. [11]).

3. The $O\left({}^3P_{j_O}\right)+OH\left(X{}^2\Pi_\Omega\right)$ system

Fragment 1 now is $O\left({}^3P_{J_1}\right)$ in the state with spin $S_1=1$, orbital momentum $L_1=1$, and total angular momentum $J_1=2,\ 1,\ 0$ with energies of the Spin-Orbit (S-O) FS components 0, $2A_{(1)}$, $3A_{(1)}$ ($A_{(1)}=0.000351$), respectively. The outer AO $2p$ of the atom is occupied with $n_1=4$ electrons and has a one-electron Coulomb asymptotic

$$\chi_1 \cong A_1 r^{1/\gamma_1-1}\exp(-\gamma_1 r) Y_{1,m_1}(\theta,\phi),\ \gamma_1^2/2=I_O \tag{16}$$

where $I_O=0.50045$ is the first ionisation potential of the atom. The matching parameter $A_1=1.3$ can be taken from [14].

Fragment 2 is $OH\left({}^2\Pi_{\tilde{\Omega}}\right)$ in the state with spin $S_2=1/2$, orbital $\tilde{\Lambda}=\pm 1$ and total angular $\tilde{\Omega}=\pm 3/2,\pm 1/2$ momenta along the molecular axis, and with energies of S-O

FS components 0, $A_{(2)}$ ($A_{(2)}$=0.000634), respectively. The outer valence MO 1π is occupied with $n_{2,1}$=3 electrons and has a one-electron Coulomb asymptotic

$$\chi_{p_{\pm1}^{c.m.}}(1\pi) \cong A_{2,1} r^{1/\gamma_{2,1}-1} \exp(-\gamma_{2,1}r) \ Y_{1\pm1}(\tilde{\theta},\tilde{\phi}), \ \gamma_{2,1}^2/2 = -e_{1\pi} \quad (17)$$

which is approximately centred at the centre of mass (c. of m.) of the molecule. The first fully occupied ($n_{2,2}$=2) inner MO 3σ has a one-electron Coulomb asymptotic

$$\chi_{p_0^{c.m.}}(3\sigma) \cong A_{2,2} r^{1/\gamma_{2,2}-1} \exp(-\gamma_{2,2}r) \ Y_{10}(\tilde{\theta},\tilde{\phi}), \ \gamma_{2,2}^2/2 = -e_{3\sigma} \quad (18)$$

which also is approximately centred at the c. of m. of the molecule. $\varepsilon_{1\pi}$ and $\varepsilon_{3\sigma}$ here are the MO binding energies.

The angles in Eqs. 17 and 18 marked with ~ correspond to the OH axis **r** directed towards H. All projections marked with ~ are those onto the molecular axis **r**. All unmarked projections are those onto the interfragment axis **R** in the direction from O to c. of m. of OH at an angle $\overline{\gamma}$ with respect to the axis **r** (i.e. conformation OHO corresponds to $\overline{\gamma}=\pi$).

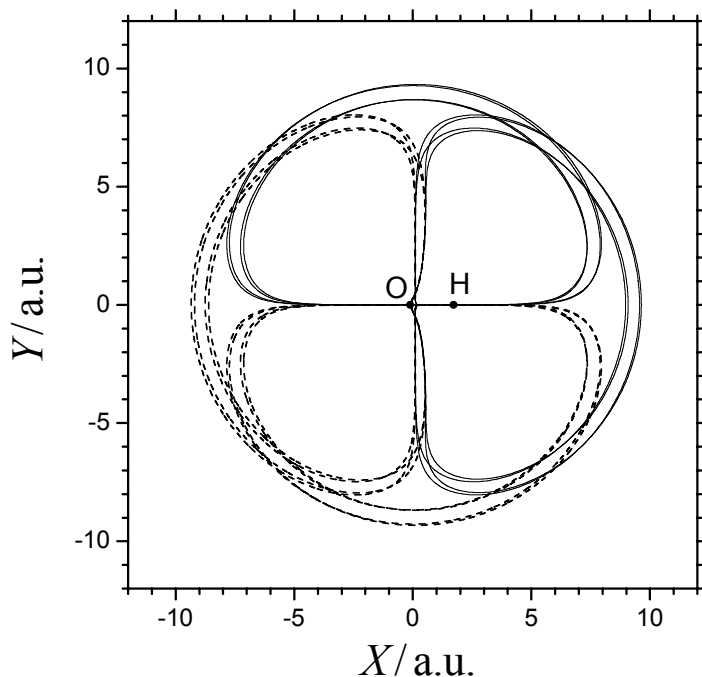*Figure 5.* Matching between HFR MO functions of OH and their one-centre one-electron asymptotics from Eqs. 17 and 18: outer and inner contours of the wave functions in the figure's plane enclosing the molecular axis are differing by the factor 2; contours with a symmetry plane enclosing the axis are for 1π, contours with a symmetry plane orthogonal to the axis are for 3σ; solid and dashed contours are differing in sign.

Hartree-Fock-Roothaan (HFR) MO functions of OH expanded in terms of Slater-type functions centred on the nuclei of O and H ($s_{O,H}$, $p_{O,H}$, $d_{O,H}$) were taken from [15]. Using these functions we start here with the estimations of the equilibrium distance R_e=1.8342, of the orbital energies $\varepsilon_{1\pi}$=-0.57215 and $\varepsilon_{3\sigma}$=-0.66041, and of the matching parameters A_{21}=1.3, A_{22}=2.6 (see *Fig.5*; a coincidence of A_{21} and A_1 was already assumed in [16]).

We write the multipolar series of the electrostatic interaction as

$$V_{1,2} = \sum_{l_1,l_2} (-1)^{l_2} \sqrt{\binom{2l_1+2l_2}{2l_1}} R^{-l_1-l_2-1} \sum_m C^{l_1+l_2\ 0}_{l_1\ m\ l_2\ -m} Q^{(1)}_{l_1\ m}(\tau_1) \sum_\mu d^{l_2}_{-m,\mu}(\overline{\gamma}) \tilde{Q}^{(2)}_{l_2\ \mu}(\tilde{\tau}_2),$$

$$Q_{p\ s}(\hat{\tau}) = \sqrt{4\pi/(2p+1)}\ \ r^p Y_{p\ s}(\theta,\phi) = \sqrt{(p-|s|)\ !/(p+|s|)\ !}\ \ e^{is\phi} r^p P^s_p(\cos\theta)$$

(19)

taking into account terms with l_1=2, l_2=1, 2, 3, and $|\mu|$=0, $2\le l_2$ only, i.e. all of the terms beginning with the dipole-quadrupole interaction ($\sim R^{-4}$) up to the quadrupole-octupole interaction ($\sim R^{-6}$; in the pioneering work of [17] there were included terms up to the quadrupole-quadrupole interaction ($\sim R^{-5}$)). The required atomic matrix elements

$$\left\langle J_1\ M_{J_1} \left| Q^{(1)}_{l_1\ m}(\tau_1) \right| J_1'\ M_{J_1}' \right\rangle = (-1)^{J_1+L_1+S_1-l_1} \sqrt{2J_1+1}\ C^{J_1' M_{J_1}'}_{J_1 M_{J_1}\ l_1 m} \left\{ {}^{L_1\ S_1\ J_1}_{J_1'\ l_1\ L_1} \right\} \left\langle (nl)^{n_1}\ L_1 S_1 \left\| Q^{(1)}_{l_1} \right\| (nl)^{n_1}\ L_1 S_1 \right\rangle \ (20)$$

are calculated using

$$\left\langle (nl)^{n_1}\ L_1 S_1 \left\| Q^{(1)}_{l_1} \right\| (nl)^{n_1}\ L_1 S_1 \right\rangle = \sqrt{2L_1+1}\ Q_0 / C^{L_1\ 0}_{L_1\ 0\ l_1\ 0} = -\sqrt{15/2}\ Q_0$$

(21)

where the maximal (in absolute value) quadrupole moment Q_0 of the $M_{L_1}=0$ component in the ${}^3P(2p)^4$ atomic state can be expressed [18] in terms of the averaged square of the radius of the outer atomic electron (see e.g. [14])

$$Q_0 \approx -2\left\langle r_1^2 \right\rangle / 5 = -0.8\ \ .$$

(22)

The molecular electrostatic multipole moments here are defined following *Buckingham* [19]:

$$q^{(2)}_{10} = d_{OH} = \int r_2 P_1(\cos\theta_2)\ \ \rho_2\ \ d\tau_2 = \int z_2\ \ \rho_2\ \ d\tau_2,$$

$$q^{(2)}_{20} = Q_{OH} = \int r_2^2 P_2(\cos\theta_2)\ \ \rho_2\ \ d\tau_2 = \frac{1}{2}\int(3z_2^2-1)\ \ \rho_2\ \ d\tau_2,$$

$$q^{(2)}_{22} = Q_{c,OH} = \int r_2^2 P_2^2(\cos\theta_2)\ \ \rho_2\ \ d\tau_2 = 3\int(x_2^2+y_2^2)\ \ \rho_2\ \ d\tau_2,$$

$$q^{(2)}_{30} = O_{OH} = \int r_2^3 P_3(\cos\theta_2)\ \ \rho_2\ \ d\tau_2 = \frac{1}{2}\int z_2(5z_2^2-3)\ \ \rho_2\ \ d\tau_2,$$

$$q^{(2)}_{32} = O_{c,OH} = \int r_2^3 P_3^2(\cos\theta_2)\ \ \rho_2\ \ d\tau_2 = 15\int z_2(x_2^2+y_2^2)\ \ \rho_2\ \ d\tau_2$$

(23)

where the integration over the density of charge ρ_2 is done taking the molecular axis **r** as z-axis with origin in the c. of m. of OH. In order to estimate these moments, we again use HFR functions from [15] (the index n here marks contributions from the nuclei)

$$d_{\overline{OH}} = d_n + d_{1\pi^3} + d_{3\sigma^2} + d_{2\sigma^2} + d_{1\sigma^2} \cong 0.70\ ;$$

$$d_n = 0.86;\ d_{1\pi^3} = 0.15;\ d_{3\sigma^2} = -0.09;\ d_{2\sigma^2} = -0.44;\ d_{1\sigma^2} = 0.22;$$

$$Q_{OH} = Q_n + Q_{1\pi^3} + Q_{3\sigma^2} + Q_{2\sigma^2} + Q_{1\sigma^2} \cong 1.30;$$

$$Q_n \cong 3.07;\ Q_{1\pi^3} \cong 1.19;\ Q_{3\sigma^2} \cong -2.50;\ Q_{2\sigma^2} \cong -0.44;\ Q_{1\sigma^2} \cong -0.02;$$

$$Q_{c,OH} = -5.13;\ O_{OH} = 2.47;\ O_{c,OH} = 0.67\ \ .$$

(24)

These estimates are in surprisingly good agreement with recent experimental and *ab initio* data [20,21]. Apparently the value of Q_{OH} from [22] (just similar to the value given in Eq.24) was used in [23] and then in [17] as defined following *Hirschfelder* [24]. As result it produces two times too shallow asymptotic shape of the linear MEP (see *Fig.6*) which in no case could be adjusted to the *ab initio* data of [25] (see also the modeling of bending frequency along the linear MEP, *Fig.7*).
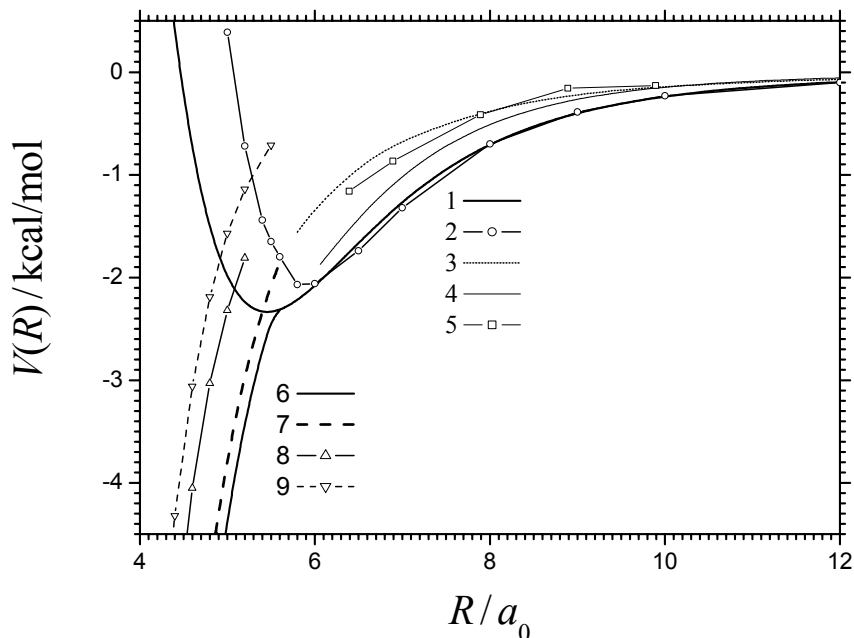

Figure.6. MEP for the two lowest doublet PES's of the $^2A''$, $^2A'$ states calculated without contribution of S-O interaction: energies are given in kcal/mol; curves 1-5 are for linear (γ=0) MEP at long distances R; curves 6-9 are for non-linear MEP at short distances; solid curves 6, 8 and dashed curves 7, 9 are for $^2A''$ and $^2A'$ states, respectively; thick curves 1, 6, 7 are from this work (after preliminary optimisation through the coefficients A_{21}, A_{22}, C_6, O_{OH} and $O_{c,OH}$) and thin curves 2, 8, 9 are from [25]; the dotted curve 3 is our recalculation (without contributions of S-O and exchange interactions) using parameters from [17] and [23]; curve 4 is the analytic representation DMBEIV from [26]; curve 5 is from the ab initio data of [27].

Then in the basis of the Hund's case *c* free fragment functions (FFC)

$$\psi_{J_1, M_{J_1}, \tilde{\Omega}, \tilde{\Lambda}} = \left\langle J_1 \ M_{J_1} \ p^{n_1} \ S_1 \ L_1 \middle| \left\langle \tilde{\Omega} \ p^{n_{2,1}} \ S_2 \ \tilde{\Omega} - \tilde{\Lambda} \ \tilde{\Lambda} \middle|, \right. \right. \tag{25}$$

the matrix elements of terms in the multipolar electrostatic expansion (19) can be reduced to the standard expressions using the definitions of Eqs. 20-23:

$$\left\langle J_1\ M_{J_1}\ p^{n_1}\ S_1\ L_1\middle|\left\langle \tilde{\Omega}\ p^{n_{2,k}}\ S_2\ \tilde{\Omega}-\tilde{\Lambda}\ \tilde{\Lambda}\middle|V_{1,2}^{(2,l_2)}\middle|J_1'\ M_{J_1}'\ p^{n_1}\ S_1\ L_1\right\rangle\middle|\tilde{\Omega}'\ p^{n_{2,k}}\ S_2\ \tilde{\Omega}'-\tilde{\Lambda}'\ \tilde{\Lambda}'\right\rangle =$$

$$= (-1)^{J_1+l_2}\ \delta_{\tilde{\Omega}'-\tilde{\Lambda}',\tilde{\Omega}-\tilde{\Lambda}}\sqrt{\frac{6(2J_1+1)}{5}}\binom{2l_2+4}{4}\left\{\begin{smallmatrix}1&1&J_1\\J_1'&2&1\end{smallmatrix}\right\}\ R^{-l_2-3}\left\langle r_1^2\right\rangle\times \tag{26}$$

$$\times\sum_m C_{2\ m\ l_2\ -m}^{l_2+2\ 0}C_{J_1M_{J_1}\ 2\ m}^{J_1'M_{J_1}'}\sum_\mu \delta_{\mu,\tilde{\Lambda}'-\tilde{\Lambda}}\sqrt{(l_2-|\mu|)\ !/(l_2+|\mu|)\ !}\ d_{-m,\mu}^{l_2}(\overline{\gamma})\ q_{l_2\ |\mu|}^{(2)}.$$
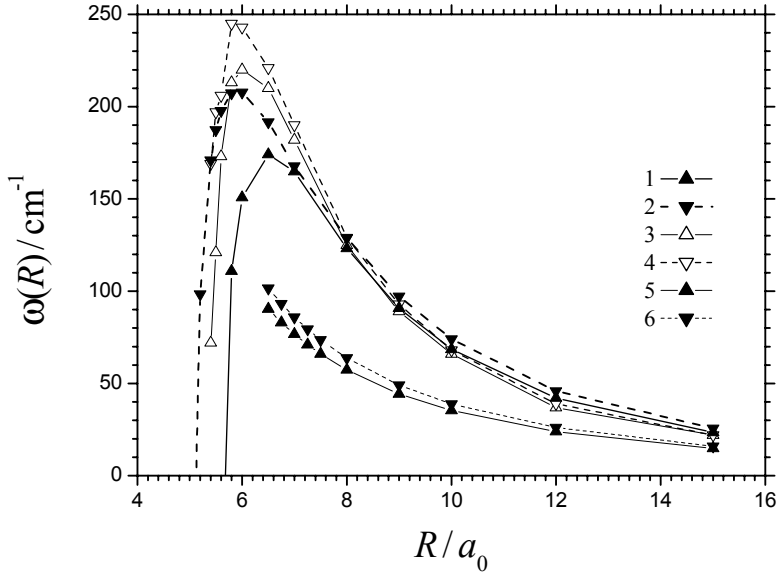

Figure 7. Harmonic bending frequencies along the linear MEP at long distances R for the two lowest doublet PES's of the $^2A''$ (solid curves 1, 3, 5) and $^2A'$ (dashed curves 2, 4, 6) states calculated without contribution of S-O interaction: frequencies are given in cm^{-1}; thick curves 1, 2 are from this work (after preliminary optimisation through the coefficients A_{21}, A_{22}, C_6, O_{OH} and $O_{c,OH}$), thin curves 3, 4 are from the ab initio data of [25] and thin curves 5, 6 are from our recalculation (without contributions of S-O and exchange interactions) using parameters from [17] and [23].

Taking into account the exchange interactions of the fragments 1 and 2 in the Heitler-London approximation (the index k equal to 1 and 2 corresponds to exchange with $1\pi^3$ outer and $3\sigma^2$ inner molecular electronic shells respectively),

$$V_{(1,2k)}^{HL} = -\sum_{i=1}^{n_1}\sum_{j=n_1+1}^{n_1+n_{2k}}\frac{1}{2}\left(1+4\mathbf{s}_i\cdot\mathbf{s}_j\right)\ V_{ij}P_{ij}^x \tag{27}$$

we use for the matrix elements the re-projecting formula from [28]

$$\left\langle J_1 \ \tilde{M}_{J_1} \ p^{n_1} \ S_1 \ L_1 \middle| \left\langle \tilde{\Omega} \ p^{n_{2,k}} \ S_2 \ \tilde{\Omega}-\tilde{\Lambda} \ \tilde{\Lambda} \middle| V_{(1,2k)}^{\text{HL}} \middle| \tilde{\Omega}^* \ p^{n_{2,k}} \ S_2 \ \tilde{\Omega}^*-\tilde{\Lambda}^* \ \tilde{\Lambda}^* \right\rangle \middle| J_1^* \ \tilde{M}_{J_1}^* \ p^{n_1} \ S_1 \ L_1 \right\rangle =$$

$$= -\sum_{\tilde{\Omega},\tilde{\Omega}^*=-3/2}^{3/2} \sum_{J_1,J_1^*=0}^{2} \sum_{\tilde{M}_{J_1},\tilde{M}_{J_1}^*} \sum_{\tilde{M}_{L_1},\tilde{M}_{L_1}^*} C_{L_1,\tilde{M}_{L_1} \ S_1,\tilde{M}_{J_1}-\tilde{M}_{L_1}}^{J_1,\tilde{M}_{J_1}} C_{L_1,\tilde{M}_{L_1}^* \ S_1,\tilde{M}_{J_1}^*-\tilde{M}_{L_1}^*}^{J_1^*,\tilde{M}_{J_1}^*} \sum_{S_1',L_1';S_2',Q_2'} \left(G_{S_1',L_1'}^{S_1,L_1} G_{S_2',Q_2'}^{S_2,Q_2} \right)^2 \times$$

$$\times \left[2^{-1} \delta_{\tilde{M}_{J_1}-\tilde{M}_{L_1},\tilde{M}_{J_1}^*-\tilde{M}_{L_1}^*} \delta_{\tilde{\Omega}-\tilde{\Lambda},\tilde{\Omega}^*-\tilde{\Lambda}^*} + C_{S_1,\tilde{M}_{J_1}^*-\tilde{M}_{L_1}^* \ 1,\tilde{M}_{J_1}-\tilde{M}_{L_1}-\tilde{M}_{J_1}^*+\tilde{M}_{L_1}^*}^{S_1,\tilde{M}_{J_1}-\tilde{M}_{L_1}} C_{S_2,\tilde{\Omega}^*-\tilde{\Lambda}^* \ 1,\tilde{M}_{J_1}^*-\tilde{M}_{L_1}^*-\tilde{M}_{J_1}+\tilde{M}_{L_1}}^{S_2,\tilde{\Omega}-\tilde{\Lambda}} \times$$

$$\times 3\sqrt{(2S_1+1)(2S_2+1)} (-1)^{\tilde{M}_{J_1}-\tilde{M}_{J_1}^*+\tilde{M}_{L_1}-\tilde{M}_{L_1}^*+S_1'+S_2'+S_1+S_2+1} \left\{ \begin{matrix} 1/2 & S_1 & S_1' \\ S_1 & 1/2 & 1 \end{matrix} \right\} \left\{ \begin{matrix} 1/2 & S_2 & S_2' \\ S_2 & 1/2 & 1 \end{matrix} \right\} \right] \times$$

$$\times \left\langle L_1' p^{n_1} L_1 \tilde{M}_{L_1} \ Q_2' p^{n_{2,k}} Q_2 \tilde{\Lambda} \middle| V_{(1,2k)} P_{(1,2k)}^x \middle| L_1' p^{n_1} L_1 \tilde{M}_{L_1}^* \ Q_2' p^{n_{2,k}} Q_2 \tilde{\Lambda}^* \right\rangle \ .$$

$$(28)$$

The transformation to the FFC basis (see Eq.25) with quantization of the atomic total angular momentum onto the intermolecular axis **R** is accomplished by the rotation

$$\left\langle J_1 \ M_{J_1} \ p^{n_1} \ S_1 \ L_1 \right| = \sum_{\tilde{M}_{J_1}} d_{\tilde{M}_{J_1},M_{J_1}}^{J_1}(\bar{\gamma}) \left\langle J_1 \ \tilde{M}_{J_1} \ p^{n_1} \ S_1 \ L_1 \right|. \tag{29}$$

All non-zero coefficients of fractional parentage in Eq.28 are atomic coefficients $G_{S_1',L_1'}^{S_1,L_1}$

$$G_{3/2,0}^{1,\,1} = -3^{-1/2}; \ G_{1/2,2}^{1,\,1} = (5/12)^{1/2}; \ G_{1/2,1}^{1,\,1} = -2^{-1} \tag{30}$$

and molecular coefficients $G_{S_2',Q_2'}^{S_2,Q_2}$ for the outer (k=1)

$$G_{0,\ 0^+}^{1/2,1} = 6^{-1/2}; \ G_{0,2}^{1,1} = -3^{-1/2}; \ G_{1,\ 0^-}^{1/2,1} = 2^{-1/2} \tag{31}$$

and for the inner (k=2)

$$G_{0,\ 1}^{1/2,1} = 2^{-1}; \ G_{1,\ 1}^{1/2,1} = (3/4)^{1/2} \tag{32}$$

molecular electronic shells.

The coordinate dependent interaction operators in the matrix elements of the last line in Eq.28 are enclosed in coordinate wave functions bound to the molecular axis **r**

$$\left\langle L_1' p^{n_1} L_1 \tilde{M}_{L_1} \ Q_2' p^{n_{2,k}} Q_2 \tilde{\Lambda} \middle| V_{(1,2k)} P_{(1,2k)}^x \middle| L_1' p^{n_1} L_1 \tilde{M}_{L_1}^* \ Q_2' p^{n_{2,k}} Q_2 \tilde{\Lambda}^* \right\rangle \cong$$

$$\cong n_1 n_{2,k} \sum_{\tilde{m}_1,\tilde{m}_1^*,\tilde{m}_2,\tilde{m}_2^*} \delta_{\tilde{M}_{L_1}-\tilde{m}_1,\tilde{M}_{L_1}^*-\tilde{m}_1^*} \delta_{\tilde{\Lambda}-\tilde{m}_2,\tilde{\Lambda}^*-\tilde{m}_2^*} C_{L_1',\tilde{M}_{L_1}-\tilde{m}_1 \ 1,\tilde{m}_1}^{L_1,\tilde{M}_{L_1}} C_{L_1',\tilde{M}_{L_1}^*-\tilde{m}_1^* \ 1,\tilde{m}_1^*}^{L_1,\tilde{M}_{L_1}^*} \tilde{J}_{\tilde{m}_1,\tilde{m}_2,\tilde{m}_1^*,\tilde{m}_2^*} \tag{33}$$

which can be easily transformed to the **R** axis using the transformation

$$\tilde{J}_{\tilde{m}_1,\tilde{m}_2,\tilde{m}_1^*,\tilde{m}_2^*} = \sum_{m_1,m_2,m_1^*,m_2^*} d_{m_1,\tilde{m}_1}^{l_1}(\bar{\gamma}) d_{m_2,\tilde{m}_2}^{l_2}(\bar{\gamma}) d_{m_1^*,\tilde{m}_1^*}^{l_1}(\bar{\gamma}) d_{m_2^*,\tilde{m}_2^*}^{l_2}(\bar{\gamma}) \left\langle l_1 m_1 \ l_2 m_2 \middle| I_{as} \middle| l_1 m_1^* \ l_2 m_2^* \right\rangle \tag{34}$$

where $l_1, l_2 = 1$. Here it is taken into account that all relevant molecular addition coefficients $\left(C_{Q_2',\tilde{\Lambda}-\tilde{m}_2 \ 1,\tilde{m}_2}^{Q_2,\tilde{\Lambda}} : Q_2 = |\tilde{\Lambda}|, Q_2' = |\tilde{\Lambda}-\tilde{m}_2|, |\tilde{m}_2| = 1 \right)$ omitted in Eq.33 are equal to 0 or 1. Two-electron matrix elements $\left\langle 1m_1 \ 1m_2 \middle| I_{as} \middle| 1m_1^* \ 1m_2^* \right\rangle$, the related integrals of the Asymptotic Theory I_{kn} (*Fig.8*), and molecular addition coefficients are found in [29].
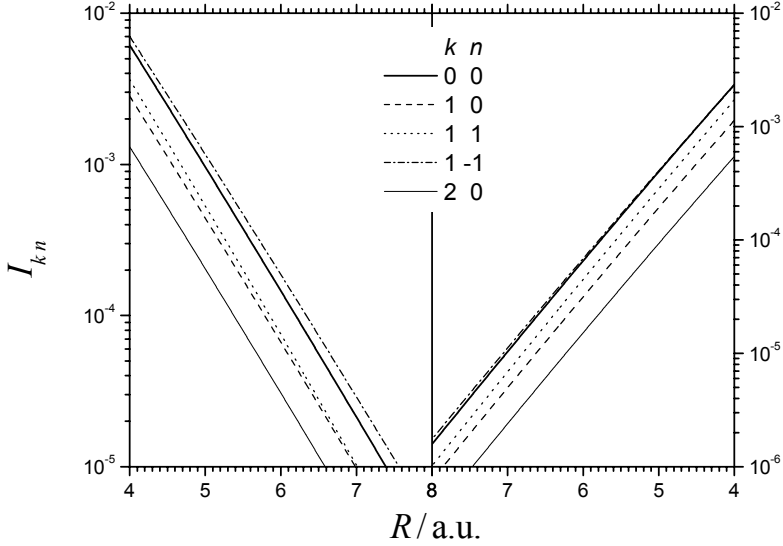
Figure. 8. Exchange integrals I_{kn} of the Asymptotic Theory for p electrons: asymptotic integrals are for the interactions of electrons from the outer AO 2p of O with electrons from the outer MO 1π (right panel) and with electrons from the inner MO 3σ (left panel) of OH.

For the evaluation of the averaged induction-dispersion interaction $-C_6R^{-6}$, we here accept based on the Slater-Kirkwood formula value $C_6=23.2$ from the work [23]. In order to create more reliable estimations of the anisotropy of C_6 term, one can again resort to the RSOF method by Meyer et al. [6] and to the related calculations of the fragment dynamic polarizabilities [20, 30]. The FFC basis of Eq.25 consists of 36 functions transforming upon time inversion as

$$I_{t\to -t}\psi_{J_1,M_{J_1},\tilde{\Omega},\tilde{\Lambda}} = (-1)^{J_1-M_{J_1}+\frac{1}{2}-\tilde{\Omega}+\tilde{\Lambda}}\,\psi_{J_1,-M_{J_1},-\tilde{\Omega},-\tilde{\Lambda}}\,. \tag{35}$$

In a system with half-integer total spin, in accordance with Kramers's theorem (see e. g. in [31]), we find the symmetry

$$I_{-t\to t}\;\;I_{t\to -t}\psi_{J_1,M_{J_1},\tilde{\Omega},\tilde{\Lambda}} = -\psi_{J_1,M_{J_1},\tilde{\Omega},\tilde{\Lambda}}\,. \tag{36}$$

The linear combinations of the FFC basis functions

$$\left(\psi_{J_1,M_{J_1},\tilde{\Omega},\tilde{\Lambda}} \pm i\, I_{t\to -t}\psi_{J_1,M_{J_1},\tilde{\Omega},\tilde{\Lambda}}\right)\!/\sqrt{2} \tag{37}$$

then constitute two uncoupled complex-valued sub-representations of the Hamiltonian reproducing, with their 18 real eigenvalues, the energies of 18 doublet eigenstates of the system (see left panels in *Figs. 9-14*; one should notice that, in these figures, $\gamma = \pi - \bar{\gamma}$).

Figure. 9. PES slices (angular potentials) $V_i(R=5.$ a.u., $\gamma)$: energies are given in kcal/mol; left panel: 18 doublet PES's calculated with the contribution of S-O interaction; right panel: 12 PES's $(3\,{}^2A' + 3\,{}^2A'' + 3\,{}^4A' + 3\,{}^4A'')$ calculated without the contribution of SO interaction.

Figure. 10. PES slices (angular potentials) $V_i(R=5.5$ a.u., $\gamma)$: details as in caption to Fig. 9.
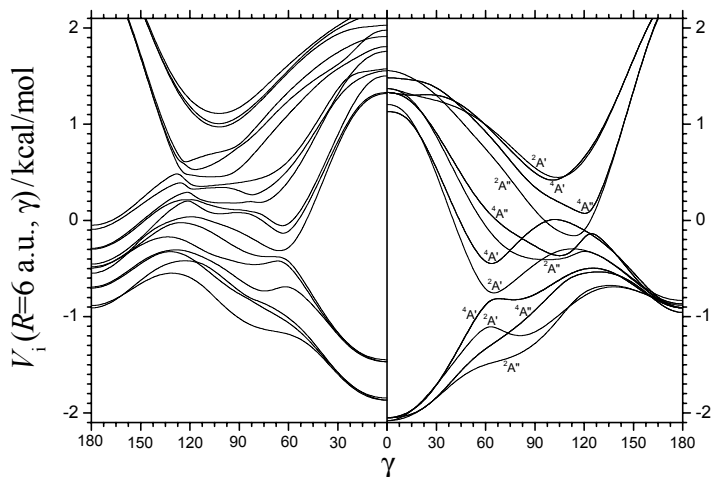
Figure. 11. PES slices (angular potentials) $V_i(R=6. a.u., \gamma)$: details as in caption to Fig. 9.

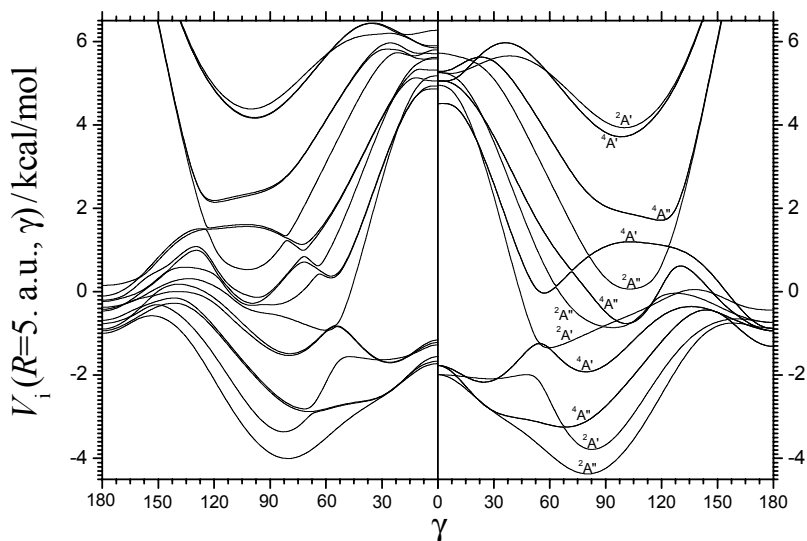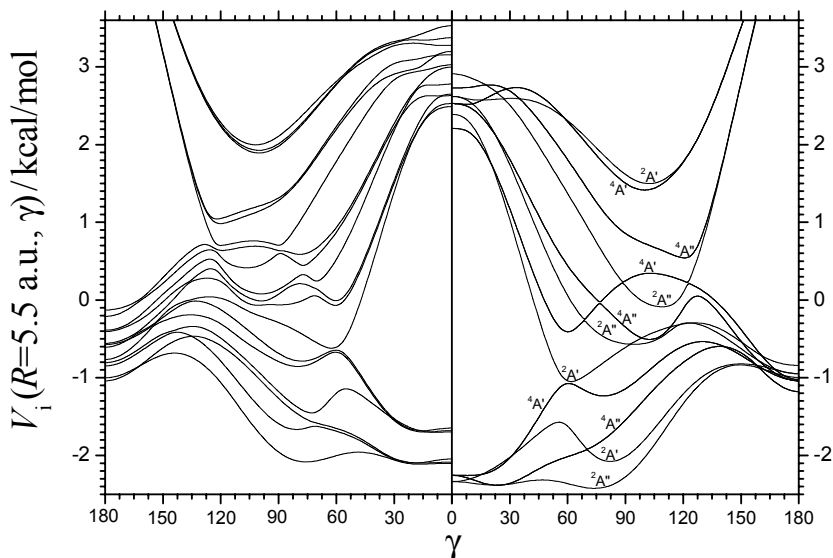*Figure. 12.* PES slices (radial potentials) $V_i(R, \gamma=0)$: energies are given in kcal/mol; left panel: 18 doublet PES's calculated with the contribution of S-O interaction are ascribed to 4 uncoupled groups of 1, 3, 6, 8 states with $|M_J|=7/2, 5/2, 3/2, 1/2$ shown with dash-dotted, dotted, dashed, and solid curves respectively; free-fragment correlations are assigned for the example of triple pseudo-crossing in the group of 8 states with $|M_J|=1/2$; right panel: 8 PES's calculated without contribution of the S-O interaction are ascribed to irreducible representations ($^2\Sigma^+ + ^2\Sigma^- + ^2\Pi + ^2\Delta + ^4\Sigma^+ + ^4\Sigma^- + ^4\Pi + ^4\Delta$) of the symmetry group $C_{\infty v}$.

In the linear configurations O-HO (γ=0) and O-OH (γ=π) there is no coupling between states differing in angular momentum projection M_J (at *Fig.12* for γ=0 and at *Fig.14* for γ=π $M_J = M_{J_1} \mp \tilde{\Omega}$ respectively). In these cases, the complex valued matrix representations of the Eq.37 consist of the 4 Jordan cells with $|M_J|$=7/2, 5/2, 3/2, 1/2 having dimensions 1, 3, 6, 8 respectively. As a result, there are a number of accidental crossings of the Renner cone type. Otherwise within the cells there exist also a number of pseudo-crossings with narrow splitting because of the coupling of the S-O components. In the asymptotic region of large R these couplings are mainly due to electrostatic interaction of the axially-polarised multipole moments ($Q_{l_1 m}^{(1)}(\tau_1)$ and $\tilde{Q}_{l_2 \mu}^{(2)}(\tau_2)$ in Eq.19 with non-equal zero m and μ respectively). We believe that some qualitative difference in the T-shaped configuration (compare *Fig.13* from this work with *Fig.5* from [17]) is because of the incorrect matrices $Q_{2,O}^1$ and $Q_{2,O}^2$ (Appendix A to [17]).

If S-O interaction is neglected, then the system can be characterised additionally by the total spin S and A′/A″ representations of C_s symmetry. In this case we have 6 doublets and 6 quartets equally presented among 6 A′ and 6 A″ states (see the right panels at *Figs. 9-11*). In the linear configurations (see right panels at *Figs. 12,14*), because of the higher symmetry $C_{\infty v}$, there exist additional degeneracies in two pairs of the doublet and in two pairs of the quartet states, i.e. we have 2 states with the degeneracy 2 ($^2\Sigma^+$, $^2\Sigma^-$), 4 states with the degeneracy 4 ($^4\Sigma^+$, $^4\Sigma^-$, $^2\Pi$(2), $^2\Delta$(2)) and 2 states with the degeneracy 8 ($^4\Pi$(2), $^4\Delta$(2)).
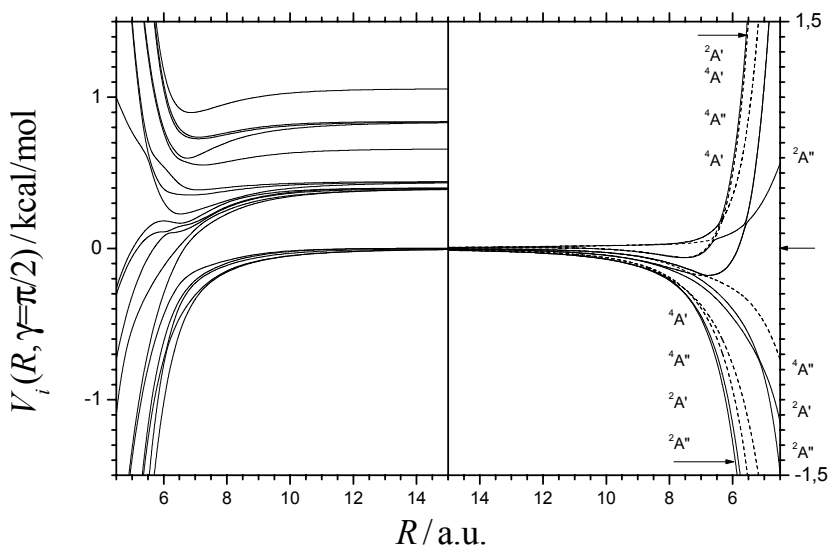
Figure. 13. PES slices (radial potentials) V_i(R, γ=π/2): energies are given in kcal/mol; left panel: 18 doublet PES's calculated with the contribution of S-O interaction; right panel: 12 PES's (3^2A′+3^2A″+3^4A′+3^4A″) calculated without the contribution of S-O interaction.

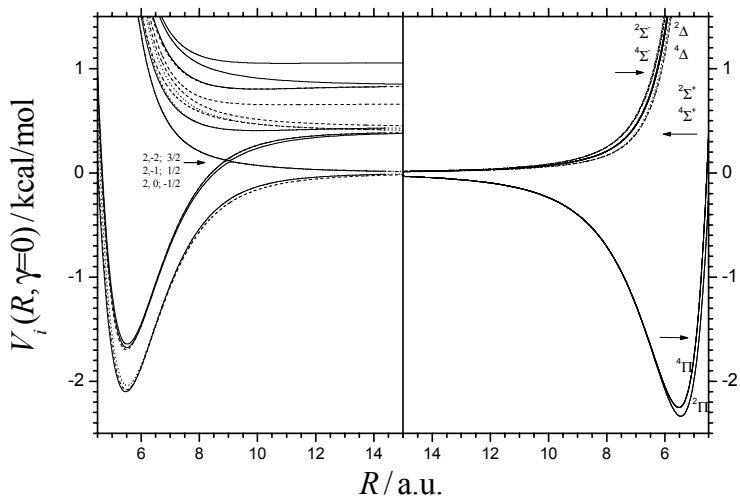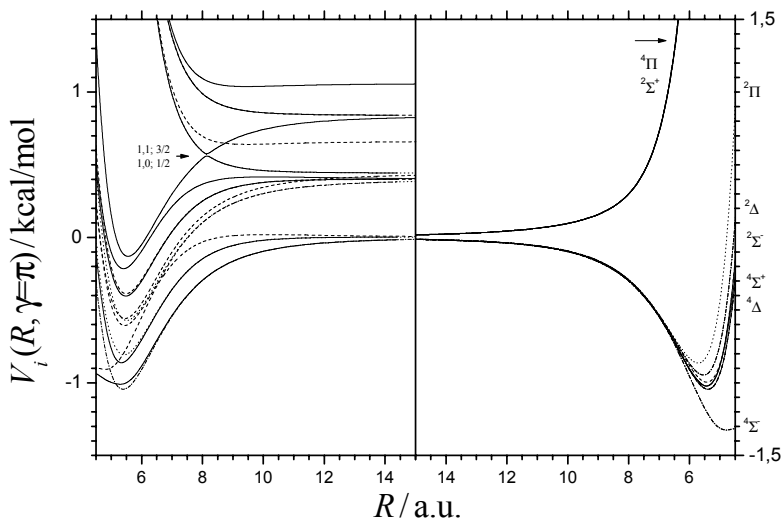*Figure. 14.* PES slices (radial potentials) $V_i(R, \gamma=\pi)$: free-fragment correlations are assigned for the example of double pseudo-crossing in the group of 8 states with $|M_J|=1/2$; other details as in caption to Fig. 12.
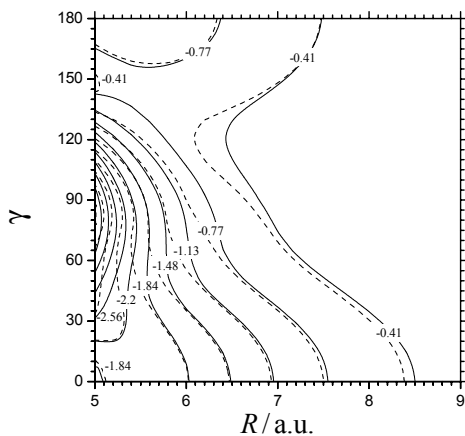
Figure. 15. Contour plots of the two lowest doublet PES, $V_{1,2}$ calculated with the contribution of S-O interaction: energies are given in kcal/mol; solid and dashed contours are for PES indicating the adiabatic correlation between the 1st and 2nd from bottom components of the lowest multiplet $O(^3P_2)+OH(^2\Pi_{3/2})$ at long distances R and the lowest $^2A''$ and $^2A'$ states at short distances, respectively.
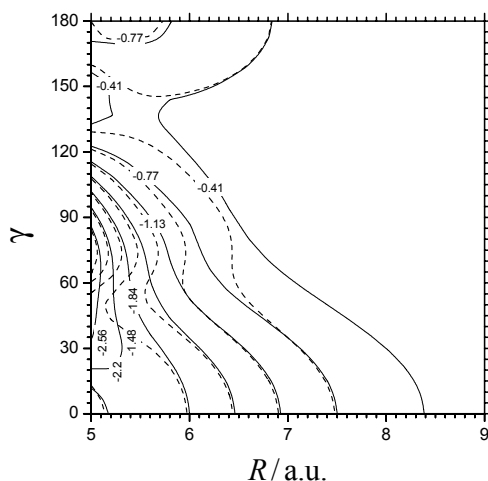
Figure. 16. Contour plots of the two doublet PES, $V_{3,4}$ calculated with contribution of the S-O interaction: energies are given in kcal/mol; solid and dashed contours are for PES indicating the adiabatic correlation between 3rd and 4th components of the lowest multiplet $O(^3P_2)+OH(^2\Pi_{3/2})$ at long distances R and the lowest $^4A''$ state at short distances, respectively.

Figure 17. Contour plots of the two doublet PES, $V_{5,6}$ calculated with the contribution of S-O interaction: energies are given in kcal/mol; solid and dashed contours are for PES indicating the adiabatic correlation between 5th ($\tilde{\Omega}=3/2$) and 1st ($\tilde{\Omega}=1/2$) components of the multiplets $O(^3P_2)+OH(X^2\Pi_{\tilde{\Omega}})$ at long distances R and the lowest $^4A'$ state at short distances, respectively.

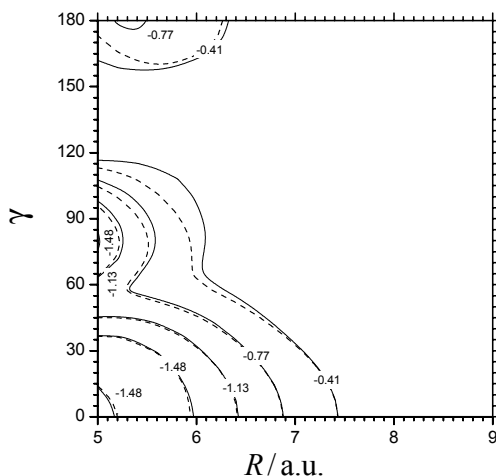In Figs. *15-17* we demonstrate the asymptotic anisotropic behaviour of the 6 lowest 2D PES indicating the correlation of the lowest S-O multiplets of fragments with the lowest adduct states of $^2A''$, $^2A'$, $^4A''$, and $^4A'$ symmetry.

For SACM applications, electronic wave functions of the FFC basis of Eq.25 are now incorporated in functions of the roronic basis

$$\Psi_{J_1,M_{J_1},J_2,M-M_{J_1},\tilde{\Omega},\tilde{\Lambda}} = \psi_{J_1,M_{J_1},\tilde{\Omega},\tilde{\Lambda}} D^{J_2}_{\tilde{\Omega},M-M_{J_1}}\left(\bar{\gamma},\bar{\phi}\right). \tag{38}$$

In this construction of the complete basis, it is taken into account that, within the standard version of the SACM (nonrotating **R**), there are no interactions responsible for the coupling of states differing in the projection of the total angular momentum M along the intermolecular axis **R**.

In the rotational Hamiltonian we keep only terms (see e.g. [12])

$$H_{\text{rot}} = B_0\left\{\mathbf{J}_2^2 - 2J_{2,z}S_{2,z} + \mathbf{S}_2^2 - 2(J_{2,z}-S_{2,z})L_{2,z} + L_{2,z}^2\right\} - B_0\left(J_{2,+}S_{2,-} + J_{2,-}S_{2,+}\right) \tag{39}$$

which, in the representation of Eq.38, generate the diagonal matrix elements

$$\left\langle\Psi_{J_1,M_{J_1},J_2,M-M_{J_1},\tilde{\Omega},\tilde{\Lambda}}\left|H_{\text{rot}}\right|\Psi_{J_1,M_{J_1},J_2,M-M_{J_1},\tilde{\Omega},\tilde{\Lambda}}\right\rangle = B_0\left\{J_2(J_2+1) - (-1)^{1/2+|\tilde{\Omega}|}|\tilde{\Omega}| - \frac{1}{4}\right\} \tag{40}$$

and the non-diagonal matrix elements:

$$\left\langle\Psi_{J_1,M_{J_1},J_2,M-M_{J_1},\tilde{\Omega},\tilde{\Lambda}}\left|H_{\text{rot}}\right|\Psi_{J_1,M_{J_1},J_2,M-M_{J_1},\tilde{\Omega}',\tilde{\Lambda}}\right\rangle = -\delta_{|\tilde{\Omega}'-\tilde{\Omega}|,1}B_0\sqrt{J_2\left(J_2+1\right)-\frac{3}{4}}. \tag{41}$$

4. Conclusion

In this contribution, within the asymptotic approach, we have elaborated the basis for the calculation either of adiabatic channel potentials (diagonalization of the full Hamiltonian in a body-fixed frame at given interfragment distances) or of axially-nonadiabatic channel potentials (diagonalization of the full Hamiltonian in a space-fixed frame at given interfragment distances). As a by-product, we have compared our asymptotic PES on different levels of approximations with available local *ab initio* data. In subsequent work, we envisage the calculation of low temperature rate constants for complex-formation of the title reactions.

Acknowledgments

References

1. Maergoiz, A.I., Nikitin E.E., Troe, J., Ushakov V.G. Classical trajectory and statistical adiabatic channel study of the dynamics of capture and unimolecular bond fission (1996) a) I. Ion-dipole capture, *J. Chem. Phys.* **105**, 6263-6269; b) II. Ion-quadrupole capture, *ibid*. 6270-6276; c) III. Dipole-dipole capture, *ibid*. 6277-6284; (1998) d) IV. Valence interactions between atoms and linear rotors, *J. Chem. Phys.* **108**, 5265-5280; e) V. Valence interactions between two linear rotors, *ibid*. 9987-9998; (2002) g) VI. Properties of transitional modes and specific rate constants $k(E,J)$, *J. Chem. Phys.* **117**, 4201-4213.
2. a) Marques, J.M.C. and Varandas, A.J.C. (2001) On the high pressure rate constants for the H/Mu+O_2 addition reaction, *Phys. Chem. Chem. Phys.* **3**, 505-507; b) Harding, L.B., Troe, J., and Ushakov, V.G. (2001) Comment, *Phys. Chem. Chem. Phys.* **3**, 2630-2631; c) Marques, J.M.C. and Varandas, A.J.C. (2001) Reply to the comment, *Phys. Chem. Chem. Phys.* **3**, 2632-2633.
3. a) Viti, S., Roueff, E., Hartquist, T.W., Pineau des Forets, G., Williams, D.A. (2001) Interstellar oxygen chemistry, *Astronomy and Astrophysics*, **370**, 557-569; b) Koehler, S.P.K., (2002) Low-temperature reaction kinetics and dynamics of the hydroxyl radical, Diploma Thesis, Institut fuer Physikalische Chemie, Universitaet Goettingen.
4. Bussery, B., Umanskii, S.Ya., Aubert-Frecon, M., and Bouty, O. (1994) Exchange interaction between two O_2 molecules using the asymptotic method, *J. Chem. Phys.* **101**, 416-423.
5. Cade, P.E. and Wahl, A.C. (1974) Atomic Data & Nuclear Data Tables **13**, 339.
6. Spelsberg, D., Lorenz, T., and Meyer, W. (1993) Dynamic multipole polarizabilities and long range interaction coefficients, *J. Chem. Phys.* **99**, 7845-7858.
7. Spelsberg, D. and Meyer, W. (1998) *Ab initio* dynamic dipole polarizabilities for O_2, *J. Chem. Phys.* **109**, 9802-9810.
8. Harding, L.B., Troe, J., and Ushakov, V.G. (2000) Classical trajectory calculations of the high pressure limiting rate constants, *Phys. Chem. Chem. Phys.* **2**, 631-642.
9. Harding, L.B., private communication.
10. Dashevskaya, E.I., Maergoiz, A.I., Troe, J., Litvin, I., Nikitin, E.E. (2003) Low- temperature behavior of capture rate constants, *J. Chem. Phys.* **118**, 7313-7320.
11. Maergoiz, A.I., Nikitin, E.E., Troe, J. (1996) Adiabatic channel study of the capture of nitrogen and oxygen molecules by an ion, *Z. Phys.* **D36**, 339-347.
12. Zare, R.N. (1986) *Angular Momentum*, Wiley, N.Y.
13. Varshalovich, D.A., Moskalev, A.N., and Khersonskii, V.K. (1988) *Quantum Theory of Angular Momentum*, World Scientific, Singapore.
14. Radzig, A.A. and Smirnov, B.M. (1985) *Reference data on atoms, molecules and ions*, Springer, Berlin.
15. Cade, P.E. and Huo, W.M. (1967) Electronic structure of first-row hydrides, *J. Chem. Phys.*, **47**, 614-648.
16. Nikitin, E.E., Ottinger, Ch., and Shalashilin, D.V. (1996) Test of the asymptotic method as applied to atom-diatom interaction potentials, *Z. Phys.* **D36**, 257-264.
17. Graff, M.M. and Wagner, A.F. (1990) Theoretical studies of fine-structure effects and long-range forces. *J. Chem. Phys.* **92**, 2423-2439.
18. Gentry, W.R. and Giese, C.F. (1977) Long-range interactions of ions with atoms having partially filled p subshells. *J. Chem. Phys.* **67**, 2355-2361.
19. Buckingham, A.D. (1967) Permanent and induced molecular moments and long-range intermolecular forces, *Adv. Chem. Phys.* **12**, 107-142.
20. Spelsberg, D. (1999) Dynamic multipole polarizabilities and reduced spectra for OH, *J. Chem. Phys.*, **111**, 9625-9633.
21. Esposti, A.D. and Werner, H.-J. (1990) OH($X^2\Pi$, $A^2\Sigma^+$)+Ar energy surfaces, *J. Chem. Phys.* **93**, 3351-3366.

22. Chu, S.I., Yoshimine, M., and Liu, B. (1974) *J. Chem. Phys.*, **61**,5389-5395.
23. Clary, D.C. and Werner, H.-J. (1984) Quantum calculations on the rate constant for the O+OH reaction*, Chem. Phys. Letters*, **112**, 346-350.
24. Hirschfelder, J.O., Curtiss, C.F., and Bird, R.B. (1964) *Molecular Theory of the Gases and Liquids*, Wiley, New York.
25. Harding, L.B., Maergoiz, A.I., Troe, J., and Ushakov, V.G. (2000) Statistical rate theory for the HO+O$\leftrightarrow$HO$_2$$\leftrightarrow$H+O$_2$ reaction system, *J. Chem. Phys.*, **113**,11019-11034.
26. Pastrana, M.R., Quintales, L.A.M., Brandao, J., and Varandas, A.J.C. (1990) Recalibration of a single-valued double many-body expansion potential energy surface for ground-state HO$_2$, *J. Phys. Chem.* **94**, 8073-8080.
27. Walch, S.P., Rohlfing, C.M., Melius, C.F., and Bauschlicher, Jr., C.W. (1988) Theoretical characterization of the minimum energy path for the reaction H+O$_2$$\rightarrow$ HO$_2$*$\rightarrow$HO+O, *J. Chem. Phys.* **88**, 6273-6281.
28. Umanskii, S.Ya. and Nikitin, E.E. (1969) Elektronenwellenfunktionen und Terme zweiatomiger Molekuele, *Theoret. chim. Acta (Berl.),* **13**, 91-105.
29. Nikitin, E.E. and Umanskii, S.Ya. (1984) *Theory of Slow Atomic Collisions*, Springer, Berlin-Heidelberg.
30. Karna, S.P. (1996) Spin-unrestricted time-dependent Hartree-Fock theory, *J. Chem. Phys.*, **104**, 6590-6605.
31. Landau, L.D. and Lifshitz, E.M. (1977) *Quantum Mechanics*, Pergamon, Oxford.

DIFFERENTIAL CROSS SECTIONS FOR ABSTRACTION REACTIONS OF HALOGEN ATOMS WITH MOLECULAR HYDROGEN INCLUDING NONADIABATIC EFFECTS

MILLARD H. ALEXANDER AND YI-REN TZENG
Department of Chemistry and Biochemistry, Institute for Physical Science and Technology, and Chemical Physics Program, University of Maryland, College Park, MD 20742-2021, USA

DIMITRIS SKOUTERIS
Dipartimento di Chimica, Università di Perugia, 06123 Perugia, Italy

Abstract We describe in detail the determination of differential cross sections for the abstraction reaction of a halogen atom with molecular hydrogen. As an illustration we give some examples of differential cross sections for the $F+H_2 \rightarrow HF+H$ and $Cl+H_2 \rightarrow HCl+H$ reactions, extending calculations described in earlier publications from our research groups.

1. Introduction

Because of their experimental accessibility, the reactions of F and Cl with H_2 and its isotopomers have become paradigms for exothermic triatomic reactions.[1] The high-quality *ab initio* $F+H_2$ potential energy surface (PES) of Stark and Werner (SW) [2] has been used in a number of quantum-scattering calculations [37] as well as quasi-classical trajectory studies.[6, 8] These theoretical studies have successfully reproduced the major features seen in both the photodetachment spectrum of the FH_2^- ion [3, 9] and the molecular-beam scattering studies of the reaction of F with H_2,[10] D_2,[11, 12] and HD.[11, 13, 14] Concurrently, numerous quasiclassical trajectory and various quantum scattering investigations have been reported for the $Cl+H_2$ reaction [15-18] on several potential energy surfaces (PESs).[19-21]

Approach of the H_2 molecule to a halogen atom splits the degeneracy of the ^2P state of the atom. Two electronic states ($1^2A'$ and $1^2A''$; $^2\Sigma^+$ and $^2\Pi$ in linear geometry) correlate adiabatically with the ground-state atomic reactant ($^2P_{3/2}$) while a third state ($2^2A'$; $^2\Pi$ in linear geometry) correlates adiabatically with the excited-state atomic reactant ($^2P_{1/2}$).[22] Of these, only the $1^2A'$ electronic state correlates with the electronic ground state of the products [$HX(X^1\Sigma^+)$ + $H(^2S)$]. The two other electronic states correlate with electronically excited states of the products [$HX(a^3\Pi)$ + $H(^2S)$] which are considerably higher in energy [23, 24] and, consequently, energetically inaccessible at low to moderate collision energies.

The presence of these three electronic states, as well as the sizable spin-orbit (SO) splitting in the F and Cl atoms (1.15 kcal/mol for F and 2.52 kcal/mol for Cl [25]) raises two important questions: (1) what is the reactivity of the excited ($^2P_{1/2}$) spin-orbit state relative to that of the ground ($^2P_{3/2}$) state and (2) how well is the dynamics of the reaction described by calculations on a single, electronically adiabatic potential energy surface (PES). If the reaction were to proceed adiabatically on a single PES, as would be predicted by the Born-Oppenheimer (BO) approximation, then the excited SO state should not react.[26, 27]

For F+H$_2$ and its isotopomers the molecular beam, scattering studies mentioned above [10, 12] indicate that the reactivity of the excited spin-orbit state is below the sensitivity level of these experiments at collision energies below 2 kcal/mol. (The barrier on the SW PES with the full spin-orbit Hamiltonian included is $\approx$ 1.9 kcal/mol [25]). In subsequent molecular-beam experiments on the F+HD reaction Liu and co-workers [13] also found that the reactivity of the spin-orbit excited state was only a few percent of that of the ground state.

In recent molecular beam experiments, Liu and co-workers [28, 29] used two different Cl atom sources to separate the reactivity of the two SO states of the Cl atom. Except at the lowest collision energies, they conclude that the excited SO state has a significantly larger reactive cross section. This result is indeed surprising, because the body of experimental studies indicates that reactions which are allowed within the BO approximation (adiabatically allowed) always dominate.[27, 30]

Theoretical investigations of the role of excited electronic surfaces in the F+H$_2$ reaction date back to the pioneering work of Tully.[31] Although scattering studies which include one (or both) of the excited electronic states have been reported by several groups,[32] these calculations have been subject to various approximations, both in the treatment of the dynamics as well as in the description of the PESs and couplings (non-adiabatic, Coriolis, and spin-orbit). The vast majority of recent scattering studies of the Cl+H$_2$ and F+H$_2$ reactions have been based on a single, electronically-adiabatic potential energy surface.

In several recent papers, we have presented the complete methodology for the time-independent, fully-quantum treatment of the abstraction reactions of halogen atoms with molecular hydrogen.[33, 34] For the first time, we account for, accurately and completely, the electronic angular momenta of the halogen reactant and the spin-orbit coupling. The treatment involves six three-dimensional hypersurfaces, four of which describe the diabatic potential energy functions and two of which describe the coordinate dependence of the spin-orbit coupling. All Coriolis terms are included. The scattering is treated fully quantum mechanically, without any dynamical approximations.

More recently we described the calculation of differential cross sections (DCSs) for the Cl+H$_2$ reaction.[35] These were used in the interpretation of ongoing crossed molecular beam studies. The rationale for this investigation is that DCSs offer, in principle, a far more detailed probe of the dynamics than the integral cross sections (ICSs). This paper [35] marked the first ever fully quantum mechanical determination of reactive DCSs for a set of coupled *ab initio* PESs. Because of space constraints, no details of the determination of the DCSs were reported.[35] The goal of the present article is to present, for future reference, these details.

The organization of this paper is as follows: The next two sections contain a brief review of the time-independent description of the collision dynamics and the details of

the application to reactions involving multiple PES's. Discussion of the determination of DCSs is the subject of Sec. IV. Section V reviews briefly the adiabatic and diabatic PESs which are necessary to describe the X+H$_2$ reaction, and, in particular, the results of *ab initio* determinations of these PESs for the FH$_2$ and ClH$_2$ systems. The results of representative calculations of DCSs for Cl+H$_2$ and F+H$_2$ are given in Sec. VI. We close with a summary and conclusion.

2. Hamiltonian and Basis Functions

The reactive scattering calculations are carried out in a manner similar to the recent work of Schatz and co-workers on the Cl+HCl exchange reaction.[36, 37] We use an extension of the ABC code of Manolopoulos and co-workers.[5, 38] The scattering wavefunction is expanded in an over-complete set of products of electronic-vibrational-rotational states for each of the arrangement channels. Canonical orthogonalization is then used to construct the surface eigenfunctions in each sector. For more details on the methodology [39] and the computer code (as applied to triatomic reactions in which the electronic fine structure of the atoms is ignored), we refer the reader to the earlier paper of Skouteris *et al.* [38]. We shall present here only those details which are relevant to the inclusion of the electronic fine structure and the participation of multiple PESs in the determination of DCSs for reaction.

We write the total Hamiltonian for collision of a halogen (X) in a ^2P electronic state and the H$_2$ (or any other diatomic) molecule as

$$H(\vec{R},\vec{r},\vec{q}) = T_{nuc}(\vec{R},\vec{r}) + H_{el}(\vec{q};\vec{R},\vec{r}) + H_{so}(\vec{q};\vec{R},\vec{r}) \qquad (1)$$

Here $\vec{q}$ is a collective notation for the electronic coordinates, H_{el} is the electronic Hamiltonian, which, in the Born-Oppenheimer sense, depends parametrically on the positions of the three nuclei, and H_{SO} is the spin-orbit Hamiltonian, which is not included in H_{el}.

The nuclear coordinates $\vec{R}$ and $\vec{r}$ in eq. 1 designate the Jacobi vectors [40] in any one of the three chemical arrangements (X+HH, H+HX, or HX+H). In terms of the mass-scaled Jacobi coordinates S and s, one defines Delves hyperspherical coordinates r and q .[40] At each value of the hyperradius r we expand the total wavefunction in an overcomplete basis of rotational-vibrational-electronic wavefunctions in each arrangement. In the X+H$_2$ arrangement there are six electronic states. For a halogen atom with a p^5 electron occupancy these states correspond to the three spatial orientations of the p hole and the two possible spin-projection quantum numbers. For the halogen halides, the lowest excited state is of Π symmetry, and lies far above the ground state ($X\ ^1\Sigma^+$) in the region of the molecular minimum.[24] If we neglect these excited Π states, then, in each H+HX arrangement, we need retain only two states, which correspond to the HX molecule in its ground electronic state ($^1\Sigma^+$) combined with the two possible spin-projection quantum numbers of the H atom.

In each arrangement the basis functions are [34, 36, 41, 42]
$$|\,J\,M\,K\,\mathrm{v}\,j\,k\,\lambda\,\sigma>=$$

$$\frac{2}{\sin(2\theta)}\left(\frac{2J+1}{4\pi}\right)^{1/2} D_{MK}^{J*}(\Omega)\,Y_{jk}(\gamma,0)\,\phi_{\mathrm{v}j}(\theta;\rho)\,|\,\lambda\,\sigma>. \qquad (2)$$

Here J is the total angular momentum, with projection M along the space-frame z-axis and projection K along the Jacobi vector $\vec{R}$ of the relevant arrangement. The quantum number j designates the rotational angular momentum of the diatomic moiety in the same arrangement, with projection k along $\vec{R}$. Here, also, $D_{MK}^{J*}(\Omega)$ is a Wigner rotation matrix element,[43] $Y_{jk}(\gamma, 0)$ is a spherical harmonic,[43] and $\phi_{vj}(\theta; \rho)$ is the solution of a "vibrational" reference problem corresponding to motion in the hyperangle q at the given (fixed) value of r.[38]

The quantities l and s in eq. 2 are the projection of the electronic orbital and spin angular momenta along $\vec{R}$. Since we consider here only doublet electronic states, the spin part of the wavefunction corresponds to $s = 1/2$ and $s = \pm 1/2$. The projection quantum numbers are related as follows

$$K = k + l + s. \tag{3}$$

Note that we are using here a fully uncoupled treatment of the electronic angular momentum of the X atom [44] (case 2A in the notation of Dubernet and Hutson [45]). By contrast, in the work of Schatz and co-workers [36, 37] on the Cl+HCl exchange reaction, a "partially-coupled" basis set is used in which the total angular momentum j_a of the atom ($\vec{j}_a = \vec{l} + \vec{s}$) appears explicitly. The advantage of the fully uncoupled electronic basis set is twofold: First, it is not necessary to specify explicitly the magnitude l of the electronic orbital angular momentum, which is a good quantum number only asymptotically. Second, use of a fully uncoupled basis set allows a direct connection with the results of *ab initio* calculations of the potential energy surface, without recourse to expansions in angular functions.[34]

To solve the close-coupled reactive scattering equations, one must first construct surface functions in each sector,[41, 46] by diagonalizing the total Hamiltonian, exclusive of the kinetic operator corresponding to radial motion in the hyperradius r, in the multiple arrangement basis consisting of the states defined by eq. 2. Because the basis is non-orthogonal, it is necessary to determine matrix elements not only of the Hamiltonian but also of the overlap between the basis functions in the various arrangements. In addition to the electrostatic interaction potential and the spin-orbit Hamiltonian, it is also necessary to determine matrix elements of the orbital angular momentum $L^2 = (J - l - s - j)^2$. For details on the determination of the matrix elements of the electronic and spin-orbit Hamiltonians and the orbital angular momentum, we refer the reader to Ref. [34].

3. Solution of the Time-Independent Close-Coupled Equations

As discussed above, for each value of the hyperradius r, we expand the total scattering wavefunction in a set of previously determined orthogonal surface functions. A log-derivative method [47] is used to propagate the solution numerically, from small r to large r. The parameters which control the accuracy of the integration are (a) the number of sectors, (b) the number of vibration-rotation states included for each electronic state in each arrangement, and (c) the maximum value of the total projection quantum number K. These are increased until the desired quantities (integral and/or

differential cross sections) have converged to within a reasonable limit. For abstraction reactions dominated by linear (or near linear) barriers, converged results can be obtained with only a few values of K, which greatly reduces the necessary computer time.

To reduce further the number of basis functions which must be simultaneously considered, we use definite-parity linear combinations of the signed-K rotation-vibration-electronic basis functions (eq. 2). These definite parity combinations are defined by [48]

$$|J M K v j k \lambda \sigma \eta > = 2^{-1/2} \left[| J M K v j k \lambda \sigma > + \eta | J M, -K, v j, -k, -\lambda, -\sigma > \right] , \quad (4)$$

where $h = \pm 1$, and the half-integer projection quantum number K is taken to be positive in this "definite-parity" basis.

Since the Hamiltonian is symmetric with respect to exchange of the two hydrogen nuclei, for reactions involving identical nuclei (X+H_2/D_2) the wavefunctions must be either symmetric or antisymmetric with respect to this operation. For the basis functions in the reactant channel, the symmetry affects only the rotational wavefunction of the H_2 moiety, which has the symmetry $(-1)^j$. Thus, only even (*para*-H_2) or odd (*ortho*-H_2) values of j need be included in the expansion in eq. 2. For the product arrangement, we use the exchange-symmetrized basis functions [49]

$$\Psi^{\pm} = 2^{-1/2} [\Psi_2 \pm (-1)^j \Psi_3] , \quad (5)$$

where Y_2 and Y_3 are basis functions [eq. 2] in each product arrangement (H+XH and HX+H) and the rotational quantum number j refers to the HX rotation. The "+" functions must be used in calculations involving the reaction of pH_2, and the "−" functions, in calculations for oH_2.

The propagation of the solutions to the CC equations are carried out entirely in the fully-uncoupled, body-frame basis of eq. 2. At the end of the propagation, but before extraction of the S matrix, we transform the log-derivative matrix into the partially coupled basis discussed above. Here, the atomic states in the reactant arrangement are labeled by the total electronic angular momentum of the atom, j_a, and the projection of j_a along $\vec{R}$, which we designate k_a. In this basis the spin-orbit operator (and, hence, the total Hamiltonian) is diagonal. These partially-coupled atomic states correspond to the Russell-Saunders spin-orbit states of the halogen atom. Instead of eq. 2, the partially-coupled basis states are defined as

$$| J M K v j k j_a k_a > =$$

$$\frac{2}{sin(2\theta)} \left(\frac{2J+1}{4\pi} \right)^{1/2} D_{MK}^{J*}(\Omega) Y_{jk}(\gamma, 0) \phi_{vj}(\theta; \rho) | l s j_a k_a > . \quad (6)$$

Since l and s are fixed ($l = 1$ and $s = 1/2$), these indices are suppressed in the state label on the left-hand-side of eq. 6. The transformation between the uncoupled states of eq. 2 and the partially coupled states of eq. 6 is diagonal in K, j, k, and v, and given by

$$| J M K v j k j_a k_a > = \sum_{\lambda \sigma} (l \lambda s \sigma | j_a k_a) | J M K v j k \lambda \sigma > , \quad (7)$$

where $(\cdots | \cdot\cdot)$ is a Clebsch-Gordan coefficient.[50] In the product arrangement, because the H atom has an electronic orbital angular momentum of zero, we need retain only a single electronic state. Consequently, it is not necessary to carry out a similar transformation of the electronic basis states in the product arrangement.

4. Differential Cross Sections

The determination of integral reactive cross sections, either fully state-specific in the product vibrational and rotational quantum numbers, or summed over all product states, has been discussed in a previous paper.[34] Basically, the probability for reaction at each value of the total angular momentum J is proportional to the square of the fully-state resolved S-matrix element for the transition in question. The ICS is then obtained by summing over all values of the total angular momentum J and multiplying by p divided by the square of the reactant wavevector.

In terms of the definite-parity S-matrix elements, we have

$$S^J(j_a\, k_a\, j\, k\, v, \sigma\, j'k'v')=S^J(j_a-k_a\, j-k\, v, -\sigma\, j'-k'v')$$

$$\tfrac{1}{2}\left[S^{J\eta=+1}(j_a\, k_a\, j\, k\, v, \sigma\, j'k'v')+S^{J\eta=-1}(j_a\, k_a\, j\, k\, v,\, \sigma\, j'k'v')\right] \tag{8a}$$

where $h = \pm 1$, and

$$S^J(j_a\, k_a\, j\, k\, v, -\sigma\, j'-k'v')=S^J(j_a-k_a\, j-k\, v, \sigma\, j'k'v')$$

$$\tfrac{1}{2}\left[S^{J\eta=+1}(j_a\, k_a\, j\, k\, v, \sigma\, j'k'v')-S^{J\eta=-1}(j_a\, k_a\, j\, k\, v, \sigma\, j'k'v')\right] \tag{8b}$$

The DCS is the square of the scattering amplitude. In the treatment of reactive scattering on a single potential energy surface, in which the only internal angular momentum (j) is the orbital (end-over-end) motion of the diatomic moiety, the DCS and scattering amplitude are often determined in the helicity representation, in which the states are defined by the vibrational (v) and rotational (j) quantum numbers of the diatomic and the projection of the latter along the reactant and arrangement channel Jacobi vectors. We have

$$d\sigma_{jkv\to j'k'v'}(\theta, E_{col})=\left|\frac{1}{2ik_i}\, f_{jkv\to j'k'v'}(\theta, E_{col})\right|^2 . \tag{9}$$

where k_j is the incident wavevector. The scattering amplitude is given by [51]

$$f_{jkv\to j'k'v'}(\theta, E_{col})=\frac{1}{2ik_i}\sum_J (2J+1)\, d^J_{kk'}(\theta)S^J(j\, k\, v, j'k'v'; E_{col}+\varepsilon_{jv}) , \tag{10}$$

where q is the center of mass scattering angle and $d^J_{kk'}$ is a Wigner reduced rotation matrix element.[43] Note that $\vec{j}=\vec{J}-\vec{L}$, where $\vec{L}$ is the orbital angular momentum of the atom with respect to the diatomic fragment. For simplicity, we shall suppress the vibrational quantum numbers. By convention, the center-of-mass scattering angle q is measured counterclockwise from the initial relative velocity vector, as shown in the schematic Newton diagram in Fig. 1.
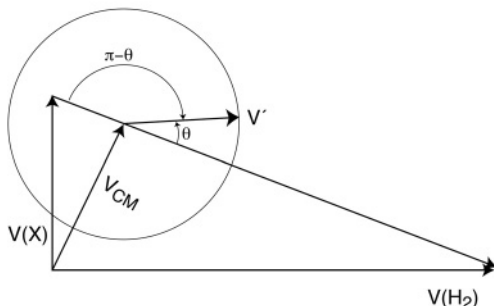
Figure 1.   Schematic Newton diagram for the reaction of a halogen atom with molecular hydrogen. The vector designated V' is the velocity vector of the HX products in the center-of-mass frame.

In cases where the cm scattering angle is measured clockwise from $\vec{R}$, then in eqs. 9 and 10 the angle θ should be replaced by. π-θ. Note that the scattering calculations, and hence the S matrix, are performed at discrete values of the total energy. Consequently, the determination of DCSs for different initial states, but at a given initial translational energy, requires scattering calculations at more than one value of the total energy.

　　We shall designate the total internal angular momentum by j_{12}, where, for reaction of a ^2P atom

$$\vec{j}_{12} = \vec{J} - \vec{L} = \vec{j}_a + \vec{j} = \vec{l} + \vec{s} + \vec{j} \ . \tag{11}$$

In the study of the X+H$_2$ reactions the expression for the scattering amplitude analogous to eq. 10 is

$$f_{j_{12}k_{12} \to j_{12}{'}k_{12}{'}}(\theta, E_{col}) =$$

$$\frac{1}{2ik_i} \sum_J (2J+1)\, d^J_{k_{12}k_{12}{'}}(\theta) S^J (j_{12}\,k_{12},\, j_{12}{'}k_{12}{'};\, E_{col} + \varepsilon_j), \tag{12}$$

where k_{12} is the helicity frame projection of the total internal angular momentum. We note that the S matrix which appears in eq. 12 is expressed in a fully-coupled basis, in which all the internal angular momenta are first coupled to form $\vec{J}_{12}$, which is then coupled with the atom-molecular orbital angular momentum $\vec{L}$, as summarized by eq. (11).

　　However, in the scattering calculations described in Secs. II and III above, the S matrix is obtained in a basis in which the reactant states, determined in a partially coupled basis, are defined by the quantum numbers $j_a\,k_a jk$ and the product states, by the quantum numbers $s\sigma jk$. The relation between these bases and the fully-coupled basis defined in the preceding paragraph is (in the reactant arrangement)

$$|\,(j_a\ j) j_{12}k_{12}\rangle = \sum_{k_a k} (j_a k_a jk\,|\,j_{12}k_{12})|\,j_a k_a j\,k\rangle \ , \tag{13}$$

where $j_a = 1/2$ or 3/2. In the product arrangement the corresponding relation is

$$|\,(s\ j') j_{12}{'}k_{12}\rangle = \sum_{\sigma k} (s\sigma j'k'\,|\,j_{12}k_{12})|\,s\sigma j'k\rangle \ . \tag{14}$$

Consequently, the *S* matrix elements in the fully-coupled basis are given by

$$S^J(j_{12}k_{12}, j_{12}'k_{12}') =$$
$$\sum_{k_a k \sigma k'} \left(j_a k_a jk \mid j_{12}k_{12} \right) \left(s\sigma j'k' \mid j_{12}'k_{12}' \right) S^J(j_a k_a jk, s\sigma j'k') \quad , \tag{15}$$

where, for simplicity, we have suppressed the energy argument in the *S*-matrix elements.

The expression for the scattering amplitude (eq. 12) can then be expressed in terms of *S*-matrix elements in the partially-coupled basis as

$$f_{j_{12}k_{12} \rightarrow j_{12}'k_{12}'}(\theta, E_{col}) = \frac{1}{2ik_i} \sum_{J}(2J+1) \, d^J_{k_{12}k_{12}'}(\theta)$$
$$\sum_{k_a k \sigma k'} \left(j_a k_a jk \mid j_{12}k_{12} \right) \left(s\sigma j'k' \mid j_{12}'k_{12}' \right) S^J(j_a k_a jk, s\sigma j'k') . \tag{16}$$

However, the expression for the scattering amplitude can be transformed, similarly to eq. 15, into an expression between states expanded in the partially coupled basis, namely (hereafter, for simplicity, we suppress the dependence on E_{col})

$$f_{j_{12}k_{12} \rightarrow j_{12}'k_{12}'}(\theta) =$$
$$\sum_{k_a' k'' \sigma' k'''} \left(j_a k_a' jk'' \mid j_{12}k_{12} \right) \left(s\sigma' j'k''' \mid j_{12}'k_{12}' \right) f_{j_a k_a' jk'' \rightarrow s\sigma' j'k'''}(\theta) \cdot \tag{17}$$

Setting these last two equations equal, and using the orthogonality of the Clebsch-Gordan coefficients, we can obtain the following equation for the scattering amplitude in the partially coupled basis in terms of the *S*-matrix elements in the same, partially-coupled basis

$$f_{j_a k_a' jk'' \rightarrow s\sigma' j'k'''}(\theta) = \frac{1}{2ik_i} \sum_{J} \sum_{j_{12}k_{12}j_{12}'k_{12}'}(2J+1) \, d^J_{k_{12}k_{12}'}(\theta)$$
$$\sum_{k_a k \sigma k'} \left(j_a k_a jk \mid j_{12}k_{12} \right) \left(j_a k_a' jk'' \mid j_{12}k_{12} \right) \left(s\sigma j'k' \mid j_{12}'k_{12}' \right) \tag{18}$$
$$\times \left(s\sigma' j'k''' \mid j_{12}'k_{12}' \right) S^J(j_a k_a jk, s\sigma j'k') .$$

Because the Clebsch-Gordan coefficient $\left(j_1\mu_1 j_2\mu_2 \mid j\mu \right)$ vanishes unless the sum of the first two projection quantum numbers equals the third $(\mu_1 + \mu_2 = \mu)$, only one value of k_{12} and only one value of k_{12}' survive on the right-hand-side of this last equation. Subsequently, we can carry out the sum over j_{12} and j_{12}' and use the orthogonality relation of the Clebsch-Gordan coefficients (with respect to summing over j_{12},k_{12} and j_{12}',k_{12}') to obtain the simplified expression, which we could have perhaps anticipated,

$$f_{j_a k_a jk \rightarrow s\sigma j'k'}(\theta) = \frac{1}{2ik_i} \sum_{J}(2J+1) \, d^J_{k_a+k, \sigma+k'}(\theta) \, S^J(j_a k_a jk, s\sigma j'k') . \tag{19}$$

If we now insert, explicitly, the reactant and product vibrational quantum numbers, we obtain

$$f_{j_a k_a j k v \to s \sigma j' k' v'}(\theta) =$$

$$\frac{1}{2ik_i} \sum_J (2J+1) d^J_{k_a+k, \sigma+k'}(\theta) \, S^J(j_a k_a j k v, s \sigma j' k' v') \cdot \quad (20)$$

The corresponding DCS is obtained by squaring this expression

$$d\sigma_{j_a k_a j k v \to s \sigma j' k' v'}(\theta) = \left| f_{j_a k_a j k v \to s \sigma j' k' v'}(\theta) \right|^2 . \quad (21)$$

The DCS, summed and averaged over projection quantum numbers, for reaction to yield HX products in rotational level j' in vibrational manifold v' is given by

$$d\sigma_{j_a j v \to s j' v'}(\theta) = \frac{1}{(2j+1)(2j_a+1)} \sum_{k_a k \sigma k'} d\sigma_{j_a k_a j k v \to s \sigma j' k' v'}(\theta) . \quad (22)$$

One can further sum over j' to obtain an expression for the total DCS for reaction to yield HX products in vibrational level v', summed over all accessible rotational levels in this vibrational manifold, namely

$$d\sigma_{j_a j v \to v'}(\theta) = \frac{1}{(2j+1)(2j_a+1)} \sum_{k_a k j' \sigma k'} d\sigma_{j_a k_a j k v \to s \sigma j' k' v'}(\theta) . \quad (23)$$

5. Potential Energy Surfaces: Adiabatic and Diabatic

Werner and co-workers [2, 21, 34] used internally-contracted multi-reference configuration-interaction (IC-MRCI) calculations, based on state-averaged (three-state) multi-configuration, self-consistent-field (MCSCF) calculations with large atomic orbital basis sets, to determine the three electronically adiabatic Cl(F)+H$_2$ PESs in the reactant arrangement: $1A'$, $2A'$, and $1A''$. These all correlate with $X(^2P) + H_2$. These three adiabatic electronic states are the IC-MRCI approximations to the three lowest eigenfunctions of H_{el}, namely

$$H_{el}(\vec{R}, \vec{r}; \vec{q}) \, \psi_i(\vec{R}, \vec{r}; \vec{q}) = E_i(\vec{R}, \vec{r}) \, \psi_i(\vec{R}, \vec{r}; \vec{q}) , \quad (24)$$

where the subscript i = 1,2,3 designates the $|1A'>$, $|2A'>$, and $|1A''>$ states. The eigenvalues E_i define the three adiabatic PESs.

We specifically subtract the energies of the reactants at infinite X–H$_2$ separation, so that

$$V_i(\vec{R}, \vec{r}) = E_i(\vec{R}, \vec{r}) - E_X - E_{H_2}(r) . \quad (25)$$

Here E_X designates the electronic energy of the X atom in its ^2P state exclusive of the spin-orbit Hamiltonian. The zero of energy will be defined by the equilibrium internuclear separation of the H$_2$ molecule as determined in the IC-MRCI calculations, so that

$$V_i(|\vec{R}| = \infty, |\vec{r}| = r_e) = 0 , \quad (26)$$

where r_e is the equilibrium internuclear separation of the H$_2$ molecule, as predicted by IC-MRCI calculations.

By analysis of the coefficients in the CI expansion of the XH$_2$ electronic wavefunctions, the two PES's of A' reflection symmetry can be transformed to an approximate diabatic basis,[2, 52] in which the orientation of the p hole on the X atom is fixed with respect to the plane defined by the three atoms. Here we take $\vec{R}$ to define

the z axis and chose the y axis to be perpendicular to the triatomic plane. We shall designate the diabatic states by the projections of the electronic orbital and spin angular momenta along $\vec{R}$. We use the compact Cartesian notation $|\Pi_x>$, $|\Pi_y>$, and $|\Sigma>$. The two adiabatic states of A' symmetry correspond to a 2 x 2 rotation of the $|\Pi_x>|$ and $|\Sigma>$ diabatic states, namely

$$\begin{bmatrix} |1A'\rangle \\ |2A'\rangle \end{bmatrix} = T \begin{bmatrix} |\Sigma\rangle \\ |\Pi_x\rangle \end{bmatrix} \quad , \tag{27}$$

where

$$T = \begin{bmatrix} \cos\zeta & \sin\zeta \\ -\sin\zeta & \cos\zeta \end{bmatrix} \quad . \tag{28}$$

Here the transformation angle ξ depends on R, θ and γ. Since there is no coupling between the $|\Pi_y>$ state, of A'' reflection symmetry, with the $|\Pi_x>$ and $|\Sigma>$ states, of A' reflection symmetry, the adiabatic and diabatic states of A'' reflection symmetry are identical. Alternatively, we can define the diabatic states in terms of signed-λ, rather than Cartesian, projections, namely $|\Pi_1>$, $|\Pi_{-1}>$, and $|\Sigma>$. These signed-λ states are those which we used above in the expansion of the scattering wavefunction. Note that the state we designate as "Σ" corresponds to $\lambda = 0$.

As presented in detail in an earlier paper,[34] the matrix of the interaction potential, in the 6 x 6 basis defined by the three Cartesian diabatic states and the two possible spin projections (which are also defined with respect to $\vec{R}$) can be described in terms of three diagonal, electronically diabatic PES's: V_{xx}, V_{yy}, and V_{zz}, [53] as well as a fourth PES, V_{xz}, which is the coupling between the two states of A' symmetry. Each of these four PES's is a function of the three internal coordinates. Thus, the description of the interaction in the electronically diabatic basis, which involves these four potential energy functions is equivalent to the description in the electronically adiabatic basis, which involves three potential energy surfaces ($V_{1A'}$, $V_{2A'}$, and $V_{1A''}$) plus the coordinate dependent mixing angle ξ .

The matrix of the spin-orbit Hamiltonian is determined fully by two components,[2]

$$A(R, r, \theta) \equiv i <\Pi_y |H_{SO}|\Pi_x> \tag{29}$$

and

$$B(R, r, \theta) \equiv <\overline{\Pi}_x |H_{SO}|\Sigma> \quad , \tag{30}$$

where

$$\lim_{R\to\infty} B = \lim_{R\to\infty} A \tag{31}$$

The spin-orbit functions A and B can be determined in the *ab initio* calculations, along with the PESs.

The three-state calculations carried out by Werner and co-workers [2, 21, 34] did not extend into the product arrangement. In these regions the lowest electronically adiabatic PES from the three-state calculations was smoothly merged to either the single F+H$_2$ PES of Stark and Werner (SW) [2] or the single Cl+H$_2$ PES of Bian and Werner (BW).[20] The excited surface of A' symmetry, as well as the single surface of A'' symmetry, was harmlessly extrapolated to a high repulsive plateau. In addition, the coupling potential was extrapolated to zero, outside of the region in which the three-state calculations were performed. Thus, outside the reactant arrangement, the

description of the FH_2 and ClH_2 systems is *unchanged* from the original SW or BW fits with the addition of two high-energy electronic states. For the $F+H_2$ system, the set of diabatic potential energy functions, along with the coordinate dependence of the two spin-orbit matrix elements is known, collectively, as the Alexander-Stark-Werner (ASW) PES,[34] and, for the $Cl+H_2$ system, as the Capecchi-Werner (CW) PES.[18, 21]

In the expression for the basis functions, the electronic states which appear in eq. (2) have a well-defined value of the projection of the electronic orbital angular momentum λ, even though l itself does not have a definite value, except when the X atom is infinitely far from the H_2.[48] In the pure-precession limit, l would everywhere fixed at its value for the separated halogen atom reactant, namely $l= 1$.

When the spin-orbit Hamiltonian is included, the lowest electronically adiabatic PES corresponds to the lowest eigenvalue of $H_{el} +H_{SO}$. Since the Π states lie so much higher than the Σ state at the barrier, the Π - Σ component of the spin-orbit coupling [the B term of eq. (20)] has only a small effect on the Σ state. [The Π–Π component, A (eq. 19), will affect the Σ state only to higher order]. By contrast, asymptotically, the presence of the spin-orbit coupling results in a lowering of the energy of the lowest electronically adiabatic state by 1/3 the value of the spin-orbit constant of the atom. As has been discussed previously,[2, 6, 9, 36] the net result is an *increase* in the height of the barrier, with respect to the $F+H_2$ reactants, by approximately 1/3 the halogen atom spin-orbit splitting. After inclusion of this spin-orbit contribution, the predicted FH_2 barrier is 2.33 kcal/mol [34] and the predicted $Cl+H_2$ barrier is 8.45 kcal/mol.[20] In addition, the spin-orbit Hamiltonian will make an appreciable contribution in the region of the van der Waals minimum. The effect of this will not be explored further in the present article.

6. Calculations

Differential cross sections were determined for the $Cl+H_2$ reaction at four different initial collision energies (3.85, 4.25, 5.2 and 5.85 kcal/mol), which correspond to those in two recent molecular-beam scattering studies.[28, 35] The details of the calculation were similar to those reported in several earlier investigations of this system.[18, 35]. Values of the total angular momentum ranging from $J = 0.5$ to $J =24.5$ were included in the calculation. Figure 2 shows the reactive DCS summed over all rotational levels of the v=0 vibrational manifold of the HCl products at these collision energies. We observe that the DCSs are all strongly backward peaked, and very small in magnitude. This is a reflection of the low collision energy relative to the height of the barrier ($E_a = 8.45$ kcal/mol).
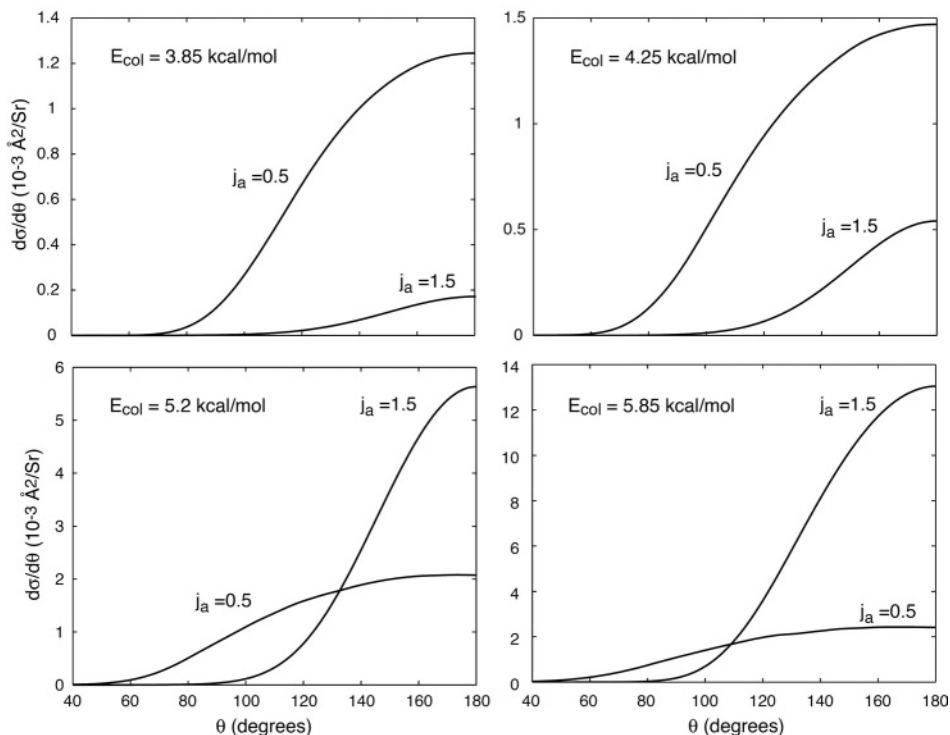
Figure 2. DCS for reaction of Cl with $H_2(j=0)$ to yield $HCl(v=0)$, summed over all rotational levels of the product. Shown are cross sections for reaction of the ground ($j_a=1.5$) and excited ($j_a=0.5$) spin-orbit states of the Cl atom.

As the collision energy increases, the magnitude of the cross sections increases, as expected. Additionally, we observe that the relative reactivity of the two spin-orbit states changes dramatically over this range. Because of the sizable spin-orbit splitting in the Cl atom (2.5 kcal/mol), at a given collision energy the total energy available in the Cl*+H_2 will be that much larger. Although reaction of Cl* is adiabatically forbidden, at very low collision energies, where the adiabatically allowed reaction (Cl+H_2) is strongly classically forbidden by the large barrier, the additional energy in the Cl*+H_2 reaction will enhance the reactivity of the adiabatically forbidden channel. This effect can also be seen, of course, in the energy dependence of the ICSs.[18]

If the sum of the electronic interaction Hamiltonian plus the SO coupling in the 6x6 electronic basis is diagonalized at each value of the coordinates, the lowest root will define a fully (electronic + spin-orbit) adiabatic X+H_2 PES. This is designated as the CWad PES for Cl+H_2 [18] and the Hartke-Stark-Werner (HSW) PES for F+H_2.[9] The reader should note that these PESs are different from the Bian-Werner (BW2) and Stark-Werner (SW) fits to the electronically adiabatic (no spin-orbit Hamiltonian) PES for, respectively, Cl+H_2 and F+H_2. Because the CWad and HSW PESs have the full spin-

orbit Hamiltonian included, they provide the single-surface analog to the CW and ASW PESs. Comparison of integral and/or differential calculations determined on the CW as compared to the CWad PESs (or the ASW as compared to the HSW PESs) will be a direct probe of the effect of nonadiabatic couplings as the reaction occurs.

In the multi-state formulations of the X+H$_2$ reaction, four states correlate with the ground-state [X($^2P_{3/2}$)] reactants. In collinear geometry these are the $^2\Sigma_{1/2}$ and $^2\Pi_{3/2}$ states.[34]   Since the $^2\Pi_{3/2}$ states are repulsive and hence unreactive, to zeroth order, only 50% of the reactants will approach on a PES which leads to reaction. However, in the single-state calculations we assume that all (100 %) of the reactants will approach on the reactive PES. Dividing the single PESs cross sections by 2 provides a simple compensation for this fundamental difference.[34, 54] Figure 3 compares the DCS for the Cl+H$_2$→HCl(v=0)+H reaction as predicted by three-state calculations on the CW PESs and single-state calculations on the CWad PES. These are compared with (dashed line) the predictions of single-surface calculations on the CWad PES. We observe (fig. 3, left panel) that the DCS predicted by the single-surface (CWad)
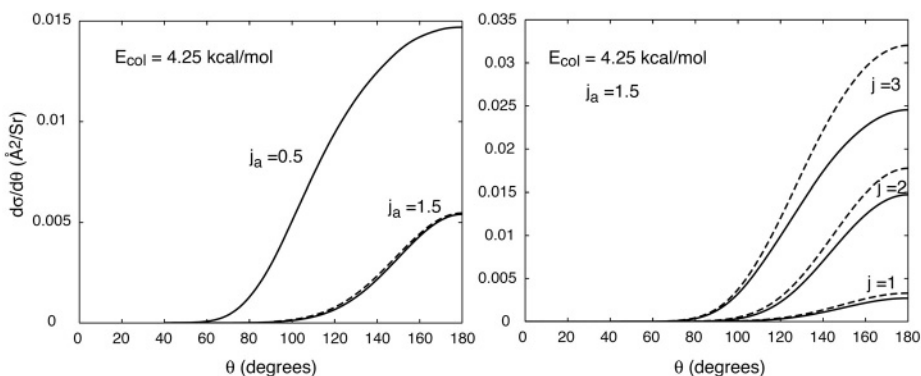

Figure 3.   (Left panel) DCS for reaction of Cl and Cl* with H$_2$(j=0) to yield HCl(v=0), summed over all rotational levels of the product. Shown are cross sections for reaction of the ground (j$_a$=1.5) and excited (j$_a$ =0.5) spin-orbit states of the Cl atom and (dashed line) predictions of single-surface calculations on the CWad PES. (Right panel) DCS for reaction of Cl with H$_2$(j=1, 2, and 3) to yield HCl(v=0), summed over all rotational levels of the product.

calculations with the single-surface ABC code [38] are (once divided by 2) virtually identical to the DCS for adiabatically allowed reaction of the $^2P_{3/2}$ state of the Cl atom from the multi-surface calculations based on the CW PESs. Since the methodology and formulation of the scattering are quite different, the good agreement confirms the accuracy of our multi-surface adaptation [34] of the ABC code.

In the right panel of fig. 3 this comparison is continued for reaction of Cl with H$_2$ in higher rotational levels. It is well known that rotational excitation of the H$_2$ greatly enhances the probability of reaction.[17]   This effect is apparent in the relative magnitudes of the DCSs shown in fig. 3. We also observe that the agreement between the single-surface CWad DCSs and the multi-surface CW DCSs deteriorates with increasing initial rotational excitation of the H$_2$ molecule. As we have already noted in our determination of ICSs for the Cl+H$_2$ reaction,[18] there are additional electronically inelastic channels in the multi-surface formulation which do not occur in the single-

surface treatment. The effect of these electronically inelastic channels is to decrease the flux leading to reaction, so that, when compared with the single-surface calculations, the multi-surface DCSs should be smaller. Coupling between reaction, which occurs on the lowest ($^2\Sigma^+$) PES, and an inelastic collision on the repulsive $^2\Pi$ PES, can be induced by several terms in the expansion of the L^2 operator, discussed at the end of Sec. II and in more detail in the Appendix to Ref. [34]. In particular, the $j \cdot l$, $j \cdot J$, and $j \cdot s$ terms will all vary linearly with the initial rotational angular momentum of the H_2 molecule. Consequently, we might anticipate that this inelastic loss mechanism will increase with increasing j, which is what is observed.
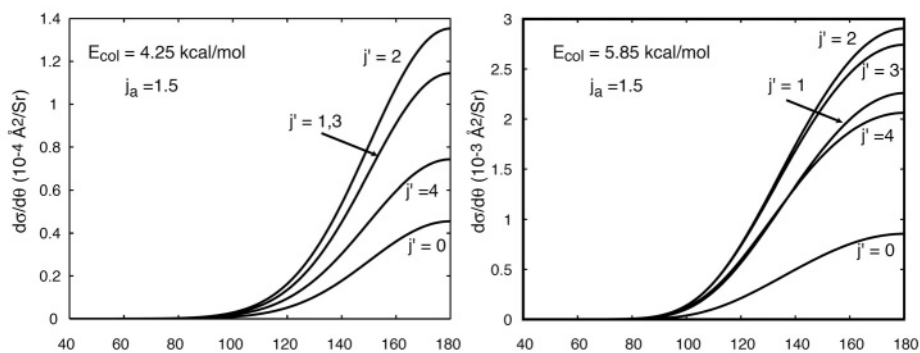

Figure 4. DCS for reaction of Cl with H_2(j=0) to yield HCl(v=0, j′) at two collision energies.

Figure 4 shows the dependence on final rotational state of the Cl+H_2(v=0, j =0)→ HCl(v=0,j′) DCSs at two different collision energies. We observe that the DCSs all have a very similar shape. Likely, this implies that the overall shape of the DCS is determined by the reactive probability (opacity) as a function of impact parameter and by an overall deflection function $\Theta(b)$, while the product final state distribution is governed by the shape of the PES in the exit region of the arrangement channels. We remark also that the determination of fully final-state resolved DCS does not present any particular difficulty for our time-independent method, but would not be feasible with some of the time-dependent methods which have been applied recently to the X+H_2 reactions.[7, 16]

We turn now to the F+H_2 system. Figure 5 shows reactive cross sections for the reaction of F($^2P_{3/2}$ and $^2P_{1/2}$) with H_2 in $j = 0$ at E_{col} =1.84, the lowest energy explored in the landmark molecular-beam experiment of Neumark *et al.*[10]   In contrast to the Cl+H_2 DCSs, we observe that even at this low energy the adiabatically allowed reaction has a considerably larger DCS than the adiabatically forbidden reaction of F*. Also in contrast to the Cl+H_2 DCSs, those for F+H_2 show a substantial sideways contribution and a pronounced forward peak. However, the DCS for reaction with H_2 in j =1, which makes up the largest fraction of a supersonic beam of nH_2, shows much less forward and sideways contributions to the DCS
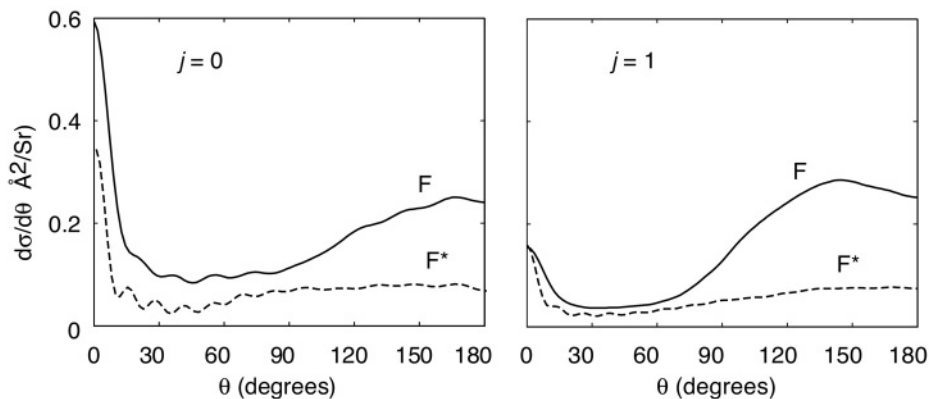
Figure 5. DCSs for reaction of F (solid curves) and F* (dashed curves) with $H_2(j=0)$ (left panel) and $H_2(j=1)$ (right panel) to yield HF, summed over all final vibrational and rotational levels, at $E_{col} = 1.84$ kcal/mol.

Figure 6 (next page) compares the prediction of the multi-surface calculations on the ASW PESs for reaction of F in its ground spin-orbit state with the predictions of single-surface calculations based on the fully adiabatic HSW PES. As in the case of the $Cl+H_2$ calculations on the fully-adiabatic CWad PES, the calculated DCSs are divided by 2 to compensate for the presence of the non-reactive $^2\Pi_{3/2}$ states with correlate with $F(^2P_{3/2})+H_2$. We observe that both in shape and magnitude the HSW DCSs and the ASW $F+H_2$ DCSs agree very well. At the same collision energy, the DCS from single surface calculations based on the SW PES (not shown here), are similar in shape but somewhat larger in magnitude. This reflects the lower barrier on the SW PES because of the absence of spin-orbit coupling, which, as discussed above, effectively lowers the barrier by ~ 1/3 the atomic spin-orbit splitting. A more careful examination shows that the ASW DCSs are slightly depressed in the backward direction, when compared with the HSW DCSs.

We also observe that the backward scattering produces primarily HF product in $v'=2$, while the forward scattering peak corresponds primarily to HF products in $v'=3$. This angular separation is virtually identical to what is predicted by the single-surface HSW calculations.

7. Summary and Conclusion

We have presented here the necessary formalism for the determination of differential cross sections for abstraction reactions of a halogen atom in a ^2P state with molecular hydrogen. The scattering is treated fully quantum-mechanically, and involves six three-dimensional hypersurfaces, four of which describe the diabatic potential energy functions and two of which describe the coordinate dependence of the spin-orbit coupling. In addition, all Coriolis terms are included. The DCSs can be obtained from a straightforward extension of the standard helicity-frame expression used in prior single-potential-surface treatments. Using the available fitted *ab initio* PESs for the
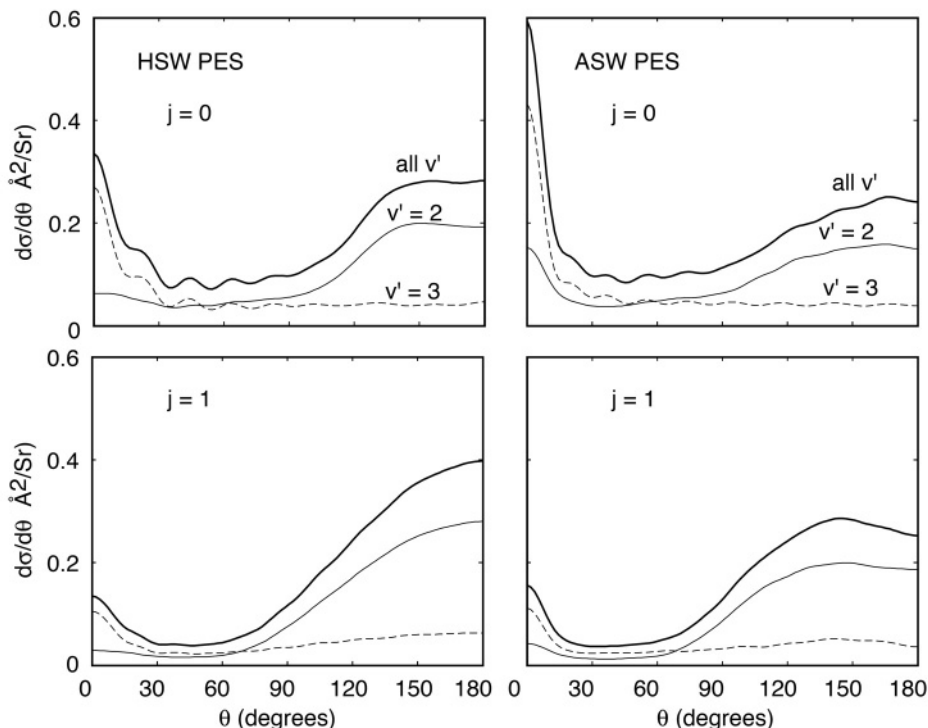
Figure 6. DCSs for reaction of F with $H_2(j=0)$ (upper panels) and $H_2(j=1)$ (lower panels) to yield HF at $E_{col} = 1.84$. The left hand panels refer to single-surface calculations on the HSW PES while the right panels refer to the multi-surface calculations with the ASW PESs. The heavy solid curve depicts the total reactive DCS, summed over all final states; the light solid and dashed curves designate the DCS for reaction into all rotational levels of HF in the $v = 2$ and $v=3$ vibrational manifolds, respectively.

$F+H_2$ and $Cl+H_2$ systems, determined by Werner and his co-workers,[2, 9, 20, 21, 34] we presented calculated DCSs in the center-of-mass frame at a number of collision energies.

For the $Cl+H_2$ system, these calculations show that the reactive DCSs are all strongly backward peaked, independent of the collision energy and the initial rotational level of the H_2 molecule. At the lowest collision energies, well below the barrier, theDCS for reactivity of the excited spin-orbit state far exceeds that of the ground spin-orbit state. When the adiabatically allowed channel becomes too strongly energetically forbidden, then Cl^* reaction, even though energetically forbidden, becomes facilitated by the additional internal energy in the excited spin-orbit state. As the collision energy increases, the adiabatically allowed reaction becomes rapidly dominant. This result mirrors, of course, the conclusions of our earlier investigation of ICSs for the $Cl+H_2$ reaction.[18] Curiously, an opposite trend is inferred from the experiments of Liu and co-workers.[28, 29] This disagreement is not yet understood.

When compared with DCSs calculated on the lowest adiabatic Cl+H_2 PES (the CWad PES), the multi-surface DCSs agree exceptionally well for transitions out of low H_2 rotational levels. This confirms the accuracy of the multi-surface methodology and scattering code. However, as the H_2 rotational level increases, the multi-surface reactive DCSs become progressively smaller than the single-surface CWad predictions. This is likely an indication of loss of reactive flux through electronically inelastic processes, which are not possible in a single-surface model. Obviously, more work should be done on this aspect of the reaction.

Because the topology of the PESs are much different and because the barrier is considerably lower, calculated DCSs for the F+H_2 reaction are much larger in magnitude and have a significant forward and sideways component not seen in the Cl+H_2 DCSs. At the collision energies considered, the DCS for reaction of the excited spin-orbit state of F is always significantly less than the DCS for adiabatically-allowed reaction of the ground spin-orbit state. Overall, the DCSs for reaction of F and F* are quite similar in shape, although the excited spin-orbit channel does not show as strong a peaking in the backward direction. Comparison of the multi-surface calculations based on the ASW PESs with single-surface calculations based on the fully adiabatic HSW PES indicate, as in the case of Cl+H_2, that the adiabatically allowed reaction of F($^2P_{3/2}$) is mimicked very well by calculations on the lowest PES which neglect all electronic fine structure of the atom.

In a recent communication we have compared calculated Cl+H_2 DCSs, transformed into the laboratory frame, with those determined in recent experiments.[35] In future papers, we shall present more detailed results of comparable simulations, for both the Cl+H_2 and F+H_2 reactions.

The formalism and computer codes developed here for the study of halogen-hydrogen could, without great difficulty, be extended to the investigation of spin-orbit and electronic nonadiabatic effects in other atom-molecule abstraction reactions.

Acknowledgement

References

1. Allison, T. C., Mielke, S. L., Schwenke, D. W., Lynch, G. C., Gordon, M. S. and Truhlar, D. G. (1996) Die Photochemischen Bildung des Chlorwasserstoffs. Dynamics of Cl + $H_2 \rightarrow$ HCl + H on a New Potential Energy Surface: The Photosynthesis of Hydrogen Chloride Revisited 100Years after Max Bodenstein in J Wolfrum, H-R Volpp, R Rannacher and J Warnatz (eds), *Gas-Phase Reaction Systems: Experiments and Models 100 Years after Max Bodenstein*, Springer, Heidelberg, pp. 111-24; Manolopoulos, D. E. (1997) The dynamics of the F+H_2 reaction, *J. Chem. Soc. Faraday Trans.* **93**, 673-83; Casavecchia, P. (2000) Chemical reaction dynamics with molecular beams, *Rep. Prog. Phys.* **63**, 355-414.

2. Stark, K. and Werner, H.-J. (1996) An accurate multireference configuration interaction calculation of the potential energy surface for the F+H$_2$ → HF+H reaction, *J. Chem. Phys.* **104**, 6515-30.

3. Manolopoulos, D. E., Stark, K., Werner, H.-J., Arnold, D. W., Bradforth, S. E. and Neumark, D. M. (1993) The Transition State of the F+H$_2$ Reaction, *Science* **262**, 1852-5.

4. Baer, M., Faubel, M., Martinez-Haya, B., Rusin, L. Y., Tappe, U. and Toennies, J. P. (1996) State-to-state differential cross sections for the reaction F + D$_2$ at 90 meV: A crossed molecular beam experiment and a quantum mechanical study, *J. Chem. Phys.* **108**, 9694-710; Honvault, P. and Launay, J.-M. (1998) Quantum mechanical study of the F + D$_2$→ DF + D reaction, *Chem. Phys. Lett.* **287**, 270-4; Honvault, P. and Launay, J.-M. (1999) Effect of spin-orbit corrections on the F+D$_2$ → DF+D reaction, *Chem. Phys. Lett.* **303**, 657-63; Baer, M., Faubel, M., Martinez-Haya, B., Rusin, L. Y., Tappe, U. and Toennies, J. P. (1999) Rotationally resolved differential scattering cross sections for the reaction F + para-H$_2$ (v = 0, j = 0) →HF(v′ = 2, 3, j′) + H, *J. Chem. Phys.* **110**, 10231-4; Skodje, R. T., Skouteris, D., Manolopoulos, D. E., Lee, S.-H., Dong, F. and Liu, K. (2000) Observation of a transition state resonance in the integral cross section for the F+HD reaction, *J. Chem. Phys.* **112**, 4536-52; Aquilanti, V., Cavalli, S., De Fazio, D., Volpi, A., Aguilar, A., Gimenez, X. and Lucas, J. M. (2002) Exact reaction dynamics by the hyperquantization algorithm: integral and differential cross sections for F+H$_2$, including long-range and spin orbit effects, *Phys. Chem. Chem. Phys.* **4**, 401-15; Krems, R. and Dalgarno, A. (2002) Electronic and rotational energy transfer in F($^2P_{1/2}$)+H$_2$ collisions at ultracold temperatures, *J. Chem. Phys.* **117**, 118-23.

5. Castillo, J. F., Manolopoulos, D. E., Stark, K. and Werner, H.-J. (1996) Quantum mechanical angular distributions for the F+H$_2$ reaction, *J. Chem. Phys.* **104**, 6531-46; Castillo, J. F. and Manolopoulos, D. E. (1998) Quantum mechanical angular distributions for the F+HD reaction, *Faraday Discuss. Chem. Soc.* **110**, 119-38.

6. Castillo, J. F., Hartke, B., Werner, H.-J., Aoiz, F. J., Bañares, B. and Martìnez-Haya, B. (1998) Quantum mechanical and quasiclassical simulations of molecular beam experiments for the F+H$_2$→HF+H reaction on two *ab intio* potential energy surfaces, *J. Chem. Phys.* **109**, 7224-37.

7. Xie, T. X., Zhang, Y., Zhao, M. Y. and Han, K. L. (2003) Calculations of the F+HD reaction on three potential energy surfaces, *Phys. Chem. Chem. Phys.* **5**, 2034-8.

8. Aoiz, F. J., Bañares, L., Martìnez-Haya, B., Castillo, J., Manolopoulos, D. E., Stark, K. and Werner, H.-J. (1997) *Ab initio* simulations of molecular beam experiments for the F+H$_2$ÆHF+H reaction, *J. Phys. Chem.* **A101**, 6403.

9. Hartke, B. and Werner, H.-J. (1997) Time-dependent quantum simulations of FH$_2^-$ photoelectron spectra on new *ab initio* potential energy surfaces for the anionic and the neutral species, *Chem. Phys. Lett.* **280**, 430-8.

10. Neumark, D. M., Wodtke, A. M., Robinson, G. N., Hayden, C. C. and Lee, Y. T. (1985) Molecular beam studies of the F+H$_2$ reaction, *J. Chem. Phys.* **82**, 3045-66.

11. Neumark, D. M., Wodtke, A. M., Robinson, G. N., Hayden, C. C., Shobatake, R., Sparks, R. K., Schafer, T. P. and Lee, Y. T. (1985) Molecular beam studies of the F+D$_2$ and F+HD reactions, *J. Chem. Phys.* **82**, 3067-77.

12. Faubel, M., Rusin, L., Schlemmer, S., Sonderman, F., Tappe, U. and Toennies, J. P. (1994) A high resolution crossed molecular beam investigation of the absolute cross sections and product rotational states for the reaction F+D$_2$ (v$_i$=0; j$_i$=0,1) →DF (v$_f$; j$_f$)+D, *J. Chem. Phys.* **101**, 2106.

13. Dong, F., Lee, S.-H. and Liu, K. (2000) Reactive excitation functions for F+p-H$_2$ / n-H$_2$ / D$_2$ and the vibrational branching for F+HD, *J. Chem. Phys.* **113**, 3633-40.

14. Liu, K., Skodje, R. T. and Manolopoulos, D. E. (2002) Resonances in bimolecular reactions, *Phys. Chem. Comm.* **4**, 27-33.

15. Aoiz, F. J. and Bañares, L. (1996) Reaction Cross Sections and Rate Constants for the Cl + $H_2(D_2) \rightarrow$ HCl(DCl) + H(D) Reaction from Quasiclassical Trajectory Calculations on an *ab Initio* Potential Energy Surface, *J. Phys. Chem.* **100**, 18108-15; Mielke, S. C., Allison, T. C., Truhlar, D. G. and Schwenke, D. W. (1996) Quantum mechanical rate coefficients for the Cl + H_2 reaction, *J. Phys. Chem.* **100**, 13588-93; Wang, H., Thompson, W. H. and Miller, W. H. (1997) Thermal rate constant calculation using flux–flux autocorrelation functions: Application to Cl + $H_2 \rightarrow$ HCl + H reaction, *J. Chem. Phys.* **107**, 7194-201; Skouteris, D., Manolopoulos, D. E., Bian, W., Werner, H.-J., Lai, L.-H. and Liu, K. (1999) van der Waals Interactions in the Cl+HD Reaction, *Science* **286**, 17136; Manthe, U., Bian, W. and Werner, H.-J. (1999) Quantum-mechanical calculation of the thermal rate constant for the H_2+Cl $\rightarrow$ H+HCl reaction, *Chem. Phys. Lett.* **313**, 647-54; Balucani, N., Cartechini, L., Casavecchi, P., Volpi, G. G., Aoiz, F. J., Bañares, L., Menéndez, M., Bian, W. and Werner, H.-J. (2000) Dynamics of the Cl+D_2 reaction: a comparison of crossed molecular beam experiments with quasi-classical trajectory calculations on a new ab initio potential energy surface, *Chem. Phys. Lett.* **328**, 500-8; Shen, C., Wu, T., Ju, G. and Bian, W. (2001) Cl+HD reaction dynamics from quasiclassical trajectory calculation on a new ab initio potential energy surface, *Chem. Phys.* **272**, 61-8.

16. Yang, B.-H., Gao, H.-T., Han, K.-L. and Zhang, J. Z. H. (2000) Time-dependent quantum dynamics study of the Cl + H_2 reaction, *J. Chem. Phys.* **113**, 1434-40.

17. Skouteris, D., Werner, H.-J., Aoiz, F. J., Bañares, L., Castillo, J. F., Menéndez, M., Balucani, N., Cartechini, L. and Casavecchia, P. (2001) Experimental and theoretical differential cross sections for the reactions Cl + H_2/D_2, *J. Chem. Phys.* **114**, 10662-72; Aoiz, F. J., Bañares, L., Castillo, J., Menéndez, M., Skouteris, D. and Werner, H.-J. (2001) A quantum mechanical and quasi-classical trajectory study of the Cl + H_2 reaction and its isotopic variants: Dependence of the integral cross section on the collision energy and reagent rotation, *J. Chem. Phys.* **115**, 2074-81.

18. Alexander, M. H., Capecchi, G. and Werner, H.-J. (2002) The validity of the Born-Oppenheimer approximation in the Cl+$H_2 \rightarrow$ HCl+H reaction, *Science* **296**, 715-8.

19. Allison, T. C., Lynch, G. C., Truhlar, D. G. and Gordon, M. S. (1996) An Improved Potential Energy Surface for the H_2Cl System and Its Use for Calculations of Rate Coefficients and Kinetic Isotope Effects, *J. Phys. Chem.* **100**, 13575-87.

20. Bian, W. and Werner, H.-J. (2000) Global *ab initio* potential energy surfaces for the ClH$_2$ reactive system, *J. Chem. Phys.* **112**, 220-9.

21. Capecchi, G. and Werner, H.-J. (to be published. Available at http://www.theochem.uni-stuttgart.de).

22. Rebentrost, F. and Lester, W. A., Jr. (1975) Nonadiabatic effects in the collision of F(^2P) with $H_2(^1\Sigma_g^+)$ I. SCF interation potentials for the $1^2A'$, $2^2A'$, and $^2A''$ states in the reactant region, *J. Chem. Phys.* **63**, 3737-40; Aquilanti, V., Cavalli, S., De Fazio, D. and Volpi, A. (1998) Hyperquantization algorithm. II. Implementation for the F + H_2 reaction dynamics including open-shell and spin-orbit interactions, *J. Chem. Phys.* **109**, 3805-18.

23. Faist, M. B. and Muckerman, J. T. (1979) On the valence bond diatomics-in-molecules method. II. Application to the valence states of FH$_2$, *J. Chem. Phys.* **71**, 233-54; Bettendorf, M., Buenker, R. J., Peyerimhoff, S. D. and Römelt, J. (1982) *Ab Initio* CI Calculations of the Effects of Rydberg-Valence Mixing in the Electronic Spectrum of the HF Molecule, *Z. Phys. A.* **304**, 125-35.

24. Alexander, M. H., Pouilly, B. and Duhoo, T. (1993) Spin-orbit branching in the photofragmentation of HCl, *J. Chem. Phys.* **99**, 1752-64.

25. Moore, C. E. (1971) *Atomic Energy Levels, NSRDS-NBS 35*, U. S. Government Printing Office, Washington.

26. Shuler, K. E. (1953) Adiabatic Correlation Rules for Reactions Involving Polyatomic Intermediate Complexes and their Application to the Formation of OH($^2\Sigma^+$) in the H_2–O_2 Flame, *J. Chem. Phys.* **21**, 624-32.

27. Donovan, R. J. and Husain, D. (1970) Recent Advances in the Chemistry of Electronically Excited Atoms, *Chem. Rev.* **70**, 489-516.

28. Lee, S.-H. and Liu, K. (1999) Exploring the spin–orbit reactivity in the simplest chlorine atom reaction, *J. Chem. Phys.* **111**, 6253-9.

29. Lee, S.-H., Lai, L.-H., Liu, K. and Chang, H. (1999) State-specific excitation function for Cl(^2P)+H_2 (v=0,j): Effects of spin-orbit and rotational states, *J. Chem. Phys.* **110**, 8229-32; Dong, F., Lee, S.-H. and Liu, K. (2001) Direct determination of the spin-orbit reactivity in Cl($^2P_{3/2}$, $^2P_{1/2}$)+H_2/D_2/HD reactions, *J. Chem. Phys.* **115**, 1197-204.

30. Dagdigian, P. J. and Campbell, M. L. (1987) Spin-Orbit Effects in Gas-Phase Chemical Reactions, *Chem. Rev.* **87**, 1-17.

31. Tully, J. C. (1974) Collisions of F($^2P_{1/2}$) with H_2, *J. Chem. Phys.* **60**, 3042-50.

32. Rebentrost, F. and Lester, W. A., Jr. (1977) Nonadiabatic effects in the collision of F(^2P) with H_2($^1\Sigma_g^+$) III. Scattering theory and coupled-channel calculations, *J. Chem. Phys.* **67**, 3367-74; Wyatt, R. E. and Walker, R. B. (1979) Quantum mechanics of electronic-rotational energy transfer in F(^2P)+H_2 collisions, *J. Chem. Phys.* **70**, 1501; Lepetit, B., Launay, J. M. and le Dourneuf, M. (1986) Quantum study of electronically non-adiabatic colinear reactions. II. Influence of spin-orbit transitions on the F+HH reaction, *Chem. Phys.* **106**, 111-22; Billing, G. D., Rusin, L. Y. and Sevryuk, M. B. (1995) A wave packet propagation study of inelastic and reactive F+D_2 scattering, *J. Chem. Phys.* **103**, 2482-94; Gilibert, M. and Baer, M. (1994) Exchange Processes via Electronic Nonadiabatic Transitions: An Accurate Three-Dimensional Quantum Mechanical Study of the F($^2P_{1/2}$, $^2P_{3/2}$) + H_2 Reactive Systems, *J. Phys. Chem.* **98**, 12822-3.

33. Alexander, M. H., Werner, H.-J. and Manolopoulos, D. E. (1998) Spin-orbit effects in the reaction of F(^2P) with H_2, *J. Chem. Phys.* **109**, 5710-3.

34. Alexander, M. H., Manolopoulos, D. E. and Werner, H. J. (2000) An investigation of the F+H_2 reaction based on a full *ab initio* description of the open-shell character of the F(^2P) atom, *J. Chem. Phys.* **113**, 11084-100.

35. Balucani, N., Skouteris, D., Cartechini, L., Capozza, G., Segoloni, E., Casavecchia, P., Alexander, M. H., Capecchi, G. and Werner, H.-J. (2003) Differential cross sections from quantum calculations on coupled *ab initio* potential energy surfaces and scattering experiments for the reaction Cl(^2P)+H_2, *Phys. Rev. Lett.* **91**, 1-4.

36. Schatz, G. C. (1995) Influence of Atomic Fine Structure on Bimolecular Rate Constants: The Cl(^2P) + HCl Reaction, *J. Phys. Chem.* **99**, 7522-9.

37. Maierle, C. S., Schatz, G. C., Gordon, M. S., McCabe, P. and Connor, J. N. L. (1997) Coupled potential energy surfaces and quantum reactive scattering for the Cl(^2P) +HCl→ClH+Cl(^2P) reaction, *J. Chem. Soc. Faraday Trans.* **93**, 709-20; Schatz, G. C., McCabe, P. and Connor, J. N. L. (1998) Quantum scattering studies of spin-orbit effects in the Cl(^2P)+HCl →ClH + Cl(^2P) reaction, *Faraday Disc. Chem. Soc.* **110**, 139-57; Whitely, T. W. J., Dobbyn, A. J., Connor, J. N. L. and Schatz, G. C. (2000) Quantum scattering on coupled ab initio potential energy surfaces for the Cl(^2P)+HCl→ ClH+Cl(^2P) reaction, *Phys. Chem. Chem. Phys.* **2**, 549-56.

38. Skouteris, D., Castillo, J. F. and Manolopoulos, D. E. (2000) ABC: A Quantum Reactive Scattering Program, *Comput. Phys. Comm.* **133**, 128.

39. Schatz, G. C. (1990) Quantum reactive scattering using hyperspherical coordinates: Results for H+H_2 and Cl+HCl, *Chem. Phys. Lett.* **150**, 92-8.

40. Schatz, G. C. and Kuppermann, A. (1976) Quantum mechanical reactive scattering for three-dimensional atom plus diatom systems. I. Theory, *J. Chem. Phys.* **65**, 4642-67.

41. Pack, R. T and Parker, G. A. (1987) Quantum reactive scattering in three dimensions using hyperspherical (APH) coordinates. Theory, *J. Chem. Phys.* **87**, 3888-921.
42. Dubernet, M.-L. and Hutson, J. M. (1994) Atom-molecule van der Waals complexes containing open-shell atoms. 2. The Bound States of Cl–HCl, *J. Phys. Chem.* **98**, 5844-54.
43. Brink, D. M. and Satchler, G. R. (1968) *Angular Momentum* 2nd edn, Clarendon, Oxford.
44. Meyer, H.-D. and Miller, W. H. (1979) Classical models for electronic degrees of freedom: Derivation via spin analogy and application to $F^*+H_2 \rightarrow F+H_2$, *J. Chem. Phys.* **71**, 2156-69.
45. Dubernet, M.-L. and Hutson, J. M. (1994) Atom-molecule van der Waals complexes containing open-shell atoms. I. General thoery and bending levels, *J. Chem. Phys.* **101**, 1939-58.
46. Lepetit, B. and Launay, J. M. (1991) Quantum mechanical study of the reaction $He+H_2^+ \rightarrow HeH^+ + H$ with hyperspherical coordinates, *J. Chem. Phys.* **95**, 5159-68.
47. Johnson, B. R. (1973) The Multichannel Log-Derivative Method for Scattering Calculations, *J. Comp. Phys.* **13**, 445-9; Manolopoulos, D. E. (1986) An improved log derivative propagator for inelastic scattering, *J. Chem. Phys.* **85**, 6425-9.
48. Lefebvre-Brion, H. and Field, R. W. (1986) *Perturbations in the Spectra of Diatomic Molecules*, Academic, New York.
49. Miller, W. H. (1969) Coupled equations and the minimum principle for collisions of an atom and a diatomic molecule, including rearrangements, *J. Chem. Phys.* **50**, 407-18.
50. Zare, R. N. (1988) *Angular Momentum*, Wiley, New York.
51. Zhang, J. Z. H. and Miller, W. H. (1989) Quantum reactive scattering via the S-matrix version of the Kohn variational principle: Differential and integral cross sections for $D+H_2 \rightarrow HD+H$, *J. Chem. Phys.* **91**, 1528-47.
52. Werner, H.-J., Follmeg, B. and Alexander, M. H. (1988) Adiabatic and Diabatic Potential Energy Surfaces for Collisions of CN ($X^2\Sigma^+$, $A^2\Pi$) with He, *J. Chem. Phys.* **89**, 3139-51.
53. Alexander, M. H. (1993) Adiabatic and Approximate Diabatic Potential Energy Surfaces for the B…H_2 van der Waals Molecule, *J. Chem. Phys.* **99**, 6014-2026.
54. Aoiz, F. J., Bañares, L. and Castillo, J. F. (1999) Spin-orbit effects in quantum mechanical rate constant calculations for the $F+H_2 \rightarrow HF+H$ reaction, *J. Chem. Phys.* **111**, 4013-24.

ON THE QUANTIZATION OF THE ELECTRONIC NON-ADIABATIC COUPLING TERMS: THE H+H$_2$ SYSTEM AS A CASE STUDY

GÁBOR HALÁSZ,[a] ÁGNES VIBÓK,[b]
ALEXANDER M. MEBEL[c] and MICHAEL BAER[d,1]

[a]*Institute of Mathematics and Informatics, University of Debrecen, H-4010 Debrecen, P.O. Box 12, Hungary*
[b]*Department of Theoretical Physics, University of Debrecen, H-4010 Debrecen, P.O. Box 5, Hungary*
[c]*Institute of Atomic and Molecular Sciences, Academia Sinica, P.O. Box 23-166, Taipei 10764, Taiwan*
[d]*Soreq Nuclear Research Center, Yavne 81800, Israel*

Abstract In this article we present a survey of the various conical intersections which govern potential transitions between the three lower electronic states for the title molecular system. It was revealed that these three states, for a given fixed HH distance, R_{HH}, usually form four conical intersections: two between the two lower states and two between the two upper states. One of the four is the well-known equilateral D_{3h} *ci* and the others are, essentially, C_{2v} *ci*s: One of them is located on the symmetry line perpendicular to the HH axis (like the D_{3h} *ci*) and the other two are located on both sides of this symmetry line and in this way form the twin C_{2v} *ci*s. The study was carried out for two R_{HH}-values, namely, R_{HH}=0.74 and 0.4777 Å.

   The second subject treated here, in some detail, is related to the possible *quantization* of the non-adiabatic coupling matrix. We show that in general for small enough regions surrounding a particular *ci* the two-state *quantization* is fulfilled. However, increasing the region surrounded by the contour shows larger and larger deviations from the two-state *quantization* but then the three-state *quantization* shows relevance as expected from pure theoretical considerations (Baer and Alijah, Chem. Phys. Lett. 319, 489 (2000)).

[1] Email of corresponding author: michaelb@fh.huji.ac.il

1. Introduction

It is well known that molecular processes are governed by Coulomb interactions and therefore are accurately treated by applying the relevant Schrödinger equation (SE). The connection between the solutions of the SE and observables such as cross sections or spectroscopic measurements is established from the early days of quantum theory, so it seems that to a large extent the only theoretical interest one can find in molecular physics is in developing numerical algorithms to solve the SE for required situations. The basic theory that enables the quantum mechanical treatment of realistic (usually complicated) molecular systems was presented by Born and Oppenheimer (BO) and later completed by Born and Huang.[1,2] Any additional theoretical treatment is considered as overdoing. Indeed, as long as the main attention is given to processes taking place on the ground electronic state no additional theoretical input from first principles is needed.

The situation changes once electronic excited states have to be included to account for possible electronic transitions. Hints towards potential difficulties follow already from the Hellmann-Feynman theorem[3] which points out the possibility that the BO approach may lead to magnitudes - *the non-adiabatic coupling terms* (NACT) - which are singular. The singularities can be considered as mishaps caused by the fact that electronic states become *degenerate* at certain points in configuration space.[4] In numerous cases it was assumed that singular NACTs are rare and therefore can be ignored. Consequently the Hellmann-Feynman theorem was overlooked for some time, even when, two decades later, Longuet-Higgins (LH) et al. revealed that the existence of the degeneracy may affect the single-valuedness of some of the adiabatic electronic eigenfunctions.[5,6] LH overcame this 'nuisance' by multiplying the (multivalued) eigenfunction by a phase factor, forcing the eigenfunctions to be singlevalued (without affecting their electronic features). This phase being available led Mead [7] to construct an *adiabatic* (nuclear) SE which is characterized by NACTs that are not necessarily identical to the original BO NACTs (as they should be). Consequently the relevant *diabatic* SE may be inadequate as well and erroneous results can be expected.

There is no doubt that treating molecular systems affected by NACTs is much more complicated than treating them in cases when these effects are ignored. The main reason is that NACTs are not only occasionally spiky functions of the coordinates and therefore numerically unfriendly but, as mentioned earlier, they are frequently singular. [3] Having singular NACTs is not just a difficulty which can be treated using some numerical recipe; in fact, these singularities form non-local effects and therefore have to be eliminated, rigorously, without their physical contents being affected. [8,9]

Scanning through the published literature it is noticed that in many cases the NACTs are not as seriously considered as they should be. In contrast to the familiar vib-rotational coupling terms which are well understood and usually handled correctly, the NACTs are in most cases, either ignored or circumvented without proper justification. If ignored, not much can be added except to say that the results have to be considered unreliable and eventually non-relevant. More serious difficulties are encountered with treatments that circumvent the need to consider NACTs and give the impression that these treatments are well established and numerically sound. As it turns out it is impossible to

circumvent the (singular) NACTs because they form *non-local* effects which determine the minimal size of the group of (adiabatic) states one has to employ in order to form singlevalued diabatic potentials [9-11] In what follows this group is termed a Hilbert sub-space.

A NACT is a vector characterized by two features: it has its origin at a degeneracy point [3] (i.e. where two electronic eigenstates become identical), known also as a conical intersection (*ci*), [12-14] and it has a spatial distribution which is well known to decreases like q^{-1}, where q is a the distance from the *ci*, but maintains an angular dependence which is of major importance. [15-16]

The BO theory enables two different approaches or frameworks for treating the interaction of the molecular species. The first is the above-mentioned adiabatic framework which consists of the adiabatic potential energy surfaces (PES) and the NACTs and the second is the diabatic framework which is expressed in terms of the *diabatic* potential matrix. Since the elements of the diabatic PES matrix are regular, smooth functions of the coordinates, the diabatic framework is preferred for treating the dynamics of the nuclei and indeed all rigorous quantum mechanical treatments aim at reaching it.[4,8,9,17-20] The diabatic framework can be formed in three ways: (1) The *direct* way, namely, deriving an electronic basis set, as well as a set of eigenvalues calculated at a given (one, single) point in configuration space, and applying them to calculate the diabatic potential matrix at any requested point (see, for instance, ref. [9c] Appendix D). (2) The *indirect* way, namely, deriving at each point in configuration space the electronic eigenvalues (which are recognized as the adiabatic potentials) and the electronic eigenfunctions, and transforming to the diabatic framework [8-9] (employing the NACTs calculated from the adiabatic eigenfunctions). This transformation is known as the *adiabatic-to-diabatic transformation*, or by its acronym ADT, and as was discussed on many other occasions the ADT yields a meaningful diabatic potential matrix if and only if certain conditions (to be discussed below) are fulfilled. [3] There is also a third way which is similar to the former one since it is based on an ADT matrix, but the relevant matrix elements are not calculated from the NACTs but by employing other considerations.[19]

There is no doubt that on the face of it the *direct* way of reaching the diabatic framework is more convenient. Indeed, as long as the various NACTs form weak coupling terms this procedure is valid and simple. However, in case certain NACTs become singular, as for instance in case of the $H+H_2$ system, where we established the existence of four strongly interacting *ci*s, coupling at least three adiabatic PES [15] this procedure is most likely to fail and therefore is expected to yield irrelevant results. Indeed numerous PESs that were derived ignoring the relevant features of the NACTs may turn out to be inadequate for studying electronic transitions. In order to find out if such singular NACTs exist one has to 'move' into the *adiabatic* framework and calculate them for a highly dense grid of points which, in turn, makes this procedure (i.e. the *direct* one) essentially redundant. Another difficulty associated with the *direct* approach has to do with the previously mentioned non-local effects which do not become apparent, at least not in an obvious way, within the diabatic framework. We showed in numerous articles that dynamic calculations are expected to be meaningless unless the non-local effects are properly treated and this can be done only by employing the NACTs.

As was shown in numerous articles, [10-11] and we briefly repeat it here, the non-local effects are properly treated if and only if the matrix, $\boldsymbol{\tau}$, that contains the NACTs is *quantized*. We will not elaborate on this issue now because it will be extensively discussed in the next section; however, for the sake of completeness, we just say the following: The ADT yields the diabatic PES matrix elements but there is no *a-priori* guarantee that these potentials are *singlevalued*. In fact if the non-local effects are not properly treated these potentials are most likely to become *multivalued*. In the numerical part that relates to the NACTs of the $H+H_2$ system, we show that the *ad-initio* electronic eigenfunctions form *quantized* nonadiabatic coupling matrices (NACM).

The article is arranged in the following way: In the next section we present the theoretical background related to the subject, namely discussing the adiabatic SE, the ADT, the single-valuedness of the diabatic potentials, the topological matrix (a subject not yet mentioned) and finally the quantization of the NACM. In the third and fourth sections is presented the numerical part of the article: in the third section we give numerical details regarding the $H+H_2$ system and in the fourth we show the results. In the fifth section the results are discussed and the conclusions are summarized.

2. Theoretical Background

2.1 THE ADIABATIC SCHRÖDINGER EQUATION

The starting point is the Born-Oppenheimer-Huang (BOH) close coupling expansion:

$$\Psi(e,v)=\sum_{j=1}^{N}\psi_{j}(v)\zeta_{j}(e|v) \tag{1}$$

where v and e stand for nuclear and electronic coordinates, respectively, $\psi_j(v)$ is the j-th nuclear-coordinate-dependent coefficient (recognized as the j-th nuclear wave function) and $\zeta_j(e|v)$ is the j-th electronic wave function, assumed to be the eigenfunctions of the electronic Hamiltonian $H_e(e|v)$:

$$\left(H_{e}(e|v)-u_{j}(v)\right)\zeta_{j}(e|v)=0; \quad j=1,...,N \tag{2}$$

Here $u_j(v)$; j=1,…,N are the adiabatic potential energy surfaces (PES) that govern the motion of the nuclei in this system.

Next are introduced the non-adiabatic coupling matrix elements (NACME), τ_{ji}, the main magnitudes considered in this article, which are defined as:

$$\boldsymbol{\tau}_{ji}=\left\langle \zeta_{j}\left|\nabla\zeta_{i}\right.\right\rangle; \quad i,j=\{1,....\} \tag{3}$$

where the grad operator is expressed with respect to the nuclear coordinates, v, and the $\zeta_k(e|v)$-functions, k=j,i are the above-mentioned eigenfunctions. The NACTs become

apparent in the SE which describes the motion of the nuclei. Assuming the electronic manifold forms a Hilbert-space, this equation takes the form: (9)

$$-\frac{\hbar^2}{2m}(\nabla + \tau)^2 \Psi + (\mathbf{u} - E)\Psi = 0 \tag{4}$$

where τ is the above-mentioned anti-symmetric NACM, $\mathbf{u}$ is a diagonal matrix that contains the adiabatic PESs (introduced through Eq. (2)), Ψ is a column vector that contains the nuclear wave functions to be solved (introduced in Eq. (1)), E is the energy and m is the mass of the system (it is assumed that the grad operator is defined with respect to mass- scaled coordinates). Eq. (4) can be shown to be valid for a group of states that does not necessarily form a Hilbert space but which is strongly coupled to itself and, at most, weakly coupled to other states belonging to this manifold (in the region of interest). In what follows such a group of states is termed a **Hilbert sub-space**.

2.2 THE ADIABATIC-TO-DIABATIC TRANSFORMATION (ADT)

Considering Eq. (4) it is well noticed that for those cases where the NACTs are singular we encounter a differential equation that contains singular functions. As was mentioned earlier these singular functions create non-local effects and therefore eliminating them has to be done *rigorously* in order not to lose the physical non-local effects. This elimination is done by applying a unitary transformation matrix **A** that, as it turns out, transforms the adiabatic framework to the diabatic one, which is characterized by the fact that the resulting NACTs are zero (or close to zero). Due to this feature the matrix **A** is termed the adiabatic-to-diabatic transformation (ADT) matrix. Considering Eq. (4) we replace Ψ by Φ where the two are related:

$$\Psi = \mathbf{A}\Phi \tag{5}$$

Substituting Eq. (5) in Eq. (4), performing the usual algebra, and demanding the elimination of the τ-matrix yields the following results: [8,9]

(a) The new (diabatic) SE is:

$$-\frac{\hbar^2}{2m}\nabla^2\Phi + (\mathbf{W} - E)\Phi = 0 \tag{6}$$

where the *diabatic* potential **W** is given in the form:

$$\mathbf{W} = \mathbf{A}^\dagger \mathbf{u} \mathbf{A} \tag{7}$$

(b) The differential equation to determine the ADT matrix, **A**:

$$\nabla \mathbf{A} + \tau \mathbf{A} = 0 \tag{8}$$

Eq. (8) is a vectorial, first-order differential equation and as such has to be solved along *contours*. Consequently all theoretical considerations with respect to the behavior of physical magnitudes (in particular the diabatic potential matrix introduced in Eq. (7)) are done along contours. Another remark concerning Eq. (8) is that its solution, the matrix **A,** has to be a unitary matrix.

The first difficulty we encounter with respect to Eq. (8) is that a solution is not always possible. In order to discuss this subject we first introduce the following tensorial matrix **F** defined as:

$$\mathbf{F}_{qp} = \frac{\partial}{\partial p}\boldsymbol{\tau}_q - \frac{\partial}{\partial q}\boldsymbol{\tau}_p - \left[\boldsymbol{\tau}_q, \boldsymbol{\tau}_p \right]; \quad \{p,q;n\} \tag{9}$$

where p and q are (Cartesian) internal coordinates (n stands for their number), $\boldsymbol{\tau}_q$ and $\boldsymbol{\tau}_p$ are, respectively, the q and the p components of $\boldsymbol{\tau}$, and $\mathbf{F}_{qp}$ is recognized as the (p,q) component of the tensorial Yang-Mills field. [21] The set of equations in Eq. (9) can also be written in a more compact way:

$$\mathbf{F} = Curl\boldsymbol{\tau} - [\boldsymbol{\tau} \times \boldsymbol{\tau}] \tag{9'}$$

It was shown that in case of a Hilbert space or even in case of a Hilbert sub-space (as introduced earlier), the components of **F** have to be zero at every point in configuration space for which the derivatives are valid [8a] (in particular see Appendix 1 in Ref.[8a]). Thus:

$$\mathbf{F} = \mathbf{0} \tag{10}$$

In other words, if for a given group of states Eq. (10) is not fulfilled in the region of interest, Eq. (8) does not have an analytic solution and the ADT cannot be carried out.

In case Eq. (10) is fulfilled a solution can be found for any contour, Γ in the region. Thus: [8b]

$$\mathbf{A}(s,s_0 \mid \Gamma) = \wp \exp\left(-\int_{s_0}^{s} ds' \cdot \boldsymbol{\tau}(s' \mid \Gamma) \right) \mathbf{A}(s_0) \tag{11}$$

where the dot stands for a scalar product between $\boldsymbol{\tau}(\mathbf{s})$ and a differential vector, **ds**, along Γ, $\mathbf{A}(s_0)$ is a given value of **A** at a boundary point s_0 and $\wp$ is a path ordering operator introduced to indicate that this integral has to be carried out in a given order.

Having the **A**-matrix we can derive the diabatic potential matrix **W(s)** as presented in Eq. (7). Until now the process of deriving **W(s)** seems to be straightforward as long as Eq. (10) is fulfilled. There is only one question, namely, whether these newly formed matrix elements are single-valued in configuration space. So far the single-valuedness issue was not raised although it is evident that in order to obtain a meaningful solution for the SE the diabatic potential matrix elements must be singlevalued. This issue is discussed next.

2.3. THE SINGLEVALUEDNESS OF THE DIABATIC POTENTIAL MATRIX W AND THE TOPOLOGICAL MATRIX D

We consider a closed path Γ defined in terms of a continuous parameter λ so that the starting point s_0 of the contour is at $\lambda=0$. Next, β is defined as the value attained by λ once the contour completes a full cycle and returns to its starting point. For instance, in case of a circle, λ is an angle and $\beta=2\pi$.[10]

With these definitions we can now look for the necessary condition(s) for having a single-valued diabatic potential. Therefore, as is usually done in mathematics, we assume the existence of the outcome and search for the conditions for that to happen. In our case we assume that at <u>each point</u> s_0 in configuration space the diabatic potential matrix $\mathbf{W}(\lambda)$ ($\equiv \mathbf{W}(s,s_0)$) fulfills the condition:

$$\mathbf{W}(\lambda=0) = \mathbf{W}(\lambda=\beta) \tag{12}$$

Recalling Eq. (7), this requirement implies that for every point s_0 we have:

$$\mathbf{A}^\dagger(0)\mathbf{u}(0)\mathbf{A}(0) = \mathbf{A}^\dagger(\beta)\mathbf{u}(\beta)\mathbf{A}(\beta) \tag{12'}$$

Where $\mathbf{A}^\dagger$ is the complex conjugate of $\mathbf{A}$. Next is introduced another transformation matrix, $\mathbf{B}$, defined as:

$$\mathbf{B} = \mathbf{A}(\beta)\mathbf{A}^\dagger(0) \tag{13}$$

which for every s_0 and a given contour Γ, connects $\mathbf{u}(\beta)$ with $\mathbf{u}(0)$:

$$\mathbf{u}(\beta) = \mathbf{B}\,\mathbf{u}(0)\,\mathbf{B}^\dagger \tag{14}$$

The $\mathbf{B}$-matrix is, by definition, a unitary matrix (it is a product of two unitary matrices) and at this stage except for being dependent on Γ and, eventually, on s_0, it is rather arbitrary. Since the electronic eigenvalues (the adiabatic PESs) are uniquely defined at each point in configuration space we have: $\mathbf{u}(0) \equiv \mathbf{u}(\beta)$ and therefore Eq. (14) implies:

$$[\mathbf{B},\mathbf{u}(0)] = 0 \tag{15}$$

or more explicitly:

$$\sum_{j=1} \left(\mathbf{B}^*_{lj}\mathbf{B}_{jk} - \delta_{lk}\delta_{jk}\right)\mathbf{u}_j(0) = 0 \tag{16}$$

Eq. (16) has to hold for every arbitrary point s_0 ($\equiv\lambda=0$) <u>on</u> the path Γ and, therefore, for an essentially arbitrary set of non-zero adiabatic eigenvalues, $\mathbf{u}_j(s_0)$; j=1,…,M. Due to the arbitrariness of the $\mathbf{u}_j(s_0)$'s Eqs. (16) can be satisfied if and only if the $\mathbf{B}$-matrix elements fulfill the relation:

$$\mathbf{B}^{*}_{lj}\mathbf{B}_{jk} = \delta_{lj}\delta_{jk}; \qquad l, j, k \le M \tag{17}$$

or

$$\mathbf{B}_{jk} = \delta_{jk}\exp(i\chi_k) \tag{18}$$

Thus, **B** is a diagonal matrix which contains in its diagonal (complex) numbers whose norm is 1 (this derivation holds as long as the adiabatic potentials are non-degenerate along the path Γ). From Eq. (13) we obtain that the **B**-matrix transforms the **A**-matrix from its initial value to its final value while tracing the closed contour:

$$\mathbf{A}(\beta) = \mathbf{B}\,\mathbf{A}(0) \tag{19}$$

We return to Eq. (11) and consider the case when the contour Γ becomes a closed contour and $\mathbf{A}(s_0)$ is the unit matrix. For this particular case we define the following matrix:

$$\mathbf{D} = \wp \exp\left(-\oint_{\Gamma} d s \cdot \mathbf{\tau}\right) \tag{20}$$

From Eq. (11) it is noticed that if the contour Γ is closed the **D**-matrix transforms $\mathbf{A}(s_0)$ to its value $\mathbf{A}(s = s_0 | s_0)$ obtained, once we reached the end of the (closed) contour, namely:

$$\mathbf{A}(s = s_0 | s_0) = \mathbf{D}\,\mathbf{A}(s_0) \tag{21}$$

Now comparing Eq. (19) with Eq. (21) it is noticed that **B** and **D** are identical. This implies that all the features that were found to exist for the **B**-matrix also apply for the matrix **D** as defined in Eq. (20).

Returning to the beginning of this Section we establish the following: The *necessary* condition for the **A**-matrix to yield single-valued diabatic potentials in a region surrounded by a close contour Γ is that the **D**-matrix, calculated along this contour (see Eq. (20)), be diagonal and that it have, in its diagonal, numbers of norm 1 (in fact the second outcome is redundant because the **D**-matrix is a unitary matrix and therefore, being diagonal, implies numbers with norm 1). Since we consider only real electronic eigenfunctions these numbers can be ±1. The diagonalization of the **D**-matrix ensures singlevalued diabatic potentials but not singlevalued ADT matrices, as is noted from Eq. (21) (because the **D**-matrix is not necessarily a unit matrix). In what follows the number of (-1)s in a given matrix **D** will be designated as K - defined as the *topological number*.[22]

It is important to mention that the relation between the phases of the **D**-matrix and Berry's phase of each of the electronic adiabatic states is discussed by R. Baer [23]. In particular, for a real electronic basis set where the two phases are shown to be identical.

2.4. THE QUANTIZATION OF THE τ-MATRIX

The **D**-matrix as introduced in Eq. (20) is not expected to be diagonal for a **τ**-matrix of an arbitrary dimension. For a given region only certain sizes of groups of eigenstates are capable of yielding diagonal **D**-matrices. In general this is a group which is strongly coupled to itself but, at most, weakly coupled to states outside the group. As one may recall we termed such a group as a Hilbert sub-space. In applications one starts with a group of two states and then, step by step increases the number of states until the calculated **D**-matrix becomes diagonal. (This we did recently in a detailed study based on the eigenfunctions obtained from the Mathieu equation (24)).

Considering a given region, Λ, in configuration space: we define those **τ**-matrices, that yield diagonal **D**-matrices in Λ, as being *quantized* in that region. The concept of *quantization* becomes clear when we consider a 2x2 **τ**-matrix which is presented in terms of one non-zero matrix element:

$$\boldsymbol{\tau}(s) = \begin{pmatrix} 0 & \tau(s) \\ -\tau(s) & 0 \end{pmatrix} \tag{22}$$

It can be shown (employing Eq. (11)) that the **A**-matrix takes the form: [8a]

$$\mathbf{A}(s \mid \Gamma) = \begin{pmatrix} \cos\gamma(s \mid \Gamma) & \sin\gamma(s \mid \Gamma) \\ -\sin\gamma(s \mid \Gamma) & \cos\gamma(s \mid \Gamma) \end{pmatrix} \tag{23}$$

where $\gamma(s|\Gamma)$ is the ADT angle presented as:

$$\gamma(s \mid \Gamma) = \gamma(s_0) + \int_{s_0}^{s} ds \cdot \tau(s|\Gamma) \tag{24}$$

Here the integration, as mentioned earlier, is carried out along a contour Γ. The **D**-matrix, just like the **A**-matrix, can be written in the form:

$$\mathbf{D}(\Gamma) = \begin{pmatrix} \cos\alpha(\Gamma) & \sin\alpha(\Gamma) \\ -\sin\alpha(\Gamma) & \cos\alpha(\Gamma) \end{pmatrix} \tag{25}$$

where $\alpha(\Gamma)$ is topological phase defined as:

$$\alpha(\Gamma) = \oint_{\Gamma} ds \cdot \tau(s \mid \Gamma) \tag{26}$$

It is noticed that in order for the 2x2 **D**-matrix in Eq. (25) to become diagonal, $\tau(s)$ has to fulfill the well known Bohr-Sommerfeld quantization rule of the angular momentum, namely: [24]

$$\alpha(\Gamma) = \oint_{\Gamma} ds \cdot \tau(s \mid \Gamma) = n\pi \tag{27}$$

where n is an integer.

3. Numerical Comments

To carry out the numerical study we fix the position of two of the hydrogens and use the third hydrogen as a probe to reveal the various *cis*. Due to symmetry it is enough to consider the motion of this atom in one fixed plane and in order to follow its motion (on that plane) we need two (polar) coordinates; q the radial coordinate and φ the angular coordinate. In what follows we assume the contours to be circles with their centers at given points and with varying radii. Since the contours are circles, we need for the calculations only the angular component of the NACTs (which are the required tangential components in this case) to be designated as $\tau_{\varphi jk}(q, \varphi)$ and defined as:

$$\tau_{\varphi jk}(\varphi \,|\, q) = \left\langle \zeta_j(\varphi \,|\, q) \left| \frac{\partial}{\partial \varphi} \zeta_k(\varphi \,|\, q) \right. \right\rangle \tag{28}$$

In case the Hilbert sub-space contains only two states, namely the j-th and the (j+1)-th states we are interested only in the ADT angle and the topological phase. The ADT angle, $\gamma(\varphi|q)$, expressed in these coordinates is:

$$\gamma_{jj+1}(\varphi \,|\, q) = \int_0^\varphi \tau_{\varphi jj+1}(\varphi \,|\, q)\, d\varphi \tag{29}$$

and the corresponding topological phase $\alpha_{jj+1}(q)$ is given in the form:

$$\alpha_{jj+1}(q) = \int_0^{2\pi} \tau_{\varphi jj+1}(\varphi \,|\, q)\, d\varphi \tag{30}$$

The situation becomes more involved in case the Hilbert sub-space contains three states. In such a case the τ_φ-matrix is of dimension 3x3, namely:

$$\tau_\varphi(\varphi|q) = \begin{pmatrix} 0 & \tau_{\varphi 12} & \tau_{\varphi 13} \\ -\tau_{\varphi 12} & 0 & \tau_{\varphi 23} \\ -\tau_{\varphi 13} & -\tau_{\varphi 23} & 0 \end{pmatrix} \tag{32}$$

and as a result the (φ-dependent) ADT matrix becomes:

$$A(\varphi \,|\, q) = \wp \, \exp\left(-\int_0^\varphi \tau_\varphi(\varphi' \,|\, q)\, d\varphi' \right) \tag{33}$$

In the forthcoming study we consider the diagonal elements of this matrix. In case φ=2π the ADT matrix becomes the topological **D**-matrix:

$$\mathbf{D}(q) = \wp \; \exp\left(-\int_0^{2\pi} \boldsymbol{\tau}_\varphi(\varphi'|q)\, d\varphi'\right) \tag{34}$$

and the diagonal elements are expected to be ± 1. The closer they are to one of these values the more is the $\boldsymbol{\tau}_\varphi$-matrix *quantized*.

The calculation of the nonadiabatic coupling terms (along chosen circles) was carried out at the state-average CASSCF level using 6-311G** (3df,3pd) basis set [26] extended with additional diffuse functions. In order to take properly into account the Rydberg states we added, to the basis set, one s diffuse function and one p diffuse function in an even tempered manner,[27] with the exponents of 0.0121424 and 0.046875 respectively. We used the active space including all three electrons distributed on nine orbitals. Five different electronic states including the three studied states, namely, $1^2A'$, $2^2A'$ and $3^2A'$ were computed by the state-average CASSCF method with equal weights. To perform the above-mentioned integrations the relevant NACTs were obtained employing the MOLPRO program. The details how to operate it for our purpose were discussed in previous publications (in particular see Appendix of Ref. 28)and are not be repeated here.

The numerical results in this article, presented Figs 1-4, are arranged in columns – each column for one situation. A column contains three sub-figures headed by a schematic drawing describing the *ci*-positions for the situation under consideration. We distinguish between two types of *ci*s: Full *squares* designate (1,2) *ci*s, and full *diamonds* designates (2,3) *ci*s. Also, full circular dots designate the positions of the two 'fixed' hydrogens (which form the *situation*). In addition, dashed circles are the closed circular contours along which the reported integrations are performed. Next we describe what is shown in the various sub-figures (for a given column): The upper sub-figure contains the three non-adiabatic coupling terms, namely $\tau_{\varphi12}(\varphi)$, $\tau_{\varphi23}(\varphi)$ and $\tau_{\varphi13}(\varphi)$ (see Eq. (28)); the middle sub-figure contains the two corresponding $\gamma(\varphi)$-angles, namely, $\gamma_{12}(\varphi)$ and $\gamma_{23}(\varphi)$ (see Eq. (29)) and the lowest one contains the three diagonal elements of the **A**-matrix, namely, $\mathbf{A}_{11}(\varphi)$, $\mathbf{A}_{22}(\varphi)$ and $\mathbf{A}_{33}(\varphi)$. Also, in the second sub-figure are reported the actual α-angles for the two relevant cases i.e. α_{12} and α_{23} (see Eq. (30)) – expected to be π or zero - and in the third sub-figure are listed the three $\mathbf{D}_{jj}$-values – expected to be ± 1 (see Eq. (34)).

4. Numerical Verifications for Quantization: A Detailed Study of the H+H$_2$ System

In what follows we define a *situation* as a configuration of the three atoms where the distance R_{HH} between two atoms is fixed (and the third atom is allowed to move essentially undisturbed). We present results for two *situations*, namely, $R_{HH} = 0.74$ and 0.4777 Å. In order to distinguish between them we term the first situation the *loose* situation and the second the *compact* situation.
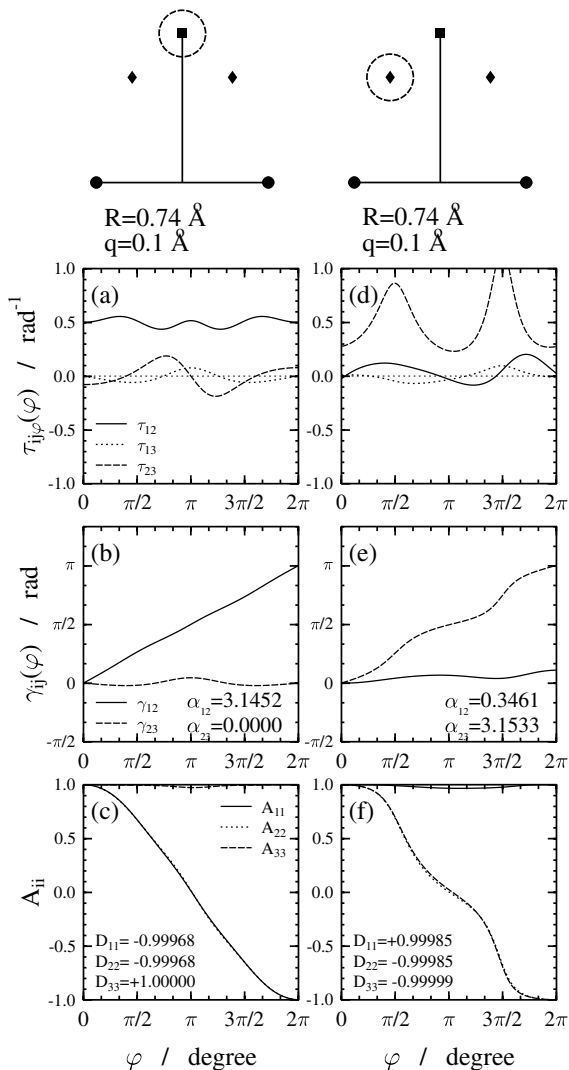
Figure 1. Results as calculated for $R_{HH} = 0.74$ Å: Sub-figs (a)-(c) are for a circle located at the (1,2) D_{3h} ci with radius q=0.1 Å; Sub-figs (d)-(f) are for a circle located at the (2,3) C_{2v} ci with radius q=0.1 Å. In Sub-Figs (a) and (d) are presented the three tangential NACTs $\tau_{\varphi ij}(\varphi|q)$; i<j (see Eq. (28)); In Sub-Figs (b) and (e) are presented the two adiabatic-to-diabatic transformation angles $\gamma_{ij+1}(\varphi|q)$; j=1,2 (see Eq. (29)); In Sub-Figs (c) and (f) are presented the three diagonal elements of the adiabatic-to-diabatic transformation matrix A (see Eq. 33), namely, $A_{jj}(\varphi|q)$; j=1,2,3 and are listed the three diagonal elements of the topological matrix D (see Eq. (34)), namely, $D_{jj}(q)$; j=1,2,3. Full dots stand for the two fixed hydrogens, full squares stand for (1,2) cis; full diamonds stand for (2,3) cis and the circles surrounding the cis are the contours. The straight line perpendicular to the HH axis connects the mid-point between the two hydrogens and the D_{3h} ci point (either the (1,2) or the (2,3) cis).

4.1 THE STUDY OF THE LOOSE CONFIGURATIONS

To study the loose configuration we consider the *situation* for which R_{HH}=0.74 Å. The results are presented in Figs. 1 and 2. Figure 1 contains two columns presenting results as obtained by surrounding single *ci*s: In the first column the circle surrounds a D_{3h} *ci* and in the second it surrounds a *sideways* C_{2v} *ci*.

The results in Figs. 1(a,b) indicate that the surrounded *ci* is a (1,2) *ci* because of the two NACTs $\tau_{jj+1}(\varphi)$; j=1,2 only $\tau_{12}(\varphi)$ is nonzero. It is noticed that $\tau_{12}(\varphi)$ is close to being constant (~0.5) along the whole φ-range and the corresponding ADT angle $\gamma_{12}(\varphi)$ is a uniformly increasing function which at φ=2π attains the value α_{12} =3.1452 Rads, a value close enough to π. In contrast to the (1,2) functions, the (2,3) functions, namely, $\tau_{23}(\varphi)$ and $\gamma_{23}(\varphi)$ possess small values and α_{23} is therefore also relatively small (~0.0 Rads.). Since this (1,2) *ci* happens for the equilateral configuration it is a D_{3h} *ci* and altogether will be labeled as the (1,2) D_{3h} *ci*. The fact that α_{12} is close to π implies that in the region surrounded by this circle $\tau_{12}(\varphi)$ is quantized, or in other words the two lower states of the H+H$_2$ system form in this region a Hilbert sub-space.

Different results are obtained for the second case presented in Figs. 1(d, e, f) (second column). Here the integration is done along a different circle so that the main activity along the φ interval is now related to the (2,3) *ci* NACT. Among other facts, it is now α_{23} (and not α_{12}) which is close to π (in fact 3.1533). Thus, in the region surrounded by this circle it is $\tau_{23}(\varphi)$ which is quantized and therefore it is the second and the third states which form, in this case, a Hilbert sub-space.

Next we briefly discuss the diagonal, φ-dependent, elements of the 3x3 **A**-matrix as presented in Figs. 1(c,f) and the listed 3x3 **D**-matrix diagonal elements. Both, the **A**- and the **D**-matrices become important if and only if the α-values, as calculated for the two-state system, are not multiples of π (or zero). In the case where *all* relevant α-values of the system are multiples of π (or zero), the j-th **A**-matrix diagonal element is expected to be close either to $\cos(\gamma_{jj+1}(\varphi))$ or to $\cos(\gamma_{j-1j}(\varphi))$, as the case may be, and therefore the diagonal **D**-matrix elements are expected to be equal to ±1. As is noticed, the results due to both matrices confirm the two-state results (and do not yield any additional information). For instance the *absolute* value of *all* the **D**-matrix diagonal elements is, indeed, ~ 1; moreover, in the first case (Fig. 1(c)), the (1,1) and the (2,2) elements are equal to –1, which implies that we encounter a (1,2) *ci*, and in the second case, the (2,2) and the (3,3) elements are equal to –1, which implies that a (2,3) *ci* is encountered (for a detailed analysis on this subject see Ref. 22).

Fig. 2 contains two columns presenting results obtained by surrounding two and three *ci*s, respectively (still for the same *situation*). In the first column the calculations are done for a highly asymmetrical case where the center of the circular contour is located at the mid-point between the (1,2) and the (2,3) *ci*s. In the second case we encounter a symmetrical situation where the contour is located at the (1,2) *ci* point. The results here
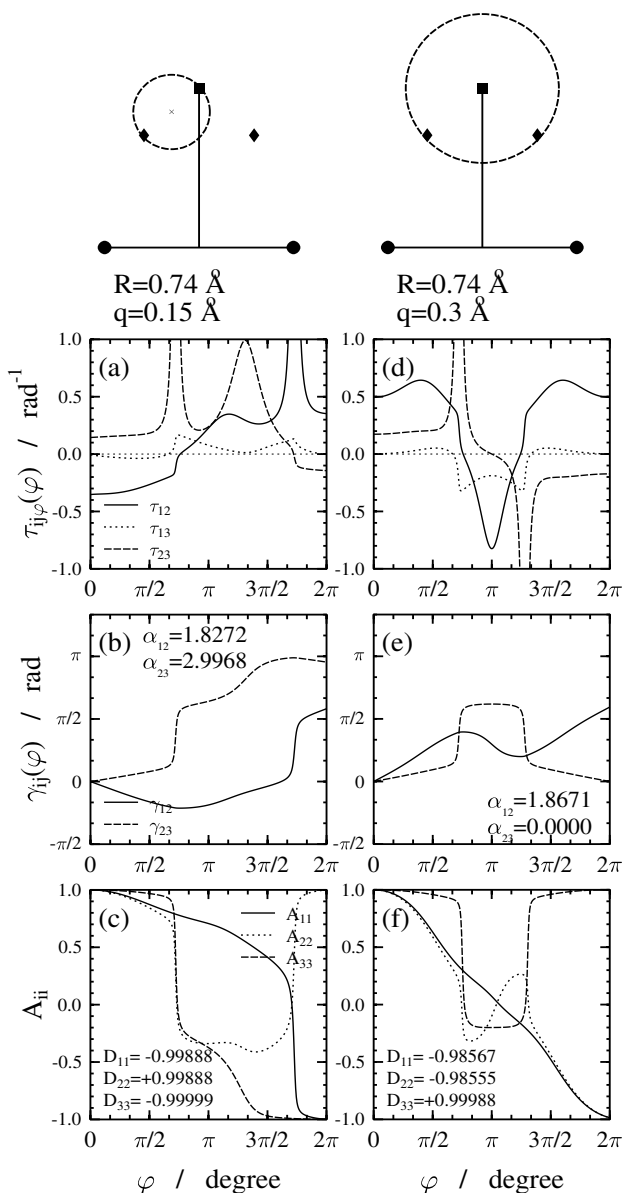
Figure 2. Results as calculated for R_{HH}= 0.74 Å: Sub-figs (a)-(c) are for a circle located at the mid-point between (1,2) D_{3h} ci and the (2,3) C_{2v} ci with radius q=0.15 Å; Sub-figs (d)-(f) are for a circle located at the(1,2) D_{3h} ci with radius q=0.3 Å. For the rest see Fig. 1.

are characterized by the fact that in both cases the values of α_{12} are 1.8004 and 1.8671 Rads., respectively which and significantly different from π (see Figs 2(b, e)). Therefore, in the two regions surrounded by these two circles, it is most likely that the third state is strongly interacting with the two-state system (mainly with the second state) so that the two-state quantization related to the two lower states is, in this case, strongly perturbed.

Next we examine the three-state quantization related to the three lower states and consider Figs. 2(c, f). The figure presents the diagonal, φ-dependent, elements of the 3x3 **A**-matrix and lists the 3x3 **D**-matrix diagonal elements. It is noticed that *all* three diagonal elements of the **A**-matrix which start with the value of +1 at $\varphi=0$ reach, at $\varphi=2\pi$, the values $\sim \pm 1$ which constitutes the diagonal elements of the **D**-matrix. Since for both circular contours we find along the **D**-matrix diagonal the values ± 1 this implies that in the regions surrounded by the above-mentioned contours, the NACM τ_{φ}, related the three lower $^2A'$, is *quantized*. In other words these results indicate that there exist circumstances where *ab initio* NACTs cannot form a two-state quantization but undoubtedly form a three-state *quantization*.

On numerous occasions we emphasized that a negative sign of the j-th diagonal element of the **D**-matrix implies that the j-th eigenfunction flips its sign while the electronic manifold traces the closed contour.[29] Thus, the results of Figs. 2(a, b, c) indicate that it is the signs of the first and the third eigenfunctions that flip their signs. This implies that the circle surrounds one (1,2) and one (2,3) *ci*s (in such a case the sign of the second eigenfunction is flipped twice and therefore the net result is no change in sign) which, indeed, is the case. Different results are obtained in Figs. 2(d, e, f). Here the calculations indicate that it is the signs of the first and the second eigenfunctions that are flipped. This implies that the circle surrounds one (or an odd number of) (1,2) *ci*(s) and (none or) an even number of (2,3) *ci*s. In such a situation the sign of the lowest (first) eigenfunction is flipped once, the sign of the second eigenfunction is flipped an odd number of times (in fact three times in this case) – and therefore the net result is, again, a change of sign, and the sign of the third eigenfunction is flipped twice and therefore, the net result is no sign-flip (similar results were obtained for the C_2H molecule– see Sec. (III.B) of Ref. 30)

4.2. THE STUDY OF THE *COMPACT* CONFIGURATIONS

To study the compact *situation* we consider the configurations defined by assuming $R_{HH}= 0.4777$ Å. The results are presented in Figs. 3 and 4. The more surprising finding that emerges from these figures is that for these configurations we encounter four (4) *ci*s in contrast to only the three (3) *ci*s that were encountered in the previous case. Since *ci*s for different R_{HH}-values are connected by *seam*s, it is inconceivable that seams (or *ci*s) can suddenly disappear or suddenly be formed (at most they may continue into the complex plane). This issue was elaborated in a previous publication (15) and will not be mentioned here as it is not immediately related to the present subject. Fig. 3 contains three columns showing results obtained by surrounding single *ci*s: In the first column the results are due to a circle surrounding a D_{3h} *ci*; in the second due to a circle surrounding a C_{2v} *ci* located on the D_{3h} symmetry line (at a distance of 0.7004 Å from

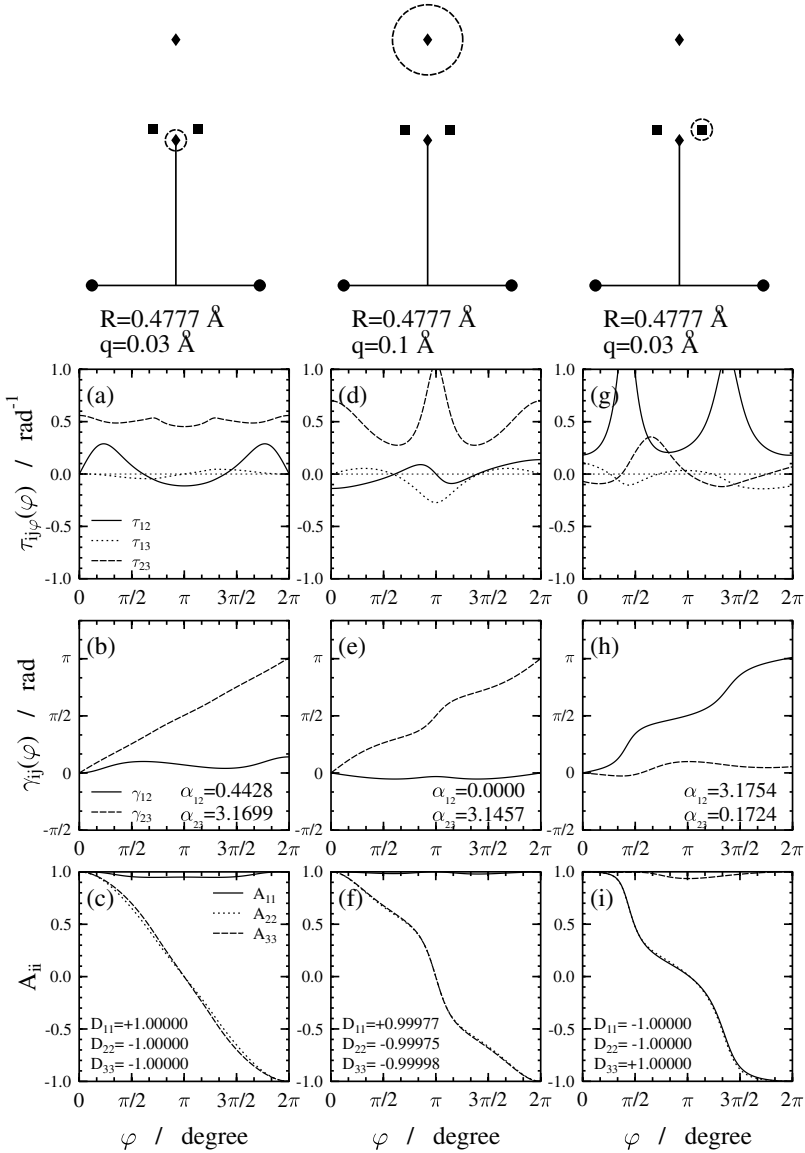*Figure 3.* Results as calculated for R_{HH}= 0.4777 Å: Sub-figs (a)-(c) are for a circle located at the (2,3) D_{3h} ci with radius q=0.03 Å; Sub-figs (d)-(f) are for a circle located at the (2,3) C_{2v} ci with radius q=0.1 Å; Sub-figs (g)-(h) are for a circle located at the (1,2) C_{2v} ci with radius q=0.03 Å. For the rest see Fig. 1 (with the obvious variations).

the HH-axis) - labeled as a *central* C_{2v} *ci* - and in the third column are presented results due to a circle surrounding one of the *sideways* C_{2v} *ci*.

The results in the first column (i.e. sub-figs. 3(a, b, c)) indicate that the D_{3h} *ci* is a (2,3) *Ci*: The only NACT that is significantly different from zero is $\tau_{23}(\varphi)$ which is a slightly φ-dependent function with a value of ~0.5 along the whole φ- range. As a result the corresponding ADT angle $\gamma_{23}(\varphi)$ is a uniformly increasing function which at $\varphi=2\pi$ attains the value $\alpha_{23} =3.167$ Rads., a value close enough to π. In contrast to the (2,3) NACT the (1,2) NACT, namely, $\tau_{12}(\varphi)$ attains small values and α_{12} is, therefore, also relatively small (=0.407 Rads.). The fact that it is α_{23} which becomes ~π and not α_{12} implies that the surrounded ci is not a (1,2) ci as expected, but a (2,3) ci. In other words, in this *situation*, the two excited states are responsible for the D_{3h} ci. A similar situation is encountered for the central C_{2v} ci as presented in the second column (Figs. 3(d, e, f)) The results indicate that it is α_{23} (and not α_{12}) which is close to π (in fact 3.146) so that the revealed ci, just like the D_{3h} ci, is a (2,3) ci.

A different *situation* is obtained for the two symmetrical sideways *ci*s (Figs. 3(g,h,i)). In each case the main activity along the φ-interval is for the (1,2) magnitudes (i.e. $\tau_{12}(\varphi)$ and $\gamma_{12}(\varphi)$) and therefore, it is now, α_{12} and not α_{23}, which becomes π (in fact 3.143) thus implying that this C_{2v} *ci*, just like its symmetrical twin, are (1,2) *ci*s. Since in all three cases the topological phase, whether it is α_{12} or $\alpha_{23,}$ are close to becoming π, this implies that the relevant NACM is a 2x2 quantized matrix.

Next we briefly relate to the diagonal, φ-dependent, elements of the 3x3 **A**-matrix as presented in Figs. 3(c, f, i) and the listed 3x3 **D**-matrix diagonal elements. Both, the **A** and **D**-matrices become important if and only if the α-values as calculated for the relevant two-state systems are not multiples of π (or zero). In case the α-values are *all* multiples of π (or zero) the j-th **A**-matrix diagonal elements is expected to be ~ equal either to $\cos(\gamma_{jj+1}(\varphi))$ or to $\cos(\gamma_{j-1j}(\varphi))$, as the case may be, and the diagonal **D**-matrix elements are expected to be ~ ±1, with the negative signs at appropriate positions. As is noticed, the results due to both matrices confirm the two-state results and do not yield any additional information (see discussion on Figs. 1(c,f)).

In comparing our findings related to the configurations for which $R_{HH} = 0.4777$ Å (see Fig. 3) to those for which $R_{HH} = 0.74$ Å (see Fig. 1), we see that they are substantially different. For $R_{HH} = 0.74$ Å the D_{3h} *ci* was a (1,2) *ci* but here it is a (2,3) *ci* which is a D_{3h} *ci*, then the sideways twin *ci*s which were (2,3) *ci*s are now, for $R_{HH} = 0.4777$ Å, two sideways twin (1,2) *ci*s. Thus the transition (1,2) *ci*s$\Leftrightarrow$ (2,3) *ci*s takes place in the interval {$0.4777<R_{HH}<0.74$Å}. This issue was analyzed, in detail, elsewhere. [15]

Fig. 4 contains three columns, presenting results as obtained by surrounding two, three and four *ci*s, respectively. The results here are characterized by two facts: (1) in all of them the values of α_{12} and α_{23} are significantly different from π and/or from zero; (2) the diagonal elements of the **D**-matrix (listed in Figs. 4(c, f, i)) are, agains ~ ±1. These two facts imply that in the regions surrounded by the relevant circles, none of the two corresponding states can form a NACN that is quantized, but NACMs formed by the three states were quantized.

Next we discuss briefly the signs of the diagonal **D**-matrix elements. We recall that a negative sign in front of the $\mathbf{D}_{jj}$ implies that the j-th eigenfunction flips it sign while the electronic manifold traces the closed contour (circle). Thus the results of the first
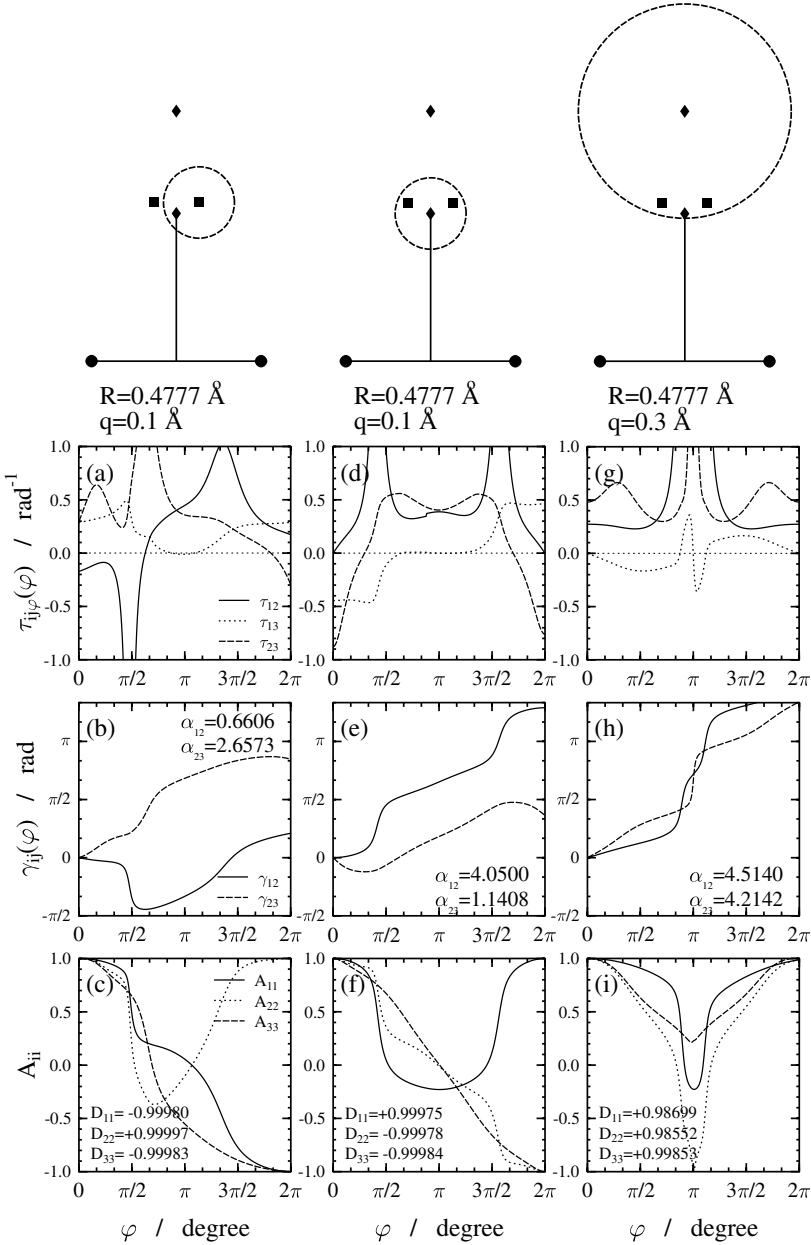
Figure 4. Results as calculated for R_{HH}= 0.4777 Å: Sub-figs (a)-(c) are for a circle located at the mid-point between the (2,3) D_{3h} ci and the (1,2) C_{2v} ci with radius q=0.03 Å; Sub-figs (d)-(f) are for a circle located at the (2,3) D_{3h} ci with radius q=0.1 Å; Sub-figs (g)-(h) are for a circle located at the C_{2v} (2,3) ci with radius q=0.3 Å. For the rest see Fig. 1 (with the obvious variations).

column indicate that it is the signs of the first and the third eigenfunctions that flip their signs (like in case of Fig. 2(c)); the results in the second column indicate that it is the signs of the second and the third eigenfunctions that flip their signs (somewhat different, as in the case in Fig. 2(f), but with a similar interpretation). The more interesting case is the third case where all three diagonal **D**-matrix elements are *positive* and therefore no sign flip takes place. This indicates that the (circular) contour surrounds an even number of (1,2) *ci*s and an even number of (2,3) *ci*s, as is really the case (we encounter, in the present case, two of each kind).

5. Discussion and Conclusions

We indicated in the Introduction that the reasons for writing this article are two-fold: (i) to present a survey of the various conical intersections which govern potential transitions between electronic states and (ii) to establish the 3-state quantization of the NACM for molecular systems.

The survey is carried out for the three lowest states of the (H_2,H) system. In what follows we summarize results and draw conclusions for two *situations* formed by fixed HH distances (labeled as R_{HH}):

(1) We revealed that for these *situations* one encounters four conical intersections: two between the two lower states and two between the two upper states. One of the four is a D_{3h} *ci* and the other three are C_{2v} *ci*s, one of which is located on the symmetry line perpendicular to the HH axis (just like the D_{3h} *ci*) and the other two are located on both sides of this symmetry line and in this way form the twin-*ci*s.

(2) We found that the D_{3h} *ci* and the single (symmetric) C_{2v} *ci* form one group of *ci*s and the (sideways) twin-*ci*s form another group. Each group couples, for a given R_{HH}-value, one pair of states. However, a given group may couple one pair of states for one R_{HH}-value, and another pair of states for a different R_{HH}-value

(3) The final point in this category is related to the fact that we termed all sideways *ci*s as C_{2v}-*ci*s although they are expected to be C_s *ci*s. We checked this finding very carefully and came to the following conclusion: The *ci*s in the $H+H_2$ system are either D_{3h}-*ci*s (the ones that form the equilateral triangles) or C_{2v}-*ci*s, (because they always form isosceles triangles). So far no C_s *ci* have been encountered.

The second subject treated here, in some detail, is related to the possible *quantization* of the non-adiabatic coupling matrix. We shall not refer to the two-state *quantization* as this issue was analyzed in numerous publications. The more intriguing subject is the 3-state *quantization* which was considered, recently, for the first time, for one single *situation* of the C_2H molecule.[15] In the present publication we consider two different *situations* defined by assigning to R_{HH} two different values, namely, R_{HH}= 0.74 and 0.4777 Å and in this way studying numerous configurations and *ci*s. In each case we applied various circular contours, some for symmetrical situations and others for non-symmetrical situations. Also, the number of *ci*s that were surrounded varied from one case to another: in some cases we surrounded two *ci*s, in others three *ci*s and in one case four *ci*s were surrounded. In all circumstances the diagonal elements of the 3x3 **D**-matrix are very close be ±1 although sometimes, in particular when the radius of the

closed circular contour becomes relatively large, deviations are seen (the largest one is 0.0145). The reason for the observed (slight) deviations is probably 'background' noise due to higher states which affects the third state (and therefore the two other states), for instance via remote (3,4) *ci*s. We tried to locate (3,4) *ci*s but we could not expose any, at least not at a reasonable distance from the ones discussed here.

Acknowledgement

References

1. M. Born and J.R. Oppenheimer, Ann. Phys. (Leipzig), 84, 457 (1927)
2. M. Born and K. Huang, Dynamical Theory of Crystal Lattices, (Oxford University, New York, 1954)
3. H. Hellmann, Einfuhrung in die Quantenchemie, Franz Deutiche, Leipzig, 1937; R. Feynman, Phys. Rev. 56, 340 (1939)
4. M. Baer and G.D Billing (Eds.), The Role of Degenerate States in Chemistry, Adv. Chem. Phys., Vol. 124 (John Willey & Sons Hoboken, N.J., 2002)
5. H.C. Longuet-Higgins, U. Opik, M.H.L. Pryce and R.A. Sack, Proc. R. Soc. Lond. A 244, 1 (1958); H.C. Longuet-Higgins, Adv. Spectrosc. 2, 429 (1961); G. Herzberg and H.C. Longuet-Higgins, Discuss. Faraday Soc. 35, 77 (1963); H.C. Longuet-Higgins, Proc. R. Soc. London Ser. A 344, 147 (1975)
6. M.S. Child, in The Role of Degenerate States in Chemistry, Eds. M. Baer and G.D. Billing, Adv. Chem. Phys., 124, Chap.1 (2002)
7. C. A. Mead, Chem. Phys. 49, 23 (1980)
8. (a) M. Baer, Chem. Phys. Lett. 35, 112(1975); (b) M. Baer, Molec. Phys., 40,1011 (1980)
9. (a) M. Baer, Chem. Phys, 259, 123 (2000); (b) *ibid*. Phys. Reps. 358, 75 (2002); (c) *ibid*. Ref. 4, Chap.2
10. M. Baer and A. Alijah, Chem. Phys. Lett., 319, 489 (2000); (b) M. Baer, J. Phys. Chem., A 104, 3181 (2000)
11. M. Baer, S.H. Lin, A. Alijah, S. Adhikari and G.D. Billing, Phys. Rev. A, 62, 032506-1 (2000)
12. R. Englman, The Jahn-Teller Effect in Molecules and Crystals (Wiley (Interscience), New York, 1972)
13. B. Bersuker and V.Z. Polinger, Vibronic Interactions in Molecules and Crystals (Springer, N.Y., 1989)
14. I. B. Bersuker Chem. Rev. 101, 1067 (2001).
15. G. Halász, A. Vibók, A.M., Mebel and M. Baer, J. Chem. Phys. 118, 3052 (2003)
16. A. Vibók, G. Halász, T. Vertesi, S. Suhai, M. Baer and J.P. Toennies (submitted for publication)
17. W. Lichten, Phys. Rev., 164 ,131 (1967); F. T. Smith, Phys. Rev. 179, 112 (1967)
18. (a) A. Kuppermann, in Dynamics of Molecules and Chemical Reactions, Eds. R.E. Wyatt, R.E. and J.Z.H. Zhang (Marcel, Dekker, Inc., N.Y., 1996) p. 411; (b) V. Sidis, in State-to-State Ion Molecule Reaction Dynamics Eds. M. Baer, M. and C.Y. Ng, (Adv. Chem. Phys. 82, 73 (1992)), Vol. II; (c) T. Pacher, L.S. Cederbaum and H. Köppel, Adv. Chem. Phys. 84,293 (1993); (d) W. Domcke and G. Stock, Adv. Chem. Phys., 100,1 (1997); (e) M. Baer,

in: Theory of Chemical Reaction Dynamics, Ed. M. Baer (CRC, Boca Raton, 1985), Vol. II, Chap. 4

19. (a) F. Rebentrost and W.A. Lester, J. Chem. Phys, 64, 3879 (1976); (b) F. Rebentrost, in Theoretical Chemistry: Advances and Perspectives, D. Henderson and H. Eyring, eds. (Academic Press, New York, 1981), Vol. VIb; (c) A. Macias and A. Riera, J. Phys. B 11, L489 (1978); (d) A. Macias and A. Riera, Int. J. Quantum Chem. 17,181 (1980);(e) C. Petrongolo, G. Hirsch, and R. Buenker, Molec. Phys., 70, 825; 835, (1990)

20. G.D. Billing, M. Baer and A.M. Mebel, Chem. Phys. Lett. 372, 1 (2003)

21. Yang, C.N. and Mills, R.L., Phys. Rev. 96, 191 (1954)

22. M. Baer, Chem. Phys. Lett. 329,450 (2000).

23. R. Baer, J. Chem. Phys, 117, 7405 (2002).

24. T. Vertesi, A. Vibók, G. Halász, A. Yahalom, R. Englman and M. Baer, J. Phys. Chem. A, (in press)

25. D. Bohm, Quantum Theory (Dover Publications, Inc. 1989, N.Y.) p. 41

26. R. Krishnan, M. Frisch and J.A. Pople, J. Chem. Phys. 72, 4244 (1980)

27. D.F. Feller and K. Ruedenberg, Theor. Chim. Acta 52, 231 (1978)

28. A. Mebel, A. Yahalom, R. Englman and M. Baer, J. Chem. Phys. 115, 3673 (2001).

29. M. Baer J. Phys. Chem. A 105, 2198 (2001)

30. A.M., Mebel, G. Halász, A. Vibók, A. Alijah, and M. Baer, J. Chem. Phys. 117, 991 (2002)

NON-ADIABATIC DYNAMICS IN THE O+H$_2$ REACTION: A TIME-INDEPENDENT QUANTUM MECHANICAL STUDY

B. MAITI AND G.C. SCHATZ*

Department of Chemistry
Northwestern University, Evanston, IL 60208-3113 USA

Abstract. A time-independent quantum scattering method has been used to study intersystem crossing (ISC) effects in the bimolecular reaction O + H$_2$. Our studies, involving a four-state one dimensional model, give fully coupled reaction probabilities that indicate significant quantum effects, including enhanced tunneling for the ground state reaction, significant Stuckelberg oscillations at energies well above threshold for certain states, and strong mixing of the product spin-orbit populations that leads to statistical behavior for some initial states and even inverted populations in some cases. Comparison of these results with those from a recently developed trajectory surface hopping (TSH) method which uses a "mixed" representation in full dimensionality are examined, and we conclude that the one-dimensional model overemphasizes coherence and interference effects, although many of the same effects occur.

1. Introduction

Spin-orbit mediated intersystem crossing plays a key role in the dynamics of chemical reactions in many areas of the chemistry, physics and particularly in biology; particularly in reactions where the ground state of the reactants/products involves a high spin state and during the course of the reaction a low spin state crosses the high spin state to provide a lower energy path for reaction. A reaction which provides an example of this behavior is O(^{3}P,^{1}D) + CH$_3$I. Here, using crossed molecular beam methods, Alagia et al [1] demonstrated that there is a significant probability of nonadiabatic transition from the triplet to the singlet state, which opens up a more reactive path to the product through the formation of a long-lived intermediate in the deep singlet well. Related behavior has been suggested for the reaction of transition metal cations with dihydrogen (and its isotopomers). Here Zhang et al. [2] predicted that because of strong spin-orbit coupling among surfaces of differing spin, the reactivity of ground state third-row transition metal cations

is much higher than that of the first and second-row transition metal cations due to the presence of low energy pathways on low-spin surfaces.

In spite of these above quoted examples, very few quantitative theoretical studies of intersystem crossing effects have been reported. This is due to the fact that the number of potential energy surfaces that one needs to generate for even the simplest atom-diatom reaction is significant (usually a minimum of three as we shall see later). Also, spin-orbit (SO) coupling surfaces are not easy to calculate, and they have rarely been determined as function of all the coordinates involved in the reaction. In addition there are serious problems with developing dynamics algorithms to study coupled states problems with multiple crossings, and asymptotic coupling.

Recently, Hoffmann and Schatz [3] made some initial progress in the development of theoretical methods for these problems by implementing a trajectory surface hopping (TSH) procedure for studying ISC in bimolecular reactions and applying it to the $O + H_2$ reaction. For this reaction, whose intersystem crossing dynamics has long been of interest [4], the ground state $O(^3P)$ (asymptotic degeneracy = 9) is coupled by spin-orbit interaction to the ^1D excited state (degeneracy = 5), including one component which crosses all the triplet states to give the deep water minimum. In addition, the singlet and triplet states interact as the products $OH(^2\Pi)+H$ (asymptotic degeneracy = 8) are formed. Hoffmann and Schatz demonstrated that it was possible to reduce the important components of the reaction dynamics to just four states (3 triplet and 1 singlet) which are coupled in the reagents, in the products and also at intermediate geometries. They developed a TSH approach to describe the reaction dynamics, but they were forced to use a diabatic representation in order to generate physically meaningful ISC probabilities. Unfortunately, this approach fails to describe the asymptotic energy states correctly, where because of asymptotic SO coupling, an adiabatic treatment is essential. Another weakness of their study was that the SO coupling surfaces were only developed for a restricted range of geometries (near the reactant and product asymptotes) and then interpolated at close range. However, in spite of these weaknesses, their results were useful for determining the role of the short range singlet-triplet crossing on reactive cross sections and product energy partitioning, and they found that this crossing produces a small but possibly measurable effect at collision energies that are well above the barrier.

Very recently, we have studied the $O(^3P,^1D) + H_2$ reaction [5] using a TSH method in full dimensionality that is based on a "mixed" representation in which the reactant and product asymptotes are treated adiabatically, and the triplet-singlet crossing seam region is treated diabatically with a smooth switch in representations in between, and with transitions between states being described throughout. In the mixed representation, the couplings between the locally defined ("mixed") states are relatively weak so the TSH approximation to the dynamics is expected to be accurate. The results of the calculations confirmed the earlier conclusions of Hoffmann and Schatz that nonadiabatic effects are relatively small

at the point of crossing between the singlet and triplet surfaces, and in addition, they provided for the first time information about the variation of reactivity with reagent fine structure (of O(^{3}P$_{2,1,0}$)) and the product fine structure distributions (of OH(^{2}Π$_{3/2,1/2}$)).

In this paper we study another aspect of the ISC dynamics associated with the O(^{3}P,^{1}D) + H$_2$ reaction, namely the quantum dynamics of the intersystem crossing process. A full three dimensional quantum dynamics treatment of this problem is still quite formidable, especially if product state-resolved cross sections are to be considered, so in this work we simplify the problem to a one dimensional model that includes the same four states that were considered previously [5]. This is somewhat like an earlier study of Hoffmann and Schatz [8] who considered a one dimensional quantum model with two coupled states, but the present model enables us to study the influence of reagent and product asymptotic coupling, in addition to the crossing between singlet and triplet states that occurs midway during the reaction. In addition, in the present model the potential curves and their couplings are derived from the ab initio calculations, rather than taken as empirically determined functions.

The rest of the article is organized as follows: after a brief description of the methodology used in our calculations in section 2, we discuss our results in section 3 and finally in section 4, we summarize our findings.

2. Potential Energies, Spin-orbit Coupling and Dynamics Calculations

We have adapted the general methodology proposed recently by Hoffmann and Schatz [3] for studying ISC effects in bimolecular reactions. In that work it was demonstrated that there are only seven electronic states that most directly are coupled by spin orbit coupling in the O + H$_2$ reaction dynamics. These seven states correspond to the six states associated with the ^{3}Π configuration of the linear OH$_2$ system and the lowest energy component of the ^1D state of O. By invoking a parity decoupling transformation, the seven state basis can further be reduced in dimension into 4×4 and 3×3 subblocks. As we are only interested in effects associated with transitions between the singlet and triplet surfaces, then only the former subblock is relevant, as it includes the components of both the singlet and triplet states: ^{3}A″($M_s = \pm 1$), ^{3}A′($M_s = 0$) and ^{1}A′($M_s = 0$), while the latter includes only triplet components: ^{3}A″($M_s = 0$), ^{3}A′($M_s = \pm 1$).

Within this four state basis, Hoffmann and Schatz used an effective nuclear charge one-electron Breit-Pauli spin-orbit Hamiltonian and CASSCF calculations to determine the spin-orbit coupling surfaces for a restricted range of geometries. Subsequently, Maiti and Schatz [5] used a two electron Breit-Pauli Hamiltonian, and determined global spin-orbit coupling surfaces. Here we use the latter coupling surfaces to define the couplings for the one dimensional model. The nonrelativistic surfaces used to define the diagonal potentials for the model are taken from the work of Rogers et al [6].
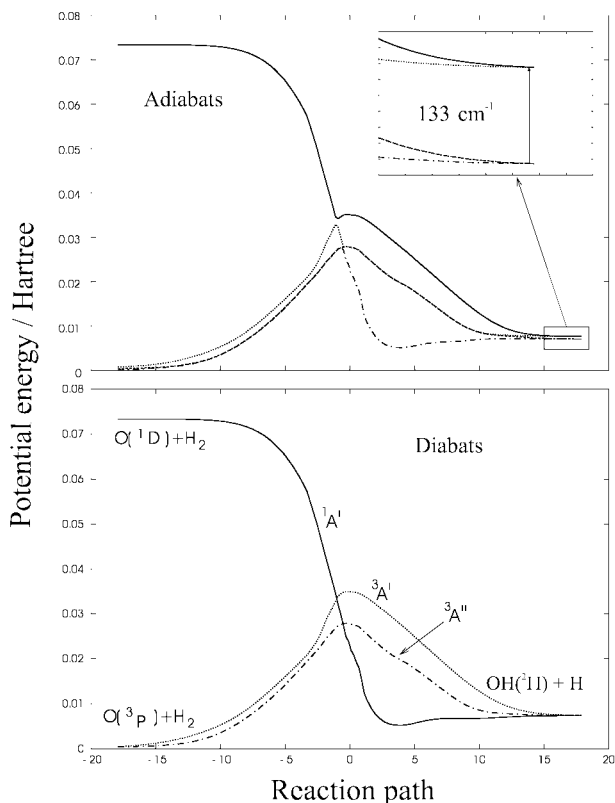
Figure 1. Reaction path model of singlet (^{1}A$'$) and triplet (^{3}A$'$ and ^{3}A$''$) potential energy surfaces associated with the O(^{3}P,^{1}D) + H$_2$ reaction. The curves refer to the potential along minimum energy path of the triplet reaction for slightly bent O-H-H geometries in: (a) diabatic and (b) adiabatic representation. Note that although there are only three diabats, the adiabats are derived from the four state basis defined in the text.

Our quantum scattering calculations refer to the reduced dimensional (reaction path) model of O + H$_2$ depicted in Figure 1. As mentioned above, the four states that we include are: one singlet (^{1}A$'$(M_s = 0)), and three triplets (^{3}A$'$(M_s = 0) and two spin states associated with ^{3}A$''$(M_s = ±1)). The figure only shows three energy levels (except in the product asymptote) because the two states in ^{3}A$''$(M_s = ±1) have the same nonrelativistic energy. The figure presents potential curves in both diabatic and adiabatic representations, where "diabatic" in this case refers to nonrelativistic while "adiabatic" refers to results in which the sum of nonrelativistic and Breit-Pauli Hamiltonians is diagonalized. In all cases the potential curve information has been derived from the potential and couplings evaluated along the minimum energy path between reactants and products, with the constraint that the O-H-H structure is slightly (10° degrees) bent. The choice
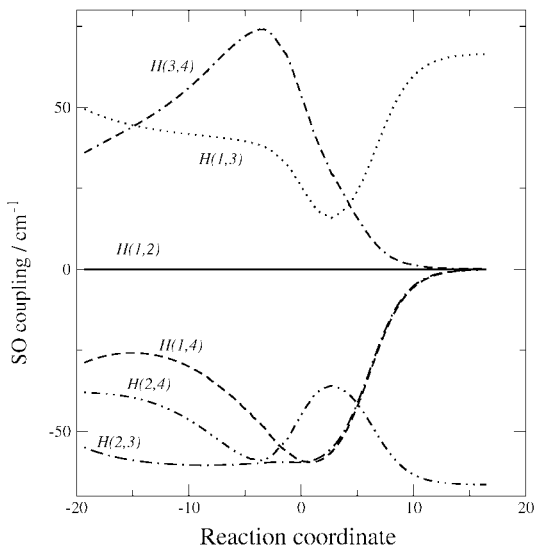
Figure 2. Spin-orbit coupling elements (in cm^{-1}) plotted against reaction coordinate for slightly bent O-H-H geometries. The numbers in parentheses refer to: $1 = {}^3A''_x$ [$= {}^3A''(+1) + {}^3A''(-1)$], $2 = {}^3A''_y$ [$= {}^3A''(+1) - {}^3A''(-1)$], $3 = {}^3A'(0)$ and $4 = {}^1A'(0)$.

of a bent structure was made because the crossing energy between the singlet and triplet surfaces is anomalously high for linear O-H-H configurations. The crossing energy is largely independent of angle for angles between 10 and 170 degrees, so the precise choice of angle is not that important provided that it is not linear.

The curves in the bottom panel of Figure 1 show expected behavior of the diabats, namely triplet states that have a 0.03 hartree barrier, with the reaction overall being endoergic by roughly 0.01 hartree, and a singlet state with a small well, and which crosses the triplets near the top of the triplet barrier. The splitting between the $^3A'$ and $^3A''$ surfaces arises because of the slightly bent structure that was used for the reaction path analysis (the states are degenerate for collinear geometries). Also, the singlet well would be much deeper if more bent structures were used.

The curves in the top panel of Figure 1 are for the most part only slightly different from those in the bottom, thereby demonstrating the weakness of the spin-orbit interaction (as will be discussed further below). The inset to the figure shows that in the product asymptote, the four adiabats split into two pairs, corresponding to the 3/2 and 1/2 components of the $^2\Pi$ state of OH. Analogous behavior occurs in the reagent asymptote, where $^3A'$ and the two components of $^3A''$ recouple to form $^3P_{2,1,0}$.

Figure 2 presents the SO matrix elements associated with the four states in our model. Here we use the following state labels: $1 = {}^3A''_x$ [$= {}^3A''(+1) + {}^3A''(-1)$], $2 = {}^3A''_y$ [$= {}^3A''(+1) - {}^3A''(-1)$], $3 = {}^3A'(0)$ and $4 = {}^1A'(0)$. The indicated linear combinations of the triplet components with M_s values +1 and -1 are used to obtain a real Hamiltonian matrix, as described by Hoffmann and Schatz. The results in Figure 2 are based on full dimensional spin-orbit surfaces presented by Maiti and Schatz, as evaluated along the same minimum energy path as used for the results in Figure 1. We see that the magnitude of the coupling elements vary in the range -80 to +80 cm^{-1}. It turns out that the coupling matrix element $H(1,2)$ between the two components of the ${}^3A''$ state is identically zero for all geometries. The other matrix elements have a complicated dependence on reaction coordinate and most are nonzero in the reagent and product asymptotes (which is why the adiabats are split in Figure 1 in the asymptotes).

The quantum scattering method which we use is related to a technique described in detail by one of us previously [7], representing a generalization of the earlier work of Hoffmann and Schatz [8] from two to four coupled states. In this method the Schrödinger equation for the four states is solved by sector propagation, integrating from $x = -20$ to $x = 20$ (where x is the reaction path coordinate), using a step size of 0.005. The reduced mass in the calculation is 3263.09 AMU (the O-H$_2$ reduced mass). The 4x4 Hamiltonian matrix is defined by the diabats in Figure 1, and the couplings in Figure 2. By propagating one set of independent solutions from negative x to positive x and then a second set from positive to negative, a complete set of solutions is obtained, and then this is matched to proper asymptotic solutions to determine the scattering matrix and the reaction probabilities. Note that the proper asymptotic solutions are defined in the adiabatic representation, but the propagation is done in the diabatic representation, so a transformation of the solutions in both the reactant and product regions is required before a reaction probability is defined. Tests of convergence of the probabilities indicate that they are converged with respect to the integration parameters.

State-to-state reaction probabilities are related to the S matrix elements by

$$P_{\alpha t \alpha' t'}(E) = |S_{\alpha t \alpha' t'}(E)|^2 . \tag{1}$$

where the index α refers to reagents or products and t refers to electronic state (t = 1, 2, 3, 4). We will also calculate probabilities $P_{\alpha t}$ which refers to the sum of the state to state probability over all possible reactive final states. Since we are only interested in reaction starting from O + H$_2$, we omit the indices α and α' in the following, implicitly assuming that α refers to O + H$_2$ and α' refers to OH + H.

3. Results and Discussion

We first consider scattering results for the limiting cases of uncoupled diabatic and adiabatic dynamics. Figure 3 presents reaction probabilities as a function of

energy for the three triplet and one singlet initial states of the reactants and going to the four possible product states (two corresponding to the ground spin-orbit state of OH, and two to the excited spin-orbit state of OH), with the top panel referring to diabatic results and the bottom to adiabatic results. Since there is no coupling, only the diagonal probabilities P$_{tt}$ are nonzero, where for the adiabatic representation the numbering convention refers to states ordered by energy in both reagents and products, while for the diabatic representation, the states are ordered by energy in the reagents but not the products.

The behavior of the diabatic and adiabatic results is easily understood based on Figure 1. Thus, in the diabatic results, the two curves $\mathbf{P}_{11}$ and $\mathbf{P}_{22}$, which refer to the $^3A''$ states, are identical, with an effective threshold (where the reaction probability first equals 0.01) of about 0.010 Hartree, while $\mathbf{P}_{33}$, which refers to the $^3A'$ state has a slightly higher effective threshold of about 0.016 Hartree. This correlates with the larger barrier height in Figure 1, and we also see that $\mathbf{P}_{44}$ has essentially a zero threshold energy relative to the O(^{1}D) energy of 0.072 Hartree.

In the adiabatic picture, Figure 3 shows that the threshold energy of the lowest energy curve, labelled $\mathbf{P}_{11}$, drops to 0.007 Hartree, while that for $\mathbf{P}_{22}$ rises to 0.012 Hartrees, and that for $\mathbf{P}_{33}$ drops to 0.012 Hartrees. These results arise because the lowest adiabat now samples the singlet well, and its effective barrier is narrower than in the corresponding diabatic system. The second adiabat, by contrast, has a barrier that is very close to the lowest diabat, being slightly higher in energy because it is repelled by the lowest adiabat. The third adiabat is very similar to the second adiabat, as they have nearly degenerate energy curves to the right of the singlet/triplet crossing. The fourth adiabat is very much the same as the fourth diabat, except that the well is replaced by part of the triplet barrier. This seems to have a negligible effect, as $\mathbf{P}_{44}$ is almost the same in the two panels in Figure 3.

Fully coupled quantum results for the total reaction probabilities $\mathbf{P}_t$ for $t = $ 1, 2, 3, 4 are plotted in Figure 4 as a function of energy. Figure 4 shows that the fully coupled results are in-between the adiabatic and diabatic results close to threshold, with the effective thresholds being at 0.009 for $\mathbf{P}_1$, and 0.012 for $\mathbf{P}_2$ and $\mathbf{P}_3$. The similar behavior of $\mathbf{P}_2$ and $\mathbf{P}_3$ is certainly closer to the adiabatic results, but a key difference between the uncoupled and coupled results is that $\mathbf{P}_2$ and $\mathbf{P}_3$ show oscillations in the coupled results, and neither probability rises above 0.9 until the energy is above the O(^{1}D) threshold.

Perhaps the most striking result in Figure 4 is the sharp peak in $\mathbf{P}_2$ and $\mathbf{P}_3$ at an energy of 0.025, while at the same time $\mathbf{P}_1$ shows no structure at all. To understand this, we note that the diabats associated with all three of the triplet states cross the singlet state (see Figure 1) at a reaction coordinate x value of about -2. Under these circumstances, one would expect to see a rising reaction probability for each triplet state at low energies (where the reaction probability is less than 0.5), and then falling probabilities at higher energies that is associated with reflection of the incident wave when the excited singlet can be accessed.
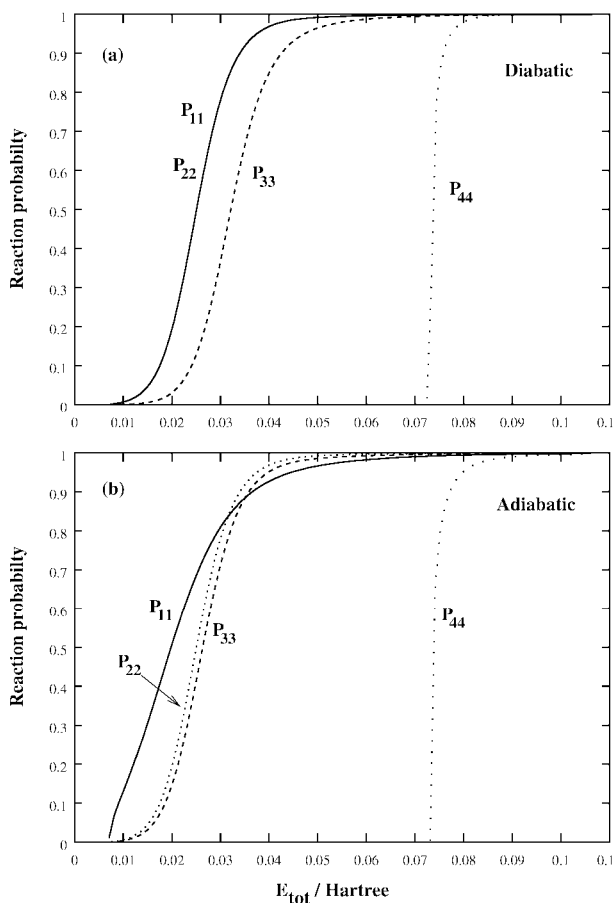
Figure 3. Reaction probabilities as a function of total energy (in Hartree) for uncoupled models: (a) Diabatic, (b) Adiabatic. In both panels, the probabilities labelled $\mathbf{P}_{11}$ and $\mathbf{P}_{22}$ are associated with the $^3A''$ initial state, while $\mathbf{P}_{33}$ is associated with $^3A'$ and $\mathbf{P}_{44}$ with $^1A'$.

In other words, the singlet state acts like a wall if the energy is high enough to allow substantial transitions to the branch of the singlet that dissociates to $O(^1D)$. However this behavior occurs for only two of the three triplet states due to a remarkable property of the spin-orbit couplings depicted in Figure 2. Here we find that the spin-orbit couplings $H(1,4)$ and $H(2,4)$ in Figure 2 are nearly identical at $x = $ -2. This means that there is a linear combination of triplet states 1 and 2 which will have no coupling to state 4. In addition since these states 1 and 2 are degenerate and have no direct coupling ($H(1,2)=0$), any linear combination of these states is acceptable, in which case the one with no coupling to state 4 will not show reflection at high energy.
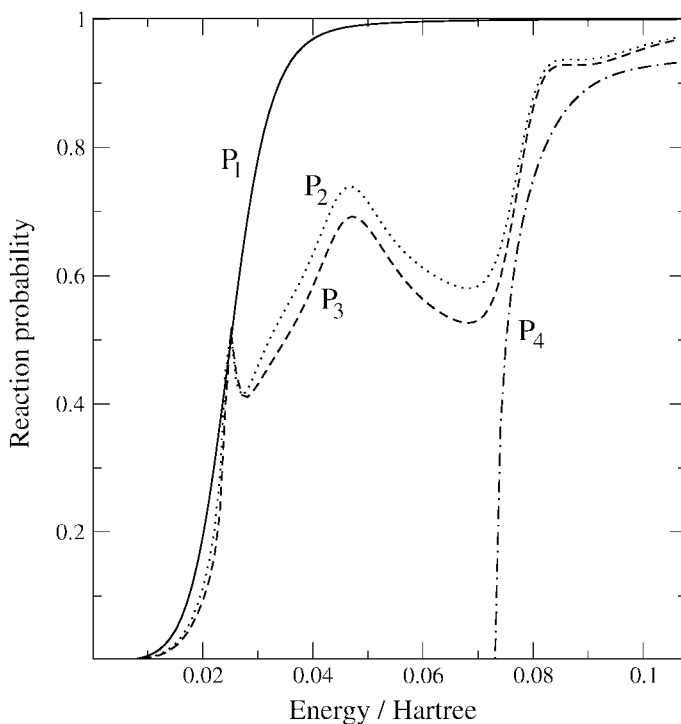
Figure 4. Fully coupled quantum reaction probabilities, summed over final states, as a function of total energy (in Hartree) for the same four initial states as in Figure 3.

To further analyze the fully coupled results, in Figure 5 we present the breakdown of each of the exact probabilities in Figure 4 into final-state-resolved probabilities, and in Figure 6 we show reaction probabilities that have been summed into groups of product states that correspond to the $^2\Pi_{3/2}$ (the solid curve) and $^2\Pi_{1/2}$ (the dotted curve) states of OH. Note that the state numbers in Figure 5 refer to the adiabatic ordering, i.e., by energy. Both figures show that the off-diagonal reaction probabilities are generally quite large, with significant interference oscillations that are similar to those seen in Figure 4. In addition, we find large probabilities for states other than the adiabatic state to be populated, with Figure 6 showing almost identical probabilities for the two spin-orbit states for reaction starting in states 1 and 4. Also, we find that reaction starting from state 2 predominantly gives the excited spin-orbit state of OH, while reaction starting from state 3 predominantly gives the ground spin-orbit state.

To understand the behavior of Figures 5 and 6, we note from Figure 2 that all

Figure 5. Fully coupled final-state-resolved reaction probabilities as a function of total energy (in Hartree). Solid curve represents branching to product channel 1, dotted curve to channel 2, dashed curve to channel 3 and separated dotted curve to channel 4. Product channel 1 and 2 correspond to $OH(^2\Pi_{3/2})$ + H, and channel 3 and 4 correspond to $OH(^2\Pi_{1/2})$ + H.

the spin-orbit matrix elements go to zero for x greater than 15 except $H(1,3)$ and $H(2,4)$. In addition, we note that the diabats in Figure 1 approach the product asymptote between $x = 10$ and $x = 15$, which means that the four product states experience strong coupling at just the point where the only significant coupling involves $H(1,3)$ and $H(2,4)$. As a result, we might expect that if the reaction dynamics was otherwise adiabatic, then the product state distributions would reflect coupling between states 1 and 3, and states 2 and 4. This then gives some insight concerning Figure 5, which shows that the largest probabilities associated with initial state 1 are to final states 1 and 3, while the largest reaction probability associated with initial state 2 is to final state 4. These simple trends do not extend to initial states 3 and 4, suggesting that the simple model of adiabatic behavior
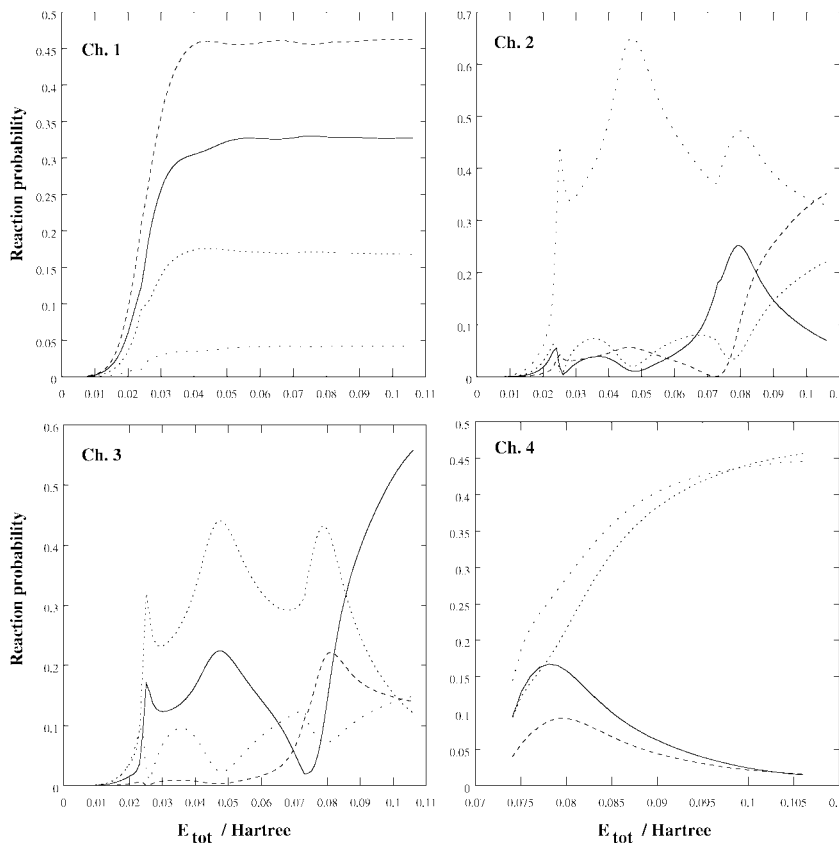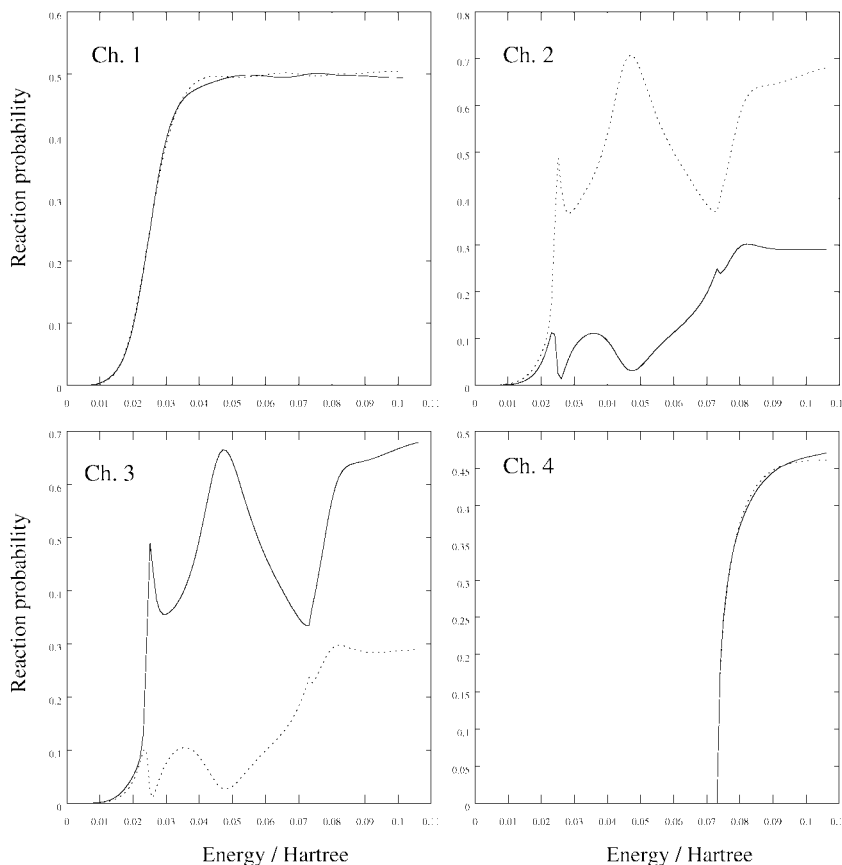
Figure 6.   Fully coupled product spin-state resolved reaction probabilities as a function of total energy (in Hartree). Solid curve represents branching to product spin-state $^2\Pi_{3/2}$ and dotted curve to $^2\Pi_{1/2}$ of the OH.

prior to the product asymptote is not correct for these states. However the results for initial states 1 and 2 demonstrate that the product asymptotic coupling is very strong, allowing in the case of initial state 1 for a larger population in final state 3 than in final state 1 (and likewise for initial state 2 yielding final state 4). In addition, we see in Figure 6 that for initial state 1, the probability of the two spin-orbit states is the same, which indicates that the excess of final state 3 over state 1 that is seen in Figure 5 is balanced by a reverse trend for the populations in states 2 and 4. This can be rationalized by realizing that initial state 1 is coupled to state 4 (but not to state 2) by coupling matrix elements that go to zero asymptotically, so any flux that is initially lost to state 4 will mostly end up in state 2 as a result of the $H(2,4)$ coupling. (Here we note that in contrast to our earlier argument concerning the lack of coupling of states 1 and 4, in the product asymptote, the
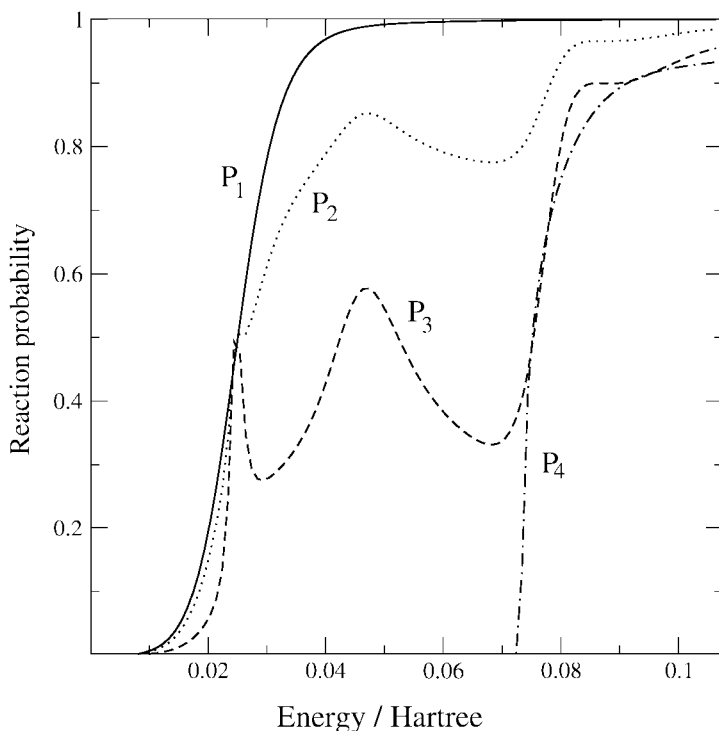
Figure 7.   Same as Figure 4, except that for reduced coupling strength by a factor of 10.

coupling terms $H(1,4)$ and $H(2,4)$ are very different in magnitude, and states 1 and 2 have different energies, so there is no linear combination of states 1 and 2 that is decoupled from state 4).

If we turn off the singlet-triplet coupling in the region where the singlet and triplet potential surfaces cross, the full quantum probabilities (not shown) are very similar to those in Figure 5. This indicates that for the one dimensional model, couplings at/near the singlet-triplet crossing do not make a noticeable difference in the state-selected reaction probabilities and hence the ISC processes. Therefore, one could infer that the nonadiabatic transitions occur mostly near the reactant and product asymptotes. Which is in accord to our recent 3D trajectory surface hopping results [5] which show that most of the hops occur near the asymptotes.

When we reduce the strength of the SO coupling by a factor of 10, there is a dramatic change in the total reaction probabilities plotted against energy in Figure 7. Here we see threshold behavior that is more like the diabats than the adiabats, with $\mathbf{P}_1$ and $\mathbf{P}_2$ being nearly equal, with a threshold of about 0.010 hartree,

while $\mathbf{P}_3$ has a somewhat higher threshold of about 0.013. Also, we still see a strong oscillation in $\mathbf{P}_3$ when the reaction probability exceeds 0.5 for the first time, however $\mathbf{P}_2$ shows only a slight kink at the same point, and then continues rising. Since the $H(3,4)$ coupling is larger (Figure 2) than $H(2,4)$ this would suggest that wave reflection associated with singlet-triplet crossing is more important for initial state 3 than for initial state 2, and indeed this is what Figure 7 shows.

4. Summary and Conclusion

The present time-independent scattering calculations indicate that even though the spin-orbit coupling matrix elements are weak (< 80 cm^{-1}), there are many noticeable effects that they produce in this reduced dimensional model of the O(^{3}P)+H$_2$ reaction. The threshold behavior of the reaction probabilities is more like that expected for the adiabats than the diabats, indicating that there can be significant tunneling through the narrow barrier that results from intersection between the triplet and singlet states than occurs through the pure triplet barrier. Above threshold, some of the reaction probabilities show strong oscillations due to reflection from the singlet state, which acts like a repulsive state in this context, but the ground state is different due to an accidental decoupling of this state from the singlet state that results because two spin-orbit matrix elements are the same at the point of the crossing, and there is no direct spin-orbit coupling between these states. In the product states, the results suggest that there is strong coupling between pairs of the four states in the product asymptotic region, and this leads to product spin-orbit distributions that on average even out the $^2\Pi_{3/2}$ and $^2\Pi_{1/2}$ populations of OH.

An important issue that we need to consider in this work is how these results will extend to quantum dynamics in three dimensions, and moreover, what we can learn from these results about the validity of the TSH calculations that have already been done. With respect to the threshold behavior, it seems likely that the enhanced tunneling that arises from the narrower barrier would be important if the singlet-triplet crossing occurs before the triplet barrier. However the work of Hoffmann and Schatz[3] demonstrated that for most orientations of the O+H$_2$ collision, the crossing occurs after the barrier. In this case, the enhanced tunneling effect is likely to be small. Further evidence for this comes from recent theory/experiment comparisons for O+H$_2$ [9] in which the excitation function observed in crossed molecular beam experiments was found to be in excellent agreement for energies close to threshold with the results of 3D wavepacket calculations using high quality potential surfaces, but without inclusion of intersystem crossing effects. Thus at this point we conclude that enhanced tunneling arising from intersystem crossing is a small effect.

With respect to sharp oscillations in reaction probability that occur at higher energy due to reflection from the excited singlet, we expect that this is a real effect that should be captured by TSH calculations. Indeed, somewhat analogous

behavior was seen by Hoffmann and Schatz in their two-state calculations [8], and similar behavior for TSH calculations done using the same two state model was also found. However, it is less clear that this effect will be as important in three dimensional dynamics as in a one-dimensional model, as the nature of the intersections between singlet and triplet states in three dimensions is much more complex, and this should lead to loss of coherence.

A related question is whether there would be differences in reactivity between different fine structure states of $O(^3P)$ due to the accidental cancellation that causes state 1 to be largely decoupled from state 4. The presence or absence of this effect in 3D TSH calculations would be crucially dependence on the underlying basis set (adiabatic or diabatic) used. For example, this would not show up if the diabatic basis set that we used to set up our problem were used, but it should in an adiabatic basis. However, the signatures of this effect are subtle, as it mostly leads to a suppression of reactivity in state 2 compared to state 1, but there is already suppression close to threshold due to the thicker barrier.

With respect to the product state distributions in Figures 5 and 6, here we found that there is very strong coupling between selected pairs of $^2\Pi_{3/2}$ and $^2\Pi_{1/2}$ states of OH, such that the average probability of these two states is about the same, but with fluctuations about this average which lead to inverted spin-orbit distributions for initial state 2 and uninverted distributions for initial state 3. In our TSH calculations [5], we found only a relatively low transition probability between $^2\Pi_{3/2}$ and $^2\Pi_{1/2}$ states in the product asymptote, indicating that this effect is much less important in three dimensions than in one dimension. Since the TSH calculations should be able to describe the transitions that would lead to this effect, we infer that the coupling is weaker for geometries sampled in three dimensions than for the specific reaction path considered here. These conclusions indicate that the one dimensional model is likely exaggerating interference and coherence effects, which is a well known flaw of low dimensional models. However, certain aspects of the present results, such as the enhanced tunneling on state 1, should have a three dimensional counterpart for some reactions, and the coherence and interference effects that we have studied will likely show up in detailed state-to-state properties.

Acknowledgements

References

1.   Alagia, M., Balucani, N., Cartechini, L., Casavecchia, P., van Beek, M., Volpi, G.C., Bennet, L. and Rayez, J. C. (1999) Crossed beam studies of the $O(^3P,^1D)$ + CH_3I reactions: Direct evidence of intersystem crossing, *Faraday Discuss.* **113**, pp. 133 150.

2. Zhang, X.-G., Rue, C., Shin, S.-Y. and Armentrout, P.B. (2002) Reaction of Ta$^+$ and W$^+$ with H$_2$, D$_2$, and HD: Effect of lanthanide contraction and spin-orbit interactions on reactivity and thermochemistry, *J. Chem. Phys.* **116**, pp. 5574–5583.

3. Hoffmann, M.R. and Schatz, G.C. (2000) Theoretical studies of intersystem crossing effects in the O + H$_2$ reaction, *J. Chem. Phys.* **113**, pp. 9456–9465.

4. Donaldson, D.J. and Wright, J.S. (1984) Singlet-triplet surface crossings and low-temperature rate enhancement for O(^3P) + H$_2$ → OH + H, *J. Chem. Phys.* **80**, pp. 221–231.

5. Maiti, B. and Schatz, G.C. (2003) Theoretical studies of intersystem crossing effects in the nonadiabatic dynamics of bimolecular reactions, *J. Chem. Phys.* – **to be submitted**.

6. Rogers, S., Wang, D., Kuppermann, A. and Walch, S. (2000) Chemically Accurate ab Initio Potential Energy Surfaces for the Lowest $^3A'$ and $^3A''$ Electronically Adiabatic States of O(^3P) + H$_2$, *J. Phys. Chem. A* **104**, 2308–2325.

7. Schatz, G.C. (1995) Influence of atomic fine structure on bimolecular rate constants: The Cl(^2P) + HCl reaction, *J. Phys. Chem.* **99**, pp. 7522–7529.

8. Hoffmann, M.R. and Schatz, G.C. (2002) Model Studies of Intersystem Crossing Effects in the O + H$_2$ Reaction, in *Low-Lying Potential Energy Surfaces*, M.R. Hoffmann and K.G. Dyall eds., ACS Symposium Series **828**, pp. 329–345.

9. Garton, D. J., Minton, T. K., Maiti, B., Troya, D., Schatz, G.C. (2003) A crossed molecular beams study of the O(^3P) + H$_2$ reaction: comparison of excitation function with accurate quantum reactive scattering calculations, *J. Chem. Phys.* **118**, pp. 1585–1588.

NONADIABATIC TRANSITIONS BETWEEN ASYMPTOTICALLY DEGENERATE STATES

V.I. OSHEROV AND V.G. USHAKOV
Institute of Problems of Chemical Physics,
Russian Academy of Sciences
Chernogolovka, Moscow 142432, Russia

AND

H. NAKAMURA
Department of Theoretical Studies,
Institute for Molecular Science,
and
Department of Functional Molecular Science,
The Graduate University for Advanced Studies
Myodaiji, Okazaki 444-8585, Japan

Abstract. The semiclassical analysis is carried out for a two-state model potential system, in which two asymptotically degenerate Morse type potentials are coupled by an exponential diabatic coupling. Both crossing and non-crossing cases are treated and explicit analytical expressions for the full scattering matrix are obtained. The analytical solution is applied to the S-P type collisional resonant excitation transfer between atoms. The corresponding cross-sections are calculated in the high energy approximation. Good agreement is obtained with the results calculated previously by Watanabe with use of the fully numerical integration of the time-dependent coupled differential equations.

1. Introduction

Nonadiabatic transitions play crucial roles in various fields of physics and chemistry [1, 2, 3, 4, 5, 7, 8, 9, 10], and it is quite important to develop basic analytical theories so that we can understand fundamental mechanisms of various dynamics. The most fundamental models among them are the Landau-Zener type curve crossing and the Rosen-Zener-Demkov type non-curve-crossing. Furthermore, there is an interesting intermediate case in which two diabatic exponential potentials are

coupled by an exponential function [1]. Quantum mechanically exact solutions of some special cases as well as a generalization of the Nikitin's semiclassical solution have been obtained [14, 15, 16, 17]. In addition to these well known cases we have found diffraction type of nonadiabatic transitions between asymptotically degenerate states [18, 19, 20, 21, 22, 23]. The properties of such transitions can be clarified analyzing the limit $\hbar \to 0$ for the solutions of semiclassical time dependent equations

$$\left(i\hbar \frac{d}{dt} + \begin{pmatrix} u(t), & -v(t) \\ -v(t), & -u(t) \end{pmatrix} \right) \begin{pmatrix} \psi_1 \\ \psi_2 \end{pmatrix} = 0. \tag{1}$$

The asymptotic at $\hbar \to 0$ behavior of diabatic amplitudes $\psi_{1,2}$ is given by

$$\begin{pmatrix} \psi_1 \\ \psi_2 \end{pmatrix} = $$

$$\begin{pmatrix} \left(1 - i\hbar\vartheta + O(\hbar^2)\right)\cos\eta, & \left(1 - i\hbar\tau + O(\hbar^2)\right)\sin\eta \\ -\left(1 + i\hbar\tau + O(\hbar^2)\right)\sin\eta, & \left(1 + i\hbar\vartheta + O(\hbar^2)\right)\cos\eta \end{pmatrix} \begin{pmatrix} c_1 e^{iS/\hbar} \\ c_2 e^{-iS/\hbar} \end{pmatrix} \tag{2}$$

with

$$S(t_0, t) = \int_{t_0}^{t} \sqrt{u^2 + v^2} \, dt, \quad \tan 2\eta = \frac{v}{u}, \tag{3}$$

and

$$\vartheta = q\sin^2\eta - \int_{t_1}^{t} \frac{v}{2} q^2 \sin 2\eta \, dt, \quad \tau = q\cos^2\eta + \int_{t_1}^{t} \frac{v}{2} q^2 \sin 2\eta \, dt, \tag{4}$$

$$q = \frac{1}{v}\frac{d\eta}{dt} = \dot\eta/v. $$

In the case of asymptotically degenerate at $t \to +\infty$ states we can assume

$$\lim_{t \to -\infty} q = 0, \quad \lim_{t \to +\infty} \sqrt{u^2 + v^2} = 0, \quad \lim_{t \to +\infty} q = -q_0 = const. \tag{5}$$

Using the expression of Eq.(2) we get the relation between asymptotic values of adiabatic amplitudes $\Psi_{1,2}$

$$\begin{pmatrix} \Psi_1 \\ \Psi_2 \end{pmatrix}_{t_2 \to +\infty} = $$

$$\begin{pmatrix} \exp(i\varphi_c), & i\hbar\frac{q_0}{2}\sin 2\eta_\infty \\ i\hbar\frac{q_0}{2}\sin 2\eta_\infty, & \exp(-i\varphi_c) \end{pmatrix} \begin{pmatrix} e^{iS(t_1,t_2)/\hbar}, & 0 \\ 0, & e^{-iS(t_1,t_2)/\hbar} \end{pmatrix} \begin{pmatrix} \Psi_1 \\ \Psi_2 \end{pmatrix}_{t_1 \to -\infty}, \tag{6}$$

where

$$\eta_\infty = \lim_{t \to +\infty} \eta \tag{7}$$

and

$$\varphi_c = \hbar \int_{-\infty}^{+\infty} \frac{v}{2} q^2 \sin 2\eta \ dt \tag{8}$$

represent the usual dynamical phase. The phase

$$\varphi_a = \pi/2 \tag{9}$$

of the amplitude of asymptotic nonadiabatic transitions can be regarded as asymptotic dynamical phase. For the probability of nonadiabatic transitions in asymptotic region we get

$$P = \left(\hbar \frac{q_0}{2} \sin 2\eta_\infty \right)^2 = \left(\lim_{t \to +\infty} \frac{\hbar}{\Delta U_{ad}} \frac{d\eta}{dt} \right)^2 = \left(\frac{1}{\xi_M} \right)^2, \tag{10}$$

where ξ_M is the asymptotic Massey parameter. $\Delta U_{ad} = 2\sqrt{u^2 + v^2}$ is the splitting between adiabatic potentials.

In this paper, we present a full analysis of the following exponential model (Eq.(11) below) of Morse type potentials coupled by an exponential function:

$$\begin{pmatrix} -\dfrac{\hbar^2}{2m} \dfrac{d^2}{dx^2} + Ae^{-\alpha x} + Be^{-2\alpha x} - E, & -Ge^{-\alpha x} \\ -Ge^{-\alpha x}, & -\dfrac{\hbar^2}{2m} \dfrac{d^2}{dx^2} + Ce^{-\alpha x} + De^{-2\alpha x} - E \end{pmatrix} \begin{pmatrix} \psi_1 \\ \psi_2 \end{pmatrix} = 0, \tag{11}$$

where

$$D > B > 0. \tag{12}$$

This model is characterized by the finite value of asymptotic Massey parameter

$$\xi_M = \frac{1}{\alpha\hbar} \sqrt{\frac{m}{2E}} \frac{\left((A - C)^2 + 4G^2 \right)^{3/2}}{G(D - B)}. \tag{13}$$

Explicit analytical expression of the $S-$matrix is derived for this model. The case $A < C$ $(A > C)$ corresponds to the non-crossing (crossing) diabatic potentials.

Introducing the dimensionless parameters,

$$(a, b, c, d, g) = (A, B, C, D, G)/E, \quad \kappa^2 = \frac{\hbar^2 \alpha^2}{2mE}, \tag{14}$$

using new functions f_i and new variable y

$$\psi_i = f_i \exp(\frac{i}{\kappa}\alpha x), \quad y = \exp(-\alpha x), \tag{15}$$

we get

$$
\begin{pmatrix}
-\kappa^2 \left[y \dfrac{d^2}{dy^2} + \left(1 - \dfrac{2i}{\kappa}\right) \dfrac{d}{dy} \right] + a + by, & -g \\[2mm]
-g, & -\kappa^2 \left[y \dfrac{d^2}{dy^2} + \left(1 - \dfrac{2i}{\kappa}\right) \dfrac{d}{dy} \right] + c + dy
\end{pmatrix}
\begin{pmatrix} f_1 \\ f_2 \end{pmatrix} = 0. \quad (16)
$$

The unitary transformation to the adiabatic states $\begin{pmatrix} \Psi_1 \\ \Psi_2 \end{pmatrix}$ is given as usual by

$$
\begin{pmatrix} \psi_1 \\ \psi_2 \end{pmatrix} = \begin{pmatrix} \cos\eta, \sin\eta \\ -\sin\eta, \cos\eta \end{pmatrix} \begin{pmatrix} \Psi_1 \\ \Psi_2 \end{pmatrix}, \quad \tan 2\eta = \frac{2g}{a - c + y(b - d)}. \quad (17)
$$

The corresponding adiabatic potentials are

$$
U_{1,2}(y) = \frac{y}{2} \left(a + c + y(b + d) \pm \sqrt{(a - c + y(b - d))^2 + 4g^2} \right). \quad (18)
$$

2. Transformation Into the Momentum Representation

The transformation into the momentum representation

$$
f_i = \int \exp\left(\frac{i}{\kappa} py\right) \Phi_i(p) \, dp \quad (19)
$$

leads to

$$
\begin{pmatrix}
i\kappa \dfrac{d}{dp} + i\kappa\pi_1 + u_1, & -g_1 \\[2mm]
-g_2, & i\kappa \dfrac{d}{dp} + i\kappa\pi_2 + u_2
\end{pmatrix}
\begin{pmatrix} \Phi_1 \\ \Phi_2 \end{pmatrix} = 0, \quad (20)
$$

where

$$
\begin{aligned}
u_1 &= \frac{a - 2p}{b + p^2}, & u_2 &= \frac{c - 2p}{d + p^2}, \\
\pi_1 &= \frac{p}{b + p^2}, & \pi_2 &= \frac{p}{d + p^2}, \\
g_1 &= \frac{g}{b + p^2}, & g_2 &= \frac{g}{d + p^2}.
\end{aligned} \quad (21)
$$

The transformation

$$
\varphi_i = \Phi_i \exp\left(\int \left(\pi_i - \frac{i}{\kappa} \frac{u_1 + u_2}{2} \right) dp \right) \quad (22)
$$

gives the following coupled equations which will be analyzed in the subsequent sections:

$$
\begin{pmatrix}
i\kappa \dfrac{d}{dp} + u, & -v \\[2mm]
-v, & i\kappa \dfrac{d}{dp} - u
\end{pmatrix}
\begin{pmatrix} \varphi_1 \\ \varphi_2 \end{pmatrix} = 0. \quad (23)
$$

Here

$$u = \frac{u_1 - u_2}{2} = \frac{p^2(a - c) - 2p(d - b) + ad - bc}{2\,(b + p^2)\,(d + p^2)} \tag{24}$$

and

$$v = \frac{g}{\sqrt{(b + p^2)\,(d + p^2)}}. \tag{25}$$

The potential matrix in Eq.(23) can be diagonalized as

$$\left(\begin{array}{cc} \cos\gamma, & -\sin\gamma \\ \sin\gamma, & \cos\gamma \end{array} \right) \left(\begin{array}{cc} u, & -v \\ -v, & -u \end{array} \right) \left(\begin{array}{cc} \cos\gamma, & \sin\gamma \\ -\sin\gamma, & \cos\gamma \end{array} \right) = \left(\begin{array}{cc} w, & 0 \\ 0, & -w \end{array} \right), \tag{26}$$

where

$$\tan 2\gamma = v/u, \quad w = \sqrt{u^2 + v^2}. \tag{27}$$

3. WKB Type Semiclassical Analysis

The semiclassical solution of Eq.(23) with the first order correction for the pre-exponential factor taken into account is given by (see Eq.(2))

$$\left(\begin{array}{c} \varphi_1 \\ \varphi_2 \end{array} \right) = \left(\begin{array}{cc} e^{-i\vartheta}\cos\gamma, & e^{-i\tau}\sin\gamma \\ -e^{i\tau}\sin\gamma, & e^{i\vartheta}\cos\gamma \end{array} \right) \left(\begin{array}{c} c_1 \exp\left(\dfrac{i}{\kappa}S\right) \\ c_2 \exp\left(-\dfrac{i}{\kappa}S\right) \end{array} \right), \tag{28}$$

where

$$S = \int w \, dp = \int \sqrt{u^2 + v^2} dp \tag{29}$$

and

$$\tau = \kappa \frac{\gamma_p'}{v} \cos^2\gamma + \kappa \int \frac{(\gamma_p')^2}{2v} \sin(2\gamma) \, dp,$$

$$\vartheta = \kappa \frac{\gamma_p'}{v} \sin^2\gamma - \kappa \int \frac{(\gamma_p')^2}{2v} \sin(2\gamma) \, dp. \tag{30}$$

The applicability condition of the semiclassical approximation is expressed as

$$|\tau| \ll 1, \quad |\vartheta| \ll 1. \tag{31}$$

¿From the total action of the functions ψ_i expressed as

$$S(p, y) = -\ln y + py + \int \frac{u_1 + u_2}{2} dp \pm \int \sqrt{u^2 + v^2} dp, \tag{32}$$

the corresponding saddle points in the $p-$space can be obtained as

$$\tilde{p}(y) = \frac{1 \pm \sqrt{1 - U_{1,2}(y)}}{y}. \tag{33}$$

Denoting the saddle points in the $p-$space corresponding to the turning points y_1 and y_2 on the adiabatic potentials U_1 and U_2 as

$$\hat{p}_{1,2} = 1/y_{1,2}, \tag{34}$$

we define actions in p-representation in the form,

$$S_{1,2}(y,p) = -\ln \frac{y}{y_{1,2}} + py - 1 + \int_{\hat{p}_{1,2}}^{p} \frac{u_1 + u_2}{2} dp \pm \int_{\hat{p}_{1,2}}^{p} \sqrt{u^2 + v^2} dp, \tag{35}$$

where indices 1 and 2 in $S_{1,2}$ correspond to the signs $+$ and $-$, respectively. Using this definition we can obtain actions in x-representation with the origin taken at the turning points,

$$S_{1,2}(y) = S_{1,2}(y, \tilde{p}_\mathcal{L}), \qquad S_{1,2}(y = y_{1,2}) = 0. \tag{36}$$

Here $\tilde{p}_\mathcal{L}$ is the left saddle point (see Eq.(33)),

$$\tilde{p}_\mathcal{L}(y) = \frac{1 - \sqrt{1 - U_{1,2}(y)}}{y}. \tag{37}$$

It should be noted that

$$S_{1,2}(y, \tilde{p}_\mathcal{L}) = -S_{1,2}(y, \tilde{p}_\mathcal{R}) > 0, \tag{38}$$

where $\tilde{p}_\mathcal{R}$ is the right saddle point (see Eq.(33)),

$$\tilde{p}_\mathcal{R} = \frac{1 + \sqrt{1 - U_{1,2}(y)}}{y}. \tag{39}$$

Using the semiclassical solution of Eq.(28) for the amplitudes in p-representation, we can obtain the diabatic wave functions in x-representation as

$$\begin{pmatrix} \psi_1(y) \\ \psi_2(y) \end{pmatrix} =$$
$$\int_{-\infty}^{\infty} \begin{pmatrix} e^{-i\vartheta} \dfrac{\cos\gamma}{\sqrt{b+p^2}}, & e^{-i\tau} \dfrac{\sin\gamma}{\sqrt{b+p^2}} \\ -e^{i\tau} \dfrac{\sin\gamma}{\sqrt{d+p^2}}, & e^{i\vartheta} \dfrac{\cos\gamma}{\sqrt{d+p^2}} \end{pmatrix} \begin{pmatrix} c_1 \exp\left(\dfrac{i}{\kappa} S_1(y,p)\right) \\ c_2 \exp\left(\dfrac{i}{\kappa} S_2(y,p)\right) \end{pmatrix} dp. \tag{40}$$

By taking into account the direction of steepest descent, the asymptotic diabatic wave functions at $x \to \infty$ can be expressed as a sum of contributions from

the left and right saddle points at $y \to 0$:

$$
\begin{pmatrix} \psi_1(y) \\ \psi_2(y) \end{pmatrix} =
$$

$$
\begin{pmatrix} e^{i\vartheta}\cos\eta, e^{i\tau}\sin\eta \\ -e^{-i\tau}\sin\eta, e^{-i\vartheta}\cos\eta \end{pmatrix} \begin{pmatrix} \dfrac{c_1}{\sqrt[4]{1-U_1}}\exp\left(\dfrac{i}{\kappa}S_1(y) - i\dfrac{\pi}{4}\right) \\ \dfrac{c_2}{\sqrt[4]{1-U_2}}\exp\left(\dfrac{i}{\kappa}S_2(y) - i\dfrac{\pi}{4}\right) \end{pmatrix}_{\mathcal{L}} +
$$

$$
+ \begin{pmatrix} e^{-i\vartheta}\cos\eta, e^{-i\tau}\sin\eta \\ -e^{i\tau}\sin\eta, e^{i\vartheta}\cos\eta \end{pmatrix} \begin{pmatrix} \dfrac{c_1}{\sqrt[4]{1-U_1}}\exp\left(-\dfrac{i}{\kappa}S_1(y) + i\dfrac{\pi}{4}\right) \\ \dfrac{c_2}{\sqrt[4]{1-U_2}}\exp\left(-\dfrac{i}{\kappa}S_2(y) + i\dfrac{\pi}{4}\right) \end{pmatrix}_{\mathcal{R}} \tag{41}
$$

with

$$
\lim_{y\to 0}(\tau+\vartheta) = \kappa \lim_{p\to\infty}\frac{\gamma_p'}{v} = -\kappa \lim_{y\to 0}\frac{2\eta_y'}{g} = \kappa\frac{2(b-d)}{(a-c)^2 + 4g^2}. \tag{42}
$$

In terms of the parameters

$$
\Delta = \frac{c-a}{\sqrt{2\kappa(d-b)}} \text{ and } \delta = \frac{g^2}{2\kappa(d-b)} \tag{43}
$$

we have

$$
\lim_{y\to 0}(\tau+\vartheta) = -\frac{1}{\Delta^2 + 4\delta} \tag{44}
$$

and also the limiting value of the angle η $(y \to 0)$ as

$$
\begin{aligned}
\sin(2\eta) &= \sqrt{\frac{4\delta}{\Delta^2 + 4\delta}}, \\
\cos(2\eta) &= \frac{-\Delta}{\sqrt{\Delta^2 + 4\delta}}.
\end{aligned} \tag{45}
$$

The connection between the amplitudes $(c_1, c_2)_{\mathcal{L}}$ and $(c_1, c_2)_{\mathcal{R}}$ is given by the nonadiabatic transition matrix L

$$
L = \frac{1}{1 + e^{-2\pi\nu}} \begin{pmatrix} 1 + e^{-2\pi\nu}e^{2i\phi/\kappa}, & 2ie^{-\pi\nu}\sin\phi/\kappa \\ 2ie^{-\pi\nu}\sin\phi/\kappa, & 1 + e^{-2\pi\nu}e^{-2i\phi/\kappa} \end{pmatrix}, \tag{46}
$$

where ν and ϕ are the Landau-Zener parameter and the Stueckelberg phase given by the usual contour integrals. Although this matrix L is unitary, it should be noted that the double exponent term $\exp(-2\pi\nu)$ has originated from the continuation of the semiclassical solution along the real axis passing between the two complex conjugate zeros of the function $\sqrt{u^2 + v^2}$. The accuracy of the semiclassical representation of the solution along this contour is not high enough to give

correct values of exponentially small terms compared to unity. Thus considering the applicability condition of the semiclassical approximation,

$$\nu \gg 1, \tag{47}$$

we should change Eq. (46) to

$$L = \begin{pmatrix} 1, & 2ie^{-\pi\nu}\sin\phi/\kappa \\ 2ie^{-\pi\nu}\sin\phi/\kappa, & 1 \end{pmatrix}. \tag{48}$$

Finally, let us try to formulate the scattering matrix within the present semiclassical treatment. Using the adiabatic wave functions obtained by the saddle point method,

$$\begin{pmatrix} \Psi_1 \\ \Psi_2 \end{pmatrix} = \begin{pmatrix} \dfrac{a_{1-}}{\sqrt[4]{1-U_1}} \exp\left(-\dfrac{i}{\kappa}S_1(y)+i\dfrac{\pi}{4}\right) \\ \dfrac{a_{2-}}{\sqrt[4]{1-U_2}} \exp\left(-\dfrac{i}{\kappa}S_2(y)+i\dfrac{\pi}{4}\right) \end{pmatrix} + $$
$$+ \begin{pmatrix} \dfrac{a_{1+}}{\sqrt[4]{1-U_1}} \exp\left(\dfrac{i}{\kappa}S_1(y)-i\dfrac{\pi}{4}\right) \\ \dfrac{a_{2+}}{\sqrt[4]{1-U_2}} \exp\left(\dfrac{i}{\kappa}S_2(y)-i\dfrac{\pi}{4}\right) \end{pmatrix}, \tag{49}$$

the $S-$matrix is defined by

$$\begin{pmatrix} a_1 \\ a_2 \end{pmatrix}_+ = \hat{S} \begin{pmatrix} a_1 \\ a_2 \end{pmatrix}_-, \tag{50}$$

where the subindexes $\mp$ correspond to the incoming and outgoing waves and $S_{1,2}(y)$ are given by Eq.(36).

Introducing the notations for the matrices of adiabatic propagation W, basis rotation R, and diffraction D,

$$W = \begin{pmatrix} e^{-iS_1(y)/\kappa+i\pi/4}, & 0 \\ 0, & e^{-iS_2(y)/\kappa+i\pi/4} \end{pmatrix}, \quad R = \begin{pmatrix} \cos\eta, & \sin\eta \\ -\sin\eta, & \cos\eta \end{pmatrix},$$
$$D = \begin{pmatrix} e^{-i\vartheta}\cos\eta, & e^{-i\tau}\sin\eta \\ -e^{i\tau}\sin\eta, & e^{i\vartheta}\cos\eta \end{pmatrix}, \tag{51}$$

and using Eqs.(17), (41), and (48), we find

$$\hat{S} = V^T L V \text{ with } V = \lim_{y\to 0} W^{-1}D^{-1}RW, \tag{52}$$

where the index T means the transposition.

The final expression for the semiclassical S-matrix is found at $\Delta < 0$ as

$$\hat{S} = \begin{pmatrix} 1, & i\sin(2\eta)(\tau+\vartheta)\cos(\zeta/\kappa) + 2ie^{-\pi\nu}\sin\phi/\kappa \\ \\ i\sin(2\eta)(\tau+\vartheta)\cos(\zeta/\kappa) + 2ie^{-\pi\nu}\sin\phi/\kappa, & 1 \end{pmatrix} =$$

$$= \begin{pmatrix} 1, & -2i\dfrac{\delta^{1/2}\cos(\zeta/\kappa)}{(\Delta^2+4\delta)^{3/2}} + 2ie^{-\pi\nu}\sin\phi/\kappa \\ \\ -2i\dfrac{\delta^{1/2}\cos(\zeta/\kappa)}{(\Delta^2+4\delta)^{3/2}} + 2ie^{-\pi\nu}\sin\phi/\kappa, & 1 \end{pmatrix}, \tag{53}$$

where

$$\zeta = \lim_{y\to 0}(S_2(y) - S_1(y)). \tag{54}$$

The formal limit $\nu \to \infty$ of the Eq.(53) gives the expression for the S-matrix at $\Delta > 0$. The applicability conditions for the present semiclassical expression of the S−matrix are given as follows

$$\kappa \ll 1, \quad \nu \gg 1, \quad \Delta^2 + 4\delta \gg 1. \tag{55}$$

The expression of the Eq.(53) demonstrates the significant role of the diffraction type nonadiabatic transitions originating from the asymptotic region $x \to \infty$. The contribution of this region to the amplitude of nonadiabatic transitions is equal to the inverse Massey parameter of Eq.(13) which has finite value at $x \to \infty$ because of the asymptotic degeneracy of potential energy curves.

4. High Energy Approximation

In this section we consider the solution of Eq.(23) at high energies,

$$E \to \infty, \quad a,b,c,d,g \to 0 \ \ (\text{in the order of } 1/E). \tag{56}$$

The zeros of the adiabatic potential $w(p) = \sqrt{u^2 + v^2}$ are the solutions of the equation

$$\left[(a-c)^2 + 4g^2\right]p^4 + 4(a-c)(b-d)p^3 + 4(b-d)^2 p^2 + \\ + 4(b-d)(ad-bc)p + (ad-bc)^2 + 4g^2 bd = 0. \tag{57}$$

The four solutions of this equation p_{1-4} can be separated into two pairs in region I: $\mid p^2 \mid \gg (a,b,c,d,g)$ and in region II: $\mid p^2 \mid \ll (a,b,c,d,g)$. The local solutions for each region can be considered separately.

4.1. LOCAL SOLUTIONS IN REGION I

Suppose p is of the order of unity. Then by taking into account only the first three terms of $o(E^{-2})$, Eq.(57) reads

$$[(a - c)p + 2(b - d)]^2 + 4g^2 p^2 = 0, \tag{58}$$

which gives

$$p_{1,2} = \frac{2(b - d)}{z_{1,2}} \tag{59}$$

with

$$z_{1,2} = c - a \pm 2ig. \tag{60}$$

Since $|p^2| \gg a, b, c, d, g$, we can express

$$u = \frac{p(a - c) - 2(d - b)}{2p^3} \text{ and } v = \frac{g}{p^2}. \tag{61}$$

Introducing

$$q = \sqrt{2\frac{d - b}{\kappa}\frac{1}{p}} + \Delta, \tag{62}$$

we obtain from Eq.(23)

$$\begin{pmatrix} i\dfrac{d}{dq} + \dfrac{q}{2}, & \sqrt{\delta} \\ \sqrt{\delta}, & i\dfrac{d}{dq} - \dfrac{q}{2} \end{pmatrix} \begin{pmatrix} \varphi_1 \\ \varphi_2 \end{pmatrix} = 0. \tag{63}$$

The point $q = 0$ corresponds to

$$p = P_1 = 2\frac{d - b}{a - c} \tag{64}$$

with $u(P_1) = 0$.

Two linearly independent solutions of Eq.(63) can be chosen as

$$\varphi_1 = \frac{e^{i\pi/4}}{\sqrt{\delta}} D_{i\delta}\left(e^{-i\pi/4}q\right), \qquad \varphi_2 = D_{i\delta-1}\left(e^{-i\pi/4}q\right)$$
$$\text{and} \tag{65}$$
$$\varphi_1 = -\frac{e^{i\pi/4}}{\sqrt{\delta}} D_{i\delta}\left(-e^{-i\pi/4}q\right), \qquad \varphi_2 = D_{i\delta-1}\left(-e^{-i\pi/4}q\right).$$

The general solution of Eq.(63) is given by the linear combination of these solutions.

The contribution of the region I to the wave function $\psi_j(y)$ at $y \to 0$ can thus be expressed as

$$\psi_i^I(y) = D_i \cdot \exp\left(-\frac{i}{\kappa}\ln y\right) \int \exp\left(\frac{i}{\kappa}py\right) \frac{\exp\left(\frac{i}{\kappa}\int_0^p \frac{u_1+u_2}{2}\,dp\right)}{p}\,dp. \quad (66)$$

Here D_i represents the value of φ_i given by Eq.(65) at $p = \infty$ ($y \to 0$). The integral in Eq.(66) can be evaluated by using the saddle point method. As a result we obtain the contribution of the region I as

$$\psi_1^I(y) = \pm\sqrt{\frac{\pi\kappa}{\delta}}\exp\left(i\frac{\pi}{2} + \frac{i}{\kappa}\xi + \frac{i}{\kappa}\ln y\right) D_{i\delta}\left(\pm e^{-i\pi/4}\Delta\right),$$
$$\psi_2^I(y) = \sqrt{\pi\kappa}\exp\left(i\frac{\pi}{4} + \frac{i}{\kappa}\xi + \frac{i}{\kappa}\ln y\right) D_{i\delta-1}\left(\pm e^{-i\pi/4}\Delta\right). \quad (67)$$

Here the upper (lower) sign corresponds to the first (second) set of solutions in Eq.(65). The phase ξ is equal to

$$\xi = \lim_{\tilde{p}\to\infty}\left(\tilde{p}y + \int_0^{\tilde{p}} \frac{u_1+u_2}{2}\,dp + 2\ln\frac{\tilde{p}}{2}\right) =$$
$$= 2 + \frac{\pi}{4}\left(\frac{a}{\sqrt{b}} + \frac{c}{\sqrt{d}}\right) + \frac{1}{2}\ln bd - 2\ln 2. \quad (68)$$

4.2. LOCAL SOLUTIONS IN REGION II.

Suppose p is much less than unity. Then by neglecting the terms of p^3 and p^4, Eq.(57) reads

$$4(b-d)^2p^2 + 4(b-d)(ad-bc)p + (ad-bc)^2 + 4g^2bd = 0, \quad (69)$$

which gives

$$p_{3,4} = \frac{bc - ad \pm 2ig\sqrt{bd}}{2(b-d)}. \quad (70)$$

Since $\left|p^2\right| \ll a, b, c, d, g$, we have

$$u = \frac{ad-bc}{2bd} - \frac{d-b}{bd}p, \; v = \frac{g}{\sqrt{bd}}. \quad (71)$$

In terms of the new variable

$$q = \sqrt{2\frac{d-b}{\kappa bd}}\,(p - P_0) \quad (72)$$

with

$$P_0 = \frac{ad - bc}{2(d - b)}, \tag{73}$$

Eq.(23) can be simplified as

$$\begin{pmatrix} i\dfrac{d}{dq} - \dfrac{q}{2}, & -\sqrt{\delta} \\[2mm] -\sqrt{\delta}, & i\dfrac{d}{dq} + \dfrac{q}{2} \end{pmatrix} \begin{pmatrix} \varphi_1 \\[2mm] \varphi_2 \end{pmatrix} = 0. \tag{74}$$

The two linearly independent solutions of this equation are

$$\varphi_1 = D_{-i\delta}\left(e^{i\pi/4}q\right), \qquad \varphi_2 = \sqrt{\delta}e^{i\pi/4}D_{-i\delta-1}\left(e^{i\pi/4}q\right)$$
$$\text{and} \tag{75}$$
$$\varphi_1 = D_{-i\delta}\left(-e^{i\pi/4}q\right), \qquad \varphi_2 = -\sqrt{\delta}e^{i\pi/4}D_{-i\delta-1}\left(-e^{i\pi/4}q\right).$$

The general solution of Eq.(74) is given by the linear combination of these solutions. It should be noted that $q = 0$ corresponds to $p = P_0$ with $u(P_0) = 0$.

Making use of the exact relation of the Weber functions[24],

$$\int_{-\infty}^{\infty} \exp\left(-\frac{(x-y)^2}{2\mu} + \frac{y^2}{4}\right) D_\delta(y)\, dy =$$

$$\sqrt{2\pi\mu}\,(1-\mu)^{\delta/2} \exp\left(\frac{x^2}{4(1-\mu)}\right) D_\delta\left(\frac{x}{\sqrt{1-\mu}}\right) \tag{76}$$

with $0 < Re\mu < 1$, we can finally obtain the contribution of the region II to the diabatic wave functions $\psi_j(y)$ in the x-representation as

$$\psi_1^{II}(y) = \sqrt{\pi\kappa} \exp\left(i\lambda - i\frac{\pi}{4} - \frac{i}{\kappa}\ln y\right) D_{-i\delta}\left(\pm e^{i\pi/4}\Delta\right),$$
$$\psi_2^{II}(y) = \pm\sqrt{\pi\kappa\delta} \exp\left(i\lambda - \frac{i}{\kappa}\ln y\right) D_{-i\delta-1}\left(\pm e^{i\pi/4}\Delta\right). \tag{77}$$

Here the upper (lower) sign in Eq.(77) corresponds to the first (second) set of solutions in Eq.(75) and the parameter λ is given by

$$\lambda = \frac{\Delta^2}{4} - \frac{\delta}{2}\ln\frac{b}{d} + \frac{a^2d^2 - c^2b^2 + 2abd(c-a)}{8\kappa bd(d-b)} =$$

$$= \frac{a^2d + c^2b}{8\kappa bd} - \frac{\delta}{2}\ln\frac{b}{d}. \tag{78}$$

4.3. SCATTERING MATRIX

Matching the general local solutions using the semiclassical type asymptotic expressions of D-functions has been carried out. As a result, the general diabatic

wave functions in x-representation in asymptotic region $x \to \infty$ can be expressed as

$$\psi_1(y) = \psi_1^+ e^{\frac{i}{\kappa} \ln y} + \psi_1^- e^{-\frac{i}{\kappa} \ln y},$$

$$\psi_2(y) = \psi_2^+ e^{\frac{i}{\kappa} \ln y} + \psi_2^- e^{-\frac{i}{\kappa} \ln y},$$

(79)

where the amplitudes $\psi_{1,2}^{\pm}$ are connected by the diabatic scattering matrix

$$\begin{pmatrix} \psi_1 \\ \psi_2 \end{pmatrix}_- = \hat{S}_d \begin{pmatrix} \psi_1 \\ \psi_2 \end{pmatrix}_+ = e^{i(s_1+s_2)/\kappa} \times$$

$$\begin{pmatrix} -e^{i\pi/4}(e^{i\epsilon} \sin^2 \chi + e^{-i\varepsilon} \cos^2 \chi), & \sin(2\chi) \sin(\frac{\epsilon + \varepsilon}{2}) \\ \sin(2\chi) \sin(\frac{\epsilon + \varepsilon}{2}), & e^{-i\pi/4}(e^{-i\epsilon} \sin^2 \chi + e^{i\varepsilon} \cos^2 \chi) \end{pmatrix} \begin{pmatrix} \psi_1 \\ \psi_2 \end{pmatrix}_+,$$

(80)

where

$$\sin \chi = e^{-\pi\delta/4} \left| D_{i\delta} \left(e^{-i\pi/4} \Delta \right) \right|,$$
$$\cos \chi = \sqrt{\delta} e^{-\pi\delta/4} \left| D_{i\delta-1} \left(e^{-i\pi/4} \Delta \right) \right|,$$
$$\epsilon = h/\kappa + \delta \ln \delta - \delta + \pi/4 - 2 \arg D_{i\delta} \left(e^{-i\pi/4} \Delta \right),$$
$$\varepsilon = h/\kappa + \delta \ln \delta - \delta + \pi/4 - 2 \arg D_{i\delta-1} \left(e^{-i\pi/4} \Delta \right),$$

(81)

$$h = \begin{cases} \int\limits_{P_0}^{P_1} \sqrt{u^2 + v^2} \, dp & \text{for the case } \Delta < 0, \\[4mm] \int\limits_{P_0}^{+\infty} \sqrt{u^2 + v^2} \, dp + \int\limits_{-\infty}^{P_1} \sqrt{u^2 + v^2} \, dp & \text{for the case } \Delta > 0. \end{cases}$$

(82)

h is equal to the Stueckelberg phase and the quantities s_1 and s_2 are defined from the action integrals $S_{1,2}(y)$ (see Eq.(36)) as

$$s_j = S_j(y) + \ln y \big|_{y \to 0}.$$

(83)

The S-matrix in the adiabatic representation is obtained as

$$\hat{S} =$$
$$\begin{bmatrix} e^{i(s_2-s_1)/\kappa} \left[R \sin \omega - i \left(R \cos \omega \cos 2\eta + r \sin 2\eta \right) \right], & i \left(r \cos 2\eta - R \cos \omega \sin 2\eta \right) \\[3mm] i \left(r \cos 2\eta - R \cos \omega \sin 2\eta \right), & e^{i(s_1-s_2)/\kappa} \left[R \sin \omega + i \left(R \cos \omega \cos 2\eta + r \sin 2\eta \right) \right] \end{bmatrix}.$$

(84)

where

$$R e^{i\omega} = e^{i\pi/4} \left(e^{i\epsilon} \sin^2 \chi + e^{-i\varepsilon} \cos^2 \chi \right),$$
$$r = \sin(2\chi) \sin \left(\frac{\epsilon + \varepsilon}{2} \right),$$

(85)

the functions $\sin 2\eta$ and $\cos 2\eta$ are given by Eq.(45), and

$$s_2 - s_1 = h - \kappa \int_0^\Delta \sqrt{q^2 + 4\delta} \; dq, \tag{86}$$

The applicability conditions for this high energy semiclassical expression for S−matrix are as follows

$$\kappa, a, b, c, d, g \ll 1. \tag{87}$$

In closing this section, let us consider some limiting cases. First, if we assume $\Delta^2 + 4\delta \gg 1$, we can use the asymptotic expressions of the D-functions and obtain

$$S_{12} = \begin{cases} -i\cos\left((s_2 - s_1)/\kappa\right) \dfrac{2\delta^{1/2}}{(\Delta^2 + 4\delta)^{3/2}} \qquad \text{for} \quad \Delta > 0, \\[4mm] -i\cos\left((s_2 - s_1)/\kappa + 2\sigma\right) \dfrac{2\delta^{1/2}}{(\Delta^2 + 4\delta)^{3/2}} + 2ie^{-\pi\delta}\sqrt{1 - e^{-2\pi\delta}} \sin\left(h/\kappa + \sigma\right) \\ \qquad\qquad\qquad\qquad \text{for} \quad \Delta < 0, \end{cases} \tag{88}$$

where

$$\sigma = \delta \ln \delta - \delta + \arg \Gamma \left(1 - i\delta\right) + \pi/4. \tag{89}$$

The expression of Eq.(88) coincides with Eq.(53) in the limits $\Delta^2 + 4\delta^2 \gg 1$ and $\delta \gg 1$.

In the case of $\Delta = 0$, we can use

$$D_n(0) = \frac{2^{n/2}\sqrt{\pi}}{\Gamma\left((1 - n)/2\right)} \tag{90}$$

and we obtain

$$S_{12} = -i\cos\left(\frac{\epsilon + \varepsilon}{2}\right)\cos\left(\frac{\pi}{4} + \frac{\epsilon - \varepsilon}{2}\right) +$$

$$+ie^{-\pi\delta}\sin\left(\frac{\epsilon + \varepsilon}{2}\right)\sin\left(\frac{\pi}{4} + \frac{\epsilon - \varepsilon}{2}\right). \tag{91}$$

Particularly when $\delta \gg 1$, this gives

$$S_{12} = -i\cos\left((s_2 - s_1)/\kappa + \frac{1}{12\delta}\right)\frac{1}{4\delta}. \tag{92}$$

The phase averaged $\mid S_{12} \mid^2$ coincides with the limit of Eq.(2.47) of the previous paper [23].

5. S-P Collisional Resonant Excitation Transfer

In order to demonstrate the physical significance of asymptotic nonadiabatic transitions and especially the analytical theory developed an application is made to the resonant collisional excitation transfer between atoms. This presents a basic physical problem in the optical line broadening [25]. The theoretical considerations were made before [25, 27, 28, 29, 25, 30] and their basic idea has been verified experimentally [31]. These theoretical treatments assumed the impact parameter method and dealt with the time-dependent coupled differential equations under the common nuclear trajectory approximation. At that time the authors could not find any analytical solutions and solved the coupled differential equations numerically. The results of calculations for the various cross sections agree well with each other and also with experiments, confirming the physical significance of the asymptotic type of transitions by the dipole-dipole interaction.

5.1. COORDINATE SYSTEMS, BASIS SETS, AND HAMILTONIAN

Two coordinate systems and basis sets describing to the collision of two identical atoms in states S and P are employed. Following Watanabe [27], first we introduce the standard space-fixed coordinate system with axis ξ along the relative nuclear angular momentum $\mathbf{l}$, i.e., axis perpendicular to the collision plane, axis ζ in the direction opposite to the asymptotic velocity vector $\vec{v}$, and axis η normal to ξ and ζ. The following notation is used for the diabatic electronic basis states:

$$
\begin{aligned}
\mid \psi_1\rangle &= \mid P_\xi\rangle_A \mid S\rangle_B, \\
\mid \psi_2\rangle &= \mid S\rangle_A \mid P_\xi\rangle_B, \\
\mid \psi_3\rangle &= \mid P_\eta\rangle_A \mid S\rangle_B, \\
\mid \psi_4\rangle &= \mid S\rangle_A \mid P_\eta\rangle_B, \\
\mid \psi_5\rangle &= \mid P_\zeta\rangle_A \mid S\rangle_B, \\
\mid \psi_6\rangle &= \mid S\rangle_A \mid P_\zeta\rangle_B.
\end{aligned}
\tag{93}
$$

This basis set is referred to as atomic basis and yields the final $S-$matrix elements.

Next, again following Watanabe [27], we introduce the body-fixed (molecular or rotating) coordinate system: axis $\overline{\pi}$ along $\mathbf{l}$, axis σ along the molecular axis $\mathbf{R}$ and axis π normal to the other two. In this system the projections of the electronic angular momentum $\mathbf{j}$ and the total angular momentum $\mathbf{J}$ onto the molecular axis $\mathbf{R}$ are equal to each other and the corresponding basis states are given by the linear combinations of the states in Eq.(93) as

$$
\begin{aligned}
\mid P_\sigma\rangle &= \sin\vartheta \mid P_\zeta\rangle + \cos\vartheta \mid P_\eta\rangle, \\
\mid P_\pi\rangle &= -\cos\vartheta \mid P_\zeta\rangle + \sin\vartheta \mid P_\eta\rangle, \\
\mid P_{\overline{\pi}}\rangle &= \mid P_\xi\rangle,
\end{aligned}
\tag{94}
$$

where ϑ is the angle between the two axes σ and η with $\vartheta \in (-\frac{\pi}{2}, \frac{\pi}{2})$. The atomic basis states with the definite projection ($\Omega = \pm 1, 0$) of the electronic angular

momentum $\mathbf{j}$ onto the molecular axis $\mathbf{R}$ are given by

$$| \ P_{+1}\rangle = -\frac{1}{\sqrt{2}}(| \ P_{\bar{\pi}}\rangle + i \ | \ P_{\pi}\rangle,$$

$$| \ P_{-1}\rangle = \frac{1}{\sqrt{2}}(| \ P_{\bar{\pi}}\rangle - i \ | \ P_{\pi}\rangle,$$

$$| \ P_0\rangle = | \ P_{\sigma}\rangle. \tag{95}$$

These define the following diabatic basis states which present the most convenient one for solving the coupled Schroedinger equations:

$$| \ \varphi_1\rangle = | \ S\rangle_A \ | \ P_0\rangle_B,$$

$$| \ \varphi_2\rangle = | \ P_0\rangle_A \ | \ S\rangle_B,$$

$$| \ \varphi_3\rangle = | \ S\rangle_A \ | \ P_{+1}\rangle_B,$$

$$| \ \varphi_4\rangle = | \ P_{+1}\rangle_A \ | \ S\rangle_B,$$

$$| \ \varphi_5\rangle = | \ S\rangle_A \ | \ P_{-1}\rangle_B,$$

$$| \ \varphi_6\rangle = | \ P_{-1}\rangle_A \ | \ S\rangle_B. \tag{96}$$

Using the standard total angular momentum representation $|JMj\Omega\rangle$ corresponding to the basis set of Eq.(96) (see for instance the book [1]) we obtain the following form of Hamiltonian for the radial nuclear motion (atomic units):

$$\langle\Omega_i \ | \ H \ | \ \Omega_k\rangle = T_R + \frac{J(J+1)}{2\mu R^2} + \langle\Omega_i \ | \ V \ | \ \Omega_k\rangle, \tag{97}$$

where

$$\langle\Omega_i \ | \ V \ | \ \Omega_k\rangle = \begin{pmatrix} \frac{1}{\mu R^2} & -\frac{2d^2}{3R^3} & V_c & 0 & V_c & 0 \\ -\frac{2d^2}{3R^3} & \frac{1}{\mu R^2} & 0 & V_c & 0 & V_c \\ V_c & 0 & 0 & \frac{d^2}{3R^3} & 0 & 0 \\ 0 & V_c & \frac{d^2}{3R^3} & 0 & 0 & 0 \\ V_c & 0 & 0 & 0 & 0 & \frac{d^2}{3R^3} \\ 0 & V_c & 0 & 0 & \frac{d^2}{3R^3} & 0 \end{pmatrix}. \tag{98}$$

Here V_c represents the Coriolis coupling

$$V_c = -\frac{\sqrt{2J(J+1)}}{2\mu R^2} \tag{99}$$

and the parameter d is defined as the $S - P$ type dipole transition moment given by the formula

$$d = \frac{3}{\sqrt{2}} \, | \, \langle S \, | \, \mathbf{d} \cdot \mathbf{n} \, | \, P_0 \rangle \, | \, .$$ (100)

Now we introduce the representation satisfying the molecular symmetry

$$| \, \boldsymbol{\Phi} \rangle = D_{\boldsymbol{\Phi} \varphi} \, | \, JMj\Omega \rangle,$$ (101)

where

$$D_{\boldsymbol{\Phi}\varphi} = \frac{1}{2} \begin{pmatrix} \sqrt{2} & \sqrt{2} & 0 & 0 & 0 & 0 \\ 0 & 0 & 1 & 1 & 1 & 1 \\ \sqrt{2} & -\sqrt{2} & 0 & 0 & 0 & 0 \\ 0 & 0 & 1 & -1 & 1 & -1 \\ 0 & 0 & 1 & 1 & -1 & -1 \\ 0 & 0 & 1 & -1 & -1 & 1 \end{pmatrix}.$$ (102)

This basis set factorizes the matrix of Eq.(98) to

$$\langle \Phi_i \, | \, V \, | \, \Phi_k \rangle = \begin{pmatrix} \dfrac{1}{\mu R^2} - \dfrac{2d^2}{3R^3} & \sqrt{2}V_c & 0 & 0 & 0 & 0 \\[2ex] \sqrt{2}V_c & \dfrac{d^2}{3R^3} & 0 & 0 & 0 & 0 \\[2ex] 0 & 0 & \dfrac{1}{\mu R^2} + \dfrac{2d^2}{3R^3} & \sqrt{2}V_c & 0 & 0 \\[2ex] 0 & 0 & \sqrt{2}V_c & -\dfrac{d^2}{3R^3} & 0 & 0 \\[2ex] 0 & 0 & 0 & 0 & \dfrac{d^2}{3R^3} & 0 \\[2ex] 0 & 0 & 0 & 0 & 0 & -\dfrac{d^2}{3R^3} \end{pmatrix}.$$ (103)

This is obviously most convenient for solving the Schroedinger equation.

At $\vartheta = \pm \pi/2$ the molecular basis set $| \, \boldsymbol{\Phi} \rangle$ determines the electronic state $| \, \boldsymbol{\Phi}_e \rangle$ connected with the original atomic one $| \, \psi \rangle$ in Eq.(93) by the relation

$$| \, \boldsymbol{\Phi}_e \rangle = D_{\boldsymbol{\Phi}\psi}(\vartheta) \, | \, \psi \rangle$$ (104)

with

$$D_{\Phi\psi}(\vartheta = \pm\pi/2) =$$

$$= 1\sqrt{2}\begin{pmatrix} 0 & 0 & \cos\vartheta & \cos\vartheta & \sin\vartheta & \sin\vartheta \\ 0 & 0 & -i\sin\vartheta & -i\sin\vartheta & i\cos\vartheta & i\cos\vartheta \\ 0 & 0 & \cos\vartheta & -\cos\vartheta & \sin\vartheta & -\sin\vartheta \\ 0 & 0 & -i\sin\vartheta & i\sin\vartheta & i\cos\vartheta & -i\cos\vartheta \\ -1 & -1 & 0 & 0 & 0 & 0 \\ -1 & 1 & 0 & 0 & 0 & 0 \end{pmatrix}(\vartheta = \pm\pi/2) =$$

$$= \begin{pmatrix} 0 & 0 & 0 & 0 & \pm1 & \pm1 \\ 0 & 0 & \mp i & \mp i & 0 & 0 \\ 0 & 0 & 0 & 0 & \pm1 & \mp1 \\ 0 & 0 & \mp i & \pm i & 0 & 0 \\ -1 & -1 & 0 & 0 & 0 & 0 \\ -1 & 1 & 0 & 0 & 0 & 0 \end{pmatrix}. \tag{105}$$

5.2. S-MATRIX, TRANSITION PROBABILITY, AND CROSS SECTION

As in the previous studies, we apply the semiclassical approach to the problem. This means that the angular momenta are considered to be large and the terms $\sim 1/\mu R^2$ in the matrix of Eq.(103) can be neglected. Then the Hamiltonian matrix can be reduced to the form

$$\langle\Phi_{1,3} \mid H \mid \Phi_{2,4}\rangle = -\frac{1}{2\mu}\frac{d^2}{dR^2} + \frac{(J+1/2)^2}{2\mu R^2} + \begin{pmatrix} \mp\dfrac{2d^2}{3R^3} & -\dfrac{J+1/2}{\mu R^2} \\ -\dfrac{J+1/2}{\mu R^2} & \pm\dfrac{d^2}{3R^3} \end{pmatrix},$$

$$\langle\Phi_{5,6} \mid H \mid \Phi_{5,6}\rangle = -\frac{1}{2\mu}\frac{d^2}{dR^2} + \frac{(J+1/2)^2}{2\mu R^2} \pm \frac{d^2}{3R^3}. \tag{106}$$

The full collision problem is now separated into two doubly-coupled and two uncoupled systems. We represent the nuclear wave vector $\mid\Psi\rangle$ of the problem in the form

$$\mid\Psi\rangle = \exp(iS_R - i\pi/4) = \exp(i\int^R \sqrt{2\mu(E-(J+1/2)^2/2\mu R^2}dR - i\pi/4)\mid\psi\rangle. \tag{107}$$

The high energy approximation leads the first equation of Eq.(106) to

$$-i\sqrt{1-\frac{b^2}{R^2}}\frac{d}{dR}\mid\psi\rangle + \begin{pmatrix} \mp\dfrac{2d^2}{3vR^3} & -\dfrac{b}{R^2} \\ -\dfrac{b}{R^2} & \pm\dfrac{d^2}{3vR^3} \end{pmatrix}\mid\psi\rangle = 0, \tag{108}$$

where the ordinary definition of the impact parameter b has been used,

$$J + 1/2 = \mu bv. \tag{109}$$

This equation can be transformed to the main coupled equations of Ref. [27] by the variable transformations $R^2 = b^2 + v^2 t^2$ and $x = \sin\vartheta$ together with the rotation of the nuclear vector with the angle ϑ. As mentioned before, the previous authors solved these coupled equations fully numerically.

Here, we try to apply our analytical theory. At first, we note that the transitions we are interested in occur in asymptotic regions, and thus we can leave only zeroth order term in the expansion of radial velocity. This leads to the equation

$$i\frac{d}{dR}\mid\psi\rangle + \begin{pmatrix} \pm\dfrac{2d^2}{3vR^3} & \dfrac{b}{R^2} \\ \dfrac{b}{R^2} & \mp\dfrac{d^2}{3vR^3} \end{pmatrix} \mid\psi\rangle = 0. \tag{110}$$

Substitution of the variable $R = e^x$ reduces the problem to the exponential model studied above. Using the $S-$matrix in the diabatic representation given by Eq.(80) we finally obtain the $S-$matrix in the representation of Eq.(101) as

$$\hat{S}_\Phi = \begin{pmatrix} S_{11} & S_{12} & 0 & 0 & 0 & 0 \\ S_{12} & S_{22} & 0 & 0 & 0 & 0 \\ 0 & 0 & S_{11}^* & -S_{12}^* & 0 & 0 \\ 0 & 0 & -S_{12}^* & S_{22}^* & 0 & 0 \\ 0 & 0 & 0 & 0 & S_{00} & 0 \\ 0 & 0 & 0 & 0 & 0 & S_{00}^* \end{pmatrix}, \tag{111}$$

where

$$S_{11} = \frac{1}{2}e^{i(s_1+s_2)-i\pi/4}(e^{i\epsilon}[1 + e^{-\pi\delta}] + e^{-i\varepsilon}[1 - e^{-\pi\delta}]),$$

$$S_{22} = \frac{1}{2}e^{i(s_1+s_2)+i\pi/4}(e^{-i\epsilon}[1 + e^{-\pi\delta}] + e^{i\varepsilon}[1 - e^{-\pi\delta}]),$$

$$S_{12} = e^{i(s_1+s_2)+i\pi/2}\sqrt{1 - e^{-2\pi\delta}}\sin\frac{\epsilon+\varepsilon}{2},$$

$$S_{00} = e^{-2i(s_1+s_2)}, \tag{112}$$

$$\epsilon = s_2 - s_1 + \delta\ln\delta/2 - \delta + \frac{\pi}{4} + 2\arg\Gamma(\frac{1}{2} - i\frac{\delta}{2}),$$

$$\varepsilon = s_2 - s_1 + \delta\ln\delta/2 - \delta + \frac{\pi}{4} + 2\arg\Gamma(1 - i\frac{\delta}{2}).$$

Here $s_{1,2}$ are the radial adiabatic phase increments in the high energy approximation given by

$$s_{1,2} = S_{1,2} - S_R = \frac{1}{6\delta} \mp \frac{1}{4\delta}\int_0^1\sqrt{\frac{z + 4\delta^2}{z(1-z)}}dz, \tag{113}$$

and δ is the principal single parameter of the model

$$\delta = \frac{b^2 v}{d^2}. \tag{114}$$

The overall transition matrix among the basis set $| \psi \rangle$ correspondent to that of Eq.(93) is given by

$$N = D_{\Phi\psi}^{-1}(\pi/2)S_\Phi D_{\Phi\psi}(-\pi/2).$$ (115)

The simple manipulation leads to

$$N = \begin{pmatrix} \mathrm{Re}S_{00} & i\mathrm{Im}S_{00} & 0 & 0 & 0 & 0 \\ i\mathrm{Im}S_{00} & \mathrm{Re}S_{00} & 0 & 0 & 0 & 0 \\ 0 & 0 & -\mathrm{Re}S_{22} & -i\mathrm{Im}S_{22} & \mathrm{Im}S_{12} & -i\mathrm{Re}S_{12} \\ 0 & 0 & -i\mathrm{Im}S_{22} & -\mathrm{Re}S_{22} & -i\mathrm{Re}S_{12} & \mathrm{Im}S_{12} \\ 0 & 0 & -\mathrm{Im}S_{12} & i\mathrm{Re}S_{12} & -\mathrm{Re}S_{11} & -i\mathrm{Im}S_{11} \\ 0 & 0 & i\mathrm{Re}S_{12} & -\mathrm{Im}S_{12} & -i\mathrm{Im}S_{11} & -\mathrm{Re}S_{11} \end{pmatrix}.$$ (116)

This matrix is unitary, because all the matrices on the right hand side of Eq.(115) are unitary. It should be noted that Eq.(115) does not describe the formal transformation from the body-fixed to space-fixed frame by coordinate transformation [1], but just gives the transformation of electronic basis sets in the asymptotic region.

Eq.(116) together with Eqs.(112)-(113) gives the analytical solution of the $S-P$ resonant excitation transfer problem in the high energy approximation and can provide all the dynamics information for this problem. In particular, we can find the total cross-sections for all the related collision processes. In the semiclassical approximation the standard expression of cross-section has the form

$$\sigma_{ik} = 2\pi \int_0^\infty P_{ik}(\delta(b))b db = \frac{\pi d^2}{v} \int_0^\infty P_{ik}(\delta)d\delta,$$ (117)

where P_{ik} are the transition probabilities for the elastic and inelastic processes:

$$\begin{aligned} P_{ik} &= |N_{ik}|^2, i \neq k, \\ P_{ii} &= |1 - N_{ii}|^2. \end{aligned}$$ (118)

The probability P_{ik} as a function of δ rapidly oscillates at $\delta \to 0$ and decreases as $1/\delta^2$ at $\delta \to \infty$. The calculated results in the unit of $\pi d^2/v$ are presented in Table 1.

Table 1 shows good agreement between the fully numerical solutions of the time-dependent coupled equations [27] and the present results obtained by matching the asymptotic analytical solutions, indicating the usefulness of the present analytical theory.

If it is possible to specify the asymptotically defined projection of the electronic angular momentum along the molecular axis, then the corresponding $S-$matrix is turned out to be

$$S_\varphi = D_{\Phi\varphi}^{-1}S_\Phi D_{\Phi\varphi}.$$ (119)

TABLE 1. Cross sections for excitation transfer (exc.tr.), depolarization (depol.), and elastic process (elas.) in unit of $\pi d^2/v$.

	exc.tr.				depol.	elas.		
	$\sigma_{\xi\xi}$	$\sigma_{\eta\eta}$	$\sigma_{\zeta\zeta}$	$\sigma_{\eta\zeta}$	$\sigma_{\eta\zeta}$	$\sigma_{\xi\xi}$	$\sigma_{\eta\eta}$	$\sigma_{\zeta\zeta}$
Ref.[27]	π	2.09	0.43	0.56	0.60	-	-	-
This work	π	1.95	0.44	0.52	0.62	π	1.49	2.08

Unlike Eq.(115), the transformation made here is just a rotation of constant angle (see Eq.(102)) and we can easily obtain the unitary and symmetric $S-$matrix as

$$S_\varphi =$$

$$
\begin{pmatrix}
\mathrm{Re}S_{11} & i\mathrm{Im}S_{11} & \frac{i}{\sqrt{2}}\mathrm{Im}S_{12} & \frac{1}{\sqrt{2}}\mathrm{Re}S_{12} & \frac{i}{\sqrt{2}}\mathrm{Im}S_{12} & \frac{1}{\sqrt{2}}\mathrm{Re}S_{12} \\
i\mathrm{Im}S_{11} & \mathrm{Re}S_{11} & \frac{1}{\sqrt{2}}\mathrm{Re}S_{12} & \frac{i}{\sqrt{2}}\mathrm{Im}S_{12} & \frac{1}{\sqrt{2}}\mathrm{Re}S_{12} & \frac{i}{\sqrt{2}}\mathrm{Im}S_{12} \\
\frac{i}{\sqrt{2}}\mathrm{Im}S_{12} & \frac{1}{\sqrt{2}}\mathrm{Re}S_{12} & \frac{1}{2}\mathrm{Re}\Sigma & \frac{i}{2}\mathrm{Im}\Sigma & \frac{1}{2}\mathrm{Re}\Upsilon & \frac{i}{2}\mathrm{Im}\Upsilon \\
\frac{1}{\sqrt{2}}\mathrm{Re}S_{12} & \frac{i}{\sqrt{2}}\mathrm{Im}S_{12} & \frac{i}{2}\mathrm{Im}\Sigma & \frac{1}{2}\mathrm{Re}\Sigma & \frac{i}{2}\mathrm{Im}\Upsilon & \frac{1}{2}\mathrm{Re}\Upsilon \\
\frac{i}{\sqrt{2}}\mathrm{Im}S_{12} & \frac{1}{\sqrt{2}}\mathrm{Re}S_{12} & \frac{1}{2}\mathrm{Re}\Upsilon & \frac{i}{2}\mathrm{Im}\Upsilon & \frac{1}{2}\mathrm{Re}\Sigma & \frac{i}{2}\mathrm{Im}\Sigma \\
\frac{1}{\sqrt{2}}\mathrm{Re}S_{12} & \frac{i}{\sqrt{2}}\mathrm{Im}S_{12} & \frac{i}{2}\mathrm{Im}\Upsilon & \frac{1}{2}\mathrm{Re}\Upsilon & \frac{i}{2}\mathrm{Im}\Sigma & \frac{1}{2}\mathrm{Re}\Sigma
\end{pmatrix}, \quad (120)
$$

where

$$\Sigma = S_{22} + S_{00}, \quad \Upsilon = S_{22} - S_{00}. \quad (121)$$

In this representation, one should take into account the fact that the molecular axis rotates with the angle π during the collision process, so that in the case of transitions $\pm 1 \to \mp 1$ the electronic angular momentum projection onto the space-fixed axis does not change, but it does change in the case of $\pm 1 \to \pm 1$. In addition, the amplitudes of elastic processes have signs opposite to the signs of the corresponding elements S_φ [1]. It redefines the transition probabilities and cross-sections. The calculated results of these cross-sections in the unit of $\pi d^2/v$ are presented in Table 2.

TABLE 2. Cross sections for excitation transfer (exc.tr.), depolarization (depol.), and elastic (elas.) processes in unit of $\pi d^2/v$ in the frame

exc.tr.				depol.	elas.		
$\sigma_{0,0}$	$\sigma_{0,\pm 1}$	$\sigma_{\pm 1,\pm 1}$	$\sigma_{\pm 1,\mp 1}$	$\sigma_{0,\pm 1}$	$\sigma_{\pm 1,\mp 1}$	$\sigma_{0,0}$	$\sigma_{\pm 1,\mp 1}$
0.44	0.52	2.35	0.20	0.62	0.43	2.08	1.88

Finally, the mean excitation transfer cross-section averaged over the initial polarizations is found to be $\langle \sigma_{et} \rangle = 2.19$, which is again in good agreement with the value 2.26 obtained from the numerical calculations [27].

6. Concluding remarks

The new type of nonadiabatic transition between asymptotically degenerate states has been fully analyzed with use of the Morse potential model, and the analytical expression of the scattering matrix has been derived. The present analysis warns that we have to be careful about this type of nonadiabatic transition whenever we encounter asymptotic degeneracy of potential energy curves. The new mechanism presented in this paper works whenever the limiting value at $x \to \infty$ of the inverse Massey type parameter is a finite quantity:

$$\lim_{x \to \infty} \frac{\hbar \eta'_x \sqrt{2E/m}}{\Delta U_{ad}(x)} = const. \tag{122}$$

The $S - P$ type collisional excitation transfer process was shown to be nicely treated analytically as one of the examples of nonadiabatic transitions between asymptotically degenerate states. The theory can be nicely represented by the asymptotic adiabatic parameter δ, and the calculated results of cross section were shown to agree well with the numerical solutions of the corresponding time-dependent coupled differential equations. This indicates the following two things: (1) appropriateness of the present analytical procedure that the transition in the asymptotic region is accurately treated and the adiabatic waves are properly matched in the region of turning point, and (2) physical significance of this type of nonadiabatic transition between asymptotically degenerate states. The usefulness of the analytical theory presented also have been clarified, since the theory is not just restricted to the Morse potential model, but it can be applied to a wider class of transitions between two asymptotically degenerate states.

Acknowledgments

References

1. Nikitin, E.E. and Umanski, S.Ya. (1984) *Theory of Slow Atomic Collisions*, Springer Verlag Berlin
2. Demkov, Yu.N. and Ostrovsky, V.N. (1988) *Zero Range Potentials and Their Applications in Atomic Physics*, Plenum New York
3. Child, M.S. (1991) *Semiclassical Mechanics with Molecular Applications*, Oxford Univ.Press
4. Crothers, D.S.F. (1971), *Adv.Phys.*, **20**, 405
5. Medvedev, E.S. and Osherov, V.I. (1994) *Radiationless Transitions in Polyatomic Molecules*, Springer Series in Chemical Physics, **57**
6. Nakamura, H. (1987), *J.Chem.Phys.*, **87**, 4031
7. Nakamura, H. (1991), *Int.Rev.Phys.Chem.*, **10**, 123
8. Nakamura, H. *(1992), Adv.Chem.Phys.*, **82**, 243

9. Nakamura, H. (1996) *Dynamics of Molecules and Chemical Reactions*, Ed. by Wyatt, R.E. and Zhang, J.Z.H. Marcel Dekker New York
10. Nakamura, H. (2002) *Nonadiabatic Transition: Concepts, Basic Theories, and Applications*, World Scientific and Imperial College Press Singapore
11. Nakamura, H. and Zhu, C. (1966) *Comments on Atom. and Molec.Physics,* **32**, 249
12. Zhu, C., Teranishi, Y. and Nakamura, H. (2001), *Adv.Chem.Phys.,* **117**, 127
13. Osherov, V.I. and Voronin, A.I. (1994), *Phys.Rev.A*, **49**, 265
14. Osherov, V.I. and Nakamura, H. (1996), *J.Chem.Phys.*, **105**, 2770
15. Osherov, V.I. and Nakamura, H. (1999), *Phys.Rev.A.,* **59**, 2486
16. Osherov, V.I., Ushakov, V.G. and Nakamura, H. (1997), *Phys.Rev.A*, **57**, 2672
17. Pichl L., Osherov V.I. and Nakamura H. (2000), *J.Phys.A*, **33**, 3361
18. Dashevskaya, E.I., Nikitin, E.E. and Troe, J. (1990), *J.Chem.Phys.*, **93**, 7803
19. Dashevskaya, E.I. and Nikitin, E.E. (1993), *J.Chem.Soc.Faraday Trans.*, **89**, 1567
20. Berengolts, A., Dashevskaya, E.I. and Nikitin, E.E. (1993), *J.Phys.B*, **26**, 3847
21. Berengolts, A., Dashevskaya, E.I., Nikitin, E.E. and Troe, J. (1995), *Chem.Phys.*, **195**, 271
22. Berengolts, A., Dashevskaya, E.I., Nikitin, E.E. and Troe, J. (1995), *Chem.Phys.*, **195**, 283
23. Osherov, V.I. and Nakamura, H. (2001), *Phys.Rev.A*, **63**, 052710
24. Bateman, H. and Erdelyi, A. (1953) *Higher Transcendental Functions*, **V.II**, McGrawHill New York
25. Berman, P.R. and Lamb, W.E. (1969), *Phys.Rev.,* **187**, 221
26. Bender, R.L. (1963), *Phys.Rev*, **132**, 2154
27. Watanabe, T. (1965), *Phys.Rev.A*, **138**, 1573. (1965), *Phys.Rev.A*, **140**, AB5
28. Omont, A.J. (1965), *J.Phys.Radium (Paris)*, **26**, 26
29. Kazansev, A.P. (1967), *Sov.Phys.JETP.*, **24**, 1183
30. Carrington, C.G., Stacey, D.N., Cooper, J. (1973), *J.Phys.B*, **6**, 417
31. Vaughan, J.M. (1966), *Phys.Lett.*, **21**, 153. (1966), *Proc.Roy.Soc.London*, **A295**, 164

COUPLING OF ELECTRON MOMENTA IN ION-ATOM COLLISIONS

B.M. SMIRNOV
Institute for High Temperatures of Russian Academy of Sciences, Izhorskaya 13/19, Moscow 127412, Russia

Abstract. Coupling of electron momenta is considered for the resonant charge exchange process in slow collisions. Since electron transfer proceeds at large distances between colliding particles compared to their sizes, where ion-atom interactions are relatively weak, one can separate different types of interactions and ascertain the character of coupling of electron momenta in a quasimolecule consisting of colliding ion and atom under real conditions. The number of types of interactions for colliding particles exceeds that used in the classical Hund scheme of momentum coupling. Momentum coupling in the case of halogen and oxygen atoms is outside the Hund scheme. In these cases of resonant charge exchange, the quantum numbers of the quasimolecule in the course of electron transfer are the total momenta J, j of colliding atom and ion, and the projection M or M_J of the atom orbital or total momentum onto the molecular axis. The ion-atom exchange interaction potential does not depend on the ion fine state, and the resonant charge exchange process is not entangled with processes of rotation of electron momenta under these conditions, as it takes place in the case "a" of Hund coupling. The partial cross section of the resonant charge exchange process depends on quantum numbers of colliding particles, while the average cross section depends weakly on the coupling scheme.

1. Introduction

The process of resonant electron transfer in slow collisions of an ion and parent atom results in transition of a valence electron from one core to the other. In the simplest case of $s-$electron transition, this process is determined by an interference of even and odd electron terms of the quasimolecule consisting of the colliding ion and atom. Correspondingly, the probability of this transition is expressed through the energy difference for the even and odd states of the quasimolecule, as well as the cross section of this process [4]. In the case of transfer of a $p-$electron with participation of an ion and atom with partially filled electron shells, the resonant charge exchange process becomes more complex, since the electron transfer

may be entangled with the processes of rotation of electron momenta and transitions between fine states of colliding particles. One can simplify the analysis of this process, constructing the hierarchy of interactions in the quasimolecule and choosing in this way a suitable case of Hund coupling [5, 6, 7], as well as certain quantum numbers of the quasimolecule. Though this scheme is constructed for a diatomic molecule when a distance between nuclei is fixed, it can be generalized to a quasimolecule consisting of colliding particles [8, 9, 10, 11]. Then, according to a general scheme by Nikitin, a certain type of Hund coupling is realized in each part of the particle trajectory. If the range of transition between different cases of Hund coupling is narrow, one can construct the wave function of the colliding particles and $S-$matrix of transition by sewing the wave functions from different parts of the transition range [10]. This allows one to divide different processes and find the probabilities for variation of quantum numbers of colliding particles at a given trajectory.

This general scheme may be used for the analysis of the resonant charge exchange process involving an ion and an atom with noncompleted electron shells when the resonant charge exchange process may be entangled with other processes (rotation of electron momenta, transitions between fine structure states). Then, within the framework of the classical Hund scheme of momentum summation [5], three types of interactions are introduced for the quasimolecule: the electrostatic interaction, V_e, the fine splitting of energy levels, δ_f, that corresponds to spin-orbit interaction and other relativistic interactions, and the rotational energy, V_{rot}, or Coriolis interaction that accounts for an interaction between the orbital and spin electron momenta with rotation of the molecular axis. Depending on the ratio between these interaction energies, one can construct six cases of Hund coupling [5, 6, 7], and for each case of momentum summation, the quasimolecule is characterized by certain quantum numbers. These cases are used as models for the analysis of some transitions in atomic collisions [10, 11, 22].

Electron transfer from one core to another takes place at large distances between colliding particles in the resonant charge exchange process in slow collisions, so that all ion-atom interaction potentials are small. This allows one to separate different interactions and to analyze the character of momentum coupling for real cases. Carrying out this analysis, we find that the number of interactions is larger than within the framework of the Hund scheme. Indeed, the electrostatic interaction, V_e, includes the exchange interaction, V_{ex}, inside atomic particles that leads to certain orbital momenta of the atom, L, and ion, l, and to certain spins S, s of these atomic particles; a long-range interaction $U(R)$, and the exchange ion-atom interaction $\Delta(R)$. In addition, the fine splitting of levels refers separately to the atom, δ_a, and ion, δ_i, and competition between all these interactions give many other cases of momentum coupling in comparison with the Hund coupling scheme. Therefore, it is more correct to analyze this problem for certain ion-atom systems when a restricted number of momentum coupling is realized. Below we consider this problem successive for resonant charge exchange of halogens and oxygen, if

ions and atoms are found in the ground electronic state, and the collision energy ranges from thermal ones up to tens eV, because this energy range is of interest for a low-temperature plasma.

2. Asymptotic theory of resonant electron transfer

First we formulate a general method to analyze this problem. We use the asymptotic theory of resonant charge exchange [14, 15, 17, 22]. This accounts for the tunneling character of electron transfer. The main contribution to the cross section of the resonant charge exchange process gives large impact parameters of collisions. Then a reciprocal value of a typical impact parameter of collisions is a small parameter of the asymptotic theory for this process. Expanding the cross section over this small parameter and restricting by two expansion terms, one can express the ion-atom exchange interaction potential and the cross section through asymptotic parameters of a transferring electron in an isolated atom and quantum numbers of ion and atom electron shells. In contrast to models, the asymptotic theory allows us to find a correct value of the cross section with an estimated accuracy. In the case of transition of a p-electron in the collision energy range under consideration this accuracy is better than 10% [19, 20].

We start from two schemes of momentum coupling for an atom and ion [2, 23, 7]. In the case of the $LS-$scheme, that is realized under the criterion $V_{ex} >> \delta_a, \delta_i$, we take $LM_L S$ as the quantum numbers of the atom and lms as the quantum numbers of the ion, where L, l are the orbital angular momenta, M, m are their projections on the molecular axis, and S, s are the spins of the atom and ion correspondingly. In the case of the $j-j$ coupling scheme for an individual atomic particle, that takes place at $V_{ex} << \delta_a, \delta_i$, we use JM_J as the atom quantum numbers, jm_j as the ion quantum numbers, where J, j are the total electron momenta, and M_J, m_j are their projections onto the molecular axis for the atom and ion correspondingly. These quantum numbers are the basis for the limiting cases of electron terms of the quasimolecule.

Let us summarize the Hund coupling scheme [5, 6, 7] that is given in Table 1 together with the quantum numbers of the quasimolecule for each case of Hund coupling. We denote by $\mathbf{L}$ the total electron angular momentum of the molecule, $\mathbf{S}$ is the total electron spin, $\mathbf{J}$ is the total electron momentum of the molecule, $\mathbf{n}$ is the unit vector along the molecular axis, $\mathbf{K}$ is the rotation momentum of nuclei, Λ is the projection of the angular momentum of electrons onto the molecular axis, Ω is the projection of the total electron momentum $\mathbf{J}$ onto the molecular axis, S_n is the projection of the electron spin onto the molecular axis, L_N, S_N, J_N are projections of these momenta onto the direction of the nuclear rotation momentum $\mathbf{N}$. Below we will take this scheme as a basis.

We now write down the possible interaction potential in the quasimolecule under consideration. In contrast to the Hund coupling scheme (Table 1), we separate various interactions of an ion and atom at large distances in the form

TABLE 1. The cases of Hund coupling.

Hund case	Relation	Quantum numbers
a	$V_e \gg \delta_f \gg V_{rot}$	Λ, S, S_n
b	$V_e \gg V_{rot} \gg \delta_f$	Λ, S, S_N
c	$\delta_f \gg V_e \gg V_{rot}$	Ω
d	$V_{rot} \gg V_e \gg \delta_f$	L, S, L_N, S_N
e	$V_{rot} \gg \delta_f \gg V_e$	J, J_N

$$V_{ex}, \; U_M = \frac{Q_{MM}}{R^3}, \; U_m = \frac{Q_{MM} q_{mm}}{R^5}, \; \Delta(R), \; \delta_i, \; \delta_a, \; V_{rot} \tag{1}$$

We divide the electrostatic interaction V_e of Table 1 into four parts: the exchange interaction, V_{ex}, inside the atom and ion that is responsible for electrostatic splitting of levels inside an isolated atom and ion, the long-range interaction, U_M, of the ion charge with the quadrupole moment of the atom, the long-range interaction, U_m, that is responsible for splitting of ion levels, and the ion-atom exchange interaction potential, Δ, that determines the cross section of resonant charge exchange. The fine splitting of levels δ_f of Table 1 is written separately for the ion, δ_i, and the atom, δ_a. Here M, m are the projections of the atom and ion angular momenta on the molecular axis, R is an ion-atom distance, Q_{ik} is the tensor of the atom quadrupole moment, q_{ik} is the quadrupole moment tensor for the ion. As is seen, the number of possible coupling cases is larger than that in the classical case. Of course, only a small fraction of these cases can be realized.

In order to find the suitable scheme of momentum coupling in real cases, we find the above ion-atom interaction potentials at distances which determine the resonant charge exchange cross section. Constructing the hierarchy of interactions, we find the quasimolecule quantum numbers in this distance range and then the partial cross sections corresponding to these quantum numbers. This allows us to ascertain the scheme of momentum summation in slow ion-atom collisions with resonant electron transfer. In turn, the character of momentum coupling may influence the value of the cross section averaged over initial quantum numbers. Below we will realize this operation for certain cases of ion-atom collisions when the colliding ion and atom are found in the ground electronic state.

3. Hierarchy of ion-atom interactions for halogens

Let us consider the resonant electron transfer involving a halogen atom and its ion in their ground electronic states

$$X^+({}^2P) + X({}^3P) \rightarrow X({}^3P) + X^+({}^2P) , \qquad (2)$$

where X is the halogen atom. We collect in Table 2 some parameters of colliding atomic particles for this case. Note that the fine structure of the lower ionic states includes the momenta of states with the total electron momenta $J = 2, 1, 0$, and the parameter δ_i in Table 2 is the splitting of the ${}^3P_2 - {}^3P_0$ ion levels. Next, the value V_{ex} is the splitting between the ground ion level ${}^3P_2$ and the level ${}^1D_2$ in notations of the $LS-$ scheme of momentum coupling. Because for all the ions the ratio δ_i/V_{ex} is less than unity, the $LS-$ scheme of momentum coupling is more or less valid. Hence, we take as a basis the LS coupling scheme for atoms and ions. The interaction potentials $U_M(R)$, $V_{rot}(R)$, $\Delta(R)$ are taken in Table 2 at a ion-atom distance R_o, so that the cross section of resonant charge exchange σ_{ex} for the case "a" of Hund coupling [19, 20, 21] is equal to

$$\sigma_{ex} = \frac{\pi}{2} R_o^2 , \qquad (3)$$

at the collision energy $1eV$.

The quantity U_M in Table 2 is equal to

$$U_M = U_{00} - U_{11} = \frac{Q_{00} - Q_{11}}{R_o^3} = \frac{6e^2 \overline{r^2}}{5R_o^3} , \qquad (4)$$

where e is the electron charge, and r is the distance of a valence atomic $p-$electron from the nucleus inside the atom. Table 2 lists the corresponding values of U_M and also the ratio U_M/δ_a that is usually less than unity, so that the fine structure of level splitting is of importance for the process under consideration. Note that an estimate of this ratio is rough because we take for U_M the difference between extreme values. The rotational energy of the quasimolecule, V_{rot}, assumes particles to be moved along straight-line trajectories. Taking the impact parameter of ion-atom collision to be R_o, we evaluate the rotation energy at closest approach of colliding particles as

$$V_{rot} = \frac{\hbar v}{R_o}, \qquad (5)$$

where v is the relative ion-atom velocity, and $\hbar$ is the Planck constant. We give in Table 2 values of the rotational energy that are found to be smaller than the other interaction potentials $(U_M, \delta_i, \delta_a)$, that determines the character of momentum coupling in this case.

On the basis of the above analysis, one can construct the hierarchy of interactions for a quasimolecule consisting of a halogen ion and its parent atom at typical distances between these particles for resonant charge exchange (2). As a result, we

TABLE 2. The parameters of halogen atoms and ions [1, 13].

	F	Cl	Br	I
δ_a, cm^{-1}	404	882	3685	7603
$\delta_i, cm^{-1\ *)}$	490	996	3840	7087
V_{ex}, cm^{-1}	20873	11654	11410	13727
δ_i/V_{ex}	0.023	0.085	0.34	0.52
R_o, a_o	10.6	13.8	15.1	17.2
$\overline{r^2}, a_o^2$	1.54	4.06	5.22	7.20
U_M, cm^{-1}	341	407	448	372
U_M/δ_a	0.84	0.46	0.12	0.049
V_{rot}, cm^{-1}	30	17	10	7.1
$\Delta(R_o), cm^{-1}$	23	14	8.4	6.1

*)The energy differences for levels of the states $^3P_2$ and ^3P_o.

have the following hierarchy of interactions which is fulfilled more or less for all the halogen cases in the range of collision energies $0.1 - 10 \, eV$:

$$V_{ex} >> \delta_i, \delta_a >> U_M >> U_m, V_{rot} \qquad (6)$$

Comparing this with the data in Table 1, the real situation is found to be between the cases "a" and "c" of Hund coupling, but case (6) does not correspond exactly to any one of the Hund cases. Now we evaluate the exchange ion-atom interaction potential $\Delta(R)$ on the basis of the formula for the resonant charge exchange cross section σ_{ex} in the case of the transition of $s-$electron [4, 14, 15]

$$\sigma_{ex} = \frac{\pi R_o^2}{2}, \quad where \quad \frac{1}{v}\sqrt{\frac{\pi R_o}{2\gamma}}\Delta(R_o) = 0.28 , \qquad (7)$$

and γ is the asymptotic parameter for the electron wave function of a transferring valence electron $(\Delta(R) \sim \exp(-\gamma R))$. From this one can compare the exchange interaction potential $\Delta(R_o)$ at a characteristic distance R_o with the rotational energy (5) of the quasimolecule at the impact parameter R_o of collision and the minimal distance between the colliding ion and atom

$$\Delta(R_o) = 0.28v\sqrt{\frac{2\gamma}{\pi R_o}} = 0.22\sqrt{\gamma R_o}V_{rot} \qquad (8)$$

We consider a small parameter of expansion of the asymptotic theory

$$\frac{1}{\gamma R_o} \ll 1 \tag{9}$$

At collisional energies in the eV range we have $\gamma R_o = 10 \div 15$, so that the values above are comparable $\Delta(R_o) \sim V_{rot}$. The values of the exchange interaction potential in Table 2 confirm this statement.

The hierarchy (6) of interactions leads to the following quantum numbers of the quasimolecule: $LSJM_Jlsjm_j$, where L, l are the atom and ion angular momenta, S, s are the atom and ion spins, J, j are the total electron momenta of the atom and ion, and M_J, m_j are their projections on the molecular axis. Correspondingly, the quasimolecule's wave function is

$$\Psi_{JM_J} = \sum_{MM_Smm_s} \left[\begin{array}{ccc} L & S & J \\ M & M_S & M_J \end{array} \right] \left[\begin{array}{ccc} l & s & j \\ m & m_s & m_j \end{array} \right] \Phi_{LMSM_S} \psi_{lmsm_s} \tag{10}$$

where Φ, ψ are the wave functions of the weakly interacting atom and ion with quantum numbers $LMSM_S$ and $lmsm_s$, respectively, if we ignore spin-orbit and other relativistic interactions.

We now find the positions of the electron levels for a quasimolecule consisting of an atom and parent ion at large distances between them being guided by the hierarchy (6) of interactions in the halogen case. We have the quasimolecule quantum numbers $LSls$ in the first approach for interactions and will be guided by the halogen case, taking the electron terms of the ground states, i.e. the electron term is ^2P for the atom and ^3P for the ion. The quasimolecule quantum numbers in the second approach are Jj, and the splitting between the fine-structure levels are determined by the corresponding values δ_a, δ_i for an isolated atom and ion. The third approach includes the quantum number M_J, the projection of the total atom electron moment onto the molecular axis, and the splitting between energy levels with different M_J due to interaction of the ion charge and atom quadrupole moment is given by

$$\begin{aligned} \Delta U(M_J) &= \left\langle \Psi_{LSJM_J} \left| \frac{Q_{MM}}{R^3} \right| \Psi_{LSJM_J} \right\rangle \\ &= \sum_{MM_S} \frac{Q_{MM}}{R^3} \left[\begin{array}{ccc} L & S & J \\ M & M_S & M_J \end{array} \right]^2 \end{aligned} \tag{11}$$

In the case of interaction of a halogen atom and ion $X(^2P) + X^+(^3P)$, where X is a halogen atom, this formula takes the form

$$\Delta U(JM_Jjm_j) = U_o \left(2 \left[\begin{array}{ccc} L & S & J \\ 0 & M_J & M_J \end{array} \right]^2 - \left[\begin{array}{ccc} L & S & J \\ 1 & M_J - 1 & M_J \end{array} \right]^2 \right), \tag{12}$$

and

$$U_o = \frac{2\overline{r_a^2}}{5R^3},\tag{12b}$$

and Q_{MM} is the component of the quadrupole moment tensor for the atom, r_a is the distance of a valence electron from the nucleus, and the bar means average over electron positions in the atom.

The fourth level of interactions leads to the quantum number m_j, the projection of the total ion electron momentum onto the molecular axis, and the energy level splitting for different M_J due to interaction between ion and atom quadrupole momenta is given by

$$\Delta V = \sum_{MM_S} \frac{Q_{MM}}{R^5} \left[\begin{array}{ccc} L & S & J \\ M & M_S & M_J \end{array} \right]^2 \sum_{mm_s} q_{mm} \left[\begin{array}{ccc} l & s & j \\ m & m_s & m_j \end{array} \right]^2,\tag{13}$$

where q_{mm} is the component of the tensor of the ion quadrupole moment. Note that the electron terms of the quasimolecule are degenerate with respect to the sign of the total momentum projections. In the case of interaction of atomic particles $X(^2P) + X^+(^3P)$, where X is a halogen atom, this formula can be rewritten in the form

$$\frac{\Delta V(JM_Jjm_j)}{V_o} = -\left(2 \left[\begin{array}{ccc} L & S & J \\ 0 & M_J & M_J \end{array} \right]^2 - \left[\begin{array}{ccc} L & S & J \\ 1 & M_J-1 & M_J \end{array} \right]^2 \right)$$
$$\left(2 \left[\begin{array}{ccc} l & s & j \\ 0 & m_j & m_j \end{array} \right]^2 - \left[\begin{array}{ccc} l & s & j \\ 1 & m_j-1 & m_j \end{array} \right]^2 \right),\tag{14}$$

where

$$V_o = \frac{4\overline{r_a^2 r_i^2}}{25R^5},\tag{15}$$

and the distances r_a, r_i refer to the atom and ion respectively.

As an example, we construct the lowest energy levels for the chlorine ion-atom quasimolecule at $R = 14a_o$ that corresponds approximately to the resonant charge exchange cross section at the collision energy of $1eV$ (see Table 2). We have for a typical energy charge-quadrupole (formula (12)) and quadrupole-quadrupole interaction (formula (15)) at this separation $U_o = 130cm^{-1}$, $V_o = 0.6cm^{-1}$. Therefore, in this case with the use of the data from Table 2 we have the hierarchy of interactions (6) in the form

$$V_{ex} \gg \delta_i, \delta_a \gg U_M \gg \Delta, V_{rot} \gg U_m\tag{16}$$

We give in Table 3 the energies E of levels according to the formula

$$E = \delta_i + \delta_a + U_M + \varepsilon_o \, , \tag{17}$$

where ε_o is taken such, that the lowest term has zero energy $E = 0$. The quasi-molecule energies of Table 3 are valid for the ground electronic state of the atom and ion, i.e. to quantum numbers $L = 1$, $l = 1$, $S = 1/2$, $s = 1$. The states of other quantum numbers $LSls$ are characterized by higher energies. Indeed, the excitation energy of the ion state $^1D_2$ is $11654cm^{-1}$, and the excitation energy of the ion state $^1S_0$ is $27878cm^{-1}$. These ion states have the same electron shell $3p^4$. Halogen atoms with an unexcited electron shell have only one electron term $L = 1$, $S = 1/2$, that simplifies the analysis.

The data of Table 3 are obtained by neglecting the interaction potentials Δ, V_{rot}, U_m which would give additional quantum numbers of the quasimolecule. Hence, the accuracy of the data in Table 3 is determined by these values: $\Delta(R) \sim V_{rot} \sim 10cm^{-1}$, $U_m \sim 1cm^{-1}$. In the used approximation the statistical weight of the quasimolecule states is

$$g = 2 \cdot 2 \cdot (2j + 1) \, . \tag{18}$$

and the first factor accounts for the degeneration over the sign of M_J, the second factor corresponds to separation of quasimolecule states into odd and even, so that this degeneration is removed by the exchange interaction $\Delta(R)$, and the third factor in formula (18) accounts for degeneration over m_j that is removed by all the neglected interactions Δ, V_{rot}, U_m.

Thus, the above analysis for interaction of a halogen ion and atom at large separations shows that the character of electron momentum coupling differs from that of the Hund coupling scheme. Along with the quantum numbers of electron shells of an isolated atom and ion within the framework of the $LS-$ coupling scheme, the quantum numbers of the quasimolecule are JjM_J (the total electron momenta of the atom and ion, and also the projection of the total atom momentum onto the molecular axis). Other quantum numbers of the quasimolecule are mixed due to the exchange Δ, rotation V_{rot}, and quadrupole-quadrupole U_m interactions between the atom and ion.

4. Ion-atom exchange interaction for halogens

We now determine the exchange ion-atom interaction that allows us to evaluate the cross section of resonant charge exchange. On this way we represent the wave function of the atom having n valence electrons of momentum l_e within the framework of the $LS-$coupling scheme in the form [2, 12, 23] :

$$\Phi_{LSM_LM_S}(1, 2, ..., n) = \frac{1}{\sqrt{n}} \hat{P} \sum_{lmsm_s\mu\sigma} G_{ls}^{LS}(l_e, n) \begin{bmatrix} l_e & l & L \\ \mu & m & M_L \end{bmatrix}$$

$$\begin{bmatrix} \frac{1}{2} & s & S \\ \sigma & m_s & M_S \end{bmatrix} \varphi_{l_e \frac{1}{2}\mu\sigma}(1) \cdot \psi_{lsmm_s}(2, ..., n) \tag{19}$$

TABLE 3. The lowest energy levels E of the quasimolecule $Cl^+ - Cl$ at the distance $R = 14a_o$ between nuclei. The energy of each state is taken with respect to the energy of isolated $Cl(^2P) + Cl^+(^3P)$. The statistical weight g relates only to the even (or odd) quasimolecule states.

JM_Jj	g	$\Delta U(M_J), cm^{-1}$	E, cm^{-1}
$\frac{3}{2}\frac{3}{2}2$	20	-130	0
$\frac{3}{2}\frac{1}{2}2$	20	130	260
$\frac{3}{2}\frac{3}{2}1$	12	-130	696
$\frac{3}{2}\frac{1}{2}1$	12	130	956
$\frac{3}{2}\frac{3}{2}0$	4	-130	996
$\frac{1}{2}\frac{1}{2}2$	20	0	102
$\frac{3}{2}\frac{1}{2}0$	4	130	1256
$\frac{1}{2}\frac{1}{2}1$	12	0	1708
$\frac{1}{2}\frac{1}{2}0$	4	0	2009

Here Φ, ψ, φ are the wave functions of the atom, ion and valence electron with indicated quantum numbers, respectively, μ, σ are the projections of the angular momentum and spin of a valence electron, the argument of the wave function indicates electrons involving in each atomic particle, the operator $\widehat{P}$ permutes these electrons, and the parentage coefficient $G_{ls}^{LS}(l_e, n)$ is responsible for addition of a valence electron to an ion for construction of an atom for given quantum numbers of these atomic particles.

The exchange interaction potential is given by the formula [11, 17]

$$\Delta(R) = 2 \left\langle \Psi_1 \left| \widehat{H} \right| \Psi_2 \right\rangle - 2 \left\langle \Psi_1 \left| \widehat{H} \right| \Psi_1 \right\rangle \left\langle \Psi_1 \left| 1 \right| \Psi_2 \right\rangle, \tag{20}$$

Here Ψ_1 is the wave function of the quasimolecule when a valence electron is located near the first core (an electron is connected with the first nucleus), and Ψ_2 corresponds to electron location near the second nucleus, $\widehat{H}$ is the Hamiltonian of electrons. Note that for an accurate evaluation of this interaction it is necessary to use the accurate wave functions of the quasimolecule which take into account interaction of a valence electron located between the cores with both cores simultaneously. We assume this to be fulfilled within the framework of the asymptotic theory. Using a general method of calculation of the exchange interaction potential $\Delta(R)$ by analogy with that for the case "a" of Hund coupling [3, 17, 20, 21], we

obtain

$$\Delta(R) \;=\; n\left(G_{ls}^{LS}\right)^2 \sum_{\mu,m,m',M,M',\,\sigma,\sigma',m_s,m_s',m_s'',\,M_S,M_S',m''',m_s'''} \begin{bmatrix} l_e & l & L \\ \mu & m' & M \end{bmatrix}$$

$$\begin{bmatrix} \tfrac{1}{2} & s & S \\ \sigma & m_s' & M_S \end{bmatrix} \begin{bmatrix} L & S & J \\ M & M_S & M_J \end{bmatrix} \begin{bmatrix} l & s & j \\ m & m_s & m_j \end{bmatrix} \begin{bmatrix} l_e & l & L \\ \mu & m'' & M' \end{bmatrix} \quad (21)$$

$$\begin{bmatrix} \tfrac{1}{2} & s & S \\ \sigma' & m_s'' & M_S' \end{bmatrix} \begin{bmatrix} L & S & J \\ M' & M_S' & M_J \end{bmatrix} \begin{bmatrix} l & s & j \\ m''' & m_s''' & m_j \end{bmatrix} \Delta_{l_e\mu}$$

Here we take into account the character of coupling of electron momenta in the quasimolecule, so that first the quantum numbers of an atomic core $lsm'm_s'$ and atomic numbers of a valence electron $l_e\mu\tfrac{1}{2}\sigma$ are summarized in the atomic quantum numbers LSM_LM_S, and then the atom quantum numbers are summed in quantum numbers $LSJM_J$, as well as ion quantum numbers $lsmm_s$ are summed in ion quantum numbers lsj. We sum or average over other quasimolecule quantum numbers which are not realized under the considered conditions. The following relations for the Clebsh-Gordan coefficients are used

$$\sum_{m,m_s,m''',m_s'''} \begin{bmatrix} l & s & j \\ m & m_s & m_j \end{bmatrix} \begin{bmatrix} l & s & j \\ m''' & m_s''' & m_j \end{bmatrix} = 1$$

$$\sum_{\sigma,\sigma',m_s'',m_s''} \begin{bmatrix} \tfrac{1}{2} & s & S \\ \sigma & m_s' & M_S \end{bmatrix} \begin{bmatrix} \tfrac{1}{2} & s & S \\ \sigma' & m_s'' & M_S' \end{bmatrix} = \delta_{M_S M_S'}$$

In formula (21) $\Delta_{l_e\mu}$ is the one-electron exchange interaction potential that respects the case when a valence electron with quantum numbers is located in the field of two structureless cores and has the same asymptotic wave function as in real atoms. As a result, we obtain by analogy with the case "a" of Hund coupling [3, 9, 17, 20, 21]

$$\Delta(R) = n\left(G_{ls}^{LS}\right)^2 \sum_{\mu,m,M,M_S} \begin{bmatrix} l_e & l & L \\ \mu & m & M \end{bmatrix}^2 \begin{bmatrix} L & S & J \\ M & M_S & M_J \end{bmatrix}^2 \Delta_{l_e\mu}(R)\,, \quad (22)$$

where the exchange interaction potential relates to certain quantum numbers JM_Jj, and this formula reduces the problem of exchange interaction between an atom and ion with noncompleted electron shells to transition of one electron between structureless cores. It is of importance that the exchange interaction potential does not depend on the ion moment j. The one-electron exchange interaction potential $\Delta_{l_e\mu}$ is given by the formula [9, 11, 16, 17]

$$\Delta_{l_e\mu}(R) = A^2 R^{\frac{2}{\gamma}-1-|\mu|} e^{-R\gamma-\frac{1}{\gamma}} \cdot \frac{(2l+1)(l_e+|\mu|)!}{(l_e-|\mu|)!\,|\mu|!\,(\gamma)^{|\mu|}} \quad (23)$$

Here l_e, μ are the quantum numbers of a valence electron, and γ, A are the parameters of the asymptotic wave function of this electron. Formula (22) contains

the first term of the asymptotic expansion of the ion-atom exchange interaction potential over a small parameter $1/\gamma R$.

Thus, formula (22) gives for the exchange interaction potential involving the halogen atom $X(^2P)$ with its ion $X^+(^3P)$

$$
\begin{aligned}
\Delta(JM_J, R) &= 3\Delta_{10}(R) \sum_M \begin{bmatrix} 1 & 1 & 1 \\ 0 & M & M \end{bmatrix}^2 \begin{bmatrix} 1 & 1/2 & J \\ M & M_J - M & M_J \end{bmatrix}^2 \\
&= \frac{3\Delta_{10}(R)}{2} \begin{bmatrix} 1 & 1/2 & J \\ 1 & M_J - 1 & M_J \end{bmatrix}^2,
\end{aligned}
\tag{24}
$$

where we extract the strongest term in the sum (22) that is proportional to $\Delta_{10}(R)$ (see formula (23)). We give in Table 4 the values of the exchange interaction potential for the ground electronic states of the halogen atom $X(^2P)$ and ion $X^+(^3P)$ at different fine-structure quantum numbers for these particles. The energies are taken at the separation $R = 14a_o$ that corresponds to the cross section (3) at the collision energy of $1eV$.

For demonstration of these results, we return to the above example of interaction of $Cl(^2P) + Cl^+(^3P)$ at the distance $R = 14a_o$ between nuclei. The energy splitting between even and odd quasimolecule states is $\Delta_{10} = 14cm^{-1}$, $\Delta_{11} = 2.0\,cm^{-1}$ if we consider the cores to be structureless. Table 4 contains the values of the exchange interaction potential under these conditions for given quantum numbers of interacting particles. We ignore the ion-atom quadrupole-quadrupole interaction as well as the rotational energy, and the energy of the even or odd state with given quantum numbers is $E \pm \Delta(R)/2$. The data of Table 4 confirm the used hierarchy of interactions between halogen atoms and their ions.

5. Resonant charge exchange for halogens

The above results for the exchange interaction potential allow us to determine the cross section of resonant charge exchange in slow collisions of halogen atoms and their ions in the ground electronic states. The asymptotic formula for the partial cross section of resonant charge exchange is given by[14, 15]

$$
\sigma_{res} = \frac{\pi R_o^2}{2}, \quad where \quad \frac{1}{v}\sqrt{\frac{\pi R_o}{2\gamma}}\,\Delta(R_o) = 0.28
\tag{25}
$$

Here v is the collision velocity, the asymptotic coefficient γ is expressed through the atom ionization potential I, and in atomic units it is equal to $\gamma = \sqrt{2I}$ (see also formula (23)). This formula is valid for transfer of an $s-$electron or in the case when transitions for states with given quantum numbers may be separated. In particular, the partial cross sections of resonant charge exchange in the chlorine case are given in Table 4.

TABLE 4.   The ion-atom exchange interaction potential $\Delta(R)$ for the ground electronic states of the quasimolecule $Cl(^2P_{JM_J}) + Cl^+(^3P_j)$ and different fine-structure states JM_Jj of this system. The exchange interaction potential is taken at $R = 14a_o$, as well as the total energy E of these states (Table 3) in neglecting the quadrupole-quadrupole ion-atom interaction, and the rotational energy. The partial cross sections of resonant charge exchange σ_{ex} are expressed in $\mathring{A}^2$ and are given at collision energies ε correspondingly 0.1; 1; and $10eV$ in the laboratory reference frame.

JM_Jj	$\Delta(R)$	Δ, cm^{-1}	E, cm^{-1}	$\sigma_{ex}, \varepsilon = 0.1; 1.0; 10eV$
$\frac{3}{2}\frac{3}{2}2$	$\frac{3}{2}\Delta_{10}$	87	0	110;92;76
$\frac{3}{2}\frac{1}{2}2$	$\frac{1}{2}\Delta_{10}$	29	260	93;77;62
$\frac{3}{2}\frac{3}{2}1$	$\frac{3}{2}\Delta_{10}$	87	696	110;92;76
$\frac{3}{2}\frac{1}{2}1$	$\frac{1}{2}\Delta_{10}$	29	956	93;77;62
$\frac{3}{2}\frac{3}{2}0$	$\frac{3}{2}\Delta_{10}$	87	996	110;92;76
$\frac{1}{2}\frac{1}{2}2$	Δ_{10}	58	1012	104;86;71
$\frac{3}{2}\frac{1}{2}0$	$\frac{1}{2}\Delta_{10}$	29	1256	93;77;62
$\frac{1}{2}\frac{1}{2}1$	Δ_{10}	58	1708	104;86;71
$\frac{1}{2}\frac{1}{2}0$	Δ_{10}	58	2009	104;86;71

We introduce the cross section of resonant charge exchange averaged over fine states assuming the initial population of atom and ion fine states to be proportional to their statistical weights

$$\overline{\sigma_{ex}} = \frac{1}{3}\left[\sigma_{ex}\left(\frac{3}{2},\frac{3}{2}\right) + \sigma_{ex}\left(\frac{3}{2},\frac{1}{2}\right) + \sigma_{ex}\left(\frac{1}{2},\frac{1}{2}\right)\right], \tag{26}$$

where the atom quantum numbers J, M_J are given as arguments of the partial cross section. If we expand the cross section of resonant charge exchange over the small parameter $1/R\gamma$ and restrict the expansion to two terms, then formula (25) for the averaged cross section (26), taking into account formula (24), takes the form

$$\sigma_{res} = \frac{\pi R_o^2}{2}, \quad where \quad \frac{2.7}{v}\sqrt{\frac{\pi R_o}{2\gamma}}\Delta_{00}(R_o) = 0.28, \tag{27}$$

and $\Delta_{00}(R)$ is the ion-atom exchange interaction potential for a transferring $s-$electron with a given asymptotic parameters γ, A of its wave function. This value

TABLE 5. The average cross sections for the halogen atom and ion in the ground electronic states $X(^2P) + X^+(^3P)$ in $10^{-15} cm^2$ at indicated collision energies ε in the laboratory frame of reference for the hierarchy (6) of interactions and for case "a" of Hund coupling[19, 21] (in parentheses).

	$\varepsilon = 0.1eV$	$\varepsilon = 1eV$	$\varepsilon = 10eV$
$F\,(\gamma = 1.132,\ A = 1.6)$	6.2(6.0)	5.1(4.9)	4.1(4.0)
$Cl\,(\gamma = 0.976,\ A = 1.8)$	10(10)	8.7(8.4)	7.1(6.9)
$Br\,(\gamma = 0.932,\ A = 1.8)$	13(12)	11(10)	8.9(8.2)
$I\,(\gamma = 0.876,\ A = 1.9)$	16(16)	14(13)	12(11)

is connected to the one-electron exchange interaction potential $\Delta_{10}(R)$ with a transferring $p-$electron in accordance with formula (23) by $\Delta_{10}(R) = 3\Delta_{00}(R)$. Table 5 contains the average cross sections of resonant charge exchange for halogen atoms and their ions in the ground electronic state $X(^2P) + X^+(^3P)$ allowing for the hierarchy (6) of interactions in a quasimolecule. These cross sections are close to the average cross sections for the ground fine states of the colliding particles, i.e. for the process $X(^2P_{3/2}) + X^+(^3P_2)$. Thus, an average over fine states of the ground electronic states and over momentum projections of the ground fine state of the colliding particles leads to similar results. In addition, these data are compared with the cross sections for the case "a" of Hund coupling which are taken from Refs. [19, 20]. As it follows from the comparison, the difference between the cross sections for different methods of momentum coupling does not exceed several percent.

One more peculiarity of the resonant charge exchange for momentum coupling at the hierarchy (6) of interactions is such that the difference between quasimolecule state energies of different projections of the atom electron momentum exceeds the rotational energy V_{rot} at ion-atom distances responsible for electron transfer. Hence, transitions between states of different quantum numbers JM_Jj are absent at these distances, and the resonant charge exchange process is not entangled with a change of these quantum numbers. Therefore, in contrast to the case "a" of Hund coupling, rotation of the molecular axis in the course of electron transfer does not influence on resonant charge exchange.

Above we evaluated precisely the cross section of resonant charge exchange accounting for the coupling of momenta of a transferring electron with momenta of atomic cores. Let us estimate the error if we ignore this coupling. Let us take a $p-$electron that has the same asymptotic parameters as valence electrons of halogen atoms, but this electron is located in the field of structureless cores. Then we obtain for the cross section of resonant charge exchange for chlorine at energies $0.1, 1,$ and $10eV$ the values $87, 71,$ and $57 \cdot 10^{-16} cm^2$, resp., instead of those of Table

5. As it is seen, ignoring the coupling between the momenta of a transferring electron and atomic cores leads to a remarkable error. Thus, resonant charge exchange proceeds at a certain value of the quantum numbers JM_Jj of the quasimolecule consisting of the colliding halogen ion and atom, and these quantum numbers do not change in this process. The partial cross sections of resonant charge exchange depend on molecular quantum numbers, whereas the average cross sections depend weakly on the scheme of momentum coupling.

6. Resonant charge exchange for oxygen

We now consider one more example of resonant charge exchange with transition of a p–electron

$$O^+(^4S) + O(^3P) \to O(^3P) + O^+(^4S) \,, \tag{28}$$
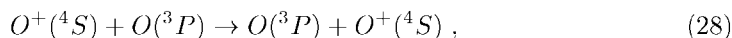
with participation of an oxygen atom and ion in the ground electronic states. Constructing the hierarchy of interactions (1) in this case, we take as a basis the previous case (6) when the quantum numbers of the quasimolecule consisting of the colliding particles are JM_J. According to formula (12), the interaction potential of the ion charge with the atom quadrupole has in this case the form

$$
\begin{aligned}
\Delta U(JM_J) &= \frac{2\overline{r_a^2}}{5R^3} \left(2 \begin{bmatrix} 1 & 1 & J \\ 0 & M_J & M_J \end{bmatrix}^2 - \begin{bmatrix} 1 & 1 & J \\ 1 & M_J - 1 & M_J \end{bmatrix}^2 \right) \\
&= U_o a(JM_J),
\end{aligned} \tag{29}
$$

where we use the notations of formula (12), and Table 6 contains the values $a(JM_J)$. On the basis of formula (22) we have in the oxygen case for the exchange interaction potential instead of formula (24) for halogens

$$\Delta(JM_J, R) = \frac{4}{3} \sum_\mu \begin{bmatrix} 1 & 1 & J \\ \mu & M_J - \mu & M_J \end{bmatrix}^2 \Delta_{1\mu}(R) \,, \tag{30}$$

and the coefficients of this formula are given in Table 6.

Note that the excitation energies of the oxygen atom fine states from the ground fine state $^3P_2$ is $158 cm^{-1}$ for the state $^3P_1$, and $220 cm^{-1}$ for the state $^3P_0$, and the parameter U_o of formula (29) at a typical separation for electron transfer is $U_o(R = 12a_o) = 102 cm^{-1}$. These values are comparable, and we have an intermediate case of momentum coupling for oxygen. In the above example for halogens $\delta_a >> U_o$, the quantum numbers of the quasimolecule are JM_Jj, while in the other limiting case $\delta_a << U_o$ the quantum numbers of the quasimolecule are JMj (M, M_J are the projections of the orbital and total atom momentum onto the quasimolecule axis). The first limiting case is used in Table 6 which contains the quasimolecule energies E in accordance with formula (17), where we consider the fine-structure splitting of levels and charge-quadrupole ion-atom interaction in the limit $\delta_a >> \Delta U$. The

TABLE   6.   The   parameters   of   interaction   for   the   quasimolecule $O^+(^4S_{3/2}) - O(^3P_J)$, and the interaction potentials at the distance $R = 12a_o$ between nuclei. The partial cross sections of resonant charge exchange σ_{ex} are expressed in $\mathring{A}^2$ and are taken at collision energies ε in the laboratory frame of reference of $0.1, 1$ and $10eV$ respectively.

JM_J	$a(JM_J)$	$\Delta(JM_J)$	E, cm^{-1}	Δ, cm^{-1}	$\sigma_{ex}, \varepsilon = 0.1; 1; 10eV$
22	-1	$\frac{4}{3}\Delta_{11}$	0	6.8	63;51;40
21	1/2	$\frac{2}{3}\Delta_{10}$	153	20	77;62;49
20	7/6	$\frac{8}{9}\Delta_{10}$	220	27	81;66;52
11	1/2	$\frac{2}{3}\Delta_{10}$	311	20	77;62;49
10	-1/2	$\frac{2}{3}\Delta_{11}$	209	4.4	56;44;34
00	1/3	$\frac{4}{9}\Delta_{10}$	363	13	72;57;45

energies are taken at the ion-atom distance $R = 12a_o$ that corresponds to typical impact parameters which determine the cross section of resonant charge exchange at the collision energy about $1eV$. Note that the rotational energy is $29cm^{-1}$ for $R = 12a_o$ and $\varepsilon = 1eV$, i.e. the rotational energy is small compared to the fine splitting of ion and atom levels and the long-range ion-atom interaction potential U_o.

The average cross section of resonant charge exchange is

$$\overline{\sigma_{ex}} = \frac{1}{9}\left[2\sigma_{ex}(22) + 2\sigma_{ex}(21) + \sigma_{ex}(20) + 2\sigma_{ex}(11) + \sigma_{ex}(10) + \sigma_{ex}(00)\right], \quad (31)$$

where the quantum numbers of the fine-structure atom state JM_J are given in parentheses, and we assume the population of these states to be proportional to their statistical weight. If we neglect the electron transitions due to rotation of the molecular axis, we have for the average cross section by analogy with formulas (25) and (27) (we use the notation of these formulas)

$$\sigma_{res} = \frac{\pi R_o^2}{2}, \quad where \quad \frac{2.9}{v(R_o\gamma)^{1/3}}\sqrt{\frac{\pi R_o}{2\gamma}}\Delta_{00}(R_o) = 0.28, \quad (32)$$

The average cross sections of Table 6 relate to formula (31) while formula (32) gives for the average cross section of resonant charge exchange the values $71, 57$, and $45 \cdot 10^{-16} cm^2$ at the collision energies $0.1, 1$, and $10eV$ respectively, while these cross sections for the case "a" of Hund coupling are equal [19, 20] to $73, 60$, and $48 \cdot 10^{-16} cm^2$, respectively. Note that averaging only over the momentum projection M_J, we obtain for the partial cross sections (i.e. for the process $O^+(^4S_{3/2}) +$

TABLE 7. The ion-atom exchange interaction potential for the quasi-molecule $O^+({}^4S_{3/2}) - O({}^3P_J)$ when its quantum numbers are J and M (the total atom moment and the projection of the atom orbital momentum onto the molecular axis). The partial cross sections of resonant charge exchange σ_{ex} at indicated quantum numbers and collision energies ε in the laboratory frame of reference are expressed in $\mathring{A}^2$.

JM	$\Delta(JM_J)$	$\sigma_{ex},, \varepsilon = 0.1eV$	$\sigma_{ex},, \varepsilon = 1eV$	$\sigma_{ex},, \varepsilon = 10eV$
20	$\frac{20}{9}\Delta_{11}$	69	56	40
21	$\frac{10}{9}\Delta_{10}$	84	68	55
10	$\frac{4}{3}\Delta_{11}$	63	51	45
11	$\frac{2}{3}\Delta_{10}$	77	62	49
00	$\frac{4}{9}\Delta_{11}$	51	41	31
01	$\frac{2}{9}\Delta_{10}$	63	50	38

$O({}^3P_2))$ the values $72, 58$, and $46 \cdot 10^{-16} cm^2$ at the collision energies $0.1, 1$, and $10 eV$. As it is seen, the difference of the above average cross sections and the average partial cross sections does not exceed their accuracy. Next, if we ignore the coupling of a transferring electron with the cores, i.e. if we consider transition of a $p-$electron between structureless cores at the same asymptotic parameters of its wave function as in the above cases, we obtain for the average cross sections of resonant charge exchange the values $64, 51$, and $40 \cdot 10^{-16} cm^2$ at the indicated collision energies. In all the cases, in order to make the comparison under identical conditions, we ignore the influence of rotation of the molecular axis on the cross section value. Rotation of the molecular axis increases the cross section of resonant charge exchange for oxygen by several percent in the case "a" of Hund coupling. From this analysis one can conclude that, though partial cross sections depend remarkably on the quantum numbers of colliding particles, the average cross sections depend weakly on the scheme of momentum coupling.

The other limiting case of the interaction hierarchy $\delta_a << U_o$ between the fine splitting of atom levels and ion-quadrupole interaction potential leads to the quasimolecule quantum numbers JMj, where M is the projection of the atom angular momentum onto the quasimolecule axis. In this limiting case formula (22) for the ion-atom exchange interaction potential takes the form for the process (28)

$$\Delta(R) = \frac{4}{3} \sum_{\mu, M_S} \begin{bmatrix} 1 & 1 & 1 \\ \mu & M-\mu & M \end{bmatrix}^2 \begin{bmatrix} 1 & 1 & J \\ M & M_S & M_S+M \end{bmatrix}^2 \Delta_{1\mu}(R), \quad (33)$$

An average of the cross sections of Table 7 over fine states of the ground electronic state gives for the average cross section of resonant charge exchange the values

$70, 56$, and $44 \cdot 10^{-16} cm^2$ at the collision energies $0.1, 1$,and $10 eV$ correspondingly, and for the ground fine state $J = 2$ these values are equal to $79, 64$, and $50 \cdot 10^{-16} cm^2$ correspondingly. In this case the average cross section differs from that for the lowest fine state. Next, for the cross section averaged over fine states with accounting for the logarithm dependence for the cross section on the collision velocity we obtain the following relation instead of formula (32)

$$\sigma_{res} = \frac{\pi R_o^2}{2} , \quad where \quad \frac{2.6}{v(R_o \gamma)^{1/3}} \sqrt{\frac{\pi R_o}{2\gamma}} \Delta_{00}(R_o) = 0.28 ,$$

and it differs from formula (32) sligthly. Thus, we find that the average cross sections depend weakly on the character of momentum coupling.

We now consider one more process of the resonant charge exchange involving an oxygen negative ion :

$$O^-(^2P) + O(^3P) \rightarrow O(^3P) + O^-(^2P) , \qquad (34)$$
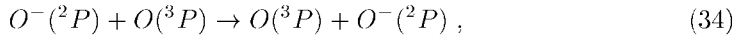
This case is of interest because the electron shells of colliding particles are identical to the halogen case (2), and the states of the oxygen atom are the same for the process (28) involving a positive oxygen ion. Nevertheless, though we are based on the same coupling scheme in all these cases, the character of coupling is different for them. As in the previous cases, we are based on formula (22) for the ion-atom exchange interaction potential and try to restrict the terms which are proportional to $\Delta_{10}(R)$, the strongest exchange interaction potential. In contrast to the case of the positive oxygen ion, the exchange interaction potentials for fine atom states are nonzero in this approximation, and we have on the basis of formula (22) for the process (34)

$$\Delta(R) = \frac{5}{3} \Delta_{10}(R) \sum_M \begin{bmatrix} 1 & 1 & 1 \\ 0 & M & M \end{bmatrix}^2 \begin{bmatrix} L & S & J \\ M & M_J - M & M_J \end{bmatrix}^2 \qquad (35)$$

Table 8 contains the values of ion-atom exchange interaction potentials for different atom fine states. Thus, the parentage coefficients are the same in this case as in the halogen case, and the fine structure parameter are identical to the case of positive oxygen atom. Because formula (22) contains the parameters of the atomic core, the exchange interaction potentials of Table 6 and 7 are different.

Using the expression for the one-electron exchange interaction potential of a negative ion and its atom at large separations [18]

$$\Delta_{10}(R) = \frac{3A^2}{R} \exp(-\gamma R) , \qquad (36)$$

and using the asymptotic formula (7) for the cross section of electron transfer, we obtain partial cross sections of the resonant charge exchange process which are

TABLE 8. The ion-atom exchange interaction potential for the quasi-molecule $O^-(^2P_j) - O(^3P_J)$ when its quantum numbers are J and M_J (the total atom moment and its projection onto the molecular axis). The partial cross sections of resonant charge exchange σ_{ex} at indicated quantum numbers and collision energies ε in the laboratory frame of reference are expressed in $10^{-15} cm^2$.

JM_J	$\Delta(JM_J)$	$\sigma_{ex},, \varepsilon = 0.1 eV$	$\sigma_{ex},, \varepsilon = 1 eV$	$\sigma_{ex}, \varepsilon = 10 eV$
22	$\frac{2}{3}\Delta_{10}$	25	19	13
21	$\frac{1}{3}\Delta_{10}$	21	16	11
20	$\frac{1}{3}\Delta_{10}$	21	16	11
11	$\frac{2}{3}\Delta_{10}$	25	19	13
10	$\frac{1}{3}\Delta_{10}$	21	16	11
00	$\frac{2}{9}\Delta_{10}$	19	14	9.2

given in Table 7. We use the parameters $\gamma = 0.328$ and $A = 0.65$ [13] for the oxygen negative ion.

7. Conclusion

Considering the character of momentum coupling for the resonant charge exchange process in slow collisions, we find that the number of possible cases of momentum coupling is larger than that in the classical Hund scheme of momentum coupling. Constructing the hierarchy of interactions for a quasimolecule consisting of the colliding ion and atom, we find the strongest interaction to be the exchange interaction of electrons in these atomic particles, and therefore the quasimolecule quantum numbers for the ion and atom electron shells are $LSls$ (the orbital momentum and spin of the atom and the same quantum numbers for the ion). For the cases under consideration (halogens and oxygen), the rotational energy V_{rot} of the colliding particles is small compared to the fine splitting of atomic ionic levels, δ_a and δ_i, as well it is small in comparison with a long-range charge-quadrupole interaction U between an ion and atom. Hence, the resonant charge exchange process in these cases proceeds at certain quantum numbers JM_Jj or JMj (J, j are the total atom and ion momenta, M, M_J are the total projections of the atom orbital and total momentum onto the quasimolecule axis) depending on the relation between δ_a and U. This character of momentum coupling does not correspond to any of the cases of the Hund coupling scheme.

In contrast to the case "a" of Hund coupling, in the halogen and oxygen cases the resonant charge exchange process is not entangled with transitions between fine states of colliding particles and rotaion of the molecular axis. This increases

the accuracy of the asymptotic theory in the evaluation of the cross section of electron transfer. The cross section depends on the initial quantum numbers of the quasimolecule, while according to the analysis for halogens and oxygen, the cross sections averaged over fine atom states depend weakly on the coupling scheme.

References

1. Bashkin, S. and Stoner, J. (1978) *Atomic Energy Levels and Grotrian Diagrams*, North Holland, Amsterdam. vol.1, 1978; vol. 2, 1978; vol. 3, 1981; vol. 4, 1982.
2. Condon, E.U. and Shortley, G.H. (1949) *Theory of Atomic Spectra*, Cambridge Univ.,Cambridge.
3. Duman, E.L. and Smirnov, B.M. (1970) *Sov. Phys. Tech. Phys.* **15**, 61.
4. Firsov, O.B. (1951) *Zh. Exp. Theor. Fiz.* **21**, 1001.
5. Mulliken, R.S. (1930) *Rev. Mod. Phys.* **2**, 60.
6. Hund, F. (1936) *Z. Phys.* **36**, 637.
7. Landau, L.D. and Lifschitz, E.M. (1980) *Quantum Mechanics*, Pergamon Press, London.
8. Nikitin, E.E.(1966) *Optika and Spectr.* **22**, 379.
9. Nikitin, E.E. and Smirnov, B.M. (1978) *Sov. Phys. Uspekhi* **21**, 95.
10. Nikitin, E.E. and Umanskii, S.Ja. (1984) *Theory of Slow Atomic Collisions*. Springer, Berlin.
11. Nikitin, E.E. and Smirnov, B.M. (1988) *Atomic and Molecular Processes.*, Nauka, Moscow.
12. Racah, G. (1942) *Phys. Rev.* **61**, 186; **62**, 438.
13. Radzig, A.A. and Smirnov, B.M. (1985) *Reference Data on Atoms, Molecules and Ions*, Springer, Berlin.
14. Smirnov, B.M. (1964) *Sov. Phys. JETP* **19**, 692.
15. Smirnov, B.M. (1965) *Sov. Phys. JETP* **20**, 345.
16. Smirnov, B.M. (1966) *Teplophys. Vys. Temp.* **4**, 429.
17. Smirnov, B.M. (1972) *Asymptotic Methods in Theory of Atomic Collisions*, Atomizdat, Moscow.
18. Smirnov, B.M. (1982) *Negative Ions*, McGraw-Hill, New York.
19. Smirnov, B.M. (2000) *Phys. Scripta.* **61**, 595.
20. Smirnov, B.M. (2001) *Sov. Phys. Uspekhi* **44**, 221.
21. Smirnov, B.M. (2001) *JETP* **92**, 951.
22. Smirnov, B.M. (2003) *Physics of Atoms and Ions*, Springer NY, New York.
23. Sobelman, I.I. (1979) *Atomic Spectra and Radiative Transitions*, Springer, Berlin.

TIME-DEPENDENT WAVEPACKET CALCULATIONS FOR REACTIVE SCATTERING AND PHOTODISSOCIATION

GABRIEL G. BALINT-KURTI
School of Chemistry
The University of Bristol, Bristol BS8 1TS, UK

AND

ALEX BROWN
Department of Chemistry
University of Alberta, Edmonton, AB, T6G 2G2, Canada

Abstract.
The theory of time-dependent wavepacket calculations of reactive scattering and photodissociation is briefly reviewed and some illustrative results presented. Particular attention will be paid to the theory of differential scattering cross sections, arising from both types of process, and to the symmetry of angular dependent scattering in a photodissociation process. Electronically non-adiabatic processes will be discussed and illustrations from the reactive scattering of $O(^1D)$ + H_2 and from the photodissociation of HF are presented.

1. Introduction

Heller [1, 2, 3] introduced and popularised wavepacket dynamics in the context of the theory of molecular photodissociation. In a photodissociation process, the molecule starts in a well defined initial state and ends up in a final scattering state. The initial bound state vibrational-rotational wavefunction provides a natural initial wavepacket in this case.

In the case of a reactive scattering process, there is no natural initial wavepacket and it must be created artificially. The artificially created wavepacket is placed in the entrance channel of the reaction and is given an inward momentum toward the strong interaction region. The wavepacket is localised in space and consequently, as a result of Heisenberg's uncertainty principle, it contains a range of energies. But as the energy is a conserved quantity for the isolated reacting system, each energy component of the wavepacket propagates independently and a correct analysis of

149

the final wavepacket dynamics should be able to provide information concerning the cross sections and reaction probabilities corresponding to all energies contained within the original wavepacket.

Photodissociation theory is in principle much simpler than reactive scattering theory. This is because only three values of the total angular momentum are involved in a photodissociation process while reactive scattering requires a summation over a very large number of total angular momentum quantum numbers.

2. Molecular Photodissociation

The key to performing a wavepacket calculation is the propagation of the wavepacket forward in time so as to solve the time-dependent Schrödinger equation. In 1983, Kosloff proposed the Chebyshev expansion technique [5, 6, 7, 8] for evaluating the action of the time evolution operator on a wavepacket. This led to a huge advance in time-dependent wavepacket dynamics [9, 10, 11, 12, 13, 14, 15, 16, 17, 18, 19, 20, 21, 22, 23, 24, 25, 26, 27, 28, 29] . Several studies have compared different propagation methods [30, 31, 32] and these show that the Chebyshev expansion method is the most accurate.

In this section, the basic formalism for calculating both integral and differential, total and partial cross sections is briefly reviewed. A fuller discussion may be found in a recent review [33].

2.1. TOTAL INTEGRAL CROSS SECTION

Within the semiclassical, perturbational treatment of the interaction of radiation with matter [35, 36] and within the dipole approximation [37] the total energy absorption cross section may be written in the form [38, 40, 41, 39]:

$$\sigma_{tot}(E) = \frac{2\pi^2\nu}{c\epsilon_0} \sum_f \int d\hat{\mathbf{k}} \mid < \psi_f|\vec{\epsilon}\cdot\vec{\mu}|\psi_i > \mid^2 \tag{1}$$

where ψ_i and ψ_f are the wavefunctions of the nuclear motion corresponding to the initial and final states respectively, $\vec{\epsilon}$ is the polarisation vector of the electric field of the light and $\vec{\mu}$ is the transition dipole vector (which depends on the nuclear geometry).

For the photodissociation of a triatomic molecule, the asymptotic form of the final state, continuum wavefunction, correctly normalised on the energy scale[42], may be written as[39]:

$$\psi_f \equiv \psi^-_{vjm_j}(\mathbf{r}, \mathbf{R}; \hat{\mathbf{k}}, E) \underset{R\to\infty}{\sim} \left(\frac{\mu k_{vj}}{\hbar^2(2\pi)^3}\right)^{\frac{1}{2}} \left\{ e^{i\mathbf{k}\cdot\mathbf{R}} \chi_{vj}(r)Y_{jm_j}(\hat{\mathbf{r}}) \right.$$

$$\left. + \sum_{v'j'm'_j} f_{v'j'm'_j,vjm_j}(\mathbf{k},\hat{\mathbf{R}})\frac{e^{-ik_{v'j'}R}}{R}\chi_{v'j'}(r)Y_{j'm'_j}(\hat{\mathbf{r}}) \right\} \tag{2}$$

where $\hat{\mathbf{k}}$ denotes the direction of observation (i.e., the direction in which the two fragments scatter), $\mathbf{r}$ is the vector joining the two atoms of the diatom fragment, R is the distance between the center-of-mass of the diatom and the atomic fragment, v is the vibrational quantum number of the final diatomic photofragment and j is its rotational quantum number. The summation over final states in Eq. (1) also includes an integration over all the directions of dissociation, $\hat{\mathbf{k}}$. The boundary conditions of the wavefunction $\psi^-_{vjm_j}(\mathbf{r},\mathbf{R};\hat{\mathbf{k}},E)$ correspond to a pure outgoing wave and with a final photofragment vibrational-rotational wavefunction $\chi_{vj}(r)Y_{jm}(\hat{\mathbf{r}})$.

Using the theory given in Refs. [33] (see especially appendix A) and [43], we can write the final state wave function in the body-fixed form (see also Refs. [4] and [39] for details of the space-fixed body-fixed transformation):

$$
\psi^-_{vjm_j}(\mathbf{r},\mathbf{R};\hat{\mathbf{k}},E) = \sum_{JM}\sum_{lm_lp} Y^*_{lm_l}(\hat{\mathbf{k}})(jlJM|jm_jlm_l)\sum_{K=\lambda}^{J}(Jjl0|JKj-K)
$$

$$
\times \sum_{K'=\lambda}^{J}\Phi^{-JvjKp}_{K'}(r,R,\theta;E)|J,K',M,p> \quad , \tag{3}
$$

where

$$
\Phi^{-JvjKp}_{K'}(r,R,\theta;E) = \left(\frac{\mu k_{vj}}{\hbar^2(2\pi)^3}\right)^{\frac{1}{2}}4\pi\sum_{v'j'}\left\{\frac{2(-1)^{j-K}}{\sqrt{2(1+\delta_{0,K})}}\right\}
$$

$$
\times\frac{\Phi^{(JvjKp)}_{v'j'K'}(R)}{R}\Theta_{j'K'}(\theta)\,\chi_{v'j'}(r)\ . \tag{4}
$$

and $|J,K,M,p\rangle$ are parity adapted eigenfunctions [43] of the total angular momentum (J) corresponding to specified space-fixed (M) and body-fixed (K) z components; $\Phi^{-JvjKp}(r,R,\theta;E)$ is a body-fixed wavefunction with the correct boundary conditions [39] so as to yield the asymptotic behaviour specified in Eq. (2); $(Jjl0|JKj-K)$ are Clebsch-Gordan angular momentum coupling coefficients [44, 45] and the coordinates r,R,θ are the body-fixed Jacobi coordinates with θ being the angle between the scattering coordinate $\mathbf{R}$ and the diatomic molecular axis direction, $\mathbf{r}$ (see Ref. [43]). $\Theta_{j'K'}(\theta)$ are normalised associated Legendre Polynomials [45]. These are just the polar angle part of the spherical harmonics.

The parity adapted total angular momentum eigenfunctions [43] are defined as:

$$
|J,K,M,p\rangle= \sqrt{\frac{2J+1}{8\pi^2}}\frac{1}{\sqrt{2(1+\delta_{0,K})}}\left\{D^J_{K,M}(\omega)+(-1)^{J+K+p}D^J_{-K,M}(\omega)\right\} \tag{5}
$$

and

$$
\lambda = \frac{1-(-1)^{J+p}}{2}. \tag{6}
$$

The parity is given by $(-1)^{J+K+p}$, where p can take the values $p = 1$ or $p = 2$, thereby yielding positive or negative parity states, depending on the values of J and $|K|$. The $D^J_{K,M}(\omega)$s are Wigner D matrices and are functions of the three Euler angles, $\omega(\equiv \alpha, \beta, \gamma)$, which orient the three atom system in the space-fixed frame [44]. The $D^J_{K,M}(\omega)$ matrix elements corresponding to the same absolute value, but different signs, of K must be combined to form parity eigenfunctions [39, 45].

The asymptotic form of the body-fixed radial scattering wavefunction, $\Phi^{(JvjK)}_{v'j'K'}(R)$, is [4, 39]:

$$
\Phi^{(JvjK)}_{v'j'K'}(R) \underset{R\to\infty}{\sim} \frac{1}{2ik_{vj}} \left[e^{ik_{v'j'}R} \delta_{vv'} \delta_{jj'} \delta_{KK'} \right.
$$
$$
\left. - S^{Jp*}_{vjK,v'j'K'} \left(\frac{k_{v'j'}}{k_{vj}} \right)^{\frac{1}{2}} e^{-ik_{v'j'}R} \right]. \tag{7}
$$

The **S** matrix elements, which occur in Eq. (7), contain information about the dynamics or scattering on the final or upper state electronic energy surface, but they do not contain information about the probability of the photodissociation process.

The initial wavefunction, ψ_i, appearing in Eq. (1) is an eigenfunction of the total angular momentum, J, of its space-fixed z component, M, and of the parity, $(-1)^{J+K+p}$. It may be written in the form:

$$
\psi_i \equiv \Psi^{J_i,M_i,p}(r, R, \theta, \omega) = \sum_{K=\lambda}^{J_i} \psi^{J_i,K_i,p}(r, R, \theta)|J_i, K, M_i, p> \tag{8}
$$

where the functions $|J, K, M, p>$ have been defined above (see Eq. (5))

2.2. PARTIAL INTEGRAL CROSS SECTION

We are interested not only in the total absorption cross section, Eqs. (1) , which gives us a measure of the total probability that the molecule will absorb light and dissociate, but also in the probability that different product quantum states will be formed. This probability is given by a *partial* cross section, $\sigma_f(E)$. ¿From Eq. (1), we see that this partial integral cross section may be written as:

$$
\sigma_f(E) = \frac{2\pi^2\nu}{c\epsilon_0} \int d\hat{\mathbf{k}} \mid < \psi_f|\vec{\epsilon}\cdot\vec{\mu}|\psi_i > \mid^2. \tag{9}
$$

The partial cross section gives the probability of absorbing light and producing a particular final product quantum state. The total photodissociation cross section is clearly given by the sum over all partial photodissociation cross sections.

$$
\sigma_{tot}(E) = \sum_f \sigma_f(E) \tag{10}
$$

By omitting the integrals over all final scattering directions in Eqs. (1) and (9), we obtain a cross section for scattering into a specific final direction. These are the differential cross sections.

These partial differential cross section are therefore given by (see Eqs. (2)) and (3))):

$$\sigma_{vjm_j}(E;\hat{\mathbf{k}}) = \frac{2\pi^2\nu}{c\,\epsilon_0}\left|\langle\psi^-_{vjm_j}(\mathbf{r},\mathbf{R};\hat{\mathbf{k}},E)|\,\vec{\epsilon}\cdot\vec{\mu}\,|\psi_i\rangle\right|^2 \quad, \tag{11}$$

Substituting Eq. (3) into the above, we obtain:

$$\begin{aligned}\sigma_{vjm_j}(E;\hat{\mathbf{k}}) &= \frac{2\pi^2\nu}{c\,\epsilon_0}\left|\sum_{JM}\sum_{KK'p}\right.\\[1mm]&\quad\left\{\sum_{lm_l}Y^*_{lm_l}(\theta_k,\phi_k)(jlJM|jm_jlm_l)(Jjl0|JKj-K)\right\}\\[1mm]&\quad\left.\times\langle J,K',M,p|\Phi^{-JvjKp}_{K'}(r,R,\theta;E)\,|\vec{\epsilon}\cdot\vec{\mu}|\psi_i>\right|^2 .\end{aligned} \tag{12}$$

Following the treatment in Refs. [39] and [33], we can show that this can be rewritten as:

$$\begin{aligned}\sigma_{vjm_j}(E;\hat{\mathbf{k}}) &= \frac{2\pi^2\nu}{c\,\epsilon_0}\frac{1}{4\pi}\left|\sum_{JM}\sum_{KK'p}(2J+1)^{\frac{1}{2}}\right.\\[1mm]&\quad\times D^J_{K,M}(\phi_k,\theta_k,0)D^j_{-K,-m_j}(\phi_k,\theta_k,0)\\[1mm]&\quad\left.\langle J,K',M,p|\Phi^{-JvjKp}_{K'}(r,R,\theta;E)\,|\vec{\epsilon}\cdot\vec{\mu}|\psi_i>\right|^2 .\end{aligned} \tag{13}$$

The form of the angular distribution of the photofragments [39, 46] is determined by the product of Wigner $D^J_{K,M}(\omega)$ matrix elements in Eq. (13), i.e., $D^J_{K,M}(\theta_k,\phi_k,0)D^j_{-K,-m_j}(\theta_k,\phi_k,0)$. In particular this form shows clearly that if either the polarisation of the initial molecular state (i.e. the M_i quantum number) or the polarisation of the product diatomic rotational state, m_j, is selected, then the angular distribution of the photofragments is more complex than is normally assumed. In particular, if linearly polarised light is used to accomplish the photodissociation, the angular distribution will require terms of the form $P_4(\cos(\theta_k))$ (i.e., fourth order Legendre polynomials in the scattering angle) for its description and the conventional β parameter, associated with second order Legendre polynomials are not sufficient [39]. Also more recently, Pe'er, Shapiro and one of the authors (GGBK) have argued [46] that the backward-forward symmetry of the angular distribution of the photofragments may be destroyed under the same circumstances. The integral on the right hand side of Eq. (13) contains the essential molecular dynamics of the photodissociation process.

2.3. THE TIME-DEPENDENT FORMULATION

The key to re-expressing the integral cross section (Eq. (1)) in terms of time-dependent quantities is the recognition that the continuum functions $\psi^-_{vjm_j}(\mathbf{r}, \mathbf{R}; \hat{\mathbf{k}}, E)$ (Eqs. (2) and (3)) form a complete set for the space of functions with energy E. This fact can be expressed as [1, 2, 47]:

$$\sum_{vjm_j} \int d\hat{\mathbf{k}} |\psi^-_{vjm_j}(\mathbf{r}, \mathbf{R}; \hat{\mathbf{k}}, E)\rangle\langle\psi^-_{vjm_j}(\mathbf{r}, \mathbf{R}; \hat{\mathbf{k}}, E)| = \delta(\hat{\mathbf{H}} - E)\hat{\mathbf{I}}. \tag{14}$$

The Dirac delta function may be represented as a Fourier transform over time:

$$\delta(\hat{\mathbf{H}} - E) = \frac{1}{2\pi\hbar} \int_{-\infty}^{\infty} dt \, \exp\left[\frac{-i(\hat{\mathbf{H}} - E)t}{\hbar}\right]. \tag{15}$$

Replacing the final state wavefunction, ψ_f, in Eq. (1) by $\psi^-_{v'j'm_{j'}}(\mathbf{r}, \mathbf{R}; \hat{\mathbf{k}}, E)$ and using Eq. (15), we obtain:

$$\sigma_{tot}(E) = \frac{\pi\nu}{c\,\epsilon_0\hbar}\langle\psi_i|\vec{\epsilon}\cdot\vec{\mu}|\left\{\int_{-\infty}^{\infty} dt \, \exp\left[\frac{-i(\hat{\mathbf{H}} - E)t}{\hbar}\right]\right\}|\vec{\epsilon}\cdot\vec{\mu}|\psi_i\rangle. \tag{16}$$

If we now define the "initial wavepacket" as

$$|\Phi_i(\mathbf{r}, \mathbf{R}, t = 0)\rangle = \vec{\epsilon}\cdot\vec{\mu}|\psi_i\rangle, \tag{17}$$

we can re-express the energy dependent total photodissociation cross section as:

$$\begin{aligned}\sigma_{tot}(E) &= \frac{\pi\nu}{c\,\epsilon_0\hbar} \int_{-\infty}^{\infty} dt \, \exp\left[\frac{iEt}{\hbar}\right] \\ &\times \langle\Phi_i(\mathbf{r}, \mathbf{R}, t = 0)|\exp\left[\frac{-i\hat{\mathbf{H}}t}{\hbar}\right]|\Phi_i(\mathbf{r}, \mathbf{R}, t = 0)\rangle.\end{aligned} \tag{18}$$

The time-dependent Schrödinger equation is:

$$i\hbar\frac{\partial\Phi(t)}{\partial t} = \hat{\mathbf{H}}\Phi(t) \tag{19}$$

If the Hamiltonian $\hat{\mathbf{H}}$ does not depend on time, this equation has the analytic solution:

$$\Phi(t) = \exp\left[\frac{-i\hat{\mathbf{H}}t}{\hbar}\right]\Phi(t = 0). \tag{20}$$

Using Eq. (20) in the right hand side of Eq. (18), we can rewrite the expression for the total absorption cross section as:

$$\sigma_{tot}(E) = \frac{\pi\nu}{c\,\epsilon_0\hbar} \int_{-\infty}^{\infty} dt \, \exp\left[\frac{iEt}{\hbar}\right]\langle\Phi_i(\mathbf{r}, \mathbf{R}, t = 0)|\Phi_i(\mathbf{r}, \mathbf{R}, t)\rangle. \tag{21}$$

The time-dependent quantity in the integrand of Eq. (21), $\langle\Phi_i(t=0)|\Phi_i(t)\rangle$, is called the auto-correlation function. It is the integral over all space of the product of the initial wavepacket with the wavepacket at time t. Krishna and Coalson [47] have shown that the Fourier transform over time in Eq. (21) can be replaced by twice the half Fourier transform where the time integral runs from $t=0$ to $t=\infty$. Using this result we obtain the final expression:

$$\sigma_{tot}(E) = \frac{2\pi\nu}{c\,\epsilon_0\hbar}\int_0^\infty dt\,\exp\left[\frac{iEt}{\hbar}\right]\langle\Phi_i(\mathbf{r},\mathbf{R},t=0)|\Phi_i(\mathbf{r},\mathbf{R},t)\rangle\quad. \tag{22}$$

Eq. (22) expresses the total absorption cross section as the half Fourier transform of an autocorrelation function, $\langle\Phi(t=0)|\Phi(t)\rangle$, where the angular brackets indicate integration over all spatial coordinates.

2.4. THE INITIAL WAVEPACKET

The initial wavefunction of the molecule has a well defined total angular momentum, J_i, and a specified space-fixed z component, M_i, of this angular momentum. It may therefore be expanded as a linear combination of the parity adapted total angular momentum eigenfunctions[43], $|J_i, K, M_i, p>$, as defined in Eq. (5). The initial wavepacket, $\Phi_i(\mathbf{r},\mathbf{R},t=0)$ (Eq. (17)), is obtained by multiplying the initial wavefunction by $\vec{\epsilon}\cdot\vec{\mu}$, where $\vec{\epsilon}$ is the electric field polarisation vector of the linearly (or circularly) polarised light and $\vec{\mu}$ is the transition dipole moment for the electronic transition involved and depends on the molecular geometry. Note that $\vec{\epsilon}$ is defined in the space-fixed reference frame and must be rotated to the body-fixed frame using Wigner D matrices. Despite the fact that the direction or sense of the electric field of the light wave oscillates, the vector $\vec{\epsilon}$ takes on a constant, though maybe arbitrarily defined, direction. For linearly polarised light, this direction is used to define the space-fixed z axis. While the actual choice of direction of $\vec{\epsilon}$ is unimportant, it has the important consequence of differentiating between the positive and negative M_i and m_j states of the initial molecule and the product diatomic, respectively. The derivation of the detailed form of the initial wavepacket and its relationship to the initial bound state wavefunction are fully discussed in Ref. [43] (see also Ref. [33]). As expected, from the vector property of the polarisation vector of the incident light beam, the result is that the initial wavepacket becomes a linear combination of functions with up to three possible values of the total angular momentum, differing from J_i by at most one, i.e.,

$$\begin{aligned}\Phi_i(\mathbf{r},\mathbf{R},t=0) &= \vec{\epsilon}\cdot\vec{\mu}|\psi_i\rangle\\ &= \sum_{J'=J_i-1}^{J_i+1}(-1)^{m+M_i}\begin{pmatrix}1 & J_i & J'\\ m & M_i & -(m+M_i)\end{pmatrix}\\ &\quad\times\left\{\sum_{K=\lambda'}^{J'}\Phi_i^{J'K}(r,R,\theta,t=0)\,|J',K,M_i+m,p'\rangle\right\}\end{aligned} \tag{23}$$

where the detailed form of $\Phi_i^{J'K}(r, R, \theta, t = 0)$ is given in Ref. [43] and in Appendix B of Ref. [33] .

It should be noted that K, which is the z component of the total angular momentum along the body-fixed z axis, is not a good quantum number and in general the initial wavefunction, ψ_i, will be a linear combination of parity adapted total angular momentum eigenfunctions corresponding to different values of K but the same J_i. The label m relates to the nature of the space-fixed electric field polarisation vector. $m = 0$ denotes linearly polarised light with the electric field vector pointing along the space-fixed z axis, while $m = \pm 1$ corresponds to circularly polarised light, with the space-fixed z axis pointing along the propagation direction of the light beam. The parity factor, $(-1)^{p'}$, of the wavefunction for nuclear motion is the same as that of the initial wavefunction if the electronic transition is perpendicular, i.e. the transition dipole moment is perpendicular to the molecular plane, and it is opposite to the initial parity for a parallel electronic transition.

The functions $\Phi_i^{J'K}(r, R, \theta, t = 0)$ involve a product of the initial wavefunction and the internal coordinate dependent vector components of the transition dipole moment (see Ref. [43] and Appendix B of Ref. [33]). As the total angular momentum is a conserved quantity during the time propagation of the wavepacket, we may divide up the initial wavepacket (Eq. (23)) into three components [43], one for each of the allowed values of J'. Thus Eq. (23) may be rewritten as:

$$\Phi_i(\mathbf{r}, \mathbf{R}, t = 0) = \sum_{J' = J_i - 1}^{J_i + 1} (-1)^{m + M_i} \begin{pmatrix} 1 & J_i & J' \\ m & M_i & -(m + M_i) \end{pmatrix}$$
$$\times \Phi_i^{J'}(\mathbf{r}, \mathbf{R}, t = 0) \tag{24}$$

where the function $\Phi_i^{J'}(\mathbf{r}, \mathbf{R}, t = 0)$ corresponds to the curly bracket in Eq. (23):

$$\Phi_i^{J'}(\mathbf{r}, \mathbf{R}, t = 0) = \sum_{K = \lambda'}^{J'} \Phi_i^{J'K}(r, R, \theta, t = 0) |J', K, M_i + m, p'\rangle \tag{25}$$

and λ' takes on the value of 0 or 1 depending on the parity number p'. Each of the wavepackets $\Phi_i^{J'}(\mathbf{r}, \mathbf{R}, t = 0)$ corresponds to a single total angular momentum value J' and each may be propagated forward in time independently of the other component wavepackets.

It should be noted that for values of $J' > 0$ there will be J' or $J' + 1$ different values of K (depending on the value of p') involved in the summation of Eq. (25). The set of body-fixed wavepackets, $\Phi_i^{J'K}(r, R, \theta, t = 0)$, corresponding to the same value of J' but to different values of K, must be propagated together as they are coupled or mixed during the propagation process by the centrifugal coupling [39, 48].

If we substitute Eqs. (24) and (25) into Eq. (22), average over the z components of the initial total angular momentum and sum over the z components of the final

total angular momentum, we obtain [43] (note the proof in Ref. [43] is specialised to the case of linearly polarised light, $m = 0$):

$$
\begin{aligned}
\sigma_{tot}(E) \quad = \quad & \frac{2\pi\nu}{3\,c\,\epsilon_0\hbar} \sum_{J'=J_i-1}^{J_i+1} \delta(J', J_i, 1) \sum_{K=0}^{J'} \int_0^\infty dt \, \exp\left[\frac{iEt}{\hbar}\right] \\
& \times \left\langle \Phi_i^{J'K}(r, R, \theta, t = 0) | \Phi_i^{J'K}(r, R, \theta, t) \right\rangle
\end{aligned} \tag{26}
$$

2.5. PARTIAL CROSS SECTIONS, PRODUCT STATE DISTRIBUTIONS, AND DIFFERENTIAL CROSS SECTIONS

Equation (22), and its widespread application [1, 3, 50, 11, 34, 43, 49] shows clearly that total absorption cross sections may be computed by propagating an initial wavepacket forward in time. The initial wavepacket is localised in space, therefore, by Heisenberg's uncertainty principle, it necessarily contains a range of relative momenta and kinetic energies. This range of initial energies is reflected in the fact that the use of Eq. (22) immediately yields the cross section over the full range of energies from a single calculation (i.e. based on the motion of a single wavepacket). The autocorrelation function is a time-dependent function. The Fourier transform of a time-dependent function yields an energy, or frequency, dependent quantity, namely, in this case, the total absorption cross section.

It seems reasonable to suppose that some alternative analysis of properties of the same time-dependent wavepacket might also yield more detailed information, such as the partial cross sections or the probability of producing different quantum states of the products. This was realised at a very early stage by Kulander and Heller [2] who discuss the evaluation of partial cross sections by projection onto the final scattering states of the system. Related methods have been developed by Kouri and coworkers [51, 52] in the context of inelastic scattering and were applied to photodissociation problems at an early stage by the groups of Gray [53] and Schinke [54]. In this section, an alternative approach, which is ideally suited for use in conjunction with a grid or Discrete Variable Representation [55] (DVR) of the final scattering coordinate is presented.

Our method relies on drawing an analysis line, perpendicular to the scattering coordinate, at some large asymptotic interfragment separation, $R = R_\infty$, and analysing the wavepacket at each time step as it passes by this line [33, 56]. The analysis consists in expanding the cut through the wavepacket along the analysis line in terms of a linear combination of fragment eigenfunctions. This yields a set of time-dependent coefficients. The half-Fourier transform of these time-dependent coefficients yields energy dependent photofragmentation $\mathbf{T}$ matrix elements in terms of which all the experimentally measurable cross sections may be expressed. The theory is outlined in detail in Appendix C of Ref. [33] (see also Ref. [56]).

The most detailed possible photofragmentation cross section is the detailed final-state resolved differential photofragmentation cross section defined in Eq.

(11) which measures the probability of the formation of a particular final state, v, j, m_j scattered into a specified scattering direction, $\hat{\mathbf{k}} = \theta_k, \phi_k$. This cross section has been discussed in Ref. [39] in the context of time-independent theory of photodissociation. The partial differential cross section may be written as (see Eqs. (13) and Appendix C of Ref. [33]):

$$
\begin{aligned}
\sigma_{vjm_j}(E; \hat{\mathbf{k}}) = \ & \frac{2\pi^2 \nu}{c\,\epsilon_0} \frac{1}{4\pi} \left| \sum_{J=J_i-1}^{J_i+1} \sum_K (2J+1)^{\frac{1}{2}} \right. \\
& \times D^J_{K,M_i+m}(\phi_k, \theta_k, 0) D^j_{-K,-m_j}(\phi_k, \theta_k, 0) \\
& \left. \times \begin{pmatrix} 1 & J_i & J \\ m & M_i & -(m+M_i) \end{pmatrix} T^{JKp'}_{vj} \right|^2 ,
\end{aligned}
$$

(27)

where $T^{JKp'}_{vj}$ is the photofragmentation **T** matrix element and is given by:

$$
T^{JKp'}_{vj} = \sum_{K'} \langle \Phi^{-JvjKp'}_{K'}(r, R, \theta; E) | \Phi^{JK'}_i(r, R, \theta, t=0) \rangle \ .
$$

(28)

Eqs. (27) and (28) have been developed and defined entirely within a time-independent framework. These equations are identical to Eqs. 35 and 32 respectively of Ref. [39]. They differ only in that a different, more appropriate, normalisation has been used here for the continuum wavefunction and that the transition dipole moment function has not been expanded in terms a spherical harmonic basis of angular functions. All the analysis previously given in Ref. [39] continues to be valid. In particular, the details of the angular distributions of the various differential cross sections and the relationships between the various possible integral and differential cross sections have been described in that paper.

The photofragmentation **T** matrix elements in Eq. (28) contain all possible information concerning the dynamics of the photodissociation process. The time-dependent theory needed for the evaluation these matrix elements has bee discussed in Ref. [33] (see Appendix C in particular). The first step is the calculation of a set of time-dependent coefficients. This is done by fixing the scattering coordinate in the time-dependent wavepacket at its value on the analysis line, R_∞, and then multiplying by the fragment eigenfunctions and integrating over all the other coordinates:

$$
C^{JK}_{vj}(t) = \langle \Theta_{jK}(\theta)\chi_{vj}(r) | \left\{ \sum_{K'} \Phi^{JK'}_i(r, R=R_\infty, \theta, t) \right\} \rangle
$$

(29)

where the angular brackets , $\langle \ \rangle$, indicate integration over the variables r and θ and it is implied that $\Theta_{jK}(\theta)$ on the left of the integral must only be associated with the same value of K on the right.
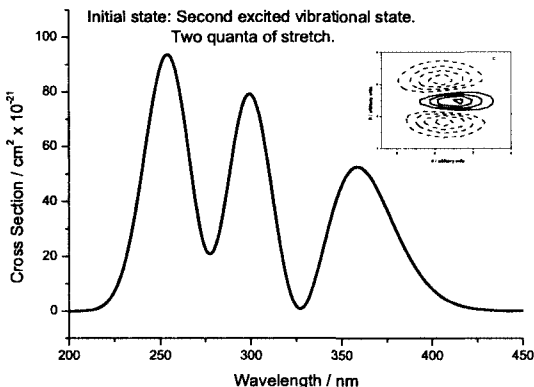
Figure 1.   Ab initio computed photoabsorption cross section for second U.V. absorption band of HOBr ($\tilde{X}^1 A' \to 2^1 A'$) from the v=2 HO–Br stretching mode See Ref. [43].

We now take the half-Fourier transform of this integral over time to give us an energy dependent quantity:

$$A_{vj}^{JK}(E) \quad = \quad \frac{1}{2\pi} \int_{t=0}^{\infty} \exp\left(iEt/\hbar\right) C_{vj}^{JK}(t) \quad .$$

(30)

In Ref. [33], it has been shown that the **T** matrix elements can be obtained from the coefficients of Eq. (30) through the relationship:

$$T_{vj}^{JKp'} \quad = \quad i\,(-1)^{K-j}\,A_{vj}^{JK}(E)\left(\frac{2\pi k_{vj}}{\mu}\right)^{\frac{1}{2}}\left\{\frac{\sqrt{2(1+\delta_{0,K})}}{2}\right\}e^{-ik_{vj}R_{\infty}} \quad . \text{(31)}$$

These equations enable us to compute all the possible photofragmentation cross sections, in particular the partial differential cross section given in Eq. (27) and the partial integral cross section below.

$$\sigma_{vjm_j}(E) \quad = \quad \frac{2\pi^2\nu}{3\,c\,\epsilon_0}\frac{1}{2J_i+1}\sum_{J=J_i-1}^{J_i+1}\sum_{K}\left|T_{vj}^{JKp'}\right|^2 \quad .$$

(32)

2.6. EXAMPLES OF PHOTODISSOCIATION PROCESSES

The absorption cross section for HOBr($\tilde{X}^1 A'$) + hν $\to$ OH + Br via excitation to the $2^1 A'$ state [43] is shown in Figure 1. The three peeks seen in the figure
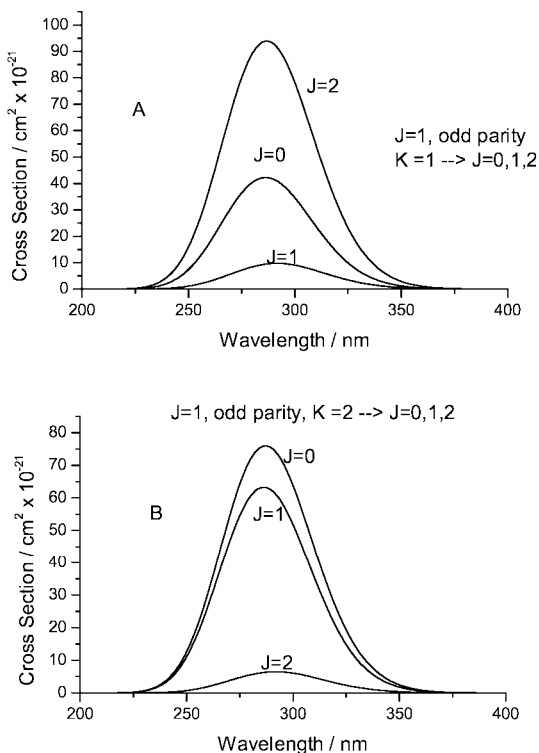
Figure 2.   Contribution of different total angular momenta to the total photodissoci-
ation cross section for the second U.V. absorption band of HOBr ($\tilde{X}^1 A' \rightarrow 2^1 A'$). The
HOBr molecule is initially in its lowest vibrational state with one unit of total angular
momentum and has odd parity. Panel A corresponds to the molecule initially in its lowest
energy state, $K = 1$, and panel B corresponds to the molecule being in the first excited
state, $K = 2$.

arise from the fact that the initial state of the molecule corresponds to an excited
vibrational state, v=2 of the HO–Br stretching motion.

Figure 2 shows the three different final total J contributions to the total ab-
sorption cross section of HOBr($\tilde{X}^1 A' \rightarrow 2^1 A'$) for HOBr initially in two different
K states of its $J = 1$ ground vibrational state [43] (note that K is used merely as
a formal label, it is not a valid quantum number). In a differential cross section
measurement, the amplitudes associated with the different J contributions shown
would interfere and might lead to characteristic angular distribution patterns.

Figure 3 illustrates the F atom branching fraction, $\Gamma = \sigma_{F^*}/[\sigma_{F^*} + \sigma_F]$, where
$F = F(^2P_{3/2})$ and $F^* = F(^2P_{1/2})$, arising from the photodissociation of HF in
its v=3 vibrational state [57]. The characteristic sharp features in the branching
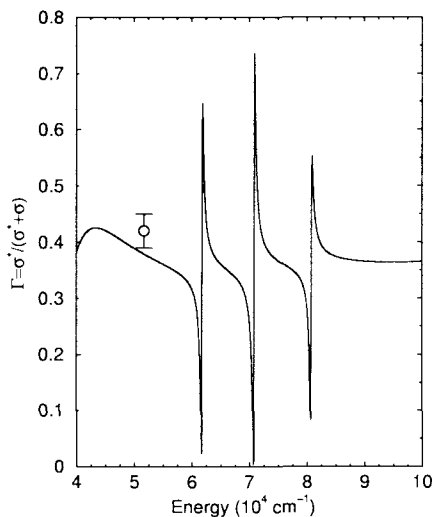
Figure 3. The F atom branching fraction, $\Gamma = \sigma[F(^2P_{1/2})]/[\sigma[F(^2P_{1/2})] + \sigma[F(^2P_{3/2})]]$, as a function of photon energy for photodissociation out of the v = 3 vibrational state for HF. Also, shown is the experimentally measured branching fraction of Wittig and co-workers [61] at 193.3 nm for HF.

fraction graph arise from the nodal structure of the initial vibrational state.

Other examples of wavepacket calculations applied to photofragmentation may be found in Refs. [34], [57] and [58]. Most recently, time-dependent methods have been used to compute vector correlations and alignment parameters [59, 60].

3. Reactive Scattering Theory

The quantum theory of reactive molecular scattering was initially based on time-independent scattering theory [4, 62, 63, 64, 65, 66, 67, 68, 69, 70, 71, 72, 73, 74, 75, 76, 77, 78, 79, 80, 81, 82, 83, 84, 85, 86, 87]. After several early attempts to apply time-dependent quantum theory to reactive scattering processes [88, 89, 90, 91, 92, 93, 94, 95], the modern era of the field really began with the seminal work of Kosloff et al. [5] on the Chebyshev expansion of the time propagation operator and their subsequent application to the reactive scattering problem by Neuhauser and Baer and co workers [96, 13, 97]. There have been many recent developments in the field [98, 99, 48, 103, 100, 102, 101] and several reviews and a book have been written on the topic [104, 105, 106, 107, 33]. The following section will outline the basic methods of time-dependent quantum theory used in reactive scattering calculations.
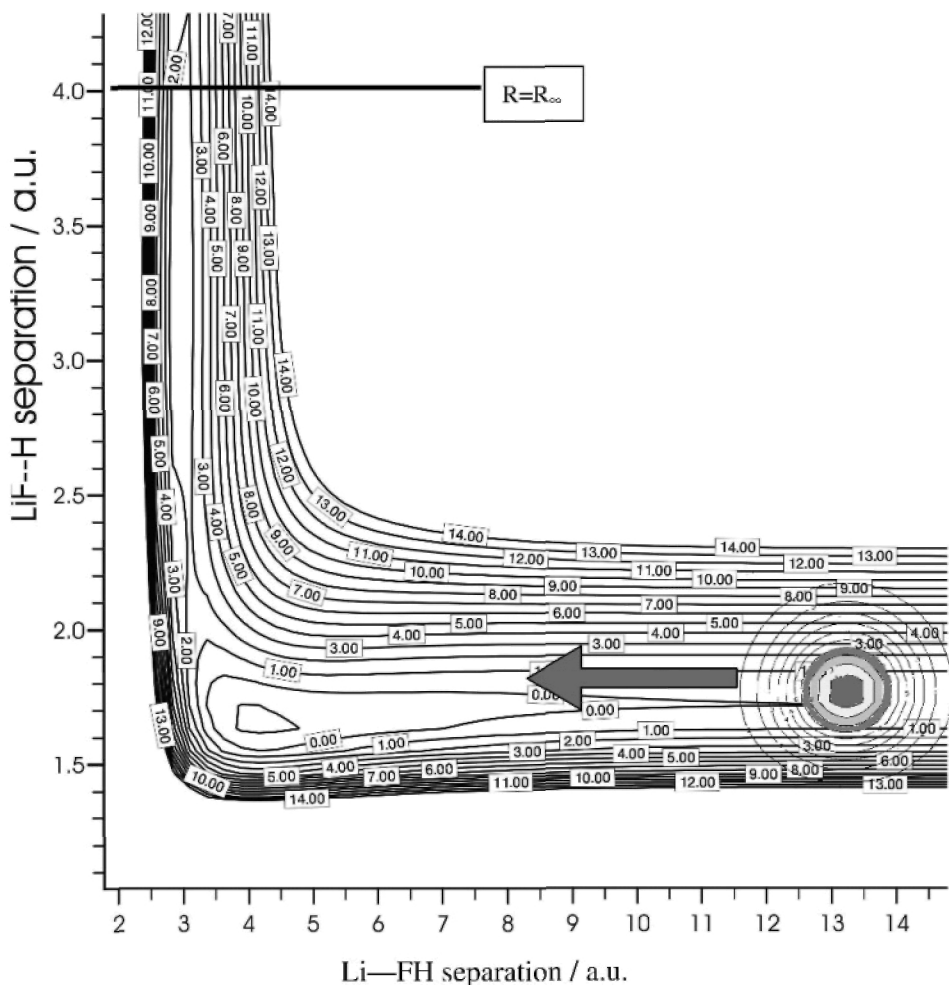
Figure 4. The initial wavepacket superimposed on an Li+HF potential energy surface. Also shown (in a schematic manner) is the analysis line, marked R_∞, in the product channel. In an actual calculation, the analysis line would be placed at a much larger value of the product scattering coordinate.

3.1. THE INITIAL WAVEPACKET

Figure 4 shows an initial wavepacket for a reactive scattering calculation superimposed on a potential energy surface for the Li + HF $\rightarrow$ LiF + H reaction [15, 108]. The initial wavepacket is placed in the asymptotic region of the reactant channel, where there is no force between the reactant molecules. It is constructed by first calculating the desired initial vibrational-rotational eigenfunctions of the reactant

fragments and multiplying the product of these by a one dimensional wavepacket, $g(R)$, where R is the scattering coordinate which is the distance between the centers of mass of the two reactants. This wavepacket is then multiplied by $\exp[-ikR]$ so as to give it a momentum of magnitude $k\hbar$ toward the strong interaction or reactive region. This leads to an initial wavepacket which is intrinsically complex (in the mathematical sense).

The most common form of the one dimensional wavepacket in R is a Gaussian wavepacket [98, 109]. This wavepacket has a Gaussian shape in both coordinate and in momentum space. Recently, we have proposed the use of an alternative form of wavepacket, a sinc wavepacket [110, 111]. In general, we will be interested in computing reactive scattering cross sections over a range of initial collision energies. When the sinc wavepacket is used, the amplitude of the wavepacket is roughly constant over most of the energy range covered by the wavepacket. The Gaussian wavepacket in contrast has a long tail at both high and low energies. This makes it more difficult to determine the energy range covered accurately by the Gaussian wavepacket, as cross sections corresponding to energies associated with a small amplitudes of the initial wavepacket will be subject to greater round-off errors and cannot be considered reliable. In practice, both types of wavepacket may be used and, with care, yield identical results.

3.2. THE ANALYSIS OF THE WAVEPACKET AND COMPUTATION OF INTEGRAL CROSS SECTIONS

One of the key aspects of time-dependent reactive scattering theory arises from the conservation of the total energy. This has the consequence that each energy component of the wavepacket propagates independently. In order to calculate the cross sections, we must therefore know the amplitude of the initial wavepacket with a given energy. Let us denote the initial one dimensional wavepacket by $g(R)$. The component of this wavepacket with momentum component $-k\hbar$ pointed toward the strong interaction or reactive scattering region is:

$$g(-k) = \frac{1}{2\pi} \int_0^\infty e^{ikR} g(R) dR \quad . \tag{33}$$

The analysis of the wavepacket proceeds in exactly the same way as described above for the case of photodissociation theory [108, 15, 98] (see section (2.5)). An analysis line is drawn corresponding to a fixed value of the product Jacobi scattering coordinate R' perpendicularly across the exit channel in the the asymptotic region of the potential energy surface [56, 98]. Specializing the formulae to the case of an atom-diatom reaction, we may write the body-fixed wavepacket as $\Phi^{JK'}(r', \theta', R', t)$, where the primes on the coordinates indicate the use of product Jacobi coordinates and the wavepackets corresponding to the different K' values are coupled by the propagation dynamics (see below). We must first take a cut through the wavepacket along the analysis line and project this onto the product vibrational-rotational eigenfunctions. In this way, we obtain a time-dependent

coefficient, $C_{v'j'}^{JK'}(t)$:

$$C_{v'j'}^{JK'}(t) = \langle \Theta_{j'K'}(\theta') \chi_{v'j'}(r') | \Phi^{JK'}(r', \theta', R' = R'_\infty, t) \rangle \quad . \tag{34}$$

We then take the half-Fourier transform of this to obtain an energy dependent quantity, $A_{v'j'}^{JK'}(E)$:

$$A_{v'j'}^{JK'}(E) = \frac{1}{2\pi} \int_0^\infty \exp(iEt/\hbar) \, C_{v'j'}^{JK'}(t) dt \quad . \tag{35}$$

The analysis of Ref. [56] (see also Ref. [98]) enables us to relate this to the reactive **S** matrix elements through the expression:

$$S_{v'j'K',vjK}^J(E) = - \left(\frac{\hbar^2 k_{vj} k'_{v'j'}}{\mu\mu'} \right)^{\frac{1}{2}} \exp(-ik'_{v'j'} R'_\infty) \frac{A_{v'j'}^{JK'}(E)}{g(-k_{vj})} \quad , \tag{36}$$

where the primed variables indicate quantities relating to the products and the unprimed to the reactants. Note the presence of the term $g(-k_{vj})$ in the denominator and the fact that the quantum numbers K and K' are associated with the z components of the total angular momentum referred to body-fixed reactant and product axes, respectively. We have purposely included here the initial state quantum numbers, vjK, which relate to the construction of the initial wavepacket as they will be needed later when we discuss the calculation of differential cross sections.

The total reaction probability for a particular value of the total angular momentum, J, , averaged over all values of m_j and M for the reactants and summed over all values of $m_{j'}$ and M' for the products, is given by:

$$P_{react}^J(E) = \frac{1}{2j+1} \sum_{v'j'} \sum_{KK'} \left| S_{v'j'K',vjK}^J(E) \right|^2 \quad . \tag{37}$$

The total integral reactive cross section for reaction from a particular initial state to all possible final states is then given by a summation over all total angular momenta which can contribute to the reaction:

$$\sigma_{all \leftarrow vj}^{tot} = \frac{\pi}{k_{vj}^2} \sum_J (2J+1) P_{react}^J(E) \quad . \tag{38}$$

3.2.1. *Reactant coordinate calculations for the total reactive cross sections*

Calculation of the total reactive cross section does not necessarily require a knowledge of the wavepacket dynamics in the exit channel of the reaction. All that is required is a knowledge of the particle flux which results in the creation of products. This can be accomplished by calculating the flux of particles passing through a plane corresponding to a large constant value of the reactant diatom separation

[114, 112, 113]. This allows us to use reactant coordinates instead of product coordinates and often greatly simplifies the calculation. It also permits the use of the helicity decoupling or centrifugal sudden approximation [112, 113], in which we ignore the coupling between different K components corresponding to a single J value (see below for further details). This important simplifying approximation is much more difficult to justify when there is a transformation from reactant to product coordinates [48].

3.2.2. *Capture model and total reactive cross sections*

The problem with Eqs. (37) and (38) is that they require the exact calculation of the scattering dynamics and the **S** matrix elements for many values of J. The computational effort required for exact $J > 0$ calculations is very great. For $J > 0$, $|K|$ takes on either $(J + 1)$ or J values depending on the parity. The wavepackets corresponding to each of these K values will be coupled by the propagation dynamics of the wavepacket. In general, quite large values of J are important for the calculation of the total reactive cross section. Thus in the case of $O(^1D) + H_2$, J values up to between 40 and 66 were required [109, 112, 113] while for heavier collision partners much higher values of J are needed [115]. The precise range of J values required depends of course on the range of collision energies covered by the calculations, but, clearly for $J > 0$, calculations are far more computationally demanding than for $J = 0$.

The calculation of total reaction cross sections may be greatly simplified by using any one of a family of approximations known as J-shifting approximations [118, 119]. In this type of approximation, the reaction probability is calculated for a limited number of J values, or even just for $J = 0$, and approximate methods are used to estimate the reaction probability for other required values of J from those for which more accurate calculations have been performed. J-shifting approximations rely on the identification of a "bottleneck" geometry, such as a transition state. The changes in rotational energy of the system, when fixed at this geometry, provide an energy shift, E_{shift}, which is used in estimating the reaction probabilities:

$$\tilde{P}^J_{react}(E) = P^{J=0}_{react}(E - E^J_{shift}) \quad , \tag{39}$$

where $P^{J=0}_{react}(E)$ is the accurately computed reaction probability for $J = 0$, at the total energy E, and $\tilde{P}^J_{react}(E)$ is the estimated reaction probability for another value of J.

The J-shifting method depends upon our ability to identify a unique bottleneck geometry and is particularly well suited to reactions which have a barrier in the entrance channel. For cases where there is no barrier to reaction in the potential energy surface, a capture model [112, 113, 115] approach has been developed. In this approach, the energy of the centrifugal barrier in an effective one-dimensional potential is used to define the energy shift needed in Eq. (39). For the case of $K = 0$, we define the one-dimensional effective potential as (see Ref. [113] for the

case of $|K| > 0$) :

$$V_{eff}^J(R) = \langle vj|V|vj\rangle - \epsilon_{vj} + \frac{\hbar^2 J(J+1)}{2\mu R^2} \quad , \tag{40}$$

where $\langle vj|V|vj\rangle$ is the potential averaged over the initial vibrational-rotational state of the reactants and is a function of the reactant scattering Jacobi coordinate. ϵ_{vj} is the vibrational-rotational energy of the initial state of the diatomic. The effective potential exhibits a centrifugal barrier in the entrance channel. Let V^{J*} be the height of the effective potential barrier corresponding to a total angular momentum quantum number J. In the capture model, the reaction probability is now estimated as:

$$\tilde{P}_{react}^J(E) = P_{react}^{J=0}(E - V^{J*}) \quad . \tag{41}$$

Both in the J-shifting model and in the capture model, it is assumed that the reaction probabilities are a function of the available energy, which is the energy in excess of the barrier height. This function of the excess energy is assumed to be universal (i.e., the same for all J values). One can then take the results for some particular J values and use them to define how reaction probability varies as a function of the excess energy.

Rather than using just calculations for $J = 0$ as a basis for approximating reaction probabilities for all higher values of J, we have adopted the technique of calculating reaction probabilities for a reasonably large number of J values, in general using the helicity decoupling approximation [112, 116, 117], and using capture model techniques to interpolate between the J values for which more accurately computed reaction probabilities are available. Suppose that we have calculated the reaction probability for J_1 and J_2 and that J lies between these two J values ($J_1 < J < J_2$). Then the reaction probability for J can be estimated as:

$$\begin{aligned}
\tilde{P}_{react}^J(E) &= P_{react}^{J_1}\left(E - [V^{J*} - V^{J_1*}]\right)\frac{(J_2 - J)}{(J_2 - J_1)} \\
&\quad + P_{react}^{J_2}\left(E + [V^{J_2*} - V^{J*}]\right)\frac{(J - J_1)}{(J_2 - J_1)} \quad .
\end{aligned} \tag{42}$$

For values of J greater than any for which actual dynamical calculations have been performed, the reaction probability may be extrapolated from that calculated for this highest value using the formula:

$$\tilde{P}_{react}^J(E) = P_{react}^{J_1}\left(E - [V^{J*} - V^{J_1*}]\right) \quad . \tag{43}$$

where, in this case, J_1 is the highest value of J for which helicity decoupled wavepacket calculations were carried out.

3.2.3. *Backward propagation method*
The theory used to analyse the wavepacket and to determine the reaction probability requires that the initial wavepacket be placed in the asymptotic region, where

there is very little interaction between the reactants [98, 114]. This is because we require knowledge of the amplitude of the initial wavepacket associated with a given relative translational energy in this asymptotic region. For large values of the total angular momentum, the centrifugal potential is very long ranged and, in practice, it is impossible to place the initial wavepacket at sufficiently large separations so as to render the centrifugal potential unimportant. In order to overcome this problem and also to overcome problems arising from the intrinsically long range nature of the potential energy surfaces, we place the initial wavepacket at a large but manageable separation of the reactants and after calculating an effective potential, as in Eq. (40), we propagate the R dependent part of the initial wavepacket (i.e., $g(R)$ as discussed in Eq. (33) see section (3.1)) backward in one dimension. We then analyse the backwards-propagated wavepacket and use the resulting momentum distribution in the analysis of the final wavepacket to yield the total reaction probability [98, 113, 115].

3.2.4. Differential reactive cross sections
The differential reactive state-to-state cross section may be written in the form [66, 120, 4, 68]:

$$\sigma_{v',j'\leftarrow v,j}(E,\theta) = \frac{1}{2j+1} \sum_{KK'} \frac{1}{4\,k_{vj}^2} \left| \sum_J (2J+1)\, S_{v'j'K',vjK}^J(E)\, d_{KK'}^J(\theta) \right|^2 . \quad (44)$$

As we have given an explicit expression for the **S** matrix in Eq. (36), there would seem to be no problem in calculating the reactive differential cross section. This is however not entirely true. The problem arises because the definition of the cross section relates to the large R asymptotic form of the wavefunction. Furthermore, the method we use for the analysis of the wavepacket relies on an analysis line, R_∞, drawn in the asymptotic region of the potential. The problem arises, as indicated in the preceding section (3.2.3), for larger values of the total angular momentum J. In such cases, the centrifugal potential and the centrifugal coupling terms are very long ranged. The long-range nature of these terms is a result of using the body-fixed coordinate system rather than the space-fixed one [39] and it is essential to transform back to the space-fixed system as part of the process of calculating the **S** matrix elements. This was clearly recognised in the recent reactive wavepacket scattering calculations of Althorpe [101, 121, 122] and the discussion below borrows heavily from this work and from the Ph.D. thesis of M. Hankel [123].

In the space-fixed axis system, the channel quantum numbers for an atom-diatom collision are jl, where j refers to the rotational quantum number of the diatomic and l is the quantum number for the orbital angular momentum of the relative motion of the two fragments. We have ignored the vibrational quantum number for the purposes of this discussion. The part of the Hamiltonian with the longest range, when working in this axis system is the effective centrifugal repulsion term $(\hbar^2 l(l+1))/(2\mu R^2)$. There is no kinetic energy coupling between the different jl channels and the long range part of the effective centrifugal repulsion is fully

accounted for analytically through the use of the spherical Bessel functions and their analytic behaviour in the asymptotically large R region [124, 4]. In contrast, as we will discuss more explicitly in the next section, the channels are labeled with the quantum numbers jK when body-fixed axes are used, K being the z component of the total angular momentum with respect to the body-fixed z axis. Rotation to the body-fixed axes simplifies the coupling arising from the potential energy term, but it creates new couplings in the kinetic energy term [4, 39]. Thus, there are couplings between different K quantum numbers when the Hamiltonian is expressed in the body-fixed axes. These couplings are, furthermore, very long ranged and there is no satisfactory means of including them analytically in the scattering formulation [39].

The solution to this problem is to transform, or half transform, the **S** matrix from the body-fixed to the space-fixed axis system; then to use the known analytic properties of the spherical Bessel functions, which are the solutions to the potential-free scattering problem in the space-fixed axes; and finally to transform back to the body-fixed axes and then to use Eq. (44) to calculate the differential cross section.

For a given value of J and the parity, p, the first step is to calculate the transformation matrix from the body-fixed jK basis to the space-fixed jl basis. This transformation matrix has been derived in Eq. (A17) of appendix A in Ref. [33]. Alternatively, the transformation matrix may be computed by using the matrix elements of the kinetic energy operator in the body-fixed axis system. These are just the diagonal and off-diagonal elements of the centrifugal coupling (see Ref. [39]). If we then diagonalise this matrix, the eigenvectors of this matrix form the desired transformation matrix from the body-fixed to the space-fixed basis [125]. We denote this transformation matrix by T_{lK}^{Jp}, where p denotes the parity, $(-1)^{J+K+p} = (-1)^{j+l}$. The **S** matrix in the space-fixed axes may then be written as:

$$
\begin{aligned}
S_{v'j'l',vjl}^{Jp}(E) &= \sum_{KK'} T_{l'K'}^{Jp} S_{v'j'K',vjK}^{J}(E) T_{lK}^{Jp} \\
&= -i^{l-l'} \left(\frac{\hbar^2 k_{vj} k_{v'j'}'}{\mu\mu'} \right)^{\frac{1}{2}} \frac{\exp(-ik_{v'j'}' R_\infty')}{g(-k_{vj})} \\
&\quad \times \left\{ \sum_{KK'} T_{l'K'}^{Jp} A_{v'j'K}^{JK'p}(E) T_{lK}^{Jp} \right\} ,
\end{aligned}
\tag{45}
$$

where the extra phase factor of $i^{l-l'}$ is discussed below.

As the kinetic energy operator has no off-diagonal elements in the space-fixed axis representation, we may more easily correct for the fact that the analysis line is not truly in the asymptotic region as far as the centrifugal representation is concerned. We do this firstly by subtracting the residual centrifugal repulsion, $l'(l'+1)/(2\mu'R'^2)$, from the radial kinetic energy at the analysis line in the product

channel. Thus we use the expression:

$$k_{v'j'} = \sqrt{2\,\mu'\left(E - \left(\varepsilon_{v'j'} + \frac{l'(l'+1)}{2\,\mu' R_\infty'^2}\right)\right)} \quad , \qquad (46)$$

to calculate the wavenumber of the products at the analysis line, which we use in evaluating the **S** matrix elements in Eq. (45).

The analysis underlying the evaluation of the **S** matrix elements was formulated for the $J = 0$ (and $l = 0$) case [56] and did not take proper account of the correct asymptotic phases of the spherical Bessel functions [124]. This phase should have been $\exp(-i(k_{v'j'}'R_\infty' - l'\pi/2)$ rather than the phase given in Eq. (45) above. To correct for this omission in both the reactant and product channels we must multiply by a phase of $\exp(-il'\pi/2) = i^{-l'}$ for the products and i^l for the reactants. These factors are included on the right hand side of Eq. (45).

After making these adjustments to allow for the fact that the analysis line cannot be located in the region of space where the centrifugal coupling in the body-fixed coordinates is negligible and also for the fact that the analysis of Ref. [56] did not take account of the long-range analytic form of the spherical Bessel functions, the space-fixed **S** matrix of Eq. (45) must be transformed back to the body-fixed axes and Eq. (44) used to compute the state-to-state differential cross sections [101, 123].

3.3. THE GRID AND THE ABSORBING POTENTIAL

In both photodissociation and reactive scattering theory, the wavepacket is eventually propagated to large values of the scattering coordinate. As we are forced to use finite sized grids for numerical reasons, the problem arises as to what is to be done with the wavepacket when it approaches the edge of the grid. If Fourier transforms are used to compute the action of the radial derivatives in the Hamiltonian operator, then serious errors will arise if the wavepacket is allowed to reach the edge of the grid. This arises from the fact that the Fourier transform method implicitly assumes a cyclic boundary condition and, if the function is non-zero at the grid edge, then it will be reflected to the opposite side of the grid causing well documented "aliasing" problems [126]. It is therefore imperative that something should be done to prevent the wavefunction reaching the grid edge.

Arbitrarily setting the wavepacket to zero at some large value of the scattering coordinate is not an acceptable solution, because this would cause reflection waves which would impact on the wavepacket in the physically important inner region of coordinate space. Therefore the crucial criteria for handling this problem is that any alteration of the wavepacket must be sufficiently gentle so as not to change the computed values of the physical observables of interest. But at the same time no part of the wavepacket must be allowed to reach the edge of the grid.

There are two general methods for addressing this problem. The first is the "gobbler" method. This involves multiplying the part of the wavepacket near the

edges of the grid, at each time step, by a positive function which is smaller than unity and which will generally decrease toward grid edge [16, 53, 11, 127, 128]. The other is the "negative imaginary potential" (NIP) method, in which a negative imaginary potential, which is non-zero only in an absorbing region close to the grid edge, is added to the potential. This method has a long tradition within scattering theory and was previously known as the "optical potential" method [129, 130]. It has been popularised within the context of time-dependent and time-independent scattering theory through the work of Neuhauser and Baer [131, 132]. Several papers have been written suggesting optimal forms and parameterisations for the NIPs [133, 134, 8, 30, 96, 135, 136, 137] and discussing the effectiveness of different functional forms of the negative imaginary potentials [136, 138].

In general, we use a complex absorbing potential of the form:

$$
V_{damp}(R) = \begin{cases} 0.0 & ; R < R_{damp} \\ -iA_{damp}\left(\frac{R - R_{damp}}{R_{max} - R_{damp}}\right)^{n_{damp}} & ; R_{damp} \leq R \leq R_{max} \end{cases} \tag{47}
$$

where n_{damp} is set equal to 2 or 3, and we choose the parameters A_{damp} and R_{damp} in accordance with the recommendations given in Refs. [136] and [137].

There have also been attempts to find optimal complex (as opposed to purely imaginary) absorbing potentials [139, 140, 141] and to relate these to the gobbler method [142]. Most recently Manolopoulos [143] has proposed a very interesting simple potential of this type which guarantees zero transmission of the wavepacket. The main practical problem with absorbing potentials is that it is very difficult to find appropriate potentials which can absorb a component of a wavepacket with a low translational energy, and therefore a long wavelength. This is at present the major challenge to the wavepacket theory of reactive scattering (see however Ref. [108] where stable threshold reactive scattering probabilities were successfully computed).

3.4. THE REAL WAVEPACKET METHOD

The initial wavepacket, described in section (3.1), above is intrinsically complex (in the mathematical sense). Furthermore, the solution of the time-dependent Schrödinger equation (Eq. (20)) also involves an intrinsically complex time evolution operator, $\exp{(-i\hat{\mathbf{H}}t/\hbar)}$. It therefore seems reasonable to assume that all the numerical operations involved with generating and analysing the time-dependent wavefunction will involve complex arithmetic. It therefore comes as a surprise to realise that this is in fact not the case and that nearly all aspects of the calculation can be performed using entirely real wavefunctions and real arithmetic. The theory of the *real wavepacket method* described in this section has been developed by S.K. Gray and one of the authors (GGBK) [98].

Consider the propagation of a wavepacket forward in time, from time t to $(t+\tau)$

(see Eq. (20)):

$$
\begin{aligned}
\Phi(t+\tau) &= \exp\left[\frac{-i\hat{\mathbf{H}}\tau}{\hbar}\right]\Phi(t) \\
&= \cos\left[\frac{\hat{\mathbf{H}}\tau}{\hbar}\right]\Phi(t) - i\,\sin\left[\frac{\hat{\mathbf{H}}\tau}{\hbar}\right]\Phi(t) \quad .
\end{aligned}
\tag{48}
$$

The corresponding expression for the backward propagation, from t to $t - \tau$ is:

$$
\Phi(t-\tau) = \cos\left[\frac{\hat{\mathbf{H}}\tau}{\hbar}\right]\Phi(t) + i\,\sin\left[\frac{\hat{\mathbf{H}}\tau}{\hbar}\right]\Phi(t) \quad .
\tag{49}
$$

By adding Eqs. (48) and (49) we obtain:

$$
\Phi(t+\tau) = -\Phi(t-\tau) + 2\cos\left[\frac{\hat{\mathbf{H}}\tau}{\hbar}\right]\Phi(t) \quad .
\tag{50}
$$

This equation is exact and constitutes an iterative equation equivalent to the time-dependent Schrödinger equation [144, 145]. The iterative process itself does not involve the imaginary number i and therefore, if $\Phi(t)$ and $\Phi(t - \tau)$ were the real parts of the wavepacket then $\Phi(t + \tau)$ would also be real and would be the real part of the exact wavepacket at time $(t + \tau)$. Therefore if $\Phi(t)$ is complex, then we can use Eq. (50) to propagate the real part of $\Phi(t)$ forward in time without reference to the imaginary part.

In Ref. [98], we show that all the observable cross sections and reaction probabilities may be obtained from an analysis of the real part of the wavepacket, without any reference to the imaginary part. The analysis itself is identical to that described in section (3.2) but when the real part of the wavepacket is used to compute $A_{v'j'}^{JK'}(E)$ in Eq. (36) we must multiply by an extra factor of 2.

The iterative relationship in Eq. (50) is still very difficult to apply, just as much so in fact as the original form of the evolution operator (Eq. (20)). The relationship can be dramatically simplified by applying a functional mapping of the Hamiltonian. The presence of the cosine term in Eq. (50) suggests an inverse cosine type mapping. If such a mapping is to be used, it is necessary to ensure that it is single valued. So the next step is to shift and scale the Hamiltonian operator in exactly the same way as in the Chebyshev expansion of the evolution operator [5, 41, 98]. This shifting and scaling ensures that the spectrum (or eigenvalues) of the Hamiltonian falls entirely within the range (-1,1). The shifted and scaled Hamiltonian, $\hat{\mathbf{H}}_s$, is then subject to the following mapping:

$$
f(\hat{\mathbf{H}}_s) = -\frac{\hbar}{\tau}\cos^{-1}(\hat{\mathbf{H}}_s) \quad .
\tag{51}
$$

The use of this mapping means that we are no longer solving the time-dependent Schrödinger equation, but rather a modified equation of the form:

$$i\hbar\frac{\partial\Phi_f(t)}{\partial t} = f(\hat{\mathbf{H}}_s)\,\Phi_f(t) \quad, \tag{52}$$

where a subscript "f" has been placed on the wavefunction to emphasize that it is the solution of a mapped equation rather than of the original time-dependent Schrödinger equation. The same arguments which led to the iterative equation, Eq. (50), now lead to the simplified form:

$$\Phi_f(t+\tau) \quad = \quad -\Phi(t-\tau) + 2\,\hat{\mathbf{H}}_{\mathbf{s}}\Phi_f(t) \quad . \tag{53}$$

In Ref. [98] we show that analysis of the real part of $\Phi_f(t)$, the solution of the mapped Schrödinger equation, can yield all the observable cross sections. Furthermore, we show that the arbitrary time-step, τ, cancels out in all expressions for the cross sections and can effectively be set to unity, i.e., $\tau = 1$.

In order to carry out the iteration process in Eq. (53), we need the wavepacket at two previous iterations (i.e., at $t - \tau$ and at t). If the initial wavepacket is taken to be $\Phi(t - \tau)$, the mapped version of Eq. (48),

$$\Phi(t) \quad = \quad \hat{\mathbf{H}}\Phi(t-\tau) - i\,\sqrt{1-\hat{\mathbf{H}}^2}\,\Phi(t-\tau) \quad, \tag{54}$$

can be used to find $\Phi(t)$, where the operator $\sqrt{1-\hat{\mathbf{H}}^2}$ is evaluated using a Chebyshev expansion [146]:

$$\sqrt{1-\hat{\mathbf{H}}^2} = \frac{2}{\pi}\left[1 - 2\sum_{s=1}^{s_{max}}\left(4s^2-1\right)^{-1}T_{2s}(\hat{\mathbf{H}})\right] \quad, \tag{55}$$

where $T_{2s}(x)$ is a Chebyshev polynomial of the first kind.

Taken together, the use of the real part of the wavepacket and the mapping of the time-dependent Schrödinger equation, lead to a very significant reduction of the computational work needed to accomplish the calculation of reactive cross sections using wavepacket techniques. To summarize, a real wavepacket calculation proceeds as follows:

1) Define an initial complex wavepacket, $\Phi^{JK'}(r',\theta',R',t=0)$, as described in section (3.1).

2) Use Eq. (54) to obtain the complete wavepacket after the first iteration at $t = \tau$, $\Phi^{JK'}(r',\theta',R',t=\tau)$.

3) Use Eq. (50) to propagate the real part of $\Phi^{JK'}(r',\theta',R',t)$ forward in time, for D + H_2 1,000 to 1,500 iterations are required [98] while for a system such as N + O_2 about 40,000 iterations are required [115].

4) The analysis proceeds as in section 3.2, except that iteration numbers are used

in performing a discrete Fourier transform rather than a trapezoid rule integration over time.

Similar techniques to those described in this section and in Ref. [98], but used within a time-independent framework, have been developed by Kouri and co-workers [147, 148] and by Mandelshtam and Taylor [149, 150]. Kroes and Neuhauser [151, 152, 153, 154] have used the methods developed in these papers to perform time-independent wavepacket calculations using only real arithmetic. The iterative equation which lies at the heart of the real wavepacket method, Eq. (50), is in fact just the Chebyshev recursion relationship [146]. This was realised by Guo who developed similar techniques based on Chebyshev iterations [18, 19, 155, 156, 157, 158, 159, 160].

3.5. EXAMPLES

Figures 5A and 5B present the total reactive cross section for reaction $N(^2D) + O_2(X^3\Sigma_g^-) \to O(^3P) + NO(X^2\Pi)$ as a function of the initial relative translational energy [115] on its two lowest adiabatic surfaces ($2^2A'$ and $1^2A''$). The O_2 reactant is in its ground vib-rotational state in both cases. The cross sections have been calculated using the real wavepacket [98] and the capture model approaches [112]. Figure 5A shows the total reactive cross section on the $2^2A'$ surface.

The reactive cross section is seen to increase smoothly with relative translational energy and reaches a constant value at an energy of around 0.4 eV. The cross section has a very small non-zero value at zero relative translational energy. This arises from a small tunneling contribution to the reaction probability [115]. Except for this, the cross section shows the typical behaviour for a reaction with an energy barrier along the minimum energy path (MEP) between reactants and products. Also shown in the figure are the values of the cross section at different energies evaluated by the quasiclassical trajectory method for $O_2(v = 0, j = 0)$ using the TRIQCT program [161]. The agreement between the QCT and the wavepacket calculations is quite satisfactory in this case showing that, except perhaps in the vicinity of the threshold energy, there are no large quantum effects for this reaction.

Figures 6 to 8 are concerned with the reaction $O(^1D) + H_2 \to OH + H$ on its lowest three potential energy surfaces ($1^1A'$, $2^1A''$ and $2^1A'$) [113]. Figure 6 shows the $J = 0$ reaction probabilities as a function of the total energy for dynamics started initially on each of these surfaces. The reaction probability for the $1^1A'$ rises sharply immediately above the threshold, i.e., the energy of the ground state reactants. This is typical of a reaction without any barrier. The probability for the $2^1A''$ is initially zero and rises more gradually starting at a higher energy. This surface has a barrier of 0.1 eV and the form of the reaction probability is typical of a reaction with a barrier. The most interesting curve is that for the $2^1A'$. This surface also has a barrier of 0.1 eV, but displays a small rise in probability immediately above the zero kinetic energy threshold. This important small peak in the reaction probability arises entirely from electronically nonadiabatic transitions from the $2^1A'$ to the $1^1A'$ surface.
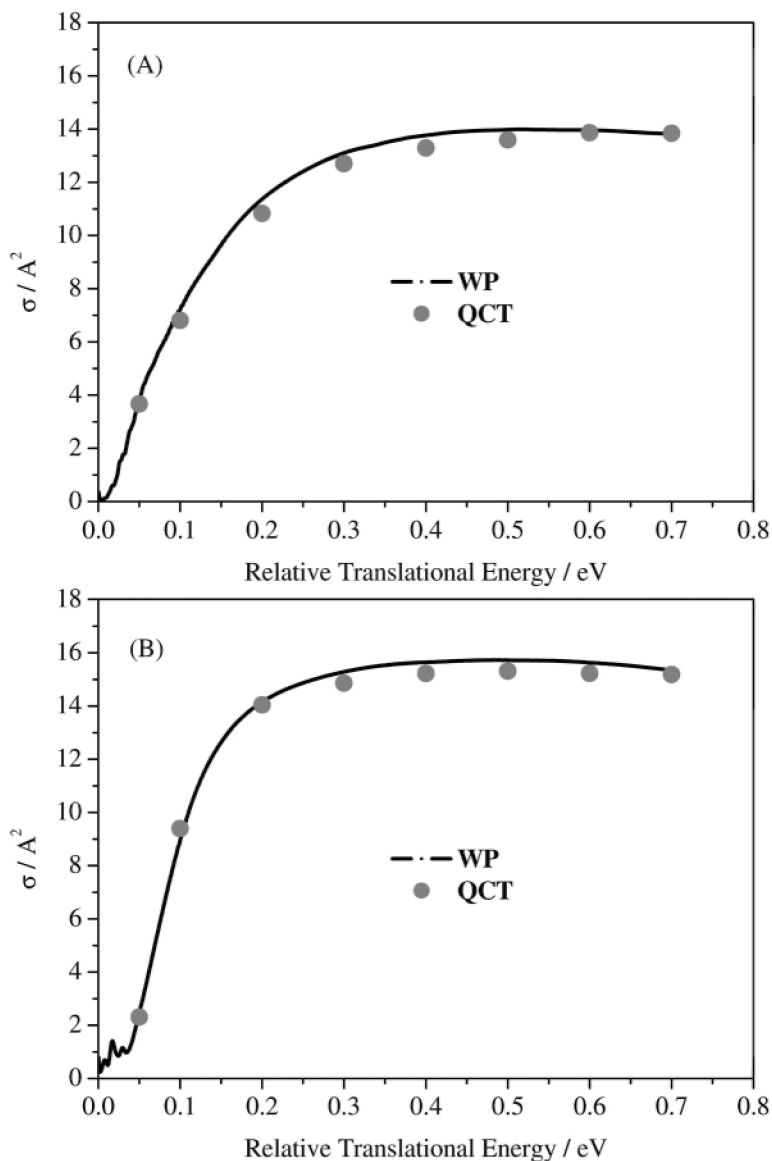
Figure 5.   Total reactive cross section, calculated using the quantum wavepacket method, for the reaction $N(^2D) + O_2(X^3\Sigma_g^-) \rightarrow O(^3P) + NO(X^2\Pi)$. The initial vibrational-rotational state of the O_2 reactant is v=0, j=0. The cross sections correspond to calculations on the two lowest adiabatic potential energy surfaces and are plotted as a function of the relative translational energy E_{trans}: (A) 2^2A PES and (B) $1^2A''$ PES. Also shown are quasiclassical trajectory results (shaded circles) (published with permission, see Ref. [115]).
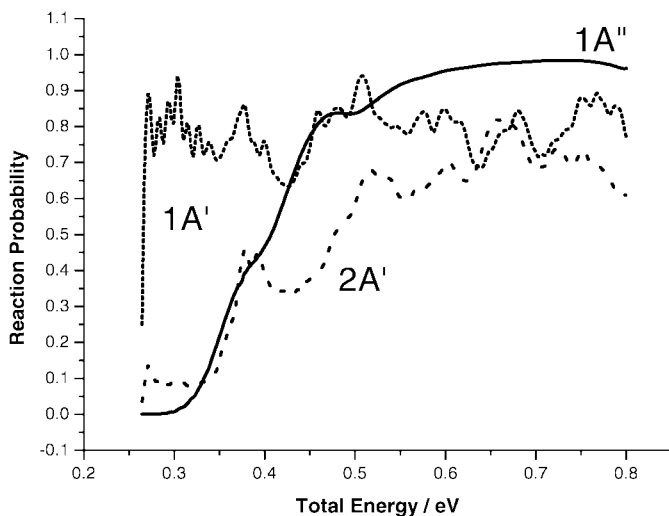
Figure 6. J=0 reaction probabilities for the reaction $O(^1D) + H_2 \rightarrow OH + H$ as a function of total energy starting on its three lowest three potential energy surfaces ($1^1A'$, $2^1A''$ and $2^1A'$) [113].
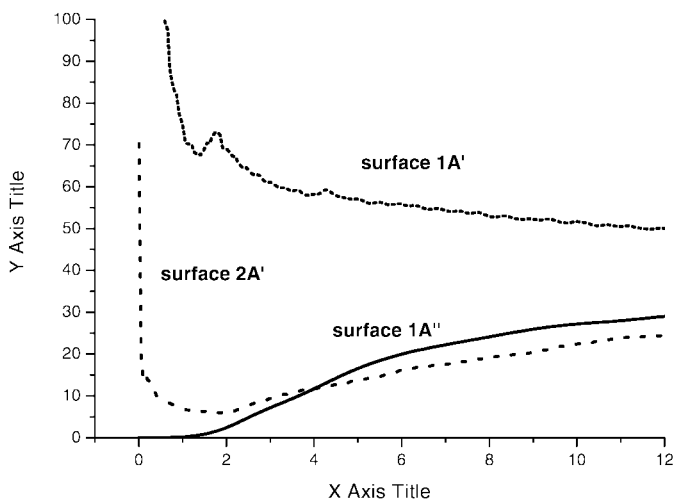
Figure 7. Reactive cross sections for the reaction $O(^1D) + H_2 \rightarrow OH + H$ as a function of total energy starting on its three lowest three potential energy surfaces ($1^1A'$, $2^1A''$ and $2^1A'$) [113].
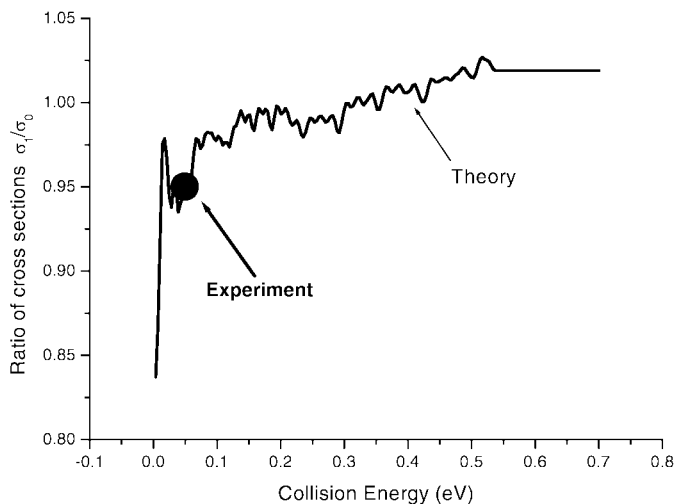
Figure 8. Ratio of cross sections for the reactions $O(^1D) + H_2(v = 0, j = 1) \rightarrow OH + H$ ($\sigma = 1$) and $O(^1D) + H_2(v = 0, j = 0) \rightarrow OH + H$ ($\sigma = 0$) as a function of collision energy.

Figure 7 shows the computed total reactive cross sections for reaction on the same potential energy surfaces as were used to compute the $J = 0$ reaction probabilities shown in figure 6. We see that reaction on the $1^1A'$ and $2^1A'$ surfaces both give cross sections which are extremely large just above the zero kinetic energy threshold. The explanation for this situation is found in Eq. 38, from which we see that if the reaction probability is non-zero when $k_{vj} = 0$ then the cross section will be infinite. We have already discussed, in connection with Fig. 6, the fact that the reaction probability is non-zero very close to threshold for reactions started on both the $1^1A'$ and $2^1A'$ surfaces.

Figure 8 shows the excellent agreement [113] achieved between theory and experiment for the ratio of cross sections for the two reactions $O(^1D) + H_2(v = 0, j = 1) \rightarrow OH + H$ ($\sigma = 1$) and $O(^1D) + H_2(v = 0, j = 0) \rightarrow OH + H$ ($\sigma = 0$). We note that similar values for this ratio have been reported by S-H Lee and K. Liu [162], but at only very slightly higher energies (0.174 eV). Their experiments show a σ_1/σ_0 ratio of 1.4, which is well above that predicted by our quantum mechanical wavepacket calculations.

4. Conclusions

This chapter has discussed some of the methods underlying the use of wavepackets in molecular dynamics. This field, which was initially popularised through

the work of Heller [1, 2, 3], has now reached maturity and is probably now the main technique used in the quantum theory of photodissociation and reactive scattering. The chapter has focused on some of the basic aspects of time-dependent wavepacket theory. To make the discussion more specific, we have concentrated on the photodissociation of triatomic molecules and on atom-diatom reactive scattering collisions. Many aspects of the theory discussed within this context apply quite generally also to larger systems.

Time independent and time-dependent theory are not really separate disciplines. This should be clear from the work of Kouri [147, 148] and Althorpe [101, 121] who use time-independent wavepacket techniques. These are easily derived from the more natural time-dependent versions by Fourier transforming the propagator over time. This is is equivalent to transforming from the time to the energy domain at the beginning of the calculation rather than at the end.

The first part of the chapter deals with aspects of photodissociation theory and the second with reactive scattering theory. Key topics covered in the chapter are the analysis of the wavepacket in the exit channel to yield product quantum state distributions, photofragmentation $\mathbf{T}$ matrix elements, state-to-state $\mathbf{S}$ matrices and the real wavepacket method, which we have applied only to reactive scattering calculations.

Perhaps the most problematic area for the wavepacket theory of reactive scattering is the treatment of the reactive scattering probabilities close to the threshold, where the wavelength of the relative translational motion of the products is extremely large and it is very difficult to absorb the wavepacket near the edge of the grid. This problem is providing a strong motivation for developing improved absorbing potentials [143].

Acknowledgements

References

1. Heller, E.J. (1978) Quantum corrections to clasical photodissociation models, *J. Chem. Phys.* **68**, 2066-2075.
2. Kulander, K.C. and Heller, E.J. (1978) Time-dependent formulation of polyatomic photofragmentation: Application to H_3^+, *J. Chem. Phys.* **69**, 2439-2449.
3. Heller, E.J. (1981) A semiclassical way to molecular spectroscopy, *Acc. Chem. Res.* **14**, 368-375.
4. Balint-Kurti, G.G. (1975) The theory of rotationally inelastic collisions, in A.D. Buckingham and C.A. Coulson (eds.), *International Review of Science, Series II, Vol 1*, Butterworths, London, pp.286-326.

5. R. Kosloff, R. (1988) Time-dependent quantum-mechanical methods for molecular dynamics, *J. Phys. Chem.* **92**, 2087-2100.

6. Kosloff, D. and Kosloff, R. (1983) A Fourier method solution for the time-dependent Schrödinger equation as a tool in molecular-dynamics, *J. Comput. Phys.* **52**, 35-53.

7. Tal-Ezer, H. and Kosloff, R. (1984) An accurate and efficient scheme for propagating the time-dependent Schrödinger equation, *J. Chem. Phys.* **81**, 3967-3971.

8. Kosloff, R. and Kosloff, D. (1986) Absorbing boundaries for wave-propagation problems, *J. Comput. Phys.* **63**, 363-376.

9. Imre, D., Kinsey, J.L., Sinha, A., and Krenos, J. (1984) Chemical dynamics studied by emission spectroscopy of dissociating molecules, *J. Phys. Chem.* **88**, 3956-3964.

10. Untch, A., Weide, K., and Schinke, R. (1985) The direct photodissociation of $ClNO(S_1)$: An exact three-dimensional wave packet analysis, *J. Chem. Phys.* **95**, 6496-6507.

11. Dixon, R.N., Marston, C.C., and Balint-Kurti, G.G. (1990) Photodissociation dynamics and emission spectroscopy of H_2S in its first absorption band: A time dependent quantum mechanical study, *J. Chem. Phys.* **93**, 6520-6534.

12. Le Quéré, F. and Leforestier, C. (1991) Hyperspherical formulation of the photodissociation of ozone, *J. Chem. Phys.* **94**, 1118-1126.

13. Neuhauser, D., Baer, M., Judson, R.S. and Kouri, D.J. (1989) Time-dependent three-dimensional body frame quantal wave packet treatment of the H + H_2 exchange reaction on the Liu-Siegbahn-Truhlar-Horowitz (LSTH) surface, *J. Chem. Phys.* **90**, 5882-5884.

14. Neuhauser, D., Baer, M., Judson, R.S. and Kouri, D.J. (1990) Time-dependent (wavepacket) quantum approach to reactive scattering: Vibrationally resolved reaction probabilities for F + $H_2 \rightarrow$ HF + H, *Chem. Phys. Lett.* **169**, 372-379.

15. Göğtas, F., Balint-Kurti, G.G. and Offer, A.R. (1996) Quantum mechanical three-dimensional wavepacket study of the Li + HF $\rightarrow$ LiF + H reaction, *J. Chem. Phys.* **104**, 7927-7939.

16. Gray, S.K. and Wozny, C.E. (1991) Fragmentation mechanisms from three-dimensional wave packet studies: Vibrational predissociation of $NeCl_2$, $HeCl_2$, NeICl, and HeICl, *J. Chem. Phys.* **94**, 2817-2832.

17. Gray, S.K. (1992) Wavepacket dynamics of resonance decay: An iterative equation approach with application to HCO $\rightarrow$ H + CO, *J. Chem. Phys.* **96**, 6543-6554.

18. Guo, H. (1993) Time-dependent quantum dynamical study of the photodissociation of hypochlorous acid, *J. Phys. Chem.* **97**, 2602-2608.

19. Xu, D.G., Xie, D.Q. and Guo, H. (2002) Theoretical study of HCN/DCN in their first absorption bands, *J. Chem. Phys.* **116**, 10626-10635.

20. Woywod, C., Stengle, M., Domcke, W., Flothmann, H. and Schinke, R. (1997) Photodissociation of ozone in the Chappuis band. I. Electronic structure calculations, *J. Chem. Phys.* **107**, 7282-7295.

21. Flothmann, H., Beck, C., Schinke, R., Woywod, C. and Domcke, W. (1997) Photodissociation of ozone in the Chappuis band. II. Time-dependent wave-packet calculations and interpretation of diffuse vibrational structures, *J. Chem. Phys.* **107**, 7296-7313.

22. Flothmann, H., Schinke, R., Woywod, C. and Domcke, W. (1998) Photodissociation of ozone in the Chappuis band. III. Product state distributions, *J. Chem. Phys.* **109**, 2680-2684.

23. Fillion, J.H., van Harrevelt, R., Ruiz, J., Castillejo, N., A.H. Zanganeh, A.H., J.L. Lemaire, J.L., M.C. van Hemert, M.C. and F. Rostas, F. (2001) Photodissociation of H_2O and D_2O in the $\tilde{B}, \tilde{C}$, and $\tilde{D}$ states (134-119 nm). Comparison between experiment and ab initio calculations, *J. Phys. Chem. A* **105**, 11414-11424.

24. Harich, S.A., Yang, X.F., Yang, X, van Harrevelt, R. and van Hemert, M.C. (2001) Single rotational product propensity in the photodissociation of HOD, *Phys. Rev. Lett.* **87**, 263001-1-263001-4.

25. van Harrevelt, R. and van Hemert, M.C. (2001) Photodissociation of water in the $\tilde{A}$ band revisited with new potential energy surfaces, *J. Chem. Phys.* **114**, 9453-9462.

26. Dixon, R.N., Hwang, D.W., Yang, X.F., Harich, S.A., Lin, J.J. and Yang, X.M. (1999) Chemical "double slits": Dynamical interference of photodissociation pathways in water, *Science* **285**, 1249-1253.

27. Harich, S.A., Hwang, D.W.H., Yang, X.F., Lin, J.J., Yang, X.M. and Dixon, R.N. (2000) Photodissociation of H_2O at 121.6 nm: A state-to-state dynamical picture, *J. Chem. Phys.* **113**, 10073-10090.

28. Harich, S.A., Yang, X.F., Hwang, D.W.H., Lin, J.J., Yang, X.M. and Dixon, R.N. (2001) Photodissociation of D_2O at 121.6 nm: A state-to-state dynamical picture, *J. Chem. Phys.* **114**, 7830-7837.

29. Kroes, G.J., van Hemert, M.C., Billing, G.D. and Neuhauser, D. (1997) Photodissociation of CH_2. VI. Three-dimensional quantum dynamics of the dissociation through the coupled $2A''$ and $3A''$ states, *J. Chem. Phys.* **107**, 5757-5770.

30. Kosloff, R. and Cerjan, C. (1984) Dynamical atom/surface effects: Quantum mechanical scattering and desorption, *J. Chem. Phys.* **81**, 3722-3729.

31. Leforestier, C., Bisseling, R., Cerjan, C., Feit, M.D., Friesner, R., Guldberg, A., Hammerich, A., Jolicard, G., Karrlein, W., Meyer, H.-D., Lipkin, N., Roncero, O. and Kosloff, R. (1991) A comparison of different propagation schemes for the time-dependent Schrödinger equation, *J. Comp. Phys.* **94**, 59-80.

32. Truong, T.N., Tanner, J.J., Bala, P., McCammon, J.A., Kouri, D.J., Lesyng, B. and Hoffman, D.K. (1992) A comparative study of time dependent quantum mechanical wave packet evolution methods, *J. Chem. Phys.* **96**, 2077-2084.

33. Balint-Kurti, G.G., Wavepacket theory of photodissociation and reactive scattering, *Adv. Chem. Phys.*, (in press).

34. Brown, A. and Balint-Kurti, G.G. (2000) Spin-orbit branching in the photodissociation of HF and DF. I. A time-dependent wave packet study for excitation from v =0, *J. Chem. Phys.* **113**, 1870-1878.

35. Pauling, L. and Wilson, E.B. (1935) *Introduction to Quantum Mechanics*, McGraw-Hill, New York.

36. Herzberg, G. (1950) *Molecular spectra and molecular structure, Vol. 1, Spectra of Diatomic molecules*, Van Nostrand, Princeton.

37. Schiff, L.I. (1955) *Quantum Mechanics*, McGraw-Hill, New York.

38. Shapiro, M. and Bersohn, R. (1982) Theories of the dynamics of photodissociation, *Ann. Rev. Phys. Chem.* **33**, 409-442.

39. Balint-Kurti, G.G. and Shapiro, M. (1981) Photofragmentation of triatomic molecules: Theory of angular and state distribution of product fragments, *Chem. Phys.* **61**, 137-155.

40. Beswick, J.A. (1993) Molecular Photofragmentation, in G. Delgado-Barrio (ed.), *Dynamical Processes in Molecular Physics*, Institute of Physics Publishing, Bristol.

41. Balint-Kurti, G.G., Dixon, R.N. and Marston, C.C. (1992) Grid methods for solving the Schrödinger equation and time dependent quantum dynamics of molecular photofragmentation and reactive scattering processes, *Internat. Rev. Phys. Chem.* **11** 317-344.

42. Levine, R.D. (1969) *Quantum Mechanics of Molecular Rate Processes*, Clarendon, Oxford.

43. Balint-Kurti, G.G., Füsti-Molnár, L. and Brown, A. (2001) Photodissociation of HOBr: Part II. Calculation of photodissociation cross-sections and photofragment quantum state distributions for the first two UV absorption bands, *Phys. Chem. Chem. Phys.* **3**, 702-710.

44. Edmonds, A.R. (1960) *Angular Momentum in Quantum Mechanics*, Princeton University Press, Princeton.

45. Zare, R.N. (1988) *Angular Momentum understanding spatial aspects in chemistry and physics*, John Wiley and Sons New York.

46. Pe'er, A., Shapiro, M. and Balint-Kurti, G.G. (1999) The breaking of forward-backward symmetry in the angular distribution of m_j-selected photofragments, *J. Chem. Phys.* **110**, 11928-11935.

47. Rama Krishna, M.V. and Coalson, R.D. (1988) Dynamic aspects of electronic exci-

tation, *Chem. Phys.* **120**, 327-333.

48. Meijer, A.J.H.M. and Goldfield, E.M. (2001) Time-dependent quantum mechanical calculations on H + O$_2$ for total angular momentum J ¿ 0: Comparing different dynamical approximations, *Phys. Chem. Chem. Phys.* **3**, 2811-2818.

49. Offer, A.R. and Balint-Kurti, G.G. (1994) Time-dependent quantum meachanical study of the photodissociation of HOCl and DOCl, *J. Chem. Phys.* **101**, 10416-10428.

50. Heller, E.J. (1978) Photofragmentation of symmetric triatomic molecules: Time dependent picture, *J.Chem.Phys.* **68**, 3891-3896.

51. Sun, Y. and Kouri, D.J. (1988) Wave packet study of gas phase atom-rigid rotor scattering, *J. Chem. Phys.* **89**, 2958-2964.

52. Sun, Y., Judson, R.S., and Kouri, D.J. (1989) Body frame close coupling wave packet approach to gas phase atom-rigid rotor inelastic collisions, *J. Chem. Phys.* **90**, 241-250.

53. Gray, S.K. and Wozny, C.E. (1989) Wave packet dynamics of van der Waals molecules: Fragmentation of NeCl$_2$ with three degrees of freedom, *J. Chem. Phys.* **91**, 7671-7684.

54. Weide, K., Kühl, K. and Schinke, R. (1989) Unstable periodic orbits, recurrences, and diffuse vibrational structures in the photodissociation of water near 128 nm, *J. Chem. Phys.* **91**, 3999-4008.

55. Light, J.C., Hamilton, I.P. and Lill, V.J. (1985) Generalized discrete variable approximation in quantum meachnics, *J. Chem. Phys.* **82**, 1400-1409.

56. Balint-Kurti, G.G., Dixon, R.N. and Marston, C.C. (1990) Time-dependent quantum dynamics of photofragmentation processes, *J. Chem. Soc. Faraday Trans. 2* **86**, 1741-1749. Eq. (3) of this reference should be multiplied by $1/(4\pi)$ and Eq. (25) by $1/(16\pi^2)$.

57. Brown, A. and Balint-Kurti, G.G. (2000) Spin-orbit branching in the photodissociation of HF and DF: II. A time-dependent wave packet study of vibrationally mediated photodissociation, *J. Chem. Phys.* **113**, 1879-1884.

58. Regan, P.M., Ascenzi, D., Brown, A., Balint-Kurti, G.G. and Orr-Ewing, A.J. (2000) Ultraviolet photodissociation of HCl in selected rovibrational states: Experiment and theory, *J. Chem. Phys.* **112**, 10259-10268.

59. Balint-Kurti, G.G., Orr-Ewing, A.J., Beswick, J.A., Brown, A. and Vasyutinskii, O.S. (2002) Vector correlations and alignment parameters in the photodissociation of HF and DF, *J. Chem. Phys.* **116**, 10760-10768.

60. Rakitzis, T.P., Samartzis, P.C., Toomes, R.L., Kitsopoulos, T.N., Brown, A., Balint-Kurti, G.G., Vasyutinskii, O.S. and Beswick,J.A. (2003) Spin-polarized hydrogen atoms from molecular photodissociation, *Science* **300**, 1936-1938.

61. Zhang, J., Riehn, C.W., Dulligan, M. and Wittig, C. (1996) An experimental study of HF photodissociation: Spin-orbit branching ratio and infrared alignment, *J. Chem. Phys.* **104**, 7027-7035.

62. Baer, M. (1985) The General Theory of Reactive Scattering: The Differential Equation Approach, in M. Baer (ed.), *Theory of Chemical Reaction Dynamics*, Vol.I, CRC Press, Inc.,Boca Raton, pp.91-161.

63. Lester, Jr., W.A. (1976) The N Coupled-Channel Problem, in W.H. Miller (ed.), *Dynamics of Molecular Collisions, Part A*, Plenum Press, New York, pp.1-80.

64. Clary, D.C. (ed.) (1986) *The Theory of Chemical Reaction Dynamics*, Reidel, Dordrecht.

65. Karplus, M. and Tang, K.T. (1967) Quantum-Mechanical Study of H + H$_2$ Reactive Scattering, *Disc. Faraday Soc.* 44, 56-67.

66. Miller, W.H. (1968) Distorted-Wave Theory for Collisions of an Atom and a Diatomic Molecule, *J. Chem. Phys.* **49**, 2373-2381.

67. Wolken, Jr., G. and Karplus, M. (1974) Theoretical Studies of H + H$_2$ Reactive Scattering, *J. Chem. Phys.* **60**, 351-367.

68. Schatz, G.C. and Kuppermann, A. (1976) Quantum mechanical reactive scattering for three-dimensional atom plus diatom systems. I. Theory, *J. Chem. Phys.* **65**,

4642-4667; Schatz, G.C. and Kuppermann, A. (1976) Quantum mechanical reactive scattering for three-dimensional atom plus diatom systems. II. Accurate cross sections for H + H$_2$, *J. Chem. Phys.* **65**, 4668-4692.

69. Kuppermann, A. (1981) in D. Henderson (ed.), *Theoretical Chemistry, Vol.6, Part A; Theory of Scattering: Papers in Honour of Henry Eyring*, Academic Press, New York, p.79.

70. Light, J.C. and Walker, R.B. (1976) An R matrix approach to the solution of coupled equations for atom-molecule reactive scattering, *J. Chem. Phys.* **65**, 4272-4282.

71. Halavee, U. and Shapiro, M. (1976) A collinear analytic model for atom-diatom chemical reactions, *J. Chem. Phys.* **64**, 2826-2839.

72. Baer, M. (1976) Adiabatic and diabatic representations for atom-diatom collisions: Treatment of the three-dimensional case, *Chem. Phys.* **15**, 49-57.

73. Kouri, D.J. (1985) The General Theory of Reactive Scattering: The Integral Equation Approach, in M. Baer (ed.), *Theory of Chemical Reaction Dynamics*, CRC Press, Inc.,Boca Raton, pp. 163-225.

74. Child, M.S. (1967) Measurable consequences of a dip in the activation barrier for an adiabatic chemical reaction,*Molec. Phys.* **12**, 401-416.

75. Connor, J.N.L. (1968) On the analytic description of resonance tunnelling reactions, *Molec. Phys.* **15**, 37-46.

76. D'Mello, M., Manolopoulos, D.E. and Wyatt, R.E. (1991) Quantum dynamics of the H + D$_2$ → D + HD reaction: Comparison with experiment, *J. Chem. Phys.* **94**, 5985-5993.

77. Launay, J.M. and le Dourneuf, M. (1989) Hyperspherical close-coupling calculations of integral cross sections for the reactions H + H$_2$ → H$_2$ + H, *Chem. Phys. Lett.* **163**, 178-188.

78. Clary, D.C. (1994) Four-atom reaction dynamics, *J. Phys. Chem.* **98**, 10678-10688.

79. Pack, R.T. and Parker, G.A. (1987) Quantum reactive scattering in three dimensions using hyperspherical (APH) coordinates. Theory, *J. Chem. Phys.* **87**, 3888-3921.

80. Truhlar, D.G., Mead, C.A. and Brandt, M.A. (1975) Time-Reversal Invariance, Representations for Scattering Wavefunctions, Symmetry of the Scattering Matrix, and Differential Cross-Sections, *Adv. Chem. Phys.* **33**, 295-344.

81. Schatz, G.C. (1988) Quantum effects in gas phase bimolecular chemical reactions, *Annu. Rev. Phys. Chem.* **39**, 317-340.

82. Manolopoulos, D.E. and Clary, D.C. (1989) Quantum Calculations on Reactive Collisions, *Annu. Rep. C. Roy. Soc. Chem.* **86**, 95-118.

83. Miller, W.H. (1990) Recent advances in quantum-mechanical reactive scattering-theory, including comparison of state-to-state cross-sections for H/D + H$_2$ → H$_2$/HD + H reactions, *Annu. Rev. Phys. Chem.* **41**, 245-281.

84. Bowman, J.M. (ed.) (1994) *Advances in Molecular Vibrations and Collision Dynamics*, Vols 2A and 2B, JAI, Greenwich.

85. Laganà, A., Pack, R.T. and Parker, G.A. (1988) *Faraday Disc. Chem. Soc.* **84**, 409.

86. Honvault, P. and Launay, J.M. (2001) A quantum-mechanical study of the dynamics of the O(^{1}D)+H$_2$ → OH + H insertion reaction, *J. Chem. Phys.* **114**, 1057-1059.

87. Jaquet, R. (2001) Quantum reactive scattering: the time-independent approach. W. Jakubetz (ed.), *Lecture Notes in Chemistry 77, Methods in Reaction Dynamics*, Springer-Verlag, Berlin, pp. 17-126.

88. Mazur, J. and Rubin, R.J. (1959) *J. Chem. Phys.* **31**, 1395.

89. McCullough, E.A. and Wyatt, R.E. (1971) Dynamics of the collinear H + H$_2$ reaction. I. Probability density and flux, *J. Chem. Phys.* **54**, 3578-3591; ibid. (1971) Dynamics of the collinear H + H$_2$ reaction. II. Energy Analysis, **54**, 3592-3600.

90. Zuhrt, Ch., Kamal, T. and Zulicke, L. (1975) Quantum mechanical investigations of the collinear collisions F + H2 and F + D2 using the wavepacket approach, *Chem. Phys. Lett.* **36**, 396-400.

91. Kellerhals, E., Sathyamurthy, N. and Raff, L.M. (1976) Comparison of quantum mechanical and quasiclassical scattering as a function of surface topology *J. Chem. Phys.* **64**, 818-825.

92. Agrawal, P.M. and Raff, L.M. (1981) Calculation of reaction probabilities and rate coefficients for collinear three-body exchange reactions using time-dependent wave packet methods, *J. Chem. Phys.* **74**, 5076-5081.

93. Leforestier, C. (1984) Competition between dissociation and exchange processes in a collinear A + BC Collision. 1. Exact Quantum Results, *Chem. Phys.* **87**, 241-261.

94. Zhang, Z.H. and Kouri, D.J. (1986) Wave-packet solution to the time-dependent arrangement-channel quantum-mechanics equations, *Phys. Rev. A* **34**, 2687-2696.

95. Mohan, V. and Sathyamurthy, N. (1987) Quantal wavepacket calculations of reactive scattering, *J. Phys. Chem.* **91**, 213-258.

96. Neuhauser, D. and Baer, M. (1989) The application of wave-packets to reactive atom-diatom systems - a new approach, *J. Chem. Phys.* **91**, 4651-4657.

97. Neuhauser, D., Baer, M., Judson, R.S. and Kouri, D.J. (1990) A time-dependent wave packet approach to atom diatom reactive collision probabilities - theory and application to H + H_2 (J=0) system, *J. Chem. Phys.* **93**, 312-322.

98. Gray, S.K. and Balint-Kurti, G.G. (1998) Quantum dynamics with real wavepackets, including application to three-dimensional (J = 0) D + H_2 → HD + H reactive scattering, *J. Chem. Phys.* **108**, 950-962.

99. Carroll, T.E. and Goldfield, E.M. (2001) Coriolis-coupled quantum dynamics for $0(^1D)$+H_2 → OH + H, *J. Phys. Chem. A* **105**, 2251-2256.

100. Kingma, S.M., Somers, M.F., Pijper, E., Kroes, G.J., Olsen, R.A. and Baerends, E.J. (2003) Diffractive and reactive scattering of (v=0, j=0) HD from Pt(111): Six-dimensional quantum dynamics compared with experiment, *J. Chem. Phys.* **118**, 4190-4197.

101. Althorpe, S.C. (2001) Quantum wavepacket method for state-to-state reactive cross sections, *J. Chem. Phys.* **114**, 1601-1616.

102. Goldfield, E.M. and Gray, S.K. (2002) A quantum dynamics study of H_2+OH -¿ H_2O+H employing the Wu-Schatz-Lendvay-Fang-Harding potential function and a four-atom implementation of the real wave packet method, *J. Chem. Phys.* **117**, 1604-1613.

103. Gray, S.K. and Goldfield, E.M. (2001) Dispersion fitted finite difference method with applications to molecular quantum mechanics *J. Chem. Phys.* **115**, 8331-8344.

104. Zhang, J.Z.H. (1999) *Theory and Application of Quantum Molecular Dynamics,* World Scientific, Singapore.

105. Mohan, V. and Sathyamurthy, N. (1988) Quantal wavepacket calculations of reactive scattering, *Computer Phys. Repts.* **7**, 213-258.

106. Balakrishnan, N., Kalyanaraman, C. and Sathyamurthy, N. (1997) Time-dependent quantum mechanical approach to reactive scattering and related processes *Phys. Repts.-Review section of Physics Letters* **280**, 80-144.

107. Althorpe, S.C., Soldán, P. and Balint-Kurti, G.G. (eds.) (2001) *Time-Dependent Quantum Dynamics* , CCP6: Collaborative Computational Project on Heavy Particle Dynamics, Daresbury Laboratory, Daresbury.

108. Balint-Kurti, G.G., Göğtas, F., Mort, S.P., Offer, A.R., Laganà, A. and Garvasi, O. (1993) Comparison of Time-Dependent and Time-Independent Quantum Reactive Scattering – Li + HF → LiF + H Model Calculations, *J. Chem. Phys.* **99**, 9567-9584.

109. Hankel, M., Balint-Kurti, G.G., and Gray, S.K. (2000) Quantum mechanical calculation of product state distributions for the $O(^1D)$+H_2 → OH + H reaction on the ground electronic state surface, *J. Chem. Phys.* **113**, 9658-9667.

110. Hankel, M., Balint-Kurti, G.G. and Gray, S.K. (2001) Quantum mechanical calculation of reaction probabilities and branching ratios for the $O(^1D)$+HD → OH(OD)+D(H) reaction on the X $^1A'$ and $1^1A''$ adiabatic potential energy surfaces, *J. Phys. Chem.* **105**, 2330-2339.

111. Hankel, M., Balint-Kurti, G.G. and Gray, S.K. (2003) Sinc wavepackets: A new form of wavepacket for time-dependent quantum mechanical reactive scattering calculations *Int. J. Quant. Chem.* **92**, 205-211.

112. Gray, S.K., Goldfield, E.M., Schatz, G.C. and Balint-Kurti, G.G. (1999) Helicity decoupled quantum dynamics and capture model cross sections and rate constants

for $O(^1D) + H_2(r) \rightarrow OH + H$, *Phys. Chem. Chem. Phys.* **1**, 1141-1148.

113. Gray, S.K., Balint-Kurti, G.G., Schatz, G.C., Lin, J.J., Liu, X., Harich, S. and Yang, X. (2000) Probing the effect of the H2 rotational state in $O(^1D) + H_2(r) \rightarrow OH + H$: Theoretical dynamics including nonadiabatic effects and a crossed molecular beam study, *J. Chem. Phys.* **113**, 7330-7344.

114. Meijer, A.J.H.M., Goldfield, E.M., Gray, S.K. and Balint-Kurti, G.G. (1998) Flux analysis for calculating reaction probabilities with real wavepackets, *Chem. Phys. Lett.* **293**, 270-276.

115. Miquel, I., Gonzalez, M., Sayos, R., Balint-Kurti, G.G., Gray, S.K. and Goldfield, E.M. (2003) Quantum reactive scattering calculations of cross sections and rate constants for the $N(^2D) + O_2 \rightarrow O(^3P) + NO(X^2\Pi$ reaction, *J. Chem. Phys.* **118**, 3111-3123.

116. Pack, R.T. (1974) Space-fixed vs. body-fixed axes in atom-diatomic molecule scattering. Sudden approximations, *J. Chem. Phys.* **60**, 633-639.

117. McGuire, P. and Kouri, D.J. (1974) Quantum mechanical close coupling approach to molecular collisions. j_z-conserving coupled states approximation, *J. Chem. Phys.* **60**, 2488-2499.

118. Bowman, J.M. (1991) Reduced dimensionality Theory of quantum reactive scattering, *J. Phys. Chem.* **95**, 4960-4968.

119. Bittererova, M. and Bowman, J.M. (2000) A wave-packet calculation of the effect of reactant rotation and alignment on product branching in the $O(^1D) + HCl \rightarrow ClO + H, OH + Cl$ reactions *J. Chem. Phys.* **113**, 1-3; Bittererova, M., Bowman, J.M. and Peterson, K. (2000) Quantum scattering calculations of the O(D-1) plus HCl reaction using a new ab initio potential and extensions of J-shifting, *J. Chem. Phys.* **113**, 6186-6196.

120. Miller, W.H. (1969) Coupled Equations and the Minimum Principle for Collisions of an Atom and a Diatomic Molecule, Including Rearrangements, *J. Chem. Phys.* **50**, 407-418.

121. Althorpe, S.C. (2002) Time-dependent plane wave packet formulation of quantum scattering with application to $H + D_2 \rightarrow HD + D$, *J. Chem. Phys.* **117**, 4623-4627.

122. Althorpe, S.C., Fernandez-Alonso, F., Bean, B.D., Ayers, J.D., Pomerantz, A.E., Zare, R.N. and Wrede, E. (2002) Observation and interpretation of a time-delayed mechanism in the hydrogen exchange reaction, *Nature* **416**, 67-70.

123. Hankel, M. (2001) Time-Dependent Wavepacket Methods for the Calculation of State-to-State Molecular Reactive Cross Sections, *Ph.D. thesis*, University of Bristol, Bristol.

124. Messiah, A. (1962)*Quantum Mechanics, Vol. II*, North-Holland, Amsterdam.

125. GGBK thanks M. Shapiro for suggesting this method to him.

126. Press, W.H., Flannery, B.P., Teukolsky, S.A. and Vetterling, W.T. (1987) *Numerical Recipes*, Cambridge University Press, Cambridge.

127. Monnerville, M., Halvick, P. and Rayez, J.C. (1992) Time-dependent calculation of the energy resolved state-to-state transition-probabilities for 3-atom exchange-reactions, *Chem. Phys.* **159**, 227-234.

128. Monnerville, M., Halvick, P. and Rayez, J.C. (1993) Collinear quantum wave-packet study of exothermic A + BC reactions involving an intermediate complex of linear geometry - application to the C + NO reaction, *Chem. Soc Faraday Trans.* **89**, 1579-1585.

129. Mott, N.F. and Massey, H.S.W. (1965) *The Theory of Atomic Collisions*, Oxford University Press, Oxford.

130. Leforestier, C. and Wyatt, R.E. (1983) Optical-potential for laser induced dissociation, *J. Chem. Phys.* **78**, 2334-2344.

131. Neuhauser, D. and Baer, M. (1989) The time-dependent Schrodinger-equation - application of absorbing boundary conditions, *J. Chem. Phys.* **90**, 4351-4355.

132. Neuhauser, D., Baer, M., Judson, R.S. and Kouri, D.J. (1991) The application of time-dependent wavepacket methods to reactive scattering, *Comp. Phys. Commun.* **63**, 460-481.

133. Child, M.S. (1991) Analysis of a complex absorbing barrier, *Molec. Phys.* **72**, 89-93.

134. Seideman, T. and Miller, W.H. (1992) Calculation of the Cumulative Reaction Probability via a Discrete Variable Representation with Absorbing Boundary-Conditions, *J. Chem. Phys.* **96**, 4412-4422.

135. Vibók,Á. and Balint-Kurti, G.G. (1992) Reflection and Transmission of Waves by a Complex Potential   A Semiclassical Jeffreys-Wentzel-Kramers-Brillouin (JWKB) Treatment, *J. Chem. Phys.* **96**, 7615-7620.

136. Vibók, Á. and Balint-Kurti, G.G. (1992) Parameterization of Complex Absorbing Potentials for use in Time Dependent Quantum Dynamics, *J. Phys. Chem.* **96**, 8712-8719.

137. Balint-Kurti, G.G. and Vibók,Á. (1993) Complex Absorbing Potentials in Time Dependent Quantum Dynamics, in C. Cerjan (ed.), *Numerical Grid Methods and their Application to Schrdinger's Equation*, NATO ASI series, Series C: Mathematical and Physical Sciences, Kluwer Academic Publishers, **412** 195-205.

138. Mahapatra, S. and Sathyamurthy, N. (1993) Negative imaginary potentials in time-dependent quantum molecular scattering, *Chem. Soc Faraday Trans.* **93**, 773-779.

139. Macias, D., Brouard, S. and Muga, J.G. (1994) Optimization of absorbing potentials, *Chem. Phys. Lett.* **228**, 672-677.

140. Brouard, S., Macias, D. and Muga, J.G. (1994) Perfect absorbers for stationary and wavepacket scattering, *J. Phys. A* **27**, L439-L445.

141. Riss, U.V. and Meyer, H.-D. (1996) Investigation on the reflection and transmission properties of complex absorbing potentials, *J. Chem. Phys.* **105**, 1409-1419.

142. Riss, U.V. and Meyer, H.-D. (1998) The transformative complex absorbing potential method: a bridge between complex absorbing potentials and smooth exterior scaling, *J. Phys. B* **31**, 2279-2304.

143. Manolopoulos, D.E. (2002) Derivation and reflection properties of a transmission-free absorbing potential, *J. Chem. Phys.* **117**, 9552-9559.

144. Gray, S.K. and Verosky, J.M. (1994) Classical Hamiltonian structures in wave-packet dynamics, *J. Chem. Phys.* **100**, 5011-5022.

145. Gray, S.K. and Manolopoulos, D.E. (1996) Symplectic integrators tailored to the time-dependent Schrodinger equation, *J. Chem. Phys.* **104** 7099-7112.

146. Arfken, G.B. and Weber, H.J. (1970) *Mathematical Methods for Physicists*, Academic Press, San Diego.

147. Huang, Y., Kouri, D.J. and Hoffman, D.K. (1994) General, energy-separable Faber polynomial representation of operator-functions - theory and application in quantum scattering, *J. Chem. Phys.* **101**, 10493-10506.

148. Huang, Y., Iyengar, S.S., Kouri, D.J. and Hoffman, D.K. (1996) Further analysis of solutions to the time-independent wave packet equations of quantum dynamics .2. Scattering as a continuous function of energy using finite, discrete approximate Hamiltonians, *J. Chem. Phys.* **105**, 927-939.

149. Mandelshtam, V.A. and Taylor, H.S. (1995) Spectral projection approach to the quantum scattering calculations, *J. Chem. Phys.* **102**, 7390-7399.

150. Mandelshtam, V.A. and Taylor, H.S. (1995) A simple recursion polynomial expansion of the Green's-function with absorbing boundary conditions - application to the reactive scattering, *J. Chem. Phys.* **103**, 2903-2907.

151. Kroes, G.-J. and Neuhauser, D. (1996) Performance of a time-independent scattering wave packet technique using real operators and wave functions, *J. Chem. Phys.* **105**, 8690-8698.

152. Kroes, G.-J., Baerends, E.J. and Mowrey, R.C. (1997) Six-Dimensional Quantum Dynamics of Dissociative Chemisorption of (v = 0, j = 0) H2 on Cu(100), *Phys. Rev. Lett.* **78**, 3583-3586.

153. Kroes, G.-J., Wall, M.R., Peng, J.W. and Neuhauser, D. (1997) Avoiding long propagation times in wave packet calculations on scattering with resonances: A new algorithm involving filter diagonalization, *J. Chem. Phys.* **106**, 1800-1807.

154. Kroes, G.-J., van Hemert, M.C., Billing, G.D. and Neuhauser, D. (1997) Photodissociation of $CH_2(1\,^3B_1)$ through the coupled 2 A" and 3 A" states: Quantitative

branching ratios for the production of CH+H and C+H_2, *Chem. Phys. Lett.* **271**, 311-319.

155.   Chen, R. and Guo, H. (1996) Evolution of quantum system in order domain of Chebyshev operator, *J. Chem. Phys.* **105**, 3569-3578.

156.   Chen, R. and Guo, H. (1996) Extraction of resonances via wave packet propagation in Chebyshev order domain: collinear H + H_2 scattering, *Chem. Phys. Lett.* **261**, 605-611.

157.   Guo, H. (1998) A time-independent theory of photodissociation based on polynomial propagation, *J. Chem. Phys.* **108**, 2466-2472.

158.   Guo, H. and Seideman, T. (1999) Quantum mechanical study of photodissociation of oriented ClNO(^{1}S), *Phys. Chem. Chem. Phys.* **1**, 1265-1272.

159.   Xie, D., Guo, H., Amatatsu, Y. and Kosloff, R. (2000) Three-dimensional photodissociation dynamics of rotational state selected methyl iodide, *J. Phys. Chem.* **104**, 1009-1019.

160.   Guo, H. (1998) An efficient method to calculate resonance Raman amplitudes via polynomial propagation, *Chem. Phys. Lett.* **289**, 396-402.

161.   Sayós, R. and González, M., TRIQCT (unpublished program).

162.   Lee, S.-H. and Liu, K. (1999) Effect of reagent rotation in O(^{1}D) + H_2(v = 0,j): A sensitive probe of the accuracy of the ab initio excited surfaces? *J. Chem. Phys.* **111**, 4351-4352.

QUANTUM DYNAMICS OF INSERTION REACTIONS

PASCAL HONVAULT AND JEAN–MICHEL LAUNAY

PALMS, UMR 6627 du CNRS, Université de Rennes 1,
Campus de Beaulieu, 35042 Rennes Cedex, FRANCE

Abstract.

We describe quantum-dynamical calculations of insertion reactions involving metastable C, N and O atoms with hydrogen molecules. We use a time independent hyperspherical body-frame formalism. Reaction probabilities, rovibrational distributions, integral and differential cross sections and product translational energy distributions have been computed and compared with recent experimental data.

1. Introduction

The detailed study of the dynamics of elementary chemical reactions of the kind A + BC → AB + C has recently undergone great progress.

On the experimental side, the coupling of crossed molecular beam techniques with sophisticated detection techniques (Laser Induced Fluorescence, CARS or REMPI spectroscopy, Rydberg tagging photoionisation using synchrotron radiation or VUV lasers) has improved considerably the detailed study of chemical reactivity. It is now possible to prepare reactants in a well defined state and to analyze the reaction products at a fixed scattering angle for a collision at a well defined kinetic energy [1].

On the theoretical side, the tremendous increase of computer power has permitted to obtain very accurate *ab initio* global Potential Energy Surfaces (PES) for triatomic systems and to develop efficient classical and quantum dynamical methods. Thus, in the last decade, good agreement between theory and experiment has been obtained for elementary reactions such as H + H$_2$ → H$_2$ + H and F + H$_2$ → FH + H.

Schematically, these reactions are of the *direct* type [2]. They involve potential surfaces which have no deep well. The reaction mechanism is of the abstraction type. The A atom approaches atom B and forms a new chemical bond while the old BC bond is broken gradually. The product angular distributions are backward peaked while rotational and vibrational distributions are very specific.

In an *indirect* reaction [2] A + BC → B-A-C → AB + C or AC + B. In a first step, the A atom inserts into the BC diatom forming an ABC complex. Two new bonds (AB and AC) are formed while the BC bond is broken. Then the complex dissociates with a breaking of one of these two bonds. This reaction mechanism is called *insertion*. In contrast with abstraction reactions, all three bonds in the triatomic molecule ABC participate actively in the reaction. Two bonds are formed temporarily while only one exists for the reactants and products. Thus, the potential energy surface involves a very deep well (several eV) which correspond to a stable ABC molecule or radical. When the lifetime of the ABC molecule is larger than its rotational period, angular distributions of the products are symetric with a backward/forward peak and the population of rovibrational states of the products presents a statistical character.

Because of the very large well in the potential energy surface, very few accurate quantum dynamical results were available five years ago, either by time-dependent or by time-independent methods. Indeed, a very large number of channels or of grid points are necessary to converge reaction probabilities and cross sections.

In this contribution, we will describe the essential features of the hyperspherical body-frame method (section 2) and of its numerical implementation (section 3). We will then present in section 4 selected recent results obtained for the three insertion reactions $O(^1D) + H_2$, $N(^2D) + H_2$ and $C(^1D) + H_2$. Our time-independent quantum-dynamical results will be compared with experiment.

2. Theory

2.1. HYPERSPHERICAL DEMOCRATIC COORDINATES

Mass–scaled Jacobi coordinates associated to a generic arrangement λ (= α for A + BC, β for B + CA and γ for C + AB) are denoted by $\vec{r}_\lambda$ (diatom vector) and $\vec{R}_\lambda$ (atom-molecule vector). They are used in the definition of hyperspherical coordinates which parametrize the nuclear motion of the system, namely the principal axis body frame hyperspherical coordinates [3, 4, 5]. These coordinates are :

(i) three external Euler angles, denoted collectively by $\mathcal{E}$, to specify the orientation of the principal axis frame in space. The principal axes of inertia are denoted by X, Y, Z, with Z the axis of smallest inertia, X the second axis in the molecular plane, and Y the axis of largest inertia, perpendicular to it.

(ii) the hyperspherical radius $\rho = \sqrt{R_\lambda^2 + r_\lambda^2}$ which is independent of the arrangement λ and is a measure of the global size of the triatomic system.

(iii) two internal angles θ and ϕ_λ (see figure 1) which specify the shape of the ABC molecule :

$$\theta = 2 \arctan \left(\frac{R_X}{R_Z} \right) \qquad \phi_\lambda = \frac{1}{2} \arctan \left(\frac{2\vec{R}_\lambda . \vec{r}_\lambda}{R_\lambda^2 - r_\lambda^2} \right) \qquad (1)$$

where R_X and R_Z are the inertial radii. The angle θ remains in the interval $[0, \pi/2]$ and is 0 for linear configurations and $\pi/2$ for symmetric top configurations. The range of variation of ϕ_λ is $[0, 2\pi]$.
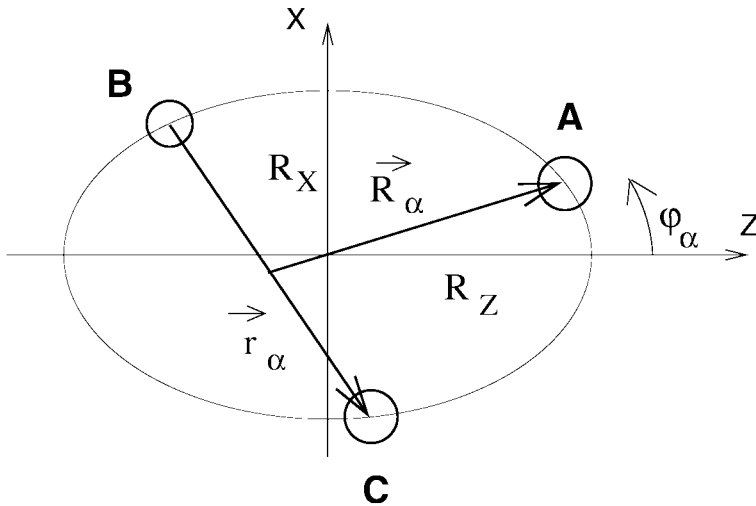
Figure 1. Definition of the θ and ϕ_α hyperangles. $\vec{R}_\alpha$ and $\vec{r}_\alpha$ are the Jacobi coordinates for arrangement α. The inertial radii are related to ρ and θ by the formulas $R_X = \rho \sin(\theta/2)$, $R_Z = \rho \cos(\theta/2)$, $R_Y = \rho$.

2.2. HAMILTONIAN

The hamiltonian of the ABC system in body-frame hyperspherical democratic coordinates is written as [4] :

$$H = -\frac{1}{2\mu\rho^5} \frac{\partial}{\partial\rho} \rho^5 \frac{\partial}{\partial\rho} + \mathcal{H} + \mathcal{C} \qquad (2)$$

where the internal hamiltonian $\mathcal{H}$ is given by

$$\mathcal{H} = \frac{1}{2\mu\rho^2} \left(-\frac{4}{\sin 2\theta} \frac{\partial}{\partial\theta} \sin 2\theta \frac{\partial}{\partial\theta} - \frac{1}{\cos^2\theta} \frac{\partial^2}{\partial\phi^2} + \frac{4J_Z^2}{\sin^2\theta} \right) + V(\rho, \theta, \phi) \qquad (3)$$

It contains deformation and rotation around the axis of least inertia at fixed-ρ and also the potential energy V. In equation (2), $\mathcal{C}$ contains the remaining rotational

terms and Coriolis coupling :

$$\mathcal{C} = \frac{1}{2\mu\rho^2} \left(\frac{J_X^2 - J_Z^2}{\cos^2 \theta/2} + \frac{J_Y^2}{\cos^2 \theta} - 2iJ_Y \frac{\sin \theta}{\cos^2 \theta} \frac{\partial}{\partial \phi} \right) \tag{4}$$

where J_X, J_Y, J_Z are the components of the total angular momentum in the principal axis frame.

2.3. HYPERSPHERICAL ADIABATIC STATES

We consider a ρ dependent basis of five dimensional functions [4] :

$$\Phi_{k\Omega}^{JM}(\rho; \theta, \phi, \mathcal{E}) = \varphi_{k\Omega}(\rho; \theta, \phi) \; N_\Omega^{JM}(\mathcal{E}) \tag{5}$$

which are eigenstates of the Hamiltonian of J_Z and $\mathcal{H}$ with eigenvalues Ω and $\epsilon_{k\Omega}(\rho)$. The functions $\varphi_{k\Omega}$ are solutions of a two–dimensional Schrödinger equation at fixed hyperradius ρ :

$$H_\Omega(\rho; \theta, \phi) \; \varphi_{k\Omega}(\rho; \theta, \phi) = \epsilon_{k\Omega}(\rho) \; \varphi_{k\Omega}(\rho; \theta, \phi) \tag{6}$$

with the Ω and ρ dependent hamiltonian :

$$H_\Omega(\rho; \theta, \phi) = \frac{1}{2\mu\rho^2} \left(-\frac{4}{\sin 2\theta} \frac{\partial}{\partial \theta} \sin 2\theta \frac{\partial}{\partial \theta} - \frac{1}{\cos^2 \theta} \frac{\partial^2}{\partial \varphi^2} + \frac{4\Omega^2}{\sin^2 \theta} \right) + V(\rho; \theta, \phi) \tag{7}$$

Equation (6) is solved by variational expansion over a basis of two-dimensional pseudo-hyperspherical harmonics (PHH) $\mathcal{Y}_{K\nu\Omega}$:

$$\mathcal{Y}_{K\nu\Omega}(\theta, \phi) = g_{K\nu\Omega}(\theta) \; h(\nu\phi - \Omega\pi/2) \tag{8}$$

where $h = \cos$ or $\sin$ (for symmetric or antisymmetric states) and the functions $g_{K\nu\Omega}(\theta)$ are solutions of the one-dimensional differential equation :

$$\left[-\frac{4}{\sin 2\theta} \frac{d}{d\theta} \sin 2\theta \frac{d}{d\theta} + \frac{\nu^2}{\cos^2 \theta} + \frac{4\Omega^2}{\sin^2 \theta} \right] g_{K\nu\Omega}(\theta) = K(K+4) \; g_{K\nu\Omega}(\theta) \tag{9}$$

with $K = \nu + 2\Omega + 4n$, n being a non negative integer [4] which is even (odd) for even (odd) parity states. The size of the basis of $\mathcal{Y}_{K\nu\Omega}$ functions can be monitored by the parameter K_{MAX}, which is the maximum value of the quantum number K. The $\mathcal{Y}_{K\nu\Omega}$ functions are delocalized in all configuration space, whereas the surface functions $\varphi_{k\Omega}$ are more and more concentrated in the arrangement valleys around $\theta = 0$ when ρ increases. As a result, the expansion of the $\varphi_{k\Omega}$ functions on the $\mathcal{Y}_{K\nu\Omega}$ basis converges slowly at large hyperspherical radius. Faster convergence is achieved by using for large ρ a contracted basis, obtained by diagonalizing the operator $1/\cos^2 \theta$ in the $\mathcal{Y}_{K\nu\Omega}$ basis and by keeping the states with eigenvalues smaller than some maximum which depends on ρ [6]. The resulting eigenfunctions

are localized in an interval $[0, \theta_{\mathrm{MAX}}(\rho)]$ and are the most useful to represent the surface states.

2.4. COUPLED HYPERRADIAL EQUATIONS

The Schrödinger equation is solved using the diabatic–by–sector method [7] in which the range of ρ is divided into small sectors $[\rho_{p-1/2}, \rho_{p+1/2}]$ centered around ρ_p. In each sector, the total wavefunction is expanded on the basis defined at ρ_p :

$$\Psi^{JM}(\rho; \theta, \phi, \mathcal{E}) = \frac{1}{\rho^{5/2}} \sum_{k\Omega} \Phi_{k\Omega}^{JM}(\rho_p; \theta, \phi, \mathcal{E}) \; F_{k\Omega}^{J}(\rho_p; \rho) \tag{10}$$

The hyperradial functions $F_{k\Omega}^{J}(\rho_p; \rho)$ are solutions of a set of coupled second order differential equations :

$$\begin{aligned} \left(-\frac{1}{2\mu} \frac{d^2}{d\rho^2} + \frac{15}{8\mu\rho^2} - E \right) F_{k\Omega}^{J}(\rho_p; \rho) &+ \sum_{k'} H_{kk'}^{\Omega}(\rho_p; \rho) F_{k'\Omega}^{J}(\rho_p; \rho) \\ &+ \sum_{k'\Omega'} \mathcal{C}_{k\Omega, k'\Omega'}^{J}(\rho_p; \rho) F_{k'\Omega'}^{J}(\rho_p; \rho) = 0 \end{aligned} \tag{11}$$

with coupling matrix elements given by :

$$H_{kk'}^{\Omega}(\rho_p; \rho) = \langle \varphi_{k\Omega}(\rho_p; \theta, \phi) | H_{\Omega}(\rho; \theta, \phi) | \varphi_{k'\Omega}(\rho_p; \theta, \phi) \rangle_{\theta\phi} \tag{12}$$

$$\mathcal{C}_{k\Omega, k'\Omega'}^{J}(\rho_p; \rho) = \langle \Phi_{k\Omega}^{JM}(\rho_p; \theta, \phi, \mathcal{E}) | \mathcal{C} | \Phi_{k'\Omega'}^{JM}(\rho_p; \theta, \phi, \mathcal{E}) \rangle_{\theta\phi\mathcal{E}} \tag{13}$$

Due to the factorisation of the basis functions $\Phi_{k\Omega}^{JM}$ into an internal part $\varphi_{k\Omega}$ which is independent of the total angular momentum J and an external part N_{Ω}^{JM}, the evaluation of matrix elements in equations (12,13) is easy. Firstly, the coupling matrix H is independent of the total angular momentum J and connects states with the same projection Ω. Secondly, when computing the $\mathcal{C}$ matrix elements, integrals over the θ, ϕ internal coordinates are independent of J while integrals over the Euler angles $\mathcal{E}$ can be performed analytically. $\mathcal{C}$ connects states with $\Delta\Omega = 0, \pm 1, \pm 2$ and needs only to be evaluated at the middle of each sector. Finally, we note that $\mathcal{C}$ is smooth and well behaved for linear configurations ($\theta = 0$) but becomes large for symmetric top configurations ($\theta = \pi/2$).

The logarithmic derivative of linearly independent solutions of the coupled equations (11) are propagated outwards in each sector $[\rho_{p-1/2}, \rho_{p+1/2}]$ using the Johnson–Manolopoulos [8] algorithm. At the boundary of each sector $\rho_{p+1/2}$, a transformation to the basis of the next sector $[\rho_{p+1/2}, \rho_{p+3/2}]$ computed at ρ_{p+1} is performed. This is repeated until the last sector (centered at ρ_m) corresponding to the asymptotic region is reached.

In practice, we retain a finite number of basis functions in this expansion. In previous work on abstraction reactions such as H + H$_2$ [4], F + H$_2$ [6] or F + D$_2$

[9], we could use at small ρ the contraction scheme decribed before. For insertion reactions, this cannot be used, because symmetric top configurations lie near the potential minimum of the triatom ABC molecule.

When computing $J \neq 0$ partial waves, we tried to use a truncated Ω-basis by including in the close-coupling expansion states with $|\Omega| \leq \Omega_{\mathrm{MAX}}$. For abstraction reactions [4, 6, 9], this procedure is very efficient in reducing the number of channels needed for convergence, provided that Ω_{MAX} is small, say 5. It is not satisfactory for insertion reactions, because of the already mentioned reason that symmetric top configurations, where Coriolis couplings are large, are energetically accessible. It is thus necessary to keep all Ω components to accurately represent this effect.

As a result of these two effects, the mentioned insertion reactions require between 3000 and 5000 channels to get convergence, whereas F + H$_2$ for example requires only 500 channels.

2.5. ASYMPTOTIC ANALYSIS

The expression (10) is not suitable to determine collisional wavefunctions because their asymptotic part is determined in Jacobi space-fixed coordinates specific for each arrangement λ. The transformation from body-frame hyperspherical democratic coordinates $(\rho, \theta, \phi, \mathcal{E})$ to space-fixed $(\vec{R}_\lambda, \vec{r}_\lambda)$ Jacobi coordinates is performed in several steps. It necessitates the introduction of Fock internal hyperspherical coordinates $(\rho, \omega_\lambda, \eta_\lambda)$ to analyze the rovibrational character of the surface functions $\varphi_{k\Omega}$ in the fragmentation region at large ρ.

2.5.1. *Transformation to Fock Body-Frame coordinates*
For a given arrangement λ, the two Fock angles $(\omega_\lambda, \eta_\lambda)$ are the hyperradial correlation angle $\omega_\lambda = \tan^{-1}(r_\lambda/R_\lambda)$ and the bending angle $\eta_\lambda = \cos^{-1}(\hat{R}_\lambda.\hat{r}_\lambda)$. The expression of the hamiltonian $\mathcal{H}$ in Fock Body-Frame coordinates is

$$\mathcal{H} = \frac{1}{2\mu\rho^2} \left(-\frac{1}{\sin^2 2\omega_\lambda} \frac{\partial}{\partial \omega_\lambda} \sin^2 2\omega_\lambda \frac{\partial}{\partial \omega_\lambda} + \frac{4\vec{j}_\lambda^2}{\sin^2 2\omega_\lambda} \right) + V(\rho; \omega_\lambda, \eta_\lambda) \qquad (14)$$

At large hyperspherical radius ρ, the potential V does not depend on the angle η_λ, hence the adiabatic states $\varphi_{k\Omega}$ converge to a rovibrational states vj in each arrangement λ :

$$\varphi_{k\Omega} \to \chi_{\lambda vj}(\rho; \omega_\lambda) \; P_{j\Omega}(\eta_\lambda) \qquad (15)$$

where $P_{j\Omega}$ is an associated Legendre function and $\chi_{\lambda vj}$ are solutions of the one–dimensional equation :

$$\left(\frac{1}{2\mu\rho^2} \left[-\frac{1}{\sin^2 2\omega_\lambda} \frac{d}{d\omega_\lambda} \sin^2 2\omega_\lambda \frac{d}{d\omega_\lambda} + \frac{4j(j+1)}{\sin^2 2\omega_\lambda} \right] + V_\lambda(\rho; \omega_\lambda) \right) \chi_{\lambda vj}(\rho; \omega_\lambda)$$
$$= \epsilon_{\lambda vj}(\rho) \chi_{\lambda vj}(\rho; \omega_\lambda) \qquad (16)$$

Hence, the wavefunction can be written as

$$\Psi^{JM} = \sum_{\lambda v j \Omega} N^{JM}_{\Omega}(\mathcal{E}) \; \chi_{\lambda v j}(\rho_m; \omega_\lambda) \; P_{j\Omega} \; (\eta_\lambda) \; F^J_{\lambda v j \Omega}(\rho_m; \rho) \tag{17}$$

2.5.2. *Transformation to Fock Space-Fixed coordinates*

The hyperradial components are then transformed to a new representation with an internal quantization axis along the Jacobi vector $\vec{R}_\lambda$. This transformation can be written as a matrix

$$U^J_{\lambda' v' j' \Omega'_\lambda \lambda v j \Omega} = \langle \chi_{\lambda v' j'}(\rho_m; \omega_\lambda) \; P_{j' \Omega'_\lambda} | d^J_{\Omega'_\lambda \Omega}(\Delta_\lambda) | \chi_{\lambda v j}(\rho_m; \omega_\lambda) \; P_{j\Omega} \rangle_{\omega_\lambda \eta_\lambda} \tag{18}$$

where Ω'_λ is the projection of $\vec{J}$ on the Jacobi vector $\vec{R}_\lambda$ and Δ_λ is the (small) angle between Z and $\vec{R}_\lambda$. Once this transformation is performed, the new expression of the wavefunction is

$$\Psi^{JM} = \sum_{\lambda v j \Omega_\lambda} N^{JM}_{\Omega_\lambda}(\mathcal{E}_\lambda) \; \chi_{\lambda v j}(\rho_m; \omega_\lambda) \; P_{j\Omega_\lambda} \; (\eta_\lambda) \; F^J_{\lambda v j \Omega_\lambda}(\rho) \tag{19}$$

Then we transform the hyperradial components to the usual Arthurs-Dalgarno representation with coupled spherical harmonics $|jlJM\rangle$. The wavefunction is thus written as :

$$\Psi^{JM} = \sum_{\lambda v j l} Y^{JM}_{jl}(\hat{r}_\lambda \hat{R}_\lambda) \; \chi_{\lambda v j}(\rho_m; \omega_\lambda) \; F^J_{\lambda v j l}(\rho) \tag{20}$$

2.5.3. *Transformation to Jacobi Space-Fixed coordinates*

Asymptotic functions are written in Jacobi coordinates

$$\Psi^{JM(\pm)}_{\lambda v j l} = Y^{JM}_{jl} \; (\hat{r}_\lambda \hat{R}_\lambda) \; \chi_{\lambda v j}(r_\lambda) \; h^{(\pm)}_{\lambda v j l}(R_\lambda) \tag{21}$$

are projected at fixed ρ on the rovibrational basis at ρ_m

$$F^{(\pm)}_{\lambda v' j' l'; \lambda v j l}(\rho) = \delta_{jj'} \; \delta_{ll'} \; \langle \chi_{\lambda v' j'}(\rho_m; \omega_\lambda) | \chi_{\lambda v j}(r_\lambda) h^{(\pm)}_{\lambda v j l}(R_\lambda) \rangle_{\omega_\lambda} \tag{22}$$

Then the matching of $F^J_{\lambda v j l}$ to $F^{(\pm)}$ permits to extract the S matrix with elements $S^J_{\lambda v j l \lambda' v' j' l'}$. Cross-sections are then given by the usual partial wave sum :

$$\sigma(\lambda v j \to \lambda' v' j') = \frac{\pi}{k^2_{\lambda v j}} \sum_J (2J+1) P^J(\lambda v j \to \lambda' v' j') \tag{23}$$

where $k_{\lambda v j}$ is the initial wavenumber and where the partial reaction probabilities are given by :

$$P^J(\lambda v j \to \lambda' v' j') = \sum_l \sum_{l'} |S^J_{\lambda v j l \lambda' v' j' l'}|^2 \tag{24}$$

3. Numerical implementation

3.1. COMPUTER CODES

A suite of computer codes permits to study the quantum dynamics of insertion reactions.

- TB computes essentially the basis of two-dimensional functions $\varphi_{k\Omega}(\rho_p; \theta\phi)$ and coupling matrix elements $H^{\Omega}_{kk'}(\rho_p; \rho)$ and the rovibrational functions χ_{vj}. This part is independent of the total energy E and of the total angular momentum J.
- TJ computes all the quantities which depend on the total angular momentum J but are independent of the total energy E, such as the couplings $\mathcal{C}^{J}_{k\Omega,k'\Omega'}(\rho_p; \rho)$ and the transformation matrices for the asymptotic analysis.
- TK solves the coupled equations (11) for each J and E using the Johnson-Manolopoulos [8] logarithmic-derivative propagator. It determines also the reactance K-matrix.
- TDCS computes the scattering matrix $S = (1+iK)/(1-iK)$ and the differential cross sections.
- TS computes the integral state-to-state cross sections.

3.2. TYPICAL COMPUTER REQUIREMENTS

In this section, we describe typical computer requirements for the $O(^1D) + H_2$ reaction. The TB, TJ and TK codes use about 2 GBytes of core memory. They have been implemented on a NEC-SX5 vector computer (8 Gflops peak performance per processor) at IDRIS/CNRS (Orsay, France). All the codes are efficiently vectorized and use the optimized BLAS and LAPACK linear algebra libraries.

The size of the PHH basis in the TB code varies from 1400 to 6200, depending on Ω and of the hyperradius ρ. Ω values range from 0 to 30 and the size of sectors ranges from $0.05a_0$ at small ρ $(2-8a_0)$ to $0.1a_0$ at large ρ $(8-14a_0)$. This results in the diagonalisation of several thousand matrices. The CPU time is 30 hours on a single processor, with a performance of 4 Gflops. The TJ code is executed for each partial wave but is independent of the total energy E.

The TK code is the most time-consuming part, because it has to be run for each J value (typically from 0 to 30). The time per partial wave varies from 30 sec. for $J = 0$ (310 channels) to 6 hours for $J = 30$ (4721 channels) for each energy, with a sustained performance of 7 Gflops.

The communication between the TB, TJ and TK codes is performed using a 2 GBytes file whose most part is dedicated to information necessary to build the coupled equations (11).

4. Selected results

4.1. $O(^1D) + H_2(X^1\Sigma_g^+) \to OH(X^2\Pi) + H$

4.1.1. *Introduction*

The $O(^1D)$ atom is a metastable species with a radiative lifetime of about 150 s. This species, with the ground $O(^3P)$ state of atomic oxygen, is an important constituent of several dilute media, such as the interstellar medium and the upper atmosphere. The rate constants of $O(^1D)$ + H_2, CH_4, H_2O and N_2O reactions is much larger than for $O(^3P)$ with the same species. Thus, even if $O(^1D)$ atoms are less abundant than $O(^3P)$, they play an important role in astrochemistry. They give highly reactive radical products as OH or NO which are for instance responsible for a significant reduction of the Earth's ozone layer. The $O(^1D)+H_2$ reaction is also important in combustion chemistry.

The $O(^1D)$ +H_2 reaction has been widely investigated both experimentally and theoretically and has become *the* prototype of insertion reactions [1, 10, 11, 12, 13, 14, 15, 16, 17, 18, 19, 20, 21, 22, 23, 24, 25, 26, 27, 28]. The combination of high resolution experiments and high accuracy of the theoretical calculations has allowed remarkable improvement in understanding of the reaction dynamics of this system. Many experimental results are available such as differential cross section (DCS), product translational energy distribution, excitation function and product rotational angular momentum polarization [15, 17, 18, 23]. Two complementary detailed experiments have recently been performed.

The group of X. Yang [25, 26] (Taiwan) has achieved a high angular and energy release resolution at a well defined collision energy of 56 meV. Yang and his coworkers used crossed molecular beams coupled with the Rydberg tagging TOF technique for the detection of the product H atoms. They obtained for the first time angle-resolved product translational energy distribution for each center-of-mass scattering angle.

In another experiment, M. Brouard and coworkers [28] (Oxford) searched a proof for the possible participation of electronic excited states in the reaction dynamics at higher collision energies. A significant fraction of the collisions takes place at energies higher than the threshold for reaction on the first excited surface. In this bulk experiment, Brouard and coworkers generated $O(^1D)$ atoms by photolysis of N_2O in a mixture of this gas with H_2. They used the Doppler-resolved polarized laser induced fluorescence technique to measure for the first time in this collision energy range the product $OH(v' = 3, 4)$ rotational distributions and $OH(v' = 3, 4)$ rotational alignment polarization parameters.

The large well depth in the ground electronic state ($\sim$ 7.2 eV) and the high exoergicity (1.9 eV) makes particularly difficult an exact QM study of the dynamics of this reaction. Theoretical studies often used the quasi-classical trajectory (QCT) method [12, 16, 18, 24]. Only a few quantum-mechanical (QM) studies have been reported. They are *exact* for the total angular momentum $J = 0$ but *approximate* for higher J. Total reaction probability has been calculated with a

time-dependent QM method for $J = 0$ [10, 13, 20, 21]. The total integral cross section (ICS) has been calculated with the centrifugal sudden [10] and capture model approaches [21]. A QM time-independent method has been reported but it used some approximations [22] such as absorbing potentials. Moreover, these approximate methods did not produce DCSs. Thus, the degree of comparison between theory and experiment was less good than for abstraction reactions, such as $F + H_2$ or $F + D_2$, where accurate QM dynamics has been performed [29, 9, 30]. Recently, we have performed the first accurate QM calculations for $J \neq 0$ and obtained converged DCSs for this reaction [27].

4.1.2. *Potential energy surfaces*

From a fundamental point of view, the $O(^1D)+H_2$ reaction adiabatically involves two different reaction pathways: the reactivity is dominated by the highly attractive ground $1^1A'$ state potential energy surface (PES) which is linked to the insertion mechanism. For the linear approach $C_{\infty v}$ (Figure 2a) the barrier is small (~0.02 eV). For the perpendicular approach C_{2v}, the PES is barrierless (figure 2b) and is characterized by a deep well (~7.2 eV) associated with the ground state of water, supporting many bound states, which is formed following the insertion of the excited atom into the H-H bond.
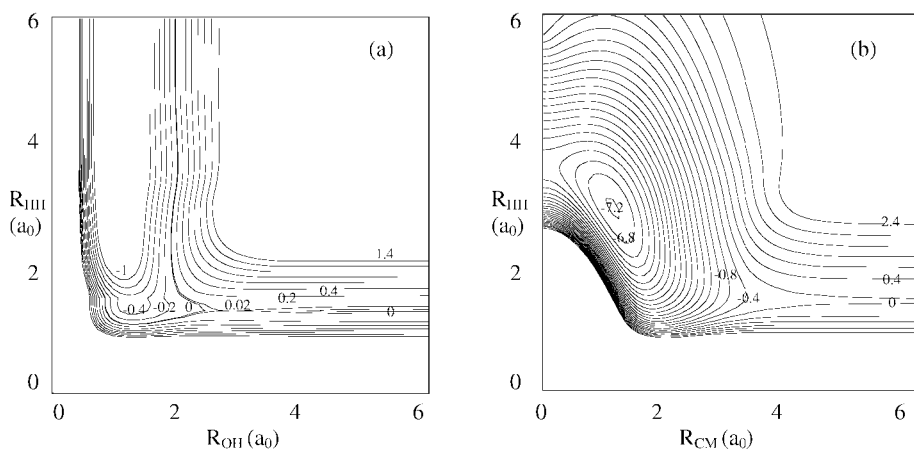
Figure 2. (a) Contour plots (in eV) of the $^1A'$ potential energy surface of OH_2 as a function of R_{HH} and R_{OH} at $\theta = 0°$. (b) Contour plots (in eV) of the $^1A'$ potential energy surface of OH_2 as a function of R_{HH} and $R_{CM} = R_{O\text{-}H2}$ at $\theta = 90°$. The origin of the energies is taken at the bottom of the $O(^1D) + H_2$ valley at infinite R_{CM} distance.

In contrast, the first excited $1^1A''$ PES (figure 3) presents a very high (~ 700 meV) barrier for the C_{2v} geometry (figure 3b), so the insertion mechanism cannot occur on this PES. Moreover the $C_{\infty v}$ collinear barrier (figure 3a) is small but significant (~ 100 meV). We therefore expected that the $1^1A''$ PES plays only a role in the reaction at collision energies higher than 100 meV and exhibits direct rebound dynamics reminiscent of the F + H_2 reaction.
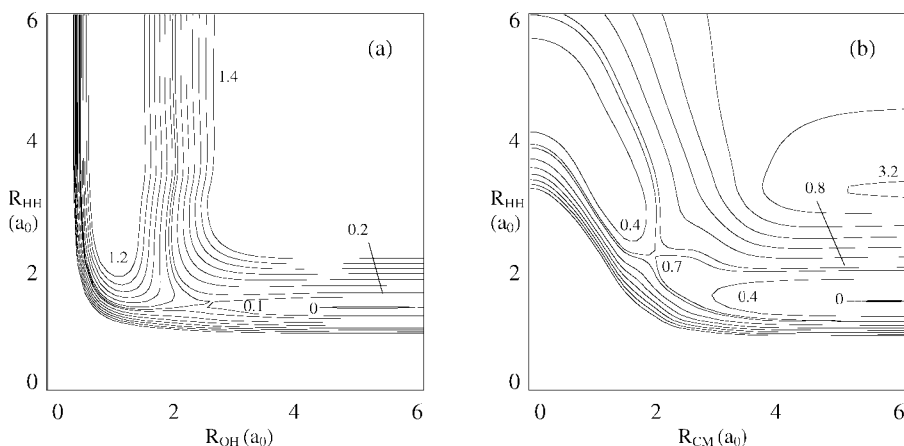
Figure 3. (a) Contour plots (in eV) of the $^1A''$ potential energy surface of OH_2 as a function of R_{HH} and R_{OH} at $\theta = 0°$. (b) Contour plots (in eV) of the $^1A''$ potential energy surface of OH_2 as a function of R_{HH} and $R_{CM} = R_{O-H2}$ at $\theta = 90°$. The origin of the energies is taken at the bottom of the $O(^1D)$ + H_2 valley at infinite R_{CM} distance.

Two sets of new high quality ab-initio PES have been proposed for both 1A' and $1^1A''$ states: the K PES [11, 12] and the DK PES [19]. They are very similar in topology but some little differences exist. For instance, the ground state H_2O well depth is smaller in the K PES than in the DK one. We used the DK PESs for scattering calculations.

4.1.3. *Convergence parameters*

The fundamentals of the QM time-independent methodology employed here can be found in Section 2. We just briefly give the relevant details for the studied reaction. QM calculations were performed for the $O(^1D)$ + $H_2(v = 0, j = 0, 1, 2)$ reaction at E_{col}=25, 56, 84, 100 and 137 meV collision energy on the ground $1^1A'$ DK PES. For the $J = 0$ partial wave, the scattering wavefunction was expanded on a basis

with 310 states dissociating at large hyperradius into the H_2 $(14, 12, 8, 2)$ and OH $(40, 38, 36, 33, 30, 28, 24, 21, 17, 11)$ rovibrational sets (this notation indicates the largest rotational level j for each vibrational manifold $v = 0, 1, \ldots$). There are three closed vibrational manifolds in the reactant arrangement and five in the product one. No restrictions were placed on the helicity quantum number Ω (the projection of the total angular momentum J of the system on each of the atom-diatom axes). Thus $\Omega_{max} = J$ and the number of coupled equations increases from 310 for $J = 0$ to 4505 for $J = 25$. Propagation goes from $\rho = 1.8$ to 14.2 a_0, including a total of 93 sectors into which the hyper-radius ρ has been divided. Two different sector sizes have been used: 0.1 a_0 from 1.8 to 8.0 a_0 and 0.2 a_0 from 8.0 to the asymptotic matching distance 14.2 a_0.
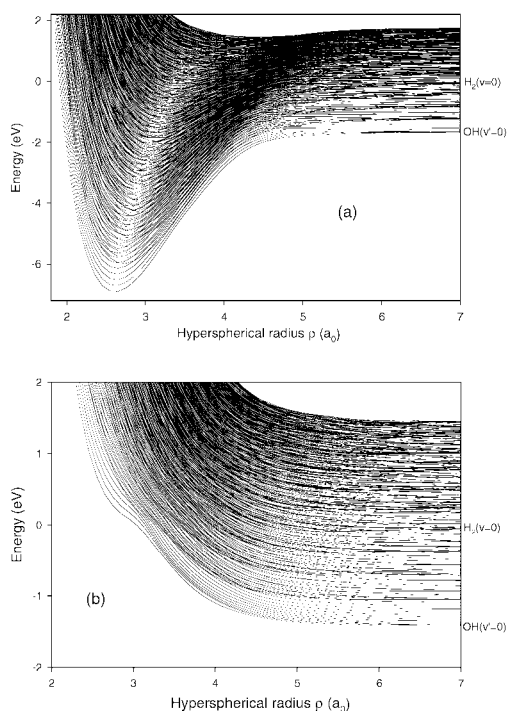
Figure 4. (a) OH_2 hyperspherical adiabatic energies for $^1A'$ as a function of hyperspherical radius ρ in a_0. (b) same for $^1A''$. The zero of the energy is taken at the asymptotic minimum of the $O(^1D) + H_2(v = 0, j = 0)$ channel.

QM calculations have been performed by J.F. Castillo [28] on the excited $1^1A''$ DK PES following a different hyperspherical coordinate scheme described in detail elsewhere [31]. In this case, the convergence of the calculations is less costly than on the ground state PES and only requires helicity quantum numbers $K = 0 - 3$. The number of coupled channels is small and constant equal to 294 for calculations at total angular momentum $J > 3$. Only partial waves with $J \leq 17$ were needed to obtain converged results.

4.1.4. *Hyperspherical adiabatic energies*

The H_2O hyperspherical adiabatic energies as a function of hyper-radius ρ for $J = 0$ are displayed in Figures 4a and 4b calculated respectively on the $1^1A'$ and $1^1A''$ PESs. They illustrate the large number of channels which have been considered in this study. At large hyperradius, the hyperspherical adiabatic energies goes to the atom-diatom energies, both $O(^1D) + H_2(v,j)$ and $OH(v',j') + H$. For the $1^1A'$ (Figure 4a), the most striking feature is the presence of a deep well. The lowest energy has a minimum of 7.2 eV relative to the $O(^1D) + H_2$ asymptote at $\rho=2.7$ a_0. In contrast, for the $1^1A''$ (Figure 4b) there is no well, such as the hyperspherical adiabatic states obtained for pure abstraction reactions ($H + H_2$, $F + H_2, \ldots$).

4.1.5. *Reaction probabilities*

In the following sections, except explicitly mentioned, all calculations have been performed on the $1^1A'$ PES.
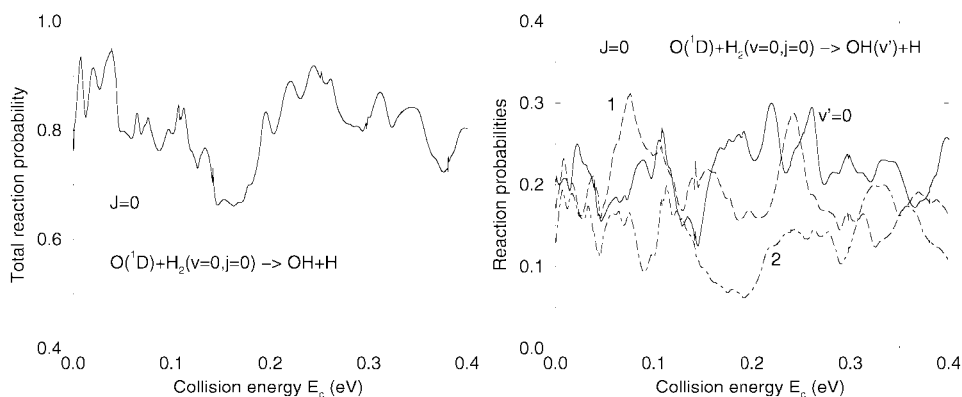
Figure 5. (a) Total reaction probabilities for $O(^1D) + H_2(v = 0, j = 0) \rightarrow OH + H$. (b) Vibrationally state-resolved probabilities for $O(^1D) + H_2(v = 0, j = 0) \rightarrow OH(v') + H$.

Figure 5a shows the total reaction probability for the reaction $O(^1D) + H_2(v = 0, j = 0) \rightarrow OH + H$ for the total angular momentum $J = 0$. This probability behaves similarly to the QM one computed by Gray et al [21] using a time-dependent method. There is no collision energy threshold as a consequence of the absence of an entrance barrier in the PES for the C_{2v} geometry. The total reaction probability presents smooth undulations. They average the more numerous structures obtained in the vibrationaly state-resolved reaction probabilities (figure 5b).

4.1.6. *Opacity and excitation functions*

We have also computed reaction probabilities for $H_2(v = 0, j = 0)$ and $J > 0$. The opacity functions $P(J)$ (total reaction probability as a function of total angular momentum J at a fixed energy) are plotted in figure 6 for four collision energies (25, 56, 84 and 100 meV).
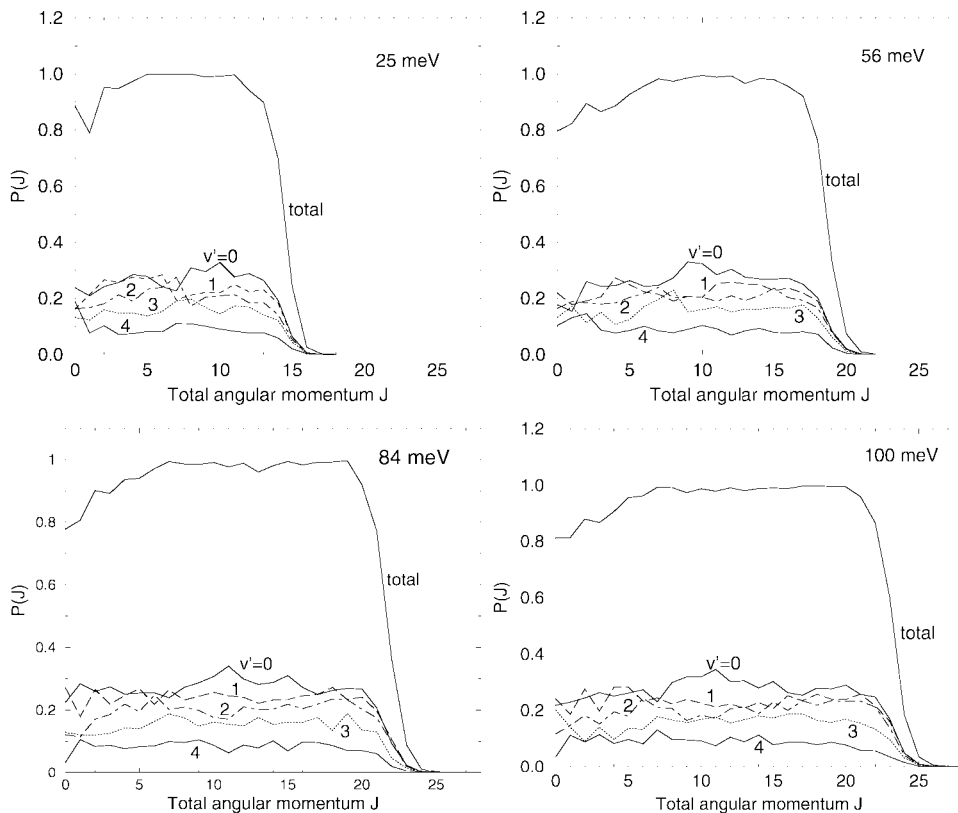
Figure 6. Reaction probabilities for $O(^1D) + H_2(v = 0, j = 0) \rightarrow OH(v') + H$ as a function of the total angular momentum J at 25, 56, 84 and 100 meV.

At all energies, $P(J)$ increases slowly with J and reaches its largest value (close to one) for $J = 6$, keeps this value up to a J_{max} (which is shifted towards larger values of J with increasing collision energy) and then decreases rapidly above J_{max} when J increases. The vibrationally state-resolved reaction probabilities $P(J, v')$ keep the same order :

$$P(J, v' = 0) > P(J, v' = 1) > P(J, v' = 2) > P(J, v' = 3) > P(J, v' = 4).$$

This non-inverted behaviour is in contrast with abstraction reactions such as F + H_2. Another difference with this latter system is the presence of many small peaks in $P(J, v')$ and even in $P(J)$.

Figure 7 shows the excitation function (the total ICS as a function of the collision energy). The cross section decreases rapidly with increasing energy. This behavior is typical for a reaction without any barrier.
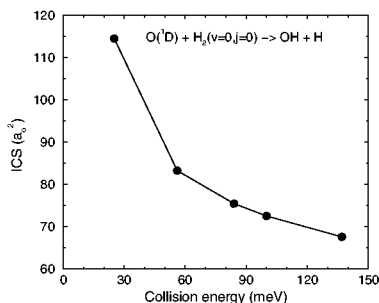
Figure 7. Total reaction cross-section for $O(^1D)$ + $H_2(v = 0, j = 0) \rightarrow OH + H$ as a function of collision energy.

The excitation function obtained using the $1^1A''$ PES is totally different, showing a threshold at about 100 meV and then a regular increase when energy increases [32].

4.1.7. *Vibrational and rotational distributions*

Figure 8 shows for the reaction $O(^1D) + H_2(v = 0, j = 0) \rightarrow OH(v', j') + H$ reaction the vibrational distribution (ICS as a function of the product vibrational quantum number v' for five collision energies (25, 56, 84, 100 and 137 meV). At all energies, the most populated vibrational level is $v' = 0$. ICS decreases when the product vibrational quantum number v' increases. This decrease reflects the diminution of open rotational states in a given vibrational manifold. For all energies, the distributions are vibrationally cold and these non-inverted vibrational populations are in sharp contrast with those computed for abstraction reactions such as F + $H_2 \rightarrow$ FH + H [29] and F + $D_2 \rightarrow$ FD + D [9] abstraction reactions which show a vibrational population inversion.
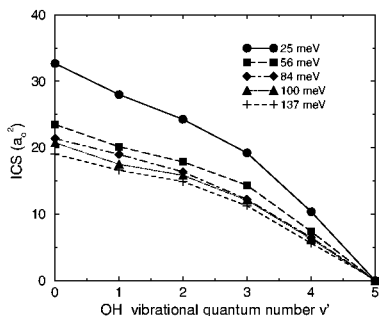
Figure 8. Integral cross sections vs final vibrational quantum number v' for $O(^1D) + H_2(v = 0, j = 0) \rightarrow OH(v') + H$ at the five collision energies 25, 56, 84, 100, and 137 meV.

This vibrational distribution for abstraction reactions is similar to that obtained on the first excited state surface, $1^1A''$ (not shown here). There is a strong population inversion and only $v' = 3, 4$ have appreciable cross sections.

Rotational distributions (QM vibrationally state-resolved ICSs as a function of the product rotational quantum number j') for the $O(^1D)+H_2(v = 0, j = 0) \rightarrow OH(v', j') + H$ reaction calculated at the 84 meV collision energy are displayed in Figure 9.
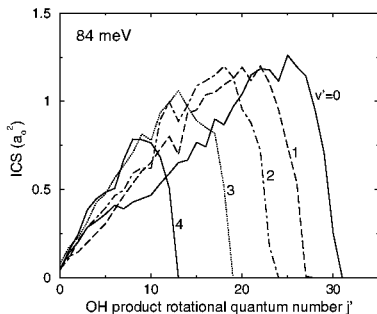
Figure 9. Rotational integral cross sections for $O(^1D) + H_2(v = 0, j = 0) \rightarrow OH(v', j') + H$ as a function of final rotational quantum number j' at 84 meV.

For each product vibrational state v', ICS increases with j' and when the energy of the product states reaches the total energy available, it decreases abruptly to zero. This typical shape of ICS suggests the existence of a long-lived intermediate complex during the collision and may therefore be considered as a signature of the insertion mechanism. A similar shape is found at other collision energies and for other insertion reactions.

Figure 10 also shows the results for $O(^1D)+H_2(v = 0, j = 1)$ at 84 meV and the influence of the initial rotational excitation of H_2 for an insertion reaction.
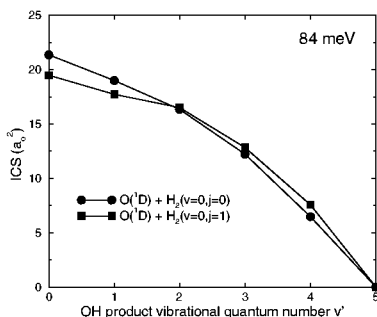
Figure 10. Integral cross sections vs final vibrational quantum number v' for $O(^1D) + H_2(v = 0, j = 0) \rightarrow OH(v') + H$ and $O(^1D) + H_2(v = 0, j = 1) \rightarrow OH(v') + H$ at 84 meV.

Vibrational distributions for each $j = 0$ and $j = 1$ are similar. However the reactivity is not exactly the same for these two initial rotational states. The vibrational distribution is slightly hotter for $j = 1$. More precisely the ratio $ICS(j_i=1)/ICS(j_i=0)$ is below 1 for $v' = 0$ and $v' = 1$, is equal to 1 for $v' = 2$ and above 1 for $v' = 3$ and $v' = 4$. Rotational distributions for $j = 0$ and $j = 1$ are

similar at all collision energies although the structures are of course not exactly the same. We also find that the effect of initial H_2 rotation is small for opacity functions.

In conclusion, when the internal rotation molecular state of H_2 going from $j = 0$ to $j = 1$, changes are minor for probabilities, vibrational and rotational distributions.

4.1.8. *Differential cross sections*

Figure 11 shows total DCSs for $O(^1D) + H_2(v = 0, j = 0) \rightarrow OH + H$ as a function of the center of mass scattering angle at 25, 56, 84, 100 and 137 meV.
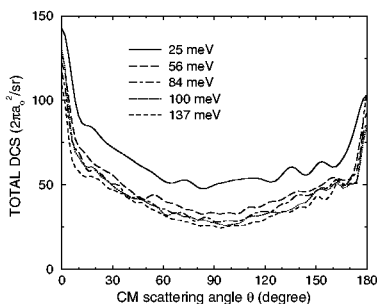
Figure 11. Total differential cross sections versus center-of-mass scattering angle θ for $O(^1D) + H_2(v = 0, j = 0) \rightarrow OH + H$ at the five collision energies 25, 56, 84, 100, and 137 meV.

We see that for each energy the total DCS has a roughly forward-backward symmetry which is a characteristic of a reaction with an intermediate complex [2]. However the full symmetry is not obtained and a slight preference for forward scattering is found. Then this insertion reaction is not purely statistical. An interesting point is related to the forward/backward peak ratio which is always larger than one for all energies.

Figure 12 shows the vibrationally-resolved DCSs and exhibits also another important feature. At all energies, we see that the forward and backward scattering and in particular the forward and backward peaks are not vibrationally specific because all product vibrational quantum number v' contribute with the largest contribution to the forward peak from $v' = 0$. This is in sharp contrast with abstraction reactions. Indeed in the $F + H_2$ ($F + D_2$) reaction, the total DCS, although preferentially backward, has a small forward peak which is due only to $v' = 3$ ($v' = 4$). Finally the relative magnitude of the vibrationally state-resolved DCSs is almost the same at all scattering angles, with a decrease when increasing v' and undulations are more pronounced than in total DCSs. Total DCS obtained with the $1^1A''$ PES (not shown here) are purely backward peaked and this behaviour is that of an abstraction mechanism. The main difference with the $F+H_2$ reaction is that OH products are not formed in the forward direction.

The effect of initial reagent molecular rotation excitation on DCSs is shown in figure 13 at 25 and 84 meV. Sideways scattering are similar for $j = 0$ and $j = 1$. Most dramatic changes appear in DCS for forward scattering (0-20 °) and
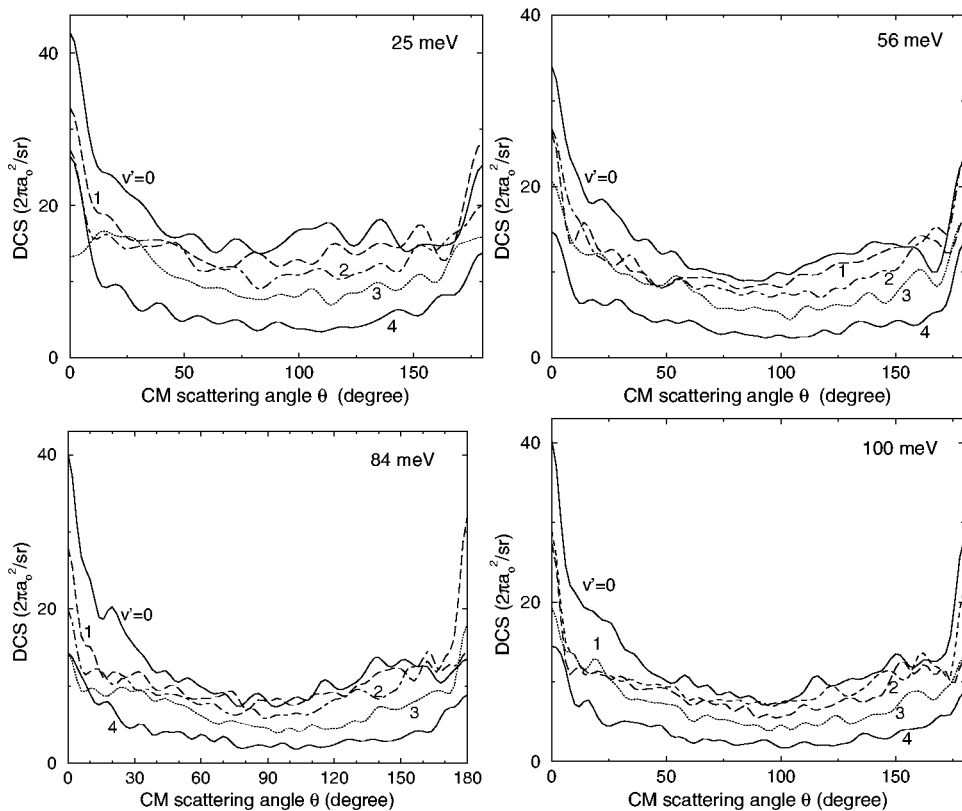
Figure 12.   Vibrationally resolved differential cross sections versus center-of-mass scattering angle θ for $O(^1D) + H_2(v = 0, j = 0) \rightarrow OH(v') + H$ at 25, 56, 84 and 100 meV.
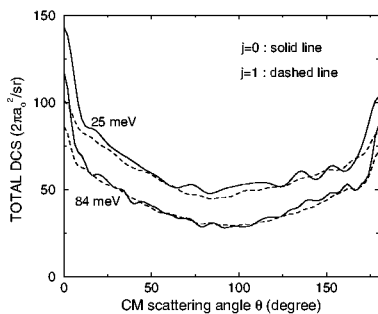
Figure 13.   Total differential cross sections versus center-of-mass scattering angle θ for $O(^1D) + H_2(v = 0, j = 0) \rightarrow OH + H$ and $O(^1D) + H_2(v = 0, j = 1) \rightarrow OH + H$ at the two collision energies 25 and 84 meV.

backward scattering (160-180 °). Forward and backward peaks become smaller and broader when increasing j. We find the same principal features at other collision energies. The QM degree of polarisation (i.e. the DCS at 90 degrees with respect to 0 degree) is also increased by initial rotational excitation. Whereas increase in j has no appreciable influence on the ICSs, rotational excitation of H_2 molecules plays a significant role for angular distributions.

4.1.9. *Comparison with experiments*

We also present some comparisons with two recent experiments. First, our QM results are compared with Yang's experiments [25, 26]. This very high resolution experiment is performed at 56 meV for $H_2(v = 0, j = 0)$, a collision energy where the reactivity on the $1^1A''$ surface is expected negligible. So the mechanism involved in the reaction should be only insertion.
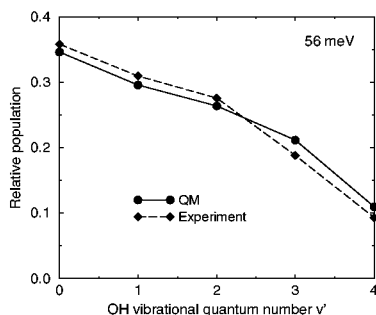
Figure 14. Comparison between the QM and experimental vibrational distributions for $O(^1D)$ + $H_2(v = 0, j = 0) \rightarrow OH(v')$ + H at 56 meV.

Figure 14 shows the comparison between the QM vibrationally state-resolved ICSs calculated on the ground state $1^1A'$ PES with the experimental data. The agreement between the experimental and QM v' state-resolved ICSs is good. For $v' = 0, 1, 2$ QM results are slightly smaller than the experimental values, whereas it is the reverse for $v' = 3, 4$. QM calculations therefore predict a somewhat hotter vibrational distribution of the OH products.

Figure 15 compares the QM and experimental rotational distributions.

A good agreement is found with the experimental data. However, the QM distributions are somewhat broader for $v' = 0$ and $v' = 1$. For all v', except $v' = 3$, the maximum peak (just before the fall) is underestimated by QM results.

The QM total DCS is compared in Figure 16 with the corresponding experimental DCS. It should be recalled that the derivation of the experimental DCS from the raw experimental data yields some uncertainties and experimental data include some degree of angular smearing, whereas the QM curves are obtained without any smoothing. QM DCS therefore appears in good agreement with the experimental angular distribution, although total QM DCS presents sharp peaks at 0° and 180°. Similar results are found for the vibrationally state-resolved DCSs.

Figure 17 shows the comparison between QM (a) and experimental (b) total product translational energy distributions $P(E'_t)$ in the center-of-mass frame.
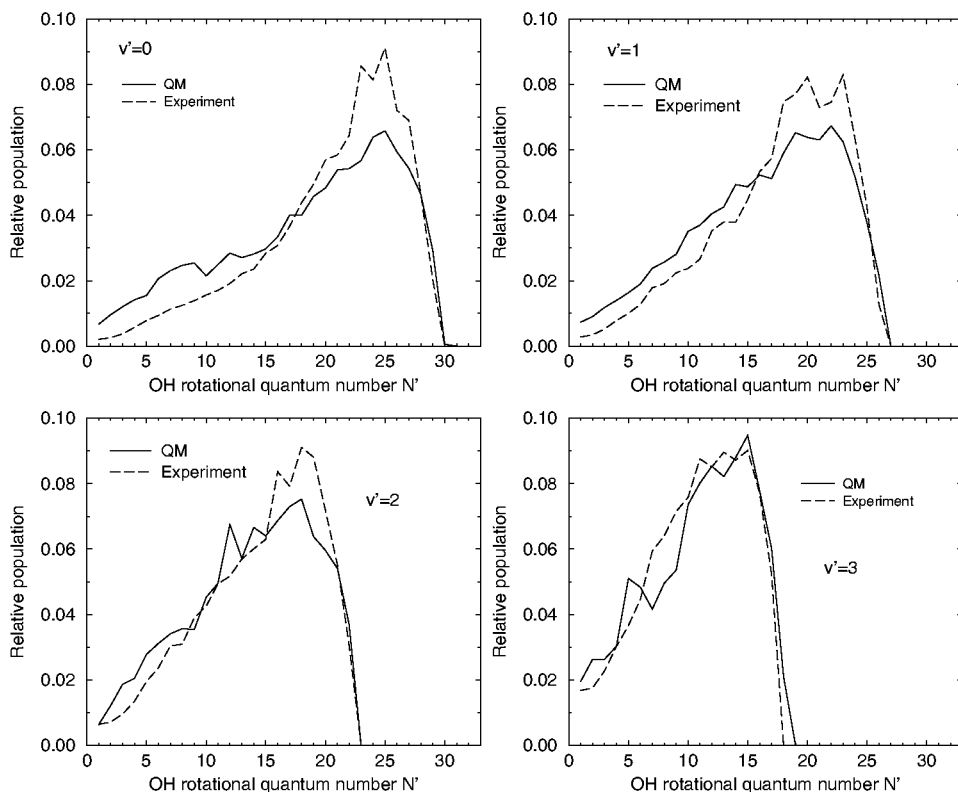
Figure 15. Comparison between the QM and experimental rotational distributions for $O(^1D) + H_2(v = 0, j = 0) \rightarrow OH(v') + H$ at 56 meV for $v' = 0, 1, 2$ and 3.
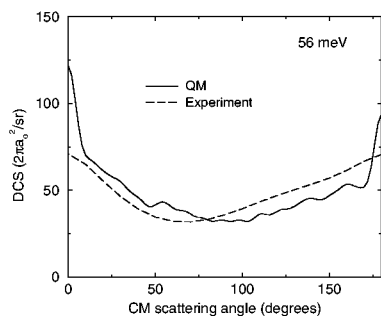
Figure 16. Comparison between the QM and experimental total differential cross section for $O(^1D) + H_2(v = 0, j = 0) \rightarrow OH + H$ at 56 meV.

It is clear that a very good agreement is obtained. However, the QM distribution is overestimated in the high energy part (14000-16000 cm^{-1}) which corresponds

to the production of only OH($v' = 0$) in low rotational states

In a recent work [33], we have compared the most detailed observable, QM angle- and (quasi)state-resolved product translational energy distribution P(E'$_t$, θ), with the experimental ones at three different angles. The agreement is excellent at $\theta = 90°$ and for other angles around it. So the sideways scattering is well reproduced by QM results. The largest discrepancies concern the forward and to a smaller extent the backward scattering. Once more the QM distribution overestimates the forward and backward scattering. A close inspection reveals that the reactivity is overestimated in the high energy part corresponding to the lower rotational states of OH($v' = 0$).
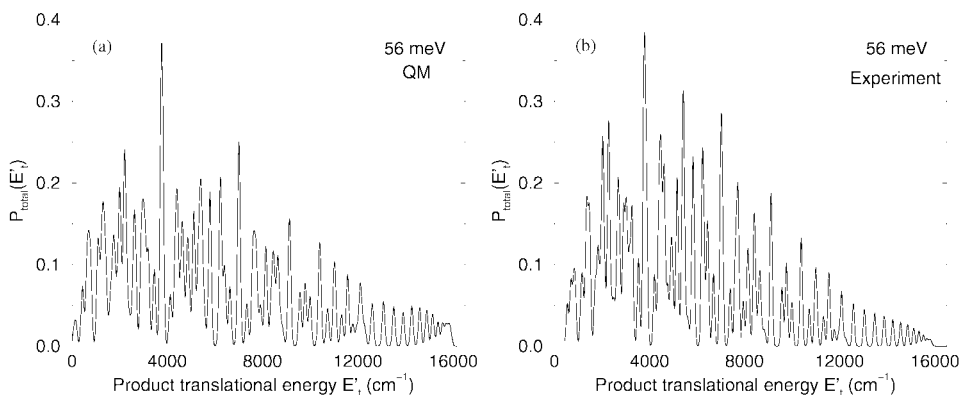
Figure 17. Comparison between the QM (a) and experimental (b) total product translational energy distributions for O(^{1}D) + H$_2$($v = 0, j = 0$) at 56 meV collision energy.

We have also studied at higher collision energy (> 100 meV) the influence of the first electronic excited $1^1A''$ state on the dynamics [28], and especially on rotational distributions for OH($v' = 4$) which have been measured by Brouard and co-workers. The agreement between QM and experimental results is largely improved by considering contributions on both the $1^1A''$ and $1^1A'$ PES. When comparing the OH rotational angular momentum alignment parameters [28], we found yet again that the best agreement is obtained when we consider both contributions.

In conclusion, at a collision energy of 56 meV, the overall good agreement obtained between QM and experimental results indicate that it is not necessary to invoke the contribution of the first excited $1^1A''$ PES to the reactivity. In contrast, at higher energy, above 100 meV, the $1^1A''$ PES plays a crucial role and we have taken it into acount to model quantitatively the experimental results. Moreover, comparisons indicate that the DK PES is accurate enough to reproduce the most detailed experimental observables.

4.2. OTHER INSERTION REACTIONS

4.2.1. $N(^2D) + H_2(X^1\Sigma_g^+) \to NH(X^3\Sigma^-) + H$

The $N(^2D) + H_2$ reaction has been less studied than $O(^1D) + H_2$. However atomic nitrogen is of fundamental interest in combustion and astrophysical and atmospheric chemistry. For instance, reactions involving this species with simple hydrocarbons play a role in the atmosphere of Saturn's moon Titan. The $N(^2D) + H_2$ reaction is perhaps a better prototype of an insertion reaction than $O(^1D)+H_2$. Here, there is no abstraction mechanism due to an excited PES [34].

An accurate ab-initio PES for the NH_2 ground state has been computed at the second-order CI level [35]. This $1^2A''$ surface has a deep potential well of 5.48 eV for a C_{2v} geometry with a HNH angle of 102.7° and a NH bond length of $1.94a_0$, corresponding to stable $NH_2(1^2B_1)$. The insertion C_{2v} barrier is 83.5 meV and the collinear $C_{\infty v}$ one is 200 meV. The dynamics may therefore be different from the $O(^1D) + H_2$ reaction,

In a recent crossed molecular beam experiment. Alagia et al. [36] measured the total DCS and product translational energy distribution for the $N(^2D)+D_2$ reaction at 165 and 220 meV collision energies. They found an exact forward-backward symmetry which is consistent with an insertion mechanism and the existence of an intermediate complex. Using a laser-induced fluorescence technique, Umemoto [37] measured nascent rotational distributions and concluded that only the insertion mechanism is important in the $N(^2D)+H_2$ reaction at low and medium energy. This result has been recently confirmed by the measure of the product vibrational population for $NH(v' = 0, 1, 2, 3, 4)$ [38].
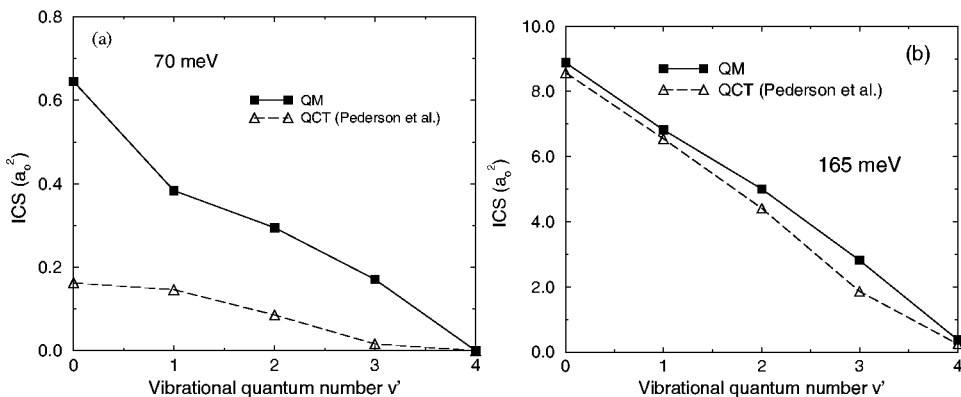
Figure 18.   (a) Integral cross sections vs final vibrational quantum number v' for $N(^2D)$ + $H_2(v = 0, j = 0) \to NH(v') + H$ at 70 meV. (b) The same for 165 meV.

For the $J = 0$ partial wave, the scattering wavefunction is expanded on a basis with 217 states dissociating at large hyperradius into the NH $(35, 32, 30, 27, 24, 20, 16, 11)$ and H_2 $(12, 8, 2)$ rovibrational sets (this notation indicates the largest rotational level j for each vibrational manifold $v = 0, 1, \dots$). There are two closed vibrational manifolds in the reactant arrangement and three in the product one. This yields 2917 coupled equations for the highest partial wave ($J = 26$). We computed integral cross sections (ICS) for the reaction N + $H_2(v = 0, j = 0) \rightarrow NH(v', j')$ + H reaction for several collision energies in the range 70-165 meV [40].

The ICS as a function of the product quantum number v' at two energies is presented in figure 18. The most populated vibrational level is $v' = 0$, with a decrease which reflects the diminution of open rotational states in a given vibrational manifold This indirect reaction yields vibrationally cold products. These non-inverted vibrational populations agree to Umemoto's experimental results [38]. The QM results are consistently greater than the QCT results of Schatz et al. [35]. the difference increasing when the kinetic energy decreases because of a tunnelling effect in the entrance arrangement. At 70 meV, the QM total reaction ICS is about four times larger than the QCT one. The low energy collision dynamics is therefore influenced by quantum effects, such as tunnelling and zero point vibrational energy effects. Rotational distributions (not shown here) agree with those measured by Umemoto et al. [37] and show a similar shape to those obtained for $O(^1D)+H_2$. Moreover, QM predictions for laboratory angular distribution and time-of-flight spectra are in a very good agreement with those derived from Casavecchia's experiments [39]. This is not the case for QCT results. QM DCSs present a forward/backward symmetry as in experiments. A comparison between experimental, QCT and QM results [39] has pointed out a quantum effect, possibly the effect of tunneling through the combined potential and centrifugal barrier.
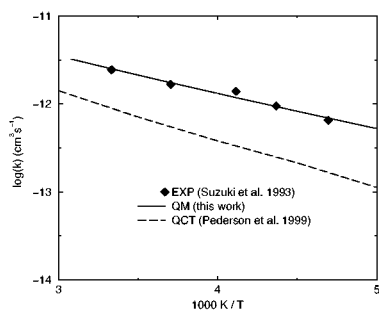
Figure 19. Comparison between the QM (solid line), QCT (dashed line) [Pederson et al. 1999] and experimental [Suzuki et al. 1993] rate coefficients for $N(^2D)$ + H_2.

We have also calculated the reaction rate constant (figure 19). We have computed the total integral cross section for $N(^2D)$ + H_2 at four collision energies (70, 110, 137 and 165 meV). The threshold is 50 meV for this reaction. We found that the total integral cross sections for $j = 0$ and $j = 1$ at 165 meV are identical (23.89 a_0^2 vs 23.90 a_0^2) and QCT calculations [35] show that the integral cross sections for $j = 0$ and $j = 1$ are similar at all collision energies. So we assume that the total

cross sections are independent of the inital state j of H_2. The excitation function is very smooth and this allows a spline interpolation. The rate constant is then obtained by averaging the calculated and interpolated cross sections over collision energies with a Boltzmann distribution. Our QM rate constant agrees very well with the experimental one [41], in contrast with QCT calculations [35] which yield a much smaller value.

Finally, these comparisons show that QM dynamics performed on the NH_2 ground state $1^2A''$ PES reproduces qualitatively both average and more detailed experimental results. Dynamics can therefore be described by using only the ground PES.

4.2.2. $C(^1D) + H_2(X^1\Sigma_g^+) \rightarrow CH(X^2\Pi) + H$

We have performed the first quantum reactive scattering calculations for the $C(^1D)$ + $H_2 \rightarrow CH$ + H reaction on a recent *ab initio* PES [46] calculated in our group. The C_{2v} geometry shows no barrier and a deep well (4.32 eV) corresponding to the 1^1A_1 electronic state of the CH_2 species. In contrast the collinear barrier is very large (0.535 eV). This reaction is similar to the $O(^1D) + H_2$ reaction because no barrier occurs for the perpendicular geometry. However there are three main differences, the well is less deep, the collinear barrier is larger and the exothermicity is much smaller (0.273 eV).

For total angular momentum $J = 0$, the scattering wave function is expanded on a basis of 289 states dissociating at large hyperradius into the $H_2(18,16,12,10,6)$ and CH(39,36,34,31,28,25,22,17,12) rovibrational sets (this notation indicates the largest rotational level j for each vibrational manifold $v = 0-4$ for H_2 and $v' = 0-8$ for CH). The number of coupled equations increases from 289 for $J = 0$ to 4210 for $J = 30$.

Figure 20 shows total and vibrationally state-resolved reaction probabilities as a function of collision energy at total angular momentum $J = 0$ in the 0-0.5 eV collision energy range. These probabilities exhibit a dense resonance structure especially at lower energies corresponding to quantum resonances associated with the deep CH_2 well in the PES. These resonances are seen for the first time for a neutral atom + H_2 reaction. Indeed we find them rather in ionic reactions, such as He + H_2^+ [42], Ne + H_2^+ [43] and N^+ + H_2 [44, 45]. A deeper study of these resonances is currently under way in our group. Vibrational and rotational distributions (not shown here) are similar to those obtained for $O(^1D) + H_2$.

QM total and vibrationally state-resolved DCSs are forward/backward peaked as for the two previous studied insertion reactions. First comparisons between QM and recent crossed beam experimental results at 80 meV lead to a fairly good agreement for laboratory angular distributions but a significant disagreement in time-of-flight spectra for some angles. This suggests that there is need to invoke a contribution from the second excited PES. This PES exhibits very high barriers at linear and perpendicular geometries, but no barrier at 60°. We are currently
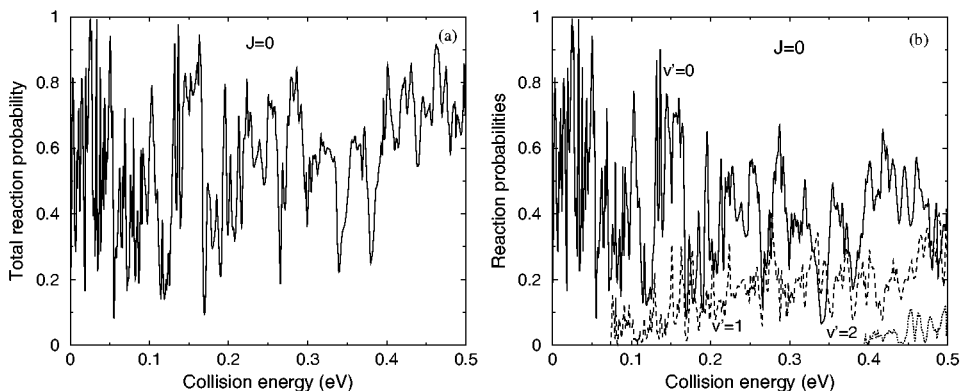
Figure 20. (a) Total reaction probabilities for $C(^1D) + H_2(v = 0, j = 0) \rightarrow CH + H$. (b) Vibrationally state-resolved probabilities for $C(^1D) + H_2(v = 0, j = 0) \rightarrow CH(v') + H$.

performing dynamical calculations on this latter PES, in order to improve the agreement with experiments.

Comparisons between our QM results and QCT results have also allowed a significant improvement of the QCT method by using the gaussian-weighted binning procedure instead of the usual histogramatic binning procedure [47].

5. Summary and prospects

Accurate quantum dynamical studies of insertion reactions involving H_2 molecules are now feasible for a single potential energy surface and we have obtained the same degree of comparison with experiment as for abstraction reactions ten years ago. The computational effort is however much larger, $O + H_2$ being roughly 100 times more expensive than $F + H_2$.

We have described in this contribution the quantum dynamics of three atom-H_2 insertion reactions $O(^1D) + H_2$, $N(^2D) + H_2$ and $C(^1D) + H_2$. The common features which appear are :

- Vibrational distributions are similar and decrease regularly with v'.
- Rotational distributions for a given v' increase regularly with j' until the limit dictated by energy conservation is reached.
- Center of mass differential cross sections (presented here only for $O(^1D) + H_2$) present a quasi forward-backward symmetry and small undulations. The degree of polarisation (ratio of DCS for forward/sideways or backward/sideways) is high (~ 3) for initial rotational state $j = 0$ and decreases with j. The for-

ward and backward peaks are present for all final vibrational states v' in contrast to the F + H_2 reaction.

However, some features are specific for each reaction :

- For $O(^1D)$ + H_2, the excited $^1A''$ surface has to be considered for energies larger than 100 meV.
- For $N(^2D)$ + H_2, the tunneling effect is very important because of the barrier in the ground electronic state.
- For $C(^1D)$ + H_2, we have found a very dense resonance structure in reaction probabilties.

In the future, we plan to investigate isotopic H → D effects for the previous insertion reactions and non adiabatic effects involving couplings between potential energy surfaces. Another fruitful route is the study of alkali-dialkali collisions for which the insertion mechanism is possible even at ultra-low temperatures [48].

References

1. Casavecchia P. (2000) Chemical reaction dynamics with molecular beams *Rep. Prog. Phys.* **63**, 355-514.
2. Levine R.D. and Bernstein R.B. (1987) *Molecular Reaction Dynamics and Chemical Reactivity*, Oxford University Press, New York.
3. Pack R.T. and Parker G.A. (1987) Quantum reactive scattering in three dimensions using hypersph Quantum reactive scattering in three dimensions using hyperspherical (APH) coordinates. Theory *J. Chem. Phys.* **87**, 3888-3921.
4. Launay J.-M. and Le Dourneuf M. (1989) Hyperspherical close–coupling calculation of integral cross–sections for the reaction H + H_2 → H_2 + H *Chem. Phys. Lett.* **163** 178-188.
5. Whitten R.C. and Smith F.T. (1968) *J. Math. Phys.* **9**, 1103.
6. Launay J.-M. and Le Dourneuf M. (1990) Quantum-mechanical calculation of integral cross sections for the reaction F + $H_2(v = 0, j = 0)$ → $FH(v' = 2, 3, j')$ + H by the hyperspherical method *Chem. Phys. Lett.* **169**, 473-481.
7. Lepetit B., Launay J.-M. and M. Le Dourneuf (1986) Quantum mechanical study of electronically non–adiabatic collinear reactions. I. Hyperspherical description of the electronuclear dynamics *Chem. Phys.* **106**, 103-110.
8. Manolopoulos D.E. (1986) An improved log derivative method for inelastic scattering *J. Chem. Phys.* **85**, 6425-6429.
9. Honvault P. and Launay J.-M. (1998) Quantum mechanical study of the F + D_2 → DF + D reaction, *Chem. Phys. Letters* **287**, 270 274.

10. Peng T., Zhang D.H., Zhang J.Z.H., and Schinke R. (1996) Reaction of $O(^1D)$ + $H_2 \to OH$ + H. A three-dimensional quantum dynamics study, *Chem. Phys. Lett.* **248**, 37-42.

11. Ho T.–S., Hollebeek T., Rabitz H., Harding L.B., and Schatz G.C. (1996) A global H_2O potential energy surface for the reaction $O(^1D)$ + $H_2 \to OH$ + H, *J. Chem. Phys.* **105**, 10472-10486.

12. Schatz G.C., Papaioannou A., Pederson L.A., Harding L.B., Hollebeek T., Ho T.S., and Rabitz H (1997) A global A-state potential surface for H_2O: Influence of excited states on the $O(^1D)$ + H_2 reaction, *J. Chem. Phys.* **107**, 2340-2350.

13. Dai J. (1997) Quantum state-resolved dynamics study for the reaction $O(^1D)$ + $H_2 \to OH$ + H (J = 0), *J. Chem. Phys.* **107**, 4934-4942.

14. Schatz G.C., Pederson L.A., and Kuntz P.J. (1997) Adiabatic and non-adiabatic dynamics studies of $O(^1D)$ + $H_2 \to OH$ + H, *Faraday Discuss.* **108**, 357-374.

15. Alexander A.J., Aoiz F.J., Brouard M., Burak I., Fujimura Y., Short J., and Simons J.P. (1996) An experimental and quasiclassical study of the product state resolved stereodynamics of the reaction $O(^1D_2)$ + H_2(v=0) $\to$ OH ($v = 0, N, f$) + H, *Chem. Phys. Lett.* **262**, 589-597.

16. Alexander A.J., Aoiz F.J., Bañares L., Brouard M., Herrero V.J., and Simons J.P. (1997) Classical reaction probabilities, cross sections and rate constants for the $O(^1D)$ + $H_2 \to OH$ + H reaction, *Chem. Phys. Lett.* **278**, 313-324.

17. Hsu Y. T., Wang J. H., and Liu K. (1997) Reaction dynamics of $O(^1D)$ + H_2, D_2, and HD: Direct evidence for the elusive abstraction pathway and the estimation of its branching, *J. Chem. Phys.* **107**, 2351-2356.

18. Alagia M., Balucani N., Cartechini L., Casavecchia P., van Kleef E.H., Volpi G.G., Kuntz P.J., and Sloan J.J. (1998) Crossed molecular beams and quasiclassical trajectory studies of the reaction $O(^1D)$ + $H_2(D_2)$, *J. Chem. Phys.* **108**, 6698-6708.

19. Dobbyn A.J. and Knowles P. (1997) A comparative study of methods for describing non-adiabatic coupling: diabatic representation of the $^1\Sigma^+/^1\Pi$ HOH and HHO conical intersections, *Mol. Phys.* **91** 1107-1124 ; Dobbyn A.J. and Knowles P. (1998) General Discussion, *Faraday Discuss.* **110**, 247.

20. Balint–Kurti G.G., González A.I., Goldfield E.M., and Gray S.K. (1998) Quantum reactive scattering of $O(^1D)$ + H_2 and $O(^1D)$ + HD, *Faraday Discuss.* **110**, 169-184.

21. Gray S.K., Goldfield E.M., Schatz G.C., and Balint-Kurti G.G. (1999) Helicity decoupled quantum dynamics and capture model cross sections and rate constants for $O(^1D)$ + $H_2 \to OH$ + H *Phys. Chem. Chem. Phys.* **1**, 1141-1149.

22. Drukker K. and Schatz G.C. (1999) Quantum scattering study of electronic Coriolis and nonadiabatic coupling effects in $O(^1D)$ + $H_2 \to OH$ + H, *J. Chem Phys.* **111**, 2451-2463.

23. Lee S.H. and Liu K. (1999) Effect of reagent rotation in $O(^1D)$ + H_2 ($v = 0, j$): A sensitive probe of the accuracy of the *ab initio* excited surfaces ?, *J. Chem. Phys.* **111**, 4351-4352.

24. Alexander A.J., Aoiz F.J., Bañares L., Brouard M., and Simons J.P. (2000) Product rotational angular momentum polarization in the reaction $O(^1D_2)$ + $H_2 \to OH$ + H, *Phys. Chem. Chem. Phys.* **2**, 571-581.

25. Liu X., Lin J.J., Harich S., and Yang X. (2000) Quantum state specific dynamics for the $O(^1D)$ + HD $\to$ OD + H reaction, *J. Chem. Phys.* **113**, 1325-1328.

26. Liu X., Lin J.J., Harich S., Schatz G.C., and Yang X. (2000) A Quantum State-Resolved Insertion Reaction: $O(^1D)$ + H_2(J = 0) $\to$ OH(v, N) + $H(^2S)$, *Science* **289**, 1536-1538.

27. Honvault P. and Launay J.-M. (2001) A quantum-mechanical study of the dynamics of the $O(^1D)$ + $H_2 \to OH$ + H insertion reaction, *J. Chem. Phys.* **114**, 1057-1059.

28. Aoiz F.J., Bañares L., Castillo J.F., Brouard M., Denzer W., Vallance C., Honvault P., Launay J.-M., Dobbyn A.J. and Knowles P. (2001) Insertion and Abstraction

Pathways in the Reaction $O(^1D_2) + H_2 \rightarrow OH + H$, *Phys. Rev. Lett.* **86**, 1729-1732.

29. Castillo J.F., Hartke B., Werner H.-J., Aoiz F.J., Banares L., and Martinez-Haya B. (1998) Quantum mechanical and quasiclassical simulations of molecular beam experiments for the $F + H_2 \rightarrow HF + H$ reaction on two *ab initio* potential energy surfaces, *J. Chem. Phys.* **109**, 7224-7237.

30. Martinez-Haya B., Aoiz F.J., Banares L., Honvault P., and Launay J.-M. (1999) Quantum mechanical and quasiclassical trajectory study of state-to-state differential cross sections for the $F + D_2 \rightarrow DF + D$ reaction in the center-of-mass and laboratory frames, *Phys. Chem. Chem. Phys.* **1**, 3415-3429.

31. Skouteris D., Castillo J.F., and Manolopoulos D.E. (2000) ABC: a quantum reactive scattering program, *Comput. Phys. Commun.* **133**, 128-135.

32. Castillo J.F., private communication.

33. Aoiz F.J., Bañares L., Castillo J.F., Herrero V.J., Martinez-Haya B., Lin X., Lin J.J., Harich S.A., Wang C.C., Yang X., Honvault P., Launay J.-M. (2002) The $O(^1D) + H_2$ reaction at 56 meV collision energy : a comparison between quantum mechanical, quasi classical trajectory and crossed beam results, *J. Chem. Phys.* **116**, 10692–10703.

34. Pederson L.A., Schatz G.C., Hollebeek T., Ho T.S., Rabitz H., and Harding L.B. (2000) Potential Energy Surface of the State of NH_2 and the Role of Excited States in the $N(^2D) + H_2$ Reaction, *J. Phys. Chem. A* **104**, 2301-2307.

35. Pederson L.A., Schatz G.C., Ho T.S., Hollebeek T., Rabitz H., Harding L.B., and Lendvay G. (1999) Potential energy surface and quasiclassical trajectory studies of the $N(^2D) + H_2$ reaction, *J. Chem. Phys.* **110**, 9091-9100.

36. Alagia M., Balucani N., Cartechini L., Casavecchia P., Volpi G.G., Pederson L.A., Schatz G.C., Lendvay G., Harding L.B., Hollebeek T., Ho T.S., Rabitz H. (1999) Exploring the reaction dynamics of nitrogen atoms: A combined crossed beam and theoretical study of $N(^2D) + D_2 \rightarrow ND + D$, *J. Chem. Phys.* **110**, 8857-8860.

37. Umemoto H. (1998) Leaving-atom isotope effect in the reactions of $N(2^2D)$ with isotopic hydrogens, *Chem. Phys. Lett.* **292** 594-600.

38. Umemoto H., Terada N., and Tanaka K. (2000) Verification of the insertion mechanism of $N(2^2D)$ into H-H bonds by the vibrational state distribution measurement of $NH(X^3\Sigma^-, 0 < v < 3)$, *J. Chem. Phys.* **112** 5762-5766.

39. Balucani N., Cartechini L., Capozza G., Segoloni E., Casavecchia P., Volpi G.G., Aoiz F.J., Bañares L., Honvault P., Launay J.-M. (2002) Quantum effects in the differential cross sections for the insertion reaction $N(^2D) + H_2$, *Phys. Rev. Lett.* **89** 013201.1–4.

40. Honvault P. and Launay J.-M. (1999) A quantum-mechanical study of the dynamics of the $N(^2D) + H_2 \rightarrow NH + H$ reaction, *J. Chem. Phys.* **111**, 6665-6667.

41. Suzuki T., Shihira Y., Dato T., Umemoto H., and Tsunashima S. (1993) Reaction of $N(2^2D)$ and $N(2^2P)$ with H_2 and D_2, *J. Chem. Soc. Faraday Trans.* **89**, 995-999.

42. Lepetit B. and Launay J.-M. (1991) Quantum mechanical study of the reaction He $+ H_2^+ \rightarrow HeH^+ + H$ with hyperspherical coordinates, *J. Chem. Phys.* **95**, 5159-5168.

43. Huarte-Larrañaga F., Giménez X., Lucas J.M., Aguilar A., and Launay J.-M. (2000) Detailed Energy Dependences of Cross Sections and Rotational Distributions for the $Ne + H_2^+ NeH^+ + H$ Reaction, *J. Phys. Chem. A* **104**, 10227-10233.

44. Russel C.L. and Manolopoulos D.E. (1999) Time-dependent wave packet study of the $N^+ + H_2$ reaction, *J. Chem. Phys.* **110**, 177-187.

45. Zhang Y.C., Zhan L.X., Zhang Q.G., Zhu W., and Zhang J.Z.H. (1999) Quantum wavepacket calculation for the ion molecule reaction $N^+ + H_2 \rightarrow NH^+ + H$, *Chem. Phys. Lett.* **300**, 27-32.

46. Bussery-Honvault B., Honvault P., and Launay J.-M. (2001) A study of the $C(^1D) + H_2 \rightarrow CH + H$ reaction: Global potential energy surface and quantum dynamics, *J. Chem. Phys.* **115**, 10701-10708.

47. Banares L., Aoiz F.J., Honvault P., Bussery-Honvault B., and Launay J.-M. (2003)

Quantum mechanical and quasi-classical trajectory study of the $C(^1D) + H_2$ reaction dynamics, *J. Chem. Phys.* **118**, 565-568.

48. P. Soldán, M.T. Cvitaš, J.M. Hutson, P. Honvault, J.-M. Launay (2002) Quantum dynamics of ultracold $Na + Na_2$ collisions *Phys. Rev. Letters* **89**, 153201.1–4.

CHEBYSHEV PROPAGATION AND APPLICATIONS TO SCATTERING PROBLEMS

H. GUO
Department of Chemistry
University of New Mexico
Albuquerque, NM 87131, USA

Abstract. The Chebyshev operator is a discrete cosine-type propagator that bears many formal similarities with the time propagator. It has some unique and desirable numerical properties that distinguish it as an optimal propagator for a wide variety of quantum mechanical studies of molecular systems. In this contribution, we discuss some recent applications of the Chebyshev propagator to scattering problems, including the calculation of resonances, cumulative reaction probabilities, S-matrix elements, cross-sections, and reaction rates.

1. Introduction

Many of the recent advances in reaction dynamics have been driven by time-dependent wave packet propagation methods.[1,2] The time-dependent approach is based on the expansion of the relevant operators, such as the Green's operator ($G = (E - \hat{H})^{-1}$), in terms of the time propagator ($e^{-i\hat{H}t}$ with $\hbar = 1$). The success of this approach can be attributed to a number of advances in wave packet propagation. First, the action of the time propagator, which is an exponential function of the Hamiltonian, can often be approximated with schemes in which repetitive application of the Hamiltonian onto the propagation wave packet is performed.[3,4] In doing so, the major numerical task in propagation becomes matrix-vector multiplication, which can be readily accomplished by a digital computer. Second, the Hamiltonian is commonly discretized in a sparse and highly structured form such that it can be readily generated on-the-fly. Thus, it is memory efficient as only a few vectors need be stored. In addition, the use of pseudo-spectral methods such as fast Fourier transform (FFT)[5] and discrete variable representation (DVR)[6] further simplifies the matrix-vector multiplication and renders favorable scaling laws with respect to the dimensionality of the system. The time-dependent wave packet propagation method has been widely and successfully used to compute S-matrix elements, total reaction probability, cross-sections, canonical and microcanonical rate constants, and other properties describing scattering processes.

For these properties in the energy domain, there is no particular reason why the propagation has to be carried out in the time domain. Recently, there has been a keen interest in search for alternative and potentially more efficient propagators to compute

the same properties. Such a propagator should be accurate, efficient in both memory and cpu requirements, easy to implement, and preferably possesses physically transparent properties. Here, we discuss such a propagator based on the Chebyshev polynomials and review some of its applications to scattering problems. We want to emphasize that this work is not meant to be a thorough review of the field. Rather, it represents a summary of some recent research in our group.

2. The Chebyshev propagator

The Chebyshev polynomials of the first kind have long been recognized as an effective basis for fitting non-periodic functions.[7] In many aspects they resemble the Fourier basis for periodic systems. This special type of classical orthogonal polynomials can be generated by the following three-term recurrence relationship:[8]

$$T_k = 2xT_{k-1} - T_{k-2} \qquad \text{for } k \geq 2 \qquad\qquad (1)$$

with $T_1 = x$ and $T_0 = 1$. The variable x is defined on the real axis in [-1, 1]. Outside this range, the polynomials diverge exponentially.

A unique property of the Chebyshev polynomials is that they can be mapped to a cosine function:

$$T_k \equiv \cos(k \arccos x), \qquad\qquad (2)$$

and the recurrence relationship in Eq. (1) is nothing but the following trigonometric identity:

$$\cos(k+1)\phi + \cos(k-1)\phi = 2\cos\phi\cos k\phi . \qquad\qquad (3)$$

In other words, the Chebyshev polynomials are essentially a cosine function in disguise. This duality underscores the effectiveness of the Chebyshev polynomials in numerical analysis, which has been recognized long ago by many,[7] including the great Hungarian applied mathematician C. Lanczos.[9] In particular, Fourier transform (and FFT) can be readily implemented in the spectral method involving the Chebyshev polynomials.

In Chemical Physics, Tal-Ezer and Kosloff were among the first to realize that the Chebyshev polynomials can be used to approximate the time propagator with a time-independent Hamiltonian [10]. In the operator form, it can be shown

$$e^{-i\hat{H}t} = \sum_{k=0}(2 - \delta_{k0})(-i)^k J_k(t)T_k(\hat{H}) , \qquad\qquad (4)$$

provided that the eigenvalues of the Hamiltonian are normalized to [-1,1], which can be readily achieved: $\hat{H}_n = (\hat{H} - H^+)/H^-$ with $H^{\pm} = (H_{max} \pm H_{min})/2$. (For discussions below, the Hamiltonian is assumed to have been normalized.) Indeed, the

approximation converges uniformly in the entire spectral range as the Bessel functions of the first kind (J_k) decay exponentially to zero when $k > t$. Subsequently, Kouri, Hoffman and coworkers demonstrated that similar expansions can be devised for the Green's function [11,12] and Dirac's delta function:[13]

$$G(E) = (E - \hat{H})^{-1} = \frac{-i}{\sqrt{1 - E^2}} \sum_{k=0}^{\infty} (2 - \delta_{k0}) e^{-ik \arccos E} T_k(\hat{H}), \tag{5a}$$

$$\delta(E - \hat{H}) = -\frac{1}{\pi} \mathrm{Im}\, G(E) = \frac{1}{\pi\sqrt{1 - E^2}} \sum_{k=0}^{\infty} (2 - \delta_{k0}) T_k(E) T_k(\hat{H}). \tag{5b}$$

In fact, any analytic function of the Hamiltonian can be expressed as an expansion in terms of the Chebyshev operator ($T_k(\hat{H})$).[14] It is interesting to note that in both Eqs. (4) and (5), the energy shows up only in the expansion coefficients. In other words, the Chebyshev recursion yields information at all energies. These advances opened the doors for both time-dependent and time-independent studies of quantum dynamics and spectra using the Chebyshev polynomials.

A closer look at the Chebyshev operator ($T_k(\hat{H})$) reveals that it possesses many similar properties with the better known time propagator. Because of the cosine mapping in Eq. (2), one can equate the Chebyshev operator to the real part of an effective time propagator:[15,16]

$$T_k(\hat{H}) \equiv \cos(k\hat{\Theta}), \tag{6}$$

in which the Chebyshev order k serves as the discrete effective time and the Chebyshev angle operator ($\hat{\Theta} \equiv \arccos \hat{H}$) defines the effective Hamiltonian. In other words, the Chebyshev operator can be considered as a discrete cosine-type propagator. In contrast to the time propagator, however, the propagation in the Chebyshev order domain with an initial state ψ_0 can be carried out exactly:

$$\psi_k \equiv T_k(\hat{H})\psi_0 = 2\hat{H}\psi_{k-1} - \psi_{k-2} \text{ for } k \geq 2 \tag{7}$$

with $\psi_1 = \hat{H}\psi_0$. The above recursion is stable and accurate as neither interpolation nor discretization error is introduced in the propagation. Unlike the time propagator, however, the Chebyshev propagator does not conserve the norm.

It can be further shown that the Chebyshev order (k) and angle ($\theta = \arccos E$) form a conjugate pair of variables, similar to energy and time.[17] The two conjugated representations, which are related by an orthogonal cosine transformation, are isomorphic. Thus, properties in the angle domain can be readily extracted from propagation in the order domain and the convergence is uniform. The Chebyshev angle does not introduce any complications as its mapping to energy is single-valued, albeit non-linear. In many cases, we are interested in the dynamics near the low end of the

spectral range of the Hamiltonian. The non-linear mapping actually provides more interpolation points in this range, and thus better convergence.

The realization of the propagator nature of the Chebyshev operator is not merely a formality, it has several important numerical implications. Indeed, any formulation based on time propagation can be readily transplanted to one that is based on the Chebyshev propagation. In addition, the propagation can be implemented easily and exactly with no interpolation errors. Like the time propagation, the major computational task is repetitive matrix-vector multiplication, which is amenable to sparse matrix techniques with favorable scaling laws. The memory request is minimal as the Hamiltonian matrix needs not be stored. Finally, the entire propagation can be performed in real space as long as a real initial wave packet and real-symmetric Hamiltonian are used. General properties of the Chebyshev propagator and its applications to spectroscopic studies have been reviewed by us earlier.[18]

When applied to scattering problems, one is forced to deal with the continuum and the implementation of the appropriate boundary conditions. This is often done in time propagation with a negative imaginary potential in the asymptote [19]. Since the Chebyshev polynomials are defined on the real axis, the use of a complex-symmetric Hamiltonian with a negative imaginary potential will lead to instability in the propagation. To solve this problem, Mandelshtam and Taylor replaced the negative imaginary potential with the following damping scheme:[20,21]

$$\psi_k^d = D(2\hat{H}\psi_{k-1}^d - D\psi_{k-2}^d)\,, \tag{8}$$

where $\psi_1^d = D\hat{H}\psi_0$. The damping function ($D$) is real and decays in the asymptote smoothly from unity. It has the effect of removing outgoing waves near the end of the grid and is thus related to an energy-dependent negative imaginary asymptotic potential. Its form can be chosen quite arbitrarily as long as it enforces the outgoing boundary conditions.[22-24] The advantage of such a damping scheme is that the corresponding wave packet can still be propagated in real space, which greatly enhanced the applicability and efficiency of the Chebyshev propagator for systems containing continua.[25]

We note here in passing that Chebyshev propagation is related to several other recursive methods based on the Krylov subspace: $\mathscr{K}^{(K)} = span\{\psi_0, \hat{H}\psi_0, ..., \hat{H}^{K-1}\psi_0\}$. A prominent example of such methods is the Lanczos algorithm.[26] Both the Chebyshev and Lanczos approaches generate the Krylov subspace recursively using three-term recurrence relationships, but the Lanczos algorithm imposes further orthogonalization among the recurring vectors. As a result, instability of the Lanczos algorithm ensues in finite precision arithmetic as a result of round-off errors.[27] On the other hand, the same round-off errors also reduce the linear independence of the Chebyshev propagation states. In many respects, their convergence behaviors and efficiency are quite similar.[28-31]

3. Applications

3.1. RESONANCES

Resonances can be considered as bound states that coupled with dissociative continua. Since these metastable states can significantly influence scattering dynamics, their studies are of great importance.[32] A resonance can be characterized by a complex eigenvalue ($E - i\Gamma/2$) of a negative imaginary potential augmented,[33] or more rigorously complex scaled,[34] Hamiltonian. The real and imaginary parts of the eigenvalue define respectively the peak position of the resonance and its width, which is inversely proportional to its lifetime. The eigenvalues can be obtained by direct diagonalization of the complex-symmetric Hamiltonian matrix.

However, the direct diagonalization is limited by the dimension of the matrix (N) as the memory and cpu scale as N^2 and N^3, respectively. A more efficient alternative is to use the low-storage filter-diagonalization (LSFD) method,[35] which constructs a series of small generalized eigenproblems in the energy range of interest from one or more correlation functions. This strategy is particularly suitable for the Chebyshev propagation as no integration over time is needed.[36-40] However, our earlier numerical tests showed that the Chebyshev-based LSFD requires roughly twice the matrix-vector multiplication steps as the complex-symmetric Lanczos method.[29]

This difference stems from the abandonment in the damped Chebyshev propagation of the doubling relation commonly used for the conventional Chebyshev autocorrelation function,[35] which can again be derived from trigonometry:

$$C_{2k} \equiv \langle \psi_0 | T_{2k} | \psi_0 \rangle = 2\langle \psi_k | \psi_k \rangle - C_0 , \qquad (9a)$$

$$C_{2k+1} = 2\langle \psi_{k+1} | \psi_k \rangle - C_1 . \qquad (9b)$$

Such doubling relations obviously do not hold for damped Chebyshev propagation prescribed by Eq. (8), but the real question is whether they will allow the extraction of the narrow resonances using the Chebyshev-based LSFD.

To answer this question, we computed the resonance positions and widths of HCO[41] and HN$_2$,[42] using both doubled and undoubled autocorrelation functions obtained from the damped Chebyshev propagation. The results indicated that the enforced doubling of the autocorrelation function yields no appreciable differences in both positions and widths of the narrow resonances when compared with those obtained from a directly calculated autocorrelation function. The differences are plotted in Fig. 1 for the low-lying resonances of HN$_2$. The largest differences are for resonances with widths on the order of a few hundred wave numbers.[42]
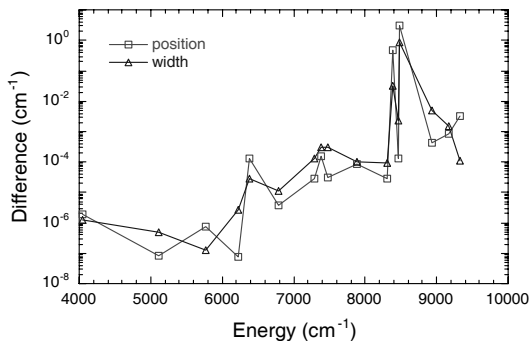
Figure 1 Differences in positions and widths for HN$_2$ resonance calculated from doubled and undoubled Chebyshev correlation functions.

The outcome should probably not be too surprising since the narrow resonances are largely localized in the interaction region and minimally affected by the damping. Consequently, its frequency information should still be accurately accounted for in the doubled autocorrelation function despite the fact that the correlation function is different from the true value because of damping. The doubling scheme results in a 50% reduction of computational costs and its implementation is trivial. In accordance to the fact that both are based on the Krylov subspace, roughly the same number of matrix-vector multiplication steps is needed for the Chebyshev-based LSFD and Lanczos algorithm, As the latter is complex, LSFD based on the (real) damped Chebyshev propagation is strongly preferred for determining the positions and widths of narrow resonances. Our work has also stimulated further exploration of the doubling of autocorrelation function in pseudo-time propagation.[43]

3.2 CUMULATIVE REACTION PROBABILITIES

In studying reaction dynamics, one may only be interested in averaged properties such as cumulative reaction probabilities and thermal rate constants. These quantities can of course be obtained from state-to-state probabilities, but as shown by Miller and coworkers they can be calculated directly and more efficiently without knowledge of the S-matrix elements.[44,45] The cumulative reaction probability, for example, can be computed as follows:

$$N(E) = 2\pi^2 Tr[\delta(E - \hat{H})\hat{F}\delta(E - \hat{H})\hat{F}], \qquad (10)$$

where $\hat{F}$ is the flux operator for a given dividing surface separating the reactants from products. Earlier approaches for calculating such attributes include direct matrix inversion or diagonalization.[46-48] Since $N(E)$ is determined largely by dynamics near the transition state, a small gird surrounded by a negative imaginary potential is often sufficient. Later work by Zhang and Light took advantage of the fact that the flux

operator has only two non-zero eigenvalues and designed a wave packet propagation approach for calculating $N(E)$.[49] This so-called transition state wave packet approach has a much better scaling with the dimensionality of the problem and is thus applicable to larger systems. Further developments include the use of recursive methods based on the Krylov subspace.[50,51] and reformulations using correlation functions.[52,53]

We follow the correlation function formulation of Miller and Carrington,[52] which rewrites the cumulative reaction probability as follows:

$$ N(E) = 4\pi^2 \lambda^2 \sum_{i,i'} \left[\left| \left\langle \phi_i^+ \left| \delta(E - \hat{H}) \right| \phi_{i'}^+ \right\rangle \right|^2 - \left| \left\langle \phi_i^- \left| \delta(E - \hat{H}) \right| \phi_{i'}^+ \right\rangle \right|^2 \right], \qquad (11) $$

where the transition state wave packets in the above equation are constructed as a product of the eigenfunctions of the flux operator and the eigenfunctions of a reduced-dimensional Hamiltonian defined on the dividing surface:

$$ \left| \phi_i^\pm \right\rangle = \left| \phi_i \right\rangle \left| \pm \right\rangle, \qquad (12) $$

where $\hat{F} |\pm\rangle = \pm\lambda |\pm\rangle$ with $\lambda \neq 0$. Instead of expanding the Dirac's delta function in terms of the time propagator, we use the Chebyshev propagation to compute the correlation functions:[54]

$$ \left\langle \phi_i^\pm \left| \delta(E - \hat{H}) \right| \phi_{i'}^+ \right\rangle = \frac{1}{\pi\sqrt{1 - E^2}} \sum_{k=0} (2 - \delta_{k0}) \cos(k \arccos E) C_k^{ii',\pm}, \qquad (13) $$

where the Chebyshev cross-correlation functions are defined as $C_k^{ii',\pm} \equiv \left\langle \phi_i^\pm \left| T_k(\hat{H}) \right| \phi_{i'}^+ \right\rangle$.

By prudently choosing the dividing surface, the numbers of surface eigenfunctions and thus the correlation functions are minimized.

The advantage of the correlation function approach is that only the storage of scalar quantities, rather than wave packets, is needed. Thus, the memory requirement is significantly reduced, an issue that may become more important for large systems. The implementation with the Chebyshev propagator takes further advantage of its numerical properties discussed above. In cases where resonances are dominant, the LSFD approach can be used to further reduce computational costs. We note in passing this approach can be extended to the calculation of thermal rate constants.

We have tested this approach for the three-dimensional H + H$_2$ exchange reaction (J=0) and found excellent agreement with the time-dependent results of Zhang and Light.[49] It was then used to calculate the cumulative reaction probability for the Li + HF → LiF + H reaction, also with zero total angular momentum.[54] Figure 2 displays the cumulative reaction probability of this reaction below 0.65 eV. It can be readily seen that the cumulative reaction probability is dominated by numerous narrow resonances. These resonances are well known in state-resolved reaction probabilities

and have apparently survived the summation over both the reactant and product states. The details of the calculations can be found in our original publication.[54]
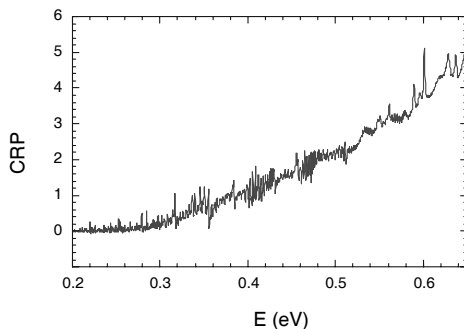
Figure 2 Cumulative reaction probability for the Li + HF → LiF + H reaction (*J*=0).

3.3. S-MATRIX ELEMENTS

Since the S-matrix provides the most detailed information for a collision process, its determination is of great interest. The S-matrix can be expressed as a Green's function matrix between the incoming (χ_i^+) and outgoing (χ_f^-) wave packets:[55,56]

$$S_{f \leftarrow i}(E) = \frac{i}{2\pi a_i(E) a_f^*(E)} \left\langle \chi_f^- \middle| G^+(E) \middle| \chi_i^+ \right\rangle, \qquad (14)$$

where $a(E) = \left\langle \Psi(E) \middle| \chi \right\rangle$ are the energy amplitudes of the wave packets. The time-dependent wave packet propagation approach can thus be considered as the direct results of expanding the Green's function operator in Eq. (14) using the time propagator.[2] Alternatively, a Chebyshev expansion can be utilized to gain further numerical advantages. Indeed, several variants of the latter approach have been explored by a number of groups.[11,12,16,20-22,25,57-60] Extensions to "half-collision" processes have also been proposed.[1,61,62]

We have recently studied rotational and vibrational inelastic scattering between two H_2 molecules using the damped Chebyshev propagation with a full-dimensional Hamiltonian.[63-65] The corresponding S-matrix elements were obtained as Fourier transforms of correlation functions ($C_k^{if} \equiv \left\langle \chi_f^- \middle| T_k(\hat{H}) \middle| \chi_i^+ \right\rangle$):

$$S_{f \leftarrow i}(E) = \frac{1}{2\pi \sqrt{1-E^2} \, a_i(E) a_f^*(E)} \sum_{k=0}^{\infty} (2 - \delta_{k0}) e^{-ik \arccos E} C_k^{if}. \qquad (15)$$

In such calculations, the initial (and final) wave packet can be conveniently chosen to be the product of an internal state eigenfunction and a real translational wave packet placed at the asymptote. A complete column of the S-matrix at all energies can be computed from a single propagation. Cross-sections and thermal rate constants can then be obtained by properly summing and averaging the state-to-state probabilities.

For the diatom-diatom collision, we have used a mixed basis/grid representation and pseudo-spectral methods for evaluating the action of the Hamiltonian matrix on to the propagation vector.[66] Both the parity and diatomic exchange symmetry were adapted for the wave packet using a method proposed earlier.[67] For $J>0$, the centrifugal sudden approximation was used.[68,69] Both *para* and *ortho*-hydrogen molecules were considered. Figure 3 shows the integral cross-sections for rotational inelastic scattering between two *para*-H_2 in their ground ro-vibrational states. Although only the inelastic channels were explored, the same approach can be readily implemented for reactive scattering.
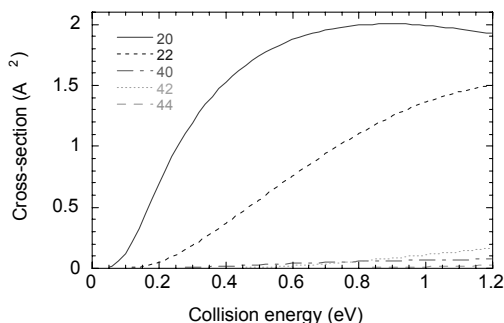
Figure 3. Integral cross-sections for rotationally inelastic collisions between two *para*-H_2 in their ground ro-vibrational states.

3.4 TOTAL REACTION PROBABILITIES AND RATES

Because of their energy global nature, wave packet methods are ideally suited for calculating the energy dependence of reaction probabilities.[2] Instead of repeating the calculation of the entire S-matrix at every energy grid point, the total reaction probability can be convinently computed at all energies from a single wave packet propagation. This becomes particularly important for reactions that are affected by shape resonances for which a very fine energy grid is needed to resolve the rich structure.

The total reaction probability is typically obtained from the reactive flux calculated at the dividing surface placed at a point-of-no-return.[70,71] This surface is often located in the product channel, but not necessarily at the asymptote where the S-matrix elements are completely converged. Consequently, such calculations can be conveniently carried out in reactant Jacobi coordinates and the computational costs are no more expensive than that for inelastic scattering. Implemented for the Chebyshev propagation, the reaction probability is given as below:[72]

$$P^r(E) = \frac{1}{2\pi\mu_r \left|a_i(E)\right|^2 (1-E^2)}$$

$$\times \text{Im}\left\langle \sum_k (2-\delta_{k0})e^{-ik\arccos E}\psi_k \left| \sum_{k'}(2-\delta_{k0})e^{-ik'\arccos E}\left[\delta(r-r_f)\frac{\partial}{\partial r}\psi_{k'}\right]\right\rangle,$$

(16)

where $r = r_f$ defines the dividing surface and μ_r is the reduced mass for the r coordinate. The derivative in the above equation can be carried out analytically. Our approach is essentially the same as that proposed by Meijer *et al.*[60] and used by the same authors.[73,74]

The above approach was recently applied to the C(^{1}D) + H$_2$ → CH + H reaction,[72] which serves as a prototype for insertion reactions. Because of a deep CH$_2$ well, a large grid and long propagation were necessary to converge all the resonance features in the total reaction probability. The calculations were carried out on a recently developed *ab initio* PES.[75,76] Figure 4 displays the total reaction probability for the C(^{1}D) + H$_2$(v=0,j=0) reaction (J=0) up to 0.5 eV of collision energy. It is clear from the figure that this reaction shows no threshold, which is consistent with the barrierless insertion pathway in this system. Strong oscillatory structures dominate the relatively large reaction probability, particularly at low collision energies. These structures can be attributed to long-lived resonance states supported by the CH$_2$ well. Our results are in reasonably good agreement with time-independent results.

Very recently, we have extended the calculation to include non-zero total angular momenta[77] with the centrifugal sudden approximation.[68,69] The resulting rate constant indicates a mild dependence on the temperature, consistent with the lack of reaction barrier in this system. At room temperature, the calculated rate constant is about a factor of two larger than experimental measurements. Considering the neglect of several important non-adiabatic channels, such as the Renner-Teller coupling between two lowest-lying singlet PESs, the agreement is very encouraging.
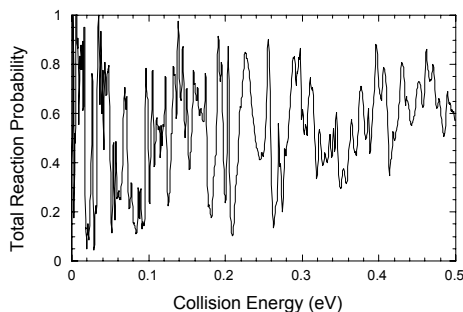
Figure 4. Total reaction probability for the C(^{1}D) + H$_2$(v=0,j=0) reaction (J=0).

4. Conclusions

In this work, we have demonstrated that the Chebyshev propagator can be used as an effective tool to study a wide range of properties in scattering dynamics, including resonances, cumulative reaction probabilities, S-matrix elements, and rate constants. It is also well known that it provides an optimal way to compute ro-vibrational spectra of polyatomic molecules. The Chebyshev approach bears many similarities with the time-dependent wave packet propagation method. Compared with the time propagator, however, it is more efficient and accurate. In particular, the Chebyshev propagator can be exactly implemented with no interpolation errors and the propagation can be carried out in real space. In addition, the Chebyshev propagation provides more favorable convergence for dynamics near the spectral extrema. It can be expected that this approach will find more and more applications in quantum studies of reactive scattering processes.

References:

1.   R. Kosloff, J. Phys. Chem. **92**, 2087 (1988).
2.   J. Z. H. Zhang, *Theory and Application of Quantum Molecular Dynamics*. (World Scientific, Singapore, 1999).
3.   C. Leforestier, R. H. Bessling, C. Cerjan, M. D. Feit, R. Friesner, A. Guldberg, A. Hammerich, G. Jolicard, W. Karrlein, H.-D. Meyer, N. Lipkin, O. Roncero, and R. Kosloff, J. Comput. Phys. **94**, 59 (1991).
4.   R. Kosloff, Annu. Rev. Phys. Chem. **45**, 145 (1994).
5.   R. Kosloff, in *Numerical Grid Methods and Their Applications to Schrodinger's Equation*, edited by C. Cerjan (Kluwer, Dordrecht, 1993).
6.   J. C. Light and T. Carrington, Adv. Chem. Phys. **114**, 263 (2000).
7.   J. P. Boyd, *Chebyshev and Fourier Spectral Methods*. (Springer-Verlag, Berlin, 1989).
8.   M. Abramowitz and I. A. Stegun, *Handbook of Mathematical Functions*. (Dover, New York, 1970).
9.   C. Lanczos, *Applied Analysis*. (Prentice Hall, Englewood Cliffs, 1956).
10.   H. Tal-Ezer and R. Kosloff, J. Chem. Phys. **81**, 3967 (1984).
11.   Y. Huang, D. J. Kouri, and D. K. Hoffman, Chem. Phys. Lett. **225**, 37 (1994).
12.   Y. Huang, D. J. Kouri, and D. K. Hoffman, J. Chem. Phys. **101**, 10493 (1994).
13.   W. Zhu, Y. Huang, D. J. Kouri, C. Chandler, and D. K. Hoffman, Chem. Phys. Lett. **217** (1,2), 73 (1994).
14.   R. Chen and H. Guo, J. Chem. Phys. **105**, 1311 (1996).
15.   R. Chen and H. Guo, J. Chem. Phys. **105**, 3569 (1996).
16.   S. K. Gray and G. G. Balint-Kurti, J. Chem. Phys. **108**, 950 (1998).
17.   R. Chen and H. Guo, J. Chem. Phys. **108**, 6068 (1998).
18.   R. Chen and H. Guo, Comput. Phys. Comm. **119**, 19 (1999).

19. D. Neuhauser, Chem. Phys. Lett. **200**, 173 (1992).
20. V. A. Mandelshtam and H. S. Taylor, J. Chem. Phys. **103** (8), 2903 (1995).
21. V. A. Mandelshtam and H. S. Taylor, J. Chem. Phys. **102**, 7390 (1995).
22. Y. Huang, S. S. Iyengar, D. J. Kouri, and D. K. Hoffman, J. Chem. Phys. **105**, 927 (1996).
23. R. Chen and H. Guo, Chem. Phys. Lett. **261**, 605 (1996).
24. H.-G. Yu and S. C. Smith, J. Chem. Phys. **107**, 9985 (1997).
25. V. A. Mandelshtam, in *Multiparticle Quantum Scattering with Applications to Nuclear, Atomic and Molecular Physics*, edited by D. G. Truhlar and B. Simon (Springer, New York, 1996).
26. C. Lanczos, J. Res. Natl. Bur. Stand. **45**, 255 (1950).
27. J. K. Cullum and R. A. Willoughby, *Lanczos Algorithms for Large Symmetric Eigenvalue Computations*. (Birkhauser, Boston, 1985).
28. S.-W. Huang and T. Carrington, Chem. Phys. Lett. **312**, 311 (1999).
29. D. Xie, R. Chen, and H. Guo, J. Chem. Phys. **112**, 5263 (2000).
30. V. A. Mandelshtam and T. Carrington, Phys. Rev. **E 65**, 028701 (2002).
31. R. Chen and H. Guo, J. Chem. Phys. **119**, 5762 (2003).
32. *Resonances in Electron-Molecule Scattering, van der Waals Complexes, and Reactive Chemical Dynamics*, edited by D. G. Truhlar (ACS, Washington D.C., 1984).
33. G. Jolicard and E. J. Austin, Chem. Phys. Lett. **121**, 106 (1985).
34. N. Moiseyev, Isreal J. Chem. **31**, 311 (1991).
35. M. R. Wall and D. Neuhauser, J. Chem. Phys. **102**, 8011 (1995).
36. V. A. Mandelshtam and H. S. Taylor, J. Chem. Phys. **106**, 5085 (1997).
37. V. A. Mandelshtam and H. S. Taylor, Phys. Rev. Lett. **78**, 3274 (1997).
38. V. A. Mandelshtam and H. S. Taylor, J. Chem. Phys. **107**, 6756 (1997).
39. R. Chen and H. Guo, Chem. Phys. Lett. **279**, 252 (1997).
40. R. Chen and H. Guo, J. Chem. Phys. **111**, 464 (1999).
41. G. Li and H. Guo, Chem. Phys. Lett. **336**, 143 (2001).
42. G. Li and H. Guo, Chem. Phys. Lett. **347**, 443 (2001).
43. A. Neumaier and V. A. Mandelshtam, Phys. Rev. Lett. **86**, 5031 (2001).
44. W. H. Miller, J. Chem. Phys. **61**, 1823 (1974).
45. W. H. Miller, S. D. Schwartz, and J. W. Tromp, J. Chem. Phys. **79**, 4889 (1983).
46. T. Seideman and W. H. Miller, J. Chem. Phys. **96**, 4412 (1992).
47. T. Seideman and W. H. Miller, J. Chem. Phys. **97**, 2499 (1992).
48. U. Manthe and W. H. Miller, J. Chem. Phys. **99**, 3411 (1993).
49. D. H. Zhang and J. C. Light, J. Chem. Phys. **104**, 6184 (1996).
50. K. M. Forsythe and S. K. Gray, J. Chem. Phys. **112**, 2623 (2000).
51. H. O. Karlsson and O. Goscinski, J. Phys. Chem. **105A**, 2599 (2001).
52. S. M. Miller and T. Carrington, Chem. Phys. Lett. **267**, 417 (1997).
53. S. Garashchuk and D. J. Tannor, J. Chem. Phys. **110**, 2761 (1999).
54. D. Xie, S. Li, and H. Guo, J. Chem. Phys. **116**, 6391 (2002).
55. D. J. Tannor and D. E. Weeks, J. Chem. Phys. **98**, 3884 (1993).
56. D. J. Kouri, Y. Huang, W. Zhu, and D. K. Hoffman, J. Chem. Phys. **100**, 3662 (1994).
57. S. S. Iyengar, D. J. Kouri, and D. K. Hoffman, Theo. Chem. Acc. **104**, 471 (2000).
58. V. A. Mandelshtam, J. Chem. Phys. **108**, 9999 (1998).
59. G.-J. Kroes and D. Neuhauser, J. Chem. Phys. **105**, 8690 (1996).
60. A. J. H. M. Meijer, E. M. Goldfield, S. K. Gray, and G. G. Balint-Kurti, Chem. Phys. Lett. **293**, 270 (1998).
61. H. Guo, J. Chem. Phys. **108**, 2466 (1998).
62. H. Guo, Chem. Phys. Lett. **289**, 396 (1998).
63. S. Y. Lin and H. Guo, J. Chem. Phys. **117**, 5183 (2002).
64. S. Y. Lin and H. Guo, Chem. Phys. **289**, 191 (2003).

65.   S. Y. Lin and H. Guo, J. Phys. Chem. **in press** (2003).
66.   R. Chen, G. Ma, and H. Guo, Chem. Phys. Lett. **320**, 567 (2000).
67.   R. Chen, G. Ma, and H. Guo, J. Chem. Phys. **114**, 4763 (2001).
68.   P. McGuire and D. J. Kouri, J. Chem. Phys. **60**, 2488 (1974).
69.   R. T. Pack, J. Chem. Phys. **60**, 633 (1974).
70.   D. Neuhauser, M. Baer, R. S. Judson, and D. J. Kouri, J. Chem. Phys. **93**, 312 (1990).
71.   D. H. Zhang and J. Z. H. Zhang, J. Chem. Phys. **101**, 1146 (1994).
72.   S. Y. Lin and H. Guo, J. Chem. Phys. (in press).
73.   G. G. Balint-Kurti, A. Gonzalez, E. M. Goldfield, and S. K. Gray, Faraday Disc. **110**, 169 (1998).
74.   S. K. Gray, C. Petrongolo, K. Drukker, and G. C. Schatz, J. Phys. Chem. **103**, 9448 (1999).
75.   B. Bussery-Honvault, P. Honvault, and J.-M. Launay, J. Chem. Phys. **115**, 10701 (2001).
76.   L. Banares, F. J. Aoiz, S. A. Vazquez, T.-S. Ho, and H. Rabitz, Chem. Phys. Lett. **374**, 243 (2003).
77.   S. Y. Lin and H. Guo, J. Phys. Chem. (submitted).

MOLECULAR DYNAMICS: ENERGY SELECTED BASES

JOHN C. LIGHT AND HEE-SEUNG LEE
Department of Chemistry and James Franck Institute University of Chicago, Chicago, IL 60637

1. Introduction

Large amplitude vibrational motions of molecules occur at high temperatures, in weakly bound complexes, in chemical reactions, and in many other circumstances. In a subset of these cases the specific quantum states and dynamics are important, *e.g.* light atom transfer reactions, unimolecular decay and isomerization of small molecules, proton transfer in liquids, photodissociation and reactions "guided" by laser control.

Small amplitude vibrational motions are well described by normal modes except in the most unusual of cases[1]. Normal modes are, in fact, extremely powerful tools for the description of molecular motions, forces, and shapes, being the most widely used representation, and for good reasons. The efficiency of normal mode descriptions comes about because of the confluence of several requirements for efficient quantum description of molecular systems. These are due to the fact that all stable molecular systems (or fragments) have a potential energy minimum which yields a quadratic approximation to the potential energy surface (PES), accurate at low energies. Since the kinetic energy operator is also quadratic in momentum or coordinate derivatives, an orthogonal transformation takes the Hamiltonian to a *separable* normal coordinate form, i.e. a sum of quadratic one dimensional Hamiltonians for each normal coordinate. Fortunately, these have analytic harmonic oscillator solutions both classically and quantum mechanically, and these approximations are quite accurate for most molecules to energies well above room temperature, making normal modes an extremely useful representation.

However, normal mode representations eventually run out of steam; they do not provide an adequate representation for large amplitude motions such as those mentioned above. As the vibrational energies increase, the PES's become anharmonic, the coupling between degrees of freedom grows in all coordinate representations, harmonic oscillators are no longer good approximate solutions, and analytic solutions are no longer available. Over the past 20 years or so, we have turned to computers to provide requisite information about large amplitude vibrational mo-

tions, both to determine the PES's for the molecular systems[7] using empirical and *ab initio* quantum mechanical methods and to determine the vibrational states or dynamics on these surfaces[8, 9, 10]. Such methods require a number of theoretical or computational steps and all of which are current activities of research. The steps are:

(i) Evaluation of the electronic energies at many molecular configurations;

(ii) Determination of a PES, i.e. a usable representation of this information;

(iii) Determination of a coordinate system in which to represent the motions of the system;

(iv) Determination of the Hamiltonians in this coordinate system;

(v) Determination of a finite representation of the Hamiltonian, i.e. a basis (or a spectroscopic or algebraic) representation which may be a coordinate grid, phase space grid, functional Hilbert space, or an abstract algebraic form;

(vi) Solution of the Schrödinger equation for the states of interest; and finally

(vii) Use of the solutions for characterization of motions and determination of the properties or dynamics of the molecules of interest.

For large molecules or very high molecular energies each step is difficult. The dimension or the number of degrees of freedom of the molecule grows by three for each additional atom and the difficulty of each step grows as some power (1 up to 3) of the dimension. In addition, the number of solutions of interest, N_{soln}, also often grows exponentially with the number of dimensions.

In this paper we present a method which, given a PES and coordinate system, promises to make the subsequent steps both more computationally efficient and simpler, and with solutions interpretable in terms of quantum numbers of characteristic motions where physically possible. While no single step in this approach is truly new, the combination of the steps into a general method is new and powerful. In the following we summarize the method, describing the reasons for the choices, present an application to H_2O to energies above dissociation. Finally we look at future applications and improvements and caveats in the approach.

2. Zero order H's, ESB's, and IRLM Solution:

In recent years the solution of problems of large amplitude motions (LAM's) has usually been based on grid representations, such as DVR,[11, 12] of the Hamiltonians coupled with solution by sequential diagonalization and truncation (SDT[13, 9]) of the basis or by Lanczos[2] or other iterative methods[14]. More recently, filter diagonalization (FD)[5, 4] and spectral transforms of the iterative operator[15] have also been used. There has usually been a trade-off between the use of a compact basis with a dense Hamiltonian matrix, or a simple but very large DVR with a sparse $\hat{H}$ and a fast matrix-vector product.

The energy selected basis (ESB) presented here has the best of both worlds. The choice of zero order reduced Hamiltonians provides a *good* zero order basis; energy selection from this basis provides an extremely compact basis with limited spectral

range; the zero order quantum numbers provide an approximate assignment of the states; and iterative solution for the eigenpairs of the Hamiltonian in this basis is simple and efficient. The efficiency of iterative solution is greatly enhanced by both the reduced size and reduced spectral range of the matrix representation of the Hamiltonian.

Since this method has been described in the literature[16], we provide here only a brief outline of the numerical algorithm, but then discuss aspects of it in some detail. The application to H_2O in Section III should clarify the implementation and performance of the method. The algorithm has three parts: definition of coordinates and coordinate groups and zero order Hamiltonians for each; generation of an ESB from solutions of the zero order Hamiltonians; and solution of the Schrödinger equation for *many* vibrational states efficiently by iterative methods.

2.1. ZERO ORDER HAMILTONIANS:

We start with the premise that we are interested in solutions for the vibrational states up to some maximum energy, $E_{max} \leq E_{cut}$. Note that with a finite range basis E_{max} and E_{cut} may be in the continuum to include resonance states. In an orthogonal coordinate system we may define each coordinate to be in a set $\{q_k\}$ and for each set $\{q_k\}$ we may define a zero order Hamiltonian and the full Hamiltonian as the sum of the zero order Hamiltonians and correction terms:

$$\hat{H} = \sum_{k=1}^{n_d} \hat{h}_k + \Delta\hat{T} + \Delta\hat{V} \tag{1}$$

$$\Delta\hat{V} = \hat{V} - \sum_{k=1}^{n_d} \hat{V}^0(q_k) \tag{2}$$

where $\hat{h}_k$ is the zero-order Hamiltonian for the kth group containing $\hat{V}^0(q_k)$, the reference potential for the $\{q_k\}$ group. $\Delta\hat{T}$ refers to the remaining terms originating from the complex kinetic energy terms, if any. The $\hat{h}_k$ are operators depending on q_k only and contain all the differential operators for q_k. However, complex kinetic energy operators may contain $f(q_{k'})$ times the differential operators in q_k (where k' and k refer to different coordinate groups). This is the usual case for kinetic energy operators for angular coordinates. The zero order Hamiltonians have $f(q_{k'})$ replaced by $f(q_{k'}^o)$, i.e fixed values so that $\hat{h}_k$ contains only q_k coordinates.

Since we want a basis which can represent motions in any degree of freedom up to the energy contour of the PES at E_{cut}, the basis for each group must extend over the PES to E_{cut}. Thus we define the reference potential for each zero order Hamiltonian, $\hat{h}_k$ to be the *minimum* of $\hat{V}(q_k)$ with respect to all variables $q_{k'}$ not in the group q_k. We then determine the zero order eigenpairs for each group k:

$$\hat{h}_k \phi_{n_k}^{(k)}(q_k) = \epsilon_{n_k}^{(k)} \phi_{n_k}^{(k)}(q_k). \tag{3}$$

The eigenfunctions, $\phi_{n_k}^{(k)}(q_k)$, can be represented in primitive direct product DVR's.

The multidimensional correlated basis functions for the full molecule are then defined as energy selected products of eigenfunctions of zero order Hamiltonians. The ith wavefunction of the system is expanded as

$$\Psi^{(i)} = \sum_{n_1, n_2, \ldots, n_{n_d}} C^{(i)}_{n_1, n_2, \ldots, n_{n_d}} \prod_{k=1}^{n_d} \phi^{(k)}_{n_k}(q_k), \tag{4}$$

where $C^{(i)}_{n_1, n_2, \ldots, n_{n_d}}$ are expansion coefficients and we include only those product basis functions that satisfy the energy cut-off:

$$\sum_{k=1}^{n_d} \epsilon^{(k)}_{n_k} \leq E_{cut}. \tag{5}$$

Thus the basis is tailored to the potential to span the ranges of coordinates for energies up to E_{cut}. This is, however, a very small basis compared to the direct product of the basis functions for each coordinate group.

2.2. COORDINATE GROUPS AND SEPARABILITY:

In order to have efficient iterative solution of the Schrödinger equation, the spectral range of the Hamiltonian matrix should be restricted. If the choice of coordinates were such that the Hamiltonian is separable into the coordinate groups q_k, then the ΔV and ΔT terms would be small or negligible and the zero order wave functions would be very accurate. In this case also the spectral range of the matrix representation of $\hat{H}$ would then be limited by E_{cut}. Even when the interactions are included, the reduced spectral range of $\hat{H}$ greatly improves the convergence of the iterative methods of solution.

However, if there is significant correlation in the potential between coordinates in different groups, (i.e. significant non-separability between groups) then the ΔV matrix will have large off-diagonal elements coupling different groups. This will increase the spectral range and slow convergence.

One clue to the appropriate grouping of coordinates are the "minimum paths" of the other coordinates $q_{k'}$ along the minimum potentials $\hat{V}^0(q_k)$. If the primed coordinates vary significantly along the minimum potential paths of the unprimed coordinates, then there is significant coupling between the two sets and a better partitioning may be sought. An example of this was given[16] for HCN where the H-CN distance and angle *are* correlated on the path between the stable H-CN minimum and the local minimum at the isomer CN-H. Thus a grouping of distance (r_{H-CN}) and angle $(\theta_{\angle HCN})$ was made for this system to reduce the spectral range of $\hat{H}$.

2.3. ITERATIVE SOLUTION:

We use the Arnoldi algorithm of the ARPACK[14] libraries which is the implementation of implicitly restarted Lanczos method (IRLM) of Sorensen[17]. The

iterative solution requires the user to provide a subroutine for the operation of the Hamiltonian on a vector. In our approach this is done by sequential transformation (as much as possible) to a DVR or other representation in which the ΔV and ΔT terms are easy to evaluate, followed by transformation back to the ESB.

For the triatomic case with one dimensional (1-D) groups of coordinates (i.e. r_1, r_2 and the interior angle θ in Jacobi or Radau coordinates), the explicit zero order Hamiltonians and the ΔV and ΔT terms can be written as:

$$\hat{h}_j = -\frac{1}{2\mu_j}\frac{\partial^2}{\partial r_j^2} + \hat{V}^0(r_j), \quad (j = 1, 2)$$

$$\hat{h}_3 = -f(r_1^e, r_2^e)\left(\frac{1}{\sin\theta}\frac{\partial}{\partial\theta}\sin\theta\frac{\partial}{\partial\theta}\right) + \hat{V}^0(\theta). \tag{6}$$

where (r_1^e, r_2^e) are the fixed values of (r_1, r_2), usually at the equilibrium geometry. For this particular partitioning of the Hamiltonian, we can remove the $\Delta\hat{T}$ term in Eq. (1) by rearranging the Hamiltonian as

$$\hat{H} = \hat{h}_1 + \hat{h}_2 + \frac{f(r_1, r_2)}{f(r_1^e, r_2^e)}\hat{h}_3 + \Delta\hat{V} \tag{7}$$

$$\Delta\hat{V} = \hat{V}(r_1, r_2, \theta) - \hat{V}^0(r_1) - \hat{V}^0(r_2) - \frac{f(r_1, r_2)}{f(r_1^e, r_2^e)}\hat{V}^0(\theta). \tag{8}$$

The three dimensional (3-D) basis functions are then defined as products of eigenfunctions of zero-order Hamiltonians with the energy cut-off criterion. The eigenfunctions for each coordinate, $\phi_n^{(k)}(q_k)$, are represented in the primitive DVR functions and they are denoted as $T_{\alpha n}^{(k)}$, where α is the index for the primitive DVR functions. The Hamiltonian matrix has a simple structure and its elements are given by ($\mid n, m, l\rangle$ is a product ESB function)

$$\langle n', m', l' \left| \hat{H} \right| n, m, l\rangle = \delta_{n'n}\delta_{m'm}\delta_{l'l}\left(\epsilon_n^{(1)} + \epsilon_m^{(2)}\right) + \delta_{l'l}\epsilon_l^{(3)}\frac{\langle n', m' \left| f(r_1, r_2)\right| n, m\rangle}{f(r_1^e, r_2^e)}$$

$$+\langle n', m', l' \left| \Delta\hat{V} \right| n, m, l\rangle. \tag{9}$$

From Eq. (9), we can divide the matrix-vector product into three parts. Since the first term in Eq. (9) is diagonal and is obtained from Eq. (3), its contribution to the cost of matrix-vector product is trivial. For the third term, we evaluate the matrix-vector product by transforming the vector in the ESB representation to the primitive DVR. For the second term, we may explicitly calculate $\langle n', m' \left| f(r_1, r_2)\right| n, m\rangle$ and save it before the matrix-vector product routine is called.

Explicitly, the (n', m', l') element of the matrix-vector product is given by

$$
u_{n'm'l'} = (\epsilon_{n'}^{(1)} + \epsilon_{m'}^{(2)})v_{n'm'l'} + \sum_{\alpha}^{n_\alpha} \tilde{T}_{\alpha n'}^{(1)} \sum_{\beta}^{n_\beta} \tilde{T}_{\beta m'}^{(2)} \times
$$

$$
\left[\epsilon_{l'}^{(3)} \frac{f(r_\alpha, r_\beta)}{f(r_1^e, r_2^e)} + \sum_{\gamma}^{n_\gamma} \tilde{T}_{\gamma l'}^{(3)} \Delta V(r_\alpha, r_\beta, \theta_\gamma) \sum_{l}^{l_{max}} T_{\gamma l}^{(3)} \right] \sum_{m}^{M(l)} T_{\beta m}^{(2)} \sum_{n}^{N(m,l)} T_{\alpha n}^{(1)} v_{nml} \quad (10)
$$

where $(n_\alpha, n_\beta, n_\gamma)$ and $(r_\alpha, r_\beta, \theta_\gamma)$ are the number and the location of primitive DVR points for (r_1, r_2, θ), respectively. Note that the upper limits for the summations over n and m depend on (m, l) and (l), respectively, due to the non-direct product nature of the basis. The limits of the summations, $N(m, l)$ and $M(l)$ may be stored in small arrays before the matrix-vector routine is called. In practice, the summation is carried out sequentially from the right to the left of Eq. (10).

In other words, the summation over n is carried out first for all values of (α, m, l), which transform the vector v into the DVR for r_1 and the $\phi_m^{(2)}(r_2)\phi_l^{(3)}(\theta)$ representation for for (r_2, θ). The subsequent summation over m for all values of (α, β, l) transforms the vector in the (α, m, l) representation to that in (α, β, l) representation. Once the vector is transformed into the primitive DVR for all three coordinates after summing over (n, m, l), the multiplication with the diagonal potential matrix, $\Delta V(r_\alpha, r_\beta, \theta_\gamma)$, is performed. The results are transformed back to the ESB representation by summing over the primitive DVR points for each (n', m', l') element of the u vector.

Since the summation limits are always less than or equal to the summation limits for a direct product basis representation, the number of operations is reduced by the ESB. A more complete description of the advantages of the sequential transformation can be found in the work of Carrington and coworkers.[18]

The overall scaling of the computer time with parameters of the calculation is not simple. It appears, however, that for this simple 3-D case the CPU time scales approximately as the product of the number of accurate solutions desired, N_{soln}, the total number of grid points, N_{grid}, and the number of ESB functions kept, N_{ESB} (which is important for the accuracy). The number of matrix-vector products required per converged eigenvalue depends on these parameters as well as the spectral density and range. This leads to an overall CPU time scaling for a given problem of approximately

$$
\tau \, \alpha \, N_{soln} N_{grid} N_{ESB}
$$

In the very high energy calculations of the vibrational states of H_2O given below, the scaling is slightly slower than this. The ESB is very efficient, with $N_{ESB} \sim 4 \times N_{soln}$ being adequate for about 7 figure accuracy, at least in the H_2O case given below.

3. A simple example: H_2O to dissociation and above

In this section we give an example of the ESB/IRLM solution for the vibrational states of H_2O to the dissociation limit and above. The potential used is reasonably accurate (the PJT2 potential[10] was used) although there may be problems near the dissociation limit. This is a non-trivial problem on which to demonstrate the efficiency and convergence characteristics of the method. The calculations reported here are meant to be representative of a simple triatomic system, not the most accurate possible for real water molecules.

The dissociation energy of this model potential is about 46,350 cm^{-1}, to the minimum of the OH potential. Thus the dissociation energy to H+OH(v=0) requires the addition of the zero point energy of OH, ~1350 cm^{-1}, yielding a D_e of ~47700 cm^{-1}. The model system has over 1340 bound states for $J = 0$, 730 even and 611 of odd symmetry with respect to H exchange.

The DVR grid used was varied from small to quite large, with up to 140 grid points for each of the three dimensions, *i.e.* 2.7x10^6 DVR points. Radau coordinates were used without symmetry reduction which meant that each calculation yielded all vibrational states. The grids were simple, evenly spaced (Chebychev) points in r_1 and r_2 and Legendre points for θ. These choices are simple but not optimal. Use of PODVR's[19, 20] might reduce the grid size by a factor of 2 to 4 with a proportionate decrease in CPU time. Use of symmetry would reduce the grid size by a factor of two.

It is instructive in this case to examine briefly the zero order potentials and eigenvalues. Using Radau coordinates the potentials for r_1 and r_2 are identical. The zero order potentials are given Figures 1 and 2 as functions of bond length (R_{OH}) and bond angle ($\cos(\theta_{\angle HOH})$). The barrier to linearity is just over 10000 cm^{-1} and the dissociation energy (given by $\hat{V}^0$ at large R_{OH}) is just over 46300 cm^{-1}. The zero order energies for $\hat{h}_1(r_1)$ (stretch) and $\hat{h}_3(\theta)$ (bend) are given in Figures 3 and 4, respectively. For $\hat{h}_3(\theta)$, r_1 and r_2 are set to equilibrium value, r_j^e, in the kinetic energy operator as defined in Eq. (6). It is worth noting that the zero order energies for both coordinates show a linear (harmonic) range followed (for stretch coordinates) by an anharmonic regime near the dissociation energy, followed by a quadratic behavior in the "square well" due to the finite range of the basis at higher energy. Thus the higher zero order energy states represent a discretization of scattering states in this energy range. The quadratic behavior of the high energy zero order angular states is due to nearly "free rotation".

The convergence was checked with respect to the grid size, the ESB size and the ranges of the coordinates. Agreement to .02 cm^{-1} was found between the largest calculations for almost all the lowest 1400 states. The largest calculation, with 140 DVR points in each dimension, corresponding to the maximum $R_{OH} = 13.3$ au, and $E_{cut} = 80,000$ cm^{-1} resulted in an ESB of 11788 3-D functions. The size of direct product 3-D basis (without imposing energy cut-off) would have been $68 \times 68 \times 42 = 194,208$ functions. This calculation required 7143 matrix vector products to converge (within the basis) 1800 eigenvalues (even and odd) and took
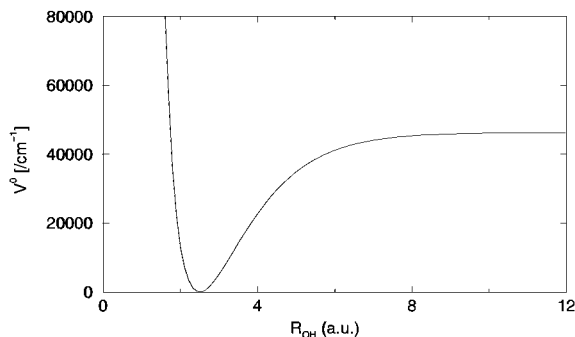
Figure 1. The minimum potential for stretch coordinate is plotted with respect to the OH bond distance, R_{OH}.
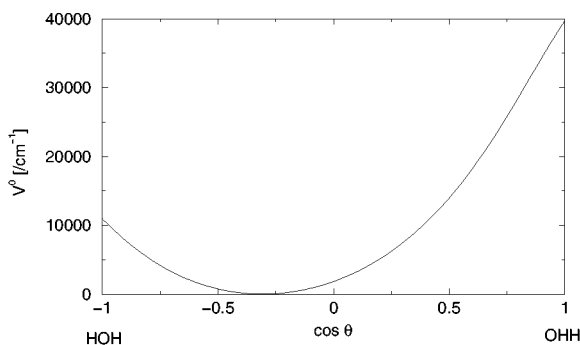
Figure 2. The minimum potential for bend coordinate is plotted with respect to the bond angle, $\cos(\theta_{\mathrm{HOH}})$.

$T_{largest} = 535$ minutes on a single 2.4 GHz Pentium IV processor. A more modest calculation with 11369 basis functions and 120 points per dimension yielded 1500 eigenvalues in $T_{modest} = 100$ minutes. This shows the scaling noted above:
$T_{largest} = (535 \text{ m}) \sim T_{modest} \times (N_{solnL}/N_{solnM}) \times (N_{DVRL}/N_{DVRM}) \times (N_{ESBL}/N_{ESBL}) = (567 \text{ m})$

Above the dissociation energy both resonance and discrete representations of the scattering states exist in the "bound" state calculation. Figure 5 shows both the convergence of the eigenvalues of the bound states and the variation of the eigenvalues above the dissociation energy with respect to the range of radial coor-
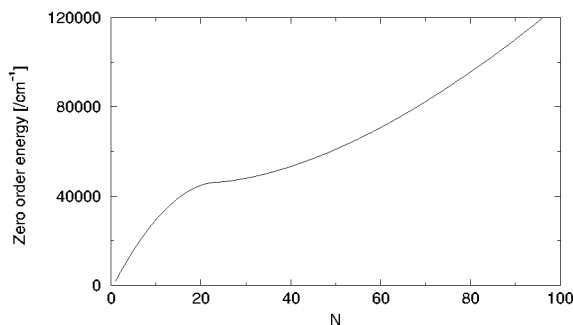
Figure 3. Zero order energies for stretch coordinate (r_i)
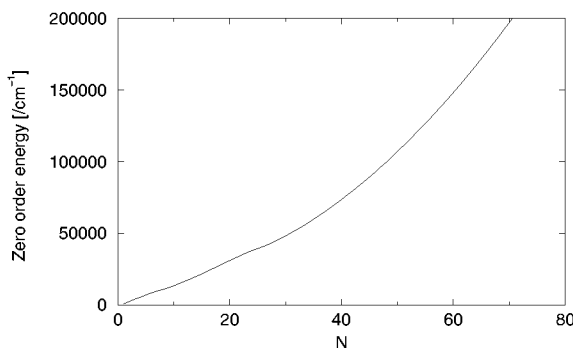
Figure 4. Zero order energies for bend coordinate (θ). The angular kinetic energy is calculated with the radial coordinates fixed at their equilibrium value.

dinate.

The resonance states are easy to identify by their stability with respect to variation of the range. Even states between number 730 and about 790 appear to be resonance states since they vary only slightly ($< .03$ cm^{-1}) with the range of the radial grid. Most even states above 790 vary substantially with range and are probably discrete representations of scattering states (or equivalently very short lived resonance states). However, even in this energy range (> 48700 cm^{-1}) there are resonance states which have very small variation with range. The lifetimes of these states can presumably be determined by adding an absorbing potential
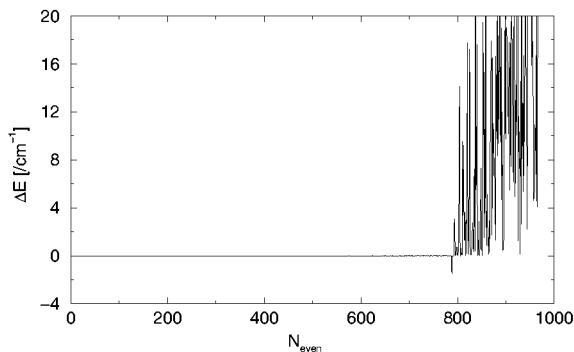
Figure 5. Variation of even vibrational energy levels of H_2O near the dissociation energy with the range of grid in stretch coordinate. Plotted is the energy difference between two calculations with maximum $R_{OH} = 12.78$ a.u. and 13.31 a.u. The last even bound state is number 730.
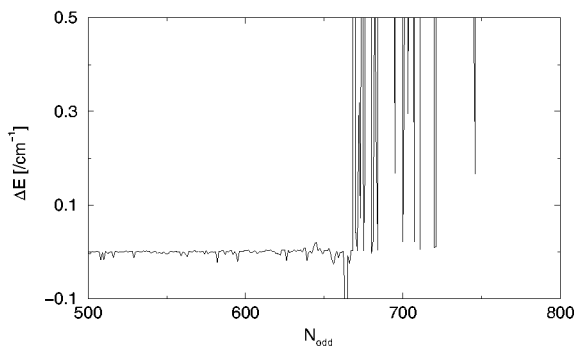
Figure 6. Variation of odd vibrational energy levels of H_2O near the dissociation energy with the range of stretch coordinate. Plotted is the energy difference between two calculations with maximum $R_{OH} = 12.80$ a.u. and 13.30 a.u.. The energy scale is expanded to show resonances for which the energy does not vary with the grid range. The last odd bound state is number 611.

to the Hamiltonian and using the last 100 or so states as a basis, diagonalizing it to yield the complex resonance energies.[6] We did not evaluate the lifetimes explicitly.

The odd states vary in a very similar fashion. In Figure 6 we show an enlarged view of the variation of the odd state energies with the range of the DVR for states

below and above the dissociation energy. The negative ΔE's near states 664 are the result of quadrature errors for the smaller calculation, all but one (# 664) of which are smaller than 0.1 cm^{-1}.

4. Conclusion and Comments:

In this paper we have reviewed briefly the ESB algorithms and in particular their application to the bound states and resonances of the PJT2 PES for the water molecule. The application demonstrates the efficiency of the approach, with all bound states below 46,200 cm^{-1} being converged to about 0.1 cm^{-1}. The last few states below dissociation are probably not converged this well since the range of stretch coordinates for the largest calculation was to $R_{OH} = 13.3$ a.u. where the potential was still ~ 10 cm^{-1} below D_e.

The results given in this paper demonstrate that the ESB generated using reduced dimensional minimum potentials and the energy cut-off provides an excellent basis for multidimensional vibrational problems. The ESB provides a very compact representation adequate for eigenfunctions up to a pre-selected energy which has a reduced spectral range and which can be used effectively in an iterative method of solution. In the calculations reported here we used the IRLM of ARPACK[14] with excellent results. Even without optimization of the grid or symmetry reduction, the combination of basis size reduction, spectral range reduction and iterative solution permitted the use of very large grids and the accurate calculation of over 1400 bound states in quite reasonable computation times. The ESB approach should also be advantageous for determination of resonances and unimolecular dissociation rates as well as for the square integrable portions of scattering calculations.

We close by discussing some remaining questions about this approach. The simplest is

"Why is $E_{cut} \sim 80000$ cm^{-1} required for accurate calculation of eigenvalues to about 52000 cm^{-1}?"

There appear to be two major reasons. First, the separability of the PES in Radau coordinates is good, but far from perfect for H_2O. Therefore the basis must be sufficiently large to yield accurate results to the desired energy. Since the density of states of the zero order ESB is close to that of the exact states and the coupling increases some energies, extra basis functions are required to converge the energies desired. Since the coupling depends on the coordinates and the PES, the number of extra functions will vary. However, the ratio of basis size to accurate eigenvalues for the ESB (< 5) is excellent for this system.

A second reason may be that the ESB may not be "well tempered", i.e. may not cover the desired phase space uniformly. In particular, the kinetic energy operator for angles is approximated in the zero order Hamiltonians. If $f(r_1, r_2)$ used in $\hat{h}_3(\theta)$ is too large, then the density of angular states will be reduced and fewer angular functions will be included in the ESB at a given E_{cut}. This appears to be the case

for H_2O where we included only 42 angular functions versus 68 for each stretch with E_{cut} of 80,000 cm^{-1}.

Finally the use of PODVR's and symmetry should improve the efficiency of the calculations substantially. We have also used the method to look at four atom (six dimensional) systems such as HOOH and H_2CO. These are, of course, much more demanding and require the use of PODVR's and symmetry reduction. These will be reported in separate publications.

References

1. P. R. Bunker and P. Jensen (1998) Molecular Symmetry and Spectroscopy, NRC, Ottawa.
2. J. Cullum and R. A. Willoughby (1985) Lanczos algorithm for large symmetric eigenvalue computation, Birkhäuser, Boston
3. D. C. Sorensen (1992) Implicit application of polynomial filters in a k-step Arnoldi method, *SIAM J. Matrix Anal. Appl.* **13**, pp. 357.
4. V. A. Mandelshtam, T. P. Grozdanov and H. S. Taylor (1995) Bound states and resonances of the hydroperoxyl radical HO_2: An accurate quantum mechanical calculation using filter diagonalization, *J. Chem. Phys* **103**, pp. 10074.
5. D. Neuhauser (1990) Bound state eigenfunctions from wave packets: Time → energy resolution, *J. Chem. Phys.* **93**, pp. 2611.
6. D. Wang and J. M. Bowman (1994) L^2 calculations of resonances and final rotational distributions for HCO → H + CO, *J. Chem. Phys.* **100**, pp. 1021.
7. J.M. Hutson (1990) Intermolecular Forces and the Spectroscopy of van der Waals molecules, *Annu. Rev. Phys. Chem.* **41**, pp. 123.
8. R. Schinke (1993) Photodissociation Dynamics, Cambridge University Press.
9. Z. Bacic and J. C. Light (1989) Theoretical Methods for Rovibrational States of Floppy Molecules, *Ann. Rev. Phys. Chem.* **40**, pp. 469.
10. H. Y. Mussa and J. Tennyson (1998) Calculation of the rotation-vibration states of water up to dissociation, *J. Chem. Phys.* **109**, pp. 10885.
11. J. V. Lill and G. A. Parker and J. C. Light (1986) The Discrete Variable-Finite Basis Approach to Quantum Scattering, *J. Chem. Phys.* **85**, pp. 900.
12. J. C. Light and T. Carrington, Jr. (2000) Discrete variable representations and their utilization, *Adv. Chem. Phys.* **114**, pp. 263.
13. Seung E. Choi and John C. Light (1992) Highly Excited Vibrational Eigenstates of Nonlinear Triatomic Molecules: Applications to H_2O *J. Chem. Phys.* **97**, pp. 7031.
14. R. B. Lehoucq and D. C. Sorensen and C. Yang (1996) ARPACK USERS GUIDE: Solution of Large Scale Eigenvalue Problems by Implicitly Restarted Arnoldi Methods, Center for Research on Parallel Computation, Rice University, CRPC-TR96665, Houston, TX.
15. Bill Poirier and Tucker Carrington Jr. (2001) Accelerating the calculation of energy levels and wavefunctions using an efficient preconditioner with the inexact spectral transform method, *J. Chem. Phys.* **114**, pp. 9254.
16. H. S. Lee and J. C. Light (2003) Molecular vibrations: Iterative solution with energy selected bases, *J. Chem. Phys.* **118**, pp. 3458.
17. D. C. Sorensen (1992) Implicit application of polynomial filters in a k-step Arnoldi method, *SIAM J. Matrix Anal. Appl.* **13**, pp. 357.
18. X. G. Wang and T. Carrington, Jr. (2002) New ideas for using contracted basis functions with a Lanczos eigensolver for computing vibra- tional spectra of molecules with four or more atoms, *J. Chem. Phys.* **117**, pp. 6923.
19. J. Echave and D. C. Clary (1992) Potential optimized discrete variable representation, *Chem. Phys. Lett* **190**, pp. 225.
20. H. Wei and T. Carrington Jr. (1992) The discrete variable representation of a Triatomic Hamiltonian, *J. Chem. Phys.* **97**, pp. 3029.

MOLECULAR REACTION STEREODYNAMICS: IN SEARCH OF PATHS TO OVERCOME STERIC HINDRANCES TO REACTIVITY

VINCENZO AQUILANTI, FERNANDO PIRANI
Dipartimento di Chimica, Università di Perugia,
06123 Perugia, Italy

DAVID CAPPELLETTI, FRANCO VECCHIOCATTIVI
Dipartimento di Ingegneria Civile ed Ambientale, Università di Perugia,
06125 Perugia, Italy

TOSHIO KASAI
Department of Chemistry, Graduate School of Science, Osaka University,
Toyonaka, Osaka 560-0043, Japan

1. Introduction

The scope of this article is to account for some aspects regarding the possibility of overcoming steric hindrances in chemical reactivity. This is one of the main themes of research in all fields of chemistry: we will present here a progress report on our understanding of elementary chemical processes and especially some recent achievements in experimental techniques for controlling the spatial orientation of molecules. For the time being, these achievements represent tools for investigations of the basic mechanisms, but perspectives are open to also exploit them for applied purposes.

Since the role of the spatial orientation of molecules in physical, chemical, and biological properties is ubiquitous, control of molecular orientation is a current challenge of advanced research in several areas of molecular sciences. Recently, this aim appears within reach as techniques for molecular alignment become available. In the next section we will illustrate the state of the art with two examples from the laboratories of the authors and then proceed with an overview of current progress in experimental and theoretical approaches and of further perspectives.

2. Aligning and orienting molecules

Two recent papers [1,2] provide updated views of advances in the production of intense and continuous beams of aligned molecules. In [1], it was demonstrated that in the prototypical case of a seeded supersonic expansion of a molecular beam of benzene, besides acceleration and cooling, orientation of the molecular plane also occurs because of the anisotropy of the intermolecular forces which govern collisions. This work is reviewed in Sec.2.1. Previous studies on the collisional alignment of the rotational

angular momentum of diatomic molecules regarded O_2 [3], for which the effect was probed by magnetic analysis, and N_2 [4] for which the probe was molecular beam scattering.

Up to now, we have been using terms like orientation and alignment as synonyms. According to current usage, we should consistently use alignment here, leaving orientation only for cases where one also specifies "heads" or "tails" spatial features of a molecule. However, "alignment of a molecular plane" is somewhat contrary to common linguistic usage and we will often employ "orientation" to obtain a more immediate picture of the phenomenon. We refer to collisional alignment techniques as "natural" ones, as compared to those where external field induce a "forced" alignment. We mention the focusing in electric fields through the Stark effect, which can be either second order for linear molecules [5] or first order for symmetric top molecules [6] (the latter being stronger than the former), the use of polarized absorption (limited to optically favorable transitions in the molecular manifold) [7], the *brute force* [8] techniques, which use strong electrical or magnetic fields and are applicable only to rotationally relaxed molecules with permanent electric or magnetic dipole moments, and the alignment in intense non-resonant laser fields [9]. Further details and updated developments toward dramatic improvement in intensity was reported in [2] and briefly summarized in Sec.2.2.
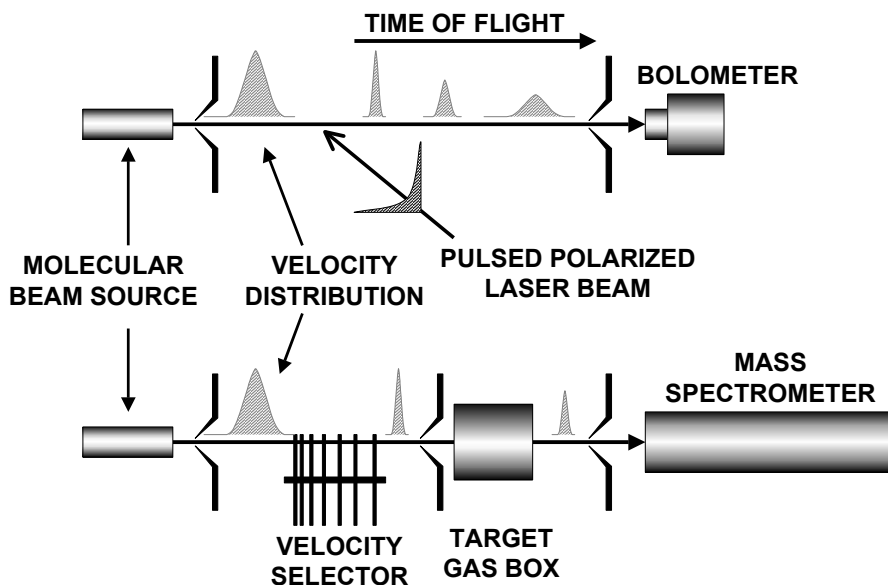
Figure 1 - The two experimental arrangements used to probe the alignment of benzene molecules in a seeded supersonic beam by direct polarized IR laser absorption (upper device) and molecular beam scattering (lower device). For further details see Ref. [1].

2.1. NATURAL ALIGNMENT IN SUPERSONIC SEEDED BEAMS

A natural and effective molecular alignment technique involves microscopic collisions in environments exhibiting anisotropic velocity distributions, such as supersonic expansions of seeded molecular beams. Simple inorganic molecules, like Na_2 [10,11], Li_2 [12], I_2 [13–17], and CO_2 [18], have been found to align their rotational angular momentum in supersonic expansions when seeded with lighter carriers. Considerable efforts were devoted to the characterization of the dependence of the phenomenon on the probed rotational levels and on the beam source conditions, such as the stagnation pressure, the gas carrier composition, and the angular displacement of the molecular beam axis [11,13–18].

In 1994, by measuring the variation of the paramagnetism of O_2 in continuous supersonic seeded molecular beams of molecular oxygen relaxed in the lowest rotovibrational states, the first experimental evidence of the strong dependence of the alignment on the final molecular speed was reported by some of the authors [3]. Later, similar effects were observed by UV spectroscopy on CO in molecular beams seeded in He [19]. These findings, depending on the analyzed rotational level, were ascribed to the sequence of state-to-state elastic and inelastic events, associated with the large number of collisions in the expansion zone [20] and to the selective dependence of their relative role on the total angular momentum of the collision complex [21,22]. Further probing of alignment by scattering cross section measurements, performed downstream of the beam source and using as projectiles velocity selected O_2- and N_2-seeded molecular beams and rare gas as targets [4,23], confirmed the correlation between molecular alignment and molecular velocity and allowed both an accurate determination of the involved interaction potential energy surfaces and characterization of the collisional dynamics of aligned molecules [24–26]. These experiments suggested that measurements of anisotropy effects in the scattering cross sections, combined with a proper velocity selection of the molecular beams, are an alternative source of information on the molecular alignment degree if the topography of the potential energy surface and details of the involved collisional dynamics are available.

Recently, our interest has been addressed to the demonstration that the disk-shaped benzene molecule in supersonic seeded molecular beams would act similarly. Note that in this case the alignment of the rotational angular momentum corresponds to a preferential orientation of the molecular plane along a particular direction. Benzene is a favorite target of organic chemists, for studies of steric effects, so we could imagine a wide range of applications for an oriented benzene molecular beam, in particular for investigation of the stereodynamics of elastic, inelastic, and reactive events. The probing of the orientation has been carried out through two complementary experiments -direct IR laser absorption and molecular beam scattering- and preliminary results have been anticipated in a Letter [27], while [1] gives a full account. An accompanying Fig.1 shows a sketch of the two experimental arrangements.

2.2. FORCED ORIENTATION BY HEXAPOLE FIELD: THE HONEYCOMB

Several molecular beam techniques to select the molecular orientation have been developed using electrostatic [28-33] or optical methods [34]. Other references have

been listed above. Here we deal in particular with the hexapole electrostatic state-selector, which is frequently employed to study the stereodynamics in chemical reactivity, such as reactive gas-phase scattering [35], surface scattering [36], photodissociation [37], and electron scattering [38], because of the high degree of molecular orientation which can be achieved with this technique. Even the selection of a single quantum rotational-state of molecule can be achieved using a long hexapole field [39,40].
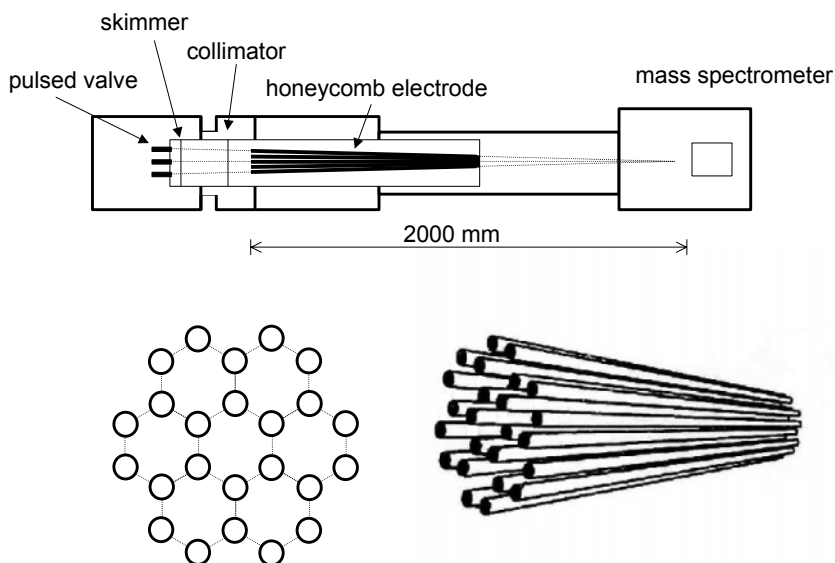

Figure 2 - The upper panel shows a global view of the apparatus, where the hexapole honeycomb electrode is installed. The geometry of the field and a perspective look of the road system to generate it are also shown. Further details can be found in Ref. [2].

The beam intensities of oriented molecules using hexapole electric field, however, turn out to be poor because the state selection requires a very large flight-length as compared with conventional molecular beam set-ups. In order to increase the beam intensity, one may propose a way to increase the stagnation pressure of the nozzle. However, the characteristics of the molecular beam such as stream velocity, rotational temperature and the size distribution of clusters are generally changed [41]. Motivation of the study of Ref.[2] has been to develop a new type of electrostatic state-selector in order to produce an intense oriented molecular beam. Basic idea of this experiment has been that the beam intensity should be simply proportional to the number of beam lines if the molecular beams can be focused on a point in space.

Fig. 2 illustrates the new apparatus for the "honeycomb electric field" which consists of seven sets of nozzle, skimmer, collimator, and electric field. This new type of electro-

static state-selector that consists of seven sets of adjacent hexapole fields forming a honeycomb field has been newly developed in order to integrate intensities of seven oriented molecular beam lines [2]. The cross section of the electric field is gradually diminished from the inlet to the outlet in order to sum up the seven molecular beam lines and focus on a focal point located at 1000-mm down-stream from the honeycomb field outlet. Again, non-focusable rare gases such as Ar and Kr were used as to check the assembly alignment, and then the polar molecule acetonitrile (CH$_3$CN, μ=3.92 D) seeded in the noble gases was employed to characterize the quantum state-selectivity of the honeycomb field. The dependence of the focused CH$_3$CN beam intensity on the honeycomb electrode voltages was obtained. It was also possible to reproduce the experimental focusing curve by use of a modified trajectory simulation applicable to the honeycomb electric field. The present beam character (i.e. rotational temperature and stream velocity) was confirmed to be maintained. Fig.2 provides some schematic views of the device and Ref. [2] gives further details.

3. Stereospecific control by molecular orientation: experiments and theory

In this section, the authors give a personalized account of the most recent (even unpublished) experiments and theoretical advances with which they are familiar.

3.1. EXPERIMENTS

Studies of the photodissociation dynamics of HCl dimers using hexapole electric fields (see for example Ref. [41]) give indication on the relative orientations of the monomers in establishing the properties of the dimer itself. In the latest activity of the group of P. R. Brooks [42-44] the process of electron transfer for K to oriented t-butyl bromide is found strongly dependent on the orientation. Systems involving metal atoms are traditional favorites of molecular beam studies, particularly of stereodynamics. In recent experiments [45], with *brute force* oriented ICl, experimental determination was made of the cone of acceptance for reactivity (steric effect) in a "harpooning" reaction, Sr + ICl leading to electronically excited products detected via their chemiluminescence [45].

The hexapole technique has been extensively exploited for the study of oriented open shell molecules such as OH (see Ref. [46] and references therein) and NO (see Ref. [47] and references therein), the latter also for scattering on surfaces [48]. This is a very important topic, because the basic tool for enhancement of chemical reactivity is catalysis at surfaces. In Ref. [49], for examples, the oxidation of Si (001) induced by incident energy of O$_2$ molecules is studied by synchrotron radiation photoemission spectroscopy and mass spectrometry, a process of a kind which may show propensities regarding molecular orientation of O$_2$ as it impinges on the surface, possibly controlled by techniques of the kind described in previous sections.

In a recent experiment [50] the sticking of ethylene molecules on a (001) Ag surface, at 80 K and saturated with O$_2$ molecules, has been studied as a function of the degree of alignment of ethylene as produced in a velocity selected supersonic seeded beam. It has been found that the sticking coefficient strongly depends on such an alignment: when

the molecules arrive on the surface rotating "helicopter"-like, they have a sticking tendency about 30% larger than that when they arrive rotating "cartwheel"-like.

3.2. THEORY

Relevant to the topic of surface scattering, the theory reviewed in [51] described an approach to surface science which specifically leads to a reaction design where the conversion yield for the ortho-para hydrogen conversion via catalysis on a copper surface is increased by molecular orientation. This is a process of possible relevance for the extremely important problem of hydrogen storage in the anticipated crucial technology of future energetic power sources. The theory is checked against early experimental findings for production of aligned molecules ["helicopter" or "cartwheel" states] in collisional dissociation at surfaces [52].

Reaction stereodynamics focuses on vector properties, such as angular momentum vector correlation and steric effects, of the reactive process under investigations. Thanks to the development of molecular beam techniques with polarized lasers as well as electric and magnetic fields, experimental observation of stereodynamics properties has become feasible [53] and also their theoretical investigation has recently been performed using a time-independent hyperspherical coordinate method. Within this approach, it is possible to calculate the full S matrix, from which exact 3-D values of stereodynamic properties can be derived. We refer e.g. to Ref. [54] for a recent comparative study of classical and quantum stereodynamics for the $O(^1D)+H_2$ reaction. We have shown some time ago that reaction stereodynamics studies can be carried out using alternative representations of the S matrix. Body-fixed representations, each of them taking a different vector of the arrangement as the quantization axis, are particularly advantageous. The stereodirected representation is characterized by the introduction of the steric quantum number, ν, the projection of an artificial vector, precessing around the Jacobi vector pointing from the diatom center of mass to the third atom of the arrangement. As the modulus of this vector increases, the grid of the discrete values of the precession angle more finely scans the angle between the Jacobi vectors. Different representations can be easily interconverted by means of orthogonal transformations, expressed in terms of Wigner $3j$ symbols, which preserve the symmetry and unitarity of the S matrix in each representation [55,56]. The exact 3-D method based on the stereodirect representation has recently been employed to calculate stereodynamic properties of the reactions Li + HF [57,58], Na + HF [59], Sr + HF [60], F + HCl [61], and C + CH [62,63] for zero total angular momentum. The extension to all partial waves has been made for the F + H_2 reaction [64].

4. Conclusions

In the preceding sections we have listed experimental progress and theoretical analysis on the theme of how to overcome obstacles to reactivity by acting on the preexponential (steric factor) ingredient of the Arrhenius equation, a not so often exploited path with respect to the conventional catalysis mechanisms which operate mainly on the

activation energy. Our point of view has been at the level of microscopic elementary processes and it is anticipated that possible practical applications will necessitate further effort at this level.

Acknowledgments

References

1. Pirani F., Bartolomei M., Aquilanti V., Scotoni M., Vescovi M., Ascenzi D., Bassi D., and Cappelletti D. (2003), *J. Chem. Phys.* **119**, 265.
2. Shimizu Y., Che D. –C., Hashinokuchi M., Fukuyama T., Suzui M., M. Watanabe, and Kasai T. (2003), *Rev. Scient. Instrum.* **74**, 3749.
3. Aquilanti V., Ascenzi D., Cappelletti D., and Pirani F. (1994), *Nature* **371**, 399; Aquilanti V., Ascenzi D., Cappelletti D., and Pirani F. (1995), *J. Phys. Chem.* **99**, 13620.
4. Aquilanti V., Ascenzi D., Cappelletti D., Fedeli R., and Pirani F. (1997), *J. Phys. Chem. A* **101**, 7648.
5. Toennies J. P. (1962), *Discuss. Faraday Soc.* **33**, 96; Bennewitz H. G., Kramer K. H., Paul W., and Toennies J. P. (1964), *Z. Phys.* **84**, 177; Lübert A., Rotzoll G., and Günther F. (1978), *J. Chem. Phys.* **69**, 5174.
6. Kramer K. H. and Bernstein R. B. (1964), *J. Chem. Phys.* **40**, 200; Brooks P. R. and Jones E. M. (1966), *J. Chem. Phys.* **45**, 3449; Brooks P. R. and Jones E. M. (1982) *Ber. Bunsenges. Phys. Chem.* **86**, 413; Kasai T., Fukawa T., Matsunami T., Che D.-C., Ohashi K., Fukunishi Y., Ohoyama H., and Kuwata K. (1993), *Rev. Sci. Instrum.* **64**, 1150.
7. Karny Z., Estler R. C., and Zare R. N. (1978), *J. Chem. Phys.* **69**, 5199; Treffers M. A. and Korving J. (1983), *Chem. Phys. Lett.* **97**, 342; Hoffmeister M., Schleysing R., and Loesch H. J. (1987), *J. Phys. Chem.* **91**, 5441; Mattheus A., Fischer A., Ziegler G., Gottwald E., and Bergmann K. (1986), *Phys. Rev. Lett.* **56**, 712; Hefter U., Ziegler G., Mattheus A., Fischer A., and Bergmann K. (1986), *J. Chem. Phys.* **85**, 286; Mc-Caffery A. J., Reid K. L., and Whitaker B. J. (1988), *Phys. Rev. Lett.* **61**, 2085; Tsubouchi M., Whitaker B. J., Wang R. L., Kohguchi H., and Suzuki T. (2001), *Phys. Rev. Lett.* **86**, 4500.
8. Loesch H. J. and Remscheid A. (1990), *J. Chem. Phys.* **93**, 4779; Friedrich B. and Herschbach D. R. (1991), *Nature* **353**, 412; Friedrich B. and Herschbach D. R. (1991) *Z. Phys. D: At., Mol. Clusters* **18**, 153; Friedrich B. and Herschbach D. R. (1992) **24**, 25.
9. Friedrich B. and Herschbach D. R. (1995), *Phys. Rev. Lett.* **74**, 4623; Seideman T (1995)., *J. Chem. Phys.* **103**, 7887; Kim W. and Felker P. M. (1996), *J. Chem. Phys.* **104**, 1147; Larsen J. J., Hald K., Bjerre N., and Stepelfeldt H. (2000), *Phys. Rev. Lett.* **85**, 2470; Velotta R., Hay N., Mason M. B., Castillejo M., and Marangos J. P. (2001), *Phys. Rev. Lett.* **87**, 183901.
10. Sinha M. P., Caldwell C. D., and Zare R. N. (1974), *J. Chem. Phys.* **61**, 491.
11. Hefter U., Ziegler G., Mattheus A., Fischer A., and Bergmann K. (1986), *J. Chem. Phys.* **85**, 286.
12. Rubahn H. G. and Toennies J. P. (1988), *J. Chem. Phys.* **89**, 287.
13. Visser A. G., Bekooy J. P., van der Meij L. K., de Vreugd C., and Korving J. (1977), *Chem. Phys.* **20**, 391.

14. Sanders W. R. and Anderson J. B. (1984), *J. Phys. Chem.* **88**, 4479.
15. Pullmann D. P., Friedrich B., and Herschbach D. R. (1990), *J. Chem. Phys.* **93**, 3224.
16. Freidrich B., Pullmann D. P., and Herschbach D. R. (1991), *J. Phys. Chem.* **95**, 8118.
17. Saleh A. J. and McCaffery A. J. (1993), *J. Chem. Soc., Faraday Trans.* **89**, 3217.
18. Weida M. J. and Nesbitt D. J. (1994), *J. Chem. Phys.* **100**, 6372.
19. Harich S. and Wodtke A. M. (1997), *J. Chem. Phys.* **107**, 5983.
20. Fair J. R. and Nesbitt D. (1999), *J. Chem. Phys.* **111**, 6821.
21. Pullmann D. P., Friedrich B., and Herschbach D. R. (1995), *J. Phys. Chem.* **99**, 7407.
22. Aquilanti V., Ascenzi D., De Castro-Vitores M., Pirani F., and Cappelletti D. (1999), *J. Chem. Phys.* **111**, 2620.
23. Aquilanti V., Ascenzi D., Cappelletti D., Franceschini S., and Pirani F. (1995), *Phys. Rev. Lett.* **74**, 2929.
24. Aquilanti V., Ascenzi D., Cappelletti D., de Castro-Vitores M., and Pirani F. (1998), *J. Chem. Phys.* **109**, 3898.
25. Aquilanti V., Ascenzi D., Bartolomei M., Cappelletti D., Cavalli S., de Castro-Vitores M., and Pirani F. (1999), *Phys. Rev. Lett.* **82**, 69.
26. Aquilanti V., Ascenzi D., Bartolomei M., Cappelletti D., Cavalli S., de Castro-Vitores M., and Pirani F. (1999), *J. Am. Chem. Soc.* **121**, 10794.
27. Pirani F., Bartolomei M., Cappelletti D., Aquilanti V., Scotoni M., Vescovi M., Ascenzi D., and Bassi D. (2001), *Phys. Rev. Lett.* **86**, 5035.
28. Kramer K. H., and Bernstein R. B. (1964), *J. Chem. Phys.* **42**, 767.
29. Brooks P. R. (1976), *Science* **91**, 5365.
30. Stolte S. (1982), *Ber. Bunsen-Ges, Phys. Chem.* **86**, 413.
31. Parker D. H., and Bernstein R. B. (1989), *Annu. Rev. Phys. Chem.* **40**, 561.
32. Loesch H. J., and Remscheid A. (1990), *J. Chem. Phys.* **93**, 4779.
33. Friedrich B., and Herschbach D. R. (1991), Nature **353**, 412; Rost J. M., Griffin J. C., Friedrich B., and Herschbach D. R. (1992), Phys. Chem. Lett. **68**, 1299.
34. Hasselbrink E., Waldeck J. R., and Zare R. N. (1988), *Chem. Phys.* **126**, 191.
35. Parker D. H., Jalink H., and Stolte S. (1987), *J. Phys. Chem.* **91**, 5427; Ohoyama H., Kasai T., Ohashi K., and Kuwata K. (1992), *Chem. Phys.* **165**, 155.
36. Kuipes E. W., Tennet M. G., and Kleyn A. W., and Stolte S. (1988), *Nature* **334**, 420; Fecher G., Volker M., and Bernstein R. B. (1989), *Chem. Phys. Lett.* **161**, 212.
37. Gandhi S. R., Curtiss T. J., and Bernstein R. B. (1987), *Phys. Rev. Lett,* **59**, 2951; Gandhi S. R., and Bernstein R. B (1988)., *J. Chem. Phys.* **88**, 1472.
38. Kasai T., Matsunami T., Fukawa T., Ohoyama H., and Kuwata K. (1993), *Phys. Rev. Lett.* **7**, 3864; Kasai T., Matsunami T., Takahashi H., Fukawa T., Ohoyama H., and Kuwata K. (1995), *J. Phys. Chem.* **99**, 13597.
39. Gandhi S. R., Curtiss T. J., Xu Q. –X., Choi S. E., and Bernstein R. B. (1986), *Chem. Phys. Lett.* **132**, 6.
40. Kasai T., Fukawa T., Matsunami T., Che D. –C., Ohashi K., Ohoyama H., and Kuwata K. (1993), *Rev. Sci. Instrum.* **64**, 1150.
41. Che D. C., Hashinokuchi M., Shimizu Y., Ohoyama H., Kasai T. (2001), *Phys. Chem. Chem. Phys.* **3**, 4979.
42. Harris S. A., Brooks P. R. (2001), *J. Chem. Phys.* **114**, 10569.
43. Brooks P. R., Harris S. A. (2002), *J. Chem. Phys.* **117**, 4220.
44. Jia B., Laib J., Lobo R. F. M., Brooks P. R. (2002), *J. Am. Chem. Soc.* **124**, 13896.
45. Woelke A. (2003), Doctoral Dissertation, Bielefeld, Germany; Woelke A., Loesch H. J. (2003), in preparation.
46. van Beeck M. C., ter Meulen J. J. (2001), *J. Chem. Phys.* **115**, 1843.
47. Alexander M. H., Stolte S. (2000), *J. Chem. Phys.* **112**, 8017.

48. Komrowski A. J., Ternow K., Razaznejad B., Berenbak B., Sexton J. Z., Zoric I., Kasemo B., Lundqvist B. I., Stolte S., Kleyn A. W., Kummel A. C. (2002), *J. Chem. Phys.* **117**, 8185.
49. Teraoka Y., Yoshigoe A. (2002), *Jpn. J. Appl. Phys.* **41**, 4253.
50. Vattuone L., Gerbi A., Rocca M., Valbusa U., Cappelletti D., Pirani F., Vecchiocattivi F., Baraldi A., Comelli G., Petaccia L., Rumiz L. (2003), *in preparation.*
51. Kasai H., Diño W. A., Muhida R. (2033), *Progr. Surf. Sci.* **72**, 53.
52. Hou H., Gulding S. J., Rettner C. T., Wodke A. M., Auerback D. J. (1997), *Science* **277**, 80.
53. Loesch H. J. (1995), *Annu. Rev. Phys. Chem.* **46**, 555.
54. Aoiz F. J., Bañares L., Castillo J. F., Martìnez-Haya B., de Miranda M. P. (2001), *J. Chem. Phys.* **114**, 8328.
55. Aquilanti V., Cavalli S., Grossi G., Anderson R. W. (1991), *J. Phys. Chem.* **95**, 8184.
56. Anderson R. W., Aquilanti V., Cavalli S., Grossi G. (1993), *J. Phys. Chem.* **97**, 2443.
57. Alvariño J. M., Aquilanti V., Cavalli S., Crocchianti S., Laganà A., Martìnez T. (1997), *J. Chem. Phys.* **107**, 3339.
58. Alvariño J. M., Aquilanti V., Cavalli S., Crocchianti S., Laganà A., Martìnez T. (1998), *J. Phys. Chem.* **102**, 9638.
59. de Miranda M. P., Gargano R. (1999), *Chem. Phys. Lett.* **309**, 257.
60. Tang B. -Y., Yang B. -H., Zhang L., Han K. -L., Zhang J. Z. H. (2000) *Chem. Phys. Lett.* **327**, 381.
61. Tang B. -Y., Yang B. -H., Han K. -L., Zhang R. -Q., Zhang J. Z. H. (2000) *J. Chem. Phys.* **113**, 10105.
62. Tang B. -Y., Chen M. -D., Han K. -L., Zhang J. Z. H. (2001) *J. Chem. Phys.* **115**, 731.
63. Tang B. -Y., Chen M. -D., Han K. -L., Zhang J. Z. H. (2001) *J. Phys. Chem.* **105**, 8629.
64. Aldegunde J., De Fazio D., unpublished results.

THE ROTATING BOND UMBRELLA MODEL APPLIED TO ATOM-METHANE REACTIONS

GUNNAR NYMAN
Göteborg University
Department of Chemistry, Physical Chemistry,
Göteborg University, SE-412 96, Göteborg, Sweden

Abstract. To accurately treat chemical reactions, methods based on quantum dynamics may be required. For most reactions involving several atoms, applying full quantum dynamics is presently prohibitive in terms of computer demand. One option is then to use reduced dimensionality approaches. Here we will focus on the Rotating Bond Umbrella (RBU) model and its application to atom-methane reactions. In the RBU model four internal motions are treated explicitly, viz. the breaking and forming bonds, the umbrella motion, and a reactant bend motion, which becomes a product CH_3 rotation. Hyperspherical coordinates are used. Here we describe how accurate boundary conditions are applied and how the matrices relating to the angular degrees of freedom are diagonalized using the iterative Guided Spectral Transform eigenproblem solver. We end by showing some illustrations of calculations for the A $(A=H,O,Cl)+CH_4 \rightarrow HA + CH_3$ reactions and a deuterated analogue.

1. Introduction

Chemistry is a broad discipline of science but central to it is chemical reactions. Studies of chemical reactions have traditionally focussed on determining thermal rate constants. With the availability of lasers, more detailed quantities such as integral and differential cross sections become accessible, even on a state-to-state level in favourable cases. While initially experimental efforts dominated, today the development goes hand in hand with theoretical efforts which become more and more accurate.

Here we are interested in the theoretical description of reaction dynamics of small gas phase reactions. In many cases a good description of how the reactions occur can be obtained by solving the classical equations of motion. This is usually the case when we are interested in highly averaged results, where state-to-state

253

information gets washed out, and if the atoms involved are reasonably heavy. We will however be particularly interested in reactions where a light atom, usually the hydrogen atom, is involved in a bond-breaking/bond-forming process. Tunneling will then play a role, particularly so at low temperatures. Our aim shall therefore be to include this effect, which here is done by solving the quantum mechanical Schrödinger equation in reduced dimensionality. We shall assume that the Born-Oppenheimer approximation is valid.

Time-independent approaches to quantum dynamics can be variational where the wavefunction for all coordinates is expanded in some basis set and the parameters optimized. The best known variational implementation is perhaps the S-matrix version of Kohn's variational principle which was introduced by Miller and Jansen op de Haar in 1987[1]. Another time-independent approach is the so called hyperspherical coordinate method. The name is unfortunate as hyperspherical coordinates may also be used in other contexts, for instance in time-dependent wavepacket calculations[2].

The hyperspherical coordinate method is the subject of the present article. In this method, one coordinate, the hyperradius, is treated by a propagator method. This leaves one coordinate less to treat by a basis set expansion than in the variational approaches. Thus the corresponding matrices are one dimension smaller. Here I will focus on two aspects of the theory, viz. the application of boundary conditions and how the matrices can be diagonalized. A short derivation of a Hamiltonian operator for umbrella type motions is also included. I will end with some illustrations of calculations that we have performed and finally there will be some concluding remarks.

2. Reduced dimensionality models

An early reduced dimensionality model is the Rotating Linear Model (RLM) of Child[3], Wyatt[4], and Connor and Child[5], developed in the late sixties. In this model the dynamics of atom-diatom reactions is treated in a collinear arrangement which is allowed to rotate. Walker and Hayes implemented a correction to include adiabatic effects of the bending degrees of freedom in their ground states. This produced the bending-corrected RLM which has been reviewed previously[6, 7]. Inclusion of these bending corrections is important and has been frequently used[6]. Nyman has used essentially the RLM model to treat larger reactions by approximately including the zero point energy of all modes not explicitly treated. This 2D model is referred to as the Rotating Line Approximation (RLA)[8, 9].

Four-atom reactions came into focus with the development by Clary of the Rotating Bond Approximation (RBA)[10, 11] and Bowman's reduced-dimensionality adiabatic bend (RD-AB) calculations of four-atom reactions. In the latter three stretching vibrational motions are treated explicitly quantum dynamically while the bending degrees of freedom are treated adiabatically and one diatom is assumed to be a spectator[12, 13, 14, 15, 16]. The RBA may be seen as an extension

of the RLM by exchanging the atom for a diatom, which is allowed to rotate. For a reaction AB+CD $\rightarrow$ A+BCD the RBA treats the breaking bond of AB, the forming bond BC, the rotation of CD, the bend of BCD and overall rotation. Sometimes the CD vibration is also treated.

Yu and Nyman have developed two reduced dimensionality models intended for A+CD$_3$H $\rightarrow$ HA+CD$_3$ reactions, where often CD$_3$H has been methane. These models have been termed the rotating line umbrella (RLU) model[17, 18] and the rotating bond umbrella (RBU) model[19]. These may again be viewed as extensions of the RLM by adding an umbrella motion (RLU) and for the RBU model additionally adding a bending motion of CD$_3$ about the line AHP where P is the center of mass of CD$_3$. For the reactions O+CH$_4$ $\rightarrow$ OH+CH$_3$ and H+CH$_4$ $\rightarrow$ H$_2$+CH$_3$ accurate rate constants, for a given potential energy surface, have been calculated and those have turned out to be in excellent agreement with previous calculations using the RBU model[20, 21].

Zhang developed a quite general reduced dimensionality model, the Semirigid Vibrating Rotating Model (SVRT)[22], which can be used to treat chemical reactions involving polyatomic molecules. For an atom-polyatom reaction the basic SVRT model treats the atom-polyatom separation, one vibration of the polyatom and the polyatom rotation. While this model gives generality, it does not treat the umbrella motion, which is often important for atom-methane reactions. In a generalised version of the model the umbrella motion has been included[23]. The SVRT model has been found to give rate constant that differ substantially from accurate calculations where such are available for atom-methane reactions[20, 21]. The reasons for this is presently not clear.

In reactive quantum dynamics, choosing coordinates is a delicate task as reactant and product geometries are best described by different coordinates. For state-to-state resolved calculations the reaction must be described all the way out to asymptotic conditions for the reactants and products. One approach to solve this problem is to use reactant-product decoupling methods which were introduced by Peng and Zhang[24] and improved by for instance Althorpe[25]. Hyperspherical coordinates attempts to solve the problem by treating both reactants and products with the same hyperradius and the same set of angles, orthogonal to each other and the hyperradius. There is thus just one coordinate that becomes infinite as all the other coordinates are angles, with bounded ranges. The hyperradius is handled separately by a propagator method, usually the R-matrix method[26, 27] or the log-derivative method[28, 29]. A drawback with the hyperspherical coordinates is that boundary conditions are best applied in Jacobi coordinates and either approximate boundary conditions are used or else a transformation between these coordinates is necessary. This we will discuss further in Sec. 2.3.

For the angular variables a basis set expansion is used. This gives rise to matrices which are to be diagonalized. Diagonalizing matrices is a subject of its own but we will discuss some aspects of this in Sec. 2.4 as we have taken a particular interest in efficient diagonalization of large sparse hermitian matrices, which ap-

pear in our implementations of the hyperspherical coordinate method. The Guided Spectral Transform matrix diagonalization method that we have developed is quite general and has also been used in the context of finding highly excited molecular vibrational states[30] which further motivates discussing it here.

2.1. THE RBU HAMILTONIAN

In the RBU model, four internal motions are treated. The model has been applied to hydrogen abstraction reactions of the type $A+CH_4 \rightarrow HA+CH_3$, with A being a hydrogen, chlorine or oxygen atom. The four motions treated are the H-C and H-A reactive bond stretches, the umbrella-type mode of the CH_3/CH_4 fragments, and a reactant bending mode which becomes a rotational motion of CH_3. The umbrella motion, where the three hydrogens move in phase, here with a fixed C-H bond length, is treated exactly within the model.

The hyperspherical coordinates used in the RBU model are defined by the mass-scaled Jacobi coordinates $(R_\alpha, r_\alpha, R_\gamma, r_\gamma)$ as

$$
\begin{aligned}
\rho^2 &= R_\alpha^2 + r_\alpha^2 = R_\gamma^2 + r_\gamma^2,\ 0 \le \rho < \infty \\
\tan\varphi &= r_\alpha/R_\alpha,\ 0 \le \varphi \le \varphi_{max} \\
z &= z,\ -r_e \le z \le r_e \\
\theta &= \theta,\ 0 \le \theta \le \pi
\end{aligned}
\tag{1}
$$

where the symbols α and γ label the reactant $A+CD_3H$ and product $HA+CD_3$ channels respectively, while β will be used to denote either channel. ρ, φ, z and θ are the hyperradius, the hyperangle, the umbrella coordinate and a rotation angle, respectively. The latter two coordinates are here actually not part of the hyperspherical coordinates, but they are of finite extent and orthogonal to ρ. The maximum value of the hyperangle is

$$
\varphi_{max} = \tan^{-1}\left[\frac{m_H m_T}{m_A m_{CD_3}}\right]^{1/2}.
$$

θ is the $\angle$HPC, where P is the CD_3 center of mass, which in the product arrangement represents the CD_3 rotation, see Fig. 1.

The umbrella coordinate z is the distance from X to C in Fig. 1. z and θ are unchanged by coordinate transformations between these hyperspherical and Jacobi coordinates.

The mass-scaled Jacobi coordinates are given by

$$
\begin{aligned}
R_\alpha &= C_\alpha^{-1} R_{A,CD_3H}, && R_\gamma = C_\gamma^{-1} R_{HA,CD_3} \\
r_\alpha &= C_\alpha R_{H,CD_3}, && r_\gamma = C_\gamma R_{HA}
\end{aligned}
$$

$$
C_\alpha = \left[\frac{m_T m_H m_{CD_3}}{m_A(m_H + m_{CD_3})^2}\right]^{1/4}, \qquad C_\gamma = \left[\frac{m_T m_A m_H}{m_{CD_3}(m_A + m_H)^2}\right]^{1/4}
$$
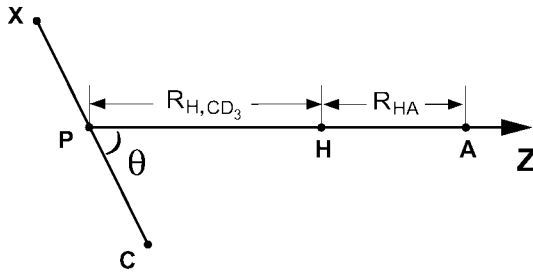
Figure 1.   Coordinates used in the RBU model.

where R_{A,CD_3H}, R_{H,CD_3}, R_{HA,CD_3} and R_{HA} are the distances of A to the CD$_3$H center of mass, of H to the CD$_3$ center of mass, of the HA center of mass to the CD$_3$ center of mass and the HA internuclear distance, respectively.

The RBU Hamiltonian in hyperspherical coordinates for the reaction A+CD$_3$H → HA+CD$_3$ is expressed as

$$
\begin{aligned}
\hat{H}(\rho,\varphi,z,\theta) \;=\; & -\frac{\hbar^2}{2\mu}\left[\frac{1}{\rho^3}\frac{\partial}{\partial\rho}\rho^3\frac{\partial}{\partial\rho}+\frac{1}{\rho^2}\frac{\partial^2}{\partial\varphi^2}\right]-\frac{\hbar^2}{2}\frac{\partial}{\partial z}G(z)\frac{\partial}{\partial z}+\frac{\hbar^2\hat{j}^2}{2I(z)} \\
& +\frac{\hbar^2}{2\mu\rho^2\sin^2\varphi}(\hat{j}^2-\Omega^2)+\frac{\hbar^2}{2\mu\rho^2}[J(J+1)-\Omega^2] \\
& +V(\rho,\varphi,z,\theta)
\end{aligned}
\tag{2}
$$

with the volume element for the internal variables

$$
d\tau=\rho^3 d\rho d\varphi dz\sin\theta d\theta,
$$

where

$$
\begin{aligned}
I(z) \;=\;& m_H r_e^2(1-\cos\eta)+\frac{m_H m_C}{m_{CD_3}}r_e^2(1+2\cos\eta), \\
\cos\eta \;=\;& \frac{3z^2-r_e^2}{2r_e^2}, \\
\mu \;=\;& \left[\frac{m_A m_H m_{CD_3}}{m_T}\right]^{1/2}, \\
\mu_z \;=\;& \frac{3m_C m_D}{m_{CD_3}}, \\
m_T \;=\;& m_A+m_H+m_{CD_3}, \\
G(z) \;=\;& \frac{r_e^2-z^2}{\mu_z(r_e^2+3m_D z^2/m_C)}
\end{aligned}
$$

and the rotational angular momentum operator is

$$\hat{j}^2 = -\frac{1}{\sin\theta}\frac{\partial}{\partial\theta}\sin\theta\frac{\partial}{\partial\theta}. \qquad (3)$$

Here m_A is the mass of the A atom with similar notation for other atoms/fragments. r_e is a fixed C-D bond length. To obtain the Hamiltonian, the centrifugal sudden approximation has been invoked, whereby both the total angular momentum J and Ω, the projection of J on the Z-axis of the body-fixed frame (along the H-A bond), are treated as good quantum numbers. Leaving out the term containing $G(z)$ and the z dependence in $I(z)$ in Eq. (2) we obtain the RBA Hamiltonian in the form derived by Nyman and Clary[11].

The potential V in Eq. 2 needs special attention in reduced dimensionality studies. It is desirable that it somehow accounts for the modes not explicitly treated in the reduced dimensionality model. This gives rise to an effective potential energy surface $V_{eff}(\mathbf{q}_D;\mathbf{q}_F)$, which is an explicit function of the explicitly treated variables $\mathbf{q}_D$, but may implicitly also depend on the other degrees of freedom, $\mathbf{q}_F$. Several approaches[31, 32, 33, 34, 35, 36] have been used to construct the potential V_{eff}. In the adiabatic approach[31], the global potential energy function $V(\mathbf{q}_D,\mathbf{q}_F)$ is minimised for given values of the dynamical variables to obtain a potential $V_{opt}(\mathbf{q}_D)$. At this geometry, vibrational energies $E_{\mathbf{q}_F}$ for the other coordinates are calculated using normal mode analysis. Finally, the effective reduced dimensionality potential function is obtained as,

$$V_{eff}(\mathbf{q}_D) = V_{opt}(\mathbf{q}_D) + E_{\mathbf{q}_F}(\mathbf{q}_D). \qquad (4)$$

This method gives the correct reaction thermicity and vibrationally adiabatic ground state barrier height, ΔV_a^G, (if it is an activated reaction) for a given potential energy surface. The adiabatic approach gives good results[31], but it requires finding $V_{opt}(\mathbf{q}_D)$ and performing the normal mode analysis for every geometry of the dynamic variables. In addition the global potential energy surface must be available.

Instead of performing the normal mode analysis we have used a more approximate method to take the $\mathbf{q}_F$-coordinates into account. For the Cl + CH_4/CD_4 reactions we have in some work used a tanh-function in the breaking bond to interpolate between the saddle point and the product asymptote to get both the reaction thermicity and ΔV_a^G consistent with the *ab initio* calculations[18]. In addition, if the effective potential energy surface of the system is modeled by the semiempirical London-Eyring-Polanyi-Sato (LEPS) function, the correction is made directly in the Morse parameters for the two reactive bonds by adjusting the Sato parameters[17, 19].

Another approach to obtain the effective potential is a sudden approximation, where the potentials are functions of the dynamical variables with the remaining coordinates fixed. This approach may give incorrect reaction thermicity and ΔV_a^G. The effects on rate coefficients and cross sections can be approximately corrected

by using an energy shifting scheme[37, 31]. We used this method for the O(^3P) + CH$_4$ → OH + CH$_3$[38] and H + CH$_4$ → H$_2$ +CH$_3$[39] reactions.

We next give a brief derivation of the $G(z)$-term in the RBU Hamiltonian, which has previously not been done. The general procedure is to derive the classical Lagrangian for the constrained motions of the model and then transforming this to the Hamiltonian form[40, 41]. Let

$$z = z_C + z_X \tag{5}$$

$$m_C z_C = m_{3D} z_X \tag{6}$$

$$\dot{z} = \dot{z}_C + \dot{z}_X \tag{7}$$

where the dot signifies time derivative and some other symbols are illustrated in Fig. 2. X is the center of mass of the three D atoms and P the center of mass of CD$_3$. From Eq. 5 we find that the kinetic energy in the z-coordinate, T_z, can be written

$$T_z = \frac{m_C \dot{z}_C^2}{2} + \frac{m_{3D} \dot{z}_X^2}{2} = \frac{\mu_z \dot{z}^2}{2} \tag{8}$$

where u_z is defined above.

Using $z = r_e \cos \chi$ gives

$$\dot{\chi} = -\frac{\dot{z}}{\sqrt{r_e^2 - z^2}} \tag{9}$$
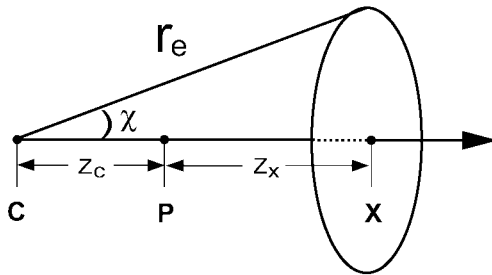
Figure 2.   Coordinates for the umbrella motion.

For the coordinate y, which is orthogonal to z, we have $y = r_e \sin \chi$ and get for the kinetic energy T_y in this coordinate

$$T_y = \frac{m_{3D} \dot{y}^2}{2} = \frac{m_{3D}}{2} (r_e \cos \chi)^2 \dot{\chi}^2 = \frac{m_{3D}}{2} \frac{z^2 \dot{z}^2}{r_e^2 - z^2}. \tag{10}$$

The Lagrangian corresponding to this umbrella motion is

$$L = T_z + T_y - V(\chi), \tag{11}$$

which gives

$$p_z = \frac{\partial L}{\partial \dot{z}} = \mu_z \dot{z} + m_{3D} \frac{z^2}{r_e{}^2 - z^2} \dot{z}. \tag{12}$$

The corresponding Hamiltonian is

$$H = \frac{p_z^2}{2(\mu_z + m_{3D} \frac{z^2}{r_e{}^2 - z^2})} + V(\chi), \tag{13}$$

from which $G(z)$ is obtained as given above.

The kinetic energy operator corresponding to $G(z)$ is hermitian above. Loss of hermiticity may lead to spurious eigenvalues appearing in the calculations[42]. To avoid this, a proper basis should be chosen. For instance, to treat the term involving $G(z)$ in the RBU Hamiltonian, a Fourier DVR basis was used[38].

2.2. COUPLED-CHANNEL EQUATIONS

We here derive the coupled channel equations in Jacobi and hyperspherical coordinates. By using Eqs. (1) and (2), we can obtain the Hamiltonian in Jacobi coordinates for either channel as

$$
\begin{aligned}
\hat{H}(R_\beta, r_\beta, z, \theta) &= -\frac{\hbar^2}{2\mu} \left[\frac{1}{\rho^2} \frac{\partial}{\partial R_\beta} \rho^2 \frac{\partial}{\partial R_\beta} + \frac{1}{\rho^2} \frac{\partial}{\partial r_\beta} \rho^2 \frac{\partial}{\partial r_\beta} \right] \\
&\quad - \frac{\hbar^2}{2} \frac{\partial}{\partial z} G(z) \frac{\partial}{\partial z} + \frac{\hbar^2 \hat{j}^2}{2I(z)} + \frac{\hbar^2}{2\mu\rho^2 \sin^2 \varphi} (\hat{j}^2 - \Omega^2) \\
&\quad + \frac{\hbar^2}{2\mu\rho^2} [J(J+1) - \Omega^2] + V \qquad (14) \\
d\tau &= \rho^2 dR_\beta dr_\beta dz \sin\theta d\theta.
\end{aligned}
$$

The hyperradius ρ is divided into L_S sectors i. For all values of J and Ω, the functions $|\psi_m^{J\Omega} >$ with initial quantum state m are expanded in the coupled channel form

$$|\psi_m^{J\Omega}(\rho, \varphi, z, \theta) >= \rho^{-3/2} \sum_{i=1}^{L_S} \sum_{n=1}^{N} h_{nm}(\rho; i, J, \Omega) |H_n(\varphi, z, \theta; i, \Omega) > \tag{15}$$

in hyperspherical coordinates, or as

$$|\psi_m^{J\Omega\beta}(R_\beta, r_\beta, z, \theta) >= \rho^{-1} \sum_{n=1}^{N} f_{nm}^\beta(R_\beta; J, \Omega) |F_n^\beta(r_\beta, z, \theta; \Omega) > \tag{16}$$

in Jacobi coordinates. Here, $|F_n^\beta(r_\beta, z, \theta; \Omega) >$ are the vibrational/rotational states with eigenvalues $\mathcal{E}_n^{F^\beta}$ in the limit of large values of R_β. These states are determined by solving

$$\hat{H}^\beta |F_n^\beta(r_\beta, z, \theta; \Omega) >= \mathcal{E}_n^{F^\beta} |F_n^\beta(r_\beta, z, \theta; \Omega) > \tag{17}$$

$$\hat{H}^\beta = -\frac{\hbar^2}{2\mu}\frac{\partial^2}{\partial r_\beta^2} - \frac{\hbar^2}{2}\frac{\partial}{\partial z}G(z)\frac{\partial}{\partial z} + \frac{\hbar^2}{2I(z)}\hat{j}^2$$

$$+\frac{\hbar^2}{2\mu\rho^2\sin^2\varphi}(\hat{j}^2 - \Omega^2) + V_F^\beta(r_\beta, z, \theta) \tag{18}$$

$$V_F^\beta(r_\beta, z, \theta) = \lim_{R_\beta\to\infty} V(\rho, \varphi, z, \theta) \tag{19}$$

and are independent of J. The potentials really refer to effective potentials as discussed in Sec. 2.1 but for notational convenience this is not made explicit here. In Eq. (15), $|H_n(\varphi, z, \theta; i, \Omega) >$ are the eigenstates of the surface Hamiltonian $\hat{H}_S$ with the potential $V_H(\varphi, z, \theta; i) = V(\rho = \rho_i, \varphi, z, \theta)$ for fixed ρ, *i.e.*

$$\hat{H}_S |H_n(\varphi, z, \theta; i, \Omega) >= \mathcal{E}_n^H |H_n(\varphi, z, \theta; i, \Omega) > \tag{20}$$

$$\hat{H}_S = -\frac{\hbar^2}{2\mu\rho_i^2}\frac{\partial^2}{\partial\varphi^2} - \frac{\hbar^2}{2}\frac{\partial}{\partial z}G(z)\frac{\partial}{\partial z} + \frac{\hbar^2}{2I(z)}\hat{j}^2$$

$$+\frac{\hbar^2}{2\mu\rho_i^2\sin^2\varphi}(\hat{j}^2 - \Omega^2) + V_H \tag{21}$$

The eigenstates are calculated by a Krylov subspace iteration method, which will be described in Sec. 2.4. The set of $\{|H_n(\varphi, z, \theta; i, \Omega) >\}$ is also independent of J and orthogonal for a constant ρ_i, *i.e.*

$$< H_{n'}(\varphi, z, \theta; i, \Omega)|H_n(\varphi, z, \theta; i, \Omega) >= \delta_{n'n} \tag{22}$$

By substituting the wavefunctions defined in Eqs. (15) and (16) into the time-independent Schrödinger equation $\hat{H}|\psi >= E|\psi >$, we obtain the coupled channel equations

$$\frac{d^2}{dR^2}f_{nm}^\beta(R_\beta; J, \Omega) + \sum_{n'=0}^N (\mathbf{D}_F^\beta)_{nn'} f_{n'm}^\beta(R_\beta; J, \Omega) = 0 \tag{23}$$

$$\frac{d^2}{d\rho^2}h_{nm}(\rho; i, J, \Omega) + \sum_{n'=0}^N (\mathbf{D}_H)_{nn'} h_{n'm}(\rho; i, J, \Omega) = 0 \tag{24}$$

where the coupling matrices have elements

$$(\mathbf{D}_F^\beta)_{nn'} = -\frac{2\mu}{\hbar^2} < F_n^\beta|\hat{H}^\beta + \frac{\hbar^2}{2\mu\rho^2}[J(J+1) - \Omega^2 + 1] - E|F_{n'}^\beta >$$

$$(\mathbf{D}_H)_{nn'} = -\frac{2\mu}{\hbar^2} < H_n|\hat{H}_S + \frac{\hbar^2}{2\mu\rho^2}[J(J+1) - \Omega^2 + \frac{3}{4}] - E|H_{n'} > \tag{25}$$

$\mathbf{D}_H$ is a diagonal matrix. We have solved the coupled channel equations in Eq. (24) using the quasi-adiabatic log-derivative algorithm of Manolopoulos[29].

2.3. BOUNDARY CONDITIONS

Here we derive boundary conditions for the RBU model using the log-derivative propagation method[29] and hyperspherical coordinates. For the log-derivative propagation we have $\mathbf{h}' = \mathbf{Y}(\rho_i)\mathbf{h}$, where $\mathbf{Y}(\rho_i)$ is the log-derivative matrix, $\mathbf{h}'$ is the derivative matrix of $\mathbf{h}$ with respect to ρ and $\mathbf{h}$ has elements h_{nm}, defined by Eq. 15. This means that we need to find expressions for the matrix elements h_{nm} and their derivatives with respect to ρ, incorporating accurate boundary conditions. The derivation here closely follows Ref. [19], which in turn is based on Refs.[43, 17]. Dropping the channel index, the asymptotic form $f_{nm}(R; J, \Omega)$ in Eq. (16) can be expressed as

$$f_{nm}(R; J, \Omega) \sim k_n^{-1/2} \hat{h}_I^{(2)}(k_n R; J, \Omega)\delta_{nm} + k_n^{-1/2} \hat{h}_I^{(1)}(k_n R; J, \Omega)S_{nm}^{J\Omega} \qquad (26)$$

where $k_n = \sqrt{2\mu(E - \mathcal{E}_n^F)}/\hbar$ is the channel wave number, and $S_{nm}^{J\Omega}$ is an S matrix element. $\hat{h}_I^{(1,2)}$ are the Riccati-Hankel functions, which can be defined by the Riccati-Bessel functions $\hat{y}_I$ and $\hat{n}_I$ as[44]

$$\begin{aligned} \hat{h}_I^{(1)}(k_n R; J, \Omega) &= \hat{y}_I(k_n R; J, \Omega) + i\hat{n}_I(k_n R; J, \Omega) \\ \hat{h}_I^{(2)}(k_n R; J, \Omega) &= \hat{y}_I(k_n R; J, \Omega) - i\hat{n}_I(k_n R; J, \Omega) \end{aligned} \qquad (27)$$

and I is defined later. Using Eqs. (15) and (22) and integrating over φ, z and θ, we have

$$h_{km} = \;\; < H_k(\varphi, z, \theta; i, \Omega)|\rho^{3/2}\psi_m^{J\Omega}(\rho, \varphi, z, \theta) >$$

Substituting for $|\rho\psi_m^{J\Omega}(\rho, \varphi, z, \theta) >$ using Eq. (16) and inserting the asymptotic form of f_{nm} in Eq. (26) yield

$$\begin{aligned} h_{km} = \;\; &\sum_n \rho^{1/2} k_n^{-1/2} \Big\{ < H_k(\varphi, z, \theta; i, \Omega)|\hat{h}_I^{(2)}(k_n R; J, \Omega)|F_n(r, z, \theta; \Omega) > \delta_{nm} \\ &+ < H_k(\varphi, z, \theta; i, \Omega)|\hat{h}_I^{(1)}(k_n R; J, \Omega)|F_n(r, z, \theta; \Omega) > S_{nm}^{J\Omega} \Big\} \end{aligned} \qquad (28)$$

Taking the derivative of h_{km} with respect to ρ, we have

$$\begin{aligned} h'_{km} &= \frac{\partial h_{km}}{\partial \rho} \\ &= \frac{1}{2}\rho^{-1}h_{km} + \sum_n \rho^{-1/2} k_n^{-1/2} \\ &\quad \times \Big\{ < H_k(\varphi, z, \theta; i, \Omega)|k_n R\hat{h}_I^{(2)'}(k_n R; J, \Omega)|F_n(r, z, \theta; \Omega) > \delta_{nm} \\ &\quad + < H_k(\varphi, z, \theta; i, \Omega)|\hat{h}_I^{(2)}(k_n R; J, \Omega)r|F_n'(r, z, \theta; \Omega) > \delta_{nm} \\ &\quad + < H_k(\varphi, z, \theta; i, \Omega)|k_n R\hat{h}_I^{(1)'}(k_n R; J, \Omega)|F_n(r, z, \theta; \Omega) > S_{nm}^{J\Omega} \\ &\quad + < H_k(\varphi, z, \theta; i, \Omega)|\hat{h}_I^{(1)}(k_n R; J, \Omega)r|F_n'(r, z, \theta; \Omega) > S_{nm}^{J\Omega} \Big\} \end{aligned} \qquad (29)$$

where

$$
\begin{aligned}
\hat{h}_I^{(i)'}(k_n R; J, \Omega) &= \frac{\partial \hat{h}_I^{(i)}(k_n R; J, \Omega)}{\partial(k_n R)} = k_n^{-1} \frac{\partial \hat{h}_I^{(i)}}{\partial R}, \\
F_n'(r, z, \theta; \Omega) &= \frac{\partial F_n(r, z, \theta; \Omega)}{\partial r}
\end{aligned}
\tag{30}
$$

and we have used the relations,

$$
\begin{aligned}
\frac{\partial(k_n R)}{\partial \rho} &= k_n R / \rho \\
\frac{\partial r}{\partial \rho} &= r / \rho.
\end{aligned}
$$

For convenience, we now introduce four real matrices

$$
\begin{aligned}
X_{kn}^{(1)} &= \rho^{1/2} < H_k(\varphi, z, \theta; i, \Omega) | \hat{y}_I(k_n R; J, \Omega) | F_n(r, z, \theta; \Omega) > \\
X_{kn}^{(2)} &= \rho^{1/2} < H_k(\varphi, z, \theta; i, \Omega) | \hat{n}_I(k_n R; J, \Omega) | F_n(r, z, \theta; \Omega) > \\
X_{kn}^{(3)} &= \rho^{-1/2} < H_k(\varphi, z, \theta; i, \Omega) | k_n R \hat{y}_I'(k_n R; J, \Omega) + \\
&\quad \frac{1}{2} \hat{y}_I(k_n R; J, \Omega) | F_n(r, z, \theta; \Omega) > \\
&\quad + \rho^{-1/2} < H_k(\varphi, z, \theta; i, \Omega) | \hat{y}_I(k_n R; J, \Omega) r | F_n'(r, z, \theta; \Omega) > \\
X_{kn}^{(4)} &= \rho^{-1/2} < H_k(\varphi, z, \theta; i, \Omega) | k_n R \hat{n}_I'(k_n R; J, \Omega) + \\
&\quad \frac{1}{2} \hat{n}_I(k_n R; J, \Omega) | F_n(r, z, \theta; \Omega) > \\
&\quad + \rho^{-1/2} < H_k(\varphi, z, \theta; i, \Omega) | \hat{n}_I(k_n R; J, \Omega) r | F_n'(r, z, \theta; \Omega) >
\end{aligned}
\tag{31}
$$

Then, h_{km} and h'_{km} can be rewritten as

$$
\begin{aligned}
h_{km} &= \sum_n k_n^{-1/2} X_{kn}^{(1)} \delta_{nm} - i \sum_n k_n^{-1/2} X_{kn}^{(2)} \delta_{nm} \\
&\quad + \sum_n k_n^{-1/2} X_{kn}^{(1)} S_{nm}^{J\Omega} + i \sum_n k_n^{-1/2} X_{kn}^{(2)} S_{nm}^{J\Omega} \\
h'_{km} &= \sum_n k_n^{-1/2} X_{kn}^{(3)} \delta_{nm} - i \sum_n k_n^{-1/2} X_{kn}^{(4)} \delta_{nm} \\
&\quad + \sum_n k_n^{-1/2} X_{kn}^{(3)} S_{nm}^{J\Omega} + i \sum_n k_n^{-1/2} X_{kn}^{(4)} S_{nm}^{J\Omega}
\end{aligned}
\tag{32}
$$

or in matrix form

$$
\begin{aligned}
\mathbf{h} &= X^{(1)} \mathbf{k}^{-1/2} \mathbf{I} - i X^{(2)} \mathbf{k}^{-1/2} \mathbf{I} + X^{(1)} \mathbf{k}^{-1/2} S^{J\Omega} + i X^{(2)} \mathbf{k}^{-1/2} S^{J\Omega} \\
\mathbf{h}' &= X^{(3)} \mathbf{k}^{-1/2} \mathbf{I} - i X^{(4)} \mathbf{k}^{-1/2} \mathbf{I} + X^{(3)} \mathbf{k}^{-1/2} S^{J\Omega} + i X^{(4)} \mathbf{k}^{-1/2} S^{J\Omega}.
\end{aligned}
$$

Using the expression for the log-derivative matrix $\mathbf{Y}(\rho_i)$ given above, we can solve these equations to obtain the S-matrix

$$S^{J\Omega}(E) = -\mathbf{k}^{1/2}\mathbf{W}^{-1}\mathbf{W}^*\mathbf{k}^{-1/2} \tag{33}$$

where

$$\mathbf{W} = \left[\mathbf{Y}(\rho_i)X^{(1)} - X^{(3)}\right] + i\left[\mathbf{Y}(\rho_i)X^{(2)} - X^{(4)}\right] \tag{34}$$

and $\mathbf{k}$ is a diagonal matrix with the elements $(\mathbf{k})_{n'n} = k_n\delta_{n'n}$. Eq. (33) is valid for large values of ρ_i. Note here that only a single ρ-sector is involved in applying the boundary conditions. To instead use the R-matrix propagation, only $\mathbf{W}$ has to be modified according to

$$\mathbf{W} = \left[\mathbf{R}_4(\rho_i)X^{(4)} - X^{(2)}\right] - i\left[\mathbf{R}_4(\rho_i)X^{(3)} - X^{(1)}\right], \tag{35}$$

where $\mathbf{R}_4$ is a block of the R matrix[43].

The order I of the Riccati-Hankel functions $\hat{h}_I^{(1,2)}$ given in Eq. (26) can be defined from the coupling matrix in Eq. (25) as

$$I(I+1) = J(J+1) - \Omega^2 + 1 \tag{36}$$

We have taken the nearest integer value of I and ignored the resulting small error in the centrifugal potential in applying boundary conditions[45, 19]. Also, we have noticed that the eigenstates of the surface Hamiltonian defined in Eq. (20) approach the asymptotic vibrational/rotational states for large ρ such that

$$|F_n(r, z, \theta; \Omega) > \approx R^{-1/2}|H_n(\varphi, z, \theta; i, \Omega) > \tag{37}$$

$$\mathcal{E}_n^F \approx \mathcal{E}_n^H. \tag{38}$$

As a result of this approximation, the asymptotic states $\{|F_n(r, z, \theta; \Omega) >\}$, need not be calculated. Further, in our applications the integrands can be integrated over the z and θ variables first. These integrations are only done once for a given Ω value, as they are independent of the scattering energy and J. Usually the scattering calculations are performed for several energies. The wavefunctions and their derivatives required to apply the boundary conditions need only be calculated for the first energy and can then be reused at other energies.

We end this section by showing reaction probabilities calculated using accurate boundary conditions as described and by applying approximate boundary conditions. The approximate boundary conditions are applied directly in the hyperspherical coordinates[46, 47]. Fig. 3 shows how the state-to-state reaction probabilities oscillate as a function of the hyperradius when using the approximate boundary conditions. The illustration here is for the Cl+CH$_4$ $\rightarrow$ HCl+CH$_3$ reaction. The straight line is an average value. Here the RLA model[9] was used and CH$_4$ had initially two quanta in a C-H stretch mode while HCl formed in the first excited vibrational state.
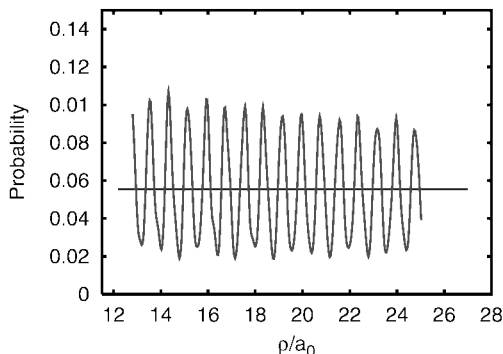
Figure 3. State-to-state reaction probabilities as a function of the hyperradius, calculated using approximate boundary conditions for the Cl+CH$_4$ → HCl+CH$_3$ reaction. CH$_4$ had initially two quanta in a C-H stretch mode while HCl formed in the first excited vibrational state.

Fig. 4 compares state-to-state reaction probabilities obtained using the accurate and approximate boundary conditions for the Cl+CH$_4$ → HCl+CH$_3$ reaction using the RLA model. The results from the approximate calculations have been averaged over sectors. CH$_4$ had initially one quantum in a C-H stretch mode while HCl formed in the ground vibrational state.
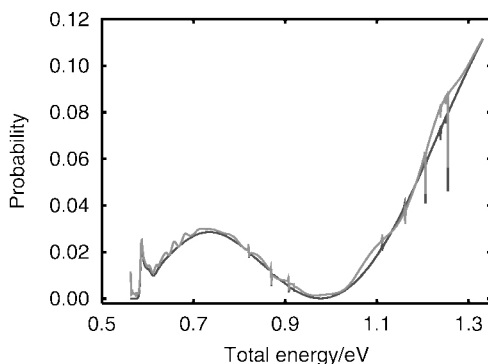
Figure 4. State-to-state reaction probabilities obtained using the accurate (solid line) and approximate boundary conditions (dashed line) for the Cl+CH$_4$ → HCl+CH$_3$ reaction. CH$_4$ had initially one quantum in a C-H stretch mode while HCl formed in the ground vibrational state.

2.4. ITERATIVE DIAGONALIZATION

Diagonalization of matrices is important in many contexts[48, 49] and a variety of efficient diagonalization routines exist. When the matrices are large, computer memory and CPU-time limitations must however be considered. If the matrices additionally are sparse and only a fraction of the eigenpairs are desired, iterative diagonalization routines can be expected to perform well. Large sparse matrices are often obtained when grid methods are used. There are a variety of grid methods available, for instance the finite element method[50, 51, 52], the collocation method[53], the adiabatic pseudo-spectral transform method[54] and the distributed approximating functional approach[55, 56, 57]. In quantum dynamics calculations the discrete variable representation (DVR) method, which is a collocation method based on orthogonal polynomials, is frequently used[40].

There is a range of iterative diagonalization routines to choose between, including classical orthogonal polynomial expansion methods[48], Davidson iteration[58] and Krylov subspace iteration methods. Here the popular Lanczos method[59] will be discussed in the context of finding the eigenstates of the surface Hamiltonian appearing in the hyperspherical coordinate method.

The Lanczos algorithm generates a set of vectors, usually from a three term recursion formula[60] and is easy to use. Two drawbacks of the standard Lanczos algorithm are the loss of orthogonality between the generated vectors and the observation that eigenvalues in dense interior regions are converged slowly. This observation can be turned into an advantage by applying a suitable spectral transform. The idea behind the Guided Spectral Transform method[61, 19] is to dilate the eigenvalue spectrum in the interesting regions, whereby these will be converged faster.

The Lanczos algorithm, using the conventional three-term recurrence[59] and incorporating a hermitian filter $F(\hat{H}_S)$, may be written

$$\beta_{j+1}|q_{j+1}> = F(\hat{H}_S)|q_j> - \alpha_j|q_j> - \beta_j|q_{j-1}> \tag{39}$$

with

$$\beta_1 \equiv 0, \ |q_0> = 0. \tag{40}$$

The generated Lanczos vectors are formally orthogonal but due to the finite precision in the calculations, loss of orthogonality occurs. This can be remedied by reorthogonalising the vectors, for instance using the partial reorthogonalization method due to Simon[62]. The recursion coefficients α_j and β_{j+1} are the mean energy and residue of the jth vector, respectively. They define the tridiagonal matrix $\mathbf{T}_j$,

$$\mathbf{T}_j = \begin{bmatrix} \alpha_1 & \beta_2 & & & \\ \beta_2 & \alpha_2 & \beta_3 & 0 & \\ & \beta_3 & \ddots & \ddots & \\ & 0 & \ddots & \ddots & \beta_j \\ & & & \beta_j & \alpha_j \end{bmatrix}. \tag{41}$$

Diagonalizing this matrix gives the eigenvalues ε_n and the expansion coefficients $\mathbf{C}^n$ of the eigenvectors in the Krylov subspace $\{|q_k>, k = 1, \cdots, j\}$ such that

$$|H_n> = \sum_{k=1}^{j} \mathbf{C}_k^n |q_k>, \tag{42}$$

where $|H_n>$ are eigenfunctions of $\hat{H}_S$ as before.

If the subspace is big enough to converge a set of N states of $F(\hat{H}_S)$, the corresponding N eigenstates of the surface Hamiltonian $\hat{H}_S$, which has the same eigenvectors but different eigenvalues $\mathcal{E}_n^{II}$, can then be obtained. This is a result of the Krylov subspace being invariant under the spectral transformation performed. The eigenvalues $\mathcal{E}_n^{II}$ of $\hat{H}_S$ can be determined from $\varepsilon_n = F(\mathcal{E}_n^{II})$.

In quantum scattering calculations we are typically interested in the eigenstates in the low energy end of the spectrum. For this purpose an exponential filter $f(\hat{H}_S) = \exp[-\alpha(\hat{H}_S - H_{min})]$ is useful as it will dilate the eigenvalues at low energies. The action of the filter on the vectors can be performed via the Chebyshev polynomials[63, 64],

$$f(\hat{H}_S) = \exp[-\alpha(\hat{H}_S - H_{min})] \approx \sum_{l=0}^{L} A_l(\alpha) T_l(\hat{H}_{norm}) \tag{43}$$

where T_l denotes the lth Chebyshev polynomial, and $\hat{H}_{norm}$ the normalized operator

$$\hat{H}_{norm} = \frac{\hat{H}_S - \overline{H}}{\Delta H} \tag{44}$$

with

$$\overline{H} = \frac{1}{2}[H_{max} + H_{min}]$$

$$\Delta H = \frac{1}{2}[H_{max} - H_{min}],$$

where H_{max} and H_{min} are respectively estimates of the maximum and minimum eigenvalues of $\hat{H}_S$.

The expansion coefficients $A_l(\alpha)$ in Eq. (43) are determined by the following integral

$$\begin{aligned} A_l(\alpha) &= \frac{2 - \delta_{l0}}{\pi} \int_{-1}^{+1} \frac{f(E) T_l(E)}{\sqrt{1 - E^2}} dE \\ &= \frac{2 - \delta_{l0}}{\pi} \int_0^{\pi} e^{-\alpha \Delta H(1 + \cos\theta)} \cos(l\theta) d\theta, \end{aligned} \tag{45}$$

which can be evaluated by Gauss-Chebyshev quadrature.

TABLE 1. Comparison of the order of the Chebyshev expansion for the exponential $f(\hat{H}_S) = e^{-\alpha(\hat{H}_S - H_{min})}$ filter with the guided filter $F(\hat{H}_S)$ defined in Eqs. (46). $H_{min} = 0.0$ and $\alpha = 0.5 \ eV^{-1}$ were used.

H_{max}/eV	L	L_G
15.0	16	6
20.0	18	7
25.0	19	7
30.0	21	8
40.0	23	9
50.0	25	9
60.0	27	10
80.0	31	11

Although the expansion in Eq. (43) converges exponentially once $l > \alpha \Delta H$, it is not necessary to converge it for the calculation of eigenstates. Instead, we use the truncated polynomials as the filter in the Lanczos iteration, *i.e.*

$$F(\hat{H}_S) = \sum_{l=0}^{L_G} A_l(\alpha) T_l(\hat{H}_{norm}), \qquad (46)$$

where the coefficients $A_l(l > L_G)$ which have an absolute value less than 0.01 have been excluded. In an application to the $Cl+CH_4 \rightarrow HCl+CH_3$ reaction we found that L_G was substantially smaller than L as listed in Table 1. This significantly enhances the efficiency of the spectral transformation as the CPU time increases approximately linearly with the number of expansion polynomials. As the exponential function is not accurately represented by the filter $F(\hat{H}_S)$, but merely acts as a guide for the filter being produced in the Chebyshev expansion, the algorithm is referred to as the guided spectral transform (GST) Lanczos method. The GST method is quite general and can also be used in other fields. It has been used to calculate all bound states of the NO_2 molecule[30] and also to calculate eigenvalues of four and five atom molecules[65, 66].

Fig. 5 shows a typical curve of the GST for the exponential filter. It is clear that the approximate spectral transform well represents the profile of the exponential filter at low energies, where the curve is also smooth and monotonous.

Although there are deviations and waves appearing at high energies, this will not affect the calculation of the lowest eigenstates required in the quantum scattering application. The eigenvalues of $\hat{H}_S$ are determined by the roots of the GST curve for obtained $F(E)$ values as shown in Fig. 5. Finding the roots is fast and can be done with several algorithms, e.g., the Newton-Raphson method[67].
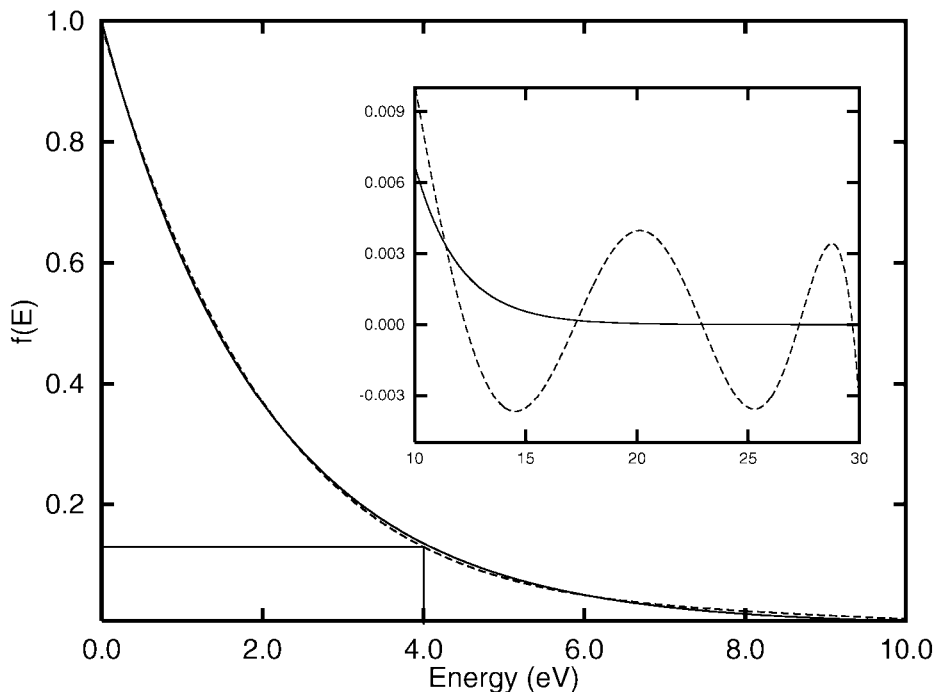
Figure 5. The curve of the guided spectral transform (dashed line) with $L_G = 8$ for the exponential function $\exp(-0.5E)$ (solid line) from $E_{min} = 0.0$ to $E_{max} = 30.0\,eV$, divided into two panels for better resolution.

The CPU scaling of the GST method with the size of the basis set expansion has been investigated in an application to Cl+CH$_4$. A scaling better than N^2, close to $N \ln N$ in fact, was observed as illustrated in Fig. 6. This is also the scaling normally found in wavepacket calculations and decidedly better than the approximately N^3 scaling observed in direct diagonalization methods. Note also that the GST method has only small requirements on primary memory.

3. Applications

The RBU model has been applied to study the hydrogen abstraction reactions, X (X=Cl, O and H) + CH$_4$ → HX + CH$_3$. These occur through a potential energy
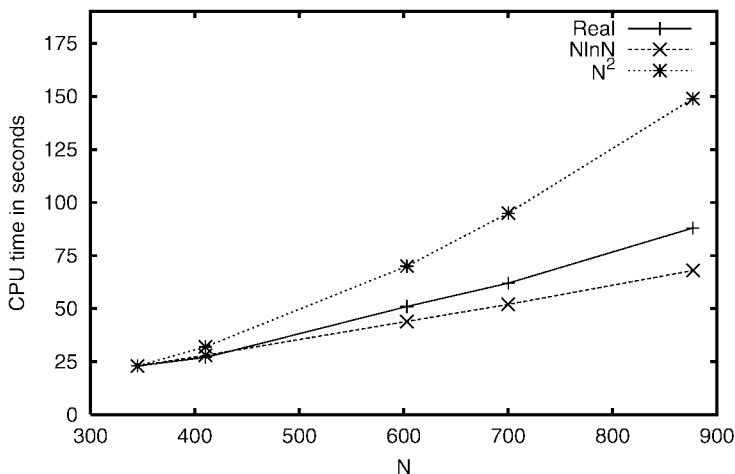
Figure 6. CPU time for diagonalizing a matrix of size N using the guided spectral transform approach in a reactive scattering application to $Cl+CH_4 \rightarrow HCl+CH_3$. $N \ln N$ and N^2 scaling laws are included for comparison.

barrier wherefore strong quantum effects are expected for these light atom transfer reactions. We here discuss thermal rate constants, effects of vibrational excitation, product rotational distributions, differential cross sections and tunneling.

3.1. THERMAL RATE COEFFICIENTS

For the $H+CH_4 \rightarrow H_2+CH_3$[20] and $O+CH_4 \rightarrow OH+CH_3$[21] reactions, accurate Multi Configurational Time Dependent Hartree (MCTDH) calculations have been performed. These calculations include all vibrational modes and are for a total angular momentum $J = 0$. The flux correlation function formalism[68, 69, 70] was employed to calculate cumulative reaction probabilities for $J = 0$, $N^{J=0}(E)$. Employing the J-shifting approximation[31] the thermal rate constant could then be found from

$$k(T) = \frac{Q_{rot}(T)}{2\pi \hbar Q_r(T)} \int_{-\infty}^{+\infty} dE \exp\left\{-E/kT\right\} N^{J=0}(E), \qquad (47)$$

where $Q_{rot}(T)$ is the partition function for the overall rotational degrees of freedom evaluated at the transition state. In some of the work on $H+CH_4$, the reactant partition function $Q_r(T)$ was evaluated harmonically[71, 72]. It was however found[73] that the anharmonicity ought to be considered, which has also been done in later work[20, 21]. In even more recent work it has been found that on a new more accurate potential energy surface, the anharmonic effects are negligible[74]. Sev-

eral reduced dimensionality quantum scattering calculations of the thermal rate constant have also appeared for the H+CH$_4$ → H$_2$+CH$_3$[75, 39, 76, 77, 78, 79] and O+CH$_4$ → OH+CH$_3$[80, 81, 82, 38, 83] reactions. The rate constants from the MCTDH and RBU calculations using the same potential energy surfaces are shown for the two reactions in Figs. 7 and 8. The agreement is seen to be very good. The O+CH$_4$ calculations by Palma and Clary[83] also agree well with the MCTDH results. The SVRT results are for these two reactions substantially below the MCTDH results. The reasons for this is at present not clear.

The reactions show a non-linear Arrhenius behaviour. For the O + CH$_4$ reaction, this is attributed to spin-orbit interactions and tunneling. For the H + CH$_4$ reaction, tunneling plays the major role. At high temperature, the curvature is also caused by the vibrational excitations of the CH$_4$ reactant, which can significantly enhance the reaction.
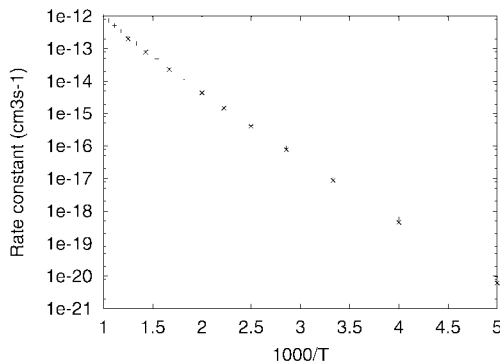
Figure 7. Thermal rate constants for the H+CH$_4$ → H$_2$+CH$_3$ reaction obtained using the RBU (x) model and full-dimensional MCTDH calculation (+). In both cases *J*-shifting is employed.

3.2. VIBRATIONAL ENHANCEMENT

The RBU model can be used to study the effect of exciting the vibrational modes treated within the model. For the reactions X (X=Cl, O and H) + CH$_4$ → HX + CH$_3$ we find that exciting a vibrational mode results in a lower threshold to reaction. It was also found that exciting the reactive C-H stretch enhances the reactivity more than exciting the CH$_4$ umbrella mode. Vibrational enhancements for the umbrella and C-H stretch vibrations have also been found in other studies of the dynamics[75, 80] and in canonical variational transition state theory (CVT) calculations[84]. Enhancement of the Cl + CH$_4$ reaction due to vibrational excitation of the H-CH$_3$ stretch has also been confirmed by experimental measurements by Zare and coworkers[85].
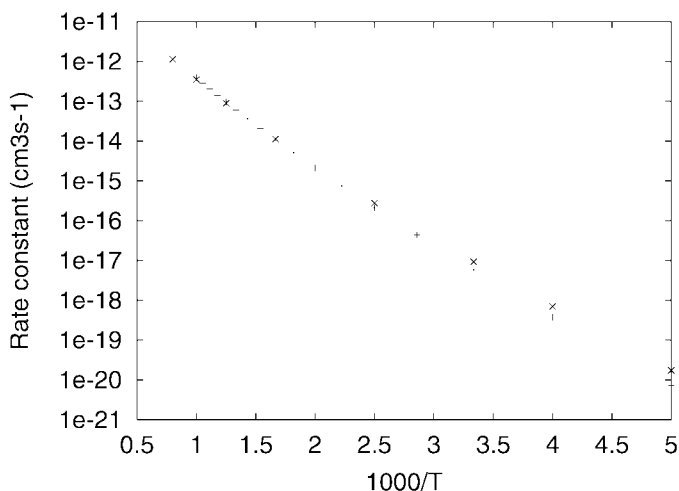
Figure 8.   Thermal rate constants for the O+CH$_4$ → OH+CH$_3$ reaction obtained using the RBU (x) model and full-dimensional MCTDH calculation (+). In both cases *J*-shifting is employed.

Interestingly, for the HCl + CH$_3$ → Cl + CH$_4$ reaction, we find that exciting the HCl stretch mode significantly enhances the rate whereas exciting the umbrella mode of CH$_3$ has the opposite effect. The same observation was made by Duncan and Truong[84] based on their CVT calculations. We have made the same observation in a study of the HBr+CH$_3$ → Br + CH$_4$ reaction using the RLU model[86]. To explain the retarding effect of the umbrella mode excitation, assume that the reaction behaves largely vibrationally adiabatic, which is reasonable at low energies considering that a light hydrogen atom transfers between two heavy atoms. Since the vibrational frequency for the umbrella motion of CH$_4$ is substantially higher than that of CH$_3$, this means that energy must be transferred into the umbrella mode as the reaction proceeds, which increases the vibrationally adiabatic threshold to reaction and slows it down. Again, in experimental measurements by Zare and coworkers on the HCl + CH$_3$ reaction it has been found that vibrational excitation of the CH$_3$ reactant has small to negative effects on the reaction rate[87].

3.3. ROTATIONAL DISTRIBUTIONS

The rotational degree of freedom about the smaller principal axis of inertia in CH$_3$ is treated in the RBU model. The corresponding rotational distributions of CH$_3$ can therefore be calculated for the X + CH$_4$ → HX + CH$_3$ reactions. The results obtained show that the rotational distribution of CH$_3$ is rather cold for the X + CH$_4$ reactions out of the vibrational ground-state of CH$_4$. This is consistent with

a collinear or nearly collinear "X-H-CH$_3$" transition state. As an example, Fig. 9 shows the distributions for Cl + CH$_4$ reacting out of the vibrational ground state at a kinetic energy of 0.159 eV. The most populated state is $j = 1$. Cold rotational distributions for the Cl + CH$_4$ reaction have been measured by Zare's group[88].
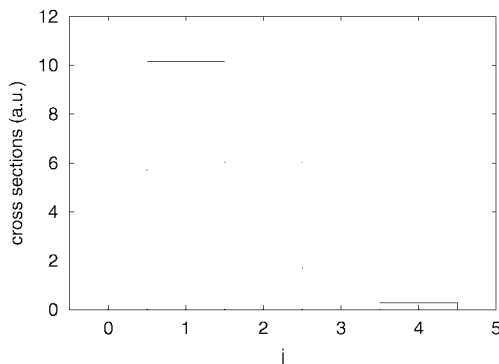
Figure 9.   Calculated rotational state distributions of CH$_3$ for Cl + CH$_4$ reacting out of the vibrational ground state to give HCl in the ground state and CH$_3$ in the vibrational ground state at a kinetic energy of 0.159 eV.

3.4. DIFFERENTIAL CROSS SECTIONS

Zare and co-workers[89] have measured differential cross sections for the Cl + CH$_4(\nu_{3b} = 0) \rightarrow$ HCl($\nu = 0, j$) + CH$_3$ and Cl + CH$_4(\nu_{3b} = 1) \rightarrow$ HCl($\nu = 0/1, j$) + CH$_3$ reactions, at an average translational energy of 0.159 eV. Here ν_{3b} is a stretch motion of H-CH$_3$ and j is the HCl rotational quantum number. In order to compare with these experimental results, we have calculated differential cross sections at this collision energy. Since the HCl rotational degree of freedom is not treated in the RBU model, we compare with the experimental results for $j = 0$.

For Cl + CH$_4$ reacting out of the vibrational ground state to form products in the vibrational ground state we find predominantly sideways and backward scattering. Also, the umbrella mode of the CH$_3$ product is not excited. These calculated results are in good agreement with the experimental measurements.

For Cl+CH$_4$ reacting out of a state with one quantum in the H-CH$_3$ stretch, HCl is formed in the ground state or in the first excited state. For HCl excited, CH$_3$ forms almost exclusively in the ground state, which is in agreement with the experiments. Forward and sideways scattering dominates which qualitatively agrees with the experimental results. For the case where HCl forms in the ground vibrational state, the products are predominantly scattered in the backward hemisphere, which again is consistent with the experimental measurements. The umbrella motion of CH$_3$ is however significantly excited in the calculations, with two quanta

in it being most probable, while the experiments indicate no, or only small vibrational excitation. We have made the same observation both in three-dimensional RLU and four dimensional RBU calculations. In the case of the RLU model a new *ab initio* potential energy surface was developed and used with the same result[18]. This discrepancy in regards to the excitation of the umbrella motion of CH_3 may be due to the constraints of the reduced dimensionality models used, where in particular the rotational degree of freedom of HCl is not treated.

Kandel and Zare[87] have measured the differential cross sections for the $Cl+CD_4$ $\rightarrow$ DCl + CD_3 reaction at collision energies of 0.18, 0.22 and 0.25 eV. Results for CD_4 initially in its ground vibrational state with DCl forming in its vibrational ground state are shown in Fig. 10 together with calculated differential cross sections using the RLU model. The agreement is good. The DCl product is backward scattered at low energy. It becomes more sideways scattered as the collision energy increases, but remains predominantly in the backward hemisphere at the energies considered here. In Table 2, relative cross sections for reaction out of the CD_4 vibrational ground state are shown. DCl is formed in its vibrational ground state. From the table it is seen that the umbrella mode of CD_3 is hardly excited at all. The results for the cross sections are in good agreement with the experimental observations as are the differential cross sections[85, 87].

In summary, the agreement with the experimental results is good except in one case. This is for the normal isotope reaction out of CH_4 with one quantum in a stretch vibration giving ground state HCl. In this case the calculations gives more umbrella mode excitation than the experiments.
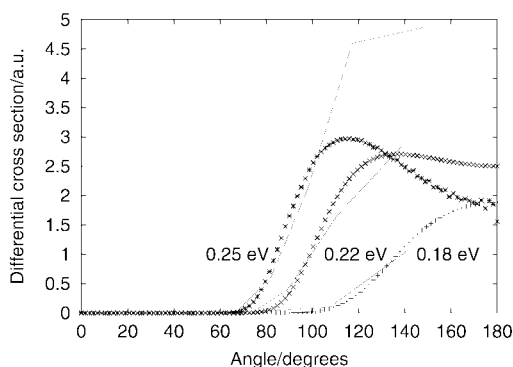
Figure 10. Differential cross sections for the reaction Cl + $CD_4(\nu_{3b} = 0, \nu_4 = 0) \rightarrow$ $DCl(\nu = 0)$ + $CH_3(\nu_2 = 0)$ at several kinetic energies. The angle 180° refers to backward scattering of the DCl product. RLU results (crosses) are compared to the experimental results of Zare and coworkers(solid lines).

TABLE 2. Relative reaction cross sections σ for Cl+CD$_4$ in the vibrational ground state giving DCl in the vibrational ground state. The umbrella excitation of CD$_3$ is indicated by ν_{umb} and the kinetic energy by E_{kin}.

E_{kin}/eV	(ν_{umb})	σ	E_{kin}/eV	(ν_{umb})	σ	E_{kin}/eV	(ν_{umb})	σ
0.15	(0)	0.15	0.22	(0)	13.01	0.25	(0)	17.48
0.18	(0)	3.70		(1)	0.11		(1)	0.23
	(1)	0.04					(2)	0.001

TABLE 3. RBU calculated ground state tunneling (η^G) and transmission (κ^G) coefficients for the X (X=Cl, O and H) + CH$_4$ → HX + CH$_3$ reactions.

T/K	Cl + CH$_4$		O + CH$_4$		H + CH$_4$	
	η^G	κ^G	η^G	κ^G	η^G	κ^G
200	13.4	2.3	264.9	33.8	71.0	66.9
250	9.9	1.6	73.7	9.0	23.0	21.7
300	7.8	1.2	34.6	4.0	12.0	11.2
400	5.3	0.9	14.8	1.6	5.8	5.4
600	3.0	0.6	6.9	0.7	3.1	2.8
800	2.2	0.5	4.8	0.4	2.3	2.0

3.5. TUNNELING

Table 3 gives the ground-state tunneling (η^G) and transmission (κ^G) coefficients for the reactions X (X=Cl, O, H) + CH$_4$ → HX + CH$_3$ as calculated within the RBU model. η^G is defined as the ratio of the thermal rate constant out of the ground state to the thermal rate constant out of the ground state obtained if reaction probabilities below the vibrationally adiabatic threshold are set to zero[36]. κ^G gives the ratio of the quantum mechanical ground state rate constant to the one where no tunneling occurs and there is no reflection at energies above the adiabatic ground state barrier[36, 90]. Thus the ratio η^G/κ^G defines the recrossing for reaction out of the ground state. It is seen that tunneling is important for all three reactions, which is related to the fact that a light hydrogen atom is transferred in these reactions.

It is also clear that recrossing is important for the heavy-light-heavy (HLH) reactions Cl/O + CH$_4$, while the recrossing is small for the H + CH$_4$ reaction. This difference is largely due to the trapped states, or Feshbach resonances, that

are associated with the region of the potential near the barrier top. Resonance scattering often plays a role in HLH reactions, which here is particularly accentuated for the Cl + CH$_4$ reaction. This is reflected in plots of cumulative reaction probabilities versus total energy where there is more structure for Cl + CH$_4$ than for H + CH$_4$. For H + CH$_4$ a smoothed step-like curve is obtained, where the steps correspond to quantized transition states[91].

4. Summary

I have here summarised some of the quantum reactive scattering work we have performed, focusing on the Rotating Bond Umbrella (RBU) model but also including some results from the Rotating Line Umbrella (RLU) model. In the RBU model four degrees of freedom are treated which are chosen to particularly efficiently treat atom-methane reactions or similar reactions with umbrella type motions. The RBU model reduces to the Rotating Bond Approximation (RBA) in its fullest form, if the RBU umbrella motion is treated in the pseudo-diatom approximation. Normally the RBU is implemented with an exact treatment of the umbrella motion, within the RBU model, and the derivation of the corresponding Hamiltonian has been explicitly given here for the first time. The RBU model reduces to the RLU model if the bend motion is not treated.

We have shown how accurate boundary conditions can be implemented into the RBU model and illustrated the effect of using approximate boundary conditions. We have also described the guided spectral transform, GST, method for iterative diagonalization of large sparse matrices.

It has been found that the RBU model gives rate constants in good agreement with accurate MCTDH calculations. The model can however additionally be used to calculate for instance state-to-state integral and differential cross sections. In particular for the Cl+CH$_4$ and Cl+CD$_4$ reactions there are many experimental results to compare with and the agreement between these and the RBU and RLU results is generally very good.

Acknowledgements

References

1. W. H. Miller and B. M. D. D. Jansen op de Haar. *J. Chem. Phys.*, 86:6213, 1987.
2. G. Barinovs, N. Markovic, and G. Nyman. *J. Chem. Phys.*, 111:6705–6711, 1999.
3. M. S. Child. *Mol. Phys.*, 12:401, 1967.
4. R. E. Wyatt. *J. Chem. Phys.*, 51:3489, 1969.
5. J. N. L. Connor and M. S. Child. *Mol. Phys.*, 18:653, 1970.

6.   R. B. Walker and E. F. Hayes. In D. C. Clary, editor, *The Theory of Chemical Reaction Dynamics*, page 105. Reidel, Dordrecht, 1986.
7.   E. F. Hayes, P. Pendergast, and R. B. Walker. In J. M. Bowman, editor, *Advances in Molecular Vibrations and Collision Dynamics: Reactive Scattering vol 2A*. JAI, Greenwich, 1994.
8.   G. Nyman. *Chem. Phys. Lett.*, 240:571, 1995.
9.   G. Nyman, H. G. Yu, and R. B. Walker. *J. Chem. Phys.*, 109:5896, 1998.
10. David C Clary. *J. Chem. Phys.*, 95:7298, 1991.
11. G. Nyman and D. C. Clary. *J. Chem. Phys.*, 100:3556, 1994.
12. Q. Sun and J. M. Bowman. *Int. J. Quant. Chem.:Quantum Chem. Symp.*, 23:115, 1989.
13. Q. Sun and J. M. Bowman. *J. Chem. Phys.*, 92:1021, 1990.
14. Q. Sun and J. M. Bowman. *J. Chem. Phys.*, 92:5201, 1990.
15. Q. Sun, D. L. Yang, N. S. Wang, J. M. Bowman, and M. C. Lin. *J. Chem. Phys.*, 93:4730, 1990.
16. J. M. Bowman and G. C. Schatz. *Annu. Rev. Phys. Chem.*, 46:169 195, 1995.
17. Hua-Gen Yu and Gunnar Nyman. *PCCP*, 1:1181, 1999.
18. Hua-Gen Yu and Gunnar Nyman. *J. Chem. Phys.*, 111:6693–6704, 1999.
19. Hua-Gen Yu and Gunnar Nyman. *J. Chem. Phys.*, 110:7233–7244, 1999.
20. Fermin Huarte-Larranaga and Uwe Manthe. *J. Chem. Phys.*, 116:2863, 2002.
21. Fermin Huarte-Larranaga and Uwe Manthe. *J. Chem. Phys.*, 117:4635, 2002.
22. J. Z. H. Zhang. *J. Chem. Phys.*, 111:3929, 1999.
23. M.L. Wang and J.Z.H. Zhang. *J. Chem. Phys.*, 117:3081, 2002.
24. T. Peng and J.Z.H. Zhang. *J. Chem. Phys.*, 105:6072, 1996.
25. S. Althorpe. *Faraday Discuss.*, 110:238, 1998.
26. J. C. Light and R. B. Walker. *J. Chem. Phys.*, 65:4272, 1976.
27. E. B. Stechel, R. B. Walker, and J. C. Light. *J. Chem. Phys.*, 69:3518, 1978.
28. B. R. Johnson. *J. Comput. Phys.*, 13:445, 1973.
29. D. E. Manolopoulos. *J. Chem. Phys.*, 85:6425, 1986.
30. Hua-Gen Yu and Gunnar Nyman. *J. Chem. Phys.*, 110:11133–11140, 1999.
31. J. M. Bowman. *J. Phys. Chem.*, 95:4960, 1991.
32. H. Szichman, I. Last, A. Baram, and M. Baer. *J. Phys. Chem.*, 97:6436, 1993.
33. H. Szichman, I. Last, and M. Baer. *J. Phys. Chem.*, 98:828, 1994.
34. David C Clary. Scattering theory. *J. Chem. Phys.*, 95:7298, 1991.
35. D. H. Zhang and J. Z. H. Zhang. *J. Chem. Phys.*, 103:6512, 1995.
36. G. Nyman and D. C. Clary. *J. Chem. Phys.*, 101:5756, 1994.
37. J. M. Bowman. *Adv. Chem. Phys.*, 61:115, 1985.
38. Hua-Gen Yu and Gunnar Nyman. *J. Chem. Phys.*, 112:238–247, 2000.
39. Hua-Gen Yu and Gunnar Nyman. *J. Chem. Phys.*, 111:3508–3516, 1999.
40. G. Nyman and Hua-Gen Yu. *Rep. Prog. Phys.*, 63:1001, 2000.
41. H. Goldstein. *Classical Mechanics*. Addison-Wesley, Oxford, 1980.
42. H. Wei. *J. Chem. Phys.*, 106:6885–6900, 1997.
43. E. F. Hayes, P. Pendergast, and R. B. Walker. In J. M. Bowman, editor, *Advances in Molecular Vibrations and Collision Dynamics: Reactive Scattering vol 2A*. JAI, Greenwich, 1994.
44. J. J. Sakurai. *Modern Quantum Mechanics*. Addison-Wesley, New York, 1994.
45. R. B. Walker and E. F. Hayes. In D. C. Clary, editor, *The Theory of Chemical Reaction Dynamics*, page 105. Reidel, Dordrecht, 1986.
46. J. Römelt. *Chem. Phys. Lett.*, 74:263, 1980.
47. G. Nyman and D. C. Clary. *J. Chem. Phys.*, 99:7774, 1993.
48. Y. Saad. *Numerical Methods for Large Eigenvalue Problems*. Manchester University Press, Manchester, UK, 1992.
49. G. Nyman and Hua-Gen Yu. *J. Comput. Meth. Sci. Eng.*, 1:229, 2001.
50. K. W. Morton. *Comput. Phys. Rep.*, 6:1, 1987.
51. A. Scrinzi and Nils Elander. *J. Chem. Phys.*, 98:3866, 1993.
52. A. Scrinzi. *Comput. Phys. Commun.*, 86:67, 1995.

53. W. Yang and A. C. Peet. *J. Chem. Phys.*, 92:522 6, 1990.
54. R. A. Friesner. *J. Chem. Phys.*, 85:1462 8, 1986.
55. C. Schwartz. *J. Math. Phys.*, 26:411, 1984.
56. I. P. Hamilton and J. C. Light. *J. Chem. Phys.*, 84:306, 1986.
57. D. K. Hoffman, M. Arnold, and D. J. Kouri. *J. Phys. Chem.*, 96:6539, 1992.
58. E. R. Davidson. *J. Comput. Phys.*, 17:87, 1975.
59. C. Lanczos. *J. Res. NBS*, 45:255, 1950.
60. H. Karlsson and S. Holmgren. *J. Chem. Phys.*, 117:9116 9123, 2002.
61. Hua-Gen Yu and Gunnar Nyman. *Chem. Phys. Lett.*, 298:27 35, 1998.
62. H. D. Simon. *Math. Comput.*, 42:115, 1984.
63. H. Tal-Ezer and R. Kosloff. *J. Chem. Phys.*, 81:3967, 1984.
64. R. Kosloff and H. Tal-Ezer. *Chem. Phys. Lett.*, 127:223, 1986.
65. Hua-Gen Yu. *Chem. Phys. Lett.*, 365:189 196, 2002.
66. Hua-Gen Yu. *J. Chem. Phys.*, 117:8190–8196, 2002.
67. W. H. Press, S. A. Teukolsky, W. T. Vetterling, and B. P. Flannery. *Numerical Recipes*. Cambridge University Press, Cambridge, 1986.
68. W. H. Miller. *J. Chem. Phys.*, 61:1823, 1974.
69. W. H. Miller, S. D. Schwartz, and J. W. Tromp. *J. Chem. Phys.*, 79:4889, 1983.
70. F. Matzkies and U. Manthe. *J. Chem. Phys.*, 108:4828, 1998.
71. Fermin Huarte-Larranaga and Uwe Manthe. *J. Chem. Phys.*, 113:5115, 2000.
72. Fermin Huarte-Larranaga and Uwe Manthe. *J. Phys. Chem.*, 105:2522, 2001.
73. J. M. Bowman, D. Wang, X. Huang, F. Huarte Larranaga, and U. Manthe. *J. Chem. Phys.*, 114:9683, 2001.
74. U. Manthe. *private communication*.
75. T. Takayanagi. *J. Chem. Phys.*, 104:2237, 1996.
76. M.L. Wang, Y. Li, J.Z.H Zhang, and D.H. Zhang. *J. Chem. Phys.*, 113:1802, 2000.
77. D. Wang and J. Bowman. *Chem. Phys.*, 115:2055, 2001.
78. Hua-Gen Yu. *Chem. Phys. Lett.*, 332:538 544, 2000.
79. H. Szichman and R. Baer. *J. Chem. Phys.*, 117:7614, 2002.
80. D. C. Clary. *Phys. Chem. Chem. Phys.*, 1:1173, 1999.
81. J. Palma and D.C. Clary. *J. Chem. Phys.*, 112:1859, 1999.
82. J. Palma and D.C. Clary. *Phys. Chem. Chem. Phys.*, 2:4105, 2000.
83. J. Palma and D.C. Clary. *J. Chem. Phys.*, 115:2188, 2001.
84. W. T. Duncan and T. N. Truong. *J. Chem. Phys.*, 103:9642, 1995.
85. W. R. Simpson, T. P. Rakitzis, S. A. Kandel, T. Lev-On, and R. N. Zare. *J. Phys. Chem.*, 100:7938, 1996.
86. Hua-Gen Yu and Gunnar Nyman. *J. Phys. Chem. A*, 105:2240–2245, 2001.
87. S. A. Kandel and R. N. Zare. *J. Chem. Phys.*, 109:9719–9727, 1998.
88. R. Zare. *private communication*.
89. W. R. Simpson, T. P. Rakitzis, S. A. Kandel, A. J. Orr-Ewing, and R. N. Zare. *J. Chem. Phys.*, 103:7313, 1995.
90. Y.-P. Liu, G. C. Lynch, T. N. Truong, D. h. Lu, D. G. Truhlar, and B. C. Garrett. *J. Am. Chem. Soc.*, 115:2408, 1993.
91. D. C. Chatfield, R. S. Friedman, D. W. Schwenke, and D. G. Truhlar. *J. Phys. Chem.*, 96:2414, 1992.

REACTION DYNAMICS OF POLYATOMIC SYSTEMS: FROM A + BCD → AB + CD TO X + YCZ$_3$ → XY + CZ$_3$

DONG H. ZHANG AND MINGHUI YANG
Department of Computational Science
National University of Singapore
Kent Ridge, Singapore 119260

MICHAEL A. COLLINS
Research School of Chemistry
Australian National University
Canberra, ACT 0200, Australia

SOO-Y. LEE
Department of Chemistry
National University of Singapore
Kent Ridge, Singapore 119260

Abstract. Over the last decade, advances in quantum dynamics, notably the development of the initial state selected time-dependent wave packet method, coupled with advances in constructing *ab initio* potential energy surfaces, have made it possible for some four-atom reactions to be addressed from first principles, in their full six internal degrees of freedom. Attempts have been made to extend the time-dependent wave packet method to reactions with more internal degrees of freedom. Here, we review the full-dimensional theory for the A + BCD four-atom reaction and use it to guide the reduced-dimensionality treatment of the X + YCZ$_3$ reaction. Comparison of rigorous calculations with recent experiments are presented for (a) the benchmark H + H$_2$O abstraction reaction, and (b) the H + CH$_4$ → H$_2$ + CH$_3$ reaction.

1. Introduction

The development of theory for reliable calculations of chemical dynamics has two components: the construction of accurate, *ab initio*, multidimensional potential energy surfaces (PESs) and the performance of reactive scattering calculations, either by time-independent (TI) or time-dependent (TD) methods, on these surfaces. Accurate TI quantum methods for describing atom-diatom reactions, in particular for the benchmark H + H$_2$ reaction, have been achieved since 1975.[1,2,3] Many exact and approximate theories have been tested with the H + H$_2$ reaction.[4,5]

The progression from accurate quantum scattering calculations of three atoms to four atoms by TI methods proved formidable.[6,7,8] It is only in recent years that we

have achieved a quantitative level of understanding for the quantum reactive scattering of some four-atom systems in their full six internal coordinates,[9,10,11,12] comparable to what was attained for three-atom systems nearly three decades ago. This has been achieved largely through the use of the initial state TD quantum wave packet approach.[13,14] The benchmark four-atom reaction has been H + H_2O ↔ H_2 + OH. Both the forward and reverse reactions have been studied in detail. The framework suggests that given an accurate PES for a four-atom reaction, quantum dynamical calculations could provide quantitative details such as state-to-state reaction probabilities, fully converged integral cross sections, and accurate thermal rate coefficients to compare with experiments.

Recently, there has been some progress made in treating polyatomic systems beyond four-atoms in full dimension.[15,16,17] However, due to the quantum nature of the reactive scattering problem, it is necessary to resort to approximation methods, e.g. a reduced dimensionality approach to overcome the exponential increase in basis set functions to be included in the scattering calculations, to remain practical. Meyer and Manthe *et al.* employed a time-dependent basis set in the multi-configuration time-dependent Hartree (MCTDH) method.[15,16,17,18,19,20] Clary *et al.* developed the rotating bond approximation (RBA).[21,22,23] Bowman *et al.* used the adiabatic bend energy-shift approximation.[24,25] Yu and Nyman deployed the rotating bond umbrella[26,27] to study reactions of the type X + CH_4 (X = H, O). Zhang *et al.* developed the semi-rigid vibrating rotor target (SVRT) model.[28,29,30] The SVRT model is capable of providing rather accurate total reaction probability by an accurate treatment of the spatial motion.

A reaction of the type X + YCZ_3, with six atoms, would have twelve internal degrees of freedom, and this poses a severe challenge for both the construction of the PES as well as the reactive scattering calculation. The H + CH_4 → H_2 + CH_3 reaction, in particular, is an important combustion reaction. It has served as a prototype for this kind of reaction, and has been the subject of both experimental[31,32] and theoretical[15,16,17,24,26,30,33,34,35,36,37] interest for many years. As five of the six atoms are hydrogens, the system is a suitable candidate for pursuing both high quality *ab initio* calculation of the PES and accurate quantum reactive calculation. By viewing the X + YCZ_3 system as similar to the atom-triatom reaction A + BCD, with CD being replaced by CZ_3 it is possible to reduce the critical internal degrees of freedom from twelve to just seven: two degrees of freedom more than the tetraatomic system with the CD bond frozen, one for the umbrella motion of CZ_3 and the other for the torsional motion of CZ_3 which is assumed to retain its C_{3v} symmetry throughout. Various other models ranging from a collinear four-atom system33 to a full twelve-dimensional quantum transition state approach have been used.[15,16]

This paper draws a parallel between the (full) six-dimensional H + H_2O → H_2 + OH and the (reduced) seven-dimensional H + CH_4 → H_2 + CH_3 abstraction reactions. In Sec. 2, we briefly present the initial state TD quantum wave packet approach for the A + BCD and X + YCZ_3 reactions. The Hamiltonians, body-fixed (BF) parity-adapted rotational basis functions, initial state construction and wave packet propagation, and extraction of reaction probabilities, reaction cross sections, and thermal rate coefficients from the propagated wave packet to compare with experiments are discussed. In Sec. 3 we briefly outline the potential energy surfaces used in the calculations. Some

interesting results for the H + H$_2$O and H + CH$_4$ abstraction reactions are presented in Sec. 4.

2. Theory

2.1 HAMILTONIAN FOR THE A + BCD REACTION AND BASIS SET EXPANSION

The A + BCD atom-triatom reaction has been discussed in detail in previous papers,[11,12] and we shall only briefly summarize the theory here. The six internal Jacobi coordinates $(R, r_1, r_2, \theta_1, \theta_2, \varphi)$ for an A+ BCD reaction are shown in Fig. 1.
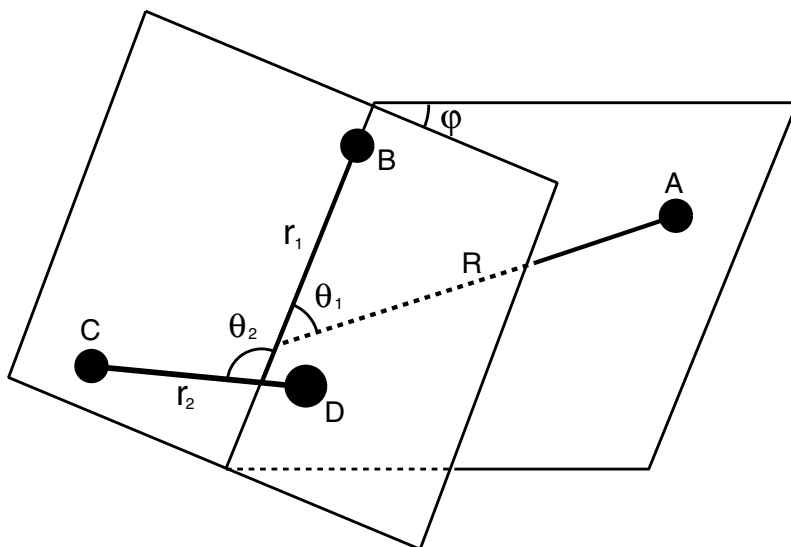

Figure 1. Jacobi coordinates for an atom-triatom reaction A + BCD.

The Hamiltonian for the "internal motion" can be written as[11]

$$H = -\frac{\hbar^2}{2\mu}\frac{\partial^2}{\partial R^2} + h_1(r_1) + h_2(r_2) + \frac{(\mathbf{J} - \mathbf{j})^2}{2\mu R^2} + \frac{\mathbf{j}_1^2}{2\mu_1 r_1^2} + \frac{\mathbf{j}_2^2}{2\mu_2 r_2^2} \\ + V(R, r_1, r_2, \theta_1, \theta_2, \varphi), \tag{1}$$

where μ is the reduced mass of A and BCD; μ_1 is the reduced mass of B and CD; μ_2 is the reduced mass of CD; R is the distance from A to the centre of mass of BCD; r_1 is the distance from B to the centre of mass of CD; r_2 is the bond length of CD; $\mathbf{J}$ is the

total angular momentum operator; $\mathbf{j}_1$ is the orbital momentum operator of B with respect to CD; $\mathbf{j}_2$ is the rotational angular momentum operator for CD; and $\mathbf{j} = \mathbf{j}_1 + \mathbf{j}_2$ is the coupled total angular momentum operator for BCD. The one-dimensional vibrational Hamiltonians $h_1(r_1)$ and $h_2(r_2)$ are defined as

$$h_i(r_i) = -\frac{\hbar^2}{2\mu_i}\frac{\partial^2}{\partial r_i^2} + V_i(r_i), \qquad i = 1,2 \tag{2}$$

where $V_1(r_1)$ and $V_2(r_2)$ are one-dimensional reference potentials obtained from the *total* global potential $V_{tot}(R,r_1,r_2,\theta_1,\theta_2,\varphi)$ with other degrees of freedom fixed as follows:

$$V_1(r_1) = V_{tot}(R \to \infty, r_1, r_2 = r_{20}, \theta_1, \theta_2 = \theta_{20}, \varphi), \tag{3}$$

$$V_2(r_2) = V_{tot}(R \to \infty, r_1 \to \infty, r_2, \theta_1, \theta_2, \varphi), \tag{4}$$

and r_{20}, θ_{20} denote the equilibrium values for r_2, θ_2 in the free triatomic BCD molecule. The interaction potential $V(R,r_1,r_2,\theta_1,\theta_2,\varphi)$ in Eq. (1) is thus given by

$$V(R,r_1,r_2,\theta_1,\theta_2,\varphi) = V_{tot}(R,r_1,r_2,\theta_1,\theta_2,\varphi) - V_1(r_1) - V_2(r_2). \tag{5}$$
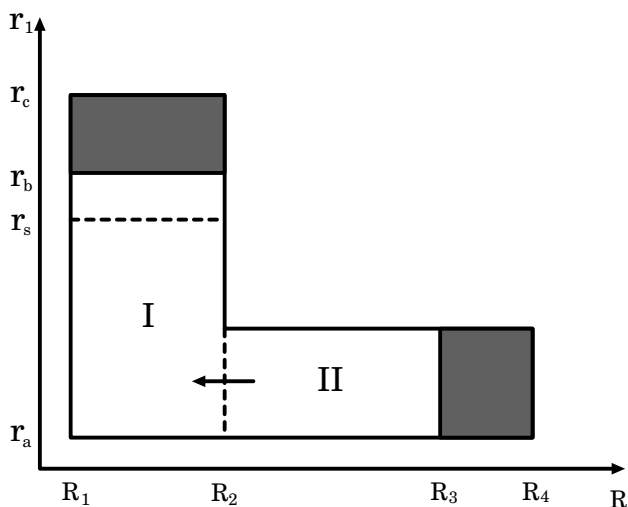
Figure 2. Schematic configuration space for the reaction A + BCD → AB + CD. R is the radial coordinate between A the centre of mass of BCD, and r_1 is the distance from B to the centre of mass of CD. The shaded regions are the absorption zones for the time-dependent wave function to avoid boundary reflections. The reactive flux is evaluated at the $r_1 = r_s$ surface.

The time-dependent wavefunction is expanded in terms of the translational basis of R, the vibrational bases $F_{v_1}(r_1), F_{v_2}(r_2)$ which are eigenfunctions of $h_1(r_1), h_2(r_2)$, respectively, and the BF parity-adapted rotational basis functions:

$$\Psi^{JM\varepsilon}(\mathbf{R}, \mathbf{r_1}, \mathbf{r_2}, t) = \sum_{n,v,\tilde{j},K} F_{nv\tilde{j}K}^{JM\varepsilon}(t) u_n^v(R) F_{v_1}(r_1) F_{v_2}(r_2) \mathbf{Y}_{\tilde{j}K}^{JM\varepsilon}(\hat{\mathbf{R}}, \hat{\mathbf{r}}_1, \hat{\mathbf{r}}_2), \tag{6}$$

where v denotes (v_1, v_2) and $\tilde{j}$ denotes (j_1, j_2, j). In order to save computational time, the configuration space for the reaction A + BCD → AB + CD is partitioned into an interaction region **I** and an asymptotic region **II**, as shown in Fig. 2, with the v dependent translational basis function $u_n^v(R)$ defined as

$$u_n^v(R) = \begin{cases} \sqrt{\dfrac{2}{R_3 - R_1}} \sin \dfrac{n\pi(R-R_1)}{R_3-R_1}, & v_1 \leq v_{1\,asy} \text{ and } v_2 \leq v_{2\,asy}, \\[2ex] \sqrt{\dfrac{2}{R_2 - R_1}} \sin \dfrac{n\pi(R-R_1)}{R_2-R_1}, & \text{otherwise}, \end{cases} \tag{7}$$

where R_2 and R_3 define the interaction and asymptotic grid ranges, respectively, and v_{1asy} and v_{2asy} are chosen to define the bases which can accurately expand the 3D rovibrational states of the free BCD molecule for the scattering calculation. The general wavefunction expansion given in Eq. (6) allows the cleavage of the CD bond, but it can also be treated as a non-reactive bond by using only a few vibrational basis functions for the CD diatom in the interaction region as well as the asymptotic region.

The parity-adapted BF total angular momentum basis functions $\mathbf{Y}_{\tilde{j}K}^{JM\varepsilon}(\hat{\mathbf{R}}, \hat{\mathbf{r}}_1, \hat{\mathbf{r}}_2)$ in Eq. (6) are the eigenfunctions for $\mathbf{J}, \mathbf{j}_1, \mathbf{j}_2, \mathbf{j}, K$ and the parity operator, where K is the projection of $\mathbf{J}$ along the BF z-axis, chosen to be along R. They are defined as

$$\mathbf{Y}_{\tilde{j}K}^{JM\varepsilon}(\hat{\mathbf{R}}, \hat{\mathbf{r}}_1, \hat{\mathbf{r}}_2) = [(1+\delta_{K0})]^{-1/2}$$
$$\times \sqrt{\frac{2J+1}{8\pi}} \Big[D_{KM}^{J*} Y_{j_1 j_2}^{jK} + \varepsilon(-1)^{j_1+j_2+j+J} D_{-KM}^{J*} Y_{j_1 j_2}^{j-K} \Big], \tag{8}$$

where D_{KM}^{J*} is the Wigner rotation matrix,[38] ε is the parity of the system, the projection of the total angular momentum on the body-fixed axis is restricted to $0 \leq K \leq \min(J, j)$, and $Y_{j_1 j_2}^{jK}$ are the angular momentum eigenfunctions of $\mathbf{j}, K$ defined as,

$$Y_{j_1 j_2}^{jK} = \sum_m D_{Km}^{j*}(\chi, \theta_1, \varphi) \sqrt{\frac{2j_1+1}{4\pi}} \langle j_2 m j_1 0 | jm \rangle y_{j_2 m}(\theta_2, 0), \tag{9}$$

where $\langle j_2 m j_1 0 | j m \rangle$ is a Clebsch-Gordon coefficient and y_{jm} are spherical harmonics. In Eq. (8), the restriction $\varepsilon(-1)^{j_1+j_2+j+J} = 1$ for $K = 0$, partitions the whole rotational basis set into even and odd parities. Thus a $K = 0$ initial state can only appear in one of these two parity blocks. For $K > 0$, however, there is no such restriction, the basis set is the same for even and odd parities; hence a $K > 0$ initial state can appear in both parities.

2.2. NITIAL STATE CONSTRUCTION AND WAVE PACKET PROPAGATION FOR A + BCD REACTIONS

The initial wavefunction is chosen to be the direct product of a localized translational wave packet for R and a specific $(JM\varepsilon)$ state for the atom-triatom system with a specific rovibrational eigenstate for the triatom BCD:

$$\Psi_{v_0 L_0 \Omega_0}^{JM\varepsilon}(\mathbf{R}, \mathbf{r}_1, \mathbf{r}_2, t = 0) = G_{k_0}(R)\psi_{v_0 L_0 \Omega_0}^{JM\varepsilon}(\hat{\mathbf{R}}, \mathbf{r}_1, \mathbf{r}_2), \tag{10}$$

where the translational wave packet $G_{k_0}(R)$ is chosen to be a Gaussian function

$$G_{k_0}(R) = \left(\frac{1}{\pi\delta^2}\right)^{1/4} \exp\left[-(R - R_0)^2 / 2\delta^2\right] e^{-ik_0 R}, \tag{11}$$

with R_0, δ as the centre and width, respectively, of the Gaussian function and $k_0 = \sqrt{2\mu E_0}$, with E_0 as the central energy of the Gaussian function, and $\psi_{v_0 L_0 \Omega_0}^{JM\varepsilon}(\hat{\mathbf{R}}, \mathbf{r}_1, \mathbf{r}_2)$ is an eigenfunction of the triatom BCD Hamiltonian

$$\begin{aligned} H_{BCD} &= h_1(r_1) + h_2(r_2) + \frac{\mathbf{j}_1^2}{2\mu_1 r_1^2} + \frac{\mathbf{j}_2^2}{2\mu_2 r_2^2} \\ &+ V(R \to \infty, r_1, r_2, \theta_1, \theta_2, \varphi), \end{aligned} \tag{12}$$

with v_0, L_0, Ω_0 representing the triatom BCD's initial vibrational state, total angular momentum, and its projection on the BF z axis, $\hat{\mathbf{R}}$, of the atom-triatom system, respectively. The initial wavefunction, Eq. (10), can be expanded as in Eq. (6) and the wave packet is propagated using the split operator method[39]:

$$\Psi(\mathbf{R}, \mathbf{r}_1, \mathbf{r}_2, t + \Delta) = e^{-iH_0\Delta/2} e^{-iU\Delta/2} e^{-iV\Delta} e^{-iU\Delta/2} e^{-iH_0\Delta/2} \Psi(\mathbf{R}, \mathbf{r}_1, \mathbf{r}_2, t), \tag{13}$$

with reference Hamiltonian H_0 given by

$$H_0 = -\frac{\hbar^2}{2\mu}\frac{\partial^2}{\partial R^2} + h_1(r_1) + h_2(r_2),$$
(14)

the potential V given by Eq. (5), and the centrifugal potential U defined by

$$U = \frac{(\mathbf{J}-\mathbf{j})^2}{2\mu R^2} + \frac{\mathbf{j}_1^2}{2\mu_1 r_1^2} + \frac{\mathbf{j}_2^2}{2\mu_2 r_2^2} \quad .$$
(15)

2.3. REDUCED DIMENSIONAL HAMILTONIAN FOR THE X + YCZ₃ SYSTEM AND BASIS SET EXPANSION

The X + YCZ$_3$ system would have 12 internal coordinates, which makes it computationally very challenging. A reduced dimensionality, taking into consideration only the most important internal coordinates for the reaction, is necessary. Here we view the system as an extension of the A + BCD system, as depicted in Fig. 3, with the CD part replaced by CZ$_3$, and imposing the requirement that the CZ$_3$ group has fixed CZ bond lengths and maintains C$_{3v}$ symmetry in the course of the reaction. Five of the Jacobi coordinates $(R, r_1, \theta_1, \theta_2, \varphi_1)$ in the A + BCD system are retained, and the sixth coordinate r_2 for the CD bond is replaced by two angles appropriate for CZ$_3$, and keeping the CZ bond length fixed.
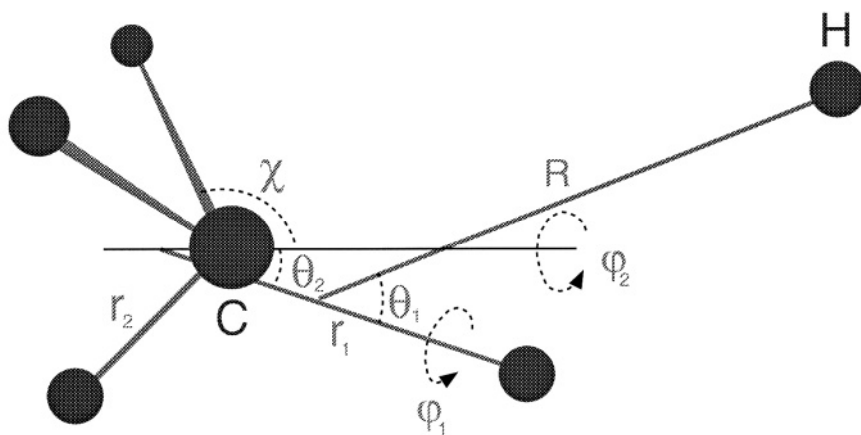
Figure 3. Jacobi coordinates for the X + YCZ$_3$ system, as exemplified by H + CH$_4$.

The CD axis now corresponds to the symmetry axis of CZ$_3$ and is described by the unit vector $\hat{\mathbf{s}}$. The umbrella motion of the CZ$_3$ group and its rotation is described by two internal angles: χ, the angle between a CZ bond and the symmetry axis $\hat{\mathbf{s}}$, and the rotation angle φ_2 of CZ$_3$ about $\hat{\mathbf{s}}$. The angles φ_1 and φ_2 are also known as the

azimuthal angles about the $\hat{\mathbf{r}}_1$ and $\hat{\mathbf{s}}$ axes, respectively. The CZ bond length, r_2, is taken to be constant. In the eight dimensional model of Palma and Clary,[40] r_2 is allowed to vary. Here, the seven Jacobi coordinates for the X + YCZ$_3$ system are taken to be $(R, r_1, \theta_1, \theta_2, \varphi_1, \varphi_2, \chi)$.

The reduced dimensionality Hamiltonian for the X + YCZ$_3$ system can be written as [40]

$$
\hat{H} = -\frac{\hbar^2}{2\mu}\frac{\partial^2}{\partial R^2} - \frac{\hbar^2}{2\mu_1}\frac{\partial^2}{\partial r_1^2} + \frac{(\mathbf{J}_{tot} - \mathbf{J})^2}{2\mu R^2} + \frac{\mathbf{l}^2}{2\mu_1 r_1^2}
$$
$$
+ \hat{K}_{CZ_3}^{vib} + \hat{K}_{CZ_3}^{rot} + V(R, r_1, \theta_1, \theta_2, \varphi_1, \varphi_2, \chi),
$$

(16)

where μ is the reduced mass of X atom and YCZ$_3$ entity, μ_1 is the reduced mass of Y atom and CZ$_3$. The first two terms are the kinetic energy operators of R and r_1, respectively. $\mathbf{J}_{tot}$ is the total angular momentum operator of the system; $\mathbf{J}$ is the rotational angular momentum operator of molecule YCZ$_3$; and $\mathbf{l}$ is the orbital angular momentum operator of Y with respect to CZ$_3$ group. $\hat{K}_{CZ_3}^{vib}$ and $\hat{K}_{CZ_3}^{rot}$ are the umbrella vibrational kinetic energy operator and the rotational kinetic energy operator of CZ$_3$, respectively. The operators have been defined by Palma and Clary40 with the following explicit forms,

$$
\hat{K}_{CZ_3}^{vib} = -\frac{\hbar^2}{2r_2^2}\left(\frac{\cos^2\chi}{\mu_x} + \frac{\sin^2\chi}{\mu_s}\right)\frac{\partial^2}{\partial\chi^2} - \frac{\hbar^2}{r_2^2}\sin\chi\cos\chi\frac{\partial}{\partial\chi},
$$

(17)

and

$$
\hat{K}_{CZ_3}^{rot} = \frac{1}{2I_A}\mathbf{j}^2 + (\frac{1}{2I_C} - \frac{1}{2I_A})\mathbf{j}_z^2,
$$

(18)

where r_2 is the fixed bond length of CZ, μ_x and μ_s are masses defined as $\mu_x = 3m_Z$ and $\mu_s = 3m_C m_Z/(m_C + 3m_Z)$. I_A and I_C are the rotational inertia of the CZ$_3$ group defined as

$$
I_A = \frac{3}{2}m_Z r_2^2\left(\sin^2\chi + \frac{2m_C}{m_C + 3m_Z}\cos^2\chi\right),
$$

(19)

and

$$
I_C = 3m_Z r_2^2 \sin^2\chi,
$$

(20)

while $\mathbf{j}$ is the rotational angular momentum of CZ$_3$ and $\mathbf{j}_z$ is its z-component. The last term in Eq. (16), $V(R, r_1, \theta_1, \theta_2, \varphi_1, \varphi_2, \chi)$, is the total global potential energy.

The rotational basis functions used in this work are very similar to those used in the initial state wave packet dynamics study of $H+H_2O$. The rotational basis function has the following explicit form

$$
\begin{aligned}
\Phi_{Jjlk}^{J_{tot}MK}(\hat{\mathbf{R}},\hat{\mathbf{r}}_1,\hat{\mathbf{s}}) &= \overline{D}_{MK}^{J_{tot}}(\hat{\mathbf{R}})Y_{jlk}^{JK}(\hat{\mathbf{r}}_1,\hat{\mathbf{s}}) \\
&= \sqrt{\frac{2J_{tot}+1}{8\pi^2}}D_{MK}^{*J_{tot}}(\alpha,\beta,\gamma)\,Y_{jlk}^{JK}(\hat{\mathbf{r}}_1,\hat{\mathbf{s}}) \quad,
\end{aligned}
\tag{21}
$$

where M and K are the projections of the total angular momentum $\mathbf{J}_{tot}$ on the z-axis of the space-fixed and body-fixed frames, respectively. The rotation matrix $D_{MK}^{*J_{tot}}(\alpha,\beta,\gamma)$ depends on the Euler angles that rotate the spaced-fixed frame on to the body-fixed frame and are eigenfuctions of $\mathbf{J}_{tot}^2$. The body-fixed internal angular momentum function in Eq. (21) is given by

$$
\begin{aligned}
Y_{jlk}^{JK}(\hat{\mathbf{r}}_1,\hat{\mathbf{s}}) &= \sum_m \overline{D}_{Km}^J(\hat{\mathbf{r}}_1)\sqrt{\frac{2l+1}{2J+1}}<jml0\,|\,Jm>\overline{D}_{mk}^j(\hat{\mathbf{s}}) \\
&= \sum_m \sqrt{\frac{2J+1}{4\pi}}D_{Km}^{*J}(0,\theta_1,\varphi_1) \\
&\times \sqrt{\frac{2l+1}{2J+1}}<jml0\,|\,Jm>\sqrt{\frac{2j+1}{4\pi}}D_{mk}^{*j}(0,\theta_2,\varphi_2).
\end{aligned}
\tag{22}
$$

By exploring the space inversion symmetry of the rotational basis functions, we can construct the parity-adapted rotational basis functions

$$
\begin{aligned}
\Phi_{Jljk}^{J_{tot}MK\varepsilon}(\hat{\mathbf{R}},\hat{\mathbf{r}}_1,\hat{\mathbf{s}}) &= \sqrt{\frac{1}{2(1+\delta_{K0}\delta_{k0})}} \\
&\times\left[\Phi_{Jljk}^{J_{tot}MK}(\hat{\mathbf{R}},\hat{\mathbf{r}}_1,\hat{\mathbf{s}}) + \varepsilon(-1)^{J_{tot}+J+l+j+k}\Phi_{Jlj-k}^{J_{tot}M-K}(\hat{\mathbf{R}},\hat{\mathbf{r}}_1,\hat{\mathbf{s}})\right] \quad,
\end{aligned}
\tag{23}
$$

where $0 \le K \le \min(J_{tot},J)$.

The time-dependent wavefunction is expanded in the parity-adapted rotational basis functions as,

$$
\begin{aligned}
\Psi^{J_{tot}M\varepsilon} &= \sum_{n_R,n_r,n_u}\sum_{KJljk} c_{n_Rn_rn_uJljk}^{J_{tot}MK\varepsilon}(t)u_{n_R}(R) \\
&\times F_{n_r}(r_1)H_{n_u}(\chi)\Phi_{Jljk}^{J_{tot}MK\varepsilon}(\hat{\mathbf{R}},\hat{\mathbf{r}}_1,\hat{\mathbf{s}})
\end{aligned}
\tag{24}
$$

where $c_{n_R n_r n_u J l j k}^{J_{tot} M K \varepsilon}(t)$ are time-dependent coefficients to be solved for. The quantum numbers n_R, n_r and n_χ labels the basis functions for the degrees of the freedom in R, r_1 and χ, respectively. In Eq. (24), the translational basis function $u_{n_R}(R)$ is defined as

$$u_{n_R}(R) = \sqrt{\frac{2}{R_2 - R_1}} \sin \frac{n_R \pi (R - R_1)}{R_2 - R_1} \quad , \tag{25}$$

while the basis functions $F_{n_r}(r_1)$ and $H_{n_u}(\chi)$ are obtained by solving one-dimensional reference Hamiltonians which are defined, respectively, as follows

$$h_1(r_1) = -\frac{\hbar^2}{2\mu_1} \frac{\partial^2}{\partial r_1^2} + v_1^{ref}(r_1) \tag{26}$$

and for the umbrella motion

$$h_u(\chi) = K_{CZ_3}^{vib} + v_u^{ref}(\chi) \tag{27}$$

where $v_1^{ref}(r_1)$ and $v_u^{ref}(\chi)$ are the corresponding reference potentials.

2.4. INITIAL STATE CONSTRUCTION AND WAVE PACKET PROPAGATION FOR X-YCZ₃ REACTION

The initial wavefunction is constructed as the direct product of a localized wave packet for R, $G_{k_0}(R)$, as defined in Eq. (11), and a specific state $(J_{tot}, M, \varepsilon)$ of the system with a specific rovibrational eigenstate (n_0, J_0, K_0, p_0) for YCZ₃, where n_0, J_0, K_0, p_0 represent, respectively, the initial vibrational state, total angular momentum, projection of total angular momentum on the body-fixed z axis of X-YCZ₃ system, and the parity of YCZ₃. The rovibrational eigenfunction of YCZ₃ is expanded as follows:

$$\psi_{n_0 J_0 K_0 p_0}^{J_{tot} M \varepsilon} = \sum_{n_r n_u l j k} d_{n_r n_u l j k}^{n_0 J_0 K_0 p_0} F_{n_r}(r) H_{n_u}(\chi) \Phi_{J_0 l j k}^{J_{tot} M \overline{K} 0 \varepsilon}(\hat{\mathbf{R}}, \hat{\mathbf{r}}_1, \hat{\mathbf{s}}) \quad , \tag{28}$$

which is a solution of the YCZ₃ Hamiltonian

$$\hat{H}_{YCZ_3} = -\frac{\hbar^2}{2\mu_1} \frac{\partial^2}{\partial r_1^2} + \frac{\mathbf{l}^2}{2\mu_1 r_1^2} + \hat{K}_{CZ_3}^{vib} + \hat{K}_{CZ_3}^{rot} + V_{YCZ_3}(r_1, \theta_2, \varphi_2, \chi) \quad , \tag{29}$$

where the potential is given by

$$V_{\text{YCZ}_3}(r_1,\theta_2,\varphi_2,\chi)=V(R\to\infty,r_1,\theta_1,\theta_2,\varphi_1,\varphi_2,\chi)\quad. \tag{30}$$

The wavefunction is propagated using the split-operator propagator.

$$\Psi(t+\Delta)=e^{-iH_0\Delta/2}e^{-iU\Delta}e^{-iH_0\Delta/2}\Psi(t)\quad, \tag{31}$$

where the reference Hamiltonian H_0 is defined as

$$H_0=-\frac{\hbar^2}{2\mu}\frac{\partial^2}{\partial R^2}+h_r^{ref}(r)+h_u^{ref}(\chi)\quad, \tag{32}$$

and the reference potential U is defined as

$$U=\frac{(\mathbf{J}_{tot}-\mathbf{J})^2}{2\mu R^2}+\frac{\mathbf{l}^2}{2\mu_1 r_1^2}+\hat{K}_{\text{CZ}_3}^{rot}$$
$$+V(R,r_1,\theta_1,\theta_2,\varphi_1,\varphi_2,\chi)-v_r^{ref}(r)-v_u^{ref}(\chi). \tag{33}$$

2.5. REACTION PROBABILITY, CROSS SECTION, AND RATE CONSTANT

For both the A + BCD and X + YCZ$_3$ reactions, the energy-dependent scattering wavefunction is obtained by a Fourier transform of the propagated wave packet[41]

$$\left|\psi_{iE}^+\right\rangle=\frac{1}{a_i(E)}\int_{-\infty}^{\infty}e^{iEt/\hbar}\,e^{-iHt/\hbar}\left|\Psi_i(0)\right\rangle dt, \tag{34}$$

where the subscript i denotes the initial rovibrational quantum state of the reactants, and the coefficient $a_i(E)$ is given by

$$a_i(E)=\left\langle\psi_{iE}^+\middle|\Psi_i(0)\right\rangle=\left\langle\phi_{iE}\middle|\Psi_i(0)\right\rangle, \tag{35}$$

where ϕ_{iE} is the free or asymptotic stationary wavefunction.

With the stationary solution ψ_{iE}^+, one can use asymptotic boundary conditions to extract the scattering matrix. However, for the total reaction probability $P_i(E)$ the calculation can be simplified by evaluating the reactive flux through any dividing surface which separates the reactant from products, e.g. at a hypersurface close to the transition state, without the need to compute the state-to-state S matrix:

$$P_i(E)=\sum_f\left|S_{fi}\right|^2=\left\langle\psi_{iE}^+\middle|\hat{F}\middle|\psi_{iE}^+\right\rangle, \tag{36}$$

where the flux operator is

$$\hat{F} = \frac{1}{2}[\delta(\hat{s} - s_0)\hat{v}_s + \hat{v}_s\delta(\hat{s} - s_0)], \tag{37}$$

with s being the coordinate perpendicular to a surface located at s_0 for the flux evaluation, and $\hat{v}_s$ is the velocity operator. In our case, it can also be simplified to

$$P_i(E) = \frac{\hbar}{\mu_1} \mathrm{Im}(\langle \psi_{iE}^+ | \psi_{iE}'^+ \rangle)|_{\eta = \eta_s} \quad , \tag{38}$$

where $\psi_{iE}'^+$ is the first derivative with respect to r_1, the coordinate of the bond that breaks.

In general, the cross section for a specific initial state can be calculated from the reaction probability,

$$\sigma_i(E) = \frac{\pi}{2\mu E} \sum_J (2J+1) P_i^J(E) \quad , \tag{39}$$

and the rate constant can be calculated from the cross section

$$r_i(T) = \left(\frac{8kT}{\pi\mu}\right)^{1/2} (kT)^{-2} \int_0^\infty E_t \exp(-E_t/kT)\sigma_i(E_t)dE_t \quad . \tag{40}$$

3. *Ab initio* potential energy surfaces

3.1 PES'S FOR THE H + H₂O ↔ H₂ + OH REACTION

The approximate, analytic Walch-Dunning-Schatz-Elgersma (WDSE) PES[42] featured prominently in facilitating the development of classical and quantum dynamical methods to study the H_2 + OH → H + H_2O reaction. Recently, some high level interpolated *ab initio* PESs were reported for the reverse abstraction reaction H + H_2O → H_2 + OH and its isotopic analogs.[43,44] The, so called, QCISD(T)/6-311++G(3df,2pd) *ab initio* PES is not defined in the region of the H_2 + OH entrance channel, due to the presence of a second low-lying electronic state, and so cannot be used to evaluate the final state distribution of H_2 + OH products from the H + H_2O reaction, or to study the H_2 + OH reaction. The near degeneracy of the ground and first excited electronic states in the H_2 + OH entrance channel has recently been addressed by employing the CASSCF/MRCI+Q/aug-cc-pVQZ level of theory, using the MOLPRO package,[45] in a substantial part of the H_2 + OH entrance channel, while elsewhere the QCISD(T)/6-311++G(3df,2pd) level of theory was used. Two new *ab initio* Yang-Zhang-Collins-Lee global PESs - YZCL1 and YZCL2 - resulted.[46] They

were constructed using the interpolation of *ab initio* data procedure of Collins *et al.*[47] The YZCL1 surface has 1,600 data points. The energy of each of these data points was then evaluated at the UCCSD(T)/aug-cc-pVQZ level of theory to produce the YZCL2 surface, considered the best global PES for H_3O today.

3.2 PES'S FOR THE H + CH₄ REACTION

Numerous PES's have been proposed for the H + CH_4 reaction. The early ones were empirical form fit to experimental results and neglected the symmetry of the methane molecule.[48] Later, semiempirical and *ab initio* surfaces, with partially correct permutation symmetry, were developed. Notable among them is the semi-empirical PES by Jordan and Gilbert (JG), symmetric with respect to all four hydrogens on methane.[49] It was built on earlier PESs given by Joseph *et al.*[50] and Duchovic *et al.*[51]

We have used a new seven-dimensional *ab initio* PES in which the CH_3 group retains C_{3v} symmetry and fixed CH bond lengths in our time-dependent calculations.[52] The energy near the minimum energy path (MEP) is described by a basis set corrected calculation using the quadratic configuration interaction treatment with all single and double excitations (QCISD):

$$E_1 = E[\text{QCISD/B1}] + E[\text{MP2/B2}] - E[\text{MP2/B1}], \tag{41}$$

where MP2 denotes the second order Moller-Plesset perturbation theory, and B1=cc-pVDZ and B2=aug-cc-pVDZ denote the correlation consistent basis sets. Similar to the construction of the H_3O PES, the CH_5 PES is given by an interpolation of second order Taylor expansions of Eq. (41) at data points scattered throughout the configuration space using the method of Collins *et al.*47 The reliability of the PES was further improved by replacing the energy E_1 at each data point by

$$E_2 = E[\text{CCSD(T)/aug} - \text{cc} - \text{pVTZ}], \tag{42}$$

where CCSD(T) denotes a coupled cluster approximation, and it is this more accurate PES that is used in the quantum dynamics calculations below.

4. Theoretical and experimental results

4.1 ABSTRACTION REACTION OF H + H₂O

There are two possible outcomes of the H + H_2O reaction:
Abstraction reaction, $\quad$ H′ + H_2O → H′H + OH
Exchange reaction, $\quad\quad\quad\quad$ → H + H′OH .
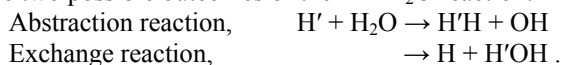
Our focus here is on the abstraction reaction. It has a saddle point with $H'\cdots H\cdots O$ close to a collinear geometry; hence the H′ atom should collide with the H_2O molecule at totally different angles in order to abstract one H atom or the other. As a result, it should be possible to treat the unbroken OH bond as a spectator bond in the abstraction

reaction, but this assumption would not be valid for the exchange reaction.[53] Figure 4 shows the total reaction probability for the abstraction reaction as a function of the translational energy for total angular momentum $J=0$ on the YZCL2 PES with the H_2O reactant in the ground rovibrational state [the (00)(0) state in the local mode notation], where the unbroken bond OH_b is treated in various ways. Using a limited number of one or five
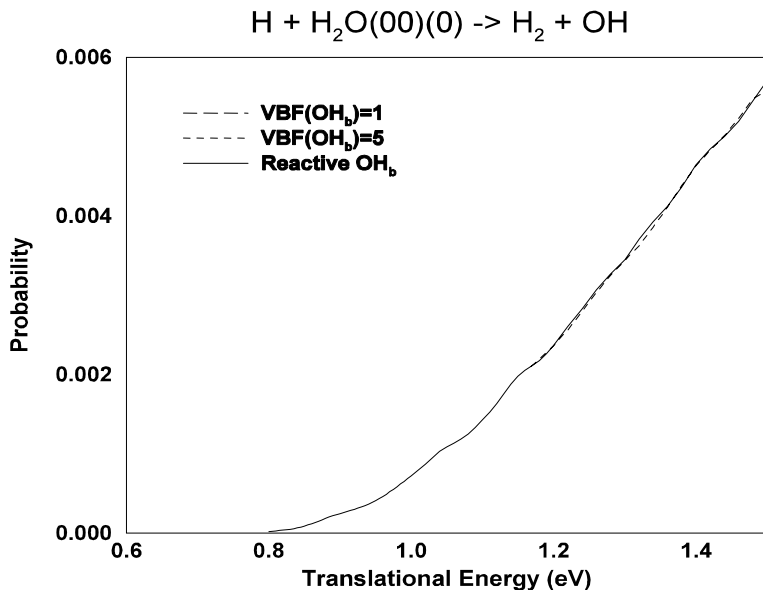
Figure 4. Total reaction probability for the H + H_2O(00)(0) $\rightarrow$ H_2 + OH abstraction reaction as a function of the translational energy on the YZCL2 PES for J = 0.

vibrational basis functions (VBF) means that the OH_b bond is unreactive, a spectator, but could be either frozen vibrationally, VBF(OH_b) = 1, or not frozen vibrationally, VBF(OH_b) = 5. The abstraction reaction probability is very small, due to the small reaction cone, but, more importantly, the results are almost identical whether the OH_b bond is treated as a spectator or as a reactive bond. It should be noted that when the OH_b bond is a spectator, then the reaction probability from OH_a alone is multiplied by two for comparison with the probability for two reactive bonds. Similar results, shown in Fig. 5, were obtained for $J=0$ with the H_2O reactant in the vibrationally excited symmetric or antisymmetric $(01)^{\pm}(0)$ stretching states. In the vibrationally frozen state for the OH_b bond, the $(01)^{\pm}$ states become one unsymmetrized local mode (10), and the result is again very close to the accurate result. For comparison, we also show the small abstraction probability for the ground state, at the bottom right in Fig. 5. Clearly, the OH stretching excitation enhances the reaction a great deal because the abstraction reaction has a later barrier which can be surmounted with the vibrational excitation energy.
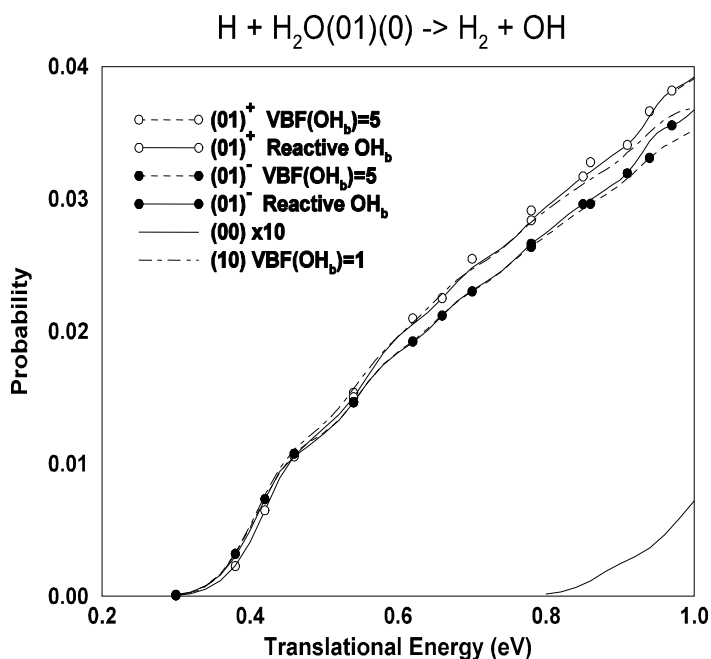
Figure 5. Same as Fig. 4, but for the $H_2O(01)(0)$ state

A recent set of calculations on the H + H_2O, D_2O abstraction reactions had taken advantage of restricting one of the OH (OD) bonds in the H_2O (D_2O) reactant from being broken, leaving just 5 degrees of freedom, to reduce the computational time.[44] A global YZCL1 PES, in hindsight, was used. The results showed that for the H + H_2O $\rightarrow$ H_2 + OH reaction there is agreement between experiment and theory for the thermal rate constant, as shown in Fig. 6. In the low temperature region, the thermal rate coefficient is dominated by contributions from the excited OH stretching states $(02)^{\pm}$ and $(01)^{\pm}$, and in the high temperature region contributions from $(03)^{\pm}$ also become important. The centrifugal sudden (CS) approximation is commonly invoked to reduce the number of rotational basis functions used in the computation. Under the CS approximation and using only the $K = 0$ rotational basis functions, there was a total of 220 million basis functions for $J = 15$ alone. Relaxing the CS approximation, for example, with $K = 0$, 1 and $J = 15$ led to 650 million basis functions. To approach the fully coupled-channel (CC) results, i.e. without the CS approximation, we had to use three K-blocks for $J = 5$, 10, 15, 20, 25, and four K-blocks for $J = 30$, 35, 40, resulting in many more rotational basis functions.11 The integral cross sections, comparing the CS versus CC for the H + $H_2O(00)(0)$ $\rightarrow$ H_2 + OH reaction on the more accurate YZCL2 PES, are shown in Fig. 7, and for the H + $H_2O(01)(0)$ $\rightarrow$ H_2 + OH reaction they are shown in Fig. 8. The quasiclassical trajectory (QCT) integral cross section at E = 1.4 eV reported on the same surface,[54] is also shown in Fig. 7. Clearly, the CS
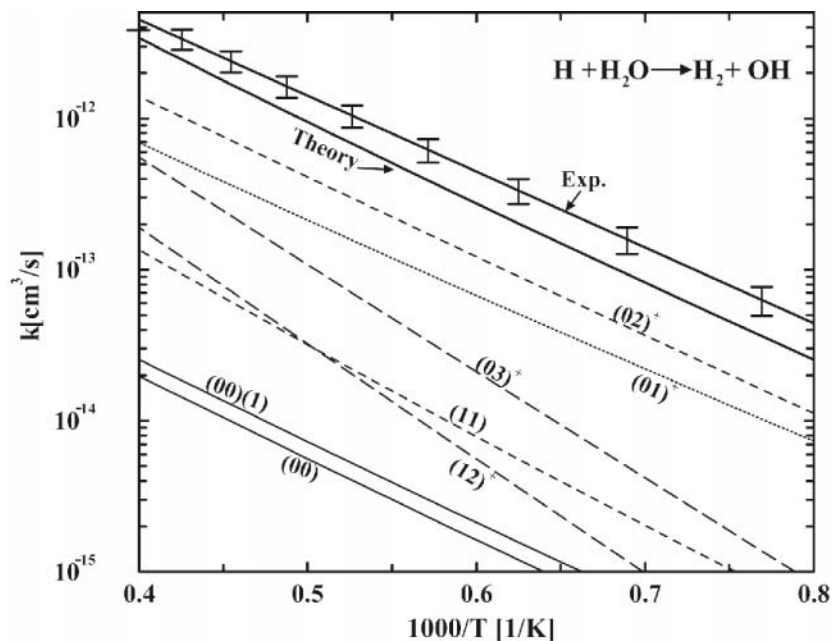
Figure 6. Comparison of theory and experiment for the thermal rate constant of the H + $H_2O \rightarrow$ H_2 + OH reaction, and the calculated contributions from the individual vibrational states of H_2O.

approximation does not work well for the abstraction reaction particularly from the ground rovibrational state. The CC cross section is larger than the CS cross section, by about 60% for the ground rovibrational state of H_2O, and by about 15% for the first excited rovibrational state.

A recent experiment[55] for the abstraction reaction gave a cross section of 0.041 ± 0.018 Å^2 at collision energies close to 2.46 eV, which is about a factor of two lower than calculations, as shown in Fig. 9. The calculations include the 5D QM results, which treat one OH bond as spectator and correspond to the CC cross section, and the quasi-classical trajectory (QCT) results of Schatz *et al.*[56] on the WSLFH PES[57] using normal and Gaussian binning procedures. Possible reasons for the discrepancy between experiment and theory include the presence of a close lying excited electronic state. At the abstraction barrier, this state is only ~2 eV above the equilibrium energy of the reactants, and could play a role at the energies sampled in the experiment.

We are now also able to calculate the state-to-state integral cross section (ICS) for the H + H_2O (00)(0) $\rightarrow$ $H_2(v_1,j_1)$ + OH(j_2) abstraction reaction, which is very demanding as it requires state-to-state reaction probabilities for $J > 0$. A 5D calculation, with one OH bond as spectator, on the YZCL2 surface has been performed.[12] From the state-to-state ICS, we can calculate the fractions of energy going into the internal motions of the products, as shown in Fig. 10. It was found that (a) the H_2 molecule is produced vibrationally cold for collision energy up to 1.6 eV, (b) the OH rotation takes away about 4% of the total available energy in the products, and (c) the fraction of energy going into H_2 rotation increases with collision energy to about 20% at 1.6 eV.

H + H₂O(00)(0) → H₂ + OH
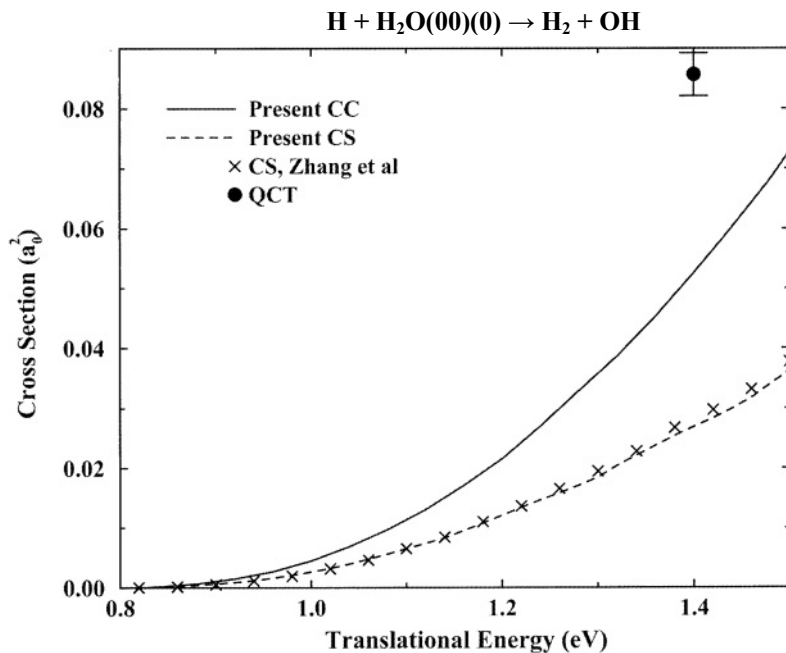
Figure 7. The coupled channel (CC) and centrifugal sudden (CS) integral cross section for the H + $H_2O(00)(0)$ abstraction reaction. Other results: x CS, Ref. 44; ● QCT, Ref. 54.

H + H₂O(01)(0) → H₂ + OH
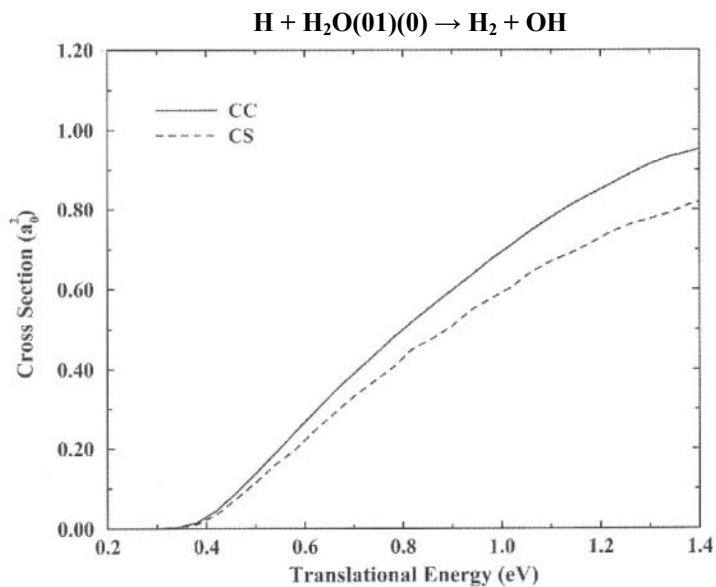
Figure 8. Same as Fig. 7, but for the H + $H_2O(01)(0)$ reaction
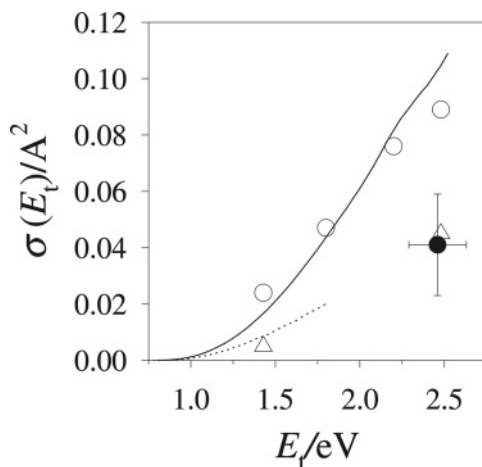
Figure 9. Comparison between the experimental abstraction reaction H + $H_2O(00)(0)$ cross section (● with error bars), the 5D QM results (solid line), the 6D QM cross sections with the CS approximation (dotted line), and the QCT data using normal (o) and Gaussian (Δ) binning procedures.

Figure 10. The fraction of the total available energy in the product channel going into rovibration of H_2 and rotation of OH as a function of the translational energy. Curves without open circles were calculated from the $J = 0$ state-to-state reaction probability.

Sometimes, the fractions obtained for the $J = 0$ reaction probabilities are used to approximately study the distribution of the total available energy among the products, and are shown (as curves without open circles) in Fig. 10 for comparison.

4.2 SEVEN DIMENSIONAL CALCULATION OF THE H + CH$_4$ ABSTRACTION REACTION

The initial state selected time-dependent wave packet method has been applied to the abstraction reaction $H + HCH_3 \rightarrow H_2 + CH_3$ using the seven-dimensional (7D) model above.[37,52] The wave packet calculation for each selected initial state of CH$_4$ was carried out with total angular momentum $J = 0$. Calculations were performed on both the Jordan-Gilbert (JG) potential,49 as well as a new interpolated *ab initio* PES.52 The new surface has a classical barrier height of 61.2 kJ mol^{-1}, in agreement with recent semiempirical PESs in which the classical barrier has been fitted to the observed reaction rate yielding a barrier height of 61.9 kJ mol^{-1}. In order to describe the quantum tunneling dynamics accurately, the PES must also accurately describe the barrier shape.

In Fig. 11, we compare the present 7D and 6D ($\chi = 107.45°$) total reaction probability for the ground rovibrational initial state with earlier results using other approximation methods – the SVRT 5D and 4D ($\chi = 107.45°$) models30 and the Wang-Bowman (WB) 6D atom-triatom model24 - on the JG PES. An obvious feature is an energy shift of 0.08-0.18 eV between the 7D probability and the WB 6D atom-triatom model. This is likely due to differences in some parameters used in the two studies to
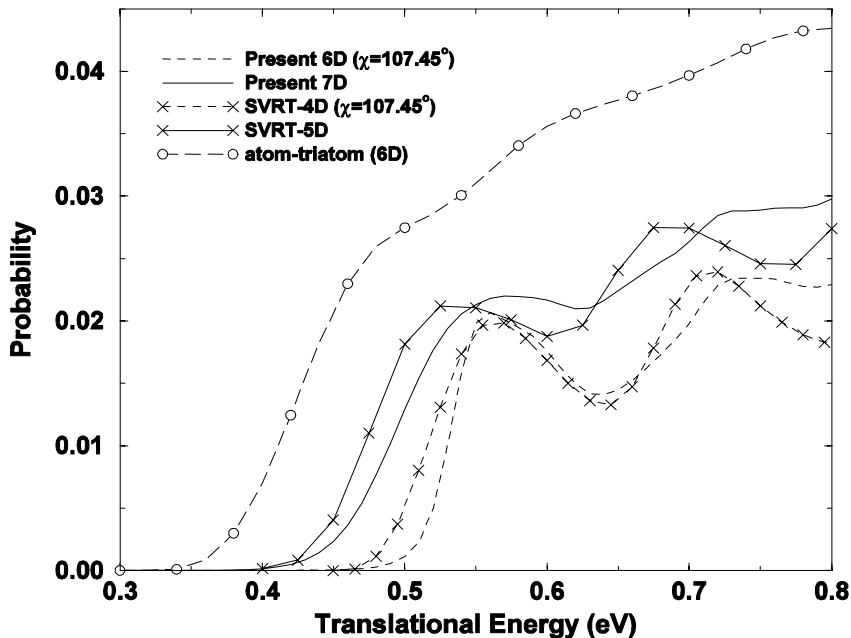
Figure 11. Comparison between the present 7D total reaction probability for the ground initial state with those of the SVRT model and the Wang-Bowman 6D atom-triatom model on the JG PES.

define the geometry of the system or the asymptotic energy. However, there is consistency in good overall agreement between the 7D and SVRT-5D probability, and between the 6D and SVRT-4D results.[37]

The importance of an accurate PES is illustrated in Fig. 12 which shows the large difference between the reaction probability calculated with the present *ab initio* global PES versus the semiclassical JG PES.52 Comparatively, the JG PES overestimates the reactivity of the ground state and underestimates that of the CH stretch excited state.
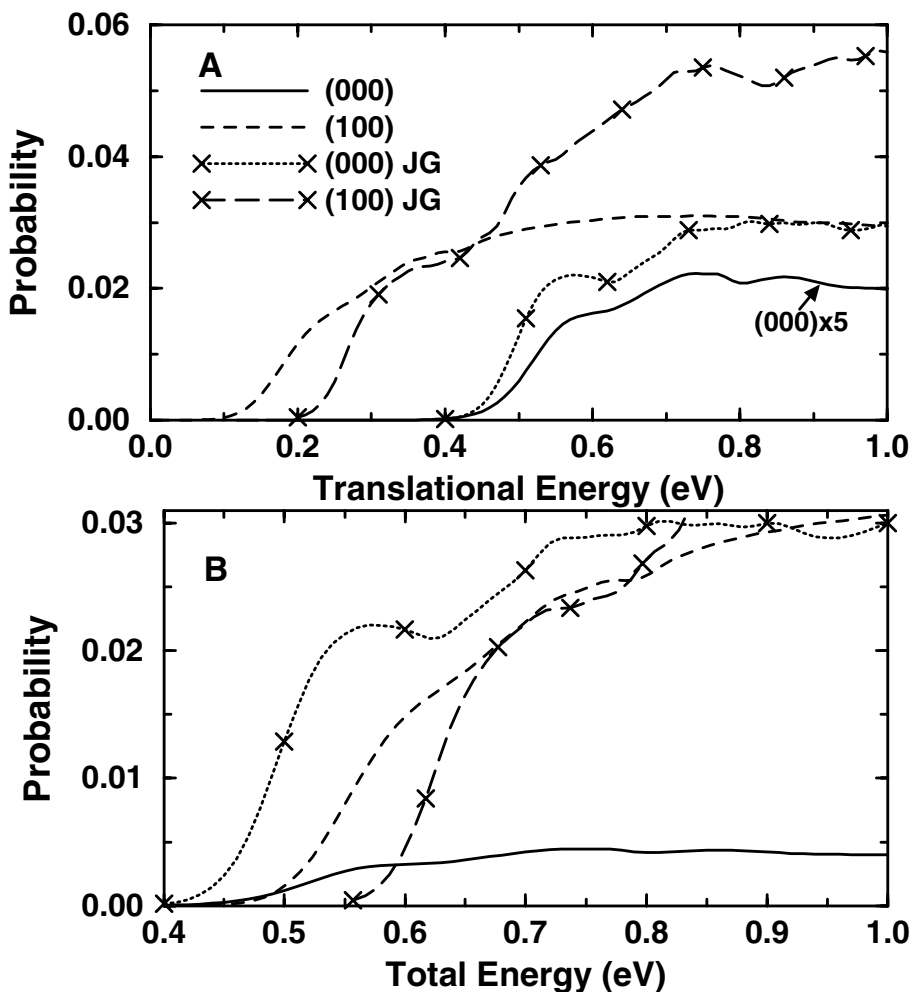
Figure 12. The reaction probability for the ground (000) and CH stretch excited (100) states of CH_4 for the ab initio PES and the Jordan-Gilbert (JG) PES as a function of the translational (A) and total (B) energy.

The necessary $J > 0$ reaction probabilities for the initial state selected rate coefficient were estimated using the centrifugal sudden approximation. Figure 13 compares the thermal rate coefficient calculated here from first principles with the JG PES, the *ab initio* global PES, and the best fit to the experimental data. The plot also shows the contribution of some initial states of CH_4 to the rate. Despite a small discrepancy at high temperatures, the agreement between experiment and the *ab initio* global PES results is excellent. The reaction at low temperature is due to tunneling from the ground state. The novel implication is that even though the population of molecules with an excited CH bond stretch is low in the temperature range of Fig. 13, they have high reactivity and account for the overall reactivity of CH_4 above 450K.
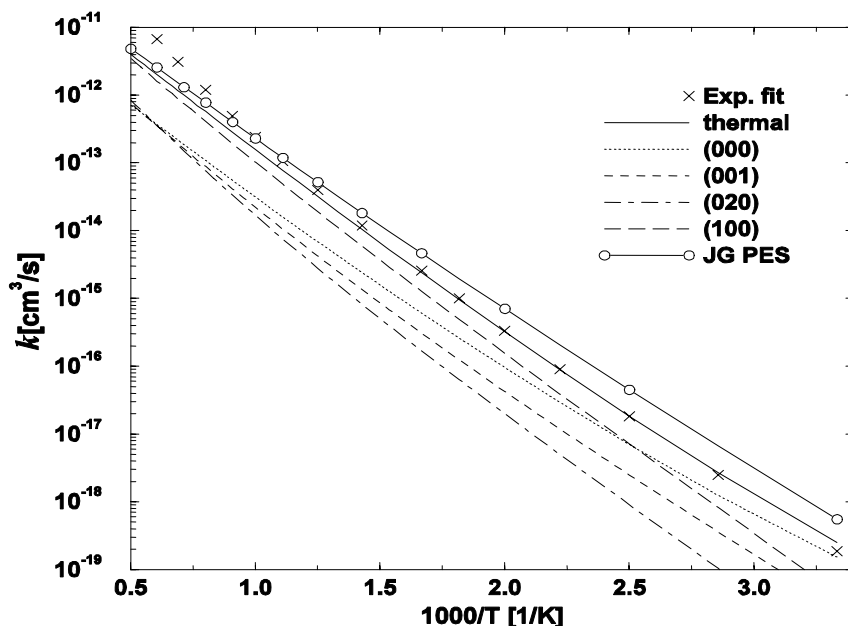
Figure 13. Comparison of the best fit experimental thermal rate coefficient with the total value for the JG PES, the ab initio PES, and the contribution from the initial CH stretch (n00), HCH bend (0n0), and umbrella (00n) states.

5.   Conclusions

The time-dependent wave packet method has been outlined to solve the A + BCD and the X + YCZ_3 reactions. The tetraatomic system could be solved in full-dimensionality, but to solve the hexaatomic system we followed the method of Palma and Clary,[40] where the CD bond is replaced by CZ_3 with C_{3v} symmetry throughout the reaction, with reduced dimensionality. Calculations were performed for the H + H_2O reaction in full-dimensionality, and the H + CH_4 reaction in seven dimensions.

We learnt that in the H + $H_2O \rightarrow H_2$ + OH abstraction reaction: (a) the unbroken OH bond can be treated as a spectator bond, (b) the OH stretching excitation in H_2O enhances the reaction greatly due to a late barrier in the abstraction reaction, (c) the centrifugal sudden approximation gives a cross section that is low compared to the exact coupled-channel results, (d) the measured abstraction reaction cross section at a collision energy of 2.46 eV is a factor of two lower than theoretical prediction on the global YZCL2 surface, and (e) much of the total internal energy of the products from the H + H_2O (00)(0) reaction appears in the H_2 rotation, followed by OH rotation.

For the H + CH_4 reaction, it is shown that: (a) there is substantial difference between the reaction probability calculated with the new *ab initio* global PES versus the semi-empirical Jordan-Gilbert PES, (b) CH_4 molecules with an excited CH bond stretch have high reactivity and accounts largely for the overall reactivity of CH_4 above 450K, and (c) the thermal rate coefficients calculated with the *ab initio* global PES agree very well with experimental data.

Acknowledgements

References

1. Schatz, G.C. and Kuppermann, A. (1975) Quantum mechanical reactive scattering: An accurate three-dimensional calculation, J. Chem. Phys. **62**, 2502-2504.
2. Elkowitz, A.B. and Wyatt, R.E. (1975) Quantum mechanical reaction cross sections for the three-dimensional hydrogen exchange reaction, J. Chem. Phys. **62**, 2504-2506.
3. Walker, R.B., Stechel, E. and Light, J.C. (1978) Accurate H_3 dynamics on an accurate H_3 potential surface, J. Chem. Phys. **69**, 2922-2923.
4. Manolopoulos, D.E. and Clary, D.C. (1989) Quantum calculations on reactive collisions, *Annu. Rep. Prog. Chem. Sect. C* **86**, 95-118; and references therein.
5. Miller, W.H. (1990) Recent advances in quantum mechanical reactive scattering theory, including comparison of recent experiments with rigorous calculations of the state-to-state cross sections for the H/D + $H_2 \rightarrow H_2$/HD + H reactions, *Annu. Rev. Phys. Chem.* **41**, 245-281; and references therein.
6. Clary, D.C. (1991) Quantum reactive scattering of four-atom reactions with nonlinear geometry: OH + $H_2 \rightarrow H_2O$ + H, *J. Chem. Phys.* **95**, 7298-7310.
7. Clary, D.C. (1992) Bond-selected reaction of HOD with H atoms, *Chem. Phys. Lett.* **192**, 34-40.
8. Wang, D. and Bowman, J.M. (1992) Reduced dimensionality quantum calculations of mode specificity in OH + H2 $\leftrightarrow$ H2O + H, *J. Chem. Phys*. **96**, 8906 - 8913.
9. Yang, M., Zhang, D.H., Collins, M.A. and Lee, S.-Y. (2001) Quantum dynamics on new potential energy surfaces for the H_2 + OH $\rightarrow H_2O$ + H reaction, *J. Chem. Phys.* **114**, 4759-4762.
10. Zhang, D.H., Yang, M. and Lee, S.-Y. (2002) Quantum dynamics of the D_2 + OH reaction, *J. Chem. Phys*. **116**, 2388-2394.

11. Zhang, D.H., Yang, M. and Lee, S.-Y. (2002) Accuracy of the centrifugal sudden approximation in the H + H$_2$O reaction and accurate integral cross sections for the H + H$_2$O → H$_2$ + OH abstraction reaction, *J. Chem. Phys.* **117**, 10067-10072.

12. Zhang, D.H., Xie, D., Yang, M. and Lee, S.-Y. (2002) State-to-state integral cross section for the H + H$_2$O → H$_2$ + OH reaction, *Phys. Rev. Lett.* **89**, 283203 (1-4).

13. Zhang, D.H. and Zhang, J.D.H. (1993) Accurate quantum calculations for the benchmark reaction H$_2$ + OH → H$_2$O + H in five-dimensional space: Reaction probabilities for J = 0, *J. Chem. Phys.* **99**, 5615-5618.

14. Zhang, D.H. and Zhang, J.D.H. (1994) Accurate quantum calculations for H$_2$ + OH → H$_2$O + H: Reaction probabilities, cross sections and rate constants, *J. Chem. Phys.* **100**, 2697-2706.

15. Huarte-Larranaga, F. and Manthe, U. (2000) Full dimensional quantum calculations of the CH$_4$ + H → CH$_3$ + H$_2$ reaction rate, *J. Chem. Phys.* **113**, 5115-5122.

16. Huarte-Larranaga, F. and Manthe, U. (2001) Quantum dynamics of the CH$_4$ + H → CH$_3$ + H$_2$ reaction: Full dimensional and reduced dimensionality rate constants, *J. Phys. Chem. A* **105**, 2522-2529.

17. Huarte-Larranaga, F. and Manthe, U. (2002) Vibrational excitation in the transition state: The CH$_4$ + H → CH$_3$ + H$_2$ reaction rate constant in an extended temperature interval, *J. Chem. Phys.* **116**, 2863-2869.

18. Meyer, H.D., Manthe, U. and Cederbaum, L.S. (1990) The multiconfigurational time-dependent Hartree approach, *Chem. Phys. Lett.* **165**, 73-78.

19. Beck, M.H., Jackle, A., Worth, G.A. and Meyer, H.D. (2000) The multiconfigurational time-dependent Hartree (MCTDH) method: a highly efficient algorithm for propagating wavepackets, *Phys. Rep.* **324**, 1-105; and references therein.

20. Sukiasyan, S. and Meyer, H.D. (2002) Reaction cross sections for the H + D$_2$ (v$_0$=1) → HD + D and D + H$_2$ (v$_0$=1) → DH + H systems. A multiconfigurational time-dependent Hartree (MCTDH) wave packet propagation study, *J. Chem. Phys.* **116**, 10641-10647.

21. Clary, D.C. (1994) Four-atom reaction dynamics, *J. Phys. Chem.* **98**, 10678-10688.

22. Clary, D.C. (1995) Product CN Rotational Distributions from the H + HCN reaction, *J. Phys. Chem.* **99**, 13664-13669.

23. Clary, D.C. and Palma, J. (1997) Quantum dynamics of the Walden inversion reaction Cl$^-$ + CH$_3$Cl → ClCH$_3$ + Cl$^-$, *J. Chem. Phys.* **106**, 575-583.

24. Wang, D. and Bowman, J.M. (2001) A reduced dimensionality, six-degree-of-freedom, quantum calculation of the H + CH$_4$ → H$_2$ + CH$_3$ reaction, *J. Chem. Phys.* **115**, 2055-2061.

25. Bowman, J.M. (2002) Overview of reduced dimensionality quantum approaches to reactive scattering, Theo. Chem. Acc. **108**, 125-133; and references therein.

26. Yu, H. and Nyman, G. (1999) Four-dimensional quantum scattering calculations on H + CH$_4$ → H$_2$ + CH$_3$ reaction, *J. Chem. Phys.* **111**, 3508-3516.

27. Yu, H. and Nyman, G. (2000) Quantum dynamics of the O(^{3}P) + CH$_4$ → OH + CH$_3$ reaction: An application of the rotating bond umbrella model and spectral transform subspace iteration, *J. Chem. Phys.* **112**, 238-247; and references therein.

28. Zhang, J.Z.H. (1999) The semirigid vibrating rotor target model for quantum polyatomic reaction dynamics, *J. Chem. Phys.* **111**, 3929-3939.

29. Zhang, D.H. and Zhang, J.Z.H. (2000) The semirigid vibrating rotor target model for atom-polyatom reaction: Application to H + H$_2$O → H$_2$ + OH, *J. Chem. Phys.* **112**, 585-591.

30. Wang, M.L. and Zhang, J.Z.H. (2002) Generalized semirigid vibrating rotor target model for atom-polyatom reaction: Inclusion of umbrella mode for the H + CH$_4$ reaction, *J. Chem. Phys.* **117**, 3081-3087; and references therein.

31. Sutherland, J.W., Su, M.-C. and Michael, J.V. (2001) Rate constants for H + CH$_4$, CH$_3$ + H$_2$, and CH$_4$ dissociation at high temperature, *Int. J. Chem. Kinet.* **33**, 669-684; and references therein.

32. Bryukov, M.G., Slagle, I.R. and Knyazev, V.D. (2001) Kinetics of reactions of H atoms with methane and chlorinated methanes, *J. Phys. Chem.* **105**, 3107-3122.

33. Takayanagi, T. (1996) Reduced dimensionality calculations of quantum reactive scattering for the H + $CH_4 \rightarrow H_2 + CH_3$ reaction, *J. Chem. Phys.* **104**, 2237-2242.

34. Bowman, J.M., Wang, D., Huang, X., Huarte-Larranaga and Manthe, U. (2001) The importance of an accurate CH4 vibrational partition function in full dimensionality calculations of the H + $CH_4 \rightarrow H_2 + CH_3$ reaction, *J. Chem. Phys.* **114**, 9683-9684.

35. Pu, J. and Truhlar, D.G. (2002) Parametrized direct dynamics study of rate constants of H with CH_4 from 250-2400K, *J. Chem. Phys.* **116**, 1468-1478.

36. Palma, J., Echave, J. and Clary, D.C. (2002) Rate constants for the $CH_4 + H \rightarrow CH_3 + H_2$ reaction calculated with a generalized reduced-dimensionality method, *J. Phys. Chem. A* **106**, 8256-8260.

37. Yang, M., Zhang, D.H. and Lee, S.-Y. (2002) A seven-dimensional quantum study of the H + CH_4 reaction, *J. Chem. Phys.* **117**, 9539-9542.

38. Rose, M.E. (1957) *Elementary Theory of Angular Momentum*, Wiley, New York.

39. Fleck, Jr., J.A., Morris, J.R. and Feit, M.D. (1976) Time-dependent propagation of high energy laser beams through the atmosphere, *Appl. Phys.* **10**, 129-160.

40. Palma, J. and Clary, D.C. (2000) A quantum model Hamiltonian to treat reactions of the type $X + YCZ_3 \rightarrow XY + CZ_3$: Application to $O(3.P) + CH_4 \rightarrow OH + CH_3$, *J. Chem. Phys.* **112**, 1859-1867.

41. Zhang, J.Z.H. (1999) *Theory and Applications of Quantum Molecular Dynamics*, World Scientific, Singapore.

42. (a) Walch, S.P. and Dunning, T.H. (1980) A theoretical study of the potential energy surface for OH + H_2, *J. Chem. Phys.* **72**, 1303-1311; (b) Schatz, G.C. (1981) A quasiclassical trajectory study of reagent vibrational excitation effects in the OH + $H_2 \rightarrow H_2O$ + H reaction, *J. Chem. Phys.* **74**, 1133-1139; (c) Elgersma, H. and Schatz, G.C. (1981) A quasiclassical trajectory study of mode specific reaction rate enhancements in H + $H_2O(v_1, v_2, v_3) \rightarrow OH + H_2$, *Intl. J. Quantum Chem., Quantum Chem. Symp.* **15**, 611-619.

43. Bettens, R.P., Collins, M.A., Jordan, M.J.T. and Zhang, D.H. (2000) *Ab initio* potential energy surface for the reactions between H_2O and H, *J. Chem. Phys.* **112**, 10162-10172.

44. Zhang, D.H., Collins, M.A. and Lee, S.-Y. (2000) First principles theory for the H + H_2O, D_2O reactions, *Science* **290**, 961-963.

45. MOLPRO is a suite of *ab initio* programs written by Werner, H.-J. and Knowles, P.J. with contributions from Almlöf, J., Amos, R.D., Berning, A. *et al.*

46. (a) Yang, M., Zhang, D.H., Collins, M.A. and Lee, S.-Y. (2001) Quantum dynamics on new potential energy surfaces for the H_2 + OH $\rightarrow H_2O$ + H reaction *J. Chem. Phys.* **114**, 4759-4762; (b) *ibid.* (2001) *Ab initio* potential energy surfaces for the reactions OH + $H_2 \leftrightarrow H_2O$ + H, *J. Chem. Phys.* **115**, 174-178.

47. Collins, M.A. (2002) Molecular potential energy surfaces for chemical reaction dynamics, *Theor. Chem, Acc.* **108**, 313-324.

48. Steckler, R., Dykema, K.J., Brown, F.B., Hancock, G.C., Truhlar, D.G. and Valencich, T. (1987) A comparative study of potential energy surfaces for $CH_3 + H_2 \leftrightarrow CH_4$ + H, *J. Chem. Phys.* **87**, 7024-7035; and references therein.

49. Jordan, M.J.T. and Gilbert, R.G. (1995) Classical trajectory studies of the reaction CH_4 + H $\rightarrow CH_3 + H_2$, *J. Chem. Phys.* **102**, 5669-5682.

50. Joseph, T.R., Steckler, R. and Truhlar, D.G. (1987) A new potential energy surface for the $CH_3 + H_2 \leftrightarrow CH_4$ + H reaction: Calibration and calculation of rate constants and kinetic isotope effects by variational transition state theory and semi-classical tunneling calculations, *J. Chem. Phys.* **87**, 7036-7049.

51. Duchovic, R.J., Hase, W.L. and Schlegel, H.B. (1984) Analytic function for the H + CH$_3$ ↔ CH$_4$ potential energy surface, *J. Phys. Chem.* **88** , 1339-1347.

52. Zhang, D.H., Yang, M., Lee, S.-Y. and Collins, M.A. (2003) Quantum dynamics study of the H + CH$_4$ → H$_2$ + CH$_3$ reaction (in preparation).

53. Zhang, D.H., Yang, M. and Lee, S.-Y. (2002) Breakdown of the spectator model for the OH bonds in studying the H + H$_2$O reaction, *Phys. Rev. Lett.* **89**, 103201 (1-4).

54. Castillo, J.F., Aoiz, F.J. and Banares, L. (2002) A quasiclassical trajectory study of the H + H$_2$O → OH + H$_2$ reaction dynamics at 1.4 eV collision energy on a new ab initio potential energy surface, *Chem. Phys. Lett.* **356**, 120-126.

55. Brouard, M., Burak, I., Marinakis, S., Minayev, D., O'Keefe, P., Vallance, C., Aoiz, F.J., Banares, L., Castillo, J.F., Zhang, D.H., Xie, D., Yang, M., Lee, S.-Y. and Collins, M.A. (2003) Cross section for the H + H$_2$O abstraction reaction: Experiment and theory, *Phys. Rev. Lett.* **90**, 93201(1-4).

56 .Troya, D., Gonzalez, M. and Schatz, G.C. (2001) A quasiclassical trajectory study of reactivity and product energy disposal in H + H$_2$O, H + D$_2$O and H + HOD, *J. Chem. Phys.* **114**, 8397-8413.

57 (a) Wu, G., Schatz, G.C., Lendvay, G., Fang, D.C. and Harding, L.B. (2000) A new potential energy surface and quasiclassical trajectory study of H + H$_2$O → OH + H$_2$, *J. Chem. Phys.* **113**, 3150-3161; (b) *ibid*. (2000) *Erratum*, *J. Chem. Phys.* **113**, 7712.

STRONG ACCELERATION OF CHEMICAL REACTIONS ARISING THROUGH THE EFFECTS OF ROTATIONAL EXCITATION OF REAGENTS ON COLLISION GEOMETRY

A. MIKLAVC
National Institute of Chemistry
Hajdrihova 19
SI-1001 Ljubljana, Slovenia

1. Introduction

Although experimental and computational methods in chemical reaction dynamics have advanced greatly over the last few decades, simple collision models of bimolecular reactions retain their importance. Comparison of their predictions with experimental results, or with the results from more sophisticated scattering calculations, can provide considerable insight into the dynamics of reactive collisions. In efforts to rationalize particular features observed in experimental data or in the results of complex calculations simple models can be very helpful. Furthermore, once they have been validated by comparison with accurate scattering calculations, such models, which require much less computational effort than accurate calculations, might be used to predict values of the rate constants outside the regimes investigated experimentally and they could be applied in the modelling of processes of technological importance or in environmental studies.

  In simple models of chemical reactions attention is focused on the reacting system at the »critical dividing surface« [1] separating reactants from products. Reaction is assumed to occur if the relevant component of the kinetic energy exceeds the potential energy, or effective potential energy, on this surface. For a long time, the venerable but simplistic, line-of-centers (LOC) model [2-4] was often used to predict the forms of the opacity and excitation functions [1] for activated bimolecular reactions. In this model, the critical energy is assumed the same at all points on the spherical critical dividing surface and consequently no allowance is made for stereodynamical effects, i.e., the dependence of reaction probability on the orientation of the reagents as they reach critical separation. The development of powerful experimental and computational techniques has exposed the shortcomings of this model and the need for improvements.

  A natural extension of the classical LOC model, in which the orientational dependence of the barrier to reaction is taken into account and which leads to the concept of a »cone-of-acceptance« which depends on collision energy, was proposed by Smith [1,5] and independently by Levine and Bernstein [6], although, as later pointed out by Levine [7], these models are similar to that suggested as long ago as in 1932 by Pelzer and Wigner [7,8]. This model, generally referred to as the angle-dependent line-of-centers (ADLOC)

model, has been modified and developed in a number of subsequent publications [9-14]. Among other developments, the original assumption of a spherical dividing surface on which the critical potential energy depends on the angle describing the orientation of the reagents at impact has been extended to systems where critical dividing surface is nonspherical [15,16,18,19] and where it is nonrigid [17].

The models referred to above have been developed essentially on the basis of energy considerations. It is assumed that reactions will occur when some portion of the kinetic energy at the critical dividing surface – either that associated with reagent motion along the line-of-centers (the ADLOC model) or that directed perpendicular to the surface (the angle-dependent line-of-normals model) [10,15,16,18,19] – exceeds the potential energy or effective potential energy at the critical dividing surface. However, the need to conserve total angular momentum is not explicitly taken into account, since, in general, the assumptions that orbital angular momentum is conserved up to the critical dividing surface and that either the energy associated with motion perpendicular to the line-of-centers or with motion parallel to the critical dividing surface is »inactive« in barrier crossing are not equivalent to conserving angular momentum. The approximation may well be justified in the ADLOC model if the interaction between the approaching reagents is nearly independent of angle, so that the equipotential contours are approximately spherical – as it is in some reactions of diatomic molecules with atoms. However, such models are likely to be less suitable for reactions of, for example, the light + light-heavy (L + LH) and heavy + light-heavy (H + LH) categories, where the interactions are less likely to be spherical and the effects of reagent rotation therefore more pronounced. This feature should be even more marked in reactions involving nonspherical polyatomic molecules when considerable coupling between the orbital and rotational angular momentum can occur en route to the critical dividing surface. Conservation of total angular momentum then restricts the amount of energy available for barrier crossing.

In [10] the energy available for barrier crossing in reactions of nonrotating molecules with ellipsoidally shaped critical dividing surfaces was considered to be restricted by rotational recoil. The available energy given in [10] differs somewhat from the results which we derive below and it is not clear to what extent it is compatible with the conservation of total angular momentum. In [18] modifications due to the conservation of total angular momentum were derived for reactions of atoms with nonrotating ($j = 0$) diatomic molecules. These results are entirely in agreement with the results which we derive below for the more general case of an atom reacting with a polyatomic molecule with arbitrary rotational angular momentum **j**.

We have more recently derived an extension of the original ADLOC model by taking explicit account of the anisotropy of the critical dividing surface as well as the anisotropy of the equipotential surfaces close to the critical dividing surface [20-22]. Both chemical and physical shape of the molecules [7] are thus considered in the model. The effects of rotational excitation of the reactants are included and total angular momentum is conserved. The model still preserves the essential simplicity of the treatment and, moreover, in the limit of »hard molecules« our formalism becomes rigorous. Although originally formulated for reactions of atoms with diatomic molcules [20] it was then extended to reactions of atoms with polyatomic molecules [21]. An extension to reactions of two polyatomic molecules is also possible but has not been

worked out yet. In order to make the model more realistic and to be able to compare its predictions with those of quasiclassical trajectory or quantum mechanical calculations, or with experimental results, an adequate treatment of vibrational zero-point energy effects had to be included in the model. The method which has been chosen for this purpose has the same basis as vibrationally adiabatic transition state theory [23-27], namely it is assumed that motion up to the critical dividing surface is vibrationally adiabatic. The essential simplicity and transparency of the model is thereby still maintained. The model has been tested on several reactions [20-22]: $H + F_2$, $O + H_2$, $O + HCl$, $O + DCl$, $O + HBr$ and $N + O_2$, for all of which quasiclassical or quantum mechanical results have been reported.

In Section 2 a derivation of the model will be given for reactions of atoms with polyatomic molecules. It will be shown that conservation of both linear and total angular momentum leads to a kinematic mass, similarly as conservation of linear momentum alone is reflected in the occurence of the usual reduced mass of collision partners. The kinematic mass in this case, however, is position-dependent. Because of the importance of this mass we called the model »kinematic mass model«. General conditions for applicability of the kinematic mass model will be discussed, particularly with regard to physical shape, i.e., equipotential contours of the molecules. Furthermore, vibrational zero-point energy effects will be briefly discussed, to provide support for our method of incorporating them into the model. Most relevant results which have been obtained with kinematic mass model so far are presented in Section 3. Surprisingly strong enhancement of reaction rates with rotational excitations found in trajectory studies of several reactions will be analysed and it will be shown that the strong enhancements in question are not due primarily to the increase of the kinetic energy available for barrier crossing but rather to favourable changes of collision geometry due to the reagent rotational excitation. Wider implications of these results for understanding the effects of excitations of rotations, internal rotations or librations in various systems will also be pointed out.

2. The Kinematic Mass Model

Simple models of activated bimolecular reactions have been founded on the assumption that reactive trajectories can be adequately approximated by straight line trajectories up to the critical dividing surface, and that »trajectory funnelling effects« could thus be neglected. The dynamics bringing about reaction is assumed to occur in a small, crucial region of the potential energy surface near the critical dividing surface. To describe the motion on such a small potential surface element dS a method can be adopted which has been successful in energy transfer studies in molecular collisions [28-33]. The underlying transformations of the energy function actually embody also earlier ideas about an effective mass in energy transfer theory [34-36].

Kinematic mass model can actually be derived for reactions of two polyatomic molecules, along the lines of reasoning developed in the energy transfer studies [30,31]. This possibility has not been explored yet. In the present case a derivation of the model will be presented for reactions of atoms with polyatomic molecules. The model will be

then applied to study mechanisms of enhancement of reactions of atoms with diatomic molecules due to rotational excitations.

Let us consider a straight line trajectory traversing an element dC of the critical dividing surface at point X (Figure 1). dS denotes an element of the potential energy surface which is near the critical dividing surface element dC and which the trajectory in question passes en route to the barrier. **n** is the unit vector normal to the surface element dS, i.e., in the direction of the gradient of the potential on dS, and **R** is the vector between the center of mass of the molecule and the atom. At the point of the trajectory which lies on dS the relative velocity can be decomposed as $\mathbf{v} = \mathbf{v}_n + \mathbf{v}_\parallel$, where $\mathbf{v}_n$ is the velocity component in the direction **n** and $\mathbf{v}_\parallel$ is parallel to the surface element dS. The system is characterized by the conserved total angular momentum $\mathbf{J}_0$
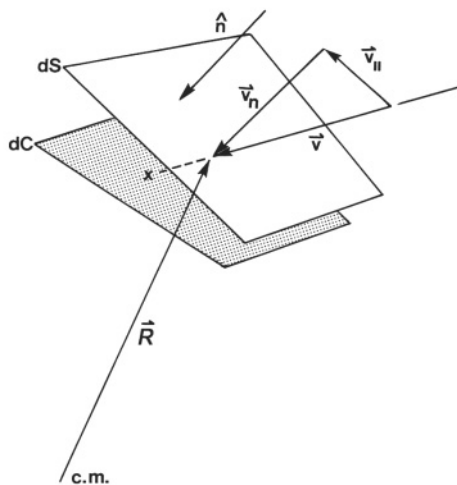
Figure 1. Schematic presentation of a short segment of a trajectory passing through an element dS of the potential energy surface near the critical dividing surface element dC. Defined are the relevant components of the relative velocity **v** of the collision partners. **R** is the vector joining the centers of mass of the colliding species, **n** is the unit vector in the direction of the potential gradient at dS.

$$\mathbf{J}_0 = \mathbf{j} + \mu \mathbf{R} \times \mathbf{v} = \mathbf{j} + \mu \mathbf{R} \times \mathbf{v}_n + \mu \mathbf{R} \times \mathbf{v}_\parallel \tag{1}$$

j is rotational angular momentum of the molecule and μ is the reduced mass of the collision partners. For the sake of convenience we write

$$\mathbf{J}_0 = \mathbf{J} + \mu \mathbf{R} \times \mathbf{v}_\parallel \tag{2}$$

where

$$\mathbf{J} = \mathbf{j} + \mu \mathbf{R} \times \mathbf{v}_n \equiv \mathbf{j} + \mu R v_n \mathbf{k} \tag{3}$$

$$\mathbf{k} \equiv \mathbf{R} \times \mathbf{n}/R \ . \tag{4}$$

The total kinetic energy E_k of the system is

$$E_k = \frac{1}{2}\mu v^2 + \sum_i \frac{j_i^2}{2I_i} \tag{5}$$

where I_i ($i = 1,2,3$) are the moments of inertia of the molecule. To derive the condition for the reaction to occur we first note that E_k can be rewritten in the following remarkable form [29,30]

$$E_k = \frac{1}{2}\mu^* v^{*2} + \frac{1}{2}\mu v_{\mathrm{II}}^2 + \frac{\mu^*}{\mu}\sum_i \frac{J_i^2}{2I_i} + \sum_{i<j}\frac{\mu^* R^2}{2I_i I_j}(J_i k_j - J_j k_i)^2 \tag{6}$$

J_i and k_i are components of vectors $\mathbf{J}$ and $\mathbf{k}$ defined by Equations 3 and 4 respectively The generalized velocity v^* and the corresponding mass μ^* are defined by [29,30]

$$\mu^* = \frac{\mu I_1 I_2 I_3}{I_1 I_2 I_3 + \mu R^2 (I_1 I_2 k_3^2 + I_1 I_3 k_2^2 + I_2 I_3 k_1^2)} \tag{7}$$

$$v^* \equiv v_n - \sum_i \frac{j_i}{I_i} R k_i = (\mathbf{v} - \boldsymbol{\omega} \times \mathbf{R}) \cdot \mathbf{n} \tag{8}$$

$\boldsymbol{\omega}$ is angular velocity vector ($\omega_i = j_i/I_i$). Equation 6 is an identity valid at any point on the trajectory. In the mass μ^*, which is position dependent, conservation of linear and total angular momentum is reflected. The transformation given by Equation 6 affords an efficient, though approximate way of dealing with processes dominated by the dynamics of the system on a potential surface element dS which is small when compared with the dimensions of the system (i.e., processes dominated by the sudden regime). $\mathbf{v}_{\parallel}$ is then nearly conserved during this crucial motion on dS during which changes of $\mathbf{n}$ and $\mathbf{R}$ can be also assumed to be negligibly small. Vectors $\mathbf{k}$ and $\mathbf{J}$ are then also nearly conserved. It should be noted, however, that changes of $\mathbf{v}_n$ and $\mathbf{j}$ can be large on the potential surface element dS in question but they are coupled through (near) conservation of $\mathbf{J}$. In the present treatment of the sudden regime translational-rotational coupling is therefore included.

It should be noted furthermore that during the motion of the collision partners on dS only the the term $\mu^* v^{*2}/2$ in Equation 6 may vary appreciably, since in the remaining terms only those quantities appear which, according to the above arguments, may be expected to change negligibly. Therefore, if the motion of the reactants is dominated by a small potential surface element dS near the critical dividing surface, the condition that reaction occurs in the encounter depicted in Figure 1 is given by

$$\tfrac{1}{2}\mu^* v^{*2} \geq E_b \tag{9}$$

where E_b is the barrier energy at the point of the critical dividing surface lying on the line of the trajectory. This equation expresses the essence of the kinematic mass model as applied to activated elementary bimolecular reactions and emphasizes its difference from the ADLOC model. In the latter, the »active« kinetic energy is assumed to be that part of the collision energy associated with the relative velocity vector directed along **R** at the critical dividing surface. In that case no account is taken of how the physical shape of the molecule serves to modify the components of relative velocity perpendicular and parallel to the equipotential contours.

The opacity function $P(E_{trans},b)$, i.e., the reaction probability averaged over all orientations at a given impact parameter b and translational energy E_{trans} can be expressed as

$$P(E_{trans},b) = \frac{1}{4\pi} \int d\Omega H(\tfrac{1}{2}\mu^* v^{*2} - E_b) \qquad (10)$$

where $H(x)$ is the unit step function, i.e., $H(x) = 1$ for $x \geq 0$ and $H(x) = 0$ for $x < 0$. The integration runs over full range of solid angles Ω describing the orientation of the molecules.

2.1 VIBRATIONAL ZERO-POINT ENERGY CORRECTIONS

In the quasiclassical trajectory calculations of reaction cross-sections, as well as in quantum mechanical calculations, the threshold energies are usually found to be shifted considerably from the values determined by the bare electronic potential energy surface, which shows that vibrational effects, associated with the presence of zero-point energy can be quite large. The model presented above must therefore be extended to include vibrational effects in order that comparison with quasiclassical trajectory calculations, or with experiments, be meaningful. In the following the present model is modified to include vibrational effects in an approximate way so that the essential simplicity of the model is preserved and reasonable agreement with trajectory calculations is obtained, in particular with respect to the threshold behavior. The conclusions as to molecular shape effects should be applicable, even when vibrational effects are present, provided that account is taken of changes in the shape of the critical dividing surface at higher vibrational excitation.

The simplest way of taking account of vibrational effects is to assume vibrational adiabaticity during the motion up to the critical dividing surface [27]. As mentioned already in the Introduction, much of the earlier work on vibrational adiabaticity was concerned with its relationship to transition-state theory, especially as applied to the prediction of thermal rate constants [24-26]. It is pointed out in [27] that the validity of the vibrationally adiabatic assumption is supported by the results of both quasiclassical and quantum scattering calculations. The effective thresholds indicated by the latter for the D + H_2(v =1) and O + H_2(v =1) reactions [37,38] are similar to those found from vibrationally adiabatic transition-state theory, which is a strong evidence for the correctness of the hypothesis of vibrational adiabaticity. Similar corroboration is provided by the combined transition-state and quasiclassical trajectory calculations [39-44]. For virtually all the A + BC systems studied [39-44], both collinearly and in three

dimensions, motion between the transition state and separated reagents was found to exhibit a high degree of vibrational adiabaticity.

The vibrationally adiabatic potential $V_{ad}(v,x)$ for an A + BC reaction is given by [27]

$$V_{ad}(v,x) = V_{el}(x) + [E_{vib}(v,x) - E_{vib}(v,-\infty)] \tag{11}$$

where x is the coordinate describing position along the minimum energy path and $V_{el}(x)$ is the electronic potential energy independent of vibrational state. $E_{vib}(v,x)$ is the energy of the v-th state of vibration orthogonal to the minimum energy path at the point x on it, and $E_{vib}(v,-\infty)$ is the vibrational energy of isolated BC(v). It is straightforward to incorporate vibrational adiabaticity into the treatment of reactions of more than three atoms.Instead of Equation 11 we have then [27]

$$V_{ad}(v_1, v_2, ..., x) = V_{el}(x) + \sum_i [E_{vib}(v_i, x) - E_{vib}(v_i, -\infty)] \tag{12}$$

To use this equation it is necessary to know how the energies associated with the states of several vibrational modes vary along the minimum energy path. This model explains why the pre-exponential factors in the rate constant expressions, as well as the activation energies, depend on the vibrational state of the reagents.

The position of the maximum value of $V_{ad}(v,x)$ depends on v because, although $V_{el}(x)$ increases toward the potential barrier, $E_{vib}(v,x)$ decreases, and this second contribution to $V_{ad}(v,x)$ assumes increasing importance as v increases. Although the $v = 0$ adiabatic maximum is usually located at the electronic saddle point, the maxima for higher states of bond-stretching vibration may be displaced into the entrance and exit valley on the potential energy surface. Vibrationally adiabatic motion is then expected up to the first of these maxima ($r_{AB} > r_{BC}$). Trajectory calculations support this expectation [39-44].

In reactions with vibrationally excited reagents additional shape effects may thus arise for two reasons [22]. First, the energies and form of the critical dividing surface for each vibrationally adiabatic state of the system will be different. Second, the physical shape of the reagent molecule may also depend on its vibrational states. In case of A + BC($v = 0$) reactions vibrational zero-point energy effects alter the barrier height but the position of the critical dividing surface is not shifted from that on the bare electronic potential surface. The vibrationally adiabatic barriers given by Equation 11 can be evaluated by noting that in collinear encounters $E_{vib}(v,0)$ can be assumed to be the energy of the $v = 0$ level of the symmetric vibrational mode of ABC at the top of the electronic barrier. For noncollinear collisions the barrier is evaluated at values of the A-B-C angle α on the critical dividing surface. A »symmetric« vibrational mode can still be defined orthogonal to the minimum energy path also in this case. It is, however, not a normal mode of the system. Approximately the problem may be treated in a »quasilinear« approximation: At each angle α, the force constants at the critical dividing surface are calculated and then the vibrational frequency is evaluated as in general nonlinear triatomic systems, with bending motion frozen. No allowance is thus made for quantization of the bending modes of ABC. The approximation introduced may thus be expected to be less appropriate for noncollinear encounters. The critical dividing surface and the barrier heights are normally calculated in terms of internal coordinates

(r_{BC}, r_{AB}, α). They have to be transformed to Jacobi coordinates (r_{BC}, R, γ) in order to be applied in the kinematic mass model.

2.2 EFFECTS OF THE SHAPE OF THE EQUIPOTENTIAL SURFACES

Although the condition for a reaction to occur, given by Equation 9, might in fact be valid quite generally, its applicability in building simple reaction models depends on the validity of the assumption that the reactive trajectories can be adequately approximated by straight line trajectories and that any »trajectory funnelling« effects could thus be neglected.

It appears to be difficult to state general conditions as to when reactive trajectories in reactions of an atom with a polyatomic molecule could be expected to be reasonably straight lines up to the barrier. In the case of A + BC reactions, however, the problem in question was studied in considerable detail for O + HCl (DCl) reactions [45-48] on two London-Eyring-Polanyi-Sato (LEPS) potential surfaces [49] usually referred to as Surface I and Surface II. The two surfaces, although perhaps not very accurate, nevertheless allow us to draw important conclusions of quite general validity. They differ mainly in the shape of the equipotential contours in the region near the H atom:
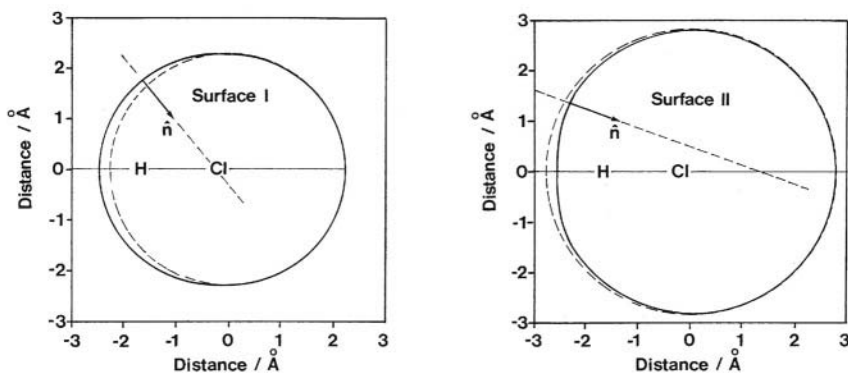
Figure 2. The shape of the prolate Surface I and the oblate Surface II for O + HCl reaction near the barrier, at E = 10 kcal/mol [47]. **n** is the direction of force exerted by the approaching atom at the point of impact. The resulting torque tends to rotate the molecule away from the atom in the first, and towards the atom in the second case. With the curved broken line the circular shape is indicated. Adapted from [47].

Surface I is prolate in this reagion whereas Surface II is oblate (Figure 2). An atom colliding with the H atom side of the HCl molecule would exert a torque that would tend to rotate the molecule away from the approaching atom in the first, and towards the approaching atom in the second case (Figure 2). The effects of this difference on the reaction dynamics are rather dramatic, as revealed by the studies presented in [45-48]. They can be explained by the behaviour of typical reactive and nonreactive trajectories on Surface I and II [46] depicted on Figure 3. We can see that the assumption of straight-line approach to the barrier is reasonably justified only in the case of Surface I. In the case of Surface II even trajectories beginning at a rather large angle are still
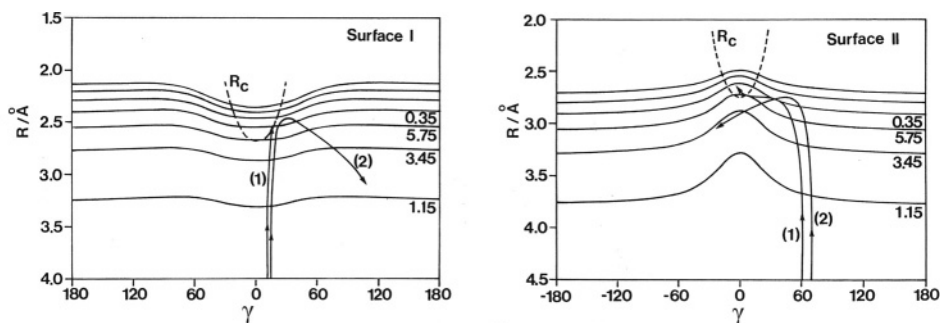
Figure3. Typical behaviour of reactive (1) and nonreactive (2) trajectories on Surfaces I and II for the O + HCl reaction. They refer to translational energy E_{trans} = 10 kcal/mol, j = 0 and zero impact parameter. R and γ are the Jacobi coordinates and R_C represents the critical dividing surface. In the case of Surface II even trajectories beginning at a rather large angle are still guided to the critical region. The assumption of straight-line trajectory approach is thus reasonably justified only in the Surface I case. The numbers on the equipotentials give energy in kcal/mol. [Reproduced from Chemical Physics, Vol. 112, Hansjuergen Loesch: "The Effects of Reagent Rotation on Reaction Cross Sections for O(3P) + HCl --> OH + Cl : A Rationale for Contradictory Predictions", pp. 85-93, copyright 1987, with permission from Elsevier]

guided to the critical region where the barrier energies are the lowest. The strong »trajectory funnelling« effects would not allow to develop simple models in this case, even if the condition expressed by Equation 9 would be still reasonably correct.

    There are two readily understandable consequences arising from the particularities of the shape properties of Surfaces I and II. The reaction cross-section for O + HCl at the rotational angular momentum $j = 0$ is much larger (more than one order of magnitude) in the case of Surface II (Figure 4), due to the trajectories being funnelled towards the low barrier energy region [46]. The two surfaces are characterized by similar barrier heights at $\gamma = 0$ [49], but the rise of the barrier height with noncolinearity is steeper for the oblate Surface II. The second important difference is in the *j* dependence of the cross-section for O + HCl(DCl) reaction [47]. In the case of Surface I the cross-section rises with increasing *j*. It will be shown in the following section that only for not too high *j* values (for *j* < 8) this effect can be ascribed as being due almost entirely to the increase of the kinetic energy available for the barrier crossing. The cross-section decreases rapidly with *j* in the case of Surface II. Increased rotational excitation in this case can be expected to disrupt the funnelling of the trajectories, so that they can no longer reach the

barrier region of low energy that they can cross. The decline in cross section is primarily a function of the ratio of the rotational and linear velocities [47].

It should be stressed that the conclusions arrived at above cannot be directly extended to reactions of an atom with a polyatomic molecule. If we take, e.g., a linear triatomic molecule and assume that the equipotential surfaces near its end-point atom are locally
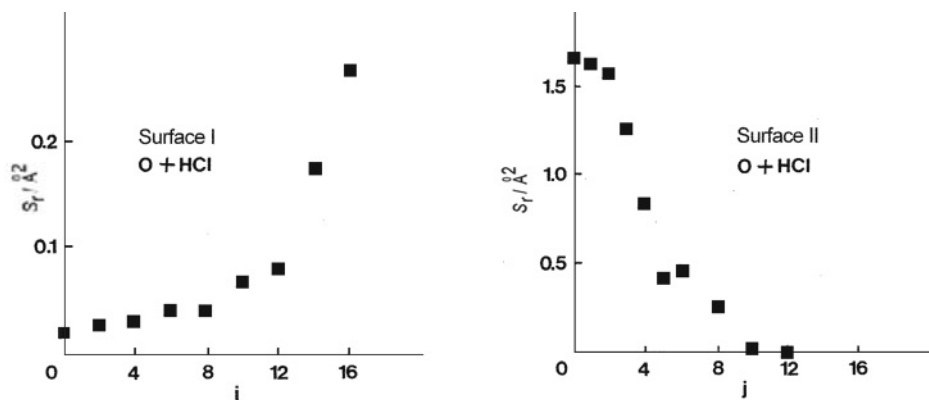

Figure 4. j dependence of the total cross section for the O + HCl reaction on Surface I and Surface II at the translational energy E_{trans} = 10 kcal/mol [47]. At j = 0 the cross section is much larger in the case of Surface II, due to the »trajectory funnelling« effect (se the text) which diminishes when j is increased Adapted from [47].

of oblate shape, similar to that of Surface II (Figure 2), the torque exerted by the approaching atom in this case does not rotate the molecule towards the approaching atom but rather away from it, as in the case of prolate diatomic. The trajectory funnelling mechanism of the kind discussed above (Figure 3) is then absent. Trajectories may be funnelled, however, due also to other features of the potential surface. This possibility would have to be explored before a judgement is made about applicability of the model in a particular case.

3. Effects of Rotational Excitation on Chemical Reaction Cross-Section

The measurement and understanding of how reaction cross-sections depend on the energy present in different motions of the reagent is a crucial element of the field of molecular reaction dynamics [1,50]. Investigation of the role played by each possible mode of reactant energy has been an active area of research for the last three decades [51-57]. In particular, for direct activated bimolecular reactions, the relative importance of translational and vibrational energy has been exhaustively investigated both experimentally and theoretically [51-53] and are now quite well-understood , at least for three-atom sytems of the A + BC → AB + C type, via the »Polanyi rules« [52]. Reagent vibrational excitation selectively enhances the reaction cross-section in the case of a »late« barrier on the potential energy surface, a situation which is expected for an endothermic reaction [52], whereas translational energy selectivity promotes reactions where the barrier is »early«, as is usually found for exothermic reactions [52]. In each

case, the effect is easily understood, since the effective motion is the one which effectively couples to the motion along the reaction coordinate which carries the system over the potential energy barrier.

The role of rotational energy in enhancing reaction rate has not been studied in comparable detail; indeed it is often summarily dismissed as ineffective. Intuitively, it is often felt that rotational motion is »perpendicular« to the reaction coordinate and hence cannot assist in crossing the barrier to reaction. The experimental data base on rotational energy effects is quite sparse, reflecting the difficulty of preparing molecules in defined rotational state and of maintaining that selectivity in the face of facile collisional relaxation. A corollary may be that rotational effects provide a more sensitive probe of the potential energy surface for a reaction, or at least of that part of the surface leading to and including the critical dividing surface between reagents and products [1]. Extensive reviews of the effects of reagent rotation on reaction cross-section have been given in [58,59]. Even in reactions of atoms with diatomic molecules the experimentally found dependence of the reaction cross-sections on the rotational excitation is often quite complex, indicating that there are several mechanisms that could play an important role in the dynamics of reactions.

The great majority of information about the effects of reagent rotation on chemical reactions comes from quasiclassical trajectory calculations. Nevertheless, there has been rather little systematic effort to unravel the separate effects, for example, of the form of the potential energy surface and of the kinematics or mass combination for the reaction. Notable results on these problems are provided, e.g by the studies of the shape effects of the surfaces already mentioned [45-48], or by the quasiclassical trajectory calculations of reaction cross-sections for the transfer of a light atom between two heavier atoms on potential energy surfaces which possess a barrier to reaction [60], where it is found that reactant rotational energy is more efficient at promoting reaction than either translation or vibration, regardless of the reaction energetics. Most quasiclassical trajectory studies, however, have aimed to quantify the rotational effects for a particular reaction. The dependence of the reaction cross-section has often been found to be quite difficult to rationalize. Moreover, it has not proven easy from quasiclassical trajectory calculations to identify the crucial elements of the collision dynamics and it remains a challenge to theory to explain how reaction cross-sections depend on j.

Broadly speaking, the mechanisms that have been put forward to explain reagent rotational effects can be classified as either »energetic« or »reorientational«. As suggested in [58], as the reagent rotational energy is increased, more product states become accessible so, at least in the phase space limit, the reaction cross-section may be expected to increase. However, direct reactions rarely, if ever, obey phase space theory, so more dynamical explanations should be sought. One such explanation would be that rotational motion in the reagent assists the system to surmount the potential energy barrier to reaction. Although, as pointed out before [60], on a simple basis it is difficult to see reactivity can be enhanced in this manner for a reaction dominated by a collinear minimum energy path, since rotational motion would be orthogonal to the motion along the reaction coordinate, rotational energy might assist in those many noncollinear collisions that lead to reaction, even in those cases where the lowest barrier to reaction is for a collinear geometry. In the examples which we discuss below rotational enhancement of the energetic origin is clearly seen to arise. The effect, however, is not

sufficient to provide an explanation for the surprisingly strong rotational enhancement of the reaction cross-sections found in the trajectory calculations in question.

Reorientational effects of reagent rotation have largely emphasized the possibility that increased reagent rotational motion will disrupt the progress of a trajectory towards the most favorable, i.e., lowest energy, geometry for reaction. Arising of such trajectory reorientation effects in interactions of diatomic reagents with atoms in the case of an oblate potential energy surface was pointed out and discussed in some detail in Section 2.2. In the systems in question the surface tends to guide the trajectories towards the region of lowest barrier energies, thereby greatly increasing the reaction cross-section. Rotational excitation disrupts this »funnelling effect« and causes a decline in reactivity with rotational quantum number in such systems.

More recently we found [61,62], assuming again that straight-line trajectories en route to the barrier are a reasonably good approximation, that rotational excitation of the reagent affects the distribution of collisions with the barrier. The effect depends strongly on the ratio of the rotational and translational velocity, v_{rot}/v_{trans} ; when this ratio is increased the distribution of collisions is shifted towards the apex region of the critical dividing surface. If the barrier energies are low in the apex region this leads to a strong increase of the reaction cross-section. The increase could be much larger than what one could reasonably expect from the »energetic« mechanism. This effect will be demonstrated and discussed in more detail using reactions $O(^3P) + H_2$ and $O(^3P) + HCl$ (DCl) as examples. Cross-sections for these reactions obtained by the trajectory calculations on well-known potential energy surfaces show peculiarly strong j dependence which can be convincingly explained by the above mechanism [61,62].

3.1 ACCELERATION OF REACTIONS O + H₂ AND O + HCl (DCl) DUE TO ROTATIONAL EXCITATION

We shall now apply the kinematic mass model introduced in Section 2 to bring out the physical content of the results of the trajectory calculations for reactions $O + H_2$ [63] and O + HCl (DCl) [47] where, as mentioned already, peculiarly strong enhancement of the reaction cross sections due to rotational excitation of the reagents was found. For each of the reactions the shape of the critical dividing surface and of the near-by equipotential surfaces in the region where the reaction could possibly occur will be approximated by the ellipsoidal surfaces (Figure 5), with axes chosen to reasonably fit the shapes derived directly from the potential energy surface for the particular reaction. The main conclusions of our analysis will be quite insensitive to the details of these fittings.

Let again **R** be the center-of-mass separation vector at a point of the trajectory, **v** the relative velocity and **n** the unit vector perpendicular to the equipotential contour at the point in question (Figure 5). In the case of a diatomic reagent the formulas given in Section 2 assume the following simpler form:
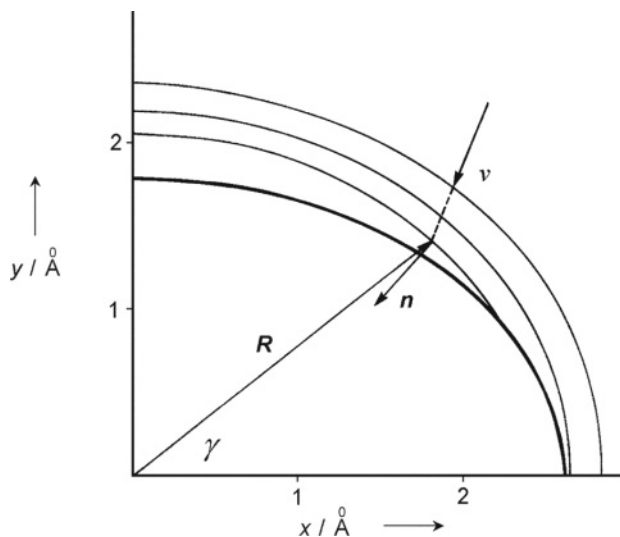
Figure 5. Schematic representation of O + H$_2$ and O + HCl (DCl) collisions. The heavy line repesents a part of the critical dividing surface, lighter lines represent equipotential contours. Ellipsoidal approximations are used for both kind of surfaces as described in the text. **v** is the relative velocity of the collision partners, **R** is their center-of-mass separation vector, γ is te Jacobi angle, **n** is the normal to the equipotential energy surfaces. The coordinate origin is at the center of mass of the molecule; axis x coincides with its longitudinal axis. In the present model calculations, straight line trajectories up to the critical dividing surface are assumed.

$$E_k = \frac{1}{2}\mu v_{II}^2 + \frac{1}{2}\mu v_n^2 + \frac{1}{2}\frac{j^2}{I} = \frac{1}{2}\mu v_{II}^2 + \frac{1}{2}\frac{\mu I}{I + \mu(\mathbf{R}\times\mathbf{n})^2}\left[\mathbf{v}_n - \frac{\mathbf{n}(\mathbf{j}\times\mathbf{R})\cdot\mathbf{n}}{I}\right]^2 +$$

$$+ \frac{1}{2}\frac{1}{I + \mu(\mathbf{R}\times\mathbf{n})^2}(\mathbf{j} + \mu\mathbf{R}\times\mathbf{v}_n)^2 \tag{13}$$

$$E_k = \frac{1}{2}\mu v_{II}^2 + \frac{1}{2}\mu^* v^{*2} + \frac{1}{2}\frac{\mathbf{J}^2}{I + \mu(\mathbf{R}\times\mathbf{n})^2} \tag{14}$$

where $\mathbf{J} = \mathbf{j} + \mu\mathbf{R}\times\mathbf{v}_n$ and μ^* is the kinematic mass,

$$\mu^* = \frac{\mu I}{I + \mu(\mathbf{R}\times\mathbf{n})^2} \tag{15}$$

The total velocity perpendicular to dS is

$$\mathbf{v}^* = \mathbf{v}_n - \frac{\mathbf{n}(\mathbf{j}\times\mathbf{R})\cdot\mathbf{n}}{I} \tag{16}$$

If it can be supposed that the process is essentially controlled by the dynamics over a potential surface element dS of dimentions which are small when compared with the dimensions of the system considered, μ^*, **n, R, v**$_\parallel$ and **J** can be regarded as nearly conserved over dS. The second term in Equation 14: $\mu^* v^*/2$ thus gives the kinetic energy of the motion perpendicular to dS which is available for the barrier crossing. The first and the third term in Equation 14 are nearly conserved on dS. They become exactly conserved in the limit when the range of force goes to zero.

   Evidence presented in [46] show that, in the case of the potential surfaces of the shape being considered here, it can be reasonably assumed that the trajectories are nearly straight lines up to the critical dividing surface. Within the above theoretical framework, the condition for the reaction to occur is given by Equation 9, where E_b is the barrier height at the point of impact and the values of μ^* and v^* must be calculated at the same point. For the present purpose, limiting the analysis to coplanar collisions was regarded to be adequate, since the trajectory studies of O + HCl (DCl) reactions referred to are for coplanar collisions. Monte Carlo methods were used to generate the impact parameter and the angle defining the initial orientation of the reagent for individual collisions.

3.1.1. *O + H$_2$ Reaction*

The reaction : $O(^3P) + H_2 \rightarrow OH + H$ is important in combustion and as a prototypical oxygen atom reaction. A considerable number of theoretical and experimental investigations of this reaction that have been reported are quoted in the trajectory study [63] devoted primarily to the effects of reagent rotation in this reaction. The work in [63] is based on Johnson-Winter LEPS potential surface [64] from which also the relevant parameters were derived for the kinematic mass model analysis [61] of the trajectory results in question.

   It should be noted that O + H$_2$, like O + HCl (DCl) and O + HBr, belongs to the few reactions for which, according to quasiclassical trajectory calculations, the cross-section increases monotonically with reagent rotation. This rather simple behaviour, however, does not seem to have a simple explanation. In [63] the qusiclassical trajectory calculations of the reaction cross-section S_r are given for $0 \leq j \leq 10$ and translational energies E_{trans} = 12, 15 and 20 kcal/mol. S_r is found to be strongly j dependent at all three collision energies considered (see Figure 7 below). As noted already in the original paper [63], such strong j dependence of S_r cannot be easily reconciled with the shape of the equipotential surfaces which, in this case, does not deviate much from the spherical, and is only slightly prolate. It has been argued therefore [63] that the observed j dependence arises because the S_r–reducing effect of trajectory reorientation by the prolate surface may be the strongest at $j = 0$ and then diminishes at larger values of j. On closer examination of the reorientation properties of trajectories in [63] one is led to the conclusion that trajectory reorientation effects in O + H$_2$ should be comparable to those found in the case of O + HCl (DCl) [46]. The j dependence of S_r for these reactions, however, is quite weak at $j < 8$, in sharp contrast to what is found in O + H$_2$. Although trajectories are reoriented to some degree towards higher barrier energies in the case of prolate equipotential surfaces [46], and the reorientation effect in question should be diminished at higher values of j, this does not provide a likely explanation for the strong j dependence of S_r found in the trajectory calculations for O + H$_2$ reaction [63]. This conclusion is further corroborated by the results of modelling O + HCl [21],

showing that most of the effects which has previously been ascribed to reorientation of trajectories in the case of a prolate surface [47] in fact comes from the anisotropy of a narrow region of the potential surface near the barrier, even if reorientation of trajectories is neglected.

In the kinematic mass model investigation of the strong j dependence of the reaction cross-section S_r in the O + H$_2$ reaction [61] the shape of the critical dividing surface in the region relevant for the reaction was approximated by an ellipsoid with the axes $a = 1.59$Å and $b = 0.75a$ which were estimated from the analysis of the potential energy surface in [63]. The equipotential surfaces were also assumed to be approximately ellipsoidal, with axes $b_1 = 0.92a_1$. These parameters were chosen to match the shape of the critical dividing surface and the equipotential surfaces near the saddle point on the potential energy surface for collision geometry [63]. The origin of the ellipsoids coincides with the center-of-mass of the diatomic reagent. Qualitatively the results should not depend much on the details of shape approximations. The dependence of the barrier height on the Jacobi angle γ for the potential surface in question is given in Figure 6. In addition to the pure electronic barrier, the vibrationally adiabatic barrier for $v = 0$ is also presented. It was determined as described in Section 2.1. Since the reaction in question was studied by quasiclassical trajectory calculations, the vibrational zero-point energy effects on the barrier crossing were included and thus have to be taken into account also in the kinematic mass model calculations.

Kinematic mass model calculations of the reaction cross-sections S_r were initially calculated as if the points of impact on the critical dividing surface were reached instantaneously, with the orientation angle, the translational energy and the rotational angular momentum having the values as initially selected. Consequently, any effects of the rotational motion on the distribution of the points of impact on the critical dividing surface were neglected: at any value of j this distribution was therefore as in the $j = 0$ case. The results of these calculations, presented in Figure 7, show a rather weak
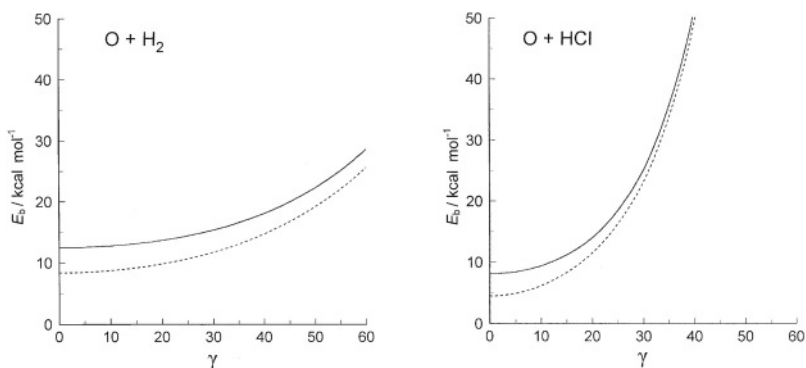

Figure 6. The dependence of the barrier height on the Jacobi angle γ for the potential energy surfaces used in the present cross section calculations for O + H$_2$ and O + HCl (DCl) reactions: (—) pure electronic barrier; (---) vibrationally adiabatic barrier ($v = 0$) [21].

dependence of the reaction cross-section on j, very much in accordance with the conventional views that rotational effects on a potential energy surface which is of an almost spherical shape should be small. The results of the model clearly are in sharp contrast with the j dependence found in the trajectory calculations.
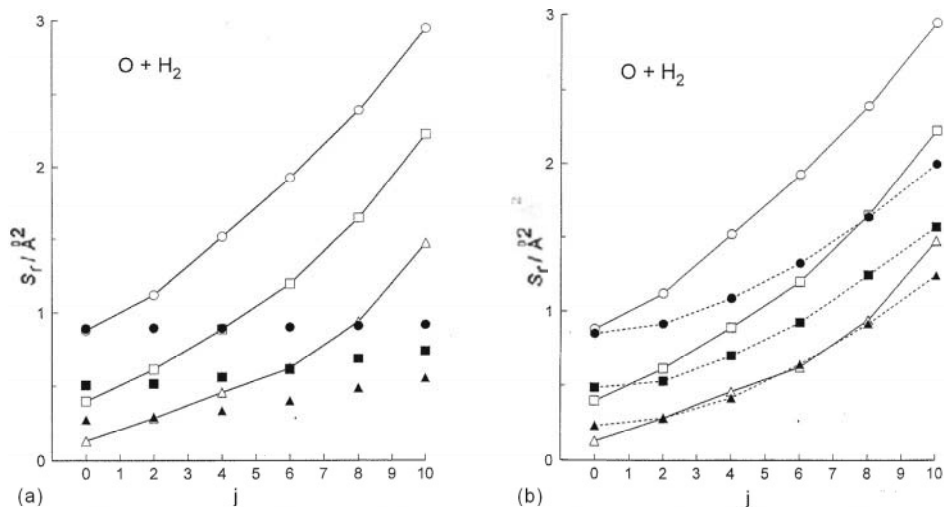

Figure 7. Reaction cross sections for O + H_2(v = 0, j) as function of j. (○,●), (□,■), and (Δ,▲) correspond to collision energies E_{trans} = 20, 15 and 12 kcal/mol respectively. Open symbols: quasiclassical trajectory results [64], full symbols: results of the kinematic mass model calculations. Effect of reagent rotation on the distribution of collisions at the barrier is neglected in (a); it is taken into account in (b)[61].

It was pointed out in [21] that effects of the rotational motion on the distribution of the points of impact may not be negligible for reactions where the critical dividing surface is nonspherical and the rotational velocitiy is comparable, or larger than, the relative translational velocity. This is the case, i.e., in O + H_2 and O + HCl (DCl) reactions presently considered. The above hypothesis was confirmed [61] by analysing the distribution of points of impact on the critical dividing surface, calculated with proper averaging, so that the distributions obtained correspond to those that should occur in calculations of the reaction cross-sections. The distribution of collisions on the critical dividing surface for $j = 0$ and $j = 10$, at collision energy E_{trans} = 12 kcal/mol, depicted in Figure 8 show that at higher rotational numbers j the distribution is shifted towards smaller values of angle γ where the barrier energy is lower (Figure 6). This leads to a mechanism of possibly strong rotational enhancement of the reaction cross-section, in addition to the enhancement due to an increase of the kinetic energy available for the barrier crossing. If changes in the distribution of collisions due to rotational excitation are taken into account in the kinematic mass model calculations the strong rotational enhancement of the cross-sections is essentially reproduced (Figure 7). Since the results of a coplanar collision model are in this case being compared with 3-dimensional quasiclassical trajectory results, a normalization factor had to be introduced which was

chosen by matching the results at $j = 0$ and $E_{trans} = 20$ kcal/mol. This may be one of the reasons for the agreement between the results in Figure 7 not being better. Even more
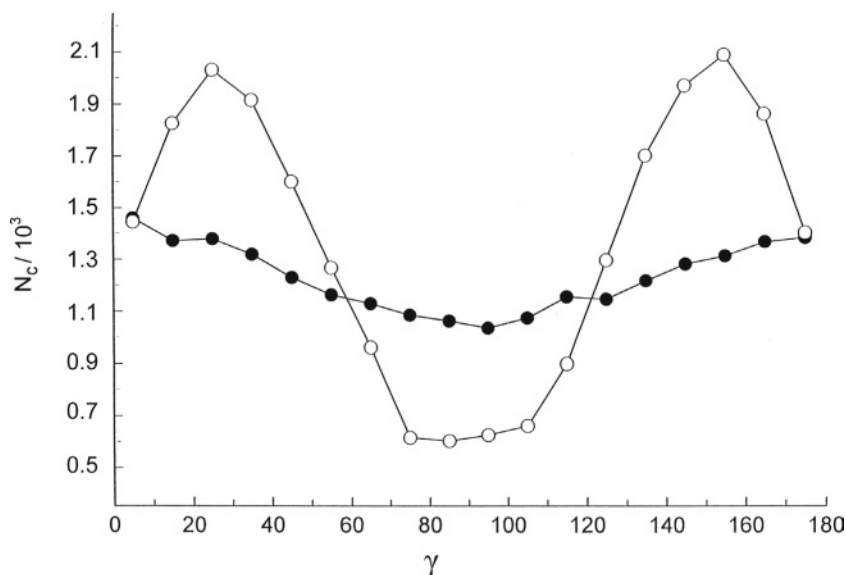

Figure 8. The effect of rotational excitation on the distribution of collisions at the barrier for O + H_2 reaction, for j = 0 (●) and for j = 10 (○). The collision energy was $E_{trans} = 12$ kcal/mol in each case[61].

important in this respect may be the fact that in the quasiclassical trajectory calculations the vibrational zero-point energy effects are included. According to the assumed potential energy surface, the barrier for O + H_2 reaction rises only slowly with the γ angle (Figure 6), which means that even collisions at fairly large values of γ can be active. As pointed out in Section 2.1, the method of calculating vibrational zero-point energy effects on the barrier in the kinematic mass model can be regarded as less reliable at larger values of γ; at such angles is thus the vibrationally adiabatic barrier (Figure 6) likely to be less accurate.

The largeness of the interval of angle γ over which the collisions O + H_2 can be reactive is also the reason for the effects of rotational excitation on the distribution of collisions being manifested already at small values of j. The situation in O + HCl (DCl) reactions, to be discussed next, is in this respect entirely different.

3.1.2 O + HCl (DCl) Reactions

The trajectory results for $O(^3P)$ + HCl (DCl) $\rightarrow$ OH (OD) + Cl reactions obtained with the Surface I [47] reveal a j dependence of the reaction cross-section S_r which differs strikingly from that in the O + H_2 case. For O + HCl, S_r rises slowly with j up to $j \sim 8$, and then increases rapidly for $j > 8$ (Figure 9). In the case of O + DCl the situation is similar, with the increase for $j > 8$, however, being much slower. There is also a weak decrease in S_r at values of j in this case which will not be addressed here.

It should be noted that in the present case the trajectory calculations were carried out for coplanar collisions with the vibration of HCl (DCl) frozen [47]. A trajectory was assumed to be reactive if it reached a point on the top of the electronic barrier. There are no corrections of the barrier height due to the vibrational zero-point energy effect in this case. These trajectory results are therefore more directly comparable with the results of the kinematic mass model than the 3-dimensional quasiclassical trajectrory calculations discussed in the previous case.

At the present level of rigour, the potential energy surface (Surface I) may be characterized by a critical dividing surface of roughly ellipsoidal shape with axes $a = 2.57$Å and $b = 0.69a$, and the equipotential surfaces near the barrier which may also be
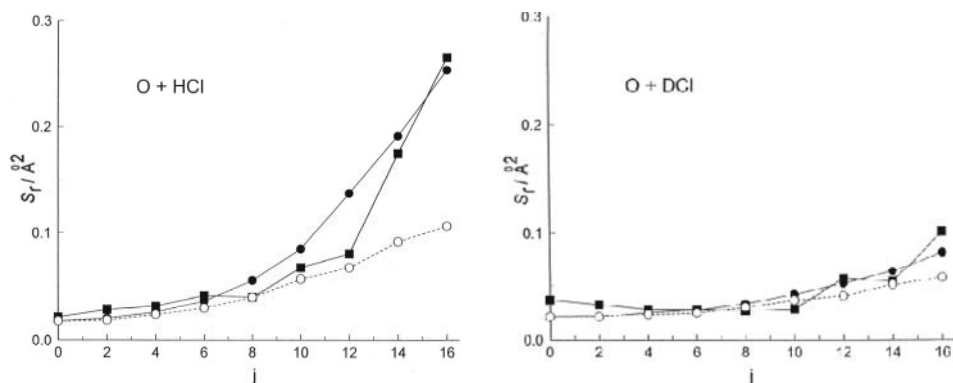

Figure 9. Rotational dependence of the reaction cross section for O + HCl and O + DCl reactions at $E_{trans} = 10$ kcal/mol. (■) classical trajectory results [48]; (●) results of the kinematic mass model with the dependence of the distribution of collisions at the barrier on reagent rotation taken into account; (○) results of the same model with the effect of rotation on the distribution of collisions neglected[61].
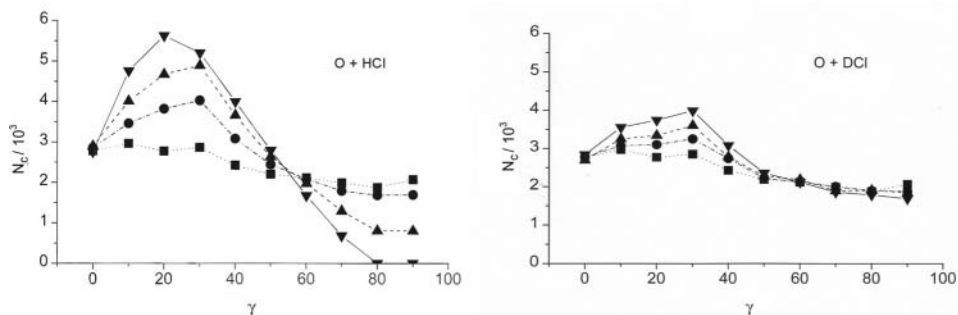

Figure 10. Effect of rotational excitation on the distribution of collisions at the barrier in O + HCl and O + DCl reactions at $E_{trans} = 10$ kcal/mol. The angle $\gamma = 0$ corresponds to the colinear Cl-H-O (Cl-D-O) geometry. Values: j = 0 (■), 8(●), 12 (▲) and 16 (▼)[62].

assumed to be roughly ellipsoidal, with $b_1 = 0.84a_1$. As in the previous case, these shapes are assumed to approximate the surfaces in question over the region relevant for the reaction and the main conclusions can be expected to depend little on finer details of these approximations. The dependence of the barrier energy on angle γ for this surface is

given in Figure 6. Its characteristic property is that it rises steeply with the angle. The range of γ values for which the reaction can occur is almost three times smaller than in the case of the O + H$_2$ reaction: at E_{trans} = 10 kcal/mol and j = 0, e.g., the maximum γ is only ~ 11°. As we shall see below, the difference in the steepness of the dependence of the barrier energy on γ is the main reason that rotational enhacements in O + H$_2$ and O + HCl reactions are strikingly different.

The results of the kinematic mass model calculations for O + HCl (DCl) in which the j dependence of distribution of collisions on the barrier was neglected , so that at each j this distribution was the same as for j = 0, are presented in Figures 9. We see that agreement with the trajectory results is quite good for j < 8, at higher values of j, however, the rotational enhancement of the reaction cross-section found in the trajectory calculations is much stronger than in the results of the model, particularly for O + HCl. By taking the effects of rotational excitation on the distribution of collisions into account, a much better agreement with the trajectories is obtained for $j \geq 8$, while the results for j < 8 remain essentially unchanged. In this respect the present results are surprisingly different from the corresponding results in the O + H$_2$ case where the effects of rotationally induced changes in the distribution of collisions become important already at small values of j. These striking peculiarities, however, can be readily explained by considering the j dependence of the collision distributions (Figure 10) and the barrier energy dependence on angle γ (Figure 6). We see that for j < 8 the rotational excitation does not affect much the number of collisions over the barrier region ($0 < \gamma <$ 15°) where the reaction is energetically possible. For $j \geq 8$, however, the number of reactive collisions increases rapidly, due, first, to the increased range of γ, but much more so due to the change of the collision distribution induced by the rotation: at higher rotational excitation collisions accumulate over the region of the barrier close to the longitudinal axis where the barrier energies are the lowest. This effect is present also in O + DCl reaction; it is, however, much weaker because the rotational velocity at a given value of j is only half of the value in the HCl case. As already mentioned, the barrier for the O + H$_2$ reaction rises rather slowly with γ: at j = 0, γ_{max} ~ 30° at E_{trans} = 12 kcal/mol and ~ 50° at E_{trans} = 20 kcal/mol. The changes in the distribution of collisions therefore become effective in increasing the cross-section already at small values of j, so that this effect cannot be neglected for any j > 0.

It is illustrative to consider also the dependence of the cross-section for the O + HCl (DCl) reactions on the rotational energy E_{rot}. The results presented in Figure 11 show that at increased rotational energy the effect of the change in the distribution of collisions can be quite large also for O + DCl, reaching about half of the value for O + HCl at the largest E_{rot} considered. For comparison, also given are the results of the calculations in which j = 0 but the translational energy E_{trans} = 10 kcal/mol is increased by E_{rot}. The cross-section for O + DCl can be larger than for O + HCl in this case because of the larger value of the mass μ^*, the velocity v^* at each translational energy being roughly the same for both reactions. The energy $\mu^* v^{*2}/2$ for barrier crossing (Equation 9) can thus be larger for O + DCl collisions in this case.
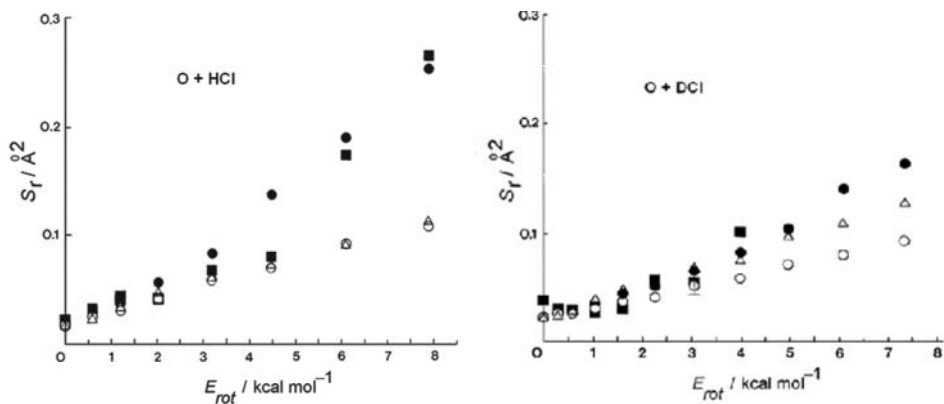
Figure 11. Rotational energy E_{rot} dependence of the cross section for O + HCl and O + DCl reactions at $E_{trans} = 10$ kcal/mol. Compared are the results of the classical trajectory calculations (■) [47], kinematic mass model results which only include the energetic effects of the reactant rotation (○), kinematic mass model results which include rotational effects on the distribution of collisions with the barrier in addition to the rotational energetic effects (●), and the kinematic mass model results for rotationally unexcited reactants (j = 0) and the translational kinetic energy increased by the amount of E_{rot} (Δ) [62].

4. Concluding Remarks

Notwithstanding the simplifications introduced in the derivation of the kinematic mass model for chemical reactions, the mechanism of strong rotational enhancement of the reaction cross-sections found in this model in the case of O + H_2 and O + HCl (DCl) reactions can be regarded as conclusively established. The »energetic effect« in the rotational enhancement, as given by the model, is rather weak, just as it is commonly expected, and the strong rotational enhancement found in the trajectory calculations is shown to be largely due to the changes of the distribution of collisions with the barrier arising through the rotational excitation. Several important characteristic properties of the mechanism in question could also be clearly pointed out: (i) the magnitude of the effect arising from this mechanism depends very much on the ratio of the rotational and translational velocity , v_{rot}/v_{trans}. This can be seen, e.g., by comparing the effect of rotational excitation in the O + HCl and O + DCl reactions. In the latter, the rotational enhancement at a particular E_{rot} is considerably weaker, due to smaller v_{rot}, v_{trans} being roughly the same in both reactions at a given E_{trans}. (ii) depending on how steeply the barrier energy rises with angle γ , the enhancement effect of the mechanism in question may set in to an appreciable extent only at a high enough value of j, say, at $j = j_0$, like in the O + HCl (DCl) reactions. For $j < j_0$ the changes in the distribution of collisions occur mostly over the regions of the barrier which cannot be crossed, the barrier energies being too high there. For such j values the rotational enhancement then is due essentially to the »energetic effect« which is generally much weaker. If the barrier energy rises slowly with angle γ, the enhancement due to the change of the distribution of collisions may be appreciable already at any $j > 0$, like in O + H_2 reaction.

The results presented here provide a convincing explanation, e.g., of the conclusion of Mayne [60] that »it appears that rotational excitation is the most efficient way to promote hydrogen atom abstraction«. He made this observation on the basis of extensive quasiclassical trajectory calculations. It is particularly noteworthy that even in the case of the reaction O + HCl on Surface II, where a decline in reactivity with rotation was found at rotational energies less than 8 kcal/mol [47,49], for higher rotational energy, and at higher translational energies rotation strongly enhances H atom transfer [60]. Although the shape of the equipotential surfaces is oblate for Surface II, the shape of the critical dividing surface is prolate (Figure 3) and at high enough rotational velocities the effect of the accumulation of collisions over the region of the barrier near the longitudinal axis prevails over the effects disrupting »trajectory funnelling« which, as discussed earlier, tend to decrease the cross-section.

As pointed out already in [62], the mechanism in question could also have a crucial role in reactions in condensed phases where it should arise due to large amplitude oscillatory motions, like internal rotations or librations, of molecules or reactive atomic groups. Such oscillatory motion could be excited, e.g., by microwaves and the mechanism in question should thus be of great importance also for understanding microwave acceleration of chemical reactions in condensed phases.

Acknowledgments

References

1. Smith, I.W.M. (1980) *Kinetics and Dynamics of Elementary Gas Reactions,* Butterworths, London.
2. Tolman, R.C. (1927) *Statistical Mechanics with Applications for Physics and Chemistry*, Chemical Catalog Co., New York.
3. Frost, A.A. and Pearson, R.G. (1953). *Kinetics and Mechanisms*, Wiley, New York.
4. Present, R.D. (1955) Note on the simple collision theory of bimolecular reactions *Proc. Natl. Acad. Sci. USA* **41**, 415-417.
5. Smith, I.W.M. (1982) A new collision theory for bimolecular reactions. *J. Chem. Ed.* **59**, 9-14.
6. Levine, R.D. and Bernstein, R.B. (1984) Opacity analysis of steric requirements in elementary chemical reactions. *Chem. Phys. Lett.* **105**, 467-471.
7. Levine, R.D. (1990) The chemical shape of molecules: An introduction to dynamical stereochemistry. *J. Phys. Chem.* **94**, 8872-8880.
8. Johnston, H. (1966) *GasPhase Reaction Rate Theory*, Ronald, New York.
9. Levine R.D. and Bernstein, R.B. (1986) Rotational state dependence of the reactivity of oriented symmetric top molecules. *Chem. Phys. Lett.* **132,** 11-15.
10. Janssen, M.H.M. and Stolte, S. (1987) Calculation of steric effects in reactive collisions employing the angle-dependent line of centers model. *J. Phys. Chem.* **91**, 5480-5486.
11. Gislason, E. A. and Sizun, M. (1991) An angle-dependent hard-sphere model for atom-diatom chemical reactions. *J. Phys. Chem.* **95**, 8462-8466.

12. Wiseman, F.L. and Rice, A.G. (1993) Modifications to the angle-dependent line of normals model for gas-phase reaction rate constants. *J. Chem. Ed.* **70**, 914-920.

13. Connor, J.N.L., Whitehead, J.C. and Jakubetz, W (1987) Orientation dependence of the F + H$_2$ reaction - analysis of the angle-dependent line-of-centers model. *J. Chem. Soc., Faraday Trans.* **83**. 1703-1718.

14. Connor, J.N.L. and Jakubetz, W. (1993) Orientation dependence of the F + H$_2$ and H + F$_2$ reactions using the line-of-centers model with angle-dependent collision diameters and barrier heights. *J. Chem. Soc., Faraday Trans.* **89**, 1481-1486.

15. Evans, G.T., She, R.S.C. and Bernstein, R.B. (1985) A simple kinetic theory model of reactive collisions of rigid nonspherical molecules. *J. Chem. Phys.* **82**, 2258-2266

16. Evans, G.T. (1987) A simple kinetic theory model of reactive collisions. III. Convex loaded bodies. *J. Chem. Phys.* **86,** 3852-3858.

17. She, R.S.C., Evans, G.T. and Bernstein, R.B. (1986) A simple kinetic theory model of reactive collisions. II. Nonrigid spherical potential with angle-dependent reactivity. *J. Chem. Phys.* **84**, 2204-2211.

18. Evans, G.T., van Kleef, E. and Stolte, S. (1990) Chemical reaction dynamics: Combination of two models. *J. Chem. Phys.* **93.** 4874-4883.

19. Esposito, M. and Evans, G.T. (1992) Steric effects and cones of reaction in gas-phase reactions. *J. Chem. Phys.* **97,** 4846-4858.

20. Miklavc, A., Perdih, M. and Smith, I.W.M. (1995) The role of kinematic mass in simple collision models of activated bimolecular reactions. *Chem. Phys. Lett.* **241**, 415-422.

21. Perdih, M., Miklavc, A. and Smith, I.W.M. (1997) Kinematic mass model of activated bimolecular reactions: Molecular shape effects and zero-point energy corrections. *J. Chem. Phys.* **106**, 5478-5493.

22. Perdih, M., Smith, I.W.M. and Miklavc, A. (1998) Kinematic mass model of activated bimolecular reactions: Reactions of vibrationally excited reactants. *J. Phys. Chem.* **A 102**, 3907-3915.

23. Hirschfelder, J.O. and Wigner, E.P. (1939) Some quantum-mechanical considerations in the theory of reactions involving an activation energy. *J. Chem. Phys.* **7**, 616-628.

24. Marcus, R.A. (1966) On the analytical mechanics of chemical reactions. Quantum mehanics of linear collisions. *J. Chem. Phys.* **45**, 4493-4499.

25. Marcus, R.A. (1966) On the analytical mechanics of chemical reactions. Classical mechanics of linear collisions. *J. Chem. Phys.* **45,** 4500-4504.

26. Truhlar, D.G., Isaacson, A.D. and Garrett, B.C. (1985) in M.J. Baer (ed.) *Theory of Chemical Reaction Dynamics*, CRC Press, Boca Raton, pp. 65-137.

27. Smith, I.W.M. (1990) Vibrational adiabaticity in chemical reactions. *Acc. Chem. Res.* **23**. 101-107.

28. Miklavc, A. and Fischer, S.F. (1978) Semi-classical theory of collision-induced vibrational-rotational transitions. Application to methyl halides. *J. Chem. Phys.* **69**, 281-287.

29. Miklavc, A. (1980) On the semi-classical theory of collision-induced vibrational-rotational transitions in molecules. *J.Chem. Phys.* **72**, 3805-3808.

30. Miklavc, A. (1980) Semi-classical theory of vibrational, rotational and translational energy exchange in collisions of polyatomic molecules. *Mol. Phys.* **39**, 855-864.

31. Miklavc, A. (1983) Quantum theory of vibrational, rotational and translational energy exchange in collisions of polyatomic molecules. Application to methyl halides. *J. Chem. Phys.* **78**, 4502-4514.

32. Cannon, B.D. and Smith, I.W.M. (1984) The relaxation of HCl(011) by V-T, R and V-V energy transfer. *Chem. Phys.* **83,** 429-443.

33. Miklavc, A. and Smith, I.W.M. (1988) Vibrational relaxation of C$_2$H$_2$ and C$_2$D$_2$ by vibration-rotation, translation (V-R,T) energy transfer. *J. Chem. Soc., Faraday Trans. 2* **84,** 227-238.

34. Kapralova, G.A., Nikitin, E.E. and Chaikin, A.M. (1968) Non-empirical calculations of the probabilities of vibrational transitions in hydrogen halide molecules. *Chem. Phys. Lett.* **2**, 581-583.

35. Zittel, P.F. and Moore, C.B. (1973) Model for V→T, R relaxation – CH_4 and CD_4 mixures. *J. Chem. Phys.* **58**, 2004-2014.

36. Steele Jr, R.V. and Moore, C.B. (1974) V→T, R energy transfer in HCl- and DCl- rare gas mixtures. *J. Chem. Phys.* **60**, 2794-2799.

37. Haug, K., Schwenke, D.W., Shima, Y., Truhlar, D.G., Zhang, Y. and Kouri, K.J. (1986) L-2 solution of the quantum-mechanical reactive scattering problem. The threshold energy for D + $H_2(v = 1) \rightarrow$ HD + H. *J. Phys. Chem.* **90**, 6751-6759.

38. Haug, K., Schwenke, D.W., Truhlar, D.G., Zhang, Y., Zhang, J.Z.H. and Kouri, K.J. (1987) Accurate quantum-mechanical reaction probabilities for the reaction O + H_2 → OH + H. *J. Chem. Phys.* **87**, 1892-19894.

39. Smith, I.W.M. (1981) Combining transition-state theory with quasiclassical trajectory calculations. 1. Collinear collisions. *J. Chem. Soc., Faraday Trans. 2* **77**, 747- 759.

40. Frost, R.J. and Smith, I.W.M. (1987) Combining transition-state calculations with quasiclassical trajectory calculations. 2. Collinear collisions involving vibrationally excited reagents. *Chem. Phys.* **111**, 389-400.

41. Frost, R.J. and Smith, I.W.M. (1987) Combining transition-state calculations with quasiclassical trajectory calculations. 3. Application to the 3-dimensional H + $H_2(v)$ reaction. *Chem. Phys.* **117**, 421-438.

42. Frost, R.J. and Smith, I.W.M. (1987) Combining transition-state theory with quasiclassical trajectory   calculations. 4. Application to the nitrogen exchange reaction N + $N_2(v)$. *Chem. Phys. Lett.* **140,** 499-505.

43. Frost, R.J. and Smith, I.W.M. (1988) Combining transition-state theory with quasiclassical trajectory calculations. 5. Canonical calculations on the reaction: F + $H_2(v = 0)$→ HF(v) + H. *J. Chem. Soc., Faraday Trans. 2* **84**, 1825-1835.

44. Frost, R.J. and Smith, I.W.M. (1988) Combining transition-state theory with quasiclassical trajectory calculations. 6. Microcanonical calculations on the reaction F + $H_2(v = 0)$→ HF(v) + H . *J. Chem.Soc., Faraday Trans. 2* **84**, 1837-1846.

45. Loesch, H. (1986) A slidig mass model to rationalize effects of reagent rotation on reaction cross sections. *Chem. Phys.* **104**, 213-227.

46. Loesch, H. (1987) The effect of reagent rotation on reaction cross sections for $O(^3P)$ + HCl→ OH + Cl: A rationale for contradictory predictions. *Chem. Phys.* **112**, 85-93.

47. Kornweitz, H., Persky, A., Schechter I. and Levine, R.D. (1990) Steric hindrance can be probed via the dependence of the reactivity on reagent rotation: O + HCl. *Chem. Phys. Lett.* **169**, 489-496.

48. Kornweitz, H., Persky, A. and Levine, R.D. (1991) Kinematic mass effect in the dynamical stereochemistry of activated bimolecular reactions. *J. Phys. Chem.* **95**, 1621-1625.

49. Persky, A. and Broida, M. (1984) Quasiclassical trajectory study of the reaction $O(^3P)$ + HCl → OH + Cl. The effects of vibrational excitation, rotational excitation and isotopic substitution on the dynamics. *J. Chem. Phys.* **81**, 4352-4362.

50. Levine, R.D. and Bernstein, R.B. (1987) *Molecular Reaction Dynamics and Chemical Reactivity*, Oxford University Press, New York.

51. Kuntz, P.J., Nemeth, E.M., Polanyi, J.C., Rosner, S.D. anf Young C.E. (1966). Energy distribution among products of exothermic reactions. II. Repulsive, mixed, and attractive energy release. *J. Chem. Phys.* **44**, 1168-1184.

52. Polanyi, J.C. (1972) Some concepts in reaction dynamics. *Acc. Chem. Res.* **5**, 161-&

53. Polanyi, J.C. (1987) Some concepts in reaction dynamics. *Science* **236**, 680-690.

54. Bauer, S.H. (1978) How energy accumulation and disposal affect rates of reactions. *Chem. Rev.* **78**, 147-184.

55. Kneba, M. and Wolfrum, J. (1980) Bimolecular reactions of vibrationally excited molecules. *Annu. Rev. Phys. Chem.* **31**, 47-79.

56. Leone, S.R. (1984) State-resolved molecular reaction dynamics. *Annu. Rev. Phys Chem.* **35**, 109-135.

57. Vandelinde, S.R. and Hase, W.L. (1989) A direct mechanism for S_N2 nucleophilic substitution enhanced by mode-selective vibrational excitation. *J. Amer. Chem. Soc.* **111**, 2349-2351.

58. Sathyamurthy, N. (1983) Effects of reagent rotation on elementary bimolecular exchange reactions. *Chem. Rev.* **83**, 601-618.

59. Grote, W., Hoffmeister, M., Schleysing, R., Zerhau-Dreihofer, H. and Loesch, H. (1988) Rotational and steric effects in three centre reactions in J.C. Whitehead (ed.) *Selectivity in Chemical Reactions*, Kluwer Academic Publishers, The Hague, pp. 47-78.

60. Mayne, H.R. (1990) Effect of reactant rotation on hydrogen atom transfer. *J. Amer. Chem. Soc.* **112**, 8165-8166.

61. Miklavc, A., Perdih, M. and Smith, I.W.M. (2000) A new mechanism for the enhancement of activated bimolecular reactions by rotational excitation. *J. Chem. Phys.* **112**, 8813-8818.

62. Miklavc, A. (2001) Strong acceleration of chemical reactions occuring through the effects of rotational excitation on collision geometry. *ChemPhysChem.* **8/9**, 552-555

63. Song, J.-B. and Gislason, E.A. (1996) Theoretical study of the effect of reagent rotation on the reaction of O + $H_2(v,j)$. *Chem. Phys.* **202**, 1.

64. Johnson, B.R. and Winter, N.W. (1977) Classical trajectory study of effect of vibrational energy on reaction of molecular hydrogen with atomic oxygen. *J. Chem. Phys* **66**, 4116-4120.

DYNAMICS STUDIES OF THE O(^{3}P) + CH$_4$, C$_2$H$_6$ AND C$_3$H$_8$ REACTIONS

DIEGO TROYA AND GEORGE C. SCHATZ
Department of Chemistry, Northwestern University
2145 Sheridan Rd., Evanston, Il. 60208-3113, USA

Abstract. We report theoretical simulations of hyperthermal O(^{3}P) collisions with CH$_4$, C$_2$H$_6$ and C$_3$H$_8$ that are related to erosion processes in low Earth orbit (LEO). In the first part of this paper, we use electronic structure calculations to show that at energies well below those accessible in LEO, there is a whole new body of reaction channels that are open in addition to the well known lowest barrier one, H abstraction to give OH + alkyl radicals. For instance, O addition to the hydrocarbon followed by H elimination to give alkoxy radicals + H is possible through barriers of about 2 eV. Similar barrier heights are found for direct carbon-carbon bond breakage processes that can take place in hydrocarbons containing C-C bonds (ethane and propane). In the second part of this paper, we carry out reaction dynamics calculations using the quasiclassical trajectory method in conjunction with a novel semiempirical Hamiltonian termed MSINDO. Cross section calculations reveal that H elimination and C-C breakage are both competitive with H abstraction in the reactions of O(^{3}P) with ethane and propane. In O(^{3}P) + methane, elimination is even more important than H abstraction under LEO conditions. Energy distributions for the majority channels show different patterns according to the kinematics of the products that are formed. For H abstraction to give OH, most of the energy is released as product translation, while OH is fairly cold. For H elimination, most energy is released as internal energy of the oxyradical. Angular distributions also depend on the product channel. H abstraction shows a trend with collision energy that matches that of reactions undergoing a direct mechanism. Near threshold H elimination and C-C breakage angular distributions reveal the presence of two different saddle points that connect reagents and products for each process.

1. Introduction

The reaction of ground electronic state atomic oxygen with short-chain hydrocarbons to give OH + alkyl radicals has been of considerable ongoing interest in

the gas phase kinetics community due to its importance in combustion chemistry [1]. As a result thermal rate constants for $O(^3P) + RH \rightarrow OH + R$ (R = short-chain saturated alkane) have been measured for a variety of alkanes over a broad temperature interval. The recommended rate constant expressions for $O(^3P) + CH_4 \rightarrow OH + CH_3$, $O(^3P) + C_2H_6 \rightarrow OH + C_2H_5$ and $O(^3P) + C_3H_8 \rightarrow OH + C_3H_7$, are (in units of cm^3 molecule^{-1} s^{-1}), respectively, $(1.15 \times 10^{-15})T^{1.56}$ exp(-4270/T) (T = 300 - 2500) [2], $(1.66 \times 10^{-15})T^{1.5}$ exp(-2920/T) (T = 300 - 1200) [3], and (1.3×10^{-21}) $T^{3.5}$ exp(-1280/T) (T = 298 - 2000) [4]. The relatively small rate constant values at room temperature ($5.5 \ 10^{-18}$, $5.1 \ 10^{-16}$, $8.5 \ 10^{-15}$ cm^3 molecule^{-1} s^{-1}, respectively) imply relatively large barriers (roughly 0.4 eV). These large barriers have limited the availability in nonthermal reaction dynamics experiments. In the early 80's, Andresen and Luntz observed rovibrational distributions of OH generated in the reaction of $O(^3P)$ atoms with several saturated hydrocarbons with energies barely above the barrier [5]. More recently, McKendrick and coworkers reported OH rovibrational distributions for $O(^3P)$ reactions with short-chain hydrocarbons, including methane and ethane [6, 7]. Energy disposal data in the partner alkyl product have been harder to obtain, and only vibrational distributions of the umbrella mode of the CH_3 generated in the $O(^3P)$ + CH_4 reaction have been published [8].

Here, we shall be interested in other aspects of the title reactions not connected with thermal processes. The surfaces of spacecraft in low Earth orbit (LEO) are eroded due to the harsh oxidizing environment encountered in that region [9, 10]. Oxygen atoms in the ground state dominate the 200-700 km altitude range associated with LEO [11]. After seminal after-flight analysis revealing important erosion patterns in spacecraft surfaces, ground-based experiments were subsequently carried out to verify the eroding character of $O(^3P)$ atoms in LEO conditions for polymer surfaces analogous to those found on spacecraft [12, 13] (for a recent review see [14]). These experiments revealed that under steady-state bombardment conditions, mass was carried away from the surfaces by means of volatile species such as CO or CO_2. It is therefore of crucial importance to examine O atom reactions with polymer surfaces in order to establish LEO erosion mechanisms. As a first step in this direction, we consider the microscopic mechanisms whereby $O(^3P)$ atoms react with gas-phase molecules that mimic the polymer surfaces, of which the simplest example is short-chain hydrocabons. Thus in the following we shall describe theoretical studies of $O(^3P)$ atoms reacting with the three shortest-chain saturated hydrocarbons under high energy (few eV) conditions, such as would be found in LEO. Insight gained in these studies will provide an initial understanding of the LEO erosion problem, and will aid in the development of theoretical models.

The novel feature of the present studies lies in the conditions upon which $O(^3P)$ reacts with hydrocarbons. Orbital motion in LEO leads to a collision energy between $O(^3P)$ atoms and spacecraft surfaces of about 5 eV [15]. Such a high collision energy has not been explored in previous thermal studies of $O(^3P)$ + hydrocarbon reactions, and it seems obvious that the thermal reactivity cannot be straightfor-

wardly extrapolated to hyperthermal conditions. These drastic energy conditions open the possibility of new reaction channels that have been unresolved until very recently [16, 17, 18, 19]. We shall focus here on these novel reaction channels as they may provide effective pathways for erosion in LEO. Our theoretical approach to the title reactions comprises two different levels of the chemical reaction theory. First, we perform quantum chemistry calculations on the electronic structure of the product reaction channels and saddle points that are accessible under LEO conditions. Second, we carry out direct dynamics studies to identify dynamics properties of the most important reaction pathways. Comparisons with experiments that are being developed by Minton and Garton at Montana State University will be made throughout [16, 19, 20].

The paper is organized as follows: the details of the electronic structure calculations are in Section II, Section III is for the dynamics studies and conclusions and future directions are given in Section IV.

2. Quantum chemistry calculations

Reagents, products and pathways connecting between them have been studied for the title reactions at different levels of electronic structure theory. Results of semiempirical PM3 [21] and MSINDO [22, 23] calculations are examined in comparison with more rigorous density functional theory (DFT) and *ab initio* predictions. Semiempirical techniques are not expected to provide accurate representations of the potential energy surfaces, however, they provide electronic structure schemes that are amenable for use in conjunction with dynamics studies (so-called direct dynamics calculations). For instance, sample gradient calculations on O(^{3}P) + CH_4 or C_2H_6 indicate that MSINDO and PM3 are about 3000 times faster than B3LYP/6-31G*. This implies that a dynamics study of the title reactions with statistical significance employing first-principles techniques poses a tremendous computational expenditure, whereas semiempirical techniques can provide detailed studies in a more timely manner. It is therefore interesting to verify the accuracy of the semiempirical techniques as they are potentially suitable candidates to be used in subsequent reaction dynamics studies.

PM3 and *ab initio* UMP2 calculations have been carried out using the GAMESS package of programs [24], JAGUAR [25] has been used for DFT B3LYP/6-31G* and MSINDO 1.1 for MSINDO calculations. All of our calculations are based on unrestricted wave-functions. Spin contamination was never larger than 7.5% of the expectation value of the exact squared spin operator ($< S^2 > = 2.0$) in any of the stationary points reported here. Likewise, all of the calculations refer to the ground electronic state (1^3A in C_s symmetry). The effects of excited triplet surfaces have been considered in dynamics studies of the O(^{3}P)+CH_4 →H + OCH_3 reaction reported elsewhere [19]. Reaction energies calculated using these methods are compared with experiments [26, 27], whereas reaction barriers are compared with highly accurate coupled-cluster calculations carried out by us for the reactions involving ethane and methane.

TABLE 1. Energetics of the most important $O(^3P)$ + CH_4, C_2H_6 and C_3H_8 reactions.[a]

Stationary Point	PM3	MSINDO	B3LYP 6-31G*	UMP2 6-311G**	Exp. (CCSD(T))[b]
$O(^3P)$+CH_4					
OH + CH_3 (abstraction)	-0.876	-0.342	0.250	0.291	0.10[c]
TS1 (abstraction)	0.304	0.564	0.264	0.774	(0.497)
H + OCH_3 (elimination)	-0.446	0.081	0.511	0.801	0.64[c]
TS2 (elimination)	1.104	1.869	1.815	2.542	(2.096)
TS3 (elimination)	1.181	1.990	2.158	2.915	(2.509)
$O(^3P)$+C_2H_6					
OH + C_2H_5 (abstraction)	-1.205	-0.758	0.040	0.175	-0.07[c]
TS1 (abstraction)	0.192	0.370	0.081	0.632	(0.415)
H + OC_2H_5 (elimination)	-0.501	-0.209	0.328	0.607	0.39[c]
TS2 (elimination)		1.701	1.857	2.571	(2.191)
TS3 (elimination)	1.119	1.671	2.050	2.789	(2.457)
CH_3 + OCH_3 (C-C breakage)	-1.257	-0.720	-0.199	0.365	-0.01[c]
TS4 (C-C breakage)		1.645	1.692	2.533	(2.062)
$O(^3P)$+C_3H_8					
OH + n-C_3H_7 (I) (abstraction)	-1.443	-0.764	0.056	0.207	-0.12[d]
OH + n-C_3H_7 (II) (abstraction)		-0.757	0.071	0.215	
TS1 (abstraction, I)	0.207	0.355	0.087	0.645	
TS2 (abstraction, II)	0.203	0.354	0.094	0.607	
H + n-OC_3H_7 (I) (elimination)	-0.508	-0.208	0.310	0.604	
H + n-OC_3H_7 (II) (elimination)	-0.484	-0.235	0.248	0.538	
TS3 (elimination, I)	1.214	1.861	1.871	2.601	
TS4 (elimination, II)	1.112	1.760	1.791	2.497	
CH_3 + OC_2H_5 (C-C breakage)	-1.282	-0.855	-0.304	0.297	-0.17[d]
OCH_3 + C_2H_5 (C-C breakage)	-1.556	-0.981	-0.329	0.387	-0.10[d]
TS5 (C-C breakage)		1.773	1.703	2.619	
TS6 (C-C breakage)		2.054	2.110	2.916	

[a] Energies in eV with respect to reagents.
[b] CCSD(T)/AUG-cc-pVTZ calculations over UMP2/AUG-cc-pVDZ geometries and frequencies for $O(^3P)$+CH_4. CCSD(T)/cc-pVTZ calculations over UMP2/cc-pVTZ geometries and frequencies for $O(^3P)$+C_2H_6.
[c] Experimental values (ΔH^o_{298K}) come from the heats of formation of Ref. [27].
[d] Experimental values (ΔH^o_{298K}) come from the heats of formation of Ref. [26].

We report in Table 1 the thermodynamics of the most important reaction channels that are open under LEO conditions. Abstraction of a hydrogen atom to generate OH and alkyl radicals is the reaction pathway that has been observed in

earlier experiments [5, 6]. However, under LEO conditions there are other possible reactive processes such as O addition to the hydrocarbon with subsequent elimination of a hydrogen atom (that we term H elimination), or direct breakage of a carbon-carbon bond in ethane and propane to generate two hydrocarbon fragments (that we term C-C breakage). Both H elimination and C-C breakage lead to the formation of oxyradicals, where oxygen atoms are directly bonded to hydrocarbon fragments. Evidence for generation of oxyradicals has been given by experiments on liquid hydrocarbons in steady-state bombardment with O(^{3}P) atoms, where volatile species such as CO or CO_2 scattering from the hydrocarbon surface were detected [14]. Initial steps for generation of these products require oxyradical formation and this is one of the reasons why H elimination or C-C breakage are particularly interesting reaction pathways. Of course, C-C breakage is also of crucial importance to materials damage in LEO as it provides a direct mechanism for the production of volatile products (small alkyl radicals or oxyradicals).

It should be noted that the hydrogen abstraction or elimination calculations reported here for O(^{3}P) + C_3H_8 only refer to processes that involve primary carbon atoms. However, it is well known that the secondary radicals coming from abstraction or elimination of hydrogen atoms initially bound to the central carbon atom are more stable than primary radicals [5]. Although we consider all of the possibilities in the dynamics studies that we report later, Table 1 only shows the thermodynamics of reactions involving primary locations so as to establish useful comparisons with ethane and methane, where radicals can only be primary. In addition, there are two possible (primary) n-C_3H_7 and n-OC_3H_7 radicals. n-C_3H_7 (I) is that in which the lacking hydrogen with respect to propane is originally in the plane defined by the carbon atoms of the molecule, whereas n-C_3H_7 (II) corresponds to the radical generated by abstraction of either of the remaining two hydrogen atoms which are symmetric by the C-C-C plane. Likewise n-OC_3H_7 (I) shows C_s symmetry, and the oxygen atom replaces an H atom initially belonging to the plane defined by the carbons chain. n-OC_3H_7 (II) is not symmetric and the oxygen atom occupies an out-of-plane position. As noted in Table 1, each of these products connects with reagents through a different saddle point.

Experimental reaction energies for the lowest energy barrier abstraction processes (O(^{3}P) + RH → OH + R) are slightly overestimated by DFT and UMP2 calculations, and strongly underestimated by semiempirical techniques in all three reactions. Only CCSD(T) calculations with correlation consistent triple zeta basis sets are able to reproduce the experimental reaction energy within chemical accuracy (0.05 eV). B3LYP/6-31G* calculations are closer to experiments than UMP2/6-311G**. For the two semiempirical techniques, the improvement of MSINDO over PM3 is quite evident from the data in Table 1, and roughly speaking, the deviation of MSINDO from experiment is 50-70% of the PM3 deviation.

For the H elimination (O(^{3}P) + RH → OR + H) channel, the reaction energies calculated using B3LYP/6-31G* are in better agreement with experiment than UMP2/6-311G**. Again, semiempirical techniques largely underestimate the

reaction energy, and MSINDO substantially improves over PM3. Note in Table 1 that for the UMP2 and B3LYP calculations the reaction energy for H elimination is larger than the barrier for H abstraction. C-C breakage is also possible in the reactions involving ethane and propane, and the reaction energies of these processes are not all that different from H abstraction. Much as happens for H elimination, the B3LYP/6-31G* predictions are closer to experiment than UMP2/6-311G** and MSINDO improves over PM3, although both semiempirical Hamiltonians largely underestimate the experiments. It should be noted that several other products are possible. For instance, double H elimination after O addition to the hydrocarbon leads to aldehydes (formaldehyde, acetaldehyde, propanal) and ketones (propanone). Also double H atom abstraction leads to water and a hydrocarbon diradical. Although we observe all of these products in our reaction dynamics studies, we have omitted them in Table 1 as they are very minor products.

Regarding the reaction barriers, it can be clearly seen in Table 1 why processes other than H abstraction have not been extensively investigated in the past. Whereas H abstraction can proceed through barriers surmountable by $O(^3P)$ atoms generated by UV laser photolysis of NO_2 or SO_2, barriers of about 2 eV make H elimination or C-C breakage inaccessible under typical laboratory conditions. However, LEO conditions involve collision energies substantially larger than these barriers, allowing for generation of oxyradicals by H elimination processes or direct C-C bond breakage. Both novel reaction pathways have been very recently detected in molecular beam experiments involving hyperthermal $O(^3P)$ atoms [16, 19]. Therefore, it is interesting to carry out a detailed analysis of the properties of the stationary points connecting reagents with H elimination and C-C breakage products. Whereas B3LYP/6-31G* calculations of reaction energies are in better agreement with experiments than UMP2/6-311G** in all cases, we observe different behavior for the reaction barriers, here using CCSD(T) data as a benchmark for comparison. The abstraction barriers are clearly underestimated by B3LYP/6-31G* but are satisfactorily reproduced by UMP2/6-311G**. For H elimination, there are at least two saddle points that connect reagents and products in all three reactions. The CCSD(T) lowest energy H elimination barrier is somewhat better reproduced by B3LYP/6-31G* than by UMP2/6-311G**, whereas neither the DFT nor UMP2 calculations cleanly agree with CCSD(T) for the higher energy barrier. It is noteworthy that B3LYP and UMP2 predictions always give a lower and upper bound to the CCSD(T) energies. C-C breakage barriers have about the same height as the H elimination barriers. For the only C-C breakage barrier where we have conducted CCSD(T) calculations, the DFT estimates seem to be more accurate than UMP2, and again both represent upper and lower bounds to the CCSD(T) values.

An illustrative comparison of abstraction, H elimination and C-C breakage processes for the reactions of $O(^3P)$ with methane, ethane and propane is depicted in Figure 1. The graph shows energies calculated at the B3LYP/6-31G* level. For H abstraction processes (Figure 1(a)) the reaction with methane seems to be the more
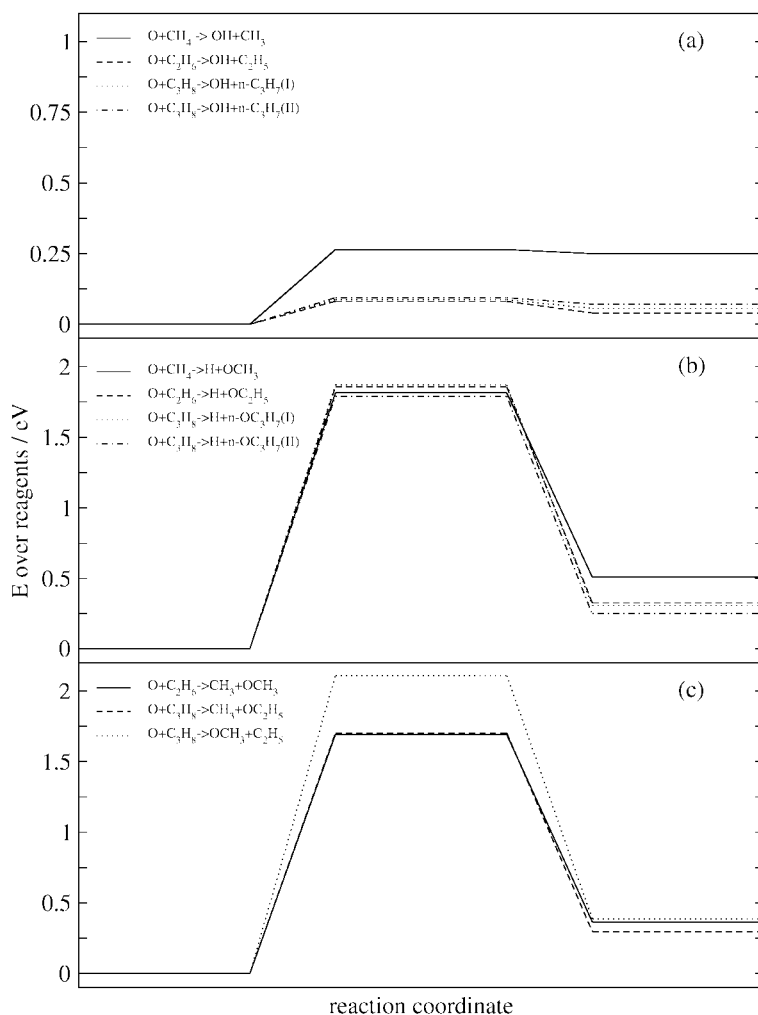
Figure 1. Energy profiles of the most important reaction channels in the O(^{3}P) + methane, ethane and propane reactions. (a) H abstraction O(^{3}P) + RH → OH + R. (b) H elimination O(^{3}P) + RH → H + RO. (c) C-C breakage O(^{3}P) + R → OR' + R". The energy scale of (a) is half that of (b) and (c). The energy of the stationary points refers to B3LYP/6-31G* calculations.

endoergic one whereas the reactions with ethane and propane show very similar reaction energies. This is in agreement with experiments. The B3LYP/6-31G* trends in the barriers are supported by CCSD(T) calculations in the reactions with methane and ethane. The reaction with methane has the largest barrier, whereas there are are only small differences between barriers for H abstraction in ethane or propane, much as it happens in the reaction energies. This agrees with the values of

the thermal rate constants at room temperature for the three systems mentioned in the introduction. B3LYP/6-31G* calculations for H elimination (see Figure 1(b)) indicate that methoxy generation is relatively more endoergic than formation of ethoxy or n-propoxy radicals, and this is supported by the rest of quantum chemistry techniques. This would indicate that longer chains more successfully stabilize oxyradicals. The lowest energy barriers for H elimination are however very similar for all three reactions, and this is supported by all the calculations reported in Table 1. Note that there are other saddle points at higher energy that can also lead to H elimination that have been omitted in the figure for clarity. Regarding C-C breakage, all the product channels considered here for the reactions with ethane and propane are within 0.1 eV according to B3LYP and UMP2 calculations and 0.2 eV according to experiments. The lowest energy barriers for C-C breakage in ethane and propane are also very similar. Independence of barrier height for C-C breakage with the hydrocarbon chain length has been previously reported for $O(^3P)$ + linear saturated hydrocarbon reactions involving hydrocarbons up to heptane [28]. However, Table 1 and Figure 1(c) show the presence of higher energy barriers that can also lead to C-C breakage under LEO conditions. We have plotted the higher energy saddle point in the $O(^3P)$ + C_3H_8 reaction as this is the lowest energy saddle point that we have located leading to the OCH_3 + C_2H_5 product. The 0.3 eV higher energy of this saddle point with respect to that leading to the CH_3 + OC_2H_5 product suggests that the preferred approach of $O(^3P)$ to propane molecules involves interaction with the secondary carbon atom rather than with the primary ones.

Semiempirical predictions of the reaction barriers show many of the trends revealed in the calculations of the reaction energies. Thus MSINDO clearly improves over PM3, particularly in regards to the saddle points involved in the H elimination and C-C breakage processes. It is also interesting to note that although the performance of MSINDO regarding the reaction energies is not as accurate as would be desired, the barrier heights are very satisfactorily described. Indeed, the root mean square deviation of the MSINDO barriers with respect to B3LYP/6-31G* values is only 0.20 eV. PM3 deviations are much larger. In addition we have failed to locate any of the C-C breakage saddle points at the PM3 level, and the geometry optimizations attempted using initial geometry guesses coming from optimized saddle points from the rest of the techniques all lead to H elimination saddle points.

What we learn from the electronic structure calculations carried out here is that short-chain hydrocarbons can experience a variety of reactions upon collisions with hyperthermal $O(^3P)$ atoms. We find that H elimination and C-C breakage may compete with the lower barrier H abstraction at energies above 2 eV, opening new mechanisms for damage in LEO. The recently developed MSINDO Hamiltonian shows improved performance with respect to PM3. Although MSINDO reaction energies substantially underestimate the experiments, MSINDO reproduces the reaction barriers calculated using higher accuracy first-principles methods very satisfactorily.

3. Dynamics

3.1. COMPUTATIONAL DETAILS

We have interfaced the MSINDO Hamiltonian with a fifth-order predictor sixth-order corrector integrator of the classical equations of motion to investigate the dynamics of the title reactions. Equations of motion are solved with a 10 a.u. time integration step. Trajectories are started with an initial distance of 12 a.u. between the O(^{3}P) projectile and the target hydrocarbon center of mass. Around 10 000 trajectories have been calculated at various collision energies relevant to LEO conditions. Initial conditions of the hydrocarbons are sampled from zero point energy motion. Results for H abstraction and elimination in the reactions involving propane take into account the possibility of both primary and secondary H atoms. The thermodynamics of these two channels are slightly different, and therefore analysis of energy partitioning has to be carried out separately. Energy disposal data for o+propane reported here is therefore an average of processes involving primary and secondary H atoms weighted according to the respective total cross sections.

As mentioned before, we detect in our reaction dynamics calculations a variety of reaction products other than H abstraction, H elimination or C-C breakage. The cross sections of these other reaction channels (such as aldehyde + 2H, or H_2O + hydrocarbon dirradical) are much smaller than those for the three more important processes, and therefore we omit a detailed analysis of these channels here.

3.2. CROSS SECTIONS

Reactive cross sections for H abstraction, H elimination and C-C breakage as a function of collision energy are presented in Figure 2.

Figure 2(a) shows the H abstraction cross sections. The size of the cross sections is apparently correlated with the length of the hydrocarbon chain. However, the small difference in the barrier heights for H abstraction is not important enough to explain the trends observed in the cross sections, particularly given that most of the energies considered in the dynamics studies are way above the barrier. Instead, the cross section correlates closely with number of H atoms in the target molecule, which obviously increases with the chain length. At E_{coll} = 3.92 eV, the propane : ethane : methane cross section ratio is 2.00 : 1.46 : 0.63, which is very close to the ratio of hydrogen atoms (2.0 : 1.5 : 1.0). Later we show that angular distributions for H abstraction at high energies is dominated by forward scattering, so a stripping process seems to dominate the reaction dynamics, which means that the cross section should scale with the number of exposed hydrogen atoms (i.e., all the hydrogen atoms for these small molecule targets).

H elimination cross sections are given in Figure 2(b). Here the dependence of the cross sections on the length of the hydrocarbon chain is not as evident like it is for H abstraction. Instead the H elimination cross sections all have a very similar size and threshold. An increase in the cross sections for the longer
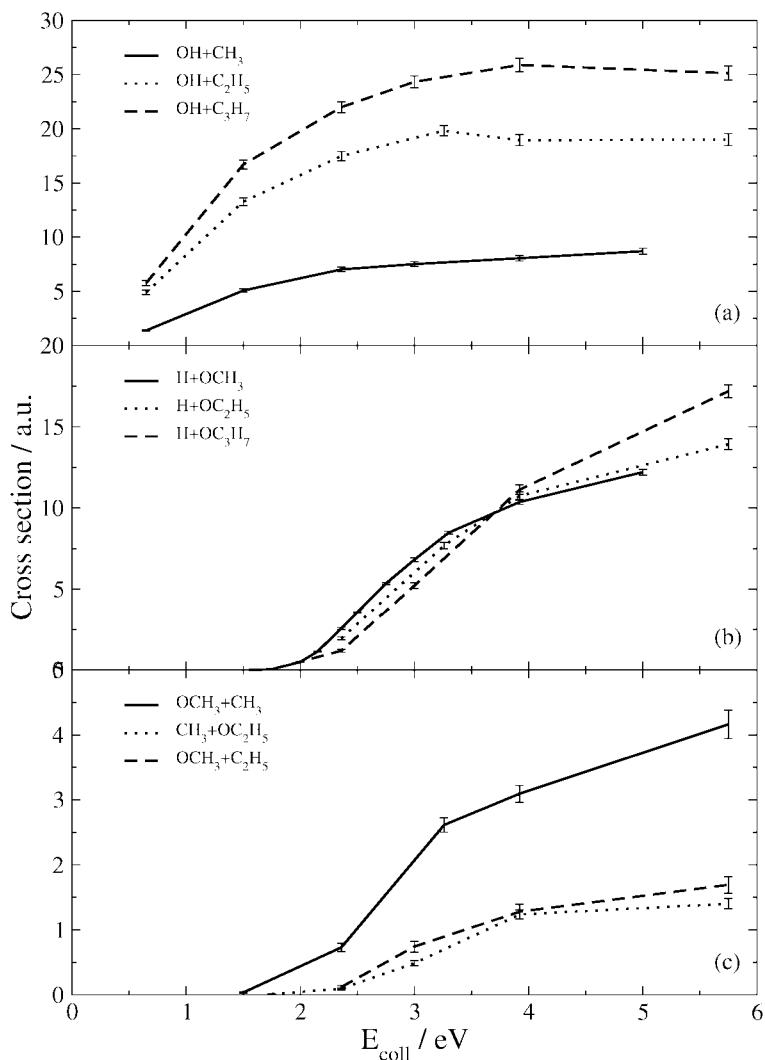
Figure 2. Excitation functions of the most important reaction channels in the O(^{3}P) + methane, ethane and propane reactions. (a) H abstraction O(^{3}P) + RH → OH + R. (b) H elimination O(^{3}P) + RH → H + RO. (c) C-C breakage O(^{3}P) + R → OR' + R".

hydrocarbon chains be inferred at high energies, but it is a minor effect. Two factors seem to be responsible for these results. First the reaction barriers for H elimination are all about the same. Second, in order for H elimination to occur, the incoming O atom needs to impulsively hit a carbon atom (rather than a hydrogen atom), which means that the number of hydrogen atoms in the molecule is not important. In addition, we find that for ethane and propane, the most effective

impulsive collisions are ones where the axis of the molecule is collinear with the incident relative velocity vector. This means that the effective area of the molecule that leads to H elimination is about the same for methane, ethane and propane.

It should also be noted that whereas in the case of the O(^{3}P) reactions with ethane and propane H elimination has a smaller cross section than H abstraction, in the case of methane H elimination takes over H abstraction at high energies. This is somewhat surprising given that there is a difference of about 1.5 eV in the reaction barriers that would favor H abstraction. This is direct evidence of the fact that knowledge of the O(^{3}P) + hydrocarbon reaction pathways at low energies cannot be directly extrapolated to LEO conditions and suggests the necessity of developing detailed studies at high energies to properly characterize the microscopic mechanisms occurring under hyperthermal conditions. Very recently [19], H elimination cross sections have been measured in a crossed-beams experiments for O(^{3}P) + CH$_4$. Comparison of those measurements with our MSINDO calculations reveals a difference in the MSINDO and experimental thresholds that is consistent with the difference between MSINDO and CCSD(T)/AUG-cc-pVTZ barrier heights. More importantly, the slope of the experimental excitation function can only be reproduced by the calculations when the excited surfaces of overall triplet multiplicity adiabatically correlating reagents and products are explicitly accounted for in our treatment.

Figure 2(c) shows the cross sections for the principal C-C breakage processes that take place in the O(^{3}P) reactions with ethane and propane. We distinguish two C-C breakage reaction channels in O + propane, OC$_2$H$_5$ + CH$_3$ and OCH$_3$ + C$_2$H$_5$. We do not observe apparent differences in the cross sections of these two channels at high energies. However, the data of Table 1 and Figure 1(a) indicate that these processes have slightly different barriers, of about 0.2 eV in the MSINDO calculations. This turns into a shift in the thresholds, and whereas we observe a very small cross section leading to OC$_2$H$_5$ + CH$_3$ at E$_{coll}$ = 1.75 eV, we do not see any reactivity to OCH$_3$ + C$_2$H$_5$. We note that although the cross sections for both propane C-C breakage channels are smaller than O + ethane C-C breakage cross sections, the global O + propane C-C breakage cross section overlaps that for ethane at high energies. Remarkably, although H elimination and C-C breakage have similar reaction barriers, H elimination has clearly a larger cross section. This can be rationalized if one imagines that the initial step for H elimination and C-C breakage is the same, namely hard impact of the O on a carbon atom, and that this is followed either by elimination of H or C-C breakage, with the probability of each channel being determined by the number of hydrogen atoms that can eliminate compared to the number of C-C bonds that can break. In fact, when an O(^{3}P) impacts directly with a C atom of C$_2$H$_6$, there are three hydrogen atoms that can eliminate but only one C-C bond that can break. The calculated H elimination : C-C breakage cross section ratio in the O(^{3}P) + C$_2$H$_6$ reaction throughout the collision energy interval considered is in fact very close to 3.0, in qualitative agreement with this statistical argument.

3.3. ENERGY DISTRIBUTIONS

Figure 3 presents product average fractions of the available energy that appear in selected product degrees of freedom as a function of collision energy for the H abstraction processes taking place in the $O(^3P)$ reactions with methane, ethane and propane. We consider energy release to translation, OH vibration and rotation, and internal energy of the hydrocarbon radical. We focus first on the high collision energy regime. Average fractions of product translational energy (Figure 4(a)) are the largest in all reactions and increase with collision energy. However, it can be seen that the larger the hydrocarbon is, the smaller the fraction of translational energy is. At high energies OH is vibrationally cold (Figure 4(b)) and there is little variation of the OH vibrational energy fractions with collision energy or with the reaction under consideration. However, OH fractions of rotational energy decrease with collision energy and depend on the hydrocarbon; the smaller the product alkyl radical is, the larger the OH average rotational energy fraction is. The reverse trend is noticed for the average fractions of the alkyl radical internal energy, and whereas the CH_3 fraction internal energy is barely above zero point at high energies, the average fraction of C_2H_5 and C_3H_7 are respectively larger and larger. In fact, in the $O(^3P)$ + C_2H_6 and C_3H_8 reactions the average fraction of internal energy of the alkyl radical is larger than the fraction in OH rotational energy.

Let us consider now the low collision energy results. McKendrick and coworkers experiments [6] indicate that OH is both vibrationally and rotationally cold at energies barely above the abstraction barrier. Although our MSINDO calculations show that OH generated in the methane reaction is vibrationally cold, OH becomes more excited as the reagent hydrocarbon becomes larger. The increase in OH vibrational energy with the hydrocarbon is much larger than is seen in the experiments, which is an effect that we demonstrated earlier is an artifact due to the QCT approach, wherein some of the reagent zero point energy ends up as product OH vibrational energy as a result of excessive intramolecular vibrational redistribution [18]. Calculations carried out with methane or ethane having half their usual zero point energies lead to colder OH products, in better agreement with experiments.

We also note that there is a much larger fraction energy released to OH rotation than seen in the experiments. This was shown earlier to be tied to the inaccuracy the MSINDO potential surface, which predicts much looser bending energy curves than is seen in *ab initio* calculations. Thus, although MSINDO is a reasonable technique for determining cross sections, as the barrier heights for the title reactions are accurate, it also contains flaws affecting regions of the potential energy surface that determine energy partitioning. Batches of a few hundred trajectories that we generated using B3LYP/6-31G* at high energies show agreement with MSINDO fractions for translation and OH vibration energy release. However, OH is rotationally cold in the B3LYP/6-31G* results, and the alkyl products are hotter than is predicted by MSINDO, which seems to be in agreement with low
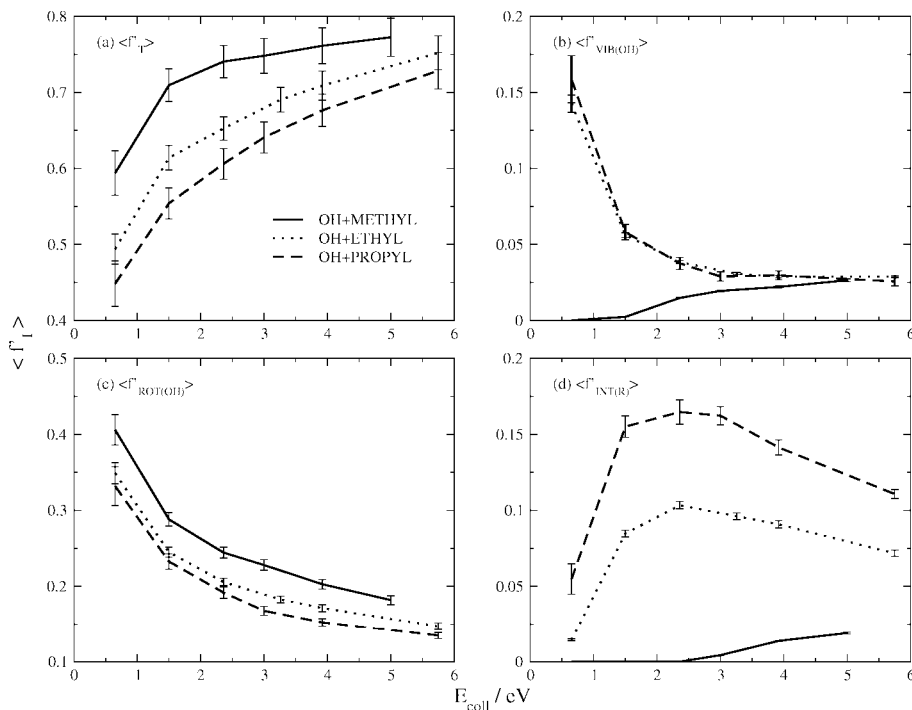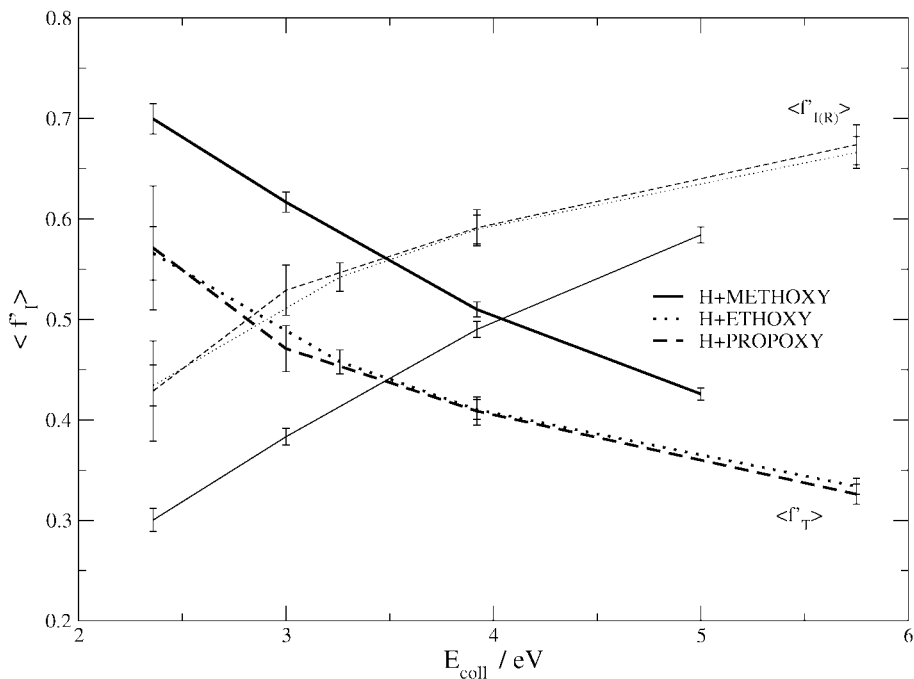
Figure 3. Average fractions of energy in products as a function of collision energy for the H abstraction reaction channel in the O(^{3}P) + methane, ethane and propane reactions. (a) Average fractions of translational energy. (b) Average fractions of OH vibrational energy. (c) Average fractions of OH rotational energy. (d) Average fractions of methyl, ethyl and propyl internal energy.

energy measurements. It should also be noted that although the average fractions of translational and OH vibrational energy calculated by MSINDO and B3LYP/6-31G* are in agreement, the absolute values of the energies differ substantially due to a large overestimation of the reaction energy by MSINDO.

Figure 4 shows the average fractions of energy released in the H elimination reactions. Here we only distinguish between product translational energy and energy released to the oxyradical. The trends are similar for all three hydrocarbons considered, with average fractions of the oxyradical product energy increasing as collision energy increases at the expense of product translation energy. This trend is opposite to that of H abstraction in Figure 3(a) which can be rationalized based on the distinct kinematics of the two reactions. H abstraction (O(^{3}P) + RH → OH + R) can be modeled as having Heavy-Light-Heavy (HLH) kinematics. In HLH systems, the reagents orbital angular momentum is preserved as final orbital angular momentum, which in turn means that larger collision energies are going to provide larger product translational energy. On the other hand, H elimination reactions (O(^{3}P) + RH → H + OR) show HHL kinematics. This implies

Figure 4. Average fractions of energy in products as a function of collision energy for the H elimination reaction channel in the $O(^3P)$ + methane, ethane and propane reactions. Thick lines show average fractions of product translational energy and thin lines are for average fractions of internal energy in the oxyradical molecules.

an inefficient tranformation of initial orbital angular momentum to final orbital angular momentum. Hence, the release of energy to translation with increasing collision energy is not promoted. It is also noticeable that although the trends for H elimination energy release are parallel for the three hydrocarbons, the reactions involving ethane and propane show very similar values of the average fractions of energy that are different from those of methane. Interestingly, akin to what we see in Figure 1(b) for B3LYP/6-31G* calculations, MSINDO reaction energies for H elimination for O + ethane and O + propane are very close, and less exoergic than that for O + methane.

We have also studied how energy is distributed among the various degrees of freedom of the products generated in the C-C breakage reactions. The picture that captures the energy distribution is a mixed contribution of the trends seen for H abstraction and H elimination, although it is much closer to H abstraction. Thus most of the energy available to products (around 70%) is released as product relative translation in all cases ($O(^3P)$ + C_2H_6 → CH_3 + OCH_3, and $O(^3P)$ + C_3H_8 → OCH_3 + C_2H_5, CH_3 + OC_2H_5). The average fractions of product translational energy slowly decrease with increasing collision energy. The remaining energy is distributed differently between the hydrocarbon fragments that result in the C-

C breakage process. The oxyradical receives more energy than the alkyl radical, the latter being barely above its zero point in all cases. In addition, the oxyradical energy increases with collision energy, a trend akin to that reported for H elimination.
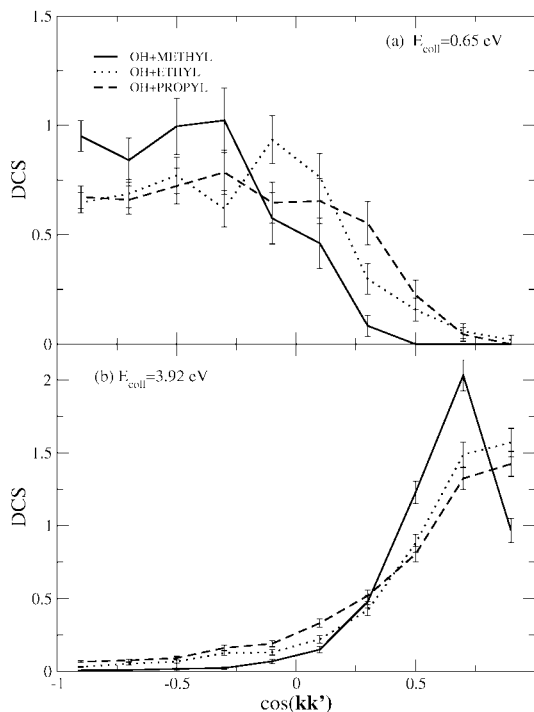
3.4. ANGULAR DISTRIBUTIONS

Figure 5. Angular ditributions expressed in terms of normalized differential cross sections $(\frac{2\sigma}{\pi})(\frac{d\sigma}{d\Omega\prime})$ for the H abstraction reaction channel in the O(^{3}P) + methane, ethane and propane reactions. (a) E_{coll}=0.65 eV. (b) E_{coll}=3.92 eV.

Analysis of angular distributions provides fundamental details of the microscopic reaction mechanisms taking place in O(^{3}P) reactions with saturated hydrocarbons. Figure 5(a) shows angular distributions for H abstraction reactions at 0.65 eV. This collision energy is representative of the reaction near the threshold, and is particularly relevant as a result of experimental measurements on homologous reactions involving larger hydrocarbons at comparable energies above the barrier by Suits and coworkers [29, 30]. Calculated differential cross sections are clearly backward, and this is in qualitative agreement with the experiments. However, the measured angular distributions seem to be more backward than those plotted in

Figure 5(a). In addition, there seems to be a trend toward less backward scattering with increasing hydrocarbon chain length. Therefore it could be argued that calculated angular distributions for hydrocarbons used in the experiments (n-butane, i-butane and cyclohexane) would be even less backward. However, preliminary studies of the $O(^3P)$ + cyclohexane reaction at E_{coll}=0.65 eV carried out by us using the MSINDO Hamiltonian give angular distributions that are coincident with those for ethane and propane within a relatively large statistical uncertainty. The clearly backward scattering for all of the $O(^3P)$ + saturated hydrocarbons reactions reported here at low energies is a direct consequence of the geometry of the saddle point for abstraction. $O(^3P)$ approaches in a nearly collinear way toward the C-H bond that is breaking, and the resulting OH is scattered back towards the direction of the incoming O atom. This behavior is analogous to what is found for a variety of H abstraction reactions with nearly collinear saddle points [31, 32]. The small mismatch between theory and experiment could be due to the quality of the MSINDO Hamiltonian, however, there are several other factors involved. For example, $O(^3P)$ + CH_4 and C_2H_6 QCT calculations in which the hydrocarbon molecules have initially half their zero point energy provide low energy scattering distributions that are more backward than are shown in Figure 5(a). As mentioned before, redistribution of the zero point energy for large molecules has the effect of vibrationally exciting the OH product molecule. Thus it seems that caution has to be used when interpreting the results of QCT calculations involving molecules that have a large zero point energy. Some of these problems were noticed before by Hase, who showed that the classical treatment of molecules having a large number of degrees of freedom provides excessively rapid intramolecular vibrational distribution in unimolecular reactions [33].

Angular distributions for high collision energy calculations (Figure 5(b)) show forward peaked distributions, in clear contrast with the low energy calculations mentioned above. The transition from low energy to large energy scattering distributions is smooth for all three reactions, and for example at E_{coll}=1.5 eV the angular distributions have an important sideways character. This behavior is typical of reactions occurring through a direct mechanism, and whereas the low energy result shows a direct 'rebound' mechanism, the high energy behavior is typical of stripping dynamics, in which the attacking atom simply picks up the atom that is abstracted, changing very little its initial momentum [34].

H elimination angular distributions are presented in Figure 6 at E_{coll} = 2.36 eV (Figure 6(a)) and E_{coll} = 3.96 eV (Figure 6(b)). The low energy distributions in O + methane are predominantly backward. However, the distributions of the $O(^3P)$ reactions with ethane and propane show bimodal character, with peaks in the backward and sideways region. This also happens for O + methane at slightly smaller energies. The two different peaks come from the two different reaction paths whereby H atoms can eliminate, as noted in Table 1. The lowest energy H elimination saddle points are characterized by a near collinear O-C-H arrangement (where H is the atom that eliminates), and is analogous to the well known SN_2

mechanism. Trajectories following this reaction path lead to backward scattering, as the H atom that eliminates exits in the same direction as the incoming O(^{3}P) atom. On the other hand, the geometry of the higher energy saddle point implies a near perpendicular O-C-H arrangement, which in turn leads to sideways scattering. Thus the bimodal distributions seen in Figure 6(a) are the result of the contribution of two different reaction paths for H elimination that can take place in all three reactions. At higher energies, the distinct contribution of both reaction paths fades, and the angular distributions become significantly broader. The flux scattered in the backward distribution is larger than that in the forward, though.
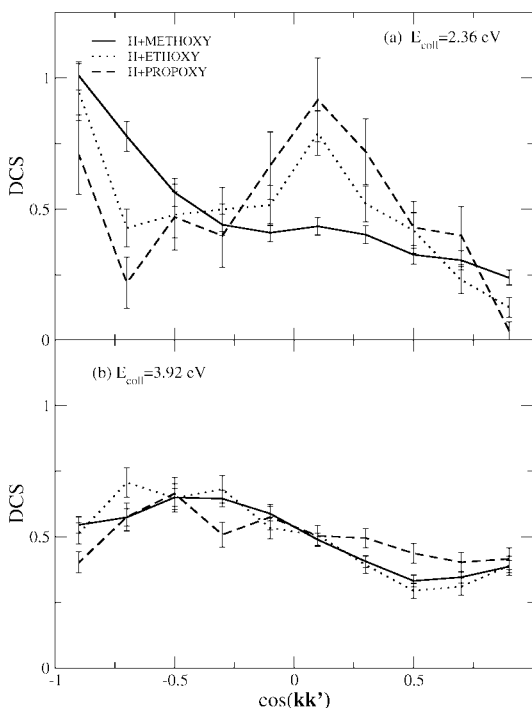
Figure 6. Angular distributions expressed in terms of normalized differential cross sections $(\frac{2\sigma}{\pi})(\frac{d\sigma}{d\Omega'})$ for the H elimination reaction channel in the O(^{3}P) + methane, ethane and propane reactions. (a) E_{coll}=2.36 eV. (b) E_{coll}=3.92 eV.

We finish our analysis by mentioning angular distributions for C-C breakage. The angular distributions at energies near threshold in O + ethane reveal the presence of two reaction pathways, much as occurs in H elimination. The predominant peak is backward and has its origin on the geometry of the C-C breakage saddle point reported in Table 1. This saddle point is characterized by a near collinear O-C-C arrangement, which implies that the CH$_3$ fragment is scattered in the same direction as the incoming O atom. The second peak comes from ap-

proach of the oxygen atom perpendicular to the C-C bond, resulting in sideways scattering. At high energies the contributions of a pure SN_2 process seem to vanish, and although the scattering distributions are rather broad, they are significantly sideways peaked. Analogous trends are observed in both C-C breakage processes that are possible in the $O(^3P) + C_3H_8$ reaction.

4. Concluding Remarks

We have performed extensive theoretical studies of the $O(^3P) + CH_4$, C_2H_6 and C_3H_8 reactions, primarily focusing on high collision energies so as to simulate low Earth orbit conditions.

   Under such high energy conditions, a variety of product channels other than the archetypal H abstraction to give OH plus an alkyl radical are open. Among these, the most important are H elimination to generate oxyradicals, and C-C breakage leading to oxy and alkyl radicals. The reaction energies and barriers for H elimination and C-C breakage have been characterized using several electronic structure techniques. Although H elimination is slightly endoergic and C-C breakage is thermoneutral, both reaction channels show similar barriers of about 2 eV. These barriers are easily surmountable under LEO conditions, and our predictions confirm experimental findings that these high energy reaction paths exist.

   Reaction dynamics investigations of cross sections reveals that at under LEO conditions H abstraction and C-C breakage are both competitive with H abstraction. In fact, in $O(^3P) + CH_4$ the H elimination cross sections are larger than the H abstraction cross sections at high energies. Analysis of energy distributions in products indicates that kinematics factors control energy partitioning. Abstraction reactions can be modeled by HLH kinematics, where product translation energy is the most excited product degree of freedom, whereas OH and alkyl radicals are both fairly cold. H elimination corresponds to HHL kinematics, and in this case the internal energy of the alkoxy radical is more significant. C-C breakage reactions are not easily associated with either of the previous models, and translational excitation of products is more important than internal excitation of the oxyradical, while the partner alkyl radical product does not receive a large amount of excitation.

   An analysis of the angular distributions reveals that the microscopic mechanism for H abstraction corresponds to a rebound mechanism at low energies and stripping dynamics at high energies. Near threshold angular distributions for H elimination and C-C breakage show contributions of two different reaction pathways. The SN_2-like mechanism is responsible for backward scattering while the slightly higher energy bent approach leads predominantly to sideways scattering.

   Although the work presented here unveils many details of novel processes that take place under LEO conditions, a thorough analysis of the fundamentals of materials damage in LEO clearly requires us to study the interactions of hyperthermal $O(^3P)$ atoms with condensed-phase surfaces analogous to those coating spacecraft. In work which is currently underway, we are investigating $O(^3P)$ hyperthermal

interactions with hydrocarbon self-assembled monolayers as a more realistic representation of erosion of a polymer surface. Preliminary results suggest the presence of reaction channels that are similar to those found here, and with dynamics properties that make contact with experiments on O(^{3}P) hyperthermal collisions with liquid hydrocarbon surfaces [35].

Acknowledgements

References

1. J. Warnatz, in *Combustion Chemistry*, ed. W. C. Gardiner, Jr. (Springer-Verlag, Berlin, 1984).
2. D. L. Baulch, C. J. Cobos, R. A. Cox, C. Esser, P. Frank, T. H. Just, J. A. Kerr, M. J. Pilling, J. J. Troe, R. W. Walker, and J. Warnatz, J. Phys. Chem. Ref. Data **21**, 445 (1992).
3. D. L. Baulch, C. J. Cobos, R. A. Cox, C. Esser, P. Frank, T. H. Just, J. A. Kerr, M. J. Pilling, J. J. Troe, R. W. Walker, and J. Warnatz, J. Phys. Chem. Ref. Data **21**, 468 (1992).
4. N. Cohen and K. E. Westberg, J. Phys. Chem. Ref. Data **20**, 1218 (1991).
5. P. Andresen and A. C. Luntz, J. Chem. Phys. **72**, 5842 (1980); A. C. Luntz and P. Andresen, *ibid* **72**, 5851 (1980).
6. G. M. Sweeney, A. Watson, and K. G. McKendrick, J. Chem. Phys. **106**, 9172 (1997).
7. F. Ausfelder and K. G. McKendrick, Prog. React. Kinet. Mec. **25**, 299 (2000).
8. T. Suzuki and E. Hirota, J. Chem. Phys. **98**, 2387 (1993).
9. L. J. Leger and J. T. Visentine, J. Spacecraft Rockets **23**, 505-511 (1986).
10. L. E. Murr and W. H. Kinard, Am. Sci. **81**, 152-165 (1993).
11. A. Jursac, *U.S. Standard Atmosphere*, (US. Government Printing Office, Washington D.C., 1976).
12. Z. A. Iskanderkova, J. I. Kleiman, Y. Gudimenko, and R. C. Tennyson, J. Spacecraft Rockets **32**, 878-884 (1995).
13. B. Cazaubon, A. Paillous, J. Siffre, and R. Thomas, J. Spacecraft Rockets **35**, 797-804 (1998).
14. T. K. Minton and D. J. Garton, in *Chemical Dynamics in Extreme Environments*, ed. R. A. Dressler (World Scientific, Singapore, 2001) p. 420-463.
15. B. A. Banks, K. K. de Groth, S. L. Rutledge, F. J. DiFilippo, *Prediction of In-Space Durability of Protected Polymers Based on Ground Laboratory Thermal Energy Atomic Oxygen*, (NASA, Washington D.C., 1996).
16. D. J. Garton, T. K. Minton, D. Troya, R. Z. Pascual, and G. C. Schatz, 2003, *Hyperthermal Reactions of O(^{3}P) Atoms with Alkanes: Observations of Novel Reaction Pathways in Crossed-Beams and Theoretical Studies*, J. Phys.Chem. A, in press, ASAP paper 10.1021/jp0226026.
17. D. Troya, R. Z. Pascual, and G. C. Schatz, 2003, *Theoretical Studies of the O(^{3}P) + Methane Reaction*, J. Phys. Chem. A, in press.
18. D. Troya, R. Z. Pascual, D. J. Garton, T. K. Minton, and G. C. Schatz, 2003, *Theoretical Studies of the O(^{3}P) + Ethane Reaction*, J. Phys. Chem. A, in press, ASAP paper 10.1021/jp034028j.

19. D. Troya, G. C. Schatz, D. J. Garton, and T. K. Minton, 2003, *Crossed-Beams and Theoretical Studies of the $O(^3P) + CH_4 \rightarrow H + OCH_3$ Reaction Excitation Function,* in preparation.
20. D. J. Garton, T. K. Minton, B. Maiti, D. Troya, and G. C. Schatz, J. Chem. Phys. **118**, 1585 (2003).
21. J. J. P. Stewart, J. Comput. Chem. **10**, 209-220 (1989).
22. B. Ahlswede and K. Jug, J. Comput. Chem. **20**, 563-571 (1999).
23. T. Bredow, G. Geudtner, and K. Jug, J. Comput. Chem. **22**, 861-887 (2001).
24. M. W. Schmidt, K. K. Baldridge, J. A. Boatz, S. T. Elbert,M. S. Gordon, J. H. Jensen, S. Koseki, N. Matsunaga,K. A. Nguyen, S. J. Su, T. L. Windus, M. Dupuis, J. A. Montgomery, J. Comput. Chem. **14**, 1347 (1993).
25. Jaguar 4.1, Schrodinger, Inc., Portland, Oregon, 2000.
26. W.B. DeMore, S.P. Sander, D.M. Golden, R.F. Hampson,M.J. Kurylo, C.J. Howard, A.R. Ravishankara, C.E. Kolb, M.J. Molina, *ChemicalKinetics and Photochemical Data for Use in Stratospheric Modeling. Evaluation No. 11,*JPL Publ. 94-26; NASA Panel for Data Evaluation, Jet PropulsionLaboratory, (California Institute of Technology, Pasadena, 1994) p. 194.
27. S. J. Blanksby and G. B. Ellison, Acc. Chem. Res. **36**, 255-263 (2003).
28. A. Gindulyte, L. Massa, B. A. Banks, and S. K. Rutledge, J. Phys. Chem. A **104**,9976 (2000).
29. X. Liu, R. L. Gross, and A. G. Suits, J. Chem. Phys. **116**, 5341 (2002).
30. X. Liu, R. L. Gross, G. E. Hall, J. T. Muckermann, and A. G. Suits, J. Chem. Phys. **117**, 7947 (2002).
31. M. J. Lakin, D. Troya, G. Lendvay, M. González, and G. C Schatz, J. Chem. Phys. **115**, 5160 (2001).
32. R. Z. Pascual, G. C. Schatz, G. Lendvay, and D. Troya, J. Phys. Chem. A **106**, 4125 (2002).
33. D.-H. Lu and W. H. Hase, J. Chem. Phys. **91**, 7490 (1989).
34. R. D. Levine and R. B. Bernstein, *Molecular Reaction Dynamics andChemical Reactivity* (Oxford University Press, New York, 1987).
35. J. Zhang, D. J. Garton, and T. K. Minton, J. Chem. Phys. **117**, 6239 (2002).

QUASICLASSICAL TRAJECTORY STUDIES OF THE DYNAMICS OF BIMOLECULAR REACTIONS OF VIBRATIONALLY HIGHLY EXCITED MOLECULES

ERIKA BENE and GYÖRGY LENDVAY
Institute of Chemistry, Hungarian Academy of Sciences
*H-1025 Budapest, P.O. Box 17, Hungary*

GYÖRGY PÓTA
Institute of Physical Chemistry, University of Debrecen
H-4010 Debrecen, P. O. Box 7, Hungary

Abstract. Excitation functions from quasiclassical trajectory calculations on the H + $H_2O \rightarrow OH + H_2$, H + HF $\rightarrow$ F + H_2 and H + H'F $\rightarrow$ H' + HF reactions indicate a different behavior at low and high low and high vibrational excitation of the breaking bond. All these reactions are activated when the reactant tri- or diatomic molecule is in vibrational ground state or in low vibrationally excited states. i.e. there is a nonzero threshold energy below which there is no reaction. In contrast, at high stretch excited states capture-type behavior is observed, i.e. at low translational energies the reactive cross section diverges. The latter induces extreme vibrational enhancement of the thermal rate consistent with the experiments. The results indicate that the speed-up observed at high vibrational excitation is beyond the applicability of Polanyi's rules; instead, it can be interpreted in terms of an attractive potential acting on the attacking H atom when it approaches the reactant with a stretched X-H bond.

1. Introduction

Collisions of highly vibrationally excited molecules is commonly a topic in the field of unimolecular reactions [1,2,3,4,5]. Collisions of vibrationally excited molecules in that field are studied in the context of energy transfer, namely, when nonreactive but inelastic collisions change the energy content of the molecule that may undergo a unimolecular reaction. The possibility that the collisions of the excited molecules in the gas phase with *reactive* partners can show specific phenomena has traditionally not been considered, except for diatomic molecules. Bimolecular reactions of vibrationally excited molecules have become a subject of intense study recently, when experimental work indicated that a remarkable speed-up and state specificity can be observed when simple molecules in vibrationally excited states collide with reactive partners [6,7,8, 9].

According to the molecular beam experiments on the reaction of vibrationally excited water with H atoms [6-10],

$$H + H_2O(00v) \rightarrow OH + H_2 \qquad \text{(R1, R-1)}$$
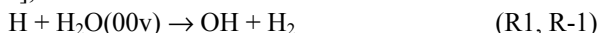
the vibrational excitation of the O-H stretch modes induces a remarkable state specificity: when the H atoms of the water molecule are tagged by isotope labeling, one can observe that the H or D atom is selectively abstracted depending on whether the O-H or O-D bond is vibrationally excited. In the experiments under thermal conditions [8,9] reaction rates exceeding the gas kinetic collision rate were observed that correspond to thermal average cross sections of around 20 $Å^2$. The classical trajectory and quantum scattering calculations indicate that reactivity increases with increasing excitation of the O-H stretch vibrational mode of water [10,11,12]. This is not surprising
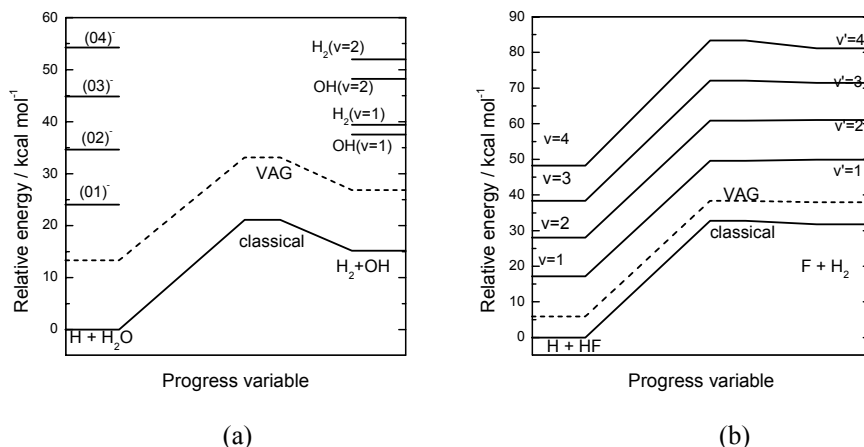
Figure. 1 Potential energy profiles together with some of the reactant energy levels for the H + $H_2O \rightarrow OH + H_2$ (a) and the H + H'F $\rightarrow$ F + H_2 reaction (b). On panel (a) the energies of the stationary points are derived from the WSLFH PES [11], the initial energy levels for water are calculated with a DVR method using Radau coordinates, and the final levels for the products are obtained from the Morse potentials corresponding to the PES. On panel (b) the energies of the stationary points are obtained from the 6-SEC PES [13]; both the initial and final energy levels are calculated from the Morse parameters obtained by fitting a Morse curve to the potential for the separated HF and H_2 oscillators.

as the reaction is characterized by a late barrier which, according to Polanyi's rules [14,15,16] can be more easily surmounted if the atom to be abstracted vibrates with larger amplitude. The magnitude of the increase is, however, much larger than what one can expect based on the bobsled effect that is beyond Polanyi's rules. The details of how and why the reactant in lower and higher vibrationally excited states reacts differently have not been investigated. It is not clear whether the extreme speed-up of the reaction is specific to the reaction of excited H_2O or can also happen in other systems. Accordingly, we studied the reactive cross sections of reaction (R1) and some other processes that are similar to it, namely, the reaction of H atoms with HF. The potential profiles for these two reactions, shown in Fig. 1, are similar: the reaction is highly endoergic. As the potential barrier is late for both, and the extra OH bond in H_2O is a well-behaved spectator bond, and the masses are similar, one can expect similar dynamics.

In this paper we summarize the results of our work performed with the purpose of elucidating the details of how the vibrational excitation increases the rate of the reaction. In the rest of the paper we first summarize the theoretical methods (section 2) then present the results of the quasiclassical study of the dynamics of the H+H$_2$O reaction in section 3 and those on the H + HF abstraction and exchange processes (section 4). In section 5 we attempt to trace back the enhancement of the rate to the properties of the potential surface.

2. Methods

The calculations of reactive cross sections for reactions with vibrationally excited reactants were performed using the standard quasiclassical trajectory method. The peculiarity of the calculations of the reaction of the triatomic water molecule is that trajectories are started from an initial state of H$_2$O which is represented by a "root" trajectory. This is obtained by searching for a periodic trajectory for which the calculated vibrational classical action variables for the three vibrational modes correspond to the selected quantum numbers (+1/2 according to the Einstein-Brillouin-Kramers quantization rule). As water in higher vibrational states is better described by local modes, the (02)$_0$, (03)$_0$, and (04)$_0$ excited states were described by 0 quantum in one O-H stretch, and 2, 3, or 4 quanta in the other, and the bend mode is in ground state (denoted by the subscript 0 after the parenthesis). In all calculations the connection between the orbital angular momentum and the initial impact parameter was considered to be purely classical. It is remarkable that in the calculations at low initial relative translational energy the maximum impact parameter has to be set to a very high value (see Fig. 4. below), otherwise the large reactive cross sections can not be observed. Similarly, as the relative velocity is very small under these conditions, the upper limit of the integration time of the trajectories must be carefully set so that no reactive trajectory should be lost. The calculations for the atom+diatom reactions were performed using an extensively modified parallel version of the VENUS code [17]. The atom + triatomic molecule reactions were performed with the code used in Ref. 11.

3. The reaction of H atoms with vibrationally excited water molecules

The H + H$_2$O $\rightarrow$ OH + H$_2$ and the reverse reaction have served as the testing ground for methods to treat reactions with four-atomic systems. Most of the earlier calculations have been performed on the WDSE potential surface [18] but recently more precise surfaces appeared. The hybrid WSLFH surface [11] combines a spline-fitted reduced dimensional section of the surface with asymptotic reactant and product potentials derived from experiments using simple analytical and switching functions. This potential surface treats the two hydrogen atoms of the water molecules or, alternatively, the two H atoms of the diatomic H$_2$ as equivalent. The OC surface [19], which is based on the rotating bond order formalism [20], treats all hydrogen atoms equivalent but the exchange reaction was not addressed and is not described correctly. The most recent and most extended is the YZCL2 potential surface [21] which is based on Sheppard

interpolation and explicitly treats the exchange channel. All hydrogen atoms are equivalent on this surface. There is a price for the increased accuracy, namely, that the calculation of the potential energy becomes more and more time-consuming in the cited order. We selected for the calculations reported in this work the WSLFH surface, because we focus our interest on the abstraction channel which is adequately described by this PES, and because the computations are much faster on this surface than on the other two.
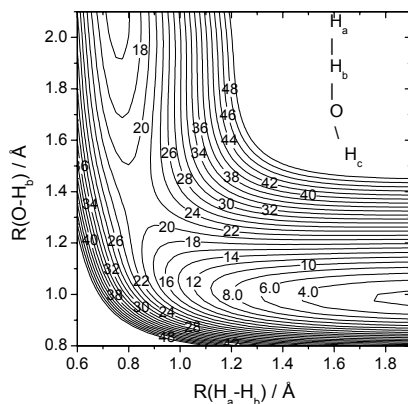
Figure. 2 The section of the WSLFH potential surface of the $H + H_2O \rightarrow OH + H_2$ reaction when the H'-H-O angle is set to 180 degrees and the spectator coordinates are fixed at their values corresponding to the saddle point
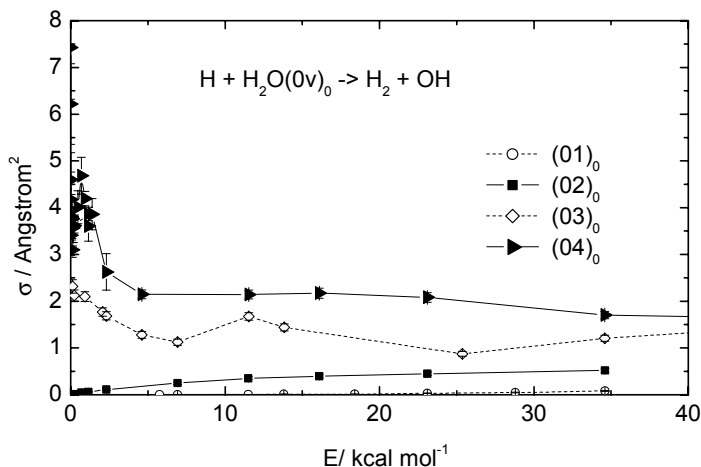
Figure. 3 Excitation function for the $H + H_2O(00v) \rightarrow OH + H_2$ reaction at various vibrational excitations v obtained on the WSLFH potential surface

The collinear section of the WSLFH PES on Fig. 2 shows that, as expected, the potential barrier is slightly in the product H_2 + OH valley. Based on Polanyi's rules one can expect that vibrational excitation of the reactant's O-H bond will be favorable for the reaction. This is what we observed in quasiclassical trajectory calculations on the H+ $H_2O(0v)_0$ reaction at low vibrational excitation (v=0,1, or 2) as shown in Fig. 3. The calculations resulted in a qualitatively different excitation function at low and high vibrational excitation, in agreement with the results reported earlier [10,11] for the OC potential surface of Ochoa and Clary [19]. At low vibrational excitation the reactive cross section is zero at low relative translational energy, and there is a finite threshold for reaction while at high vibrational excitation the reactive cross section diverges at low excitation energy and drops with increasing E_{tr}. At v=0,1,2 the threshold energy decreases with increasing vibrational excitation, being about 17.3, 4.6 and 0.1 kcal mol^{-1}, respectively. The magnitude of the reactive cross section increases with the initial relative translational energy, and at large E_{tr} it is approximately proportional to the initial vibrational quantum number. At v=3,4 the limiting high-energy cross section is also much larger than at lower v, but the large difference as compared to v=0,1,2 is that the reactive cross section decreases with increasing initial relative kinetic energy. At low E_{tr} the cross section increases roughly according to an inverse power law with decreasing E_{tr}. This behavior is characteristic of capture processes [22]. Further details can be obtained from the opacity functions presented in Fig. 4. At low relative translational energy larger reactive probability is observed at large impact parameters than in close to head-on collisions, indicating that the slowly moving reactants are attracted into a reactive arrangement. Increasing the initial relative translational energy, the reactive cross section becomes larger at small impact parameters, which means that if the partners approach fast, the influence of the small attractive force is quickly overridden.
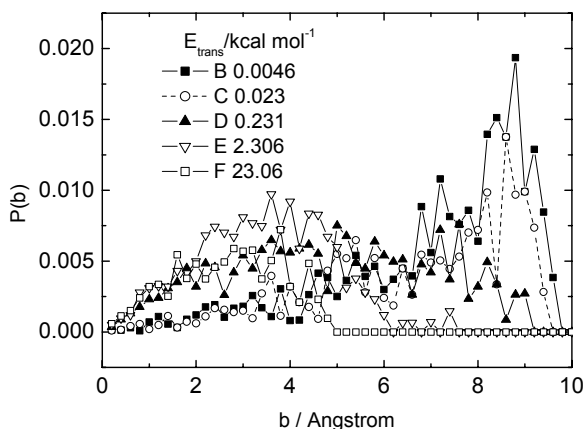

Figure 4 Opacity function for the H + $H_2O(004) \rightarrow$ OH + H_2 reaction at various initial relative kinetic energies

The thermal rate coefficients calculated for the inverse power law excitation functions for the $(04)_0$ state on both the WSLFH and the OC potential surfaces are in very good agreement with the experiments [23]

4. The reaction of H atoms with vibrationally excited HF molecules

The

$$H + HF(v) \rightarrow F + H_2 \qquad\qquad (R2, R-2)$$

reaction is the elementary reaction for which the best potential surfaces are available. Both the 6-SEC surface of Truhlar et al. [13] and the Stark-Werner potential surface [24] are based on ab initio calculations that cover almost all of the electron correlation energy. The saddle point on both surfaces is in the product valley, but both at a non-linear arrangement. In our calculations both the 6-SEC and the SW surfaces were studied with similar results. In this paper we report results based on the 6-SEC surface.

The excitation functions for H abstraction from vibrationally excited HF at various initial vibrational quantum numbers are shown in Fig. 5. The pattern is very similar to
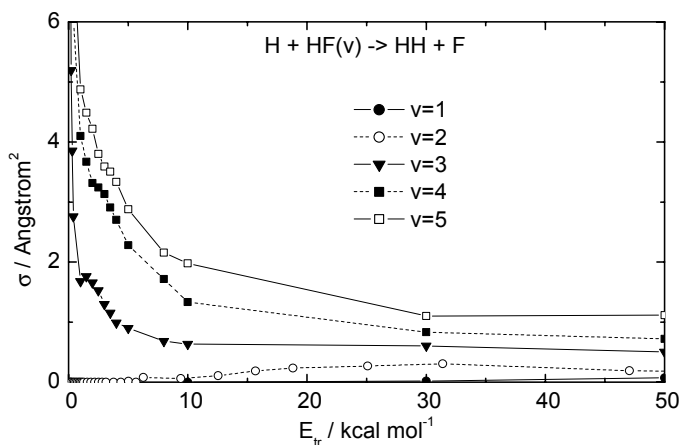

Figure. 5 Excitation function for the $H + HF(v) \rightarrow F + H_2$ reaction at various vibrational excitations v obtained on the 6-SEC potential surface

that of the H + water reaction: activated behavior at low vibrational excitation, up to $v=2$, and capture type excitation functions at higher vibrational excitation beginning with $v=3$. The higher the vibrational excitation the higher is the reactive cross section at any translational energy (so that the $\sigma - E_{tr}$ curves do not cross). The quasiclassical trajectory method allows fine tuning of vibrational excitation and determining more precisely when the reaction switches from activated to capture-like. The excitation functions calculated at non-integer vibrational quantum numbers are shown in Fig. 6. The comparison of Figs. 5 and 6 shows the details of the switch from activated to capture type behavior. At the very high vibrational excitations of Fig. 5 ($v=5,4,3$) at low

initial relative translational energy the cross sections drop smoothly with increasing E_{tr} and follow an inverse power law up to around $E_{tr}=1$ kcal mol^{-1}. At slightly smaller vibrational excitation, $v=2.8$, (Fig. 6) a dip appears at around $E_{tr}=1$ kcal mol^{-1} after which the reactive cross section increases first, then passes a local maximum and continues the pattern started at low translational energies, i.e., drops further (a slight sign of this can already be seen on the $v=3$ curve in Fig. 5 in the form of a shoulder). As
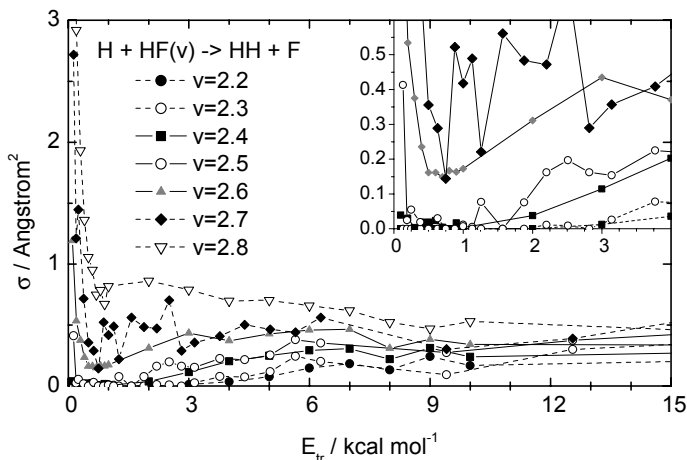
Figure. 6 Same as Fig. 5 but at non-integer HF vibrational "quantum numbers"

section up to a threshold energy with $E_{threshold} \approx 1$ kcal mol^{-1} at $v=2.2$ and ≈ 3 kcal mol^{-1} at $v=2.1$. Except for the statistical scatter in the cross sections, the excitation functions seem not to cross each other at the low excitation range shown in Fig. 6. In particular, at very high translational energies the cross sections increase with increasing v. The final state distributions for the H$_2$ product of this reaction are peaked at $v=0$ independently of the initial vibrational excitation, indicating that the process is vibrationally highly non-adiabatic. The switch from activated to capture type behavior seems not to be restricted to the H + HF abstraction reaction. The excitation function for the exchange channel,

$$H + H'F(v) \rightarrow FH + H' \qquad \text{(R3, R-3)}$$

is shown in Fig. 7 for integer initial vibrational quantum numbers and in Fig. 8. for non-integer "quantum numbers". Activated behavior can be seen for $v=1$ and 2, and beginning with $v=3$ capture-type cross sections are observed. On these capture-type excitation functions a very well expressed feature is what was seen for the abstraction reaction near the switching point between activated and capture-type behavior. Namely, the inverse power decrease of the cross section at low E_{tr} leads to a local minimum from which the cross sections start rising again with increasing relative translational energy. The switching between the activated and capture-type behavior is at around $v=2.4$ or 2.5, very close to that for the abstraction reaction.
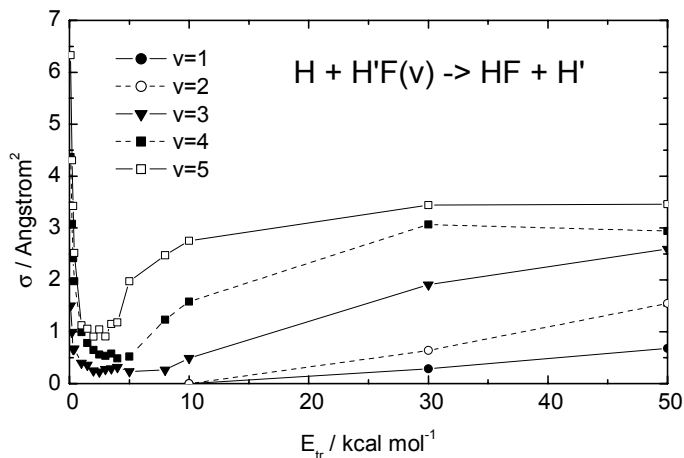
Figure. 7 Excitation function for the H + H'F(v) → FH + H' reaction at various vibrational excitations v obtained on the 6-SEC potential surface
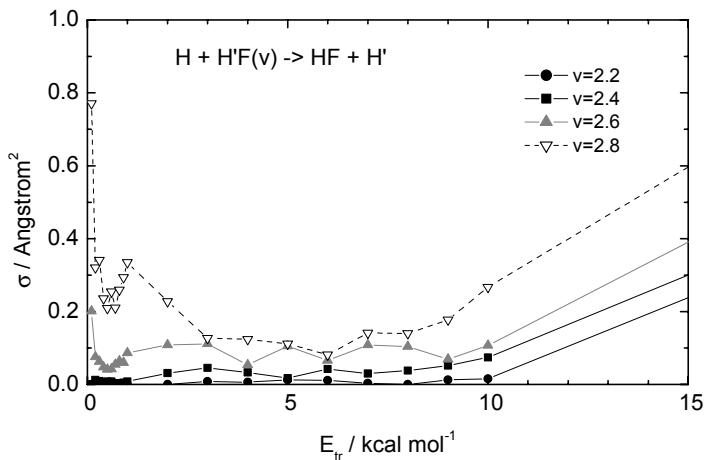

Figure. 8 Same as Fig. 7 but at non-integer HF vibrational "quantum numbers"

5. Reverse reactions

As the change of the excitation function from activated to capture type is not unique to the H + H$_2$O reaction where it was first observed, it seems to be promising to check other reactions. Really, the unusual features of high reactivity can also be observed for the reverse OH + H$_2$($v=1$) reaction on the OC potential surface, while Fig. 7. shows the excitation functions for the very exothermic F + H$_2$(v) reaction for $v=0$ to 4. The

threshold energy is very low even for the reaction of H_2 in vibrational ground state (around 0.9 kcal mol^{-1} at this QCT approximation) in agreement with the low barrier on the PES in the exothermic direction, and quickly decreases to 0.6 and 0.2 kcal mol^{-1} at v=1 and 2, respectively. The switch from activated to capture-type behavior occurs between v=2 and 3, where the threshold disappears and the cross section quickly increases with the decrease of the initial relative translational energy.
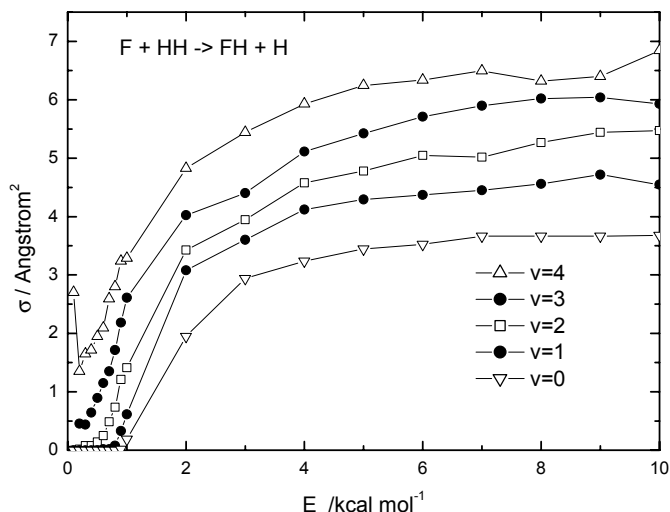

Figure. 9 Excitation function for the F + H_2 (v) → H + HF reaction at various vibrational excitations v obtained on the 6-SEC potential surface

6. Discussion

The quasiclassical trajectory calculations on both exothermic and endothermic (as well as thermoneutral) atom-transfer reactions indicate that the excitation functions for the reaction of an atom with a vibrationally excited reactant undergoes a qualitative change as the vibrational excitation increases. For an endothermic reaction at low vibrational excitation the expectations based on Polanyi's rule are fulfilled. At low kinetic energy there is no reaction, the cross sections increase above zero at a high threshold, and increase slowly and monotonously with the initial relative translational energy. The threshold energy decreases as the vibrational excitation increases, and the rate of increase is similar at different vibrational energies. The same amount of energy is more efficient for enhancing reactivity if invested in the form of vibrational energy than in the form of translational energy, which is one formulation of Polanyi's rule. At higher vibrational excitation energy a different type of excitation function is observed. The cross section is very large at low relative translational energy, and drops quickly, at a close to inverse power law with increasing E_{tr}. The decrease slows down when E_{tr} is around a few kcal mol^{-1}. In certain cases the excitation functions keep decreasing

monotonously, but more and more slowly as E_{tr} increases. In several cases, however, a well defined minimum can be observed. The cross sections start to increase again after the minimum, and may pass a flat maximum. The composite nature of the excitation function indicates that there are two different features that determine its shape: one that is responsible for the divergence of the cross section with decreasing E_{tr} at low relative kinetic energies, and one that causes the slow increase at larger kinetic energies. The latter is very probably the manifestation of Polanyi's rule, similarly to what we described for low vibrational excitation. It is easy to visualize that as the amplitude of the reactant's vibrational motion increases, the reaction rate should increase. However,
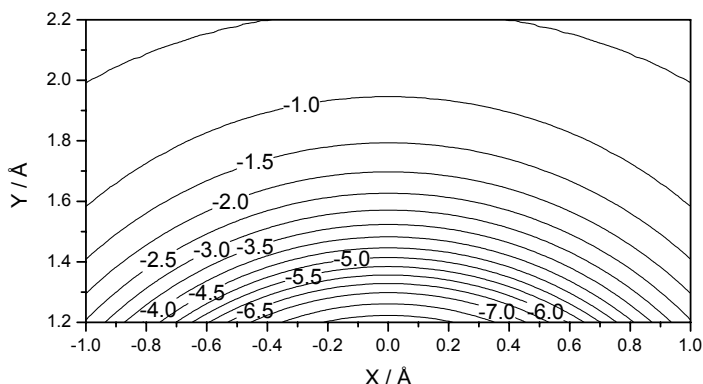

Figure 10 The cross section of the potential surface of the H+ HF(v) $\rightarrow$ H$_2$ + F reaction taken at the HF bond length of 1.3 Å. The potential felt by an H atom at coordinates X and Y approaching the H of HF positioned at the origin of the coordinate system is plotted as a function of the location of the attacking H. The H-F bond points down along the Y axis. Contour lines are spaced 0.5 kcal mol^{-1} from each other. The energy is referred to an HF molecule expanded to 1.3 Å and an H atom at the infinity.

that picture would not explain why the reactive cross section should diverge at low translational energy: it looks like the beneficial effect of the increased vibrational amplitude can be better manifested if the reactants approach slowly. Capture-type excitation functions are characteristic of collisions between partners that exert an attractive force on each other. Investigating potential surfaces for atom-transfer reactions, one can find that there is an attractive interaction between a vibrationally highly excited molecule and an atom for situations that do not occur when the reactant is not vibrationally highly excited, namely, when the breaking bond is significantly stretched. The existence of such an attraction was shown for several ab initio potential surfaces for H + H$_2$O [10,11], but it is not unique to that reaction. Figure 10 shows the potential experienced by the H atom approaching the H atom of an HF molecule when the F-H bonds is extended to the turning point of at the collinear arrangement and at the bent arrangement corresponding to the saddle point of the 6-SEC PES. The potential is attractive already at large distances. The bond of a highly excited molecule can often be relatively long, and if the attacking atom arrives at the right phase, "passing the barrier"

may be a smooth downhill walk. Such an attraction can also be observed on the SW potential surface and not only for H-atom abstraction but also for the exchange reaction.

The idea that the vibrational enhancement of the rate is due to the attractive potential for excited vibrational states of the reactant is closely related to the observation made long ago based on transition state theory [25,26]. Pollak [25] found that for vibrationally highly excited reactants the repulsive pods (periodic orbit dividing surface) is way out in the reactant valley, and the corresponding adiabatic barrier is shallow. Based on this theory one can explain why dynamical thresholds are observed in reactions with vibrationally excited reactants. The simplicity of the theory and its success for mostly collinear reactions has a real appeal. However, to reconcile the existence of a vibrationally adiabatic barrier with the capture-type behavior – which seems to be supported by the agreement of the calculated and experimental rate coefficients [23] – needs further study.

The explanation for the capture-type behavior displayed in the theoretical studies of reactions of vibrationally highly excited reactants can help to make the connection between the properties of the potential surface and the extreme speed-up of the reaction observed experimentally.

7. Acknowledgments

8. References

1. Holbrook, K. A.; Pilling, M. J.; Robertson, S. H. (1996) *Unimolecular Reactions*, John Wiley & Sons, Chichester

2. Forst, W. (1973) *Theory of Unimolecular Reactions*, Academic Press, New York

3. Oref, I. and Tardy, D.C. (1990) Energy transfer in highly excited large polyatomic molecules, *Chem. Rev.*, **90**, 1407-1445

4. Gilbert, R. G.; Smith, S. C. (1990) *Theory of Unimolecular and Recombination Reactions*; Blackwell Scientific Publications, Oxford

5. Hippler, H.; Troe, J. (1989) In *Bimolecular Reactions*; Baggott, J. E., Ashfold, M. N. R., Eds.; The Chemical Society: London.

6. (a) Sinha A. (1990) Bimolecular reaction of a local mode vibrational state: hydrogen atom + water ($4v_{OH}$) -> hydroxyl(v,J) + hydrogen, *J. Phys. Chem.* **94**, 4391-4393 (b) Sinha, A. Hsiao M. C. and Crim F. F. (1991) Controlling bimolecular reactions: Mode and bond selected reaction of water with hydrogen atoms, *J. Chem. Phys.* **94**, 4928-4935; (c) Hsiao M. C., Sinha A. and Crim F. F. (1991) Energy disposal in the vibrational-state- and bond-selected reaction of water with hydrogen atoms, *J. Phys.*

Chem. **95**, 8263-8267; (d) Metz R. B., Thoemke J. D., Pfeiffer J. M. and Crim F. F. (1993) Selectively breaking either bond in the bimolecular reaction of HOD with hydrogen atoms, *J. Chem. Phys.* **99**, 1744-1751; (f) Thoemke J. D., Pfeiffer J. M., Metz R. B. and Crim F. F. (1995) Mode- and Bond-Selective Reactions of Chlorine Atoms with Highly Vibrationally Excited H_2O and HOD, *J. Phys. Chem.* **99**, 13748 – 13754

7. (a) Bronikowski M. J., Simpson W. R. and Zare R. N. (1991) Bond-specific chemistry: 0D:OH product ratios for the reactions H + HOD(100) and H +HOD(001), *J. Chem. Phys.* **95**, 8647-8648 (b) Bronikowski M. J., Simpson W. R. and Zare R. N. (1993) Effect of reagent vibration on the hydrogen atom + water-d reaction: an example of bond-specific chemistry *J. Phys. Chem.* **97**, 2194-2203 (c) Bronikowski M. J., Simpson W. R. and Zare R. N. (1993) Comparison of reagent stretch vs. bend excitation in the hydrogen atom + water-d2 reaction: an example of mode-selective chemistry *J. Phys. Chem.* **97**, 2204-2208 (d) Adelman D. E., Filseth S. V. and Zare R. N. (1993) Integral rate constant measurements of the reaction H +D_2O + HD(v',j')+OD, *J. Chem. Phys.* **98**, 4636-4643.

8. Hawthorne G., Sharkey P. and Smith I.W.M. (1998) Rate coefficients for the reaction and relaxation of vibrationally excited $H_2O|04>^-$ with H atoms and H_2O *J. Chem. Phys.* **108**, 4693-4696.

9. Barnes P. W., Sharkey P., Sims I. R. and Smith I. W. M. (1999) Rate coefficients for the reaction and relaxation of in H2O specific vibrational states with H atoms and H_2O Faraday Discuss. **113**, 167-180.

10. Schatz G.C., Wu G., Lendvay G., Fang D.-C. and Harding L. B. (1999) Reaction of H with highly vibrationally excited water: activated or not?, Faraday Discuss. **113**, 151-165.

11. (a) Wu G., Schatz G.C., Lendvay G., Fang D.C. and Harding L.B. (2000) A new potential energy surface and quasiclassical trajectory study of H + H_2O → OH + H_2, *J. Chem. Phys.* **113**, 3150-3161; (b) *ibid.* (2000) *Erratum, J. Chem. Phys.* **113**, 7712.

12. Zhang D. H., Yang M., Collins M. A. and Lee S.-Y. (2003) Reaction Dynamics of Polyatomic Systems: From A + BCD → AB + CD to X + YCZ_3 → XY + CZ_3, This volume.

13. Mielke S. L., Lynch G. C., Truhlar D. G. and Schwenke D. W. (1993) A more accurate potential energy surface and quantum mechanical cross section calculations for the F+ H_2 reaction, *Chem. Phys. Lett.* **213**, 10-16; Erratum (1994) **217**, 173.

14. Polanyi J.C. (1972) Some Concepts in Reaction Dynamics, *Acc. Chem. Res.* **5**, 161-168.

15. Kuntz P.J., Nemeth E.M., Polanyi J.C., Rosner S.D. and Young C.E. (1966) Energy distribution among products of exothermic reactions. II. Repulsive, mixed, and attractive energy release, *J. Chem. Phys.* **44**, 1168-1184.

16. Smith, I.W.M. (1980) *Kinetics and Dynamics of Elementary Gas Reactions,* Butterworths, London.

17. Hase W.L., Duchovic R.J., Lu D.-H., Swamy K.N., Vande Linde S.R. and Wolf R.J. (1988) VENUS, A General Chemical Dynamics Computer Program.

18. (a) Walch, S.P. and Dunning, T.H. (1980) A theoretical study of the potential energy surface for OH + H_2, *J. Chem. Phys.* **72**, 1303-1311; (b) Schatz, G.C. (1981) A quasiclassical trajectory study of reagent vibrational excitation effects in the OH + H_2

→ H_2O + H reaction, *J. Chem. Phys.* **74**, 1133-1139; (c) Elgersma, H. and Schatz, G.C. (1981) A quasiclassical trajectory study of mode specific reaction rate enhancements in H + $H_2O(v_1, v_2, v_3)$ → OH + H_2, *Intl. J. Quantum Chem., Quantum Chem. Symp.* **15**, 611-619.

19. G. Ochoa de Aspuru and D. C. Clary (1998) New potential energy function for four-atom reactions. Application to OH+H_2, *J. Phys. Chem. A*., **102**, 9631-9637.

20. A. Laganà A., Ochoa de Aspuru G. and E. Garcia (1998) The largest angle generalization of the rotating bond order potential: Three different atom reactions, *J. Chem. Phys.* **108**, 3886-3896.

21. (a) Yang, M., Zhang, D.H., Collins, M.A. and Lee, S.-Y. (2001) Quantum dynamics on new potential energy surfaces for the H_2 + OH → H_2O + H reaction, *J. Chem. Phys.* **114**, 4759-4762; (b) *ibid*. (2001) *Ab initio* potential energy surfaces for the reactions OH + H_2 ↔ H_2O + H, *J. Chem. Phys.* **115**, 174-178.

22. see e.g. Clary D.C. (1995) Reactions of strongly polar ions with molecules, *Chem. Phys. Lett.* **232**, 267-272 and references therein.

23. Barnes P.W., Sims I.R., Smith I.W.M., Lendvay G. and Schatz G.C. (2001) The branching ratio between reaction and relaxation in the removal of H_2O from its |04>⁻ vibrational state in collisions with H atoms, *J. Chem. Phys.* **115**, 4586-4592.

24 Stark K. and Werner H.-J. (1996) An accurate multireference configuration interaction calculation of the potential energy surface for the F+H_2->HF+H reaction, *J. Chem. Phys.* **104**, 6515-6530.

25. see e.g. Pollak E. (1981) A classical determination of vibrationally adiabatic barriers and wells of a collinear potential energy surface, *J. Chem. Phys.* **74**, 5586-5594 and references therein.

26. Garrett B. C. and Truhlar D. G. (1979) Generalized Transition State Theory. Quantum Effects for Collinear Reactions of Hydrogen Molecules and Isotopically Substituted Hydrogen Molecules, *J. Phys. Chem.* **79**, 1079-1112.

TOWARDS A GRID BASED UNIVERSAL MOLECULAR SIMULATOR

ANTONIO LAGANÀ
Dipartimento di Chimica
Università di Perugia, Perugia, Italy

1. Introduction

The evolution of computer technologies from single extremely sophisticated processor machines to clusters of commodity computing nodes and assemblies of heterogeneous computing Grids has shifted the focus of computational chemistry from simple to complex systems and from models to realistic a priori simulations.

A sketch of the present situation in Grid computing is given in ref. [1]. A key advantage of Grid platforms is the flexibility of their operating environments in which either codes or data can be distributed for a total or a partial coordinated concurrent execution on the subset of available machines of the Grid system most suited for the job. Another important feature of these platforms is the capability to operate through interfaces making the utilization of the highly different computer hardware and basic software of these heterogeneous architectures more user friendly. This makes the Grid not only a powerful scalable virtual computer offering to the partner laboratories a significant amount of extra resources, but also a computing environment particularly suited to enhance the development of complex computational applications resulting from the collaboration of geographically distributed laboratories. This has stimulated a great deal of research on the exploitation of the network as an infrastructure for running coarse-grained parallel applications [2, 3, 4] and on the design of tools allowing scientists to use Grid platforms and still rely on the microlanguage of their specific scientific field (with no need for learning about related underlying technicalities [5, 6]).

As a matter of fact, a significant amount of Grid software (like Globus, StaMPI, Pacx-MPI, MPICH-G) has been produced with the specific purpose of enabling multi-institutional research efforts aimed at providing a high performance worldwide computing environment for complex computation oriented applications [7]. This type of environment is appropriate to complement geographically distributed computing platforms and networking infrastructures with a specific middleware acting as a problem solving environment (PSE) [8] devoted to the management of coordinated investigations. The aim of these PSEs is mainly to allow researchers

to build complex computational applications by assembling already available or
ad hoc constructed blocks.

The European Union (EU) is also active in promoting the development of
complex computational applications based on the collaboration of geographically
distributed European scientific laboratories and centers with the aim of "solving
complex problems which cannot be solved with current technologies" [9]. In this
spirit COST [10](European Cooperation in the field of Science and Technical Re-
search whose initiatives follow a bottom up approach allowing scientists to group
and collaborate on common research projects) in Chemistry has launched the D23
Action "*METACHEM: Metalaboratories for complex computational applications
in chemistry*" [11, 12]. Its aim is to promote Grid based collaborative laborato-
ries (Meta-laboratories) committed to deal with the realistic modeling of materials
and processes using *a priori* molecular approaches. A key feature of the Metalab-
oratories is, therefore, the coordinated use of the distributed computer hardware
and software resources, the development of specific Grid based problem solving
environments and the design of Grid oriented computational approaches.

This has pushed the evolution of chemical reactivity computer codes towards
approaches better allowing multiscale treatments based on loosely coupled algo-
rithms building complexity out of a large number of simpler computational tasks.
This has led to the development of Grid based molecular simulations (GMS). A
first prototype GMS has been developed within *METACHEM* for an *a priori* sim-
ulation of molecular beam experiments (*SIMBEX* [13]).

The paper discusses in section 2 the high level structure of the simulator, in
section 3 illustrates the use of advanced tools for concurrent computing and in
section 4 some new approaches designed having in mind large systems.

---

[1] The SIMBEX COST in Chemistry project (D23 003/01) [13] is at present being devel-
oped (mainly for atom diatom systems) by two groups of laboratories gathered together
on a Metacomputer. Some laboratories take care of developing and implementing friendly
computer tools for dealing with metacomputers. The other participating laboratories are
active in developing computational approaches dealing with the molecular nature of re-
active chemical processes. To the first group belong the Department of Mathematics and
Informatics of the University of Perugia that coordinates the project, the Unit for parallel
and distributed computing of CNUCE, Pisa, the Computer Science Department of the
Complutense University, Madrid, the Centre of Excellence for Computing, Budapest, the
Polish Supercomputing and Networking Center, Poznan, and the Central Laboratory for
High Performance Computing of the Research Council, Daresbury. To the second group
belong the Department of Physical Chemistry of the University of the Basque Country,
Vitoria, the School of Chemistry, University of Bristol, Bristol, the Department of Chem-
istry, University of Goteborg, Goteborg, and the Institute of Chemistry of the Academy
of Science, Budapest. More recently, collaborations with other Chemistry, Physics and
Informatics Departments are being established within national and transnational initia-
tives. The prototype SIMBEX application is described in more detail in ref. [14, 15, 16].
The client level consists of a Web browser connected to the portal of SIMBEX. The web
page drives the user to the selection of the specific application, to the collection of the
related input data and to the recollection of the results obtained from the calculations
performed on the Grid. Then the user can start running the application and choose the
virtual monitors needed to follow the evolution of the calculation and the pile up of the
results into relevant statistical indices.

2. The high level structure of the simulator

The assemblage of a GMS requires the convergence of the competences and the action of various experts in calculating molecular electronic structures, heavy particle dynamics and collective measurable properties.

The present version of SIMBEX is implemented on a prototype Grid platform made of three Internet connected Beowulf-like workstation clusters. On this model Grid platform we installed Globus Toolkit 2 [7] for use within Globus Grid. We have also implemented (still within Globus Grid) a local topology-aware distribution system using MPI. This minimizes point-to-point communications over slow links and hides slow-bandwidth communication behind fast traffic and process activity [14].

The high level structure of SIMBEX is articulated into three computational blocks each taking care of a different aspect of the calculation: INTERACTION, DYNAMICS and OBSERVABLES. Each of these blocks is taken care by one or more laboratories of the Metalaboratory.

The first block, INTERACTION, is devoted to the calculation of electronic energies determining the potential energy surface (PES) on which the nuclear motion takes place. The second block, DYNAMICS, is devoted to the integration of the scattering equations to determine the outcome of the molecular process. The third block, OBSERVABLES, is devoted to the reconstruction of the observable properties of the beam from the calculated dynamical quantities. All these blocks require not only different skills and expertise but also specialized computer software and hardware.

The Metalaboratory environment facilitates these tasks by allowing the investigators to use on the network complex packages, to deal with the various steps implemented and maintained in a proper environment, to collect the necessary information from specialized data banks on the web, to perform locally the necessary statistical manipulations as well as to render the results using graphics, animation and virtual reality techniques.

2.1. INTERACTION

The INTERACTION block usually involves the activation of the ABINITIO procedure for the calculation of a sufficiently extended set of *ab initio* values of the electronic energy when these are not available on the web or no routine evaluating the PES in an accurate way is available. To perform *ab initio* calculations of the electronic energy values it is possible to use a wide choice of standard quantum chemistry computational packages like NWChem[17], Gaussian[18], CADPAC[19], Turbomole[20], HONDO[21], etc. involving the expertise of various laboratories. The package presently adopted by SIMBEX is GAMESS-UK[22] and has been specialized for three atom systems. If *ab initio* calculations are impractical to perform, empirical or semiempirical approaches can be adopted. This is often the

case when the system is very large. This part of the procedure is computationally very heavy and particularly suited for being distributed for Grid computing.

A different approach ("on-the-fly") to the use of the ABINITIO procedure is its incorporation as a single value call inside the DYNAMICS block when the potential energy is calculated only at the time it is needed by the integration of the equations of motion.

Once defined the level of accuracy and the modality of use of ABINITIO, one has to define also the characteristics of the grid of points to be considered as well as all the other parameters characterizing the system and the *ab initio* calculations.

A separate group of programs is then used to fit the calculated *ab initio* values (often after some adjustments to reproduce the known spectroscopic properties of the system) to produce a global functional representation of the interaction to be used in the DYNAMICS block. The fitting procedures are not yet standardized to the point of making use of commercial packages. This step still involves a significant amount of human intervention, specific know how and, possibly, ad hoc graphic software and visual manipulation tools.

2.2. DYNAMICS

DYNAMICS, is the second block of the GMS in which dynamical calculations are carried out using either quasiclassical (QCT) or quantum (QM) mechanics approaches.

If the system is small enough (a few light atoms) one can tackle the problem of solving exactly the QM coupled differential equations in the nuclear coordinates generated by the expansion of the global wavefunction of the system [23] in terms of the electronic eigenfunctions and the averaging over the electronic coordinates.

In QM approaches either a time-dependent or a time-independent technique can be chosen. In the time-dependent technique, the wavepacket associated with the system is collocated on a spatial grid. The resulting time-dependent scattering equations are integrated in time by repeatedly applying the time step propagator. The wavepacket is mapped onto the local basis set in the product region. The coefficients of the expansion are half Fourier transformed from a time to an energy representation to produce the corresponding elements of the scattering ($\mathbf{S}$) matrix [24]. When the whole information over all the open states is needed in a single fixed energy QM calculation, a method based on a time-independent approach is used. In this approach, the time variable is factored out and the stationary wavefunction is expanded in terms of a set of one-dimension-less functions of the bound coordinates. This expansion and the subsequent integration over all the bound variables leads to a set of coupled differential equations on the coordinate connecting reactants to products (reaction coordinate) [25].

For larger systems mixed QM-QCT or pure QCT codes are used. QCT codes integrate the equations of the classical mechanics to directly produce the probability matrix ($\mathbf{P}$) or even more averaged quantities. One has also the option,

especially convenient for very large systems, of introducing (a certain amount of) statistical considerations.

The present version of SIMBEX is designed to use both QM and QCT calculations. However, only one QCT computational engine (ABCtraj [26] for three atom systems) is fully operative while other two (Venus[27] for more than three atom systems and DL_POLY [28] for many atom systems) are still in the process of being implemented.

It is worth pointing out here that for reactive scattering calculations (especially the quantum ones) most of the codes are non commercial and are designed from scratch or largely readapted from academic software.

2.3. OBSERVABLES

In the third block OBSERVABLES, macroscopic (observable) properties are evaluated by manipulating the scattering **S** matrix and/or the probability matrix **P** calculated in the DYNAMICS block or by making direct use of the outcome of the INTERACTION block. If only thermodynamic properties are of interest, as is more often the case of condensed phases or complex gas mixtures like air, ionized media, high temperature plasma these are determined using computing programs based on standard statistical treatments of the potential energy values associated with the various geometries of the system calculated in the INTERACTION block. This task entails the development of chemical equilibrium models as well as the calculation of the partition functions for ions and/or excited species. When dynamical information is needed use is made of other programs manipulating the elements of the **S** or of the **P** matrix. This is the case, for example, of the simulation of molecular beams [13] or jets and shock waves [29]. For molecular beams, in which a single collision regime holds, the postprocessing of DYNAMICS outcomes is mainly limited to the calculation of cross sections and product distributions for which only an averaging over the unobserved parameters has to be performed. In the case of jets and shock waves, due to higher density of the gas, single collision regime does not apply and kinetic equations as well as fluid dynamics equations may need to be integrated. Transport properties can be evaluated from the collision integrals calculated from the **S** or the **P** matrix state to state elements. For ionized gases these have to include the effect of electromagnetic fields and the related anisotropy of the transport coefficients. Flows in the transient regime or in strong shock conditions can be treated using either a state to state approach or a Direct Simulation Monte Carlo (DSMC) method (or mixed ones like those based on the density matrix formalism). An example of particular relevance for concurrent computing is the DSMC method in which a kinetic description of the state to state nature of the process can be given and microscopic cross sections can be used to describe the intervening elementary processes. Concurrency is also vital to extend the calculations to three dimensions and to render the results (as well as the evolving value of the observables) using virtual monitors.

Most of these quantities, in fact, can be visualized as graphs or movies on

dedicated Virtual Monitors. This is extended to other non observable quantities of the DYNAMICS block in order to provide useful means for rationalizing the molecular process.

3.   The use of innovative tools for concurrent computing

To make Grid computing effective, concurrency has to be exploited both at coarse grain (like, for example, the one between the blocks of the GMS) and at fine grain (like, for example, the one between the various instructions of a given routine) level. This implies the use of specific software tools allowing the parallel restructuring with a high degree of code reuse and portability.

A standard software for parallel computing restructuring is MPI[30]. MPI is a set of portable libraries allowing the concurrent management of the activities of the computing nodes through simple calls. We used MPI to restructure some of our codes on parallel machines [31, 32]. Recently, some attempts to adapt MPI for managing Grid calculations have been made (see for example [33, 34, 35]). Unfortunately, MPI is a low level formalism that does not allow an easy estimate of computing costs since it cannot make use of the information on the status of the system made available by the middleware. Therefore, the price to pay for using MPI (and taking advantage of its simplicity) is the lack of control of the efficiency parameters.

3.1. SKELETON BASED COORDINATION LANGUAGES

An interesting approach to this problem is the use of a structured approach having constraints which allow the programmer to deal with the code as an ensemble of modules (skeletons) organized according to specific schemes. This is the basic feature of the structured concurrent programming environments based on the use of a coordination language and of the already mentioned skeletons (elementary structured parallel modules).

We are presently experimenting a programming environment based on skeletons whose name is SkiE (Skeleton Integrated Environment) [36]. Skeletons refer either to stream (the flow sequence of the information) or to data (the allocation of the information) models. Typical stream-parallel modules are farms, pipelines and loops. The farm consists of a replication of a function into a number of identical and independent workers, to which the stream elements are scheduled according to a load balance strategy. The pipeline consists of a parallel implementation of a set of functions into cascade stages through which the elements flow. The loop consists of a data-driven iterative computation through which the stream elements and their transformations flow until a certain condition is satisfied. Typical data-parallel structures are the map, the reduce and the compose. The map consists of a replication of a function into a number of identical and independent workers to which the elements of the data structure are distributed. The reduce consists of a parallel reduction of a data structure by binary associative and commutative

operations. The compose consists of a sequential set of functions expressing a parallel computation-replication and partitioning of data with communications designed according to a predetermined stencil [37]. In both stream-parallel and data-parallel paradigms, some data can be replicated.

The skeletons, usually employed as building blocks to construct complex parallel applications, are also useful perspective tools for managing concurrent computing on the Grid. In SkiE, in fact, the skeletons can be encapsulated and glued in more complex structures using the related coordination language SkiE-CL. SkiE-CL allows, in this way, a uniform and rapid development and prototyping of Grid applications thanks also to the use of *de facto* standards (like MPI itself), monitoring and debugging tools, application oriented environments. Moreover, SkiE offers the user the possibility of a "reuse" of large sections of the sequential code if this is written in one of the most popular sequential languages.

3.2. ASSIST-CL

The most recent evolution of SkiE is ASSIST[38]. Using the related coordination language, ASSIST-CL, the programmer can organize parallel/distributed programs as generic graphs without losing the possibility of making also use of already structured specific modules (the classical Skeletons) for which some interesting cost models already exist. These components can be sequential or parallel and exhibit high flexibility to meet the requirements of the applications and the characteristics of the platform.

One of the key features of ASSIST-CL is the introduction of a new parallel construct, more powerful and flexible than classical skeletons. This construct, called *parallel module* or *parmod*, can be considered as a sort of generic skeleton that can be structured so as to either emulate some specific classic skeleton of SkiE or their personalized variants and combinations to the end of achieving a more satisfactory degree of high and low level structuring, expressive power, reuse and efficiency. This is linked to the possibility of implementing simple and efficient cost models and the consequent possibility of optimizing the code not only at compiling time but also at running time. The exploitation of run time support is particularly useful since the parallel modules can have a non deterministic behaviour. The optimization of the composition of the parallel codes using the *parmod* exploits therefore in a very general way the mechanisms of streams. An extremely important additional feature of ASSIST-CL is the fact that the *parmod* modules can make use of *shared object* implemented by forms of a Distributed Shared Memory-like feature. In fact, while the stream based composition is the basic mechanism for structuring the applications and defining the component interfaces, shared memory objects are the basic mechanism for saving memory. This increases the programmability of highly dynamic structures and the communicability of the heavy data sets. Moreover, the modules for a parallel application can refer to any kind of existing *external objects*.

ASSIST is based upon a library of extremely powerful classes and methods which presents significant advantages. For illustrative purposes a test has been

carried out to distribute efficiently the matrices in blocks of columns and rows using the parametric class *Collective* $< IMP >$ of the ASSIST library. In this way it has been possible to implement *broadcast* and *scatter* classes to send information to the nodes. At the same time, on the way back, it has been possible to collect the results produced by the nodes by using a *reduce* operation implemented via a gathering function. I/O operations on a communication channel have been, in turn, implemented using the put and get methods of the used collectives of communication [39].

3.3. CONCURRENCY FOR QUANTUM DYNAMICS CODES

The parallel execution of the dynamical calculations is already built in into SIM-BEX. In the present version of the simulator the introduction of concurrency has been fairly simple due to the fact that only classical mechanics approaches are available. To the end of implementing also quantum approaches we have carried out performance tests of the relevant quantum dynamics suites of codes.

The time-independent codes have an articulation that more naturally fits into a coarse grain parallel and distributed organization. In particular, since these codes need first to calculate a suitable function basis set and then use them to carry out the propagation of the solution along the reaction coordinate one can divide the application in a first section (or program) running in parallel the calculation of the surface functions at different values of the reaction coordinate and then running in parallel the integration of the coupled propagation differential equations at different energies.

More monolithic is the coarse grain structure of the time-dependent (TIDEP) code that is considered here in more detail. The high level structure of TIDEP is:

Read input data: v, j, energy, atomic masses, ...
Perform preliminary calculations
LOOP on J
    LOOP on t
        LOOP on Λ
            Perform time step integration
            Perform the asymptotic analysis
            Store $C(t)$ coefficients
        END loop on Λ
    END loop on t
END loop on J
Calculate final quantities
Print outputs

in which the most time consuming component is the propagation step that has to be iterated for several thousand times. As can be seen from the scheme

given above, calculations are performed at fixed value of the vibrational (v) and rotational (j) quantum number of the reactant diatom as well as for a given range of translational energy and a single J value. Therefore, the coarsest grain of parallelism that can be adopted is the one distributing the calculation for a pair of initial vibrational and rotational states, a given interval of the relative translational energy and a fixed value of J. In this case, a task farm dynamically assigning the computational workload has to be adopted. This very coarse grain approach was fruitfully implemented on a cluster of powerful workstations for a limited number of J values.

However, when calculating a state to state cross section or, even worse, a state to state rate coefficient, the amount of time needed to perform the calculation goes beyond any acceptable limit if simplifications are not introduced. In fact, to evaluate a vibrational state selected rate coefficient, the calculation needs to be performed for the whole accessible translational energy and to be repeated for all the reactant rotational states j populated at the temperature considered. In addition, the calculations need to be converged with J and convergence is usually reached only at $J > 100$. This increases enormously the computational load not only because calculations have to be repeated for all J values but also because the dimension of the matrices to be handled in a single J calculation is $J + 1$ times larger than that of $J = 0$. As a matter of fact, computing time, that depends on the third power of the matrix dimension, rapidly becomes exceedingly large even at small J values to make the calculation unfeasible on the machines presently available for academic use at the large scale computing facilities in Europe.

A next lower level of parallelization is the one based on the combined distribution of fixed J and fixed Λ calculations. There is no problem in distributing fixed J calculations: J is a good quantum number (*i.e.* calculations for different J values are fully decoupled) and, accordingly, the parallelization on J is natural. On the contrary, the decoupling of Λ is artificial since one has to introduce physical constraints of the infinite order sudden type (*i.e.* the projection of J on the z axis of the body fixed frame remains constant during the collision). This allows to perform separately the step-propagation of the wavepacket for blocks of fixed Λ values and the recombination of the various contributions only at the end of the propagation step. This is a key feature of the adopted computational scheme since it allows a decomposition of the domain of the wavepacket that otherwise would lead to a drastic increase of the demand for memory when J increases. Moreover, fixed J calculations were carried out in pairs for all the $J + 1$ components of Λ in order to further save computer time and allow a better load balance. However, since for this parallel model I/O is a real bottleneck, when generalizing the model node zero was exclusively dedicated to act as a master and the centralized management of I/O was abandoned.

3.4. A TIME PROPAGATOR TEST CASE

For TIDEP the parallelization can be pushed at a fine grain level by focusing on the time propagation routine (AV) that in our code is based on a Discrete variable representation (DVR) approach [24, 40]. The routine propagates the system wavepacket by repeating at each time step the following stream of matrix operations

$$\mathbf{G} = \mathbf{A} \cdot \mathbf{C} + \mathbf{C} \cdot \mathbf{B}^{\mathbf{T}} + \mathbf{V} \odot \mathbf{C} \tag{1}$$

where $\mathbf{A}$ and $\mathbf{B}$ are terms of the matrix representation of the Laplacian operator (whose blocks of rows and columns are broadcasted, like $\mathbf{V}$, once for ever at the beginning of the calculation to the worker nodes), $\mathbf{C}$ is the collocation matrix of the wavefunction, $\mathbf{V}$ is the matrix representation of the potential ($\mathbf{V} \odot \mathbf{C}$ is the direct product of the single component $\mathbf{V}$ matrix with $\mathbf{C}$). Eq. (1) is recursive since the value of $\mathbf{C}$ is taken at time $\tau - 1$ while that of $\mathbf{G}$ is taken at time τ (the value of $\mathbf{C}$ at time τ, in turns, depends on that of $\mathbf{G}$ at the same time τ even though, in order to simplify the notation, we have dropped the time subindex). The matrices used here are square matrices of order N. Such a constraint, however, can be easily removed with no prejudice for the results.

To make the propagator run concurrently at first use was made of MPI and of a Task Farm model [41]. In the startup phase the Master process distributes the rows of $\mathbf{C}$ using a cyclic policy. This implies that in the startup phase if $j \equiv i \bmod M$ (with M being the number of scheduled Workers) the vector $Row(j, \mathbf{C})$ is sent to the worker W_i. At the end of the startup phase each Worker has stored the rows received from the Master in a local (unshared) secondary space storage hereafter called $Dataset(W_i, \mathbf{C})$. Similarly, all the elements of the matrices $\mathbf{A}$ and $\mathbf{B}$ referred by the Worker W_i are stored in an analogous $Dataset$ during the wavepacket initialization (immediately before the first step $\tau = 0$).

To carry out the subsequent operations, the Master process adopts a scheduling policy to *broadcast* $Row(j, \mathbf{C})$ to each Worker. Each scheduled Worker loads from a local (unshared) secondary memory space all the elements needed to carry out the calculation of:

$w_i = \sum_{k \in D_i} A(j, k) \cdot Row(k, \mathbf{C})$

$w_i(h) = w_i(h) + Row(j, \mathbf{C}) \cdot Row(h, \mathbf{B}) \qquad \forall h \in E_i$

with i being the index of the Worker process, j being the index of the Row of $\mathbf{G}$ to be calculated, $D_i = [i]_M$ with M being the number of scheduled Workers and E_i being the set of contiguous indexes assigned to Worker W_i allowing an optimum balancing of the load among the Workers. Through a reduce operation the Master reassembles the resulting rows of matrix $\mathbf{G}$.

ASSIST turned out to be very useful to restructure the code at this level and some attempts have been made by using some parametric classes of ASSISTlib (the library of ASSIST). To this end, in the *AV* routine the Scattering collective (SCATTER) is used on the producer side to distribute the matrices of Eq. 1. More in detail, SCATTER_P carries out the distribution of blocks of rows and

columns of **A**, **B** and **C** from the Master to the workers (this has been obtained by writing a simple template). In a similar way SCATTER_C takes care of the scatter operation on the consumer side. The blocks of **G** resulting from the activity of the workers are re-collected by the Master using a Gathering function implementing through the related parametric class of ASSISTlib. Read and write operations on the communication channel are performed synchronously using the **put** and **get** methods of the communication collectives. The **put** and **get** methods are simpler to execute than their asynchronous analogues and its choice is made possible by the fact that the communications considered are not a bottle neck of the computation. A detailed report on the implementation of the *AV* routine using ASSIST is given in the reports of the PQE 2000 project [39].

4. The impact on the calculations for large systems

As already mentioned, the impact of concurrent computing can be accounted for at a finer level by reconsidering the theoretical framework. The key point is, in fact, the adoption of approaches allowing a high level of locality for the calculation. For this reason, in the followings, we revisit some features of the usual formulation of the scattering equations (by confining our attention to the prototype collinear A + BC reaction) in a search for alternative approaches.

Quantum reactive scattering calculations are based on the integration of the time-dependent Schrödinger equation

$$\hat{H}\Psi(\{x\},t) = i\hbar \frac{\partial}{\partial t}\Psi(\{x\},t) \tag{2}$$

where $\hat{H}$ is the Hamiltonian of the system, $\Psi(\{x\},t)$ is its wavefunction and $\{x\}$ is a suitable set of coordinates. When using a time-dependent approach to integrate Eq. 2, the time variable t is taken as a continuity variable even when the Hamiltonian $\hat{H}$ is time-independent. In time-independent approaches, the time dependence is separated and, in order to integrate the resulting stationary Schrödinger equation, a proper combination of spatial coordinates is taken as a continuity variable.

The $\{x\}$ variables are usually taken to be some kind of internal orthogonal coordinates. Moving to large systems it becomes more convenient to use non orthogonal coordinates like the internuclear distances or other related variables.

4.1. THE BOND ORDER FORMULATION OF THE INTERACTION

The coordinates in which the potentials are usually formulated are the internuclear distances. However, in order to avoid redundancy problems one cannot use the whole set of internuclear distances since their values are not mutually independent. For this reason more often use is made of process coordinates considering a mixed set of internuclear distances and related angles [42, 43]. Accordingly, interactions are usually formulated using a many-body expansion (MBE) [44] whose individual terms are expressed as polynomials in damped internuclear distances.

Particularly suitable coordinates not needing damping corrections are the bond-order (BO) ones which for the collinear A + BC atom diatom systems are defined as

$$n_{BC} = \exp\left[-\beta_{BC}(r_{BC} - r_{BC}^o)\right] \qquad (3)$$
$$n_{AB} = \exp\left[-\beta_{AB}(r_{AB} - r_{AB}^o)\right]$$

with β_i and r_i^o being empirical parameters linked to the vibrational spectroscopic properties of the related diatomic molecule [45]. BO coordinates have a clear advantage over internuclear distances since they are defined over a limited spatial range and converge at large distance (they tend to zero as the related internuclear distances tend to infinity). This makes polynomials in the BO coordinates a suitable functional representation for the interaction [46].

We currently use the BO polynomials in a systematic way to fit the potential energy surfaces of few-atom systems. An extension of BO functional forms to the formulation of more than three atom systems can also be made. For this purpose one can adopt a polynomial in more than three BO variables or derive from them at each geometry local normal coordinates. This makes the treatment more complex and may in certain cases introduce numerical instabilities.

A simpler approach that we introduce here for the first time is the ALBO functional form. In the ALBO approach the potential is expressed in a form that makes the optimization of the parameters easier by pivoting the search for their optimum value by means of physical considerations. To this end the overall potential is formulated in the following pseudo pair additive form

$$V(\{n\}) = \sum_j D_j(1 + Q_j(\{n_k\}_{k \neq j}))P_j(n_j) \qquad (4)$$

where j runs over all diatomic pairs making the functional a sum of pseudo ("effective") diatomic model potentials having a shape depending on the vicinity of the other atoms. For this reason, Q_j and P_j are expressed as (low order) polynomials in the BO variables of the (other) pairs of atoms. In particular, Q_j depends on all the BO variables but n_j and makes the depth of the effective diatomic potential depend on the vicinity of the other atoms. Due to the nature of the BO variables these contributions vanish, as it should be, as the other atoms fly away. P_j depends on n_j and its coefficients depend parametrically on the other n_k variables.

Usually, in the BO polynomial approach the jth diatomic component (to which P_j tends as all the other atoms fly away) is expressed as a pure fourth (sometimes sixth) order polynomial. For illustrative purposes the ALBO formulation of the interaction can be compared with the LEPS one. To this end, the polynomial is truncated to the second order so as to make the resulting ALBO asymptotic Morse like expression $(n_j/n_{0j})^2 - 2(n_j/n_{0j})$ coincide with that of the LEPS. In particular, the dependence of P_j on the other BO variables is enforced via n_{0j} which tends to 1 as the other atoms move to infinity (so as to coincide with the polynomial of the

isolated diatom). In the strong interaction region n_{0j} deviates from 1 to account for the displacement of the minimum of the effective diatomic potential from 1 due to the action of multi- (larger than 2) body interaction when the other atoms gets closer. Therefore, a reasonable formulation of n_{0j} for a triatomic system is $n_{0j} = 1 + b_1 n_k + b_2 n_l + b_3 n_k^2 + b_4 n_l^2 + b_5 n_k n_l$.

The formulation adopted for Q_j ($Q_j = a_1 n_k + a_2 n_l + a_3 n_k^2 + a_4 n_l^2 + a_5 n_k n_l$) is similar. This formulation allows the dissociation energy to tend to the correct asymptotic value at both asymptotes and strong interaction limits. This leads to a functional representation of the interaction that is more flexible than the LEPS one thanks to the larger number of parameters and to the incorporation of the asymptotic limits. As a matter of fact one can obtain quite small root mean square deviations when using the ALBO potential to fit the LEPS values. An obvious advantage of this formulation is that it automatically extends to larger systems by adding further pseudo diatomic terms and by reusing the parameters worked out for smaller systems. This can be used also on the way down to restricted geometries to build up fast estimates of the potential parameters.

4.2. THE HYPERSPHERICAL BOND ORDER FORMULATION OF THE INTERACTION

A different way of tackling the problem is to describe the reactive process in terms of the variation of the parameters of a diatomic-like interaction that evolves for the reactant to the product arrangement while rotating [47]. For the atom diatom collinear system, the rotation angle α of this BO potential (ROBO, rotating BO) is the continuity variable of the reactive process while the pseudo diatomic like bond length ρ is a collective coordinate that accounts for the deformation of the geometry of the system [48, 49, 50]. The α and ρ variables are the polar coordinates of the BO space (HYBO, hyperspherical BO coordinates). For collinear systems α and ρ read as

$$\rho = \sqrt{n_{AB}^2 + n_{BC}^2} \tag{5}$$
$$\alpha = \arctan n_{BC}/n_{AB}.$$

(whose extension to higher dimensionality is obtained by adding more angles). Accordingly, a simple formulation of the ROBO potential for the process P analogue of the Rotating Morse potential reads as:

$$V^P(\rho, \alpha) = D^P(\alpha) \left[\left(\frac{\rho}{\rho_o(\alpha)} \right)^2 - 2 \frac{\rho}{\rho_o(\alpha)} \right] \tag{6}$$

The reaction channel is then shaped by assuming a proper functional dependence of D^P and ρ_o from α. In this respect, the HYBO α angle clearly plays the role of reaction coordinate [47, 50] of the P process (for this reason these coordinates are called process coordinates). The whole potential V is then obtained by a weighed

(through the weights w^P) combination of the three ROBO functionals V^P of the three possible reaction channels (A + BC, B + CA, C + AB)

$$V = \frac{\sum_P w^P V^P}{\sum_P w^P} \tag{7}$$

This generalized form of the ROBO potential (called LAGROBO) has been successfully used to fit the potential energy surface of several three-atom systems and has been also extended to four-atom systems [51]. Other successful applications to four atom reactions have been made [52, 53] by modifying the original definition of the angles and by composing the fixed angle minimum energy paths as piecewise functions. This has allowed the reproduction of highly structured potential energy surfaces including entrance and exit channel wells and barriers.

Application of the three and four atom HYBO functional form to the formulation of the interaction of larger systems is not straightforward. However, since the MBE expansion of the interaction of large systems is, in general, truncated to the four body terms one can easily assemble the related force field by composing related HYBO three and four atom blocks.

4.3. PROCESS COORDINATE FORMULATIONS OF THE LAPLACIAN

The coordinates more commonly used to formulate reactive scattering equations are of the orthogonal arrangement type [54]. The fact that these coordinates are orthogonal makes the formulation of the Laplacian simpler and the scattering equations diagonal. However, all arrangement coordinates are, as already seen, scarcely suited to describe the interaction during the entire reactive process. Moreover, when using arrangement coordinates, only small deviations from the reference geometry (like in inelastic and elastic encounters when using the reactant Jacobi coordinates) can be dealt without varying the reference geometry. This means that in order to obtain a homogeneous description of the Laplacian arrangement coordinates need to undergo appropriate transformations at each step of the reactive process. This implies also heavy computational overheads.

On the contrary, internuclear and bond order coordinates can be considered as process coordinates since they apply to the whole (specific) reactive process connecting a given set of reactants to a given set of products. The formulation of the Hamiltonian using process coordinates eliminates the need for carrying out coordinate transformations and allows a homogeneous description of both the Laplacian and the potential energy operators of the Hamiltonian at each step of the dynamical calculation. As a matter of fact, bond length coordinates [43] have already been used in the literature to calculate static and dynamic properties of three-atom systems (see, for example, refs. [55, 56, 57]). This is also true for the BO coordinates.

As for the BO coordinates, the additional properties of being inverted with respect to the bond length ones (the zero of the BO coordinates corresponds to an infinite bond length while large BO values correspond to short bond lengths) and

being confined into a finite volume make HYBO coordinates particularly appealing for formulating the Hamiltonian and studying reaction dynamics [42, 48, 49]. These properties are particularly useful when using collocation methods and grid-point techniques.

Alike in the case of bond length coordinates the Hamiltonian is more complicated with respect to that of the Jacobi coordinates and a (trivial in the collinear case) conversion to Jacobi coordinates at the asymptotes is needed to perform the related analysis.

The collinear Hamiltonian reads, in fact, in bond order coordinates as

$$\hat{H} = C_{nnx} \left[n_{\mathrm{BC}}^2 \frac{\partial^2}{\partial n_{\mathrm{BC}}^2} + n_{\mathrm{BC}} \frac{\partial}{\partial n_{\mathrm{BC}}} \right] + C_{nny} \left[n_{\mathrm{AB}}^2 \frac{\partial^2}{\partial n_{\mathrm{AB}}^2} + n_{\mathrm{AB}} \frac{\partial}{\partial n_{\mathrm{AB}}} \right] +$$
$$C_{nxy} n_{\mathrm{AB}} n_{\mathrm{BC}} \frac{\partial^2}{\partial n_{\mathrm{BC}} \partial n_{\mathrm{AB}}} + V(n_{\mathrm{BC}}, n_{\mathrm{AB}}) \qquad (8)$$

with the coefficients being $C_{nnx} = -(\hbar \beta_{\mathrm{BC}})^2 / 2\mu_{\mathrm{BC}}$, $C_{nny} = -(\hbar \beta_{\mathrm{AB}})^2 / 2\mu_{\mathrm{AB}}$ and $C_{nxy} = \hbar^2 \beta_{\mathrm{BC}} \beta_{\mathrm{AB}} / m_{\mathrm{B}}$ when the breaking and forming diatoms have the same force constant β. The BO formulation of the Hamiltonian is currently being used for classical trajectory [42] and quantum time-dependent [49] calculations. It has also been tested in variational [48, 49] reactive calculations.

In HYBO coordinates the collinear atom diatom Hamiltonian has the more complex form

$$\hat{H} = C_{\alpha\alpha}(\alpha) \frac{\partial^2}{\partial \alpha^2} + C_\alpha(\alpha) \frac{\partial}{\partial \alpha} + C_{\rho\alpha}(\rho, \alpha) \frac{\partial}{\partial \rho} \frac{\partial}{\partial \alpha} + C_{\rho\rho}(\rho, \alpha) \frac{\partial^2}{\partial \rho^2} +$$
$$C_\rho(\rho, \alpha) \frac{\partial}{\partial \rho} + V(\alpha, \rho) \qquad (9)$$

where

$$C_{\alpha\alpha}(\alpha) = -\frac{\hbar^2 \sin^2 2\alpha}{8} \left[\frac{\beta_{\mathrm{BC}}^2}{\mu_{\mathrm{BC}}} + \frac{\beta_{\mathrm{AB}}^2}{\mu_{\mathrm{AB}}} + 2 \frac{\beta_{\mathrm{BC}} \beta_{\mathrm{AB}}}{m_{\mathrm{B}}} \right] \qquad (10)$$

$$C_\alpha(\alpha) = -\frac{\hbar^2 \sin 4\alpha}{8} \left[\frac{\beta_{\mathrm{BC}}^2}{\mu_{\mathrm{BC}}} + \frac{\beta_{\mathrm{AB}}^2}{\mu_{\mathrm{AB}}} + 2 \frac{\beta_{\mathrm{BC}} \beta_{\mathrm{AB}}}{m_{\mathrm{B}}} \right] \qquad (11)$$

$$C_{\rho\alpha}(\rho, \alpha) = -\frac{\hbar^2}{2} \rho \left[\sin 2\alpha \left(\frac{\beta_{\mathrm{AB}}^2}{\mu_{\mathrm{AB}}} \sin^2 \alpha - \frac{\beta_{\mathrm{BC}}^2}{\mu_{\mathrm{BC}}} \cos^2 \alpha \right) - \frac{\beta_{\mathrm{AB}} \beta_{\mathrm{BC}}}{2m_{\mathrm{B}}} \sin 4\alpha \right] \quad (12)$$

$$C_{\rho\rho}(\rho, \alpha) = -\frac{\hbar^2}{2} \rho^2 \left[\frac{\beta_{\mathrm{AB}}^2}{\mu_{\mathrm{AB}}} \sin^4 \alpha + \frac{\beta_{\mathrm{BC}}^2}{\mu_{\mathrm{BC}}} \cos^4 \alpha - \frac{\beta_{\mathrm{AB}} \beta_{\mathrm{BC}}}{2m_{\mathrm{B}}} \sin^2 2\alpha \right] \qquad (13)$$

$$C_\rho(\rho, \alpha) = -\frac{\hbar^2}{2}\rho \left[\frac{\beta_{BC}^2}{\mu_{BC}} \cos^2 \alpha \left(1 + \sin^2 \alpha\right) + \frac{\beta_{AB}^2}{\mu_{AB}} \sin^2 \alpha \left(1 + \cos^2 \alpha\right) + \frac{\beta_{BC}\beta_{AB}}{2m_B} \sin^2 2\alpha \right] \quad (14)$$

5. Conclusions

The impact produced by the evolution of computer technologies towards Grid systems on the size and the complexity of the problems that theoretical and computational studies of chemical reactions can afford is discussed. The analysis is extended on one side to how this affects the way computer codes are structured to gain significant efficiency and on the opposite side to how alternative formulation of the reactive scattering equations can be written to exploit the advantages of concurrent computing. In particular, the use of traditional low level parallelization libraries has been considered and compared with that of coordination languages based on skeletons and related extensions. As for alternative approaches those based on BO coordinates which have the advantage of formulating in a homogeneous way the potential and the Laplacian operator, are analyzed. In particular new formulations of the functional representations of the interaction are discussed and the formulation of the Hamiltonian in terms of both BO and HYBO coordinates are given.

Acknowledgments

References

1. Baker, M., Buyya, R., Laforenza, D. (2002) Grids and Grid technologies for wide-area distributed computing, *Software: Practice and Experience*, **32(15)**, Wiley Press, USA
2. Gentzsch, W. (1999) *Future Generation Computer Systems*, **15**, 537.
3. (1999), *The Grid: Blueprint for a Future Computing Infrastructure*, I. Foster, and C. Kesselman Eds., Morgan Kaufmann Publishers, USA.
4. Baker, M., Buyya, R., Laforenza, D. (2000) *The Grid: International Efforts in Global Computing*, SSGRR2000, L'Aquila, Italy, July.
5. Gentzsch, W. (1999) *Future Generation Computer Systems*, **15**, 1.
6. Baker, M., Fox, G. (1999) Metacomputing: Harnessing Informal Supercomputers, *High Performance Cluster Computing: Architectures and Systems*, Buyya, R., Ed., Volume 1, Prentice Hall PTR, NJ, USA.
7. Foster, I., Kesselman, K. (1997) *Int. J. Supercomputing Applications*, **115**, 28; Foster, I., Kesselman, K. (1998) The Globus Project: a status report *IPPS/SPDP'98 Heterogeneous Computing Workshop* S.4-18, http://www.fp.globus.org/documentation/papers.html; http://www.globus.org
8. Gallopoulos, S., Houstis, E., Rice, J. (1994) Computer as Thinker/Doer: Problem-Solving Environments for Computational Science, *IEEE Computational Science and Engineering*, Summer 94.

9. Information Society Technologies, 2003-2004 Workprogramme http://cost.cordis.lu/ist page 30
10. http://cost.cordis.lu/src/home.cfm.
11. Laganà, A., METACHEM: Metalaboratories for cooperative innovative computational chemical applications, *METACHEM workshop*, Brussels, November (1999).
12. COST Action N. D23, *METACHEM: Metalaboratories for complex computational applications in chemistry.*
13. COST Action N. D23, Project 003/2001, *SIMBEX: a Metalaboratory for the a priori Simulation of Crossed Molecular Beam Experiments.*
14. Storchi, L., Manuali, C., Gervasi, O., Vitillaro G., Laganà, A., Tarantelli, F. (2003) *Lecture Notes in Computer Science,* **2658**, 297.
15. Gervasi, O., Laganà, A., Lobbiani, M. (2002) *Lecture Notes in Computer Science,* **2331**, 956.
16. Baraglia, R.; Laforenza, D.; Laganà, A. A Web based Metacomputing Problem-Solving Environment for Complex Applications, *Workshop on Grid Computing,* Bangalore, December 2000. Errata corrige: In Fig. 4 of this paper the first arrow down on the upper left hand side should have a YES instead of a NO. ASI PQE200 project workpackage 4 and 5.
17. see the homepage http://www.pnl.gov.2080/
18. Gaussian Inc. 4415 Fifth Ave, Pittsburgh, PA 15213 USA (1992).
19. Amos, R.D., Alberts, L.L., Andrews, J.S., Colwell, S.M., Handy, N.C., Jayatilaka, D., Knowles, P.J., Kobayashi, P., Koga, N., Laidig, K.E., Maslen, P.E., Murray, C.W., Rice, J.E., Sanz, J., Simandiras, E.D., Stone, A.J., Su, M.-D. (1995) CADPAC, Issue 6, University of Cambridge.
20. Ahlrichs, R., Br, M., Hser, M., Horn, H., Klmel, C. (1989) *Chem. Phys. Letters,* **162**, 165.
21. Dupuis, M., Watts, J.D., Villar, H.O., Hurst, G.J.B. (1989) *Comput. Phys. Commun.,* **52**, 415.
22. Dupuis, M., Spangler, D., Wendoloski, J. (1980) *NRCC Software Catalog,* Vol. 1, Progr. No. QG01.
23. Laganà, A., Riganelli, A. (2000) *Lecture Notes in Chemistry,* **75**, 1.
24. An atom diatom time-dependent quantum program (see Balint-Kurti, G.G. (2000) *Lecture Notes in Chemistry,* **75**, 74).
25. An atom diatom quantum program based on APH coordinates (see Parker, G.A., Crocchianti, S., Kiel, M. (2000) *Lecture Notes in Chemistry,* **75**, 88).
26. An atom diatom trajectory program derived from Chapman, S., QCPE N. 273, Bloomington, Indiana.
27. A polyatomic reactive program derived from that of Hase, W.H., Duchovic, R.J., Hu, X., Komornicki, A., Lim, K.F., Lu, D.G. Peslherbe, H. Swamy, K.N., Vande Linde, S.R. Varandas, A., Wang, H., Wolf, R.Y. *VENUS96: A General Chemical Dynamics Program,* QCPE Program N. 671, Indiana University, Bloomington, Indiana.
28. DL_POLY is a package of molecular simulation routines written by Smith, W., Forester, T.R. copyright The Council for the Central Laboratory of the Research Councils, Daresbury Laboratory at Daresbury, Warrington, UK (1996).
29. Longo, S., Milella, A. (2001) *Chem. Phys. Letters,* **274**, 219.
30. a) Message Passing Interface Forum, *Int. J. Supercomput. Appl.* 8(3/4), 1994; b) Smir, M., Otto, S., Huss-Ledermam, S., Walker, D., Dongarra, J.: *MPI: The complete reference,* MIT Press, 1996.
31. D'Agosto, G., Piermarini, V., Pacifici, L., Crocchianti, S., Laganà, A. Tasso, S. (2001) *Lecture Notes in Computer Science* **2073**, 367.
32. Bolloni, A., Crocchianti, S., Laganà, A. (2000) *Lecture Notes in Computer Science,* **1908**, 338.
33. Kielmann, T. Hofman, R.H.F., Bal, H.E., Plaat, A., Bhoedjang, R.A.F. (1993) "Magpie: MPI's collective communication operations via clustered wide area systems" In *Proc. Symposium on Principles and Practice of Parallel Programming,* Sand Diego.

34. Foster, I., Karonis, N. (1998) "A Grid enabled MPI: Message passing in heteroge-
     neous distributing computing systems" In Proc. Supercomputing '98".
35. Karonis, N., de Supinski, B., Foster, I., Gropp, W., Lusk, E., Bresnahan, J. (2000)
     "Exploiting hierarchy in parallel computer networks to optimize collective opera-
     tion performance" In Proc. International Parallel and Distributed Processing Sym-
     posium.
36. Danelutto, M., Di Meglio, R., Orlando, S., Pelagatti, S., Vanneschi, M. (1992) *Future
     Generation Comput. Syst.*, **8**, 205; Pelagatti, S., *Structured development of parallel
     programs*, Taylor & Francis Ltd, London, 1998.
37. Vanneschi, M. (2000) *Lecture Notes in Chemistry* **75**, 168.
38. Ciullo, P., Danelutto, M., Vaglini, L., Vanneschi, M., Guerri, D., Lettere, M. (2001)
     Ambiente ASSIST: modello di programmazione e linguaggio Assist (versione 1.0),
     Progetto ASSIST PQE 2000, Università di Pisa, February; Vanneschi, M. (2002)
     ASSIST: An Environment for Parallel and Distributed Portable Applications, Tech-
     nical Report TR-02-07, Università di Pisa.
39. Laganà, A., Tarantelli, F., Gervasi, O., Pacifici, L., Villani, C., Storchi, L. (2002)
     ASI PQE2000, Work package n.4: Demostrators and benchmarking.
40. Piermarini, V., Pacifici, L., Crocchianti, S., Laganà, A., D'Agosto, G., Tasso, S.
     (2001) *Lecture Notes in Computer Science*, **2073**, 567.
41. Bellucci, D., Tasso, S., Laganà, A. (2002) *Lecture Notes in Computer Science* **2331**,
     918.
42. Laganà, A., Faginas Lago, N., Riganelli, A., Ferraro, G. (2001) *An approach to reac-
     tive scattering based on nonorthogonal coordinates*, XIX International Symposium
     on Molecular Beams, p. 281; Faginas Lago, N. (2002) Phd Thesis, Perugia.
43. Laganà, A., Crocchianti, S., Faginas Lago, N., Pacifici, L., Ferraro, G. (2003) *Coll.
     Czech. Chem. Comm.*, **68**, 386.
44. Murrell, J.N., Carter, S., Farantos, S.C., Huxley, P., Varandas, A.J.C. (1984) *Molec-
     ular Energy Functionals*, Wiley, New York.
45. Garcia, E., Laganà, A. (1985) *Mol. Phys.* **56**, 621.
46. Garcia, E., Laganà, A. (1985) *Mol. Phys.* **56**, 629.
47. Laganà, A. (1991) *J. Chem. Phys.* **95**, 2216.
48. Laganà, A., Spatola, P., Ochoa de Aspuru, G., Ferraro, G., Gervasi, O. (1997) *Chem.
     Phys. Lett.*, **267**, 403.
49. Ferraro, G., Laganà, A. *Scattering calculations using a nonorthogonal coordinate
     formalism* (in preparation).
50. Garcia, E., Laganà, A. (1995) *J. Chem. Phys.* **103**, 5410.
51. Ochoa de Aspuru, G., Clary, D.C. (1998) *J. Phys. Chem. A* **102**, 9631.
52. Ceballos, A., Garcia, E., Rodriguez, A., Laganà, A. (2000), *Chem. Phys. Letters*
     333(6) 471.
53. Rodriguez, A., Garcia, E., Hernández, M.L., Laganà, A., (2002), *Chem. Phys. Let-
     ters* **3360**,2.
54. Zhang, J.Z.H. (1998) Theory and Application of Quantum Molecular Dynamics,
     World Scientific.
55. Carter, S., Handy, C. (1982) *Mol. Phys.*, **47**, 1445.
56. Carter, S., Handy, C. (1986) *Mol. Phys.*, **57**, 175.
57. Lara, M., Aguado, A., Paniagua, M., Roncero, O. (2000) *J. Chem. Phys.*, **113**, 1781.

VIBRATIONAL PREDISSOCIATION: QUASICLASSICAL TUNNELING THROUGH CLASSICAL CHAOTIC SEA

E. NIKITIN[a,b] and J. TROE[b]

[a]*Department of Chemistry, Technion - Israel Institute of Technology, Haifa, 32000 Israel,*
[b]*Institut für Physikalische Chemie der Universität Göttingen, Tammannstrasse 6, D-37077 Göttingen, Germany*

Abstract   Vibrational predissociation (VP) of van der Waals complexes occurs via an isolated resonance. An isolated resonance possesses no classical counterpart. And yet, classical calculations of the decay yield the rates that are sometimes not too different from the quantum rates. We resolve this puzzle by addressing the following points:
i)   Quantum theory of VP: accurate and perturbative approaches;
ii) Quasiclassical theory of VP: Landau method and recovery of VP transition probabilities from the correspondence principle transition probabilities;
iii) Classical theory of VP: diffusional description of long-time chaotic dynamics.
  We calculate the ratio of the classical to quantum VP rates, determine the conditions when the rates of quantum dynamical tunneling is close to the classical diffusional rates across the chaotic sea and establish a classical counterpart of quantum perturbation approach.

1. Introduction

Vibrational predissociation (VP) of a van der Waals triatomic complex A..BC is an example of a unimolecular reaction the rate of which is controlled by the intramolecular vibrational energy redistribution (IVR) [1]. Within a rigorous quantum mechanical approach, the VP dynamics is completely characterized by the complex-valued energies $\mathsf{E}_n = E_n - i\Gamma_n / 2$ that lie above the dissociation threshold of A..BC into an atom A and a diatomic molecule BC. The important property of VP is that the widths of the levels, Γ_n, are small compared to the spacing between neighboring levels, $E_{n+1} - E_n$. It means that the quasistationary state $\left| \mathsf{E}_n \right\rangle$ decays exponentially with a VP rate constant $k_n = \Gamma_n / \hbar$ and that the energy E_n of the complex can be split, to a good approximation, into the energy E_{BC} of a free diatomic molecule BC and the energy E_{vdW} of the van der Waals bond [2]. We therefore can specify the state-specific VP event as

$$A \overset{E_{vdW}}{\cdots} BC(E_{BC}) \rightarrow A \overset{E'_{vdW}}{+} BC(E'_{BC}) \qquad (1)$$

In what follows, we will discuss the IVR dynamics and VP event for a collinear non-rotating triatomic vdW complex A..BC. For this model, all the complications that arise from the partitioning of the total angular momentum of the complex into the relative angular momentum of the dissociation fragments and intrinsic angular momentum of the diatomic fragment do not appear, and the quantum (Q) state-specific rate constant of the VP event in Eq.(1) can be written in more details as $k_n = k^Q(E_{vdW}, E_{BC}; E'_{vdW}, E'_{BC})$. With four variables, one is redundant because of the conservation of total energy. Introducing the energy transfer to the vdW bond, ΔE, one can write the VP rate constant as $k^Q = k^Q(E_{vdW}, E_{BC}; \Delta E)$ where all three variable assume discrete (quantized) values. Here the energy transfer ΔE can be expressed, of course, through the transition frequency as $\Delta E = \hbar\omega_{\Delta E}$, $k^Q = k^Q(E_{vdW}, E_{BC}; \hbar\omega_{\Delta E})$. The quasiclassical (QCl) counterpart of k^Q, k^{QCl}, will depend on the classical frequency of the BC fragment, associated with the initial quasiclassical energy E_{BC}, $k^{QCl} = k^{QCl}(E_{vdW}, E_{BC}; \hbar\omega(E_{BC}))$. The definition of the classical (Cl) VP rate is not straightforward as their quantum counterpart, because the classical decay is not exponential. One has, therefore, to adopt a certain way of extracting a reasonable parameter from the decay curves, which can be considered as an effective VP rate constant, k^{Cl}_{eff}. The latter will depend on three classical quantities, $E_{vdW}, E_{BC}, \omega(E_{BC})$, i.e. $k^{Cl}_{eff} = k^{Cl}_{eff}(E_{vdW}, E_{BC}, \omega(E_{BC}))$.

Comparative discussion of three functions, $k^Q, k^{QCl}, k^{Cl}_{eff}$ and the approximations, which are used to derive them, sheds light onto the quantum, quasiclassical and classical dynamics of vibrational predissociation.

Quantum numerical calculations of k^Q for a given potential surface are nowadays quite straightforward, especially when one uses the complex scaling technique that formally reduces a nonstationary problem to finding complex-valued eigenvalues of a non-Hermitian Hamiltonian [3]. Since the resultant eigenvalues fall into the category of non-overlapping resonances, it is clear that a perturbation scheme must exist for calculation of k^Q. However, a question arises here as to the zero-order basis to be used in calculating k^Q. This question can hardly be answered by purely numerical methods since they can not unambiguously indicate the optimal separation of the Hamiltonian into the zero-order Hamiltonian and a perturbation.

Quasiclassical perturbative calculations to be discussed here are based on the Landau method of calculation of the transition matrix elements [2] and the recovery of the Landau quasiclassical exponent from the classical encounter time [4-6]. The quasiclassical VP rate constants, k^{QCl}, contain classical dynamical parameters that characterize a vdW complex motion in the classically allowed regions. In this respect, quasiclassical Landau approach indicates a possible way of transition from quantum to classical dynamics. This transition is not at all trivial, since the correspondence principal limit ($\hbar \rightarrow 0$) of k^{QCl} yields zero rate.

Classical calculation of decay plots by integrating classical equation of motion is also straightforward. A recovery from these plots such kinetic coefficients as $k_{\text{eff}}^{\text{Cl}}$ requires some approximate scheme (see above). Though the classical decay is slow on the timescale of vdW motion, there is no standard perturbation method for calculation of $k_{\text{eff}}^{\text{Cl}}$. This is due to the fact that the classical VP dynamics is chaotic [7-12].

With the above comments in mind, we first briefly discuss a hierarchy of models for VP (Section 2), then dwell on the quantum (Section 3), quasiclassical (Section 4) and classical (Section 5) theories of VP. After that, we compare different approaches (Section 6) and summarize our results on the quantum-classical correspondence for isolated resonances, which is the case for vibrational predissociation.

2. Hierarchy of models

A standard model of VP, which is repeatedly used in the study of VP dynamics, corresponds to two coupled Morse (M) oscillators, one low-frequency (LF) dissociating oscillator, coordinate R, and the other high-frequency (HF) oscillator, coordinate r, in bound states. The Hamiltonian of such a Morse-Morse system is written as

$$\hat{H}_{\text{MM}}(\hat{P}_R, R; \hat{p}_r, r) = H_{\text{LFM}}(\hat{P}_R, R) + H_{\text{HFM}}(\hat{p}_R, r) + V_{\text{MM}}(R, r) \tag{2}$$

This Hamiltonian can be simplified without losing any interesting features of VP by using special conditions pertinent to the VP event. The simplification is carried out in several steps thus creating a hierarchy of models.
i) Since in a VP event the HF oscillator suffers a one-quantum transition, it can be replaced, for a given transition, by a harmonic (H) oscillator of the same transition frequency and properly modified coupling strength [11]. We thus replace the Morse-Morse system by a Morse-Harmonic system with the Hamiltonian:

$$\hat{H}_{\text{MH}}(\hat{P}_R, R; \hat{p}_r, r) = H_{\text{LFM}}(\hat{P}_R, R) + H_{\text{HFH}}(\hat{p}_R, r) + V_{\text{MH}}(R, r) \tag{3}$$

ii) If the energy of a harmonic oscillator is noticeably higher than the energy loss in the VP event, the HFH oscillator can be considered as a source of time-dependent perturbation acting on LFM oscillator. Accordingly, the two-degree-of-freedom Hamiltonian in Eq.(3) is replaced by one-degree-of-freedom time-dependent Hamiltonian of a driven Morse (DM) oscillator [13]:

$$\hat{H}_{\text{DM}}(\hat{P}_R, R; t) = H_{\text{LFM}}(\hat{P}_R, R) + V_{\text{DM}}(R, t) \tag{4}$$

where $V_{\text{DM}}(R, t) = V_{\text{MH}}(R, r(t))$ with $r(t)$ being the trajectory of unperturbed harmonic oscillator.
iii) Because of large disparity of frequencies of LF and HF oscillators, the time-dependent interaction in Eq.(4) can be represented adequately by the two terms of its

Fourier expansion [14]. This would correspond to the harmonically-driven Morse oscillator with the Hamiltonian:

$$\hat{H}_{\text{HDM}}(\hat{P}_R, R; t) = \hat{H}_{\text{LFM}}(\hat{P}_R, R) + V_{\text{DM,0}}(R) + V_{\text{DM,1}}(R) \cos(\omega_D t + \varphi) \tag{5}$$

In what follows, we will use the Hamiltonian from Eq.(3) in assessing the applicability of first order diabatic perturbation theory for calculation of k^Q, and the Hamiltonian from Eq.(5) for calculation of k^{QCl} and $k_{\text{eff}}^{\text{Cl}}$.

The VP dynamics for the Hamiltonian in Eq.(5) is most conveniently discussed in terms of dimensionless energy of a Morse oscillator for a system "A + center of mass BC", ε, dimensionless frequency Ω of a harmonic oscillator, the dimensionless time τ and the dimensionless "Planck constant" $\tilde{\hbar}$. The initial energy of a harmonic oscillator affects the VP dynamics only through yet another dimensionless parameter that characterizes the coupling strength between the Morse oscillator and the harmonic perturbation. The explicit expressions for $\varepsilon, \Omega, \tau, \tilde{\hbar}$ are

$$\varepsilon = \frac{E_{\text{vdW}}}{2D_{\text{M}}} \quad , \qquad \Omega = \omega_{\text{BC}} / \omega_{\text{M},e} \ , \ \tau = t\omega_{\text{M},e} \ , \ \tilde{\hbar} = \hbar\omega_{\text{M},e} / 2D_{\text{M}} \tag{6}$$

where E_{vdW} is counted from the dissociation threshold of the Morse potential well of the depth D_{M}, ω_{BC} is the frequency of the harmonic oscillator, and $\omega_{\text{M,e}}$ is the small-amplitude frequency of the Morse oscillator. In this parameterization, the Hamiltonian H_{HDM} is transformed into dimensionless Hamiltonian $\eta_{\text{HDM}} = H_{\text{HDM}} / 2D_{\text{M}}$ which contains dimensionless coordinate q and time τ [14].

3. Quantum VP rate.

The quantum approach to the VP dynamics was formulated by Rosen [15] who used the first order perturbation theory for description the intermode energy transfer. The partition of the total energy in two parts was done ignoring the kinematic coupling between two modes. It was shown that the large disparity between frequencies of the vdW mode and that of the molecular moiety is responsible for a very slow decay rate on the time scale of the slow vdW vibrational motion. Much later, a comprehensive theoretical model of VP was developed by Beswick and Jortner [16-18]. They also relied on the perturbative approach and used a model of weakly coupled Morse oscillators that permitted deriving an analytical expression for the VP rate through the golden rule formula. Their approach corresponded to the partitioning of the energy by identifying E_{vdW} with the energy of the vdW complex for the non-vibrating BC oscillator. In the current nomenclature, this approach is dubbed as first order diabatic (FOD) approximation; the respective rate constant $k^{\text{Q,FOD}}$ reads:

$$k_{\text{MM}}^{\text{Q,FOD}}(E_{\text{vdW}}, \Delta E) = \frac{2\pi}{\hbar} \left| {}^{\text{D}}\left\langle E'_{\text{vdW}}, E'_{\text{BC}} \middle| V_{\text{MM}} \middle| E_{\text{vdW}}, E_{\text{BC}} \right\rangle^{\text{D}} \right|^2 \tag{7}$$

where $\left|...\right\rangle^{\mathrm{D}}$ are the eigenfunctions of the Hamiltonian $\hat{H}_{\mathrm{LFM}} + \hat{H}_{\mathrm{LFM}}$. The HDM counterpart of Eq.(7) reads:

$$k_{\mathrm{HDM}}^{\mathrm{Q,FOD}}(\varepsilon, \Delta\varepsilon) = \frac{2\pi}{\hbar}\left|{}^{\mathrm{D}}\left\langle\varepsilon'\left|V_{DM,1}/2\right|\varepsilon\right\rangle^{\mathrm{D}}\right|^2 \tag{8}$$

where the zero-order functions $\left|\varepsilon\right\rangle^{\mathrm{D}}$ are the eigenfunctions of the Hamiltonian $\hat{H}_{\mathrm{LFM}}$ and ε, ε' are related as $\varepsilon' = \varepsilon + \Delta\varepsilon$, $\quad \Delta\varepsilon = \tilde{\hbar}\Omega$.

The rate constant $k^{\mathrm{Q,FOD}}$ is an increasing function of initial state energies, and therefore a question arises about the high-energy limit below which the FOD approach provides a reasonable approximation to the accurate rate constant k^{Q}. As an example, Fig.1 shows the low-lying complex energy levels (in reduced units, see [11]) for a model linear ICl...Ne system calculated accurately by the complex scaling method and within the FOD approximation. For this model $\Omega=8.36$ and the Morse potential supports three bound states. The energy levels $\mathrm{E}_{v,n} = \varepsilon_{v,n} - i\gamma_{v,n}/2$ counted from the dissociation threshold correspond to the vibrational quantum numbers $v = 1,2,3,4,5,6,7,8$ for the BC high frequency mode and $n = 0,1,2$ for vdW low-frequency mode (for clarity, Fig.1 shows the ground vdW states, $n = 0$, only).

It is seen that though the VP rate constant is very small (the VP transition probability is of the order of 10^{-5} per one vibration of the vdW bond), the FOD approximation, at least for this particular example, is reasonable only for the VP induced by transition from the state $v=1$. Therefore, one can ask what are particular physical effects, which are ignored within the FOD approach. The following might be the reasons for noticeable overestimation of the rates by FOD approach compared to the accurate rates:

i) Ignoring a decrease in the steepness of the repulsive part of the interaction potential which is due to a springy property of the high-frequency *vibrating* oscillator (the mattress effect).

ii) Ignoring an increase in the force constant of the high-frequency *vibrating* oscillator upon its compression by a low-frequency motion (the stiffening effect).

The above effects are properly taken into account when one passes from diabatic zero-order basis to the adiabatic zero-order basis, and uses first order adiabatic (FOA) perturbation theory [19,20]. This passage is easily seen in terms of the HDM Hamiltonian, when Eq.(8) is modified as

$$k_{\mathrm{HDM}}^{\mathrm{Q,FOA}} = \frac{2\pi}{\hbar}\left|{}^{\mathrm{A}}\left\langle\varepsilon'\left|V_{DM,1}/2\right|\varepsilon\right\rangle^{\mathrm{A}}\right|^2 \tag{9}$$

where $\left|\varepsilon\right\rangle^{\mathrm{A}}$ are the eigenfunctions of adiabatically-corrected Hamiltonian $\hat{H}_{\mathrm{ALFM}} = \hat{H}_{\mathrm{LFM}} + V_{DM,0}$. The same approximation can be used to calculate complex
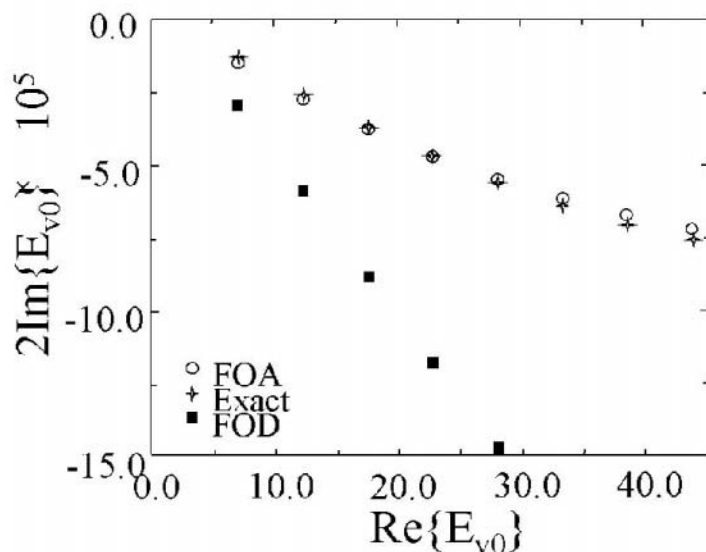
Figure 1. Complex energy levels for a model ICl-Ne system (in reduced units). Shown are the accurate results (complex scaling method, crosses), first-order diabatic (FOD, filled squares) and first-order adiabatic (FOA, open circles).

eigenvalues of the initial Hamiltonian in Eq.(2). The result is also shown in Fig.1. We indeed see that the adiabatic basis serves as a very good zero-order approximation. A very noticeable difference between FOD and FOA eigenvalues can be traced back to the fact that FOA approximation takes into account the mattress and stiffening effects. These two effects cause a small relative change in the large Massey parameter of the VP problem thus noticeably affecting the absolute value of the VP rate. In other words, the convergence of the perturbation series in the adiabatic basis is much quicker compared to that in the diabatic basis. This indicates that the Beswick-Jortner rates, based on the FOD approximation, can not be unconditionally used for comparison of accurate quantum and classical rates, though this procedure was adopted in the first paper devoted to the classical VP dynamics [21].

4. Quasiclassical VP rate

In adopting the quasiclassical approximation, we use the important property of the VP dynamics that VP transition probability is induced by the interaction close to the inner turning point of the LF oscillator. Then, the expression for the rate constant $k^{QCl}(\varepsilon, \Delta\varepsilon)$ can be split in two factors, the classical frequency $\nu(\varepsilon)$ and the quasiclassical probability $P^{QCl}(\varepsilon, \Delta\varepsilon)$ for VP transition per one excursion of the LF oscillator to the repulsive part of the potential.

$$\kappa^{\mathrm{QCl}}(\varepsilon, \Delta\varepsilon) = \nu(\varepsilon) P^{\mathrm{QCl}}(\varepsilon, \Delta\varepsilon) \tag{10}$$

According to Landau [2], the first order probability $P^{\mathrm{QCl,FO}}$ is proportional to an exponential function which contains the absolute value of the difference in the classical actions for the initial and final states, calculated from the classical turning points q_{ti} and q_{tf} to the stationary phase point q_{stph} which in our case lies in the classically forbidden region of motion. Explicitly,

$$P^{\mathrm{QCl,FO}}(\varepsilon, \Delta\varepsilon) = B \exp\left(-\frac{2}{\tilde{\hbar}} |\Delta\sigma(\varepsilon, \Delta\varepsilon)| \right) \tag{11}$$

with

$$\Delta\sigma(\varepsilon, \Delta\varepsilon) = \int_{q_t}^{q_{stph}} p_q(q, \varepsilon) dq - \int_{q_t'}^{q_{stph}} p_q(q, \varepsilon') dq \tag{12}$$

The momentum p_{q} is found from the equation

$$\frac{p_q^2}{2} + \upsilon(q) = \varepsilon \tag{13}$$

where $\upsilon(q)$ is a potential that determines the unperturbed motion of the LF oscillator. For FOD approximation, $\upsilon(q)$ is identified with the Morse potential $\upsilon_{\mathrm{M}}(q)$, while for FOA approximation $\upsilon(q)$ is equal to the adiabatically-corrected Morse potential, $\upsilon_{\mathrm{M}}^{\mathrm{A}}(q) = \upsilon_{\mathrm{M}}(q) + \upsilon_{\mathrm{DM},0}(q)$.

A path $q_t \to q_{stph} \to q_t'$ is the classically forbidden part of the VP trajectory (we call it a "trajectory" since it is defined by the classical Hamiltonian; however, it is "classically forbidden" since for this part of the trajectory the momenta are imaginary). Taken together with the classically allowed parts of the incoming and outgoing trajectories, it defines the full trajectory for the VP event, see Fig.2.

The preexponential factor in Eq. (11) can be found either by calculating the transition amplitude within the stationary phase approximation as explained in [2], or by considering the correspondence-principle (CP) limit of the QCl transition amplitude. We will follow the latter prescription since it allows an easier comparison of classical and quantum rates in Sect.6.

The VP quasiclassical expression for the rate can be expressed through classical dynamical quantities following our suggestion for recovering the Landau matrix elements from the Fourier components of classical functions [4-6].

According to [6], the Landau exponent in Eq. (11) is related to the encounter time τ_{en} as

$$|\Delta\sigma(\varepsilon, \Delta\varepsilon)| = \int_{\varepsilon}^{\varepsilon+\Delta\varepsilon} \tau_{\mathrm{en}}(\bar{\varepsilon}) d\bar{\varepsilon} \tag{14}$$
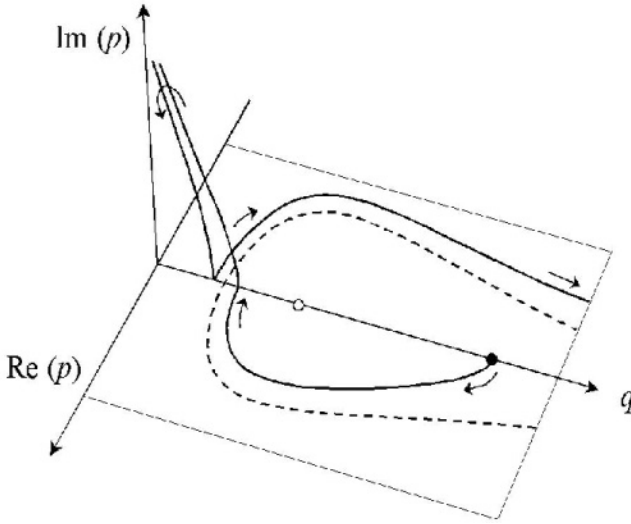
Figure 2. The Landau "classical" VP trajectory in the $q, \mathrm{Re}(p), \mathrm{Im}(p)$ space (bold line) The dashed line indicates the potential energy contour at the dissociation threshold. The solid circle represents the initial point of the trajectory, the open circle represents the equilibrium point of the potential; arrows show the direction of the motion.

Here the energy-dependent encounter time τ_{en} is given by

$$\tau_{en}(\bar{\varepsilon}) = \int_{q_{stph}}^{q(\bar{\varepsilon})} \frac{dq'}{\sqrt{2\upsilon(q') - 2\bar{\varepsilon}}} \tag{15}$$

The preexponential factor in Eq.(11) can be found by comparing the correspondence principle (CP) limit of this expression (condition $\varepsilon \gg \Delta\varepsilon$) with the FO CP transition probability $P^{CP,FO}(\varepsilon, \Delta\varepsilon)$. The latter can be expressed by using CP relation between the classical and quantum FO mean-square energy transfer per one encounter (one excursion of the vdW oscillator into the repulsive region of the interaction). In this way we get:

$$\left\langle (\Delta\varepsilon)^2 \right\rangle^{\mathrm{Cl,FO}} = \left\langle (\Delta\varepsilon)^2 \right\rangle^{\mathrm{CP,FO}} = 2(\Delta\varepsilon)^2 P^{CP,FO}(\varepsilon, \Delta\varepsilon) \tag{16}$$

wherefrom

$$P^{CP,FO}(\varepsilon, \Delta\varepsilon) = \frac{\left\langle (\Delta\varepsilon)^2 \right\rangle^{\mathrm{Cl,FO}}}{2(\Delta\varepsilon)^2} \tag{17}$$

On the other hand, the CP limit of Eq.(11) is:

$$P^{QCl,FO}(\varepsilon, \Delta\varepsilon)_{\Delta\varepsilon \ll \varepsilon} = P^{CP,FO}(\varepsilon, \Delta\varepsilon) = B\exp\left(-\frac{2\Delta\varepsilon}{\widetilde{\hbar}}\tau_{en}(\varepsilon)\right) \qquad (18)$$

From the comparison of Eqs.(17) and (18) we determine B and finally express $P^{QCl,FO}(\varepsilon,\Delta\varepsilon)$ as

$$\kappa^{QCl,FO}(\varepsilon, \Delta\varepsilon) =$$
$$= \frac{\nu(\varepsilon)}{2}\frac{\left\langle(\Delta\varepsilon(\varepsilon)^2\right\rangle^{Cl,FO}}{(\Delta\varepsilon)^2}\exp\bigl[2\Omega\bigl(\tau_{en}(\varepsilon) - \tau_{tun}(\varepsilon_i, \Delta\varepsilon)\bigr)\bigr]\Theta(\varepsilon + \Delta\varepsilon) \qquad (19)$$

where the dynamical tunneling time from the level ε to the level $\varepsilon'=\varepsilon+ \varepsilon$ is defined as

$$\tau_{tun}(\varepsilon, \Delta\varepsilon) = \frac{1}{\Delta\varepsilon}\int_{\varepsilon}^{\varepsilon+\Delta\varepsilon}\tau_{en}(\overline{\varepsilon})d\overline{\varepsilon} \qquad (20)$$

The plots of the encounter and tunneling times vs. energy are shown Fig. 3.
The Heaviside step function $\Theta(\varepsilon+\Delta\varepsilon)$ in Eq.(19) indicates that the FO VP rate is nonzero only when the final energy $\varepsilon + \Delta\varepsilon$ is positive. Since $\Delta\varepsilon = \widetilde{\hbar}\Omega$ and ε is negative, it is clear that the classical limit of QCl FO VP rate is zero (the limit $\widetilde{\hbar} \to 0, \Omega$ fixed). This is expected since an isolated resonance has no classical counterpart, and the one-quantum vibrational predissociation does not belong to the events that conform to the
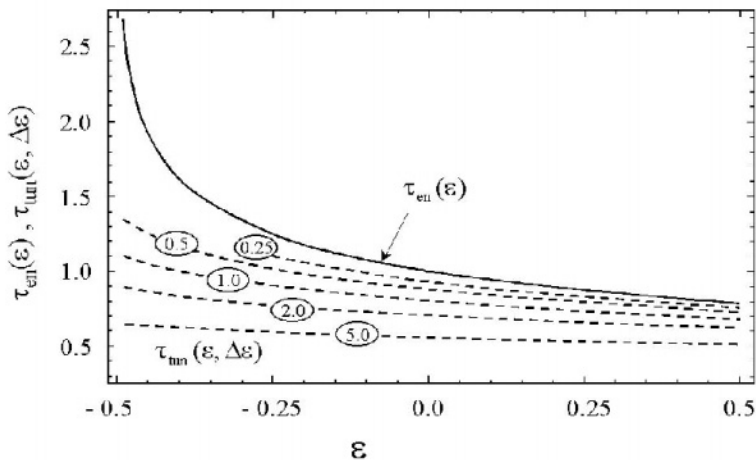
Figure 3. Classical encounter time $\tau_{en}(\varepsilon)$, and quasiclassical tunneling times $\tau_{tun}(\varepsilon, \Delta\varepsilon)$ (dashed curves) for a Morse oscillator. (The curves for $\tau_{tun}(\varepsilon, \Delta\varepsilon)$ are labeled by the values of $\Delta\varepsilon$).

correspondence principle. On the other hand, the QCl FOA approach provides a very good approximation to accurate VP rates [11,19,20].

5. Classical effective VP rate

Classical VP occurs as a result of chaotic motion of the driven LF oscillator toward the dissociation threshold. The effective dynamic rate constant $k_{\text{eff}}^{\text{Cl}}(\varepsilon,\Omega)$ for the crossing the chaotic sea that separates the initial state of energy ε from the dissociation threshold can be defined as a reciprocal time during which the initial population drops by a factor of e. It has been shown that a fair approximation to $k_{\text{eff}}^{\text{Cl}}(\varepsilon,\Omega)$ is given by the effective diffusion rate constant $k_{\text{eff}}^{\text{Cl,Diff}}(\varepsilon,\Omega)$ [12] which is recovered from the solution of the Kramers equation that simulates the chaotic dynamical behavior of the driven LF oscillator. In turn, $k_{\text{eff}}^{\text{Cl,Diff}}(\varepsilon,\Omega)$ can be reproduced by an analytical formula $k_{\text{bottl}}^{\text{Cl,Diff}}(\varepsilon,\Omega)$ when one exploits the fact that the energy diffusion coefficient in the Kramers equation increases strongly with the energy [22]. In this (so-called bottleneck) approximation we write

$$k_{\text{eff}}^{\text{Cl}} \approx k_{\text{eff}}^{\text{Cl,Diff}} \approx k_{\text{bottl}}^{\text{Cl,Diff}} \qquad \text{`} \tag{21}$$

The rate constant $k_{\text{bottl}}^{\text{Cl,Diff}}(\varepsilon,\Omega)$ reads [22]:

$$\kappa_{\text{bottl}}^{\text{Cl,Diff}}(\varepsilon) = \frac{\nu(\varepsilon)}{4}\frac{\left\langle \Delta\varepsilon^2(\varepsilon)\right\rangle^{\text{Cl}}}{(\delta\varepsilon(\varepsilon))^2} \tag{22}$$

Here $\left\langle \Delta\varepsilon^2(\varepsilon)\right\rangle^{\text{Cl}}$ is the mean-square energy transfer per one encounter (one excursion) of the LF oscillator into the repulsive region of the interaction for the initial energy ε, and δε(ε) is the width of the energy bottleneck layer that is adjacent to the initial energy level. The inverse width of this layer is determined by the rate of increase of the energy transfer with the energy:

$$\frac{1}{\delta\varepsilon(\varepsilon)} = \frac{d}{d\varepsilon}\ln\left\langle \Delta\varepsilon^2(\varepsilon)\right\rangle^{\text{Cl}} \tag{23}$$

Under the condition when one can use FO perturbation approach in quantum and quasiclassical calculations, the classical mean square energy transfer can also be calculated in the FO classical perturbation theory. This again opens a possibility for comparison of FOD and FOA (now classical) approximations. Fig.4 shows the

dependence of $\left\langle \Delta\varepsilon^2(\varepsilon) \right\rangle^{Cl}$ (trajectory calculations), $\left\langle \Delta\varepsilon^2(\varepsilon) \right\rangle^{Cl,FOD}$ and $\left\langle \Delta\varepsilon^2(\varepsilon) \right\rangle^{Cl,FOA}$ on the initial energy of the LF oscillator. Once again, we see that the classical adiabatic perturbation approach performs much better than the diabatic one. Within the FO treatment (both diabatic and adiabatic), the mean-square energy transfer is of the following form [14]:

$$\left\langle (\Delta\varepsilon)^2 \right\rangle^{Cl,FO} = A \exp\left(-2\Omega\tau_{en}(\varepsilon)\right) \tag{24}$$

which defines the FO bottleneck layer as

$$\frac{1}{\delta\varepsilon^{FO}(\varepsilon)} = -2\Omega\frac{d\tau_{en}(\varepsilon)}{d\varepsilon} \tag{25}$$

Thus, the FO counterpart of Eq.(22) reads:

$$\kappa_{bottl}^{Cl,Diff,FO}(\varepsilon) = \frac{\nu(\varepsilon)}{4}\frac{\left\langle \Delta\varepsilon^2(\varepsilon) \right\rangle^{Cl,FO}}{(\delta\varepsilon^{FO}(\varepsilon))^2}\Theta(\varepsilon - \varepsilon^{Ch}) \tag{26}$$
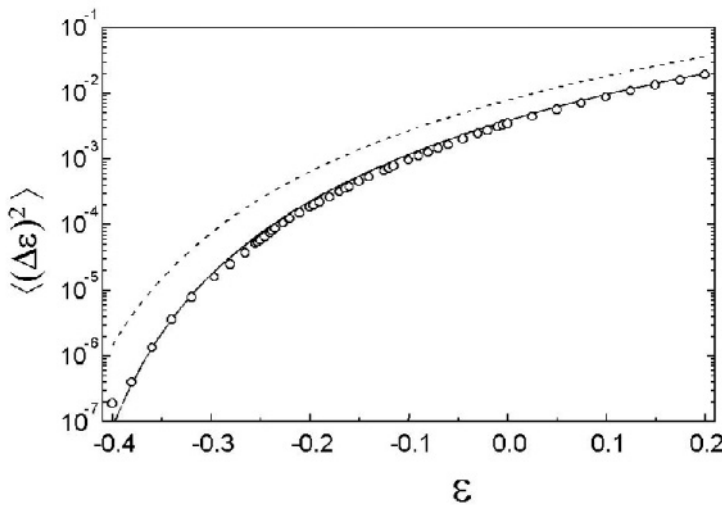
Figure 4. An example of the dependence of the mean square energy transfer per encounter, $\left\langle (\Delta\varepsilon)^2 \right\rangle$, on the energy ε of the driven oscillator with $\Omega = 7$. The open circles represent accurate trajectory results, the dashed line the FOD treatment, and the full line FOA treatment. Negative values of ε correspond to the bound states of the Morse oscillator, positive to the dissociative states.

The Heaviside step function $\Theta(\varepsilon+\Delta\varepsilon)$ in Eq.(26) symbolically emphasizes the fact that the FO VP diffusion description is valid when the initial energy level lies above the chaos onset limit $\varepsilon = \varepsilon^{Ch}$.

According to Chirikov [23], the onset of chaos is associated with the overlap of neighboring nonlinear resonances. The overlap criterion, which bears the qualitative significance, uses the model of isolated resonances. Each resonance is characterized by its width, the maximum distance (in the action variable) from the elliptic fixed point. The overlap means that the sum of the widths of two neighboring resonances is equal to the distance between two fixed points of these isolated resonances. We start with the pendulum Hamiltonian, which describes an isolated $1{:}N$ resonance under the periodic perturbation of frequency Ω:

$$\eta_N^{\text{pend}}(\delta_N\iota, \beta) = -(1/2)(\delta_N\iota)^2 + (1/2)\upsilon_{1N}(\Omega)\cos N\phi \tag{27}$$

Here $\delta_N\iota$ and ϕ are the conjugate action-angle variables, with $\delta_N\iota$ counted from the resonance action ι_N, and $\upsilon_{1N}(\Omega)$ is the interaction parameter that is generated from the interaction energy $\upsilon(\varepsilon,\Omega)$ at the $1:N$ resonance: $\upsilon_{1N}(\Omega) = \upsilon(\varepsilon,\Omega)\big|_{\varepsilon=\varepsilon_N}$ with ε_N found from the $1:N$ resonance condition $N\omega(\varepsilon_N)=\Omega$. The resonance width, $(\delta_N\iota)_{\max}$, for the Hamiltonian (27) is:

$$(\delta_N\iota)_{\max} = \sqrt{2\upsilon_{1N}} \tag{28}$$

We write the overlap criterion as

$$[(\delta_{N+1}\iota)_{\max} + (\delta_N\iota)_{\max}] = |\iota_{N+1} - \iota_N| \tag{29}$$

and, furthermore, $\iota_{N+1} - \iota_N = d\iota_N/dN$, $(\delta_{N+1}\iota)_{\max} = (\delta_N\iota)_{\max}$ (which is valid since $N \gg 1$), and $\omega_N = 1 - \iota_N = \Omega/N$ (which is valid for a Morse oscillator described by the scaled Hamiltonian.). Eqs. (28) and (29) now yield an equation for the resonance $N = N_{Ch}$ which corresponds to the chaos onset

$$\upsilon_{1N_{\text{ch}}}(\Omega) = \frac{\Omega^2}{8N_{ch}^4} \tag{30}$$

Once this equation is solved for N_{Ch}, it also determines the critical energy ε_{Ch} and the critical value of the interaction $\upsilon_{1N_{\text{ch}}}$ for the chaos onset. Eq.(30) can be rephrased in terms of a condition which insures that the energy level ε lies in the chaotic region:

$$\upsilon(\varepsilon,\Omega) \geq \frac{\omega^4(\varepsilon)}{8\Omega^2} \tag{31}$$

Now, the quantity $\upsilon(\varepsilon,\Omega)$ can be related to the mean square energy transfer for the Morse oscillator per one excursion into the repulsive region of the potential:

$$\upsilon^2(\varepsilon,\Omega) = 2\left(\frac{\omega(\varepsilon)}{\pi\Omega}\right)^2 \left\langle (\Delta\varepsilon(\varepsilon))^2 \right\rangle^{\text{Cl,FO}} \tag{32}$$

In turn, $\left\langle (\Delta\varepsilon(\varepsilon))^2 \right\rangle^{\text{Cl, FO}}$ determines the effective bottleneck rate constant in Eq.(26). Therefore the Chirikov condition for the interaction strength $\upsilon(\varepsilon,\Omega)$ in Eq.(31) can be reformulated as a condition for the effective rate constant

$$\kappa_{\text{bottl}}^{\text{Cl,Diff,FO}}(\varepsilon) \geq \lambda(\varepsilon); \qquad \lambda(\varepsilon) = \left(\frac{\omega(\varepsilon)}{2}\right)^7 \left(\frac{d\tau_{\text{en}}(\varepsilon)}{d\varepsilon}\right)^2 \tag{33}$$

An interesting property of an inequality in Eq.(33) is that rate constant $\kappa_{\text{bottl}}^{\text{Cl,Diff,FO}}$ depends, beside the energy ε, on the coupling strength and the driving frequency, while the "chaos onset boundary" λ depend only on ε. This makes it possible to discuss different classical models on equal footing [14]. We indeed found out that the chaos onset limit for the VP events is given by the criterion of overlapping resonances, Eq.(33), and that the transition from the regular motion (from where the VP is forbidden) to the chaotic motion is quite abrupt. The latter property permits symbolic use of the step function in Eq.(26), where the energy of the chaos onset ε^{Ch} is found from the Chirikov criterion:

$$\kappa_{\text{bottl}}^{\text{Cl,Diff,FO}}(\varepsilon^{\text{Ch}}) = \lambda(\varepsilon^{\text{Ch}}) \tag{34}$$

6. Comparison of classical and quantum predissociation rates

The classical effective predissociation rate, $\kappa_{\text{eff}}^{\text{Cl}}(\varepsilon)$, out of the energy level $\varepsilon = \varepsilon_n$, can now be compared with the quantum predissociation rate $\kappa^Q(\varepsilon_n,\Delta\varepsilon)$ via their diffusional and quasiclassical counterparts, $\kappa_{\text{bottl}}^{\text{Cl,Diff,FO}}(\varepsilon_n)$ from Eq.(26) and $\kappa^{\text{QCl,FO}}(\varepsilon,\Delta\varepsilon)$ from Eq.(19). For this purpose, we calculate the ratio R of the bottleneck classical to quasiclassical rate constants:

$$R(\varepsilon_n,\Delta\varepsilon) = \frac{\kappa_{\text{bottl}}^{\text{Cl,Diff,FO}}(\varepsilon_n)}{\kappa^{\text{QCl,FO}}(\varepsilon_n,\Delta\varepsilon)} =$$

$$= 2\left[\Delta\varepsilon\Omega \cdot \left.\frac{d\tau_{\text{en}}(\varepsilon)}{d\varepsilon}\right|_{\varepsilon=\varepsilon_n}\right]^2 \exp\left\{-2\Omega(\tau_{\text{en}}(\varepsilon_n) - \tau_{\text{tun}}(\varepsilon_n,\Delta\varepsilon))\right\} \tag{35}$$

Two important properties of this expression are:

i) The ratio R depends on the coupling strength only through its manifestation in the adiabatically-corrected interaction potential.

ii) The ratio R depends on the adiabatically-corrected interaction potential only through its manifestation in the encounter time. In this respect, Eq. (35) has more general significance than an expression applicable only to the dissociating Morse oscillator. Note, however, that the adiabatic correction to the encounter time affects the difference in the exponent of the r.h.s. of Eq.(35) in much smaller degree than it does for the individual terms. Therefore, the ratio $R(\varepsilon_n, \Delta\varepsilon)$ can be considered in the FOD approximation.

iii) For a given value of ε_n, the Planck constant enters into R only through the transferred energy $\Delta\varepsilon = \tilde{\hbar}\Omega$.

The quantity R in Eq.(35) should provide a fair estimate of the ratio of classical/quantum rate constants, if the following basic conditions are fulfilled: the initial energy ε_n should be above the chaos threshold energy $\varepsilon^{Ch}, \varepsilon_n > \varepsilon^{Ch}$, and the final energy should be positive, $\varepsilon_n + \Delta\varepsilon > 0$. Of course, the whole discussion is valid only if Ω, the ratio of the driving frequency to the frequency of the vdW moiety, is noticeably larger than one.

One sees that the ratio R can be larger or smaller than unity. This follows from the following observation. The preexponential factor in Eq (35) is always larger than unity since it equals the square of the ratio of the transferred energy $\Delta\varepsilon$ to the classical diffusional energy layer $\delta\varepsilon$, $(\Delta\varepsilon/\delta\varepsilon)^2 \gg 1$. On the other hand, the exponential factor may be substantially smaller than unity since the classical encounter time τ_{en} is always longer than the quasiclassical tunneling time τ_{tun}, such as illustrated in Fig. 3.

A useful insight into the ratio R can be gained if one plots R as a function of Ω for given value of ε_n and the scaled Planck constant $\tilde{\hbar}$. First we note that ε_n for as Morse potential is given by formula:

$$\varepsilon_n = \tilde{\hbar}(n+1/2)\left[1 - \tilde{\hbar}(n+1/2)\right] - 1/2, \quad n = 0,1,....N \tag{36}$$

where $\tilde{\hbar}$ is defined by Eq.(6). Second, we put $\tilde{\hbar} = 1/(N+1/2)$. This means that the Morse potential supports just $N+1$ levels with the upper lever at the dissociation boundary. We then write

$$R_{n,N}(\Omega) = R(\varepsilon_n, \Delta\varepsilon)\big|_{\tilde{\hbar}=1/(N+1/2)} \tag{37}$$

The plots of the functions $R_{n,N}(\Omega)$ are presented in Fig. 5 for $N=1,2,3$ and discussed in detail in [14].

Here we only note that for the classical models studied earlier [7-12, 21] the classical VP rates are higher than the quantum rates. We interpret this as a consequence of inability for a quantum system to follow available classical paths, which turn out to be too narrow to allow the minimal finite action of volume $\hbar$ to squeeze through them.
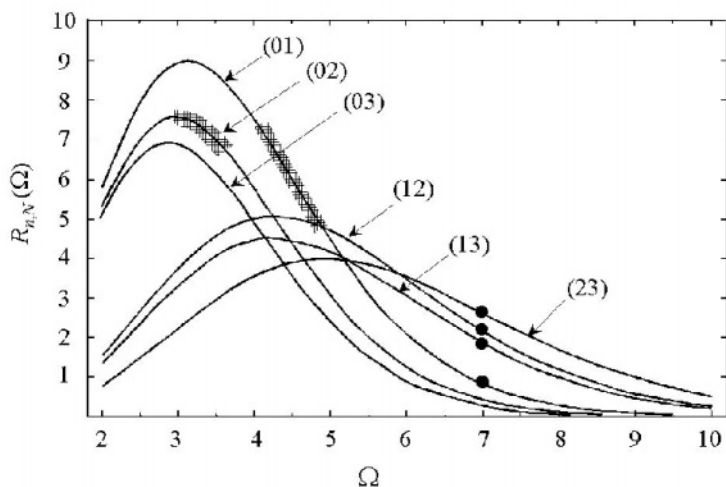
Figure 5. Ratios $R_{n,N}(\Omega)$ of the classical bottleneck VP rates to the quasiclassical VP rates vs. driving frequency Ω for different initial vibrational states n of the vdW oscillator with a Morse potential well that supports just $N+1$ 0 states, $N=1,2,3$. The curves are labeled by (n,N) quantum numbers; filled points correspond to the model of [12] (states (01), (13), (12) and (23) for fixed frequency Ω; shaded areas correspond to the models of [8] and [21] (states (02) and (01), respectively) for a ranges of frequencies such as indicated.

Nonetheless, with an increase of the driving frequency, the tunneling quantum decay eventually takes over. This is predicted by Eq (35), since $\lim_{\Omega\to\infty} R_{nN}(\Omega) = 0$. However, this limit is not very interesting because the initial classical states fall into the regular regime where the diffusional description becomes inapplicable.

We believe that the above comparison clarifies the statement in [1] that if the quantum decomposition occurs via isolated resonances, only in special cases do the classical and quantum rates coincide.

7. Conclusion

Summarizing, we note that the single-quantum vibrational predissociation of a weak van-der-Waals bond in a triatomic molecule and the classical dissociation of the same system do not represent processes which can be compared in the correspondence principle limit. Our study explains why the classical and quantum rates sometimes are close to each other and show the same trends with a change of the interaction parameters. The underlying logic in comparing of classical and quantum and VP rates is as follows:

i)   The classical motion, which leads to dissociation, is chaotic;

ii) The chaotic motion can be approximately described by the diffusion model, and the effective classical VP rate can be related to the energy diffusion coefficient in the initial state;

iii) The diffusion coefficient is related, *within the first-order classical perturbation approach*, to certain Fourier components of the interaction potential;

iv) The same Fourier components can be used to recover the quasiclassical transition matrix element that connects the initial and final states;

v) The quasiclassical transition matrix elements approximate well the respective quantum mechanical matrix elements;

vi) These quantum mechanical matrix elements determine the dissociation rate *within the first-order quantum perturbation approach*.

However, the classical approach should not be used for a quantitative interpretation of the experimental results for single-quantum vibrational predissociation. The classical process, which should show the correspondence with the quantum one, is the cleavage of a bond under a condition when the quantum of energy transferred to this bond from a diatomic fragment, $\hbar\Omega$, is much smaller than the dissociation energy, E_D, of the bond, i.e. $\hbar\Omega \ll E_D$. This condition does not contradict the classical limit, $\hbar \to 0$. The actual study of this limit (small but finite value of $\hbar$) is rather complicated, as it is already evident from the chaotic classical dynamics and from the inapplicability of a first-order perturbation approach in the quantum dynamics. However, at least the classical limit under the condition that the dissociation energy is large compared to the "vibrational temperature" of the molecule is clear: it is the diffusional description of IVR supplemented with the standard mean first passage time approach for calculation of the rate constant [24-28].

Acknowledgments

References

1. Baer, T. and W. L. Hase, (1996) *Unimolecular Reaction Dynamics,* Oxford University Press, Oxford.

2. Landau L. D. and Lifshitz, E. M., (1977) *Quantum Mechanics*, Pergamon Press, Oxford.

3. Moiseyev, N. (1998) Quantum theory of resonances: calculating energies, widths and cross-sections by complex scaling, *Phys. Rep.*, **302**, 211-293.

4. Nikitin, E.E. , Noda, C. and Zare, R.N. (1993) On the quasiclassical calculation of fundamental and overtone intensities, *J.Chem.Phys.*, **98**, 47-59.

5. Karni, Y., and Nikitin, E.E., (1994) Recovery of the Landau matrix elements from the classical Fourier components:one-dimensional dissociating oscillator, (1994) *J.Chem. Phys.*, **100**, 2027-2033.

6. Nikitin, E.E. and Pitaevskii, L. (1994) Calculation of the Landau quasi-classical exponent from the Fourier components of classical functions, *Phys.Rev.*, **A49**, 695-703.

7. Noid, D.W., Gray, S.K. and Rice S.A., (1986) Fractal behavior in classical collisional energy transfer *J.Chem.Phys.* **84**, 2649-2652.

8. Gray, S.K., Rice, S.A. and Noid, D.W. (1986) The classical mechanics of vibrational predissociation: A model based study of phase space structure and its influence on fragmentation rates, *J.Chem.Phys*. **84**, 3745-3752.

9. Davis, M.J. and Gray, S.K. (1986) Unimolecular reactions and phase space bottlenecks, *J.Chem.Phys*. **84**, 5389-5411.

10. Gray, S.K., Rice, S.A. and Davis, M.J. (1986) Bottlenecks to unimolecular reactions and alternative form for classical RRKM Theory, *J.Phys.Chem.* **90**, 3470-3482.

11. Karni, Y. and Nikitin, E.E. (1996) Vibrational predissociation: quasiclassical tunneling and classical diffusion, *Mol.Phys*. **89**, 1327-1343.

12. Dashevskaya, E. I. Litvin, I., Nikitin, E. E. and Troe, J. (2001) Classical diffusion model of vibrational predissociation of van der Waals complexes: II. Comparison with trajectory calculations and analytical approximations, *Phys. Chem. Chem. Phys.*, **3,** 2315-2324.

13. Gray, S.K. (1987) A periodically forced oscillator model of van der Waals fragmentation: Classical and quantum dynamics, *J.Chem.Phys.* **87**, 2051-2061.

14. Dashevskaya, E. I., Litvin, I., Nikitin, E. E., Oref, I. and Troe, J. (2002) Classical diffusion model of vibrational predissociation of van der Waals complexes: III. Comparison with quantum calculations, *Phys. Chem. Chem. Phys.* **4**, 3330-3340.

15. Rosen, N. (1933) Lifetimes of unstable molecules, *J.Chem.Phys.,* **1**, 319-326.

16. Beswick, J.A. and Jortner J., (1978) Vibrational predissociation of triatomic van der Waals molecules, *J.Chem.Phys.*, **68**, 2277-2297.

17. Beswick, J. A. and Jortner, J. (1978) Perpendicular vibrational predissociation of T-shaped van der Waals molecules, *J. Chem. Phys.*, **69**, 512-518.

18. Beswick, J. A. and Jortner, J. (1981) Intramolecular dynamics of van der Waals molecules, *Adv.Chem.Phys.*, **47**, 363-506.

19. Karni, Y. and Nikitin. E.E. (1994) Vibrational predissociation rate from dynamics of the full collision: a test of the Landau method against the exact results, *J.Chem.Phys.*, **100**, 8065-8071.

20. Karni, Y. and Nikitin, E.E. (1995) Adiabatically corrected quasiclassical model for the vibrational predissociation of van der Waals complexes, *Chem.Phys.,* **191**, 235-246.

21. Woodruff, S.B. and Thompson, D. (1979) A quasiclassical trajectory study of vibrational predissociation of van der Waals molecules: Collinear He··I$_2$($B^3\Pi$)*, J.Chem.Phys.* **71**, 376-380.

22. Dashevskaya, E.I., Litvin, I., Nikitin, E. E., Oref, I. and Troe, J. (2000) Classical diffusion model of vibrational predissociation of van der Waals complexes: I. Truncated mean first passage time approximation.*Phys. Chem. Chem. Phys* **2**, 2251-2259.

23. G.M. Zaslavskii, (1985), *Chaos in Dynamical Systems*, Harwood Academic Publishers.

24. Shalashilin, D.V. and Thompson, D.L. (1996) Intrinsic non-RRK behaviour: Classical trajectory, statistical theory, and diffusional theory studies of a unimolecular reaction, *J.Chem.Phys.* **105**, 1833-1845.

25. Shalashilin, D.V. and Thompson, D.L. (1997) Method for predicting IVR-limited unimolecular reaction rate coefficients, *J.Chem.Phys.* **107**, 6204-6212.

26. Guo, Y., Shalashilin, D. V., Krouse, J. A. and Thompson, D. L. (1999) Predicting nonstatistical unimolecular reaction rates using Kramers' theory, *J. Chem. Phys.* **110**, 5514-5520.

27. Guo, Y., Shalashilin, D. V., Krouse, J. A. and Thompson, D. L.(1999) Intramolecular dynamics diffusion theory approach to complex unimolecular reactions, *J. Chem. Phys.* **110**, 5521-5525.

28. Guo, Y., Thompson, D. L. and Miller, W. (1999) Thermal and microcanonical rates of unimolecular reactions from an energy diffusion theory approach, *J.Phys.Chem. A*, **103**, 10308-10311.

SOME RECENT ADVANCES IN THE MODELING OF ION-MOLECULE ASSOCIATION REACTIONS

J. TROE

Institut für Physikalische Chemie, Universität Göttingen
Tammannstrasse 6, D-37077 Göttingen, Germany

1. Introduction

Ion-molecule reactions and reactions of neutral species in the gas phase have much in common. Nevertheless, because different communities were concerned, theories of the kinetics of these processes have often been developed separately, missing the chances for synergism and for more rapid progress. Fortunately, this unsatisfactory situation is changing and the common aspects, but also the characteristic differences are becoming identified more clearly.

This report describes the state-of-the-art of modeling ion-molecule association reactions. For these reactions, the rate coefficients depend on the temperature T, the chemical nature and the concentration [M] of the bath gases M. The modeling of the corresponding recombination reactions of neutral species has been a traditional part of unimolecular rate theory. The "falloff curves", i.e., the dependences of the second-order rate coefficients k on [M], together with the limiting low pressure (k_0) and high pressure (k_∞) rate coefficients, have been analyzed in detail (see e.g. [1]) and amply documented (see e.g. [2]). Experimental studies of the falloff curves covered wide pressure ranges, from fractions of a millibar to a thousand bar (see e.g. [3]). Such wide variations have not been realized for ion-molecule associations. First, it is essential that truly thermal conditions are being applied. Second, experiments should be conducted up to high gas pressures. Using laser-induced ionization for reactant preparation and laser-induced fluorescence for product detection, falloff curves for ion-molecule association, however, are now also becoming accessible up to relatively high pressures [4]. In the following, we consider the framework for modeling falloff curves of association reactions in general and, subsequently, we try to specify where ionic and neutral reaction systems differ or agree.

2. General Formalism

The energy-transfer (ET) mechanism of association reactions involves the following steps

$$A + B \rightarrow AB* \qquad (1)$$

$$AB^* \rightarrow A + B \tag{-1}$$
$$AB^* + M \rightarrow AB^* M \tag{2}$$

The second-order rate coefficient

$$k = ([A][B])^{-1} d[AB]/dt \tag{3}$$

at steady-state takes the form

$$k = k_1 \{ k_2 [M]/(k_2 [M] + k_{-1}) \}. \tag{4}$$

The corresponding thermal dissociation starts with the reverse of reaction (2),

$$AB + M \rightarrow AB^* + M \tag{-2}$$

and is completed by a competition of reactions (-1) and (2) so that a first-order rate coefficient

$$k_{diss} = -([AB])^{-1} d[AB]/dt, \tag{5}$$

given by

$$k_{diss} = k_{-2}[M] \{ k_{-1}/(k_2[M] + k_{-1}) \}, \tag{6}$$

is obtained. Obviously, k and k_{diss} are linked by the equilibrium constant K_{eq} through

$$k/k_{diss} = K_{eq} = k_1 k_2 / k_{-1} k_{-2}. \tag{7}$$

In reality, more complicated expressions apply because of the multi-step character of the reaction: k_1 and k_{-1} depend on the energy E and the angular momentum (quantum number J), and the collisional energy transfer is a multi-step process with activations and deactivations, to be characterized by a master equation. It has become customary to consider "strong collisions" first and to introduce "weak collision effects" afterwards. For strong collisions, equation (6) takes the form

$$k_{diss}^{SC} = Z[M] \sum_{J=0}^{\infty} \int_{E_o(J)}^{\infty} dE \, f(E,J) k(E,J) / \{ Z[M] + k(E,J) \} \tag{8}$$

where k_2 is replaced by a total energy transfer collision frequency Z, k_{-1} is represented by the specific rate constants $k(E,J)$ for dissociation of the excited adducts AB*, $E_o(J)$ denotes the J-dependent threshold energies for dissociation of AB*, and $f(E,J)$ are equilibrium populations of the states of the adduct in that part of the metastable range

which is populated or depopulated by collisions. The corresponding strong collision rate coefficient k for association follows through eq. (7).

In the low pressure limit, eq. (8) approaches

$$k_{diss,0}^{SC} = Z[\text{M}] \sum_{J=0}^{\infty} \int_{E_o(J)}^{\infty} dE f(E,J) \tag{9}$$

which can be expressed in an economical way [1] as

$$k_{diss,0}^{SC} \cong Z[\text{M}] \frac{\rho_{vib,h}(E_o)\text{k}T}{Q_{vib}} F_E F_{anh} F_{rot} \exp[-E_o(J=0)/\text{k}T] \tag{10}$$

with the vibrational harmonic density of states $\rho_{vib,h}(E)$, the vibrational partition function Q_{vib}, a factor F_E accounting for the E-dependence of $\rho_{vib,h}(E)$, a factor F_{anh} accounting for the anharmonicity of the vibrational density of states, and a factor F_{rot} accounting for the rotational contributions to eq. (9). Provided that the relevant molecular parameters of AB are known, the evaluation of eq. (10) is straightforward. Likewise, the conversion to k_0 via eq. (7) can easily be made; however, an internally consistent set of molecular parameters has to be used.

   In reality, collisions will not be "strong" which is expressed by a collision efficiency β_c through

$$k_{diss,0} = \beta_c k_{diss,0}^{SC} . \tag{11}$$

Solution of the master equation has related β_c to the average energy $\langle \Delta E \rangle$ transferred per collision [1] by

$$\beta_c / \left(1 - \beta_c^{\frac{1}{2}}\right) \approx -\Delta E / F_E \text{k}T . \tag{12}$$

In the high-pressure limit, eq. (8) approaches

$$k_{diss,\infty}^{SC} = \sum_{J=0}^{\infty} \int_{E_o(J)}^{\infty} dE \, f(E,J) k(E,J) . \tag{13}$$

Statistical unimolecular rate theory expresses $k(E,J)$ by

$$k(E,J) = W(E,J)/\text{h}\rho(E,J) \tag{14}$$

where $W(E,J)$ is the number of "open channels", of "activated complexes", or of "capture channels". The features of $W(E,J)$ in ionic and neutral systems need to be analyzed, since $W(E,J)$ is determined by the properties of the potential energy surface of the reaction system, see below.

Reduced falloff curves k/k_∞ as a function of a "reduced pressure scale" k_0/k_∞, being proportional to [M], are identical for dissociation and association reactions. In the simplified mechanism given above, they take the form

$$\frac{k}{k_\infty} = \frac{k_0/k_\infty}{1+k_0/k_\infty}.$$ (15)

Because of the described multi-step character of the mechanism, broadening factors $F(k_0/k_\infty)$ have to be introduced, i.e.,

$$\frac{k}{k_\infty} = \frac{k_0/k_\infty}{1+k_0/k_\infty} F(k_0/k_\infty).$$ (16)

It was shown in [1] that, in the simplest way, $F(k_0/k_\infty)$ is approximated by

$$F(k_0/k_\infty) \approx F_{center}^{1/\left\{1+[\log(k_0/k_\infty)/N]^2\right\}}.$$ (17)

with $N \approx 0.75\text{-}1.27 \log F_{center}$. More accurate, although more complicated, representations of $F(k_0/k_\infty)$ require detailed models for $k(E,J)$. Examples have been calculated recently in [5],[6]. Some asymmetries of $F(k_0/k_\infty)$ and minor shifts of the minimum were observed. The center broadening factor F_{center} can either be used as a fitting parameter or it can be calculated from unimolecular rate theory, see below.

In rare cases [7],[8] a different mechanism has been identified in neutral association reactions, named the radical-complex (RC) or chaperon mechanism. It involves complexes AM and proceeds by the steps

$$A + M \rightarrow AM$$ (18)
$$AM \rightarrow A + M$$ (-18)
$$AM + B \rightarrow AB + M$$ (19)

such that

$$k = (k_{18}/k_{-18})k_{19}[M].$$ (20)

This mechanism sometimes dominates the low-pressure range for reactions involving only few atoms; more generally the high-pressure range can be influenced. As ions A more easily form complexes AM with the bath gas M with stronger bonds, one has to look for RC-contributions more regularly in ionic than in neutral reaction systems, see below.

In the following, we shall discuss the properties of k_0, k_∞, and of the reduced falloff curves in more detail, trying to identify common and different contributions for ionic and neutral reaction systems.

3. High pressure limit of association reactions

Converting eqs. (13) and (14) to high pressure association rate coefficients, leads to

$$k_\infty = \frac{kT}{h}\left(\frac{h^2}{2\pi\mu kT}\right)^{3\!/\!2} \frac{Q_{el}(AB)}{Q_{el}(A)Q_{el}(B)} \frac{Q^*}{Q_{vibrot}(A)Q_{vibrot})(B)} \tag{21}$$

with an "activated complex partition function" Q^* given by

$$Q^* = \sum_{J=0}^{\infty} \int_{E_o(J)}^{\infty} dE\, W(E,J)\exp(-E/kT). \tag{22}$$

Q_{el} and Q_{vibrot} denote electronic and rovibrational partition functions, respectively. In general, the contributions of the internal degrees of freedom of A and B cancel in Q^* and $Q_{vibrot}(A)Q_{vibrot}(B)$, such that only contributions from the external rotations of A and B and the relative motion, summarized as "transitional modes", need to be considered. Under low temperature quantum conditions, these can be obtained by statistical adiabatic channel (SACM) calculations [9],[10] while classical trajectory (CT) calculations [11]-[14] are the method of choice for higher temperatures. CT calculations are run in the capture mode, i.e. trajectories are followed from large separations of A and B to such small distances that subsequent collisions of AB* can stabilize the adduct.

In the case of isotropic potential energy surfaces, such as appropriate (approximately) for ion A - induced dipole B systems, the situation is even simpler. In this case, the external rotational levels of A and B transfer unchanged into W(E,J) and Q^* becomes a centrifugal partition function

$$Q^* = \sum_{J=0}^{\infty} \exp\left[- E_o(J)/kT\right]. \tag{23}$$

For an ion - induced dipole (α) potential

$$V(r) = -\alpha q^2 / 2r^4, \tag{24}$$

$E_o(J)$ follows as

$$E_o(J) = \left[\frac{J(J+1)\hbar^2}{(2\alpha)^{1\!/\!2}2\mu q}\right]^2, \tag{25}$$

such that

$$Q^* = \left(\frac{2\mu q}{\hbar^2}\right)\left(\frac{\pi\alpha kT}{2}\right)^{\frac{1}{2}} \qquad (26)$$

and

$$k_\infty = k_L = 2\pi q(\alpha/\mu)^{\frac{1}{2}} \qquad (27)$$

(as long as $Q_{el}(AB)/Q_{el}(A)Q_{el}(B) = 1$). Eq. (27) is the well-known Langevin rate constant for capture of induced dipoles by ions which here is represented as part of a general formulation of association rate coefficients.

When the potential becomes anisotropic, such as in ion - permanent dipole (μ_D) and ion - quadrupole potentials, the situation immediately becomes more complicated. Earlier treatments like the average dipole (or quadrupole) orientation (ADO or AQO) methods were not physically correct because thermal averaging was done before the treatment of capture, while the opposite order is required. Classical trajectory calculations by Su and Chesnavich [11], for ion - permanent dipole capture, instead led to

$$k_\infty/k_L \approx 1 + 0.0967x + 0.0950x^2 \qquad (28)$$

and

$$k_\infty/k_L \approx 0.4767x + 0.6200 \qquad (29)$$

where $x = \mu_D/(2\alpha kT)^{1/2}$, and eq. (28) applies for $x \leq 2$ while eq. (29) is for $x \geq 2$. These were confirmed and extended over the full range between adiabatic and sudden dynamics in [12]. At very low temperatures (kT/B, B = rotational constant of the dipole rotor), eqs. (28) and (29) cease to be valid. Instead, a transition to

$$k_\infty(T \to 0)/k_L = (1 + \mu_D^2/3\alpha B)^{\frac{1}{2}} \qquad (30)$$

takes place [9] which prevents the divergence of eq. (29). CT calculations for ion - quadrupole capture have also been done in detail and represented analytically in [13],[14].

Eqs. (28) and (29) show that ion - induced + permanent dipole association reactions at high pressures should be dominated by the permanent dipole at low temperatures while they are governed by the induced dipole at high temperatures. At very high temperatures, finally the valence part of the potential comes into play [15]. In the following, we confront this expectation with experimental observations [16] for the formation of the proton-bound dimer of ammonia

$$NH_3 + NH_4^+ + M \to NH_3H^+NH_3 + M. \qquad (31)$$
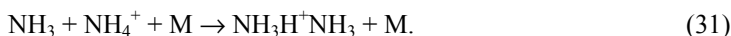
Figure 1 shows second-order rate coefficients measured in a CRESU flow apparatus over a wide temperature range at a variety of pressures and bath gases.
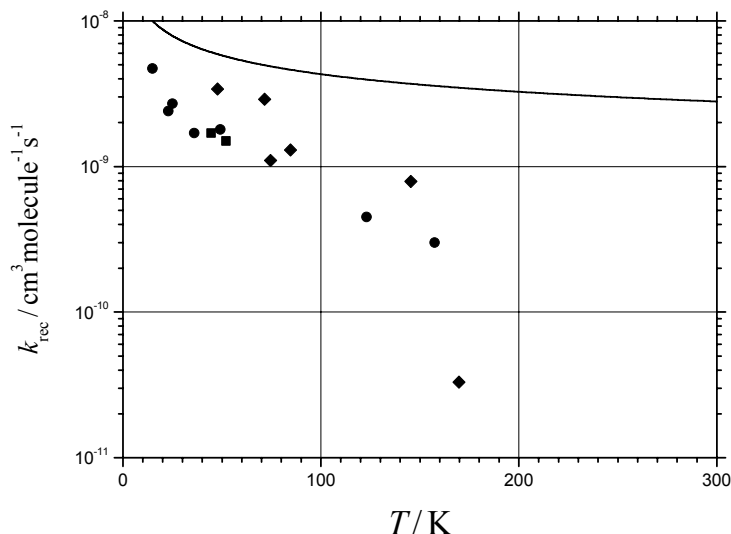
Figure. 1   Second-order rate coefficients for the reaction $NH_3 + NH_4^+ + M \rightarrow N_2H_7^+ + M$ from CRESU experiments in [16] (full line = Su-Chesnavich prediction of eqs. (28) and (29), circles: M = He, squares: M = Ar, diamonds: M = N_2).

The Su-Chesnavich line corresponds to eqs. (28) and (29), illustrating the changing contribution of the induced and permanent dipoles of NH_3. As $k_\infty(T \rightarrow 0) = 1.65 \times 10^{-8}$ cm^3 molecule^{-1} s^{-1} is derived from eq. (30) and $B_{eff}(NH_3)/k = 7$ K, the quantum range of k is not reached in the measurements down to 15 K, and CT calculations are fully appropriate for all measurements. The deviations of the experiments from the Su-Chesnavich line, therefore, have to be attributed to falloff effects, see below. In order to reach the high-pressure limit, higher pressures would have had to be applied in these experiments. With increasing molecular size of A and B, the transition to the high pressure limit shifts to lower pressures. Going from reaction (31) to larger amines, this was demonstrated in [17].

Quantum effects become important only at very low temperatures, i.e. for $B/kT \approx 1$. The best candidates for observing these effects thus are hydrides. Quantum effects become more pronounced when A and/or B are species with open electronic shells; see e.g. the differences between the associations $N_2 + N_2^+ \rightarrow N_4^+$ and $O_2 + O_2^+ \rightarrow O_4^+$ at temperatures below 10 K [10]. Before leaving this section, it should be mentioned that alternative approaches such as the ACCSA treatment from [18], the perturbed rotational state treatment from [19] and the semiclassical adiabatic invariance method from [20] all represent simplified variants of the here described SACM/CT approach and, like the

ADO and AQO approaches, today are superseded by the more accurate and more general treatments from [9]-[15].

4. Low pressure limit of association reactions

An experimental illustration for the approach of the low pressure limit $k \to k_0$, where k_0 is proportional to the bath gas concentration [M] and the association reaction is a termolecular process, is shown in figure 2 for the reaction
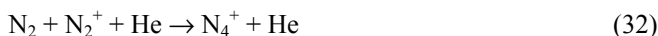
$$N_2 + N_2^+ + He \to N_4^+ + He \tag{32}$$

In this case, pressures below about 10 Torr would be required for reaching the low
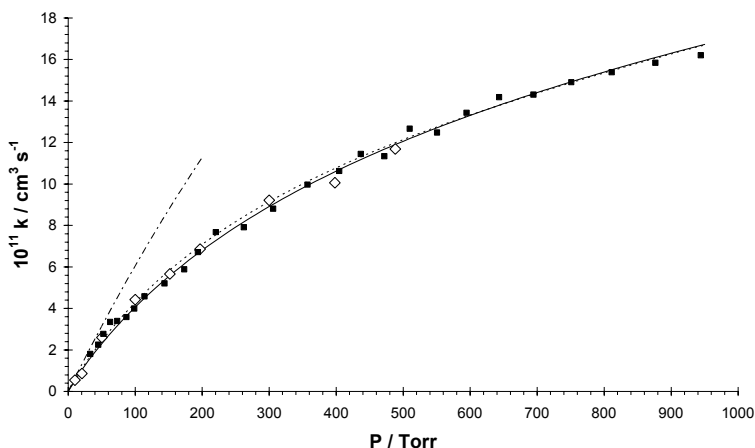
Figure. 2   Second order rate coefficients for the reaction $N_2 + N_2^+ + He \to N_4^+ + He$ from [4] (dash-dotted line = low pressure limit, dotted line = eqs. (16)-(17), full line = more rigorous falloff fit, see [4], diamonds = flow system, squares = static system).

pressure limit. An analysis of k_0 has been made in [4] on the basis of eqs. (10)-(12). Since the required molecular parameters for N_4^+ are fairly well known today, most of the factors in eq. (10) can be calculated easily following the prescriptions of [1]. In these factors there is no principle difference between ionic and neutral systems. There is the same basic uncertainty about anharmonicity factors F_{anh}. The rotational factors F_{rot} for ionic AB should rather use centrifugal barriers from electrostatic potentials such as given by eq. (25), than relying on short-range valence potentials; in any case F_{rot} reaches the order of magnitude of its maximum value in the absence of centrifugal barriers and determined by the bond strength of AB [1]. The major difference between the ionic and neutral systems is in the product $Z \beta_c$. At present, there exists much less direct information on collisional energy transfer of highly excited molecular ions than for excited neutrals. For the latter, Z generally is approximated by the Lennard-Jones

collision frequency and β_c is consistent with directly measured $\langle\Delta E\rangle$-values, typically being in the -hc 100 cm^{-1}-range for M = He and in the -hc 200 cm^{-1}-range for M = N$_2$. In [4], Z was assumed to be given by the Langevin rate constant for N$_4^+$ + M - collisions. Then $\beta_c \approx 0.4$ for M = He, and $\beta_c \approx 0.9$ for M = N$_2$ was derived. Underestimating F_{anh} and F_{rot} would have led to an overestimate of β_c which seems not improbable. In any case, the assumption of $Z \approx k_L$ appears highly reasonable, leading to β_c-values not far away from the corresponding values for neutrals. However, this approach to β_c, and hence to $\langle\Delta E\rangle$, is much too uncertain to decide whether energy transfer of highly excited ions and neutrals have similar properties or not. This question has recently been answered for highly excited ethylbenzene ions in collision with M = He and N$_2$ [21]. By chemical activation experiments, where energy transfer was measured relative to the known $k(E)$ for fragmentation, quite similar $\langle\Delta E\rangle$-values for ions were derived as for the corresponding neutrals. One, therefore, can conclude that the modeling of k_0 by eqs. (10)-(12) for neutrals and ions can be made in the same way, except for the different total collision frequencies Z which for ions can be identified with the AB + M - capture rate constants from section 3. Apart from this difference, termolecular ion - molecule association rate constants, therefore, should be modeled within the general formalism of section 2 and should not follow special formulations developed separately.

5. Falloff curves for ion-molecule association reactions

It remains to be discussed, whether eq. (17) provides an adequate representation of the falloff curves interpolating between k_0 and k_∞, and how the parameter F_{center} can be predicted. This question applies as well to neutrals as to ionic systems. The question has a strong collision and a weak collision aspect. If one concludes that $\langle\Delta E\rangle$ and β_c are similar for ionic and for neutral systems, then the weak collision broadening factor F_{center}^{WC} in $F_{center} = F_{center}^{WC} F_{center}^{SC}$ can be estimated [1] by

$$F_{center}^{WC} \approx \beta_c^{0.14}. \tag{33}$$

The strong collision broadening factor F_{center}^{SC} requires the knowledge of all details of $k(E,J)$ and of $W(E,J)$ such as given by unimolecular rate theory. Details of this treatment cannot be given here. It should, however, be mentioned that the dominant ingredients for this treatment are the same as described in section 3. For isotropic potentials, $W(E,J)$ directly follows from phase space theory (PST) and can be easily calculated. The effects of anisotropy of the potential are represented by specific rigidity factors $f_{rigid}(E,J)$ such that

$$W(E,J) = f_{rigid}(E,J) W(E,J)_{PST} \tag{34}$$

$f_{rigid}(E,J)$ generally follows from CT calculations such as shown in [22]. For ion - permanent dipole capture, however, a simple expression for $f_{rigid}(E,J)$ was derived by SACM methods in [9], giving

$$f_{rigid}(E,J) \approx 1 - J(J+1)\hbar^2 / 2\mu q \mu_D . \tag{35}$$

On this basis, strong collision broadening factors were calculated for reaction (31) in [16]. Figure 3 shows the results. F_{center}^{SC} is close to 0.2 and does not show a particular
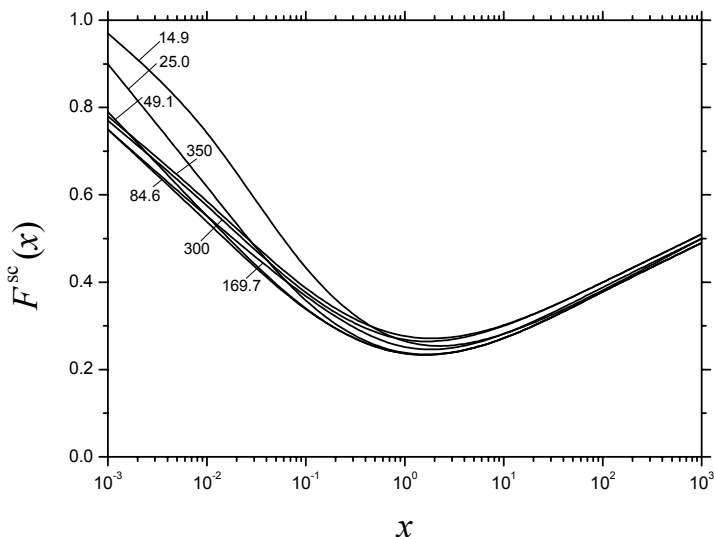
Figure. 3 Strong collision broadening factors $F^{SC}(x)$ for the reaction $NH_3 + NH_4^+ + M \rightarrow N_2H_7^+ + M$ from [16] (numbers in the figure = T/K, $x = k_0/k_\infty$).

temperature dependence. The considered ion - permanent dipole - system is characterized by vanishing centrifugal barriers as long as $J(J+1)\hbar^2 \leq 2\mu q \mu_D$. It is, therefore, special and different from ion-induced dipole- and neutral radical - radical systems. For the latter, one would have expected [6] F_{center}^{SC} to be close to 0.42. Some deviations of figure 3 from eq. (17) are also noted. For neutral radical - radical associations, asymmetries of $F(k_0/k_\infty)$ were observed which are opposite to those of figure 3. Unless one can do the complete treatment, eq. (17) provides a good first approximation, F_{center}^{SC} being of the order of 0.42 for nonlinear A + nonlinear B, 0.47 for nonlinear A + linear B, 0.53 for linear A + linear B, 0.59 for atomic A + nonlinear B, and 0.63 for atomic A + linear B [23]. The fitted $F_{center} \approx 0.47$ for M = He and $F_{center} \approx 0.52$ for M = N_2 in reaction (32) from [4] are well consistent with these values and eq. (33).

The described procedure for modeling the limiting low and high pressure rate coefficients k_0 and k_∞, and the falloff curves interpolating between these values, can be

employed for localizing experimental data such as illustrated in figure 1. As an example, in figure 4 we compare modeled strong collision falloff curves for reaction (31) in the bath gas M = He with the measurements from figure 1. One realizes that
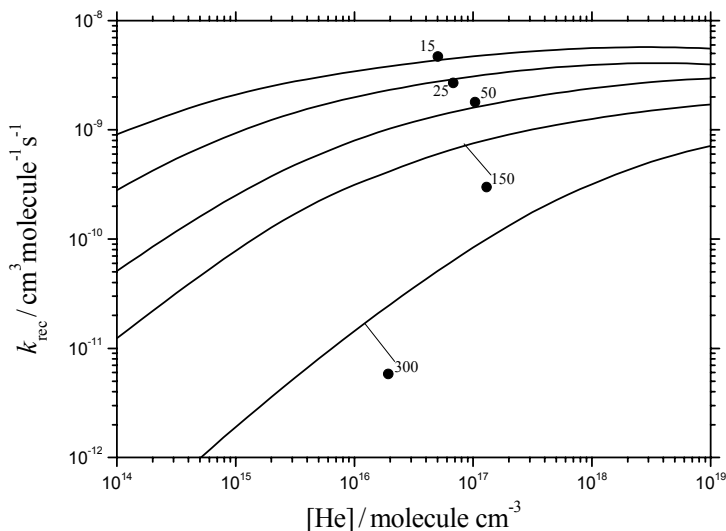
Figure. 4   Experimental second-order rate coefficients (points) for the reaction
 $NH_3 + NH_4^+ + He \rightarrow N_2H_7^+ + He$ with modeled strong collision falloff curves (lines)
(numbers = T/K, results from [16]).

the experimental data at the higher temperatures are systematically lower than the modeled curves whereas they nearly fall on the curves at lower temperatures. This is easily explained by weak collision effects. Taking into account collision efficiencies β_c of the order of 0.2 over the range 150-300 K, leads to shifts of the curves from left to right such the experiments scatter around the modeled curves. At lower temperatures, on the one hand, according to eq. (12) (with temperature independent $\langle \Delta E \rangle$) β_c increases, on the other hand, because of the approach of the experiments to the high-pressure limit, weak collision effects do not influence much the position of the curves relative to the measurements. One can, therefore, conclude that the modeled rate coefficients of reaction (31) with M = He very well agree with the measurements over a wide temperature range. Without this modeling, the data points such as obtained from the CRESU experiments in figure 1 could not have been understood.

   One may try to apply the same analysis of the experimental data for reaction (31) with different bath gases M. It was shown in [16] that low pressure rate coefficients for strong colliders such as M = CH_4 or NH_3 at 200-350 K are well reproduced by the modeled k_0. On the other hand, there is a problem with the data for M = N_2 from figure

1. Figure 5 compares the experiments from figure 1 with modeled falloff curves for M = N_2. The low temperature results are systematically above the
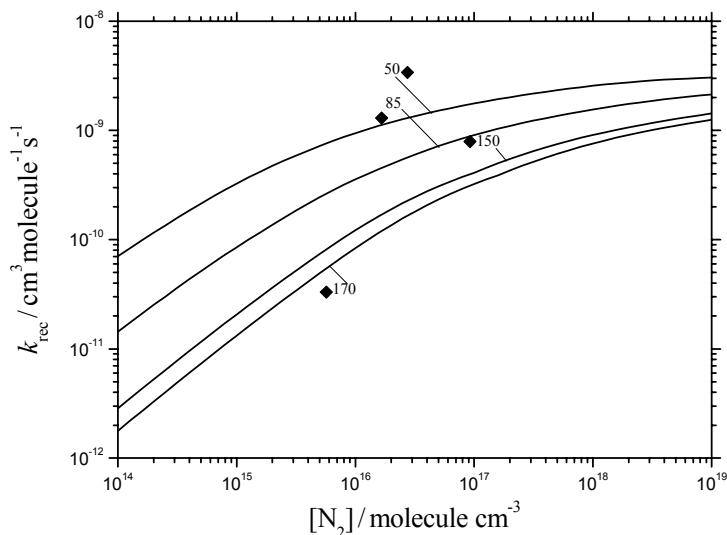
Figure. 5   As figure 4, for $NH_3 + NH_4^+ + N_2 \rightarrow N_2H_7^+ + N_2$.

modeled strong collision falloff curves and at higher temperatures the results are less below the curves than one would have expected with typical β_c. In view of the good agreement between experiment and theory for M = He this is surprising. However, an interpretation of the discrepancy can be found [16] by considering the interaction between NH_4^+ and N_2: $NH_4^+N_2$ complexes are known to have binding energies of the order of $D/k \approx 3000$ K and higher complexes $NH_4^+(N_2)_n$ are similarly strongly bound. As a consequence, at lower temperatures NH_4^+ will be fully solvated by N_2 and the reaction proceeds by the radical-complex mechanism

$$NH_4^+(N_2)_n + NH_3 \rightarrow N_2H_7^+(N_2)_n. \tag{36}$$
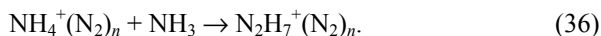
The rate of this reaction can again be estimated by the capture theory from section 3 under the assumption that NH_4^+ is heavily clustered (reduced mass $\mu[NH_4^+(N_2)_n + NH_3] \approx m[NH_3]$) and that the charge of NH_4^+ is shielded by the solvation shell (charge $q \approx q/\varepsilon$ with ε = dielectric constant of liquid nitrogen). Using this interpretation, the modeling of the combined ET- and RC-mechanism such as given in [16] succeeds to reproduce the experimental results from figure 6.

6. Conclusions

Ion-molecule association reactions and the corresponding reactions of neutral species have much in common and, therefore, should be interpreted and modeled by the same theoretical framework. Nevertheless, there are also characteristic differences which require specific changes of the analysis. On the energy transfer side, different collision frequencies Z have to be considered while average energies $\langle \Delta E \rangle$ appear to be of similar size in ionic and related neutral systems. Specific rigidity factors $f_{rigid}(E,J)$ and centrifugal barriers $E_o(E,J)$ may also be characteristically different, but such differences have only minor influences on reduced falloff curves. Finally, capture rate constants determining the high pressure rate coefficients in ionic systems are governed by long range electrostatic potentials in a way which can well be expressed by the analytical representation of classical trajectory results.

Acknowledgments

References

1. Troe, J. (1979) *J. Phys. Chem.* **83**, 114.
2. Atkinson, R., Baulch, D.L., Cox, R.A., Hampson, R.F., Kerr, J.A., Rossi, M.J., and Troe, J. (1997), *J. Phys. Chem. Ref. Data* **26**, 521.
3. Croce de Cobos, A.E., Hippler, H., and Troe, J. (1984), *J. Phys. Chem.* **88**, 5083.
4. Frost, M.J. and Sharpe, C.R.J. (2001), *Phys. Chem. Chem. Phys.* **3**, 4536.
5. Troe, J. (2001) *Int. J. Chem. Kinet.* **33**, 878.
6. Cobos, C.J. and Troe, J. (2003) *Z. Phys. Chem.* **217**, 1.
7. Hippler, H., Rahn, R., and Troe, J. (1990) *J. Chem. Phys.* **93**, 6560.
8. Oum, K., Sekiguchi, K., Luther, K., and Troe, J. (2003) *Phys. Chem. Chem. Phys.* **5**, in press.
9. Troe, J. (1987) *J. Chem. Phys.* **87**, 2773; (1996) *J. Chem. Phys.* **105**, 6249.
10. Maergoiz, A.I., Nikitin, E.E., and Troe, J. (1996) *Z. Phys. D* **36**, 339.
11. Su, T. and Chesnavich, W.J. (1982), *J. Chem. Phys.* **72**, 2641.
12. Maergoiz, A.I., Nikitin, E.E., Troe, J., and Ushakov, V.G. (1996) *J. Chem. Phys.* **105**, 6263.
13. Bhowmic, P.K. and Su, T. (1991) *J. Chem. Phys.* **94,** 6444.
14. Maergoiz, A.I., Nikitin, E.E., Troe, J., and Ushakov, V.G. (1996) *J. Chem. Phys.* **105**, 6270.
15. Troe, J. and Ushakov, V.G. (2003) *J. Chem. Phys.*, to be published.
16. Hamon, S., Speck, T., Mitchell, J.B.A., Rowe, B.R., and Troe, J. (2002) *J. Chem. Phys.* **117**, 2557.
17. Olmstead, W.N., Lev-On, M., Golden, D.M., and Brauman, J.I. (1977) *J. Am. Chem. Soc.* **99**, 992.
18. Clary, D.C. (1987) *J. Chem. Soc. Faraday Trans 2* **83**, 139.
19. Takayanagi, K. (1978) *J. Phys. Soc. Jpn.* **45**, 976.
20. Bates, D.R. (1982) *Proc. Roy. Soc. London A* **384**, 289.
21. Troe, J., Viggiano, A.A., and Williams, S. (2003) *J. Phys. Chem. A* **107**, in press.
22. Maergoiz, A.I., Nikitin, E.E., Troe, J., and Ushakov, V.G. (2002) *J. Chem. Phys.* **117**, 4201.

VIBRATIONAL RELAXATION OF DIATOMS IN COLLISIONS WITH ATOMS AT VERY LOW ENERGIES

E. I. DASHEVSKAYA[a], E. NIKITIN[a,b], I. OREF[a], and J. TROE[b]

[a]*Department of Chemistry, Technion - Israel Institute of Technology, Haifa, 32000 Israel,*
[b]*Institut für Physikalische Chemie der Universität Göttingen, Tammannstrasse 6, D-37077 Göttingen, Germany*

Abstract A generalization of the Landau-Teller model for vibrational relaxation of diatoms in collisions with atoms at very low energies is presented. The extrapolation of the semiclassical Landau-Teller approach to the zero-energy Bethe-Wigner limit is based on the quasiclassical Landau method for calculation of transition probabilities, and the recovery of the Landau exponent from the classical collision time. The quantum suppression-enhancement probabilities are calculated for a general potential well, which supports several bound states, and for a Morse potential with arbitrary number of states. The model is applied to interpretation of quantum scattering calculations for the vibrational relaxation of H_2 in collisions with He.

1. Introduction

Vibrational relaxation (VR) of diatomic molecules in collisions with atoms (the loss of the vibrational energy of a diatom released as the relative translational energy of the partners and the rotational energy of a molecule) represents a simplest example of non-reactive collisions between molecular species (see, e.g. [1,2]). The VR event in a collision

$$A + BC(n, j) \rightarrow A + BC(n', j') \qquad (1)$$
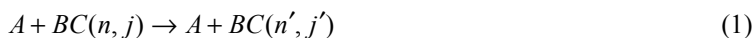
is schematically represented in Fig.1, with *n,j* being the vibrational and rotational quantum numbers of a diatom. Shown are an interpartner interaction potential of A and BC coupled to an oscillator BC, and energy levels for the relative motion before, E, and after, E', the collision.

The increase in the energy $E \rightarrow E' = E + \Delta E$ is accompanied by the decrease of the energy of the oscillator, which is depicted as a lowering of the vibrational amplitudes. Two limiting collision regimes are presented here.

 i) The high-energy regime, valid under the condition $E >> \Delta E$, corresponds to the well-known Landau-Teller (LT) model, with the VR transition probability P^{VR} given by the
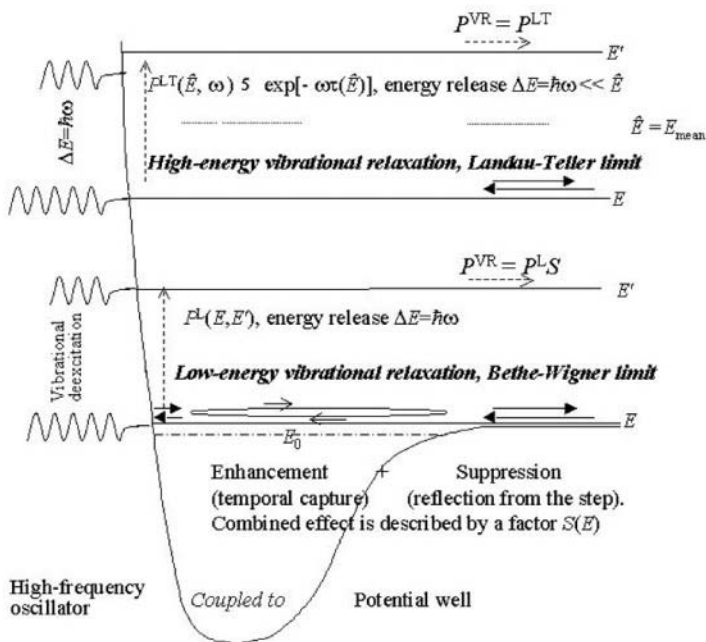
Figure 1. Schematic representation of VR collision in the high and low energy regimes.

Landau-Teller expression $P^{VR} = P^{LT} \propto \exp(-2\pi\Delta E/\hbar \alpha v)$ for a head-on collision. Here v is the collision velocity and α is the logarithmic derivative of the repulsive exponential potential [3].

The exponential dependence of P^{VR} on velocity is the manifestation of the Ehrenfest adiabatic principle [4], once $\Delta E/\hbar$ is identified with the frequency ω of a perturbed system (the BC diatom) and $2\pi/\hbar\,\alpha v$ with the characteristic time of the perturbing force $\tau(E)$ for the exponential interaction. A representation

$$P^{VR} = P^{LT}(E, \Delta E) = A\exp(-\Delta E \tau(E)/\hbar) \tag{2}$$

suggests a generalization of the LT approach for an arbitrary interaction provided that the change of the action variable of a perturbed system is small compared to the initial action. Note also that LT transition probability P^{LT} is an example of the correspondence principle transition probability, which is based on the fundamental relation between the quasiclassical matrix elements and the Fourier components of the respective classical quantities [5].

ii) The low-energy regime corresponds to the condition when the de Broglie wave length of the relative motion $\lambda = 1/k$ (with k being the wave vector) is much larger then the length characterizing the collision complex. In the limit of vanishingly small k, the VR s-wave transition probability in the case of attractive interaction is given by the general Bethe-Wigner (BW) expression [6,7]:

$$P^{VR} = P^{BW}(E, \Delta E) = 4L''(\Delta E)k \tag{3}$$

where L'' is the inelastic scattering length that contains all the information on the dynamics of an inelastic event. The universal k dependence (or velocity dependence) of the transition probability in the low-energy exoergic collisions follows from the general unitary properties of the scattering matrix [5].

  In this contribution we will discuss the VR event in the BW limit and beyond it and also consider the energy dependence of the VR cross section in a wide energy range for a particular case with A = He and BC = H_2. The plan of the presentation is the following. Section 2 describes the problem. Section 3 is devoted to the quantum suppression in the case of quasiclassical potential well of the intermolecular interaction. Section 4 deals with specific model of the Morse potential which allows one to relax the quasiclassical conditions for the motion in the well region. In Section 5 we discuss the Landau transition probability for the Morse potential. Section 6 describes the bridging between the low- and high-energy regimes of the VR cross sections for H_2-He collisions. We conclude by indicating key parameters that determine the energy dependence of the VR cross section over wide energy range.

2. State-specific VR cross sections

State-specific rovibrational relaxation cross section ($n' < n$) in a collision (1) has a standard form:

$$\sigma_{n'j';nj}(k) = \frac{\pi}{k^2(2j+1)} \sum_J (2J+1) P^J_{n'j';nj}(k) \tag{4}$$

where k is the wave vector in the initial state, $E = \hbar^2 k^2 / 2\mu$, $P^J_{n'j';nj}$ is the probability of the transition $n, j \to n', j'$, and J is the total angular momentum J. In turn, $P^J_{n'j';nj}$ is a sum of probabilities $P^J_{n'j'\ell';nj\ell}$ that correspond to all possible relative angular momenta ℓ, ℓ' compatible with j, j', J, $P^J_{n'j';nj} = \sum_{\ell,\ell'} P^J_{n'j'\ell';nj\ell}$. In order to avoid a complicated algebra of angular momentum addition we will consider a specific transition between initial and final rotationless states $j=0 \to j'=0$. Then the sum $\sum_{\ell,\ell'} P^J_{n'j'\ell';nj\ell}$ reduces to a single term $P^J_{n'0J;n0J}$. Also, for definiteness, we assume that VR corresponds to

deactivation of the first vibrational state of a diatom, i.e. we will discuss the transition, $n=1 \rightarrow n=0$. Omitting all unessential subscripts we put $P_{10J;00J}^{J}(k) = P_{J}^{VR}(k,k')$, $\sigma_{10;00}(k) = \sigma^{VR}(k,k')$, where we emphasized the dependence of the VR transition probabilities and VR cross section on initial and final wave vectors k, k'. Then Eq. (4) assumes the form:

$$\sigma^{VR}(k,k') = \frac{\pi}{k^2}\sum_{J}(2J+1)P_J^{VR}(k,k') \tag{5}$$

If the probability $P_J^{VR}(k,k')$ is calculated within first-order perturbation approach and if the motion in the exit channel is quasiclassical, then, as follows from the generalized Landau method [8], $P_J^{VR}(k,k')$ can be factorized into the quasiclassical Landau probability $P_J^{L}(k,k')$ and the so-called a suppression-enhancement factor $S_J(k)$ [6], i.e.

$$P_J^{VR}(k,k') = P_J^{L}(k,k')S_J(k) \tag{6}$$

In this approximation, the nonquasiclassical character of motion in the entrance channel is associated with the elastic scattering in this channel (S_J depends only on k, and not on k'). The two possibilities, $S_J(k) < 1$) or $S_J(k) > 1$ correspond to the suppression or enhancement of the VR probability compared to the quasiclassical probability.

The LT limit of Eq.(5) corresponds to high collision energies, when $S_J(k) = 1$, and many partial waves contribute to the cross section:

$$\sigma^{VR}(k,k')_{E \gg \Delta E} = \sigma^{VR,LT}(E,\Delta E) =$$
$$= \pi\int\frac{2J}{k^2}P_J^{VR,LT}(E,\Delta E)dJ = Q^{LT}\exp(-\Delta E\tau(E)/\hbar) \tag{7}$$

Here $\Delta E\tau(E)/\hbar$ is assumed to be large, and Q^{LT} depends on E much weaker than the exponential does.

The BW limit of Eq.(5) refers to extremely small values of the wave vector, when only the s-wave contributes to the cross section [7,8]:

$$\sigma^{VR}(k,k')\Big|_{k \to 0} = \frac{4\pi L''}{k} = \frac{\pi}{k^2}P_0^{VR}(k,k')\Big|_{k \to 0} = \frac{\pi}{k}\lim_{k \to 0}P_0^{L}(k,k')\frac{S_0(k)}{k} \tag{8}$$

In what follows, we discuss a simple model, which allows one to interrelate quantities entering in Eqs. (2) and (3), identify the key parameters that clarify the meaning of the BW limit $k \to 0$, determine the basic features of the low-energy VR relaxation, and

suggest an interpolation formula that bridges the gap between the LT and BW limits. This proves to be possible due to two important features of the VR event: rather small probability of the VR event and the quasiclassical character of motion of the partners in the exit channel. The former feature allows one to rely on the perturbation approach in an appropriate basis (say, adiabatic channel basis [9]), while the latter permits to use the generalized Landau method of calculating transition probabilities [10,11].

3. *s*-wave inelastic VR scattering for a potential with a quasiclassical well

It is well known that the VR energy transfer is induced by short-range repulsive part of the intermolecular interaction A-BC [1,2,12]. This part is separated from the long-range attractive part by a potential well, which may or may not support bound states of a complex A-BC. If the well supports at least several bound states, the motion inside the well for the energies not too close to the bottom and to the dissociation threshold is quasiclassical. We call this well a quasiclassical well. The VR event occurs as a result of the travel of an atom A above the well to the repulsive part (the entrance channel) where the atom A gains the energy and then departs (exit channel). An inelastic event occurs close to the turning point with the quasiclassical transition probability P^L which can be calculated by the Landau method [4]. On the way to the repulsive part, the incoming wave in the entrance channel can suffer a partial reflection from the potential step of the long-range attractive part. The attenuation of the wave in traversing the step towards the turning point is the reason of the quantum suppression (compared to the quasiclassical behavior) [13]. Clearly, the quantum suppression disappears if the step is traversed quasiclassically. A part of the wave that elastically reflected from the repulsive part of the potential suffers the reflection from the potential step in its attempt to exit the well. A succession of these reflections (from the turning point and from the step) leads to a temporary trapping of the collision pair. This trapping increases the overall VR transition probability, which is the reason for the quantum enhancement. This event is also schematically depicted in Fig.1.

The interplay of the suppression and enhancement can be comparatively easily described for a quasiclassical well when the inelastic transition and transmission across the step can be considered independently [14,15]. Under this condition, the suppression-enhancement factor $S_0(k) = S_0^{QCl}(k)$ is expressed via the probability of transmission across the potential step $T(k)$, and the phase $\Psi(k)$, which is accumulated during the motion in the region of the well. The phase $\Psi(k)$ equals to a certain quasiclassical phase integral complemented with a non-quasiclassical correction. The explicit expression for $S_0(k)$ reads [15]:

$$S_0^{QCl}(k) = \frac{T(k)}{1 + 2\sqrt{1 - T(k)}\,\cos 2\Psi(k) + (1 - T(k))} \qquad (9)$$

With increase in k, when $T(k) \rightarrow 1$, $S_0^{QCl}(k)$ tends to its quasiclassical limit $S_0^{QCl}(k)_{T\rightarrow\infty} \rightarrow 1$. Here, however, we are interested in the case when k is small. In this

case T is small and linear in k [16], and the function $\Psi(k)$ can be identified with its value for $k=0$:

$$T \to kR^* << 1$$
$$\Psi(k) = \Psi(k)\big|_{k=0} = \psi \tag{10}$$

Then

$$S^{QCl}(k)\big|_{kR^*<<1} = \frac{4(kR^*)}{(kR^*)^2 + 16\cos^2\psi} \tag{11}$$

3.1. VR TRANSITION PROBABILITY IN THE BETHE-WIGNER LIMIT AND BEYOND IT

Consider first the BW limit of Eq.(11). It corresponds to the case when $S_0^{QCl}(k)$ is linear in k, that is when $kR^* << 4|\cos\psi|$

$$S^{QCl}(k)\big|_{kR^*<<4|\cos\psi|} = S^{QCl,BW}(k) = \frac{kR^*}{4\cos^2\psi} \tag{12}$$

Eq.(12) defines the inelastic scattering length as

$$L'' = \frac{S_0^{QC,BW} p^L}{4k} = \frac{R^* p^L}{16\cos^2\psi} \tag{13}$$

where

$$p^L = \lim_{k \to 0} P^L(k,k') \tag{14}$$

Consider now two quantities, R^* and ψ, that determine L'' in Eq.(13). They have been discussed in [13,16].

The length parameter R^* is related to the long-range attractive part of the interaction as:

$$R^* = \begin{cases} A(s)\left(2\mu C/\hbar^2\right)^{1/(s-2)}, & \text{for } U_{att}(R) = -C/R^s \\ 4\pi a, & \text{for } U_{att}(R) \propto -\exp(-R/a) \end{cases} \tag{15}$$

with

$$A(s) = \left(\frac{1}{s-2}\right)^{2/(2-s)} \frac{4\pi}{\Gamma(1/(s-2))\Gamma(1+1/(s-2))} \tag{16}$$

The phase integral ψ is related to the elastic scattering length L'. This relation is especially simple when the deviation $\Delta\psi$ of the phase ψ from the value $\pi(n*+1/2)$ with an integer $n*$ is small, ($|\Delta\psi| \ll 1$):

$$\Delta\psi = \psi - \pi(n*+1/2) = \frac{1}{\hbar}\int_{R_{in}}^{\infty}\sqrt{-2\mu U(R)}dR - \phi* - \pi(n*+1/2),\tag{17}$$

Here

$$\phi* = \begin{cases} \pi/2(s-2), & \text{for } U_{att}(R) = -C/R^s \\ 0, & \text{for } U_{att}(R) \propto -\exp(-R/a) \end{cases}\tag{18}$$

Then, when $|\Delta\psi| \ll 1$,

$$\cos\psi \approx \Delta\psi = \frac{R^*}{4L'}\tag{19}$$

If $n*$ in Eq.(17) equals the quantum number of the upper bound state N, $n*=N$, L' is positive, and it determines the energy of a weakly bound (upper) state E_N:

$$E_N = -\frac{\hbar^2}{2\mu(L')^2}\tag{20}$$

If $n*$ in Eq.(17) equals $N+1$, then the quantity L' is associated with a virtual state [5]. In terms of L', Eq.(12) reads:

$$S^{QCl,BW} = \frac{4k(L')^2}{R^*}\tag{21}$$

Finally, the expression for the inelastic scattering length reads:

$$L'' = \frac{(L')^2}{R^*}p^L\tag{22}$$

This equation expresses the inelastic scattering length L'' in terms of the elastic scattering length L', which is determined by the energy of a weakly-bound state, the zero-energy quasiclassical Landau probability p^L, which is governed by the short–range behavior of the potential, and a length parameter R^*, which characterizes the transmission through the long-range part of the interaction potential.

The quantities L' and L'' determine the complex scattering length $L=L'+iL''$ that enters into the scattering matrix in the BW limit. The condition of small transition probability is now written as $L'' \ll |L'|$, i.e. $p^L \ll R^*/|L'| \ll 1$. The limit $k\to 0$ (the Bethe limit) means $kL' \ll 1$. Note, that Eqs. (21) and (22) are valid for the following hierarchy of

lengths: $\Delta R_{rep}<<\Delta R_e<<R^*<<|L'|<<1/k$ where ΔR_{rep} is the range of the repulsive part of the potential well and R_e is the position of its minimum.

We go now beyond the BW limit, but assume that $kR^*<<1$. Expressed through L' (under the condition $R^*<<L'$) Eq.(12) assumes the form

$$S^{QCl}\Big|_{\substack{kR^*<<1\\R^*<<L'}}=\frac{4L'}{R^*}\frac{kL'}{1+(kL')^2} \tag{23}$$

We see that under the condition $|L'|/R^*>>1$ the function S^{QCl} in Eq.(23), after a linear increase with k, passes through the maximum $S_{max}^{QCl}=2|L'|/R_c^* >>1$ at $kL'=1$. Thus, the function $S^{QCl}(k)$ in Eq.(23) describes the quantum **suppression** of the quasiclassical probability p^L, if $S^{QCl}(k)<1$, and the quantum **enhancement** of the quasiclassical probability p^L if $S^{QCl}(k)>1$. Both effects can exist not only for $kR_S^*<<1$ but also in the Bethe region ($k|L'|<<1$). This interesting feature persists for a non-quasiclassical Morse well (see Section 4) and can be also seen in the results of accurate numerical calculations for a system with a realistic potential (see Section 6). Of course, the prerequisite of these effects is an existence of a weakly bound state.

3.2. LOW-ENERGY s-WAVE CROSS SECTIONS

From Eq.(23) one gets the expression for $\sigma^{VR}(k)$ under condition $kR^*<<1$:

$$\sigma^{VR}(k)=\frac{4\pi(L')^2}{kR^*}\frac{p^L}{1+(kL')^2} \tag{24}$$

The quasiclassical counterpart of $\sigma^{VR}(k)$, $\sigma^{VR,QCl}(k)$, is of the form:

$$\sigma^{VR,QCl}(k)=\frac{\pi}{k^2}p^L \tag{25}$$

For a comparison, we cite the expression for the elastic cross section, $\sigma^{el}(k)$, written in the same approximation:

$$\sigma^{el}(k)=4\pi(L')^2\frac{1}{1+(kL')^2} \tag{26}$$

From Eqs.(24) and (26) we get the relation between the elastic and inelastic cross sections:

$$\frac{\sigma^{VR}(k)}{\sigma^{el}(k)}=\frac{p^L}{kR^*} \tag{27}$$

Note that this ratio does not depend on L', that is on the energy of a weakly-bound state. We also see that depending on k, the low-energy ($kR^* \ll 1$) VR cross section σ^{VR} can be suppressed or enhanced compared to the quasiclassical cross section $\sigma^{VR,QCl}$. The suppression occurs in the BW regime ($k|L'| \ll 1$). The enhancement can be seen in the BW regime, though it reaches its maximum beyond the BW range (at about $k|L'| \approx 1$). Eqs.(24) and (26) are valid for $R_e \ll R^* \ll 1/k$. If the condition $R^* \ll 1/k$ is not well fulfilled, one should go beyond the scattering length approximation, and resort, for instance, to the effective range approach [5].

4. *S*-wave inelastic VR scattering for a Morse potential with an arbitrary well

The suppression factor $S_0(k)$ for a non-quasiclassical potential can be found by solving the Schroedinger equation for the energy E across the whole potential range with subsequent correlation of JWKB asymptotics in the region of free motion and in the classically forbidden region. If such a potential is taken to be a linear function of the coordinate near the turning point, this procedure yields the standard JWKB result for which $S_0(k)=1$ [5]. In our case we consider a Morse potential in the form

$$U^M(R) = D\left[1 - \exp\left(-(R - R_e)/a\right)\right]^2 - D \tag{28}$$

Calculation of the suppression factor for a Morse potential, $S_0(k)=S_0^M(k)$, allows one to see the effect of the potential well in both quasiclassical (large D) and non-quasiclassical (small D) conditions. Of course, in the limit of high energies ($E \gg D$, $ka \gg 1$) the linear approximation to the Morse potential close to the turning point can be used, and the Morse comparison equation goes over to the Airy equation.

The solution of the Schroedinger equation for a Morse potential is well known (see e.g. [5]), so that the suppression-enhancement amplitude can be calculated using the available information on the solution of the respective equation (see, e.g. [17]). Let us introduce two dimensionless quantities, the reduced wave vector κ, associated with the incoming wave, and the wave-vector-like quantity κ_D, associated with the potential well depth:

$$\kappa = \sqrt{2\mu E}\, a/\hbar, \quad \kappa_D = \sqrt{2\mu D}\, a/\hbar \tag{29}$$

The number of bound states N supported by the Morse potential is $N=\text{integer}(\kappa_D+1/2)$ and the negative bound-state energy levels are

$$E_n = -D + \hbar\omega_e(n+1/2)\left[1 - \frac{\hbar\omega_e}{4D}(n+1/2)\right], \tag{30}$$

$$\omega_e = (1/a)\sqrt{2D/\mu}, \qquad n = 0,1,....N-1$$

The energy of the last bound state is

$$E_{N-1} = -\frac{\hbar^2}{2\mu a^2}(\kappa_D + 1/2 - N)^2 \qquad \kappa_D \geq 1/2 \tag{31}$$

which identifies the scattering length as

$$L = \frac{a}{[\kappa_D + 1/2 - N]} \tag{32}$$

The suppression-enhancement probability for the VR event with the Morse interaction potential reads [6]:

$$S_0^M(\kappa, \kappa_D) = \frac{\sinh(2\pi\kappa)}{2[\sinh^2(\pi\kappa) + \cos^2(\pi\kappa_D)]} \cdot \frac{As\Gamma(\kappa_D, \kappa)}{\left|\Gamma\left(\frac{1}{2} + \kappa_D + i\kappa\right)\right|^2} \tag{33}$$

$$As\Gamma(\kappa, \kappa_D) = 2\pi(\kappa_D^2 + \kappa^2)^{\kappa_D} \exp[-2\kappa_D - 2\kappa\arctan(\kappa/\kappa_D)]$$

The surface plot of the function $S_0^M(\kappa_D, \kappa)$ is shown in Fig.2. It is seen that $S_0^M(\kappa_D, \kappa)$ can be lower (suppression) and higher (enhancement) than unity; the latter occurs only when $\cos^2(\pi\kappa_D) \leq 1/2$.
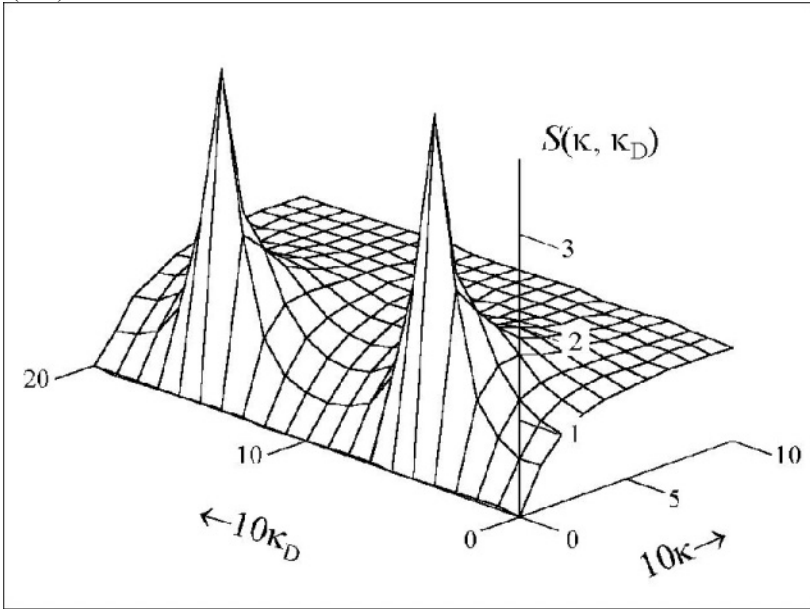
Figure 2. Surface plot of the probability $S_0^M(\kappa, \kappa_D)$ for the Morse potential.

The function $As\Gamma(\kappa, \kappa_D,)$ defined by Eq.(33) is actually the asymptotic expression of $|\Gamma(1/2 + \kappa_D + i\kappa)|^2$ so that the last factor in r.h.s. of Eq.(33) tends to unity if the motion in

the region of the potential well is quasiclassical, $\sqrt{\kappa_D^2 + \kappa^2} \gg 1$. Thus, the quasiclassical limit of S_0^M reads:

$$S_0^{M,QCl} = \frac{\sinh(2\pi\kappa)}{2[\sinh^2(\pi\kappa) + \cos^2(\pi\kappa_D)]} \tag{34}$$

This expression coincides with a general expression (9) provided T is identified with the transmission probability through the exponential potential step, which corresponds to the attractive part of the Morse potential $U_{attr}(R) \propto -\exp(-R/a)$, and ψ is taken as the quasiclassical phase integral for the Morse potential:

$$T = 1 - \exp(-4\pi\kappa) = 1 - \exp(-4\pi a k) \tag{35}$$
$$\Psi = \psi^M = \pi\kappa_D$$

If $\Delta\psi = \pi(\kappa_D + 1/2) - \pi N$ is small, $\Delta\psi \ll 1$, it defines the scattering length

$$L' = \pi a/\Delta\psi \tag{36}$$

This expression can be obtained from Eqs.(19) by substitution $R^* \rightarrow 4\pi\alpha$. Therefore, the expression for the BW-limit of the suppression factor assumes the form:

$$S_0^{M,QCl}\Big|_{\substack{k \rightarrow 0, \\ |\kappa_D + 1/2 - N| \ll 1, \\ N \gg 1}} = \frac{(L')^2 k}{\pi a} \tag{37}$$

that corresponds to the inelastic scattering length

$$(L'')^{M,QCl} = \frac{(L')^2}{4\pi a} p^{L,M} \tag{38}$$

Two interesting non-quasiclassical limits of Eq.(33) correspond to purely repulsive potential and to the case when the potential well supports a single bound state.
i) If $\kappa_D = 0$, the Morse potential becomes a purely repulsive exponential potential $U_{rep}(R) \propto \exp(-2R/a)$. For this case, Eq.(33) yields:

$$S_0^M(\kappa, \kappa_D)\Big|_{\kappa_D = 0} = S_0^{exp}(\kappa) = 1 - \exp(-2\pi\kappa) = 1 - \exp(-2\pi a k) \tag{39}$$

In this case we have a pure suppression of the quasiclassical probability, so that the BW limit $P^{VR,BW}$ for $4\pi k a \ll 1$ yields the following expression for L'':

$$(L'')^{M}\Big|_{\kappa_D=0} = (L'')^{\exp} = \pi a p^{L,\exp} \tag{40}$$

where $p^{L,\exp}$ is the zero-energy Landau transition probability for the repulsive exponential interaction.

ii) If κ_D is close to ½, the suppression probability behaves as in Eq.(22) but with an additional factor π/e. In this case, the expression for the BW-limit of the suppression-enhanced factor assumes the form:

$$S_0^{M}\Big|_{\substack{k\to 0,\\|\kappa_D-1/2|<<1}} = \frac{(L')^2 k}{ea} \tag{41}$$

This expression for S_0^{M} corresponds to the following inelastic scattering length:

$$(L'')^{M}\Big|_{|\kappa_D-1/2|<<1} = \frac{(L')^2}{4ea} p^{L,M} \tag{42}$$

where $p^{L,M}$ is the zero-energy Landau transition probability for the Morse potential.

A comparison of Eqs.(42) and (22) with $R^*=4\pi a$ shows that the breakdown of the quasiclassical conditions does not dramatically change the relation between the inelastic and elastic scattering lengths.

5. Landau transition probability: application to a Morse potential

Calculation of the transition probability by the Landau method is based on the analytical continuation of classical dynamical variables into the classically forbidden region of the potential [5]. Alternatively, the Landau transition probability can be recovered from the Fourier components of certain classical quantities, related to the transitions in question [10,11]. This allows one to write the Landau VR probability as

$$P^{L} = A\exp\left(-\frac{1}{\hbar}\int_{E}^{E+\Delta E}\tau(\bar{E})d\bar{E}\right) \tag{43}$$

where $\tau(\bar{E})$ is the classical characteristic time for the collision energy $\bar{E}$ in the field of a given potential. Eq.(43) can be regarded as a generalization of the Ehrenfest theorem for a quasiclassical case when the change of the action variable is not small, but the probability of this change is small [18].

For the model of a Morse oscillator $\tau(\bar{E}) \equiv \tau^{M}(\bar{E})$, and the Landau transition probability depends, beside κ, κ_D, on one more parameter, $\kappa_{\Delta E}$, which is associated with the energy transfer ΔE or on the final wave vector κ':

$$\kappa_{\Delta E} = \sqrt{2\mu\Delta E}\, a/\hbar; \quad \kappa' = \sqrt{\kappa^2 + \kappa_{\Delta E}^2} \tag{44}$$

The explicit expression for $P^{L,M}$ reads [10]:

$$P^{L,M}(\kappa, \kappa', \kappa_D) = A\exp\left[-M(\kappa', \kappa_D) + M(\kappa, \kappa_D)\right], \tag{45}$$

where the prefactor A does not depend on $\kappa,\ \kappa',\ \kappa_D$, and $M(\kappa,\kappa_D)$ is

$$M(\kappa, \kappa_D) = 2\kappa\arctan(\kappa/\kappa_D) - \kappa_D \ln\left[1 + (\kappa/\kappa_D)^2\right]. \tag{46}$$

In the low-energy limit, the exponent in Eq. (45) is:

$$M(\kappa', \kappa_D) - M(\kappa, \kappa_D)\big|_{\substack{\kappa\to 0,\\ \kappa'\to\kappa_{\Delta E}}} = \pi\kappa_{\Delta E} + 2\kappa_D - 2\kappa_D \ln(\kappa_{\Delta E}/\kappa_D), \tag{47}$$

and the Landau probability tends to a constant

$$P^{L,M}(\kappa \to 0, \kappa_{\Delta E}, \kappa_D) \equiv p^{L,M}(\kappa_{\Delta E}, \kappa_D) = A\left(\kappa_{\Delta E}/\kappa_D\right)^{2\kappa_D} \exp(-\pi\kappa_{\Delta E} + 2\kappa_D) \tag{48}$$

In the high-energy limit, the exponent in Eq. (45) is:

$$M(\kappa', \kappa_D) - M(\kappa, \kappa_D)\big|_{\kappa,\kappa' \gg \kappa_D, \kappa_{\Delta E}} = \pi\kappa_{\Delta E}^2/2\kappa \tag{49}$$

The transition probability from Eq. (45) with the exponent given by Eq.(49) coincides with the LT probability.

6. VR cross section for H_2 - He collisions over a wide energy range

Vibrational relaxation of H_2 in collisions with He atom provides an interesting realistic example that illustrates low-energy features of the collisional energy transfer. The cross sections for the collision

$$H_2(n=1, j=0) + He \rightarrow H_2(n=0, j=0) + He \tag{50}$$

were accurately calculated by Balakrishnan, Forrey and Dalgarno (BFD) [19] for the potential surfaces from [20]. The PES used possesses a potential well of about 10cm⁻¹ depth, and this well supports a weakly bound state of binding energy of 0.0016 cm⁻¹. The energy range covered by calculations extends from the BW to LT limits. In addition VR cross section for this PES, calculations were performed for a modified PES in which the attractive interaction was ignored. In this section we compare the results for the Morse model with accurate quantum calculations. We first consider the

s-wave scattering and then the quasiclassical scattering where a noticeable number of partial waves contribute.

6.1. LOW-ENERGY CROSS SECTION AND THE ISOTOPE EFFECT

At low energies only the first partial cross section contributes to the sum over J, so that

$$\sigma^{VR,M}(\kappa, \kappa', \kappa_D) \approx \frac{\pi a^2}{\kappa^2} P_0^{VR}(\kappa, \kappa', \kappa_D) = \frac{\pi a^2}{\kappa^2} S_0^M(\kappa, \kappa_D) P_0^{L,M}(\kappa, \kappa', \kappa_D) \tag{51}$$

In the BW limit, $S_0^M(\kappa, \kappa_D)$ should be considered as a linear function of κ, $S_0^M(\kappa, \kappa_D) = B^M(\kappa_D)\kappa$ and $P^{M,L}$ can be replaced by its zero-κ limit. Referring to Eqs.(33) and Eq.(48), we thus get

$$\sigma^{VR,M}(\kappa, \kappa_D, \kappa_{\Delta E})_{\kappa \to 0} = \sigma^{VR,M,BW}(\kappa, \kappa_D, \kappa_{\Delta E}) =$$
$$= \frac{\pi a^2 B^M(\kappa_D)}{\kappa} A\left(\frac{\kappa_{\Delta E}}{\kappa_D}\right)^{2\kappa_D} \exp\left(-\pi \kappa_{\Delta E} + 2\kappa_D\right) \tag{52}$$

where

$$B^M(\kappa_D) = \frac{\pi}{\cos^2(\pi \kappa_D)} \cdot \frac{2\pi \kappa_D^{2\kappa_D} \exp(-2\kappa_D)}{\left|\Gamma(1/2 + \kappa_D)\right|^2} \tag{53}$$

Two liming expressions for $B(\kappa)$ correspond to a pure repulsive potential ($\kappa_D \to 0$) and a potential that supports a single weakly-bound state ($\Delta\kappa_D = \kappa_D - 1/2 \ll 1$)

$$B^M(\kappa_D) = \begin{cases} 2\pi, & \text{for} \quad \kappa_D \ll 1 \\[2mm] \dfrac{1}{e(\Delta\kappa_D)^2}, & \text{for} \quad \Delta\kappa_D \ll 1 \end{cases} \tag{54}$$

6.2. MEDIUM AND HIGH ENERGY CROSS SECTION

With increase in the collision energy, more and more partial cross sections contribute to the total VR cross section, so that one has to calculate the transition probabilities P_J^{VR} for $J>0$. If the suppression-enhancement effects are ignored for $J>0$, one can use the so-called effective quantum number approximation [21].This amounts to the following:

$$P_J^{VR}(k, k') = P_J^L(k, k'), \quad J > 0; \tag{55}$$
$$P_J^L(k, k') = P^L(k_J, k_J')$$

where

$$k_J = \sqrt{k^2 - \hbar^2 J(J+1)/R_0^2}; \quad k'_J = \sqrt{k'^2 - \hbar^2 J(J+1)/R_0^2}, \tag{56}$$

Here R_0 is the distance of closest approach for the collision with $J=0$. This approximation is valid when the radius R_0 is considerably larger that the length parameter of the repulsive interaction. In this way we get:

$$\sigma^{\mathrm{VR,M}}(\kappa, \kappa', \kappa_D, \rho_0) = \frac{\pi a^2}{\kappa^2} S_0^{\mathrm{M}}(\kappa, \kappa_D) P_0^{\mathrm{M,L}}(\kappa, \kappa', \kappa_D) +$$
$$+ \frac{\pi a^2}{\kappa^2} \sum_{J=1}^{J^*(\kappa,\rho_0)} (2J+1) P_0^{\mathrm{M,L}}(\kappa_J, \kappa'_J, \kappa_D) \tag{57}$$

Here $J^* = J^*(\kappa, \rho_0)$ is the largest integer for which the radicand in the expression for $\kappa_J = \sqrt{\kappa^2 - J(J+1)/\rho_0^2}$, with $\rho_0 = R_0/a$, is positive. If the number of terms that contribute to the cross section in Eq.(57) is large, and the kinetic energy substantially exceeds both the transferred energy and the potential well depth, the cross section $\sigma^{VR}(E)$ becomes the LT cross section:

$$\sigma^{\mathrm{VR,M}}(\kappa)\Big|_{\kappa \gg \kappa_{\Delta E}} = \sigma^{\mathrm{LT,M}}(\kappa, \kappa_{\Delta E}) = \frac{\pi}{k^2} \int_0^{J^*} 2J P^{M,L}(E_J)\Big|_{\kappa \gg \kappa_{\Delta E} \gg \kappa_D} dJ =$$
$$= R_0^2 \frac{2A\hbar v}{\Delta Ea} \exp\left(-\frac{\pi \Delta E a}{\hbar v}\right) = R_0^2 \frac{4A\kappa}{\kappa_{\Delta E}^2} \exp\left(-\frac{\pi \kappa_{\Delta E}^2}{2\kappa}\right) \tag{58}$$

The following comments about Eq.(57) will be in order:
i) Beside three parameters $\kappa, \kappa', \kappa_D$ discussed in Sections 4 and 5, the VR cross section within our model depends on yet another parameter ρ_0, which controls the contributions from higher angular momenta. In the approximation adopted, the tunneling through the centrifugal barriers towards the repulsive wall of the potential and the overbarrier reflection that prevents reaching this region are ignored. As follows from our recent results on the calculation of the capture cross sections at low energies [21], to a good approximation these two effects can be accounted for by simply replacing the sum over J by an integral, $\sum_{J=1}^{J^*(\kappa,\rho_0)} ... \rightarrow \int_{J=1}^{J^*(\kappa,\rho_0)} ...dJ$. However, we will not discuss this modification here since the peaks, associated with sudden onset of successive partial contributions to the VR cross section in Eq.(55) provide useful bookkeeping of the number of essential partial cross sections. This bookkeeping disappears, of course, in the LT limit, Eq.(56).
ii) The energy dependence of the VR cross section is controlled by parameter κ, see Eq.(29).

iii) The dependence of the VR cross section on the potential depth is controlled by parameter κ_D, see Eq.(29).

iv) The dependence of the VR cross section on the energy release is controlled by parameter $\kappa_{\Delta E}$, see Eq.(44).

Presumably, these parameters constitute a minimal set for a physically adequate model of VR over a wide energy range.

6.3. COMPARISON OF THE MODEL CROSS SECTION WITH THE ACCURATE QUANTUM RESULTS

Since the variation of energy from the BW region to the LT region produces a very large change in the cross sections, we will use the log-log representation of σ^{GL} vs. κ. This choice is dictated also by our intent to compare our results with numerical results from [19] where the same representation of the VR cross section σ^{BFD} versus the collision energy was used. Since the energy-independent coupling strength factor A is not specified in $\sigma^{VR,M}$, the log σ^{BFD} – log E graph can be superimposed onto the graph log $\sigma^{VR,M}$ – log κ (or vice versa) by a vertical shift and with the proper adjustment of the energy scale. The latter is set by the value of $\kappa_{\Delta E}$ since $(E/\Delta E)=(\kappa/\kappa_{\Delta E})^2$. After this adjustment, the general shape of the curve log σ^{VR} – log E is determined by the values of three parameters: κ_D, $\kappa_{\Delta E,}$ and ρ_0. Two parameters, κ_D and $\kappa_{\Delta E}$, control the s-wave cross section. The value of κ_D is very sensitive to the interaction potential and cannot be deduced from our model. Therefore, we have determined it from the ratio of elastic scattering lengths for $H_2(v=0,j=0)+{}^4He$ and $H_2(v=0,j=0)+{}^3He$ collisions. In this way we find $\kappa_D\approx0.533$. The value of $\kappa_{\Delta E}$ is related, for given μ and ΔE, to the length parameter α of the Morse potential. It can, therefore, be estimated from the repulsive portion of the interaction potential adopted in the numerical calculations [19]. Once α is determined, it sets, through the relation $\kappa_{\Delta E} = \sqrt{2\mu\Delta E}\,a/\hbar$, the energy scale in the dependence of the cross section on the collision energy, or log $\sigma^{VR,M}$ – log E plot.

In order to use the general formula given in Eq.(58) for higher energies, one has to adopt a value for the collision radius ρ_0. The value of ρ_0 can be expected to be close or somewhat less than the equilibrium distance of the H_2He complex [22]. From Fig.2. of Ref.[20] we find $R_e \approx 3.3A$ that is $\rho_0\approx6-7$. A slight variation of ρ_0 about this value allows one to make the uppermost right points of the two graphs, log $\sigma^{VR,M}$ – log E and log σ^{BFD} – log E coincide. The final result of the fitting with parameters $\rho_0=6$, $\kappa_{\Delta E}=9.5$, $\kappa_D=0.533$ is shown in Fig.3. Note that in this fitting, we have forced coincidence of only three points: two at the left side of the figure (one for each curve, with the attraction and without it), and one at the right part (where the two curves coalesce). The region across the minimum of the cross section was not fitted (for details see [22]).

Fig.3 shows a good qualitative agreement between the model and *ab initio* BFD cross sections for the collision in Eq. (51). Here, the upper set of curves represents scattering on a potential with a well, and the lower set represents scattering on a purely repulsive potential. In both cases the solid lines give the cross sections, Eq.(51), the dashed curves give the cross sections without quantum correction (Eq.(51) with $S_0^M=1$) and squares are
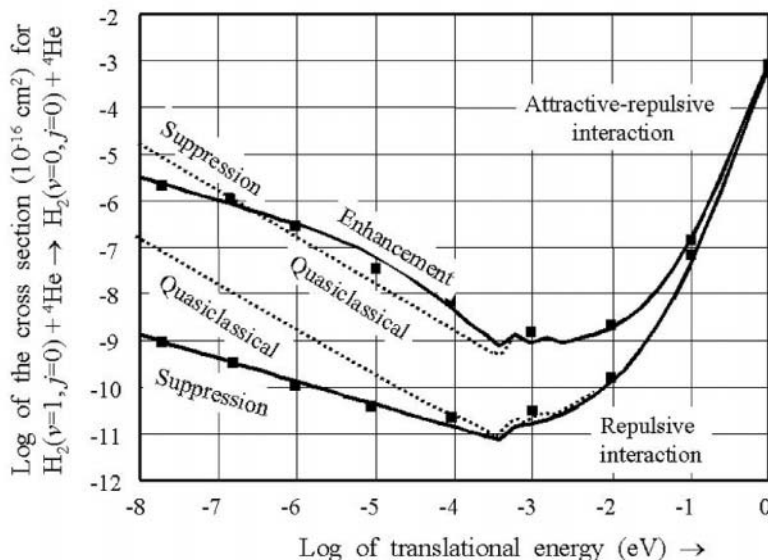
Figure 3. Comparison of the model (full and dotted lines) and numerical (squares) cross sections for VR collisions $H_2(v=1, j=0)+^4He \rightarrow H_2(v=0, j=0)+^4He$. Lower curves and symbols correspond to a pure repulsive interaction, upper to the interaction with the potential well.

the numerically computed points from Ref. [19].

The present model adequately reproduces the VR cross sections and can be used to explain the main features of the plots in Fig.3.

i) The cross sections for both potentials used have minima in the region where the *p*-wave scattering sets on. The corresponding energy E_m (of about $10^{-3.3}$ eV) is marked by the small "tips" in both curves. They are due to the approximation used, (Eq.(51)), which ignores the tunneling through the centrifugal barrier. This is also the energy, below which the *s*-wave quasiclassical (Landau) cross section and the quantum cross section begin to differ. The reason why the two features (the onset of the *p*-scattering for $E>E_m$ and the onset of the quantum effects for $E<E_m$) correspond to the same energy $E \approx E_m$ can be traced to the fact that the threshold value of the momentum for the *p*-wave scattering, $\kappa_p^{th} = \sqrt{2}/\rho_0 \approx 0.24$, matches the beginning of the quantum suppression (or enhancement) for the s-wave scattering. Note that the value of $E_m \approx 10^{3.3} eV \approx cm^{-1}$ is of the same order of magnitude as is the energy of the cross section minimum for VR in I_2 - He collisions (at about 10cm^{-1}) [23].

ii) The quantum *s*-wave scattering cross section for the repulsive potential lies below the quasiclassical one; this is consistent with the quantum suppression. The ratio of slopes of the linear portions of the cross sections agrees with *1/v* (BW) and *1/v²* (quasiclassical) predictions. The quantum *s*-wave scattering cross section for the potential with a well

also lies below the quasiclassical one at very low energies (the BW limit), but before it reaches this limit it surpasses the quasiclassical cross section. This quantum enhancement of the quasiclassical scattering is due to a resonance phenomenon, which is associated with the existence of a weakly bound complex H$_2$He. We also see that the BW threshold law is valid for energies just below E_m while for interaction with attraction it is valid at much lower energies, by four orders0 of magnitude, at $E_m<10^{-6}$eV. This agrees with the findings for I$_2$ - He collisions calculated for a potential surface with an attractive well [23].

iii) A huge effect of the attraction on the cross section at low energies can be understood in terms of "resonance" and "potential" (Landau) contributions to the enhancement ratio of the BW cross sections, R^{BW}, for attractive and repulsive interactions. We thus write:

$$R^{BW}(\kappa_{\Delta E}, \kappa_D) = \frac{\sigma^{VR,M,BW}(\kappa, \kappa_{\Delta E}, \kappa_D)\big|_{\kappa_D \ll \kappa_{\Delta E}}}{\sigma^{VR,M,BW}(\kappa, \kappa_{\Delta E}, \kappa_D)\big|_{\kappa_D=0}} = R^{res}(\kappa_D) \cdot R^{pot}(\kappa_{\Delta E}, \kappa_D) \qquad (59)$$

where $R^{res}(\kappa_D)$ is the ratio of the suppression-enhancement factors for the potential with the well and a pure repulsive potential, and $R^{pot}(\kappa_{\Delta E}, \kappa_D)$ is the ratio of the Landau cross sections for the same potentials:

$$R^{res}(\kappa_D) = \frac{B(\kappa_D)}{B(\kappa_D)\big|_{\kappa_D=0}} \qquad (60)$$

$$R^{pot}(\kappa_{\Delta E}, \kappa_D) = \frac{p^L(\kappa_D, \kappa_{\Delta E})\big|_{\kappa_D \ll \kappa_{\Delta E}}}{p^L(\kappa_D, \kappa_{\Delta E})\big|_{\kappa_D=0}} = \left(\frac{\kappa_{\Delta E}}{\kappa_D}\right)^{2\kappa_D} \exp(2\kappa_D) \qquad (61)$$

Plots of the functions R^{pot}, R^{res}, R^{BW} vs. κ_D for $\kappa_{\Delta E}=10$ are shown in Fig.4. A point on the R^{BW} curve corresponds to H$_2$-He collisions on the Morse potential surface. One can see that the attractive enhancement of the VR cross section under consideration comes roughly evenly from resonance and potential effects.

iv) The effect of the attraction on the cross section at high collision energies, $\kappa \gg \kappa_D$, can easily be seen when one calculates the ratio of the Landau cross section to the LT cross section:

$$\frac{\sigma^L(\kappa, \kappa_{\Delta E}, \kappa_D, \rho_0)}{\sigma^{LT}(\kappa, \kappa_{\Delta E}, \rho_0)} = \exp\left(\frac{\kappa_{\Delta E}^2 \kappa_D}{\kappa^2}\right). \qquad (62)$$

One can see that even when the ratio $\kappa_D / \kappa = \sqrt{D/E}$ is small (the collision energy is high compared to the well depth) the effect of the attraction can be significant since the ratio $\kappa_{\Delta E}^2 / \kappa$ is large, and the exponent in Eq.(62) can exceed unity. This is illustrated in Fig.3 by the divergence of the curves (one for the potential with the attraction, and the

other for a pure repulsive potential) with decrease in the collision energy at the right-hand side of the graph.
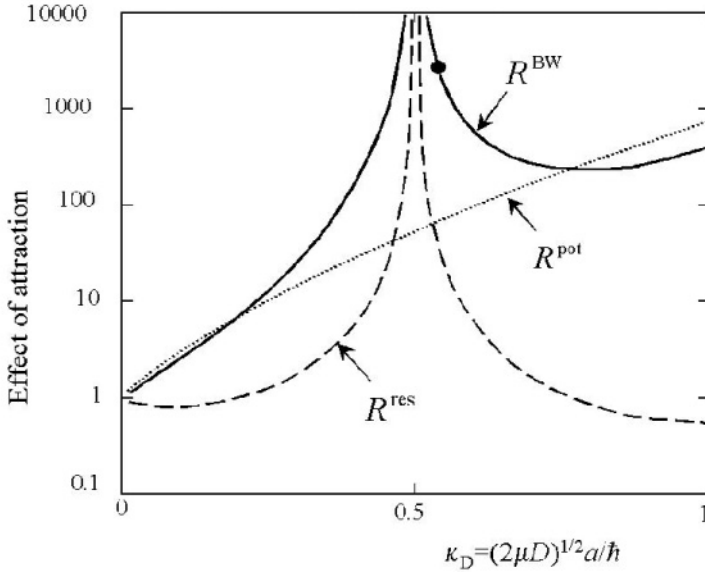
Figure 4. Attractive enhancement ratio for the BW cross sections with increase of κ_D across the first resonance at $\kappa_D =1/2$ for $\kappa_{\Delta E}=10$. Shown are the resonance contribution R^{res}, potential contribution R^{pot} and the total enhancement ratio $R^{\text{BW}}= R^{\text{res}}R^{\text{pot}}$. A point on the R^{BW} curve corresponds to H_2-He collisions on the Morse potential surface in the BW limit.

Finally, consider the isotope effect, which is due to the change of the reduced mass of colliding partners (change of mass of an atom A). Let μ and $\widetilde{\mu}$ be the reduced masses in collisions with participation of two isotopes of atom A. Assume for simplicity that the mass difference, $\widetilde{\mu} - \mu$, is small compared to μ. We thus want to investigate the effect of a small parameter $\delta = (\widetilde{\mu} - \mu)/\mu$ on the ratio $\widetilde{L}''/L''$ assuming the Morse interaction potential. Referring to Eq.(38), we write:

$$\frac{(\widetilde{L}'')^{\text{M}}}{(L'')^{\text{M}}} = \left(\frac{\widetilde{L}'}{L'}\right)^2 \cdot \left(\frac{\widetilde{p}^L}{p^L}\right) = \left(\frac{\Delta \psi^M}{\Delta \widetilde{\psi}^M}\right)^2 \cdot \left(\frac{\widetilde{p}_a^{L,M}}{p_b^{L,M}}\right) \tag{63}$$

Expanding $\widetilde{\kappa}_D$ and $\widetilde{\kappa}_E$ through first order in δ, we have

$$\frac{(\widetilde{L}'')^{\text{M}}}{(L'')^{\text{M}}} = \left(\frac{\kappa_D -1/2}{\kappa_D (1+\delta/2)-1/2}\right)^2 \cdot \left(\frac{\kappa_{\Delta E}}{\kappa_D}\right)^{\kappa_D \delta} \exp\left(-\frac{\pi}{2}\kappa_{\Delta E}\delta + \kappa_D\delta\right) \tag{64}$$

If κ_D is close to ½ and δ is negative (atom $\widetilde{A}$ is lighter than atom A), the first factor in the r.h.s. of Eq.(62) can depend on δ very strongly. The second factor can noticeably depend on δ if $\kappa_{\Delta E} >> 1$.

We illustrate this result by comparing $H_2 + {}^4He$ and $H_2 + {}^3He$ collisions. The values of the parameters which are needed for estimation of the ratio of inelastic scattering lengths from Eq.(64) are $\kappa_D = 0.533$, $\kappa_{\Delta E} = 9.5$, $\delta = 0.1$. In this way we have

$$\frac{{}^3L''}{{}^4L''} = \left(\frac{{}^3L'}{{}^4L'} \right)^2 \cdot \frac{{}^3p^L}{{}^4p^L} = 16 \cdot 3.64 = 58.2 \tag{65}$$

This value is close to 50 that can be inferred from the numerical data points of Fig.2 and 3 of Ref.[19]. The difference of about 20% between the model estimate and accurate result can be presumably blamed for an erroneous long-range behavior of the model Morse potential (exponential long-range attraction) compared to the accurate potential (van der Waals attraction). Nonetheless, a simple model explains a large difference between the ratios of inelastic and elastic scattering lengths in collisions for two isotopes of He (50 and 4 respectively).

7. Conclusion

We conclude that the qualitative pattern of the energy dependence of the VR cross section for collision energies above E_m (incipient p-wave scattering) can be reconstructed from knowledge of three basic parameters of the atom-molecule interaction: the collision radius, the well depth and the steepness of the repulsive part of the interaction. At energies below E_m, one has to know the value of yet another parameter, which is related to the elastic scattering length of collision partners or to the position of the real or virtual energy level close to the dissociation threshold of the complex.

Acknowledgement

References

1. Capitelli, M.(ed). (1968) *Nonequlibrium Vibrational Kinetics*, Springer Verlag, New York.
2. Yardley, J. T. (1980) *Introduction to molecular energy transfer*, Academic, New York.
3. Landau L. and Teller, E. (1936) Zur Theorie der Schalldispersion, *Phys.Z.Sowet.* **10**, 34-40.
4. Landau, L. D. and Lifshitz, E. M. (1977) *Classical Mechanics,* Pergamon Press, Oxford
5. Landau, L. D. and Lifshitz, E. M. (1977) *Quantum Mechanics,* Pergamon Press, Oxford.

6. Dashevskaya, E. I. and Nikitin, E. E. (2000) Quantum suppression and enhancement of the quasiclassical Landau-Lifshitz matrix elements. Application to the inelastic H_2-He scattering at ultra-low energies, *Phys.Rev.A*, **63**, 012711-1 - 012711-7

7. Bethe, H. A. (1937) Nuclear physics B. Nuclear dynamics, Theoretical, *Rev.Mod.Phys.* **9**, 69-244.

8. Wigner, E. (1948) On the behavior of cross sections near threshold, *Phys.Rev.* **73**, 1002-1009.

9. Troe, J. (1992) Statistical aspects of ion-molecule reaction, *Adv.Chem.Phys.* **82**, 485-529.

10. Karni, Y., and Nikitin, E.E., (1994) Recovery of the Landau matrix elements from the classical Fourier components: one-dimensional dissociating oscillator, *J.Chem. Phys.*, **100**, 2027-2033.

11. Nikitin, E.E. and Pitaevskii, L. (1994) Calculation of the Landau quasi-classical exponent from the Fourier components of classical functions, *Phys.Rev.A*, **49**, 695-703.

12. E. E. Nikitin , (1974) *Theory of Elementary Atomic and Molecular Processes in Gases,* Clarendon Press, Oxford.

13. Côté, R., Heller, E.J. and Dalgarno, A. (1996) Quantum suppression of cold atom collisions, *Phys.Rev. A,* **53**, 234-241.

14. E.E.Nikitin, S.Ya.Umanskii, (1984) *Theory of Slow Atomic Collisions,* Springer, Berlin.

15. Côté, R., Dashevskaya, E. I., Nikitin E. E. and Troe, J. Quantum enhancement of vibrational predissociation near the dissociation threshold (submitted to *Phys.Rev A*).

16. Côté, R., Friedrich, H. and Trost, (1997) Reflection above potential step, *Phys.Rev A,* **56**,1781-1787.

17. Gradshteyn, I. S. and Ryzhik, I. M. (1980) *Tables of Integrals, Series and Products,* Academic Press, New-York.

18. E. E. Nikitin, (1996) Pathways of vibrational relaxation of diatoms in collisions with atoms: Manifestation of the Ehrenfest adiabatic principle, in J.Wolfrum, H.-R.Volpp, R. Rannacher, J. Warnatz (eds) *Gas Phase Chemical Reaction System*, Springer, Berlin- Heidelberg, pp 231-242.

19. Balakrishnan, N., Forrey R. C. and Dalgarno, A. (1998) Quenching of H_2 vibrations in ultracold ^{3}He and ^{4}He collisions, *Phys.Rev.Lett.* **80**, 3224-3227.

20. Muchnik, P. and Russek, A. (1994) The HeH_2 energy surface. *J. Chem. Phys.* **100,** 4336-4346.

21. Dashevskaya, E.I., Litvin, I., Maergoiz, A., Nikitin, E. E. and Troe, J. (2003) On the low-temperature limit of the capture rate constants for inverse power potentials, *J.Chem.Phys.* **118**, 7313-7321.

22. Dashevskaya, E. I., Kunc, J. A., Nikitin, E. E. and Oref, I. (2003) Two-channel vibrational relaxation of H_2 by He: a bridge between the Landau-Teller and Bethe-Wigner limits, *J.Chem.Phys.*, **118**, 3141-3141.

23. Schwenke D. W. and Truhlar, D. G. (1985) The effect of Wigner singularities on low-temperature vibrational relaxation rates J. Chem. Phys. **83,** 3454-3461.

COLLISIONAL ENERGY TRANSFER IN THE GAS PHASE BY CLASSICAL TRAJECTORY CALCULATIONS

V. BERNSTEIN, I. OREF
Department of Chemistry, Technion – Israel Institute of Technology
32000 Haifa, Israel

Abstract   Classical trajectory calculations provide useful information about molecular collisions in the gas phase. Various energy transfer quantities such as the average energy transferred per collision <ΔE>, the lifetime of the collision complex and their dependence on temperature, pressure and intermolecular potential can be calculated by this method and clues as to the mechanism of collision and energy transfer may come to light as a result of these calculations. Examples from our work are provided below for energy transfer between Ar and benzene and toluene and between Li^+ and C_{60} under a variety of experimental conditions.

1. Introduction

Collisional energy transfer (CET) plays a major role in chemical, photochemical and photo physical processes [1]. Binary collisions are an important means by which energy is transferred in and out of molecules enabling them to undergo chemical transformation. What is less known, is the overall detailed picture of the collisional energy transfer process, especially in polyatomic molecule, which is the subject of the present paper. Over the years, a large amount of experimental and theoretical information on CET has been accumulated by various groups. This work gave a glimpse of the various, complicated, aspects that comprise the process of energy transfer in large molecules. The early work on CET in polyatomics can be divided into work on highly excited molecules and on molecules with low level internal excitation. The latter shed light on level-to-level energy transfer. The subject matter of the present paper constitutes only theoretical work on CET of highly excited polyatomic molecules. Until the 1980's the theoretical work on CET of large, highly excited, molecules was mostly involved in developing empirical models for CET probability density functions that, when used in the context of master equations gave average quantities such as average energy transferred in a collision, <ΔE>, that could be compared with experiment. However, in the mid-eighties, classical trajectory calculations, CTC , were applied to CET with great success. Hase, Gilbert, Miller, Schatz, Lendvay, Luther, Barker and their coworkers as well as others have all used CTC , and their computations have added to our present understanding of CET. This paper, not being a review, will discuss only work done by the authors without meaning to imply a diminution of the seminal

work of all those who have contributed to our present knowledge of CET in polyatomic molecules. This report summarizes work which is reported in 20 papers and deals with various aspects of CET between Ar and toluene and benzene and between C_{60} and Li^+.

2. Theory

The numerical methods which were used in our work were discussed in detail previously [2, 3] and only a general outline will be presented here. The equations of motion were integrated by using a modified public domain program Venus [4]. For an intermolecular potential we have used a potential calculated by Bludsky, Spirko, Herouda, and Hobza [5] (BSHH) who reported *ab initio* calculations of an Ar-benzene cluster and fitted the results to a potential function which is based on pair-wise atom-atom interactions. This is called the BSHH potential.

$$V_{ij} = \frac{A_{ij}}{r_{ij}^\alpha} - B_{ij}\left(\frac{1}{r_{ij}^6} - \frac{C_{ij}}{r_{ij}^7}\right); \qquad i, j = 1-6 \qquad (1)$$

A, B and C are constants, r is the CM relative distance, i indicates a carbon or a hydrogen atom and j indicates an argon atom. The parameters for the benzene/Ar system can be found in ref. 6. In some cases a Lenard-Jones pair-wise potential was used.

$$V_{ij} = A_{ij}r_{ij}^{-12} - B_{ij}r_{ij}^{-6} \qquad (2)$$

The intramolecular potential includes all the normal mode contributions, stretching, bending, wagging and torsion. The values of the parameters for the potential for benzene were obtained from the modified valence force field calculations by Draeger [7] and are given also in references 2 and 3. The initial translational and rotational energies were chosen from the appropriate thermal energy distributions and the initial vibrational energies were the average thermal energies at the temperatures of the calculations or, when so desired, chosen value. The energy was distributed statistically among all the normal modes of the molecule. The initial impact parameter (b) was chosen randomly from values between 0 and its maximum value b_m. The maximum value of the impact parameter b_m was determined separately [2, 3]. The number of trajectories used was chosen to give good statistics. In some cases it was over 100000 for a given set of initial conditions.

One of the major problems in classical calculations is how to define the beginning and the end of an effective collision since trajectories of events that occur at very large distances do not contribute to CET. To separate effective collisions from long-distance non-effective events we have developed a method which we call Forward and Backward Sensing (FOBS) [2, 3]. In this method, events that affect the internal energy of the polyatomic molecule even temporarily are defined as collisions. Each trajectory is scanned forward and the first instance that a change ε in the internal energy

of the hot molecule in a time period Δt occurred is noted,. Then, the trajectory is scanned backward and again, when a change ε is detected in a time period Δt, the time is noted again. These two points in the trajectory time bracket the collisional event. The value of the gradient $\Delta\varepsilon/\Delta t$ was optimized after a careful study in which ε was changed systematically and it was verified that all effective collisions are counted and that a small variation in ε did not change the initial time or duration of the collision.

Average quantities $<x>$ such as $<\Delta E>$ or average lifetime of a collision, $<\tau>$ were calculated from the following formula:

$$< x >= \frac{\sum_{i=1}^{N} x_i}{N}.$$

(3)

where x_i is the individual quantity in trajectory i and N is the total number of FOBS effective collisions.

Termolecular collision were also studied. Such collisions may be regarded as a sequence of two binary collisions. In the first, a single Ar atom collides with a benzene molecule and in the second the binary collision complex collides with an additional Ar atom. The beginning and the end of each collision was determined by FOBS. The starting distance between the centers of mass of the binary complex, BAr and the second atom Ar', R_{in}, of the second collision is chosen randomly from the free paths probability density function

$$P(R_{in}) = \exp(-R_{in} / \lambda) / \lambda$$

(4)

between the values of the collision radius, r_c, and infinity. λ is the mean free path determined by the pressure of the system. The number of **termolecular** trajectories was weighted by the probability density function

$$P(N) = 3(R + r_c)^2 / (R_{max}^3 - r_c^3)$$

(5)

The combined distance-volume probability density distribution function has the general form

$$P = R_{in}^2 \exp(-R_{in} / \lambda) / C$$

(6)

where C is a normalization factor. This type of a distribution ensures that the termolecular trajectories that are initiated at large distances will not have an undue effect on energy transfer quantities. It should be noted that R_{in} includes the excluded volume of the binary collision complex. Taking just the center-of-mass distances will bias the results, especially at high pressure where the mean free path is short.

There are many details that relate to individual subjects. For details of the calculation for Ar colliding with benzene and toluene and for Li^+ colliding with C_{60} the interested reader may consult references cited below.

2.1. MECHANISM OF ENERGY TRANSFER

When CET occurs between an atom and an excited polyatom the collision partners approach each other and at a certain center-of-mass, CM, or minimal distance, MD, from the closest atom of the polyatom, FOBS become operational. The colliding pair forms or does not form a collision complex depending on how the latter is defined. At 300K the Ar-toluene collision complex lifetime is 0.68 ps while at 1500K it is 0.23 ps [2]. These timescales are long enough for the excited molecule to execute few vibrations even of low lying internal modes but they are not long enough for rotations to take place. They also hardly affect the toluene-Ar van der Waals modes. This tells us right away that, at least in the present system, sequential pumping and un-pumping by the atom is unrealistic. ΔE for up and down collisions has a narrow temporal distribution [2] with the averages reported above. However, the averages are misleading from mechanistic point of view. The actual energy transfer occurs on a much shorter timescale in a kick that may last around 50 fs. That is to say, the average complex lifetime is not related to the actual time of the energy transfer process.

The collision lifetime of benzene with Ar increases as the relative kinetic energy of the colliding partners decreases [8]. The long lifetimes of the collision complex at low kinetic energies enable stabilizing termolecular collisions to occur and this fact explains the formation of clusters in low-temperature molecular beams.

The minimal initial separation or MD at the moment of the collision as defined by FOBS, does not change much with temperature being 0.299 nm at 300K and 0.308 nm at 1500 K [3]. The distribution of ΔE with MD is narrow and there is no correlation between the collision lifetime and the MD [8]. The MD varies during the course of the collision as the atom moves around the molecule and the latter executes its internal vibrations. Even a greater insight on the detailed mechanism of CET can be obtained by studying the relative CM velocities of the colliding pair [9]. Few types of collisions were observed. In collisions lasting less than 300 fs the relative velocities as a function of time are straight lines [9]. These impulsive Ar-toluene collisions which do not form a collision complex comprise 62% of all inelastic collisions. To the second group of collisions belong those with duration greater than 300 fs and less than the chracteristic time for intramolecular vibrational redistribution, (IVR), ~600 fs [10]. In these chattering collisions the relative CM velocity is close to zero while the atom interact with various parts of the molecule. The van der Waals modes have a much slower period and therefore chattering does not lead to significant energy transfer between the atom and the molecule. Rather, the sort of collision which results in large energy transfer may be characterized as a sudden, impulsive kick. This type of collisions amount to over 30% of all inelastic collisions. The balance of the inelastic collisions, those of longer duration, do not contribute much to the overall value of <ΔE>.

By now we have a fairly detailed understanding of the mechanism of CET between highly excited molecules and a bath atom. We turn next to understanding of the relative contribution of rotation and vibration to the CET process. We performed clasical trajectory calculations of the average energy transferred per collision, <ΔE>, between an exited benzene molecule and an argon atom [11] in which three cases were investigated. a) collisions with unconstrained "normal" initial conditions. b) collisions where the rotations of the benzene molecule are initially "frozen". c) collisions where

the out-of-plane vibrations of the benzene molecule are initially "frozen". The distributions of <ΔE> vs. collision durations and the values of <ΔE> for collisions with frozen degrees of freedom are different than those obtained in normal collisions. Rotations were found to have the largest effect on CET. Next in efficiency are the out-of-plane vibrations. This corroborates quantum mechanical calculations which show that out-of-plane motions are particularly efficient in energy transfer compared with in-plane vibrations, for example [12]. It was found that in rotational CET and in vibrational CET, the C-H group is the vehicle for CET and that CET does not take place when the Ar hits the center of the benzene ring. Measurements of C-Ar and H-Ar van der Waals distances in the energy transferring moiety show that C is the prominent atom in the energy transfer mechanism [13].

As mentioned above, rotations play a major role in CET. Most of the CET occurs via a T/R mechanism in which the translational energy goes into rotation. This is confirmed in a detailed study of single mode excitation [14] where each mode of the benzene was pumped separately. It was found that the values of $<\Delta E_r>_{all}$ are a factor of ~3-5 larger than the values of $<\Delta E_v>_d$. The conclusion that rotations are the major contributors to the values of $<\Delta E>_{all}$ in all specific-modes excitation energies is supported by the work of Rosenblum *et al.* [15] who found that in SO_2 rare gas collisions, rotations are the major energy transferring mode.

By now we know quite a lot about the mechanism of energy transfer, but we can take it even one step further. We know that out-of-plane vibrations are more efficient than the in-plane in transferring energy but are they all equally efficient, or is there a hierarchy of efficiencies among them? Using single mode excitation, we found that there are two factors that affect energy transfer: the frequency and the type of molecular motion that is associated with the mode [14]. We found that the lowest frequency, out of plane torsion mode of the benzene molecule, is the gateway mode for energy transfer. When the same frequency is assigned also to the in plane mode, the out of plane mode is still more efficient. Only when the frequencies of the out of plane and the in plane modes are switched does the in plane mode becomes the gateway mode for energy transfer. Therefore, the lowest frequency is always the gateway mode and given two modes of identical frequencies the molecular motions determine the efficiency of energy transfer. These results agree with quantum calculations by Clary *et al.* [12].

2.2. SUPERCOLLISIONS

Supercollisions are collisions which transfer an inordinate amount of energy in a single event. They were found experimentally [16-19] and in trajectory calculations [2, 3, 9, 11, 13, 20-24] and transfer as much as 3000 cm^{-1} in a single collision between an Ar atom and an excited toluene or benzene or as much as 10000 cm^{-1} in a collision between an excited CS_2 and a cold CO. There seems to be a probability of 1 in a 800 for a 3000 cm^{-1} transfer to occur [2, 3]. These supercollisions, by virtue of the large value of ΔE which is transferred, affect the values of the rate coefficient, collisional efficiency and the average energy transferred per collision <ΔE> in a very prominent way. One supercollision (SC) of 10 000 cm^{-1} in 1000 collisions changes the value of the rate coefficient by a factor of 9 in the low pressure region. Five SC of the same magnitude in

1000 collisions change the value of the rate coefficient by a factor of 20 [23]. Similar results have been found for the collisional efficiency and the values of <ΔE> [23].

All the SC trajectories indicate that the energy transfer event takes place when the atom approaches perpendicularly to the plane of the molecule. There are two ways in which this particular configuration affects a SC. In one the atom receives a sudden kick from an out-of-plane vibration of the molecule when it is in phase with the out-of-plane motion. The other way is that the plane of a fast rotating molecule hits in phase the incoming atom. This tennis-ball effect, which appears in both modes of energy transfer, is probably responsible for the large energy transfer quantities exchanged in supercollisions. However, these two conditions, perpendicularity and phase, are not sufficient to affect large vibrational energy transfers. A third very important condition must be fulfilled as well. Large quantities of internal energy must be present in a moiety from which energy is transferred. The out of plane motions have low frequencies and they must be highly excited to affect large energy transfers. The probability of having large values of excitation energy in a small moiety in a highly excited benzene molecule is actually rather high [25], and it does not appear to be a bottleneck in the CET process. When the three conditions are fulfilled simultaneously, a supercollision may occur.

2.3. GLOBAL POTENTIAL

There are a number of ways of using an intermolecular potential in trajectory calculations. One is to use a pairwise potential, the other is to calculate it on-the-fly as the trajectory progresses. There is a basic difference between the pairwise potential between the individual atoms in the system and the overall, global potential which is the sum of the individual interactions. We have calculated [26-28] an average, or global, dynamic potential by averaging many single-trajectory potentials. It represents a quantity that is based on averaging tens of thousand of trajectories with all possible orientations and impact parameters chosen by Monte Carlo sampling of impact parameters and Euler's angles. It is obtained by binning the potential energy as a function of the CM distance for all the trajectories and averaging it by dividing the sum in each bin by the number of times the atom traverses a given CM distance that is represented by a particular bin. Global potentials are especially useful for non-spherical molecules like benzene [26, 28]. The dynamic global potential is a function of the temperature and explanations, which take into consideration the anisotropic potential of the benzene molecule and the effects of the vibrational, rotational, and translational energies on the dynamic global potential are provided in reference 28. It is to be noted that Lennard-Jones or *ab initio* pairwise potentials yield Buckingham-type global potentials.

2.4. VIRIAL COEFFICIENTS

Using trajectory calculations with an *ab initio* pair-wise potential or an assumed Lennard-Jones pair-wise potential, we can calculate the intermolecular dynamic global potential which can be used to calculate experimentally obtained quantities such as a second virial coefficient. From classical statistical mechanics one obtains the following, well known, equation for the second virial coefficient:

$$B(T) = 2\pi N_A \int_0^\infty \left(1 - \exp(-V(r)/kT\right) r^2 dr \qquad (7)$$

where *V(r)* is the dynamic intermolecular global potential and r is the separation between the centers of mass of the colliding pair. The agreement between calculated and experimental quantities is a measure of the quality of the intermolecular potential that is used in such calculations. The method was demonstrated for benzene-Ar collisions [28]. An *ab initio* and a Lennard-Jones pair-wise potentials were used, and calculations of the dynamic global potential and the second virial coefficient were performed at various temperatures. Comparison with publish results shows large discrepancies between classical calculations with isotropic potentials and the present work. The method applies to neat gases as well as to binary gas mixtures.

2.5. INTERMOLECULAR ENERGY TRANSFER PROBABILITY DENSITY FUNCTION

One of the most important and elusive quantities in molecular dynamics calculations of reacting system is the intermolecular energy transfer probability density function P(E',E) which is used in master equation calculations of reaction rate coefficients [1].
        We have used trajectory calculations to calculate this quantity [26]. Our method distinguishes between effective trajectories that contribute to P(E',E) and those with very large impact parameter which do not. The P(E',E) thus found, obeys conservation of probability and detailed balance and is independent of the impact parameter. The method is demonstrated for benzene-Ar collisions at various temperatures and internal energies. With this method, it is possible to combine *ab initio* inter and intramolecular potentials with trajectory calculations, obtain P(E',E) and use that in master equation calculations to obtain rate coefficients and population distributions without resorting to any *a priori* assumptions and energy transfer models.

2.6. DYNAMICS AND ENERGY RELEASE IN BENZENE/AR-CLUSTER DISSOCIATION

The breakdown of a dimer, or a binary cluster, is referred to, mistakenly, as half-collision because the partners carry away energy thus deactivating the excited molecule. It differs from an actual collision because of the absence of relative translational energy and rotations of the monomers. We have studied the energy disposal distributions and lifetimes of Ar-benzene clusters, ABC [6,29]. Four intermolecular potentials, Lennard-Jones, *ab initio*, and two Buckingham-type potentials, were used in the calculations. The Ar atom was placed in one of the five minima of the potential surface at 0 K. The benzene monomer in ABC at 0 K was excited to various internal energies, and internal energy loss of the monomer following dissociation was calculated. The average energy removed, <ΔE>, depends on the depth of the potential well and on the initial structure of the cluster. The highest value was obtained when the cluster was formed at the deepest well, in which the Ar atom is above the center of the ring. Regardless of the initial structure, it was found that the atom migrated from well to well including the deepest,

and dissociation occurred from a structure different from the initial one. No correlation was found between the energy removed and the cluster lifetime, i. e. the dissociation process is history independent. Rotations and out-of-plane vibrations play a major role in the dissociation process. Except for the lowest values of ΔE, the energy disposal probability density function, $P(E',E)$, is exponential in ΔE. The cluster lifetime distributions depend on the potential, and can be fit by multi-exponential functions. Within a given potential, the shallower the well the narrower the temporal distribution, and the higher the internal energy of ABC the shorter the lifetime. Application of RRKM Theory to cluster modes, which contain an amount of energy ΔE, yields lifetimes with values similar to those obtained directly from trajectory calculations. A comparison between $P(E',E)$, $<\Delta E>$, and lifetimes obtained in cluster-dissociation and gas-phase collisions for identical inter- and intramolecular potentials show that energy transfer quantities and lifetimes are larger in clusters. On the other hand, the mechanism of energy transfer, and the contribution to it of rotations and out-of-plane vibrations are found to be similar in both systems.

2.7. INTRAMOLECULAR ENERGY REDISTRIBUTION IN C_{60} FOLLOWING HIGH-ENERGY COLLISIONS

It is interesting to consider energy flow in a large polyatom following initial impact by a small, energetic collider. We have addressed this issue by investigating high energy collisions between a C_{60} molecule and a Li^+ ion [17, 30]. When an inelastic collision occurs, the sudden internal excitation of the C_{60} sets in motion an intramolecular dynamics that ends up in the molecule being ergodic. The non mode-specific excitation of a moiety in the molecule by a collision involves a number of internal modes that in turn are coupled to additional modes and it is of interest to determine the rate of IVR for such a collisional event. We have monitored specific collisional events where the Li^+ hits the molecule at pre-specified locations: a five-member ring, a double bond, a single bond, and a carbon atom. The criteria used to follow the temporal evolution of the excitation in the molecule are bond lengthening and energy contents in the stretchings and bendings at various points in the molecule. For example, the IVR dynamics of a 5 member ring excitation was followed by observing the average lengths of the 5 bonds in the ring being impacted (front), of the 5 bonds in the ring directly opposite to the front ring at the back of the molecule (back), and of the 5 bonds in the side rings (side) as a function of time. In addition, the average energies in the 5 bonds of the rings were determined as a function of time.

Figure 1. A schematic drawing of a C_{60} molecule used in conjunction with studies of IVR. Front indicates the location of the impact of the Li^+ ion. Back indicates the ring opposite to the location of the front ring and Side indicates the side ring depicted in the drawing.

As an example, a collision of C_{60} with Li^+ with relative translational energy of 15 eV deposits 13.7 eV in a 5 member ring of a C_{60} at 613 K. The initial excitation is of the stretches of the C-C bonds in the ring. This manifests itself in the lengthening of these bonds while excitation of the bends takes place much more slowly, i.e. on a time scale

of 600 fs. Excitation of the local stretches of the back ring begins after about 67 fs. The bends follow with a longer time delay. There is "beating", excitation exchange, between back and front rings that slowly decays to a steady state. While the back and front rings are "communicating" with each other, the stretches in the side rings are hardly affected. Their excitation is modest with little fluctuations and beatings. The bending modes, on the other hand, are excited relatively soon, only 70 fs after the stretches in the ring are first excited. This is in contrast to the situation in the front and back rings where the bends are relatively passive in the initial stage of the energy exchange.

The initial rate of IVR is extremely fast. Only 67 fs after the initial excitation of the front ring, energy appears in the back ring. This does not mean, of course, that the energy randomizes on this time scale, but it indicates that local clustering of energy in a molecule for an extended period of time is impossible. The methode of fast Fourier Transforms was used to identified the modes that participated in the IVR. Only four normal modes, out of the available 174 modes, were excited and participated in the initial phase of IVR. Even though it took 60 fs for the excitation to move from the front to the back of the molecule, total relaxation was obtained however, only after few ps.

2.8. TERMOLECULAR COLLISIONS

Three-body collisions play a major role in many atmospheric and combustion reactions. A much cited explanation for third-body-assisted bimolecular reactions in the gas phase is the following sequence of two binary collisions.

$$A + B \rightarrow AB^*$$
$$AB^* + M \rightarrow AB + M$$
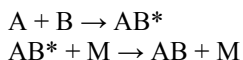
The first step is formation of a long-lived excited complex and the second is stabilization by energy transfer. A modification of this mechanism is the Chaperon mechanism,

$$A + M \rightarrow AM$$
$$B + AM \rightarrow AB + M$$
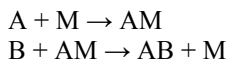
The chaperon M forms a weak complex with A in the first step and stabilizes the product by removing energy in the second step. The relative importance of the two mechanisms depends on the details of the potential energy surface of the system, namely, whether the reactants are radicals or polar and whether M is a noble gas atom or a polyatom. These types of reactions are of current theoretical and experimental interest.

We have studied termolecular collisions between a benzene molecule and two Ar atoms as a function of pressure, temperature and intermolecular potential without presupposing a given mechanism but, instead, letting the calculations dictate the final results [31]. The results show that termolecular collisions form termolecular complexes and occur by three mechanisms: a) the Chaperon mechanism, in which the first Ar in is the first Ar out of the termolecular complex, is the dominant one at high pressures. Two thirds of all termolecular collisions go by this mechanism. b) The Energy Transfer mechanism, in which the first Ar in is the last Ar out of the termolecular complex,

comprises about a quarter of all termolecular collisions at high pressures. c) The concerted channel, in which both argon atoms depart from the benzene simultaneously and does not lead to products in reactive systems, comprises about 10% of all termolecular collisions. We have evaluated and reported energy transfer quantities and collision complex lifetimes and their dependence on inter and intramolecular harmonic and anharmonic potentials, temperature, pressure, and internal energy of the benzene molecule. It was found that: a) The value of energy transfer quantities increase with internal energy, temperature and the well depth of the intermolecular potential. b) Termolecular collision complex lifetime increases with increase in internal energy, decreases with temperature, and increases with increase in the well depth of the intermolecular potential and depends in a very weak way on pressure. c) Anharmonic coupling does not significantly change energy transfer quantities, which were obtained by harmonic potential. d) Lowering the temperature increases the termolecular collision-complex lifetime because it reduces the translational/rotational energies. For that reason, it decreases the energy transfer quantities. Even though at first glance trajectory calculations of termolecular collisions seem a simple extension of bimolecular collisions this is not the case at all. The density of the gas is a major factor here while in binary collisions it does not enter at all. This inflicts major computational difficulties and use of proper probability density functions for random gas is required.

3. Conclusion

Trajectory calculations together with *ab initio* inter and intramolecular potential are efficient and productive in producing detailed information on the mechanism of binary and termolecular collisions and provide numerical values of collisional energy transfer quantities such as the average energy transferred in a collision, the average lifetime of binary and ternary collision complex, the energy transfer probability density function, supercollisions and the second virial coefficient.

References

1. Oref, I. and Tardy, D.C. (1990) Energy transfer in highly excited large polyatomic molecules, *Chem. Rev.*, **90**, 1407-1445.
2. Bernshtein, V., Lim, K.F. and Oref, I. (1995) Temporal dependence of collisional energy transfer by classical trajectory calculations of the toluene-argon system, *J. Phys. Chem.*, **99**, 4531-4535.
3. Bernshtein, V. and Oref, I. (1995) Minimal separation distance in energy transferring collisions – trajectory calculations, *Chem. Phys. Lett.*, **233,** 173-178.
4. VENUS. Quantum Chemistry Program Exchange by Hase, W.L., Duchovic, R.J., Hu, X., Komornicki, A., Lim, K.F., Lu, D.H., Peslherbe, G., Swamy, K.N., Vande-Linde, S.R., Varandas, A., Wang, H., and Rolf, R.J. (1996), *Quantum Chemistry Program. Exchange Bull*. (QCPE Program 671), **16** (4) , 43.
5. Bludsky, O., Spirko, V., Hrouda, V., and Hobza, P. (1992) Vibrational dynamics of the benzene/argon complex, *Chem. Phys. Lett.*, **196**, 410-416.
6. Bernshtein, V. and Oref, I. (2000) Dynamics and energy release in benzene/Ar cluster-dissociation, *J. Chem. Phys.*, **112**, 686-697.

7.   Draeger, J.A.   (1985) The methylbenzenes. 1. Vapor-phase vibrational fundamentals, internal rotations and a modified valence force-field, *Spectrochim. Acta.*, **41A**, 607-627.
8.   Bernshtein, V. and Oref, I. (2001) Dependence of collisions lifetimes on translational energy, *J. Phys. Chem. A.* **105**, 3454-3457.
9.   Bernshtein, V. and Oref, I. (1996) Trajectory calculations of relative center of mass velocities in collisions between Ar and toluene, *J. Chem. Phys.*, **104**, 1958-1965.
10. Rabinovitch, B.S. and Oref, I. (1979) Ergodicity in highly excited Polyatomic molecules, *Acc. Chem. Res.*, **12**, 166-175.
11. Bernshtein, V. and Oref, I. (1997) Collisional energy transfer between Ar and normal and vibrationally and rotationally frozen internally excited benzene-trajectory calculation, *J. Chem. Phys.,* **106**, 7080-7089.
12. Clary, D.C., Gilbert, R.G., Bernshtein, V., and Oref, I. (1995) Mechanisms for supercollisions, *Faraday Discuss.*, **102**, 423-433.
13. Bernshtein, V. and Oref, I. (1997) The contribution of wide angle motions to collisional energy transfer between benzene and Ar, *ACS Sym. Ser.*, **678**, 251-265.
14. Bernshtein, V. and Oref, I. (2001) The effect of magnitude and geometry on the gateway frequencies for collisional energy transfer between benzene and Ar, *J. Phys. Chem. A.*, **105**, 10646-10650.
15. Rosenblum, I., Dashevskaya, E.I., Nikitin, E.E., and Oref, I. (1997) Effect of the vibrational/rotational energy partitioning on the energy transfer in atom-triatomic molecule collisions, *Mol. Eng.*, **7**, 169-183.
16. Pashutzky, A. and Oref, I. (1980) *J. Phys. Chem.*, **92**, 178.
17. Hassoon, S., Oref, I. and Steel, C. (1988) Collisional activation of quadricyclane by azulene: an example of very strong collisions, *J. Chem. Phys.* **89**, 1743-1744.
18. Margulis, I.M., Sapers, S.S., Steel, C., and Oref, I. (1989) A chemical probe for highly energetic collisions in reactive systems, *J. Chem. Phys.* **90**, 923-929.
19. Mullin, A.S., Park, J., Chou, J.Z., Flynn, G.W., and Weston, R.E. (1993) Chem. Phys. **53**, 175.
20. Clarke, D.L., Thompson, K.G. and Gilbert, R.G. (1991) *Chem. Phys. Lett.*, **182**, 357.
21. Lendvay, G. and Schatz, G.C. (1990) *J. Phys. Chem.*, **94**, 8864.
22. Oref, I. (1995) Supercollisions, in Barker, J.R. (ed.) *Vibrational Energy Transfer Involving Small and Large Molecule,* Volume 2B of *Advances in Chemical Kinetics and Dynamics*, JAI, Greenwich, CT, pp. 285-298.
23. Bernshtein, V. and Oref, I. (1993) Effect of supercollisions on chemical reactions in the gas phase, *J. Phys. Chem.*, **97**, 12811-12818.
24. Bernshtein, V. and Oref, I. (1994) Effect of supercollisions analytical expressions for collision efficiency and average energy transferred in collisions, *J. Phys. Chem.*, **98**, 3782.
25. Oref, I. (1994) Local excitation in statistical systems, dynamics and supercollision effects, *Chem. Phys.*, **187**, 163-170.
26. Oref, I. and Bernshtein, V. (1998) Intermolecular energy transfer probabilities from trajectory calculations - A new approach, *J. Chem. Phys.,* **108**, 3543.
27. Bernshtein, V. and Oref, I. (1998) Endohedral formation, energy transfer and dissociation in collisions between L_i^+ and C_{60}, *J. Chem. Phys.*, **109**, 9811-9819.
28. Bernshtein, V. and Oref, I. (2000) Dynamic global potentials and second virial coefficients from trajectory calculations, *J. Phys. Chem.* **104**, 706.
29. Bernshtein, V. and Oref, I. (1999) Energy release in benzene-argon cluster-quasiclassical trajectory calculations, *Chem. Phys. Lett.*, **300**,104-108.
30. Bernshtein, V. and Oref, I. (1999) Intramolecular energy redistribution in C_{60} following high energy collisions with L_i^+ , *Chem. Phys. Lett.* **313**, 52-56.
31. Bernshtein, V. and Oref, I. (in press), Termolecular collisions between benzene and Ar, *J. Chem. Phys.*

MANIPULATION OF ATOMS AND MOLECULES WITH LASER RADIATION AND EXTERNAL FIELDS

MARCIS AUZINSH
Department of Physics, University of Latvia, 19 Rainis boulevard, Riga, LV-1586, Latvia, mauzins@latnet.lv

Abstract. The paper provides analysis of a process, when a laser radiation absorption of a specific polarization creates a specific spatial distribution of molecular bonds and angular momenta of small molecules. It is discussed how an external fields — electric or magnetic — can influence this distribution. Some practical examples involving optical polarization of molecules in magnetic and electric fields are presented. [1]

1. Introduction

Laser radiation has proved to be an efficient tool to control the shape of wave functions. The ability to control the shape of a quantum state may lead to methods for bond-selective chemistry and novel quantum technologies such as quantum computing. The classical coherence of laser light has been used to guide quantum systems into desired target states through interfering pathways. These experiments allow to control properties of the target state such as light absorption, fluorescence, angular momentum or molecular bond spatial orientation etc.

Probably coherent effects in atomic excitation with light were studied first by Wilhelm Hanle. The very first publication about the effect, which is now called Hanle effect, appeared in *Zeitschrift für Physik* as early as in 1924 [1]. In the paper it was shown that the resonance fluorescence of Hg excited with linear polarized light is depolarized by an external magnetic field. That publication does

---

[1] I have a privilege to know Prof. Evgueni Nikitin for many years. For the first time as a young student I met him at a conference in the former Soviet Union at which optical polarization of atoms and molecules was discussed. Later on our ways crossed several times and I had an opportunity to work with Prof. Nikitin on several projects and to admire his scientific intuition, deep knowledge and skills in application of advanced mathematical techniques to solve problems in physics elegantly. I feel very delighted and honored to dedicate this paper to Prof. Evgueni Nikitin on the occasion of his seventieth birthday.

not provide solely the measurements of this depolarization. It also shows that the plane of polarization of the fluorescence is rotated by the external magnetic field. To analyze this effect W. Hanle used a model of decaying linear oscillators that precess in the magnetic field with an angular velocity depending on the magnetic field strength. In this first paper the quantum theoretical importance of the effect was already discussed.

During the following years, efforts to provide a consistent interpretation of the effect played an important role in the development of quantum theory. The essence of Hanle effect, as we understand it today, is the creation of low frequency coherences between magnetic Zeeman sublevels of an atomic state and the destruction of these coherences by lifting of the magnetic sublevel degeneracy by an applied external magnetic field. These Zeeman coherences are associated with spatial polarization (orientation or alignment) of angular momenta of atoms or molecules. To this day Hanle effect still is an effective tool to study atomic [2] and molecular structure [3].

If the optical field that excites atoms or molecules is strong enough, it can create Zeeman coherences not only in the excited state of atoms or molecules, but also in the ground state. In a slightly different context this effect for the first time was studied as an optical pumping of atomic states.

As early as in 1949 Kastler [4] draws attention to the remarkable properties of the interaction of resonance light with atoms. Kastler points out that the absorption and scattering of resonance light could lead to large population imbalances along with atomic excited state also in atomic ground state. Ground state optical pumping soon was observed experimentally by Brossel, Kastler and Winter [5] and by Hawkins and Dicke [6].

In the absence of the external fields, the effect of optical pumping can easily be analyzed without using the concept of atomic coherences, but if one is willing to consider the influence of the external fields on optically pumped atoms or molecules then the idea about Zeeman coherences in the ground state of atoms or molecules becomes vital. In this case, we are speaking about creation of dark states or coherent population trapping. This effect was first directly observed in 1976 in the interaction of sodium atoms with a laser field [7]. In the case of coherent population trapping the destructive quantum interference between different excitation pathways causes the trapping of population in a coherent superposition of ground state sublevels. Once established, such a superposition (a dark state) [8] is immune against further radiative interaction. As a result, a fluorescence from an ensemble of atoms decreases, while the intensity of the transmitted light increases. An external magnetic field **B** applied perpendicularly to the light polarization vector **E** destroys the coherence between ground state sublevels and restores the absorption and fluorescence of the ensemble of atoms.

To describe all phenomena related to the creation and evolution of coherences created in an ensemble of atoms or molecules, one can deal with probability amplitudes for different quantum states involved in the process of light — matter

interaction. Nevertheless, it is a rather complicated business to follow all the amplitudes and, what is most important, all the phase relations between the states involved in the process. It is much more convenient to describe an ensemble of particles by means of quantum density matrix. The application of quantum density matrix for the description of atomic processes was pioneered by U. Fano (see, for example [9]). Currently this approach is recognized as very fruitful and is used in various contexts. In a standard form the interaction of laser radiation with gaseous atoms or molecules is described by means of the Liouville or optical Bloch equation for the quantum density matrix [8]. In the case of optical Bloch equations the use of monochromatic, intense optical field is assumed.

At the same time very often the real optical field interacting with atoms has rather broad spectral profile, width of which is broader or comparable with the inhomogeneous width of the atomic transition. In this case, a broad spectral line approximation for quantum density matrix approach has proved to be very rewarding. This approximation was introduced in the 1960s by C. Cohen-Tannoudji for excitation of atoms with ordinary light sources [10]. This was an era before lasers. Later on it was adjusted for application for excitation of atoms with multimode lasers [11] and for excitation of molecules in the case of large angular momentum states [3, 12].

It is demonstrated in different occasions that the quantum density matrix solutions for atomic or molecular states can be connected to a form of created wave function and spatial distribution of atomic angular momentum [13, 14]. This approach proved to be especially fruitful in the case of molecules. For example, for diatomic molecules that typically possess states with very large angular momentum quantum numbers $J \propto 100$, the spatial orientation of this angular momentum with respect to a chosen direction of quantization axis varies almost continuously. As a result, the transition from the quantum density matrix solution to the spatial distribution of angular momentum and molecular axes seems to allow to have a very clear insight into the processes taking place during the interaction of molecular ensemble with the optical fields [3, 15]. This method allows one to prepare molecules in a desired state of their orientation in a laboratory frame as well. It also allows one to study different stereoscopic or spatial effects of molecular interactions and interaction of molecule with the laser radiation.

2. Angular momentum polarization by laser radiation

2.1. VECTOR MODEL

The main purpose of this vector model treatment of light absorption in molecules is to provide a simple visual model for the absorption of light by diatomic molecules in which the geometrical implications of light polarization and molecular spatial orientation may be made appearent.

Let us start with the following picture of laser light interacting with diatomic molecule. We have a rotating diatomic molecule with a large total angular momen-

tum J. It is largely created by molecular rotation, which contributes an angular momentum N as a main part of J. Additionally, it is created also from an electronic angular momentum L, and, more precisely, from its projection Λ on an internuclear axis of the molecule. Due to the axial symmetry of the internal fields in the molecule this is a quantity, which is conserved in a molecular frame (see Fig. 1).
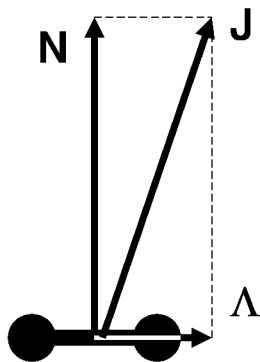
Figure 1.   The main angular momentum components in a diatomic molecule.

If we ask a simple question   what is changing, if such a molecule absorbs radiation in an electronic transition? The answer is obvious. Light can change an electron motion in the molecule and it means that electronic angular momentum in molecule and along with it the projection of this angular momentum on internuclear axis will be changed. In molecular spectroscopy one can distinguish two different types of transitions between electronic states of diatomic molecule. One is a perpendicular transition in which Λ is changed by ± 1 and another one is a parallel transition when Λ remains constant. For example $\Sigma \longleftrightarrow \Sigma$ or $\Pi \longleftrightarrow \Pi$ are parallel molecular transitions, but $\Sigma \longleftrightarrow \Pi$ is a perpendicular transition. The notation of the transition as being parallel or perpendicular is coming from the vector model and an analysis of the behavior of transition dipole momentum during the transition in this model. For the parallel transition this dipole moment oscillates along the internuclear axis, while in the case of perpendicular transition it rotates in a plane perpendicular to the internuclear axis. It is obvious, how this behavior of the transition dipole moment is coming into existence. If, for example, we have a $\Sigma \rightarrow \Pi$ absorption, then as a part of the transition probability we will need to calculate a dipole transition matrix element

$$\langle J'\Lambda = 1 | \widehat{d} | J''\Lambda = 0 \rangle, \tag{1}$$

where $\widehat{d}$ denotes transition dipole operator and J' and J'' denote the angular momentum quantum numbers of an excited and ground state respectively. As we see,

during this transition projection of an angular momentum J on the internuclear axis is increased by 1. This can be provided only by the dipole moment component d_{mol}^{+1} which in an angular momentum vector model can be associated with a rotation of the transition dipole momentum in a counterclockwise direction in a plane perpendicular to the quantization axis with a frequency ω [13], in this particular case – internuclear axis (see Fig. 2 a). In a similar way the behavior of the transition dipole momentum of molecule during the parallel type of transition, for example $\Sigma \longleftrightarrow \Sigma$ transition
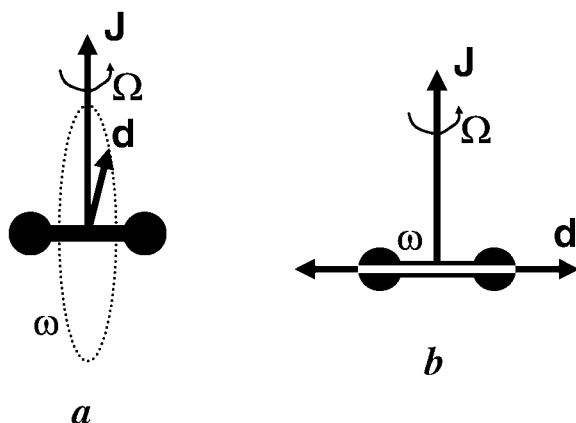
Figure 2. Perpendicular (a) and parallel (b) type of molecular transition.

$$\langle J'\Lambda = 0| \, \widehat{d} \, |J''\Lambda = 0\rangle \tag{2}$$

in a straightforward way can be associated with an oscillation with a frequency ω of a transition dipole momentum along the internuclear axis (see Fig. 2 b). Unfortunately, this picture alone is not sufficient to understand what will be the spatial distribution of molecular axes or angular momentum of molecules after the molecules absorb the polarized light with a fixed polarization in the laboratory frame. The transition dipole, which follow its own motion with frequency ω, simultaneously rotates together with the molecule with a frequency Ω. In order to understand what will be the angular momentum or molecular axis spatial distribution in the laboratory frame when a molecule absorbs polarized light, one needs to decompose the composite motion of the transition dipole momentum into components fixed in the laboratory frame. Most suitable for this purpose are the cyclic components of the vector. The unit vectors of this reference frame can be written as [3, 16, 17]

$$\mathbf{e}_{+1} = -1/\sqrt{2}(\mathbf{e_x} + i\mathbf{e_y}), \tag{3}$$
$$\mathbf{e_0} = \mathbf{e_z}, \tag{4}$$

$$\mathbf{e_{-1}} \;=\; 1/\sqrt{2}(\mathbf{e_x} - i\mathbf{e_y}).\tag{5}$$

These vectors can easily represent the linear oscillations along the z axis ($\mathbf{e_0}$) and a circular motion in the clockwise ($\mathbf{e_{-1}}$), as well as counterclockwise ($\mathbf{e_{+1}}$) direction in the xy plane [13]. In these coordinates a transition, which corresponds to the transition angular momenta component in a laboratory frame d^{+1}, increases the total angular momentum J of the molecule by 1. This is a so-called R type of the molecular transition and it is associated with the rotation of transition dipole momentum in a system of coordinates which is fixed to the total angular momentum of molecule in a counterclockwise direction — in a direction that coincides with a direction of the molecular rotation. The transition dipole momentum rotation frequency in this case is $\omega + \Omega$. The transition, which corresponds to the transition dipole momenta d^{-1} component, decreases the angular momentum of the molecule by 1. This is a so-called P type of molecular transition and it is associated with the rotation of the transition dipole momentum in a clockwise direction — in a direction which is opposite to the direction of molecular rotation. The transition dipole momentum rotation frequency in this case is $\omega - \Omega$. As far as there is a transition dipole momentum component in the plane perpendicular to the total angular momentum of the molecule for both cases of molecular transition – parallel as well as perpendicular   both transition types (P and R) exist for both parallel and perpendicular molecular transition [3, 18]. Additionally, for the perpendicular type of molecular transition there is a component of transition dipole momentum in a direction perpendicular to the molecular axis. This component of transition dipole can be associated with linear oscillations along the total angular momentum of the molecule. Frequency of these oscillations is ω. This is a so-called Q type of the molecular transition [3, 18]. All three types of molecular transition are shown in Fig. 3.
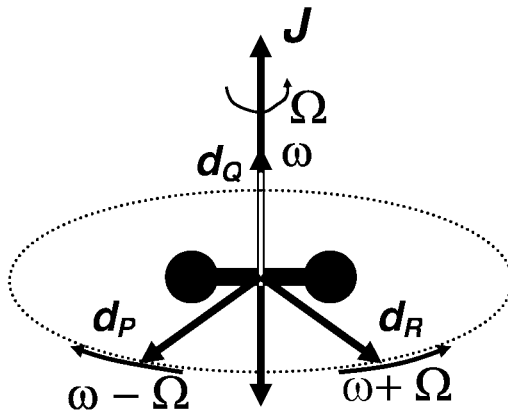
Figure 3.   Spatial orientation of transition dipole moment for P , Q and R types of molecular transitions.

This vector model of the transition dipole moment behavior provides a very simple and straightforward way to analyze the kind of spatial distribution of angular momenta or molecular axis that will be created by the absorption of the light of a definite polarization. For example, let us assume that we have light polarized along the z axis and the frequency of the light is equal to the frequency at which the transition dipole oscillates — ω. This light is absorbed by the molecules undergoing Q type transition (transition dipole moment parallel to angular moment). As far as the classical probability to absorb light by a linear dipole is proportional to $\cos^2\theta$, where angle θ is an angle between transition dipole moment and an electric vector of the light (see Fig. 4a), it is obvious that in this vector model the spatial distribution $\rho_{cl}(\theta,\varphi)$ of the angular momentum of molecules will be represented by the dumb bell shape probability density function $\rho_{cl}(\theta,\varphi) \sim \cos^2\theta$, (see Fig. 5a).

Let us now consider the absorption of circularly polarized light. We will describe the handedness of the light in accordance with the definition accepted in optics [19]. It means that if we are looking at the light beam, which is approaching us, and in this beam the electric field vector $\mathbf{E}$ rotates from left to right (clockwise direction) then we will call this light a right-polarized light, but if the electric field vector rotates from right to left (counterclockwise direction) then we will call this light a left-polarized light. Now, for example, a left-polarized light is propagating along the z axis. Its frequency coincides with the frequency $\omega - \Omega$ of the P type transition in a particular molecule (see Fig. 4b). According to the figure, if the angular momentum of the molecule is in the positive direction of the z axis, then the transition dipole momentum and the electric field vector of the light rotate in the opposite direction and the molecule is not able to absorb the light. On the contrary, if the angular momentum of the molecules is pointed in the negative direction of the z axis, then the transition dipole moment of the molecule and the light electric field rotate in the same direction with the same angular frequency. This means that such a molecule can absorb the light efficiently. If we are putting the analysis we performed in quantitative terms, then it means that the probability of the molecule to absorb left-hand circularly polarized light that travels in positive direction of z axis in case of P type of molecular transition is proportional to $\rho_{cl}(\theta,\varphi) \sim (1 - \cos\theta)^2/4$, see, Fig. 5b.

Such type of analysis in each particular case of light polarization and type of molecular transition allows to obtain a simple and comprehensive picture, which shows, what kind of angular momentum distribution we can expect if the ensemble of molecules absorbs the light with a specific polarization.

2.2. LIOUVILLE (OPTICAL BLOCH) EQUATIONS

Of course, a vector model described above has strong limitations. It can be applied only in the case of large angular momentum quantum number values. To have a precise quantum mechanical description of light interaction with atoms and molecules, one should use a quantum mechanical description. Usage of monochro-
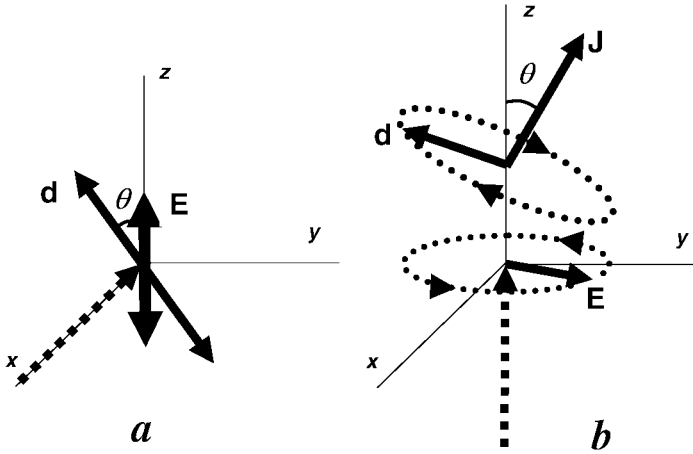
Figure 4.   *a*   absorption of lineal polarized light by a Q type of molecular transition and *b*   of the left hand circular polarized light by a P type of molecular transition.

matic, intense and continuously tunable radiation sources permits a very precise control of atomic and molecular states. To describe this interaction for intense laser radiation, one can use an optical Bloch equation [8, 20]

$$i\hbar \frac{d\rho(t)}{dt} = [H, \rho(t)] + \Gamma\rho(t), \tag{6}$$

where $\rho(t)$ is a density matrix describing population of the levels and coherences created in a system. H is a Hamilton operator, which describes atom or molecule and its interaction with the laser radiation. Finally, Γ is the relaxation matrix, which phenomenologically describes all the relaxation processes in a system. Usually this system of equations is solved in the rotating wave approximation, which eliminates fast oscillations with a frequency of the order of optical transition frequency for the density matrix elements.

For example, in the simplest possible case of two non-degenerated level system interacting with laser radiation, we have the following Liouville equations

$$\dot{\rho}_{11} = \Gamma_1 - \Gamma_1\rho_{11} + \Gamma_{21}\rho_{22} + \frac{i}{2}(\rho_{12} - \rho_{21})\Omega, \tag{7}$$

$$\dot{\rho}_{12} = -\left(\gamma - i\Delta + \frac{\Gamma_{21} + \Gamma_2 + \Gamma_1}{2}\right)\rho_{12} + \frac{i}{2}(\rho_{11} - \rho_{22})\Omega, \tag{8}$$

$$\dot{\rho}_{22} = -(\Gamma_2 + \Gamma_{21})\rho_{22} - \frac{i}{2}(\rho_{12} - \rho_{21})\Omega, \tag{9}$$

where Γ_{21} is a spontaneous emission rate from level 2 to level 1 and Γ_i is an additional loss rate from level i, $i = 1, 2$. Excitation is parameterized by a Rabi frequency $\Omega = d_{12}\mathcal{E}/\hbar$, where d_{12} is a dipole operator matrix element between
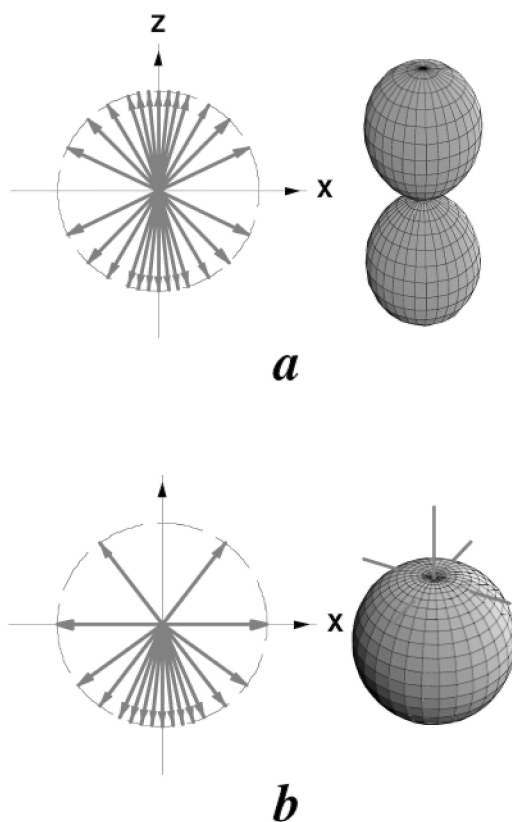
Figure 5.   *a* — angular momentum alignment (angular momentum spatial distribution probability density) created by an absorption of linear polarized light on a *Q* type of molecular transition and *b* — angular momentum orientation created by a left-hand polarized light on a *P* type of molecular transition.

states 1 and 2 and $\mathcal{E}$ is an electric field strength of the laser radiation. Parameter Δ describes a detuning of the laser frequency from the exact resonance, γ is equal to the laser radiation spectral line-width, $\rho_{ik} = \rho_{ki}^*$. These equations represent the excitation processes of a two level system with an accuracy which is adequate for most experiments that study collision dynamics or chemical reactions. Even more, molecular systems are often open systems. This means that excited molecules usually decay to very many molecular states and there is a very small chance for a molecule in a spontaneous process to return to the initial level. Consequently, we are arriving at a situation when $\Gamma_{21} = 0$ and even in case of degenerated molecular

states the problem very often can be treated as a set of many independent two level systems. Each system of equations describes an independent pairs of levels from the degenerated two level transition.

This system in many cases can be simplified further. For example, if we have a broad spectral line excitation with a not very intense laser radiation, we have a situation for an open transition when $\gamma \gg \Gamma_i, \Omega$. In practical cases this condition is often fulfilled at excitation with *cw* lasers operating in a multimode regime. If the homogeneous width of spectral transition usually is in the range of 10 MHz, then the laser radiation spectral width broader than 100 MHz usually can be considered as a broad line excitation. In this case we can use a procedure known as adiabatic elimination. It means that we are assuming that optical coherence ρ_{12} decays much faster than the populations of the levels $\rho_{ii}, i = 1, 2$. Then we can find stationary solution for off-diagonal elements for the density matrix and afterwards find a rate equations for populations in this limit. For the two level system we will have

$$
\dot{\rho}_{11} = \Gamma_1 - \Gamma_1\rho_{11} + \Gamma_{21}\rho_{22} - \frac{(2\gamma + \Gamma_1 + \Gamma_2 + \Gamma_{21})\Omega^2}{(2\gamma + \Gamma_1 + \Gamma_2 + \Gamma_{21})^2 + 4\Delta^2}\rho_{11} +
$$
$$
\frac{(2\gamma + \Gamma_1 + \Gamma_2 + \Gamma_{21})\Omega^2}{(2\gamma + \Gamma_1 + \Gamma_2 + \Gamma_{21})^2 + 4\Delta^2}\rho_{22}, \tag{10}
$$
$$
\dot{\rho}_{22} = -(\Gamma_2 + \Gamma_{21})\rho_{22} + \frac{(2\gamma + \Gamma_1 + \Gamma_2 + \Gamma_{21})\Omega^2}{(2\gamma + \Gamma_1 + \Gamma_2 + \Gamma_{21})^2 + 4\Delta^2}\rho_{11} -
$$
$$
\frac{(2\gamma + \Gamma_1 + \Gamma_2 + \Gamma_{21})\Omega^2}{(2\gamma + \Gamma_1 + \Gamma_2 + \Gamma_{21})^2 + 4\Delta^2}\rho_{22}, \tag{11}
$$

In these equations that are valid for broad spectral line excitation (large γ) and arbitrary values for all other parameters, one can easily see a simple rate equations if we assume that absorption rate is expressed as

$$
\Gamma_{pump} = \frac{(2\gamma + \Gamma_1 + \Gamma_2 + \Gamma_{21})\Omega^2}{(2\gamma + \Gamma_1 + \Gamma_2 + \Gamma_{21})^2 + 4\Delta^2}. \tag{12}
$$

If we are interested in a stationary solution of Eqs. (10 and 11), then balance equations that can be obtained from Eqs. (10 and 11) setting right-hand-side of equations equal to zero are valid for any values of parameters and the broad spectral line assumption is not necessary any more. It means that very often for two level system Liouville equations can be replaced with a simple rate equations.

Situation becomes much more complicated if we have a two-step excitation. For example, the first laser excites transition $1 \to 2$ and the second laser further excites transition $2 \to 3$. In this case for nondegenerated three level system we will have the following Liouville equations:

For the diagonal elements or the populations of three levels we have

$$
\dot{\rho}_{11} = \Gamma_1 - \Gamma_1\rho_{11} + \Gamma_{21}\rho_{22} + \Gamma_{31}\rho_{33} + \frac{i}{2}(\rho_{12} - \rho_{21})\Omega_{12}, \tag{13}
$$
$$
\dot{\rho}_{22} = -(\Gamma_2 + \Gamma_{21})\rho_{22} + \Gamma_{32}\rho_{33} -
$$

$$\frac{i}{2} \left(\rho_{12} - \rho_{21} \right) \Omega_{12} + \frac{i}{2} \left(\rho_{23} - \rho_{32} \right) \Omega_{23}, \tag{14}$$

$$\dot{\rho}_{33} = -\left(\Gamma_3 + \Gamma_{31} + \Gamma_{32} \right) \rho_{33} - \frac{i}{2} \left(\rho_{23} - \rho_{32} \right) \Omega_{23}. \tag{15}$$

The density matrix equations for the single-photon coherences are

$$\dot{\rho}_{12} = -\left(\gamma - i\Delta_{12} + \frac{\Gamma_{21} + \Gamma_1 + \Gamma_2}{2} \right) \rho_{12} +$$

$$\frac{i}{2} \left(\rho_{11} - \rho_{22} \right) \Omega_{12} + \frac{i}{2} \rho_{13} \Omega_{23}, \tag{16}$$

$$\dot{\rho}_{23} = -\left(\gamma - i\Delta_{23} + \frac{\Gamma_{21} + \Gamma_2 + \Gamma_{31} + \Gamma_{32} + \Gamma_3}{2} \right) \rho_{23} -$$

$$\frac{i}{2} \rho_{13} \Omega_{12} + \frac{i}{2} \left(\rho_{22} - \rho_{33} \right) \Omega_{23}, \tag{17}$$

while the equation for the two-photon coherence is

$$\dot{\rho}_{13} = -\frac{1}{2} \left(-i\Delta_{13} + \Gamma_{31} + \Gamma_{32} + \Gamma_1 + \Gamma_3 \right) \rho_{13} -$$

$$\frac{i}{2} \rho_{23} \Omega_{12} + \frac{i}{2} \rho_{12} \Omega_{23}. \tag{18}$$

In these equations all the notations are similar to the notations used for the two level system.

The procedure of adiabatic elimination in this case leads to rather complicated equations for diagonal elements of the density matrix, which in a general case can not be reduced to simple rate equations for populations. To examine the essential characteristics of the equations for populations we shall make a number of simplifying assumptions. First, let us consider an exact resonance

$$\Delta_{ij} = 0. \tag{19}$$

Next, we neglect all spontaneous emission between states $1, 2$ and 3. (Such terms are essential when one deals with a closed system, but can often be neglected for such an open system as most of molecules.) We assume that the remaining relaxation rates, to other levels, are all equal:

$$\Gamma_{ij} = 0, \qquad \Gamma_j = \Gamma. \tag{20}$$

Finally, we take the two Rabi frequencies to be equal,

$$\Omega_{ij} = \Omega. \tag{21}$$

With these assumptions we have the following rate equations for populations in an assumption of broad spectral line excitation

$$\dot{\rho}_{11} = \Gamma(1 - \rho_{11}) - \frac{\Gamma \Omega^2 (\rho_{11} - \rho_{22})}{2\Gamma(\gamma + \Gamma) + \Omega^2} + \frac{\Omega^4 (\rho_{11} - \rho_{33})}{4(\gamma + \Gamma)[2\Gamma(\gamma + \Gamma) + \Omega^2]}, \tag{22}$$

$$\dot{\rho}_{22} = -\Gamma\rho_{22} + \frac{\Gamma\Omega^2(\rho_{11} - \rho_{22})}{2\Gamma(\gamma + \Gamma) + \Omega^2} + \frac{\Gamma\Omega^2(\rho_{33} - \rho_{22})}{2\Gamma(\gamma + \Gamma) + \Omega^2}, \tag{23}$$

$$\dot{\rho}_{33} = -\Gamma\rho_{33} - \frac{\Gamma\Omega^2(\rho_{33} - \rho_{22})}{2\Gamma(\gamma + \Gamma) + \Omega^2} + \frac{\Omega^4(\rho_{11} - \rho_{33})}{4(\gamma + \Gamma)[2\Gamma(\gamma + \Gamma) + \Omega^2]}. \tag{24}$$

from where one and two photon absorption rates can be defined as

$$\Gamma_{pump}(1) = \frac{\Omega^2\Gamma}{2\Gamma(\gamma + \Gamma) + \Omega^2}, \tag{25}$$

$$\Gamma_{pump}(2) = \frac{\Omega^4}{4(\gamma + \Gamma)[2\Gamma(\gamma + \Gamma) + \Omega^2]}. \tag{26}$$

If, as before, we are interested only in the steady state solution (steady state populations) for three levels, then the obtained equations are valid for arbitrary values of all the parameters and the assumption of broad spectral line (large γ) is not needed.

In these equations we can clearly see the two photon transition probabilities that directly connect levels 1 and 3 and are proportional to the fourth power of Rabi frequency. These equations in the limit of weak excitation (small Ω) lead to the "phenomenological" rate equations, which do not take into account two photon transitions

$$\dot{\rho}_{11} = \Gamma(1 - \rho_{11}) - \frac{\Omega^2(\rho_{11} - \rho_{22})}{2(\gamma + \Gamma)}, \tag{27}$$

$$\dot{\rho}_{22} = -\Gamma\rho_{22} + \frac{\Omega^2(\rho_{11} - \rho_{22})}{2(\gamma + \Gamma)} + \frac{\Omega^2(\rho_{33} - \rho_{22})}{2(\gamma + \Gamma)}, \tag{28}$$

$$\dot{\rho}_{33} = -\Gamma\rho_{33} - \frac{\Omega^2(\rho_{33} - \rho_{22})}{2(\gamma + \Gamma)}. \tag{29}$$

We see that, taking into account assumptions made with respect to the relaxation rates and other parameters, we basically have arrived at the same absorption rate that we had for a two level system, compare to Eq. (12). It is interesting to note the ratio between two-photon transition rate and one-photon transition rate. This ratio is

$$\frac{\Gamma_{pump}(2)}{\Gamma_{pump}(1)} = \frac{\Omega^2}{4\Gamma(\gamma + \Gamma)}, \tag{30}$$

which means that the transition rate for two photon transitions is negligible for weak excitation, but can play a dominant role for strong laser radiation and cannot be neglected.

To illustrate the method described above, let us consider now one particular example (see Fig. 6). The diatomic molecule, for example Na_2, is excited in two steps by two weak linear polarized lasers, which are at an exact resonance ($\Delta = 0$) — first one with the first molecular transition, but the second one with the second molecular transition. In the first case lasers are polarized parallel to each other.

Angular momenta of the molecular states involved in the transition are $J'' = 7 \rightarrow J'_1 = 8 \rightarrow J'_2 = 9$. As a result we have molecular axis distribution in the second excited state as depicted in the Fig. 6a. The z axis in this figure is directed along the direction of polarization of both lasers. As we see, molecular axes are very strongly aligned along the direction of quantization axis (direction of polarization of a laser beams).

On the contrary, if we have lasers polarized in perpendicular directions to each other, we point the z-axis in the direction of polarization of second laser and consider molecular transitions in a sequence $J'' = 7 \rightarrow J'_1 = 8 \rightarrow J'_2 = 8$, then we have molecular axes distribution in the second excited state as shown in Fig. 6b. Now molecular axes are very strongly aligned in the plane that is perpendicular to the axis of quantization. This example demonstrates, how efficiently we can manipulate the molecular axes distribution just by varying angular momentum of the states excited by laser beams and mutual polarization of lasers.
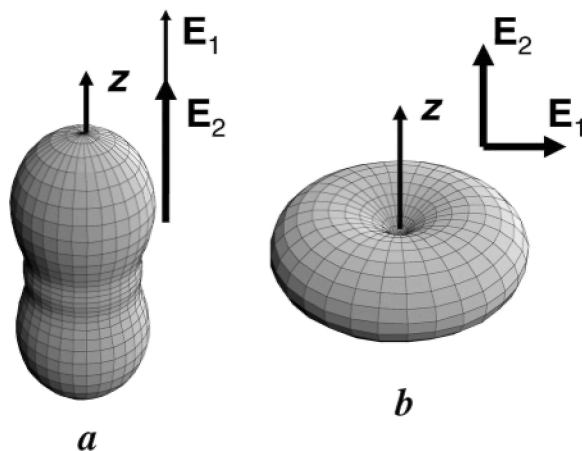
Figure 6.   The probability distribution of molecular axes for two step laser excitation of diatomic molecules. For case *a* we have angular momentum quantum number sequence 7-8-9 in molecular transitions, but for case *b* we have 7-8-8 sequence. Mutual laser polarization for both cases is shown in the figure.

3.   Rate equations for degenerate levels

Let us analyze further to what consequences assumption of spectrally broad laser excitation leads. We shall assume that we have degenerate ground and excited state of optical transition. For example, it can be an optical transition between two molecular states that consists of a large number of degenerate magnetic (Zeeman) sublevels. It means that this large width of laser line will prevent the formation of the optical coherences between pairs of magnetic sublevels, in which one sublevel

belongs to the ground sate and another to the excited state   optical coherences. At the same time there is no reason why, with the spectrally broad radiation, coherences between pairs of magnetic sublevels for which both sublevels belong either to the ground or to the excited state could not be created. To analyze these Zeeman coherences, the density matrix equations for degenerated two level system for a broad spectral line excitation can be used [3, 12]

$$
\begin{aligned}
\dot{f}_{M_e M_e'} \;=\;& \Gamma_p \sum_{M_g M_g'} \langle M_e | \mathbf{E}^\star \mathbf{d} | M_g \rangle \langle M_e' | \mathbf{E}^\star \mathbf{d} | M_g' \rangle^\star \varphi_{M_g M_g'} - \\
& (\frac{\Gamma_p}{2} + i\omega_S) \sum_{M_e'' M_g} \langle M_e | \mathbf{E}^\star \mathbf{d} | M_g \rangle \langle M_e'' | \mathbf{E}^\star \mathbf{d} | M_g \rangle^\star f_{M_e'' M_e'} - \\
& (\frac{\Gamma_p}{2} - i\omega_S) \sum_{M_e'' M_g} \langle M_e'' | \mathbf{E}^\star \mathbf{d} | M_g \rangle \langle M_e' | \mathbf{E}^\star \mathbf{d} | M_g \rangle^\star f_{M_e M_e''} - \\
& \Gamma f_{M_e M_e'} - i\omega_{M_e M_e'} f_{M_e M_e'} \qquad\qquad\qquad (31)
\end{aligned}
$$

$$
\begin{aligned}
\dot{\varphi}_{M_g M_g'} \;=\;& -(\frac{\Gamma_p}{2} + i\omega_S) \sum_{M_g'' M_e} \langle M_g | \mathbf{E}^\star \mathbf{d} | M_e \rangle \langle M_g'' | \mathbf{E}^\star \mathbf{d} | M_e \rangle^\star \varphi_{M_g'' M_g'} - \\
& (\frac{\Gamma_p}{2} - i\omega_S) \sum_{M_g'' M_e} \langle M_g'' | \mathbf{E}^\star \mathbf{d} | M_e \rangle \langle M_g' | \mathbf{E}^\star \mathbf{d} | M_e \rangle^\star \varphi_{M_g M_g''} + \\
& \Gamma_p \sum_{M_e M_e'} \langle M_g | \mathbf{E}^\star \mathbf{d} | M_e \rangle \langle M_g' | \mathbf{E}^\star \mathbf{d} | M_e' \rangle^\star f_{M_e M_e'} - \gamma \varphi_{M_g M_g'} - \\
& i\omega_{M_g M_g'} \varphi_{M_g M_g'} + \sum_{M_e M_e'} \Gamma_{M_g M_g'}^{M_e M_e'} f_{M_e M_e'} + \lambda \delta_{M_g M_g'} \qquad (32)
\end{aligned}
$$

where by $f_{M_e M_e'}$ and $\varphi_{M_g M_g'}$ are denoted the density matrices of an excited and ground state level respectively. The first term on the right-hand side of Eq.(31) describes the absorption of light at the rate Γ_p. The transition matrix elements of the form $\langle M_e | \mathbf{E}^\star \mathbf{d} | M_g \rangle$ account for the conservation of angular momentum during photon absorption with $\mathbf{E}$ being the light polarization vector. The second and the third terms describe the stimulated emission of the light and the dynamic Stark shift ω_S. The fourth term characterizes the relaxation of the density matrix $f_{M_e M_e'}$ with a rate constant Γ. Finally, the fifth term describes the Zeeman splitting of the magnetic sublevels M_e and M_e' by a value of $\omega_{M_e M_e'} = (E_{M_e} - E_{M_{e'}})/\hbar$.

The first and the second terms on the right-hand side of Eq.(32) describe a light absorption and the dynamic Stark shift, the third term — the stimulated light emission, the fourth term — the relaxation processes in the ground state, the fifth term — the Zeeman interaction, the sixth term — the repopulation by spontaneous transitions at a rate $\Gamma_{M_g M_g'}^{M_e M_e'}$, and the seventh term — the relaxation of the density matrix of the ground state atoms interacting with the gas in a cell, not influenced by the radiation.

The matrix element of electric dipole transition $\langle M_e| \mathbf{E}^\star \mathbf{d} |M_g\rangle$ is expanded as [3, 16, 17]

$$\langle M_e| \mathbf{E}^\star \mathbf{d} |M_g\rangle = \sum_q (E^q)^* \langle M_e| d^q |M_g\rangle, \tag{33}$$

where the superscript q denotes the cyclic components of the respective vectors. The matrix element at the right-hand side of equation (33) are further expanded, applying the Wigner–Eckart theorem, as [3, 16, 17]

$$\langle M_e| d^q |M_g\rangle = \frac{1}{\sqrt{2F_e + 1}} C^{J_e M_e}_{J_g M_g 1 q} (F_e \,||d||\, F_g), \tag{34}$$

where $(J_e \,||d||\, J_g)$ is the reduced matrix element. Under conditions of stationary excitation the system of equations (31) and (32) becomes a system of linear equations for the ground and excited state density matrix elements. The coefficients of this system are calculated using angular momentum algebra and the formulas presented above. For further details see, for example [3].

Solution of this equation allows to calculate spatial distribution and its evolution in time for angular part of probability density, which in case of atoms means angular distribution of valence electron but in case of diatomic molecules   the spatial distribution of molecular axis. This is an important information, if the stereo effects for different interactions are under the study. Hence, for example, if we know the density matrix of the excited state of diatomic molecule, then the molecular axes distribution can simply be calculated as [15]

$$\rho_{ax}(\theta, \varphi) = \sum_{M_1 M_2} f_{M_1 M_2} Y_{J M_1}(\theta, \varphi) Y^*_{J M_2}(\theta, \varphi). \tag{35}$$

If one is interested in a spatial distribution of angular momentum created by laser radiation, then there is a method how to make a transition from quantum density matrix to the continuous angular momentum spatial distribution probability density. As it is shown in [21], a classical probability density $\rho_{cl}(\theta, \varphi)$ for angular momentum spatial distribution can be connected to the density matrix elements $f_{MM'}$. At the $J \to \infty$ limit these elements can be considered as coefficients of the Fourier expansion of a classical probability density $\rho_{cl}(\theta, \varphi)$

$$\rho_J(\theta, \varphi) = \sum_{\varepsilon=-\infty}^{\infty} e^{i\varepsilon\varphi} f_{M+\frac{\varepsilon}{2}, M-\frac{\varepsilon}{2}}; \qquad \cos\theta = \frac{2M}{2J+1}. \tag{36}$$

The last equation is not restricted to the case when we have a coherent superposition of two M states belonging to the same J. If they belong to different J states, all we need to do is replace J with $(J_1 + J_2)/2$. The inverse of (36) can be written as

$$f_{M+\frac{\varepsilon}{2}, M-\frac{\varepsilon}{2}} = \frac{1}{2\pi} \int\limits_0^{2\pi} e^{-i\varepsilon\varphi} \rho_{cl}(\theta, \varphi) \, d\varphi. \tag{37}$$

In practice, we almost always have the situation when for those $f_{M+\frac{\varepsilon}{2}, M-\frac{\varepsilon}{2}}$ that differ from zero, values of ε are small in comparison to the interval of all allowed M values. For most cases of practical interest it makes the calculation of (36) rather simple.

4. Influence of external fields

The action of the external fields like electric or magnetic can be taken into account in a very general way. External fields, as a rule, lift the degeneracy of different magnetic sublevels of the angular momentum state. It means that in the external field magnetic sublevels are split and cause appearance of the nonzero Zeeman frequencies $\omega_{M_e M'_e} = (E_{M_e} - E_{M_{e'}})/\hbar$. For different molecules in different (electric or magnetic) fields pattern of magnetic sublevel splitting can be very different. It means that Zeeman frequencies $\omega_{M_e M'_c}$ can have different dependence on M_e, M'_e for different cases. The simplest case is the linear Zeeman effect, when in the magnetic field each magnetic sublevel obtains additional energy, which is directly proportional to the magnetic field strength and magnetic quantum number. The coefficient of proportionality is the Bohr magneton μ_B multiplied by the Lande factor g

$$E_M = g\mu_B B M. \tag{38}$$

As a result, Zeeman frequencies are simply $\omega_{M_e M'_e} = g\mu_B B \Delta M/\hbar$, where $\Delta M = M - M'$. In terms of the vector model described above, this means that the linear Zeeman effect causes precession of the angular momentum probability distribution around the magnetic field with Larmor frequency $\omega_{Larmor} = g\mu_B B/\hbar$. Shape of probability density during this precession is preserved [15]. However, in many cases Zeeman effect deviates from a simple linear behavior and then the influence of the external field on the polarization of molecules created by the laser field can be a sensitive probe of this nonlinearity of Zeeman effect. As it was shown, for example, for Te$_2$ in [22] and [23], the nonlinearity of the Zeeman effect can cause a symmetry breaking of the angular momentum spatial distribution, which exhibits itself as an appearance of the orientation of angular momentum in the initially aligned ensemble and appearance of the circularly polarized laser induced fluorescence after linear polarized laser excitation, as a consequence. Observation of such type of effects allows to study the reasons for nonlinearity of the Zeeman effect and to determine such molecular constants as the rate of magnetic predissociation and state mixing matrix elements in external fields. In this particular case a rather strong circularity (up to 5%) was observed at a magnetic field strength of 0.4 T (see Fig. 7)

In the case of an electric field, situation can be even more peculiar. In most cases Stark effect in molecules is in principle nonlinear (quadratic) over the electric field strength $\mathcal{E}$ and magnetic quantum number M. This allows to exploit this intrinsic nonlinearity and to manipulate angular momentum spatial distribution of
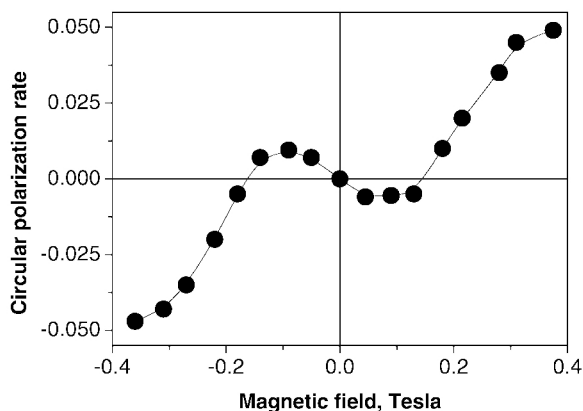
Figure 7. Circular polarization rate created by an alignment to orientation conversion in laser excited fluorescence of the Te_2 molecule due to magnetic intramolecular interactions and magnetic predissociation.
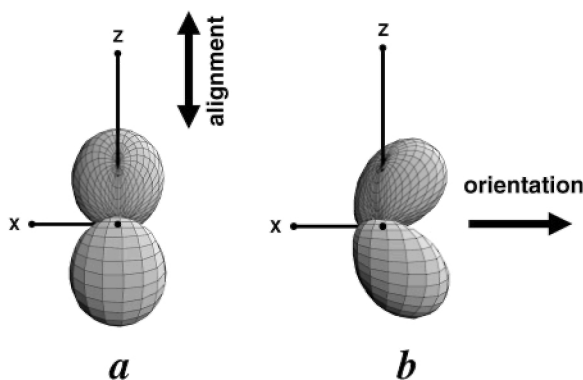
Figure 8. The angular momentum probability distribution of diatomic molecule in absence of an electric field — case a and when electric field is applied along the z axis — case b.

molecules. Let us consider one example. In Fig. 8 angular momenta spatial distribution are shown for two cases. In case a we have initially aligned molecules. This alignment is created by a linerly polarized laser radiation in Q type of molecular transition. Laser is polarized in yz plane at an angle $\pi/4$ with respect to z axis. Molecules are aligned along the laser polarization vector. If now an electric field is applied along z axis angular momenta distribution is changed in such a way that more angular momenta are pointed in the negative direction of x axis than in the

positive direction. As a result, we have transverse (perpendicular to the axis of quantization) orientation of angular momenta of molecules. For more details, see [15].

This alignment to orientation conversion can be exploited for practical purposes. In molecular beams alignment of angular momentum of molecules due to collisions during the beam formation usually occurs almost automatically [24]. If we apply an electric field in the direction of $\pi/4$ to the beam direction, this alignment can be efficiently converted into orientation. Choosing appropriate region length along the beam direction in which field is applied and field strength one can orient molecules in a selected rotational state and even for a selected isotopomer of the molecule. For details, see [25].

When speaking about nonlinear Zeeman or Stark effects in molecules as well as in atoms, we should keep in mind that usually these nonlinearities are caused by mixing in the external field of the different molecular states — be that rotational states of the molecules or other close lying states like, for example, Lambda doublet components in the Π states of the diatomic molecules. This state mixing does not only cause nonlinear magnetic sublevel splitting but also modifies state wave functions between which light causes transitions. It means that the matrix elements of a type $\langle M_e | \mathbf{E}^\star \mathbf{d} | M_g \rangle$ do not describe any more transition probabilities between states with well defined angular momentum J but between states the wave function of which, in general case, can be represented as

$$|\chi M_g\rangle = \sum_{J_i} c_{J_i} |J_i M_g\rangle. \tag{39}$$

As it was shown in [26], this leads to the substantial modification of the transition probabilities between molecular states and it can happen that transitions that are strictly forbidden in absence of the external field, in presence of the field become to be allowed and exhibit high probability.

5. Conclusions

In this paper it was very briefly demonstrated that the laser radiation in combination with external fields can be a powerful tool to prepare molecules in specific quantum state that can be characterized with a well pronounced spatial anisotropy of molecular axes (chemical bonds) and angular momentum. These states in past have been exploited in studies of molecular properties including dynamics of chemical reactions, but it seems that full capacity of this method still needs to be explored.

Acknowledgements

References

1. W. Hanle, Uber magnetische Beeinflussung der Polarisation der Resonanzfluorescenz, Z. Phys. **30**, p. 93 – 105, (1924); English translation in ref. 2.
2. *The Hanle Effect and Level-Crossing Spectroscopy*, Edited by G. Morruzi and F. Strumia (Plenum Press, New York, London, 1991), 371 pp.
3. M. Auzinsh and R. Ferber, *Optical Polarization of Molecules* (Cambridge University Press, Cambridge, 1995), 306 pp.
4. A. Kastler, Quelques suggestion concenteant la production optique et la detection optique d'une inegelite de population des niveaux, J. Phys. Radium, **11,** p. 225 – 265, (1950).
5. Brossel, J., A. Kastler, and J. Winter, Optical method of creating an inequality of population between Zeeman sub-levels of atomic ground states. J. Phys. Radium, **13**, p. 668-669, (1952).
6. W.B. Hawkin, R.H. Dicke, The Polarization of Sodium Atoms, Phys. Rev., **91**, p. 1008 1009, (1953).
7. G. Alzetta, A. Gozzini, L. Moi, and G. Orrioli, An Experimental Method for the Observation of R.F. Transitions and Laser Bear Resonance in Oriented Na Vapour, Novo Cimento, **36**, p. 5 – 20, (1976).
8. E. Arimondo, Coherent population trapping in laser spectroscopy, Progr. Opt. **35**, p. 257 354, (1996).
9. U. Fano, Description of States in Quantum Mechanics by Density Matrix and Operator Techniques, Rev. Mod. Phys., **29**, p. 74 – 93, (1957).
10. C. Cohen-Tannoudji, Theorie quantique du cycle de pompage optique. Verification experimentale des nouveaux effets prevus (1-e partie), Ann. De Phys. **7**, p. 423 – 461, (1962); C. Cohen-Tannoudji, (2-e partie), Ann. De Phys. **7**, p. 469 – 504, (1962).
11. Ducloy, M., Nonlinear Effects in Optical Pumping of Atoms by a High-Intensity Multimode Gas Laser. Genaral Theory. Phys. Rev. A, **8** (4): p. 1844 – 1859, (1973).
12. Auzinsh, M.P. and R.S. Ferber, Optical-Pumping of Diatomic Molecules in the Electronic Ground State — Classical and Quantum Approaches. Phys. Rev. A, **43** (5): p. 2374 – 2386, (1991).
13. Auzinsh, M., The evolution and revival structure of angular momentum quantum wave packets. Canadian Journal of Physics, **77** (7): p. 491 – 503, (1999).
14. Rochester, S.M. and D. Budker, Atomic polarization visualized. Am. J. Phys., **69** (4): p. 450 – 454, (2001).
15. Auzinsh, M., Angular momenta dynamics in magnetic and electric field: Classical and quantum approach. Canadian Journal of Physics, **75** (12): p. 853-872, (1997).
16. R.N. Zare, *Angular momentum* (J. Wiley & sons, New York, 1988), 280 pp.
17. D.A. Varshalovich, A.N. Moskalev, V.K. Khersonskii, *Quantum theory of angular momenta* (World Scientific, Singapore, 1988), 514 pp.
18. D.A Case, G.M. McClelland, and D.R Herschbach, Angular Momentum Polarization in Molecular Collisions: Classical and quantum theory for measurements using resonance fluorescence, Mol. Phys., **35**, 541 – 573, (1978).
19. M. Born, E. Wolf, *Principles of Optics* (Pergamon Press, Oxford, London, Edinburgh, New York, Paris, Frankfurt, 1968), 566 pp.
20. B.W. Shore, *The Theory of Coherent Atomic Excitation*, (John Wiley & Sons, New York, Chichester, Brisbene, Toronto, Singapore, 1991), vol. 1 and vol. 2, 1735 pp.
21. Nasyrov, K.A., Wigner representation of rotational motion. J. Phys. A: Math. Gen., **32**, p. 6663 – 6678 (1999).
22. Klincare, I.P., M.Y. Tamanis, A.V. Stolyarov, M.P. Auzinsh, and R.S. Ferber, Alignment-Orientation Conversion by Quadratic Zeeman-Effect Analysis and Observation for Te_2, J. Chem. Phys., **99** (8): p. 5748 5753, (1993).
23. Auzinsh, M., A.V. Stolyarov, M. Tamanis, and R. Ferber, Magnetic field induced alignment - orientation conversion: Non-linear energy shift and predissociation in Te_2 B 1_u state, J. Chem. Phys., **105** p. 37 49 (1996).

24. Aquilanti, V., D. Ascenzi, M.d. Castro, Vitores, F. Pirani, and D. Cappelletti, A quantum mechanical view of molecular alignment and cooling in seeded supersonic expansions. J. Chem. Phys. **111** (6), p. 2620 - 2632, (1999).
25. Auzinsh, M.P. and R.S. Ferber, J-Selective Stark Orientation of Molecular Rotation in a Beam., Phys. Rev. Lett., **69** (24): p. 3463   3466, (1992).
26. Tamanis, M., M. Auzinsh, I. Klincare, O. Nikolayeva, A.V. Stolyarov, and R. Ferber, NaK D 1^{II} electric dipole moment measurement by Stark level crossing and e-f mixing spectroscopy., J. Chem. Phys. **106** (6), p. 2195   2204 (1997).

PHOTODISSOCIATION OF HYDROGEN HALIDES IN A CRYOGENIC RARE GAS ENVIRONMENT: A COMPLEX APPROACH TO SIMULATIONS OF CLUSTER EXPERIMENTS

PETR SLAVÍČEK AND PAVEL JUNGWIRTH

J. Heyrovský Institute of Physical Chemistry, Academy of Sciences of the Czech Republic and Center for Complex Molecular Systems and Biomolecules, Dolejškova 3, 18223 Prague 8, Czech Republic

Abstract. Simulation of the photodissociation experiment performed in a large neutral cryogenic clusters is described in this chapter. The emphasize is put on the methodological aspects of the simulations, namely on the correct preparation of the initial state. Possible control of photodissociation process is discussed. The good agreement between theory and experiment not only indicates the quantitative predictive power of the calculations, but also confirms that the experimental concepts and analysis of cluster production in supersonic beams are quite reliable.

1. Introduction

Photodissociation of small molecules in different cluster environments has attracted much attention in recent years. The reason is the possibility to explore physical properties as a function of a cluster size. One can thus address the question of the onset of surface and bulk solvation. Moreover, for molecular cluster certain quantities such as the kinetic energy distribution of the photodissociated fragments are experimentally available and direct comparison with theoretical calculations is feasible. Hydrogen halide molecules interacting with different rare gas clusters have served as a prototypal systems for such investigations using different levels of theoretical treatment [1, 8, 22, 23, 24, 25, 28, 29, 31, 32, 36, 37, 41, 45, 46]. Photodissociation in a cryogenic rare gas environment have several appealing features from the theoretical point of view. First, rare gas atoms serve as simplest, structureless solvents. Rare gas atoms exhibit only elementary features of solvation. Basically, the only important solute-solvent interaction is the repulsion between the photodissociation fragments and the rare gas atoms. Second, under cryogenic conditions the system is usually prepared in a well defined state. We can thus avoid complications connected with averaging over thermodynamical distributions. On

the other hand, nuclear quantum effects such as the zero point energy motion can play a crucial role.

Recently, a lot of new experimental results in supersonic beams have been produced in this field [8]. The basic setup of a cluster experiment is following. First, the clusters are prepared in a supersonic beam. Second, the clusters are photodissociated by a polarized laser beam, and, third the photodissociated fragments are ionized and detected by techniques of mass spectrometry.

The experimental setup has its counterpart in the theoretical methodology. First, the doped cluster has to be prepared. In theory this means to construct the multidimensional potential energy surface for the interaction of particles in the ground state (even simple systems like Lennard-Jones clusters can form surprisingly rich energy landscapes). The potential energy surface of the $HX-Rg_n$ system can be constructed from the known interactions between cluster fragments. If these are not available, it is required to calculate them by means of *ab initio* quantum chemistry methods. The cluster is prepared under cryogenic conditions and quantum vibrational and rotational effects can thus be of a vital importance. The initial ground state wavefunction of the system is constructed. Since we deal with large systems, usually approximations are applied. The experiment is, however, not performed at T = 0 K, therefore, we have to ask what is the role of entropic effects on the initial state of the doped cluster. The thermodynamical averaging via a certain simulation tool, e.g., molecular dynamics, is thus performed.

The second experimental step is photodissociation. From a theoretical point of view this means (i) changing the potential energy surface of the system and (ii) time evolution of the system. As for the ground state, also after the photoexcitation the potential energy surface has to be constructed from known or calculated interactions between cluster fragments. In the excited state, open shell systems occur. A simple and elegant method for the construction of the potential energy surface of large systems containing an open shell particle is the Diatomics-in-Molecules approach. Then, an appropriate method has to be chosen for the dynamics. Fully quantum description of the dynamics is not computationally feasible and certain approximations have to be adopted. Approximations can basically go in two directions. The first one is to connect the quantum dynamics with its classical counterpart. The second option is the factorization of the problem. The actual choice depends not only on the system under study but also on the type of questions we raise. A certain level of treatment is used when the dominant quantum effect is the change in the energetics, while a different approach is used if interference and coherence effects are of interest.

The third step in the experiment is detection. On the simulation side this is equal to visualizing the results. A time evolution of the calculated wavefunction (or a swarm of classical trajectories) has to be translated into a physically meaningful pictorial representation. Finally, at this stage we should link our simulations with the measurements. This means to find measurable quantities which can be compared with the experiment. We can calculate quantities both in the time and

in the energy domain. Both can be in principial reached experimentally.

In this chapter we concentrate namely on the methodological aspects of the simulations of photodissociation process in large clusters. The aim is, however, not only to describe the process but also to address the question about how to actively influence the process, i.e., how to control photodissociation by employing weak forces, external fields or an IR laser pulse.

The organization of this chapter follows the above mentioned division: in section 2 we discus the theoretical tools for initial state description, section 3 describes the methodology of photodissociation simulations in extended systems, in section 4 we describe the analysis of experimental results and in section 5 we discuss the possible control of photodissociation process.

2. Preparation of clusters

As is further stressed in section 5, the initial state of the cluster, i.e., the state prior to the photodissociation is of a fundamental importance for the subsequent photodissociation dynamics. The determination of the initial cluster structure consists of three steps: first we find the optimized structure, i.e., the minimum on the potential energy surface of the ground state. In a second step, we calculate the ground state vibrational wavefunction. This second step can qualitatively change the initial structure. The final step is to explore what is the distribution of isomers at a thermodynamic equilibrium corresponding to experimental temperature. Even though this temperature is quite low, its non-zero value may play a significant role for weakly bound clusters.

2.1. OPTIMAL STRUCTURES

For finding optimal classical structures it is first required to construct reliable potential energy surface for the system in the ground state. Usually, several approximations are employed. First, we neglect three body interactions within rare gas atoms, and second we assume that the interaction between the hydrogen halide and the rare gas atom is within a certain range independent of the HX bond distance. The latter approximation is not necessarily always justified [9]. With these approximations we can write the PES of a HX-Rg$_n$ cluster as a following sum

$$V(HX - Rg_n) = \sum_{i=1,n} V_{HX-Rg} + \sum_{i=1,n} \sum_{j=i,n} V_{Rg-Rg} + V(HX), \qquad (1)$$

where V_{HX-Rg} is a three body term for the interaction between a rare gas atom and a hydrogen halide molecule with a fixed bond length, V_{Rg-Rg} is a pair rare gas-rare gas potential and $V(HX)$ is a potential of HX in the $^1\Sigma$ state. The expression 1 has been found to provide good estimates of structural properties of larger HX-Rg$_n$ clusters [3].

To find the classical structure of a molecular cluster basically means a minimization of the potential energy function 1. Since we treat systems with as many as
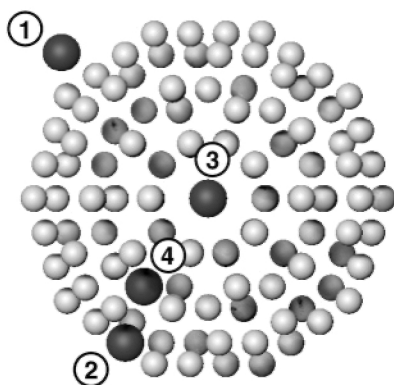
Figure 1. Possible positions of the HX dopant in or on the surface of large rare gas cluster. 1. Smooth adsorption, 2. Incorporation in the surface, 3. Central solvation, 4. Subsurface solvation.

300 particles, this task is generally very difficult to perform. We have performed the optimization in two steps: in the first one we have obtained the optimized structure of the impurity free rare gas cluster. Then we have chosen a position where the dopant is placed and we have locally re-optimized the structure.

Once we have a structure of the rare gas cluster, we have to decide into which position the dopant is placed. On Fig. 1 all the possibilities are described. The dopant may occupy a smooth adsorption site, i.e., it can stay on the surface of the cluster, interacting thus basically only with three nearest neighbors (1). Other position is the substitutional surface place, in which the dopant replaces one of the rare gas atoms from the most outer shell (2). The cluster can replace the central argon atom of the cluster (3), or can be placed also in the subsurface substitutional place (4). After adding the dopant, a local optimization is performed. The choice of the dopant position should reflect the way the cluster is prepared, either by a pick-up procedure or by co-expansion. Under experimental conditions we may expect both the surface and the embedded isomers to be kinetically stable even though the global minimum can be energetically well bellow the second isomer. This turns out to be the case of argon clusters. For the weakly bound neon clusters, however, one has to be cautious. At the experimental temperature the dopant can be distributed over several positions.

2.2. INITIAL VIBRATIONAL WAVEFUNCTION OF LARGE CLUSTERS: SEPARABLE APPROACH AND DIFFUSION MONTE CARLO METHOD

The quantum delocalization of the particles has two consequences for the photodissociation experiment. First, the smearing of the initial state changes the sampling statistics during the photodissociation. This is especially important for the HX librational motion. This motion has a highly delocalized character (e.g., the dopant

inside the cluster cage the HX behaves almost as a free rotor). Starting the dynamical calculations from the minimum of the potential energy surface has then little physical justification. We discuss in more detail this issue in the next chapter. Another consequence of the quantum delocalization is that one is forced to rethink the concept of structure in certain molecular clusters.

For a correct description of the cluster state at a temperature T=0 K it is, therefore, inevitable to treat the effect of quantum delocalization. Technically, this means to solve the N-dimensional vibrational Schrödinger equation. One can calculate the ground state wavefunctions for systems of interest either exactly (for small systems) or by dividing the system degrees of freedom into several groups and treating them separately. Finally, one can calculate the exact N-dimensional ground state wavefunction by mean of the stochastic Diffusion Monte Carlo method. This method can not, however, be directly used as a starting point for the subsequent quasi-classical molecular dynamics simulations, and it is also not straightforward to extend this method for excited states calculations. In following paragraphs, we briefly describe the employed methodology of the vibrational calculations. Generally, we aim to solve the stationary Schrödinger equation with Hamiltonian

$$\hat{H}_I = \sum_{i=1,n} \hat{T}_{Ar,i} + \hat{T}_X + \hat{T}_H + V_{GS}(HX - Rg_n). \qquad (2)$$

Here $\hat{T}$ stands for the kinetic energy operator and $V_{GS}(HX - Rg_n)$ is the potential energy surface in the ground state. The first approximation which we introduce is a separation of the fast HX vibrational (stretching) motion from all other degrees of freedom. The HX distance is thus held constant during the calculations.

So far, we have only separated out the HX vibrational motion. Generally, such a solution of the stationary Schrödinger equation is not computationally feasible for clusters with more atoms. Therefore, other approximations have to be employed. At the same time, all phenomena important for the cluster structure have to be properly included. We have performed an adiabatic separation of the HX librational motion from the motion of the heavy particles, i.e., from the cage modes. Moreover, the cage modes have been calculated within the harmonic approach, i.e., by a diagonalization of the Hessian matrix. Formally, the wavefunction is expressed as

$$\Psi(\rho, q_1, q_2, ..., q_{3n-6}, \Theta, \Phi) = \frac{\chi(\rho)}{\rho} \phi_1(q_1)....\phi_{3n-6}(q_{3n-6}) \phi_{lib}(\Theta, \Phi, \{q_i\}), \qquad (3)$$

where q_i are the normal coordinates of cage (i.e., heavy atoms), and ρ is the H-X separation. The factor $1/\rho$ comes from the use of spherical coordinates. As has been already said, the cage modes are taken into account within the harmonic approximation, while the librational wavefunction of the HX molecule $\phi_{lib}(\Theta, \Phi)$

is calculated by a diagonalization of the HX (hindered) rotational Hamiltonian in the basis of spherical harmonics

$$\hat{H}_{rot} = \frac{\hbar^2}{2\mu_2 r^2}\hat{j}^2 + V(\Theta, \Phi, \{q_i\}). \tag{4}$$

The term connected with the overall rotation of the cluster is neglected since $\mu_1 R^2$ is much larger than $\mu_2 r^2$. Due to the loss of cylindrical symmetry the potential V becomes also Φ–dependent. Both the potential for the hindered rotation of HX and the librational wavefunctions are parametrically dependent on the cage coordinates.

   This approach is satisfactory for systems, where the minima corresponding to HX–Rg$_n$ and XH–Rg$_n$ structures are well separated or correspond to similar heavy atom geometries and, therefore, we can separate the librational and cage modes. The energy gap between minima corresponding to possible isomeric structures is increasing with the number of rare gas atoms. Thus, the coupling between vibration and internal rotation does not usually have a strong effect on the ground state structure of the explored complexes (Ar$\cdots$HI and Ne$\cdots$HI), however, it can seriously influence the bound states. Another concern is connected with the role of cage anharmonicity.

   Principally exact solution of the vibrational Schrödinger equation can be found by applying the Diffusion Monte Carlo (DMC) method [40], where the accuracy for ground state calculations is limited only by the statistical noise, which can be reduced to a desired level by a sufficient investment of computer time.

   We demonstrate the importance of proper description of initial vibrational wavefunction on the case of small HI(Ar)$_n$ complexes [36]. For the correct description of HX-Rg$_n$ photodissociation dynamics the HX librational wavefunction ϕ_{lib} is the key component of the vibrational wavefunction. If the hydrogen halide molecule is embedded in the cluster, we observe an almost free rotation of HI. This is a consequence of the high symmetry of this solvation site and the short range character of the van der Waals forces. On the other hand, the HI molecule on the surface of an argon cluster is strongly oriented. This is caused by the asymmetry of the surface site. To properly describe the orientation of the HI molecule on the surface of an argon cluster is not trivial. The interaction potential between HI and argon manifests two collinear minima. The lower minimum corresponds to the H-I...Ar arrangement while the secondary minimum has a hydrogen atom pointing towards the argon atom (I-H...Ar). The first minimum is energetically preferred by approximately 50 cm^{-1}. After accounting for zero point motions, the ground state energies D_0 differs, however, by only 8 cm^{-1}. For the HI-Ar system the hydrogen wavefunction is oriented away from the argon atom. If this would be also the case for larger argon clusters, then no caging can be observed for the surface isomer. With the use of reduced dimensionality vibrational calculations we found a flip of the librational wavefunction when going from HI-Ar$_2$ to HI-Ar$_3$ cluster, then a

back-flip for HI-Ar$_4$ (with librational wavefunction pointing outside of the cluster once again). Starting from HI-Ar$_5$ all larger clusters are characterized by hydrogen pointing towards the argon cluster. It is important to emphasize that quantum delocalization (i.e., the zero point energy) plays a major role in the determination of the cluster structure.

Since quantum effects are so important in this case, we have decided to recalculate the ground state wavefunctions for these clusters with the use of Diffusion Monte Carlo Method. A composite Fig. 2 depicts the square of the wavefunction as a function of cosΘ, where Θ is the angle between the HI molecular axis and the vector connecting the argon cluster center of mass with the HI center of mass. The librational wavefunction corresponds to hydrogen pointing away from the rare gas atoms for HI-Ar and HI-Ar$_2$ clusters. Starting from the HI-Ar$_3$ cluster, hydrogen is oriented towards the argon cluster. Unlike the reduced dimensionality calculations, the change is gradual and there is still some wavefunction component with the hydrogen atom pointing outside of the cluster for the HI-Ar$_3$ cluster. No back-flip at HI-Ar$_4$ is observed. We conclude that the general trend of the change of the hydrogen orientation has been confirmed by the DMC calculations, while the back-flip has been found to be an artefact of the previous approximate vibrational calculations. The implications of the size evolution of the librational wavefunction on the photodissociation dynamics are obvious. It suggests that no cage effect should be observed upon photodissociating the HI-Ar complex. Indeed, no low energy signal in the KED spectrum has been observed for this system [4], while for a similar Ar-HBr cluster a weak single atom cage effect has been observed [33]. On the other hand, the cage effect for larger cluster should be pronounced and this is exactly what has been measured and calculated [35].

One of the goals is to use the results of DMC simulations for subsequent quasi-classical studies of photodissociation process. For this purpose, one needs to have a swarm of walkers sampling the square of the wavefunction (or even better a set of walkers in the classical phase space sampling the Wigner distribution). We have reached this goal by the descendant weighting method [6]. DMC sampling of the Wigner distribution is still difficult due to the oscillatory character of the integrand and the problem is still open. Recently, there has been an attempt to overcome the difficulties by approximative separating of the momentum and coordinate space probability distributions, which are evaluated by the DMC wavefunction [5]. This approach, however, is not universal.

2.3. SIMULATION OF PICK-UP PROCEDURE AND PHASE BEHAVIOR ANALYSIS

Mixed molecular clusters can be prepared by two different techniques: (i) by a co-expansion, where a mixture of the dopant with a rare gas is expanded into the vacuum, or (ii) by a pick-up procedure, in which case the neat rare gas clusters prepared by a supersonic expansion travel through a chamber with a dopant and a buffer gas. For solid systems one is thus able to prepare clusters with the dopants
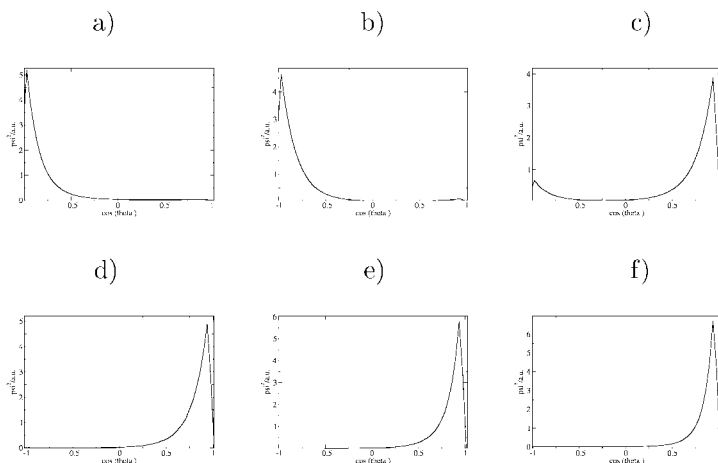
Figure 2. Size dependence of the DMC calculated ground vibrational (librational) wavefunction for HI on Ar_n ($n = 1 - 6$, corresponding with labels a) to f)). Wavefunction is depicted as a function of $\cos \Theta$ where Θ is the angle between the cluster center of mass and the center of mass of the dopant. Note the flip of the H wavefunction towards the rare gas clusters upon increasing cluster size seen for the calculations in reduced dimensionality is no more observed.

in different positions in or on the cluster according to the way of preparation. However, for ergodic systems (e.g., for liquids) the final dopant sites are simply given by the equilibrium thermodynamical distributions, and they are thus independent of the cluster preparation. The question concerning the degree of ergodicity is interesting particularly in the case of pick-up procedure. The dopant can significantly increase the temperature in this case and even liquidify an originally solid cluster. Molecular dynamics simulation can help in answering the question what is the distribution of positions under experimental conditions corresponding to the pick-up process. Classical molecular dynamics has a limited validity for neon clusters with intermediate quantum effects. Indeed, these quantum effects influence the binding energy per particle (the ground state binding energy is only about 60% of the well depth for a neon dimer) and the mean particle distances and will foreseeably have an important effect on the dopant embedding dynamics, the dopant mobility inside the cluster, and the number of neon atoms evaporating after an impact. For description of these clusters, dynamical methods accounting for at least the principal quantum effects have to be used.

Molecular dynamics is an appropriate tool for the study of the pick-up procedure. It is imperative to perform dynamical (and not thermodynamical) simulation because (i) we do not know in forward the final temperature of the system and (ii) for non-ergodic systems the final distribution can represent just a local minimum on the free energy surface of the system, i.e., a metastable state with a high ki-

netical stability. Thus, equilibrium techniques such as Path Integral Monte Carlo (PIMC) can not be used. Full quantum dynamical simulation of dynamic properties of neon clusters at finite temperature is impossible with present computational techniques. Thus we now face a question how to simulate the quantum systems using essentially classical equations of motion.

We have resorted to an approximate technique which attempts to include the above mentioned main quantum effects via the construction of effective potentials V_q. Basically, each particle is represented by a single particle wavefunction and the Ehrenfest theorem is applied. Similar ideas have been used with good success even for quantum solids like hydrogen [38]. Effective quantum potentials are also among the results of the Feynman-Hibbs treatment [12] which have been applied to pure neon clusters in the past [34].

While it is possible to construct quantum effective potentials for bulk systems by fitting particle binding energies, bulk densities, and pair correlation functions, our strategy for the construction of the effective quantum potential for clusters avoids the use of empirical information. We use a self consistent iterative procedure, which has been applied previously with surprising success to pure and doped helium clusters [30]. This method is particularly suitable for clusters where empirical density and pair correlation information are unavailable. Conceptually, each particle is replaced by a probability distribution $\phi^2(r)$, centered around its classical position, and assumed to have a spherical symmetry. Starting from the original pair potential $V_{cl}(R) = V_{q,0}(R)$, a delta distribution $\phi_0^2(r)$, and known masses the construction is based on the following sequence of calculations, which is repeated until the n-th order potential and distributions have reached self consistency

1. Construction of the pair correlation function $P_n(R)$ between classical particle positions from a classical molecular dynamics simulation at temperature T with the current potential $V_{q;n}(R)$.
2. Convolution of the pair correlation function with the current single particle distribution $\phi_n^2(s)$ according to

$$P_{q;n}(|\mathbf{R}|) = \int P_n(|\mathbf{R}|)\phi_n^2(|\mathbf{R} - \mathbf{R}'|)d\mathbf{R}'. \tag{5}$$

3. Construction of the radial potential $V_{rad;n}(r)$ experienced by each particle in the 'cage' formed by the others by integration over the current pair potential and the particle distribution following

$$V_{rad;n}(|\mathbf{r}|) = \int V_{cl}(|\mathbf{r} - \mathbf{R}|)P_{q;n}(|\mathbf{R}|)d\mathbf{R}. \tag{6}$$

4. Solution of the radial Schrödinger equation in the radial potential $V_{rad;n}(r)$ in order to find $\phi_{n+1}(r)$ for each particle in the mean field of the others.
5. Construction of the next generation effective pair potential $V_{q;n+1}(R)$ by the convolution

$$V_{q;n+1}(R) = \int\int V_{cl}(|\mathbf{R} + \mathbf{r} - \mathbf{r}'|)\phi_{n+1}^2(|\mathbf{r}|)\phi_{n+1}^2(|\mathbf{r}'|)d\mathbf{r}d\mathbf{r}'. \tag{7}$$
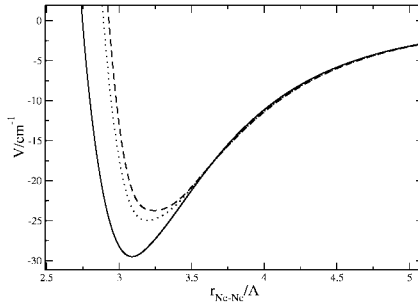
Figure 3.   Convergence of the Ne-Ne effective quantum potential during its iteration.

    The algorithm was described for a construction of an effective potential for the Ne-Ne interaction. Analogically, one can construct the potential for a Ne-dopant interaction. All radial and pair potentials are computed on a grid and spline interpolated for the molecular dynamics simulations and for the solution of the Schrödinger equation. The number of iterations required to reach self consistency is modest. On Fig. 3 the convergence of the effective potential is shown. The figure depicts the classical potential, the first iteration and the 10th iteration which is fully converged. Actually, only 4 iterations are required for a fully converged effective quantum potential in this case. The 'broadening' of each particle described by ϕ_n tends to fill in the potential well and leads to a shift to larger mean particle distances clearly accounting qualitatively for the quantum zero point effects. The resulting potentials are clearly temperature dependent and could in principle be reconstructed periodically during a non equilibrium impact simulation. This would have sense if we were interested in the first stage of the pick-up process, i.e., in the collision. We address, however, a question what is the final dopant distribution, therefore, this recalculation of the effective quantum potential is not required. Note also that (unlike, e.g., the Feynman-Hibbs potential) our effective quantum potential is size dependent. This corresponds to a fact that smaller systems exhibit generally a stronger quantum character. Thus, this approach is well suited for the study of large moderately quantum clusters.

    Figure 4 displays the result of the HBr pick-up on a cluster with 130 neon atoms. The simulation can be visualized in two ways. On Fig. 4a the density of the dopant atom as a function of the distance from the center of mass of the cluster is depicted. For comparison also the density of neon atoms is added in the graph. The majority of the dopant atoms stays in the surface area of the cluster, i.e., in the third shell. There is also a peak in the very central position of the cluster. Note, however, that the depicted quantity is a density, which should be multiplied by a factor $4\pi r^2$ to obtain the number of dopant atoms. Thus, only
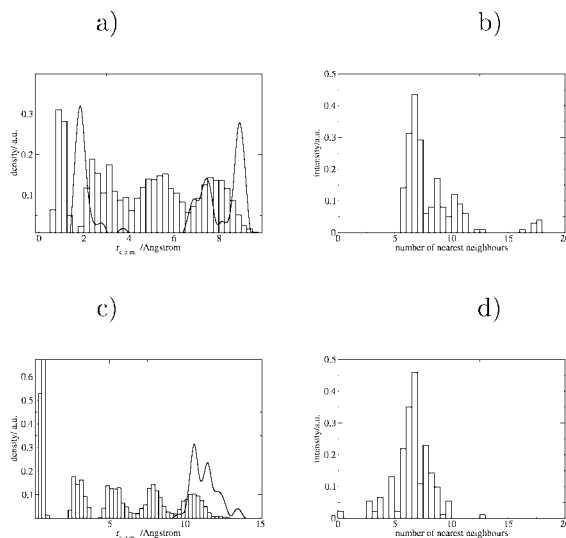
Figure 4. Pick-up of HBr on neon clusters. a) Density of dopant atoms (solid line) in comparison with the density of neon atoms (histogram) (Ne_{130}). b) Distribution of number of nearest neighbors to the dopant atom (Ne_{130}). c) Density of dopant atoms for the Ne_{300} case. d) Nearest neighbors for the Ne_{300} case.

some 7 % of the dopants land in the fully embedded positions. Most of the dopants stay deeply in the third shell, often on the border with a second shell. The Ne_{130} cluster is apparently of a semiliquid character after the impact of the dopant, enabling occasionally the dopant to come to the center. However, the position in the surface is preferred. Another way how to visualize the final solute distribution in the cluster is to display the number of neon atoms in the proximity of the dopant (i.e., closer than 4.3 Å) . The resulting distribution is displayed on Fig. 4b. Fully embedded dopants are those with the number of nearest neighbors larger than 15 (also some of the neon atoms from second solvation layers are occasionally counted). Most of the dopants are interacting with either 6 neon atoms or with around 10 neon atoms (this corresponds to the dopant position between the third and the second layers). There is no evidence for smooth adsorption of the HBr dopant on the neon clusters, in which case, one would expect the HBr molecule to directly interact only with approximately 3 neon atoms.

The situation for Ne_{300} cluster is different. Neon clusters with four solvation layers are much more stiff than clusters with tree layers. Moreover, quantum effects are less important for larger clusters since neon atoms are now more confined. As a result, none of the HBr dopants penetrates into the fully embedded position (corresponding densities for dopant and neon atoms are depicted in Fig. 4c). Most of the HBr particles stay deeply solvated in the outer, fourth neon layer. There is also a small portion (6 %) of dopants in the smooth adsorption position. This

amount is, however, too small to allow to decide whether it is only an artefact of a short duration of the pick-up simulation or whether the occupation of this position actually reflects a genuine thermodynamical distribution. Fig 4d shows the number of nearest neighbors of the HBr dopant for the same system. We can observe the typical feature of the surface solvation with 6-10 solvent atoms closer than 4.3 Å. This result indicates that the cluster is solid after the pick-up of the dopant and the part of the phase space with embedded dopant is virtually not accessible under the experimental conditions.

One of the important issues addressed in our simulations is the character of clusters under study. Are these clusters solid or liquid under experimental conditions? If they are liquid, then the distribution we observe in the pick-up and consequently in the photodissociation simulations corresponds to a statistical distribution at a given temperature. If, however, the cluster is solid then both in the simulations and in the experiment we observe a quasi-stationary state with a very long lifetime rather than an equilibrium thermodynamical state. This question can be resolved by means of the instantaneous normal modes (INM) density of states (DOS) spectrum. To calculate INM DOS we construct the Hessian matrix in a mass-weighted atomic Cartesian coordinate basis of N atoms $x_{n\mu}$ with $\mu=\{x,y,z\}$. The 3N eigenvectors in the form $c_{1x}, c_{1y}, c_{1z}, c_{2x}, c_{2y}, c_{2z}, ...c_{Nx}, c_{Ny}, c_{Nz}$ describe the contribution of each atom to the i-th mode. A quantity which is the basic output of the INM procedure is the density of states. This is nothing more than a histogram of frequencies averaged over an ensemble of configurations obtained by molecular simulation techniques:

$$\rho(\omega) = \left\langle \sum_{i=1}^{3N-6} \delta(\omega - \omega_i) \right\rangle. \tag{8}$$

We have omitted the six frequencies corresponding to rotational and translational motions of the whole cluster. One of the advantages of the INM analysis is that we can perform projections of the density of states. One can decompose the density of states spectrum, e.g., into molecular rotational and translational motion [39]. For molecular clusters it is interesting to explore the localization of the motion described by the Hessian eigenvectors at different frequencies. Even though the harmonic motion is inherently collective, certain motions can be attributed to a limited area. This is the case of non-homogeneous systems, where the spectral characteristics can be quite different for different spatial parts. We define a projector P_{area}

$$P_{area} = \sum_{n \in area} \sum_{\mu=x,y,z} c_{n\mu}^2, \tag{9}$$

where area can be, e.g., a certain cavity around a host molecule. The projected density of state is then given as:

$$\rho^{area}(\omega) = \left\langle \sum_{i=1}^{3N-6} P_{area}\delta(\omega - \omega_i) \right\rangle. \tag{10}$$

A critical issue is the sampling of instantaneous configurations for the INM analysis. We have sampled the instantaneous configurations via classical molecular dynamics run on effective quantum potentials (the same as we have used for simulating the pick-up procedure).

The typical INM DOS spectrum for a liquid differs significantly from that for a solid. A typical DOS spectrum of an atomic liquid consists of a right triangular pattern for the real frequencies distribution corresponding to translational atomic motion [39]. This shape is caused by a dominant presence of the slow, soft modes in liquids. Furthermore, a significant fraction of imaginary frequencies is present in liquids (imaginary modes are usually depicted for convenience on the negative axis of the DOS spectra). Imaginary frequencies dissappear in solid systems. Moreover, the right-triangular shape of the positive part of the spectrum disappears. The spectrum for an atomic bulk solid shows different spectral features, corresponding to longitudinal and transversal mode peaks. We can see the onset of these features in clusters. They become more important for larger clusters where the fraction of the interior neon atoms is larger. We calculated the INM DOS spectra for clusters of the same size as those in the pick-up simulations, i.e., with 130 neon atoms and with 300 neon atoms. We took the advantage of the projection technique to investigate the phase behavior of the neon atoms in different cluster layers.

Figure 5a depicts the INM DOS of Ne_{127} cluster at 10 K. The DOS of the interior part of the cluster has the imaginary frequencies strongly suppressed. However, there is still a certain fraction of them and we may conclude that a cluster of this size is a border line case, close to the phase transition. This is in agreement with previous experiments on the doped neon clusters [43]. Still, the core of the cluster is more solid than liquid. Moving closer to the surface of the cluster, the character of the density of states changes. Now, it is a typical spectrum for a liquid state with the right triangular shape in the real part of the spectrum and with a significant imaginary frequency contribution.

The INM DOS spectrum for the interior part of the Ne_{293} cluster (Fig. 5b) exhibits feature typical for a solid. Frequency distribution is shifted towards higher values and no imaginary frequencies are observed. This is basically true for all the layers except for the outermost one, which is apparently liquid. We may thus conclude that both clusters explored (Ne_{127} and Ne_{293}) have a solid core with a liquid surface. This enables the dopant to be deeply solvated in the surface. The character of the cluster, however, prevents the dopant to penetrate deeper into the inner layers. It is interesting to compare these cluster DOS with those calculated or measured for the bulk (phonon spectrum) [10, 21]. Clusters should represent "the bridge between the isolated molecule and the bulk". Typical bulk features are boson peaks observed in the phonon DOS. We can observe such a feature for the interior neon atoms. However, the convergence to the bulk limit is rather

a)   b)
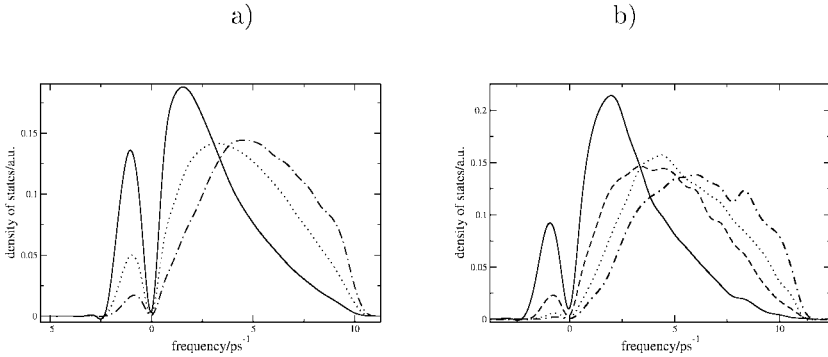
Figure 5. INM density of states of different layers in neon clusters. All density distributions are normalized. Imaginary frequencies are displayed on the negative part of the axis. a) Ne$_{130}$ cluster. Outer shell-solid line, medium layer-dotted line, inner part of the cluster-dashed-dotted line. b) Ne$_{300}$ cluster. Outer shell-solid line, third shell-dashed line, second layer-dotted line, inner part of the cluster-dashed-dotted line.

slow. This is not surprising if we assume that even for the largest cluster explored approximately one half of the neon atoms form the outer shell.

3. Photodissociation

Once the cluster is prepared in its initial state, described usually by the ground state wavefunction $\Psi_0(\vec{r})$, the exciting laser pulse is switched on. Let's assume for the moment that the laser pulse is infinitely short (we modify this assumption later). This simply means that the whole wavefunction is promoted into the excited state, i.e., the Hamiltonian has instantaneously changed from $\hat{H}_I$ into the excited state Hamiltonian $\hat{H}$. The wavefunction is then no more an eigenfunction of the Hamiltonian $\hat{H}$ and the system starts to evolve according to the time-dependent Schrödinger equation

$$i\hbar\frac{\partial\Psi(\vec{r},t)}{\partial t} = (\hat{T} + \hat{V}(\vec{r}))\Psi(\vec{r},t). \tag{11}$$

If we neglect the spatial dependence of the transition dipole moment, the initial condition for the eq. 11 is

$$\Psi(\vec{r},0) = \Psi_0(\vec{r}). \tag{12}$$

We now face the task to numerically solve equation 11 and to analyze the final wavefunction. Note at this moment that the vector $\vec{r}$ has a dimension $3N$ (N is number of particles). Although there are efficient numerical algorithms for propagating the time-dependent Schrödinger equation both on a grid or in a suitable

basis [20], these can hardly be used for systems exceeding several particles. Therefore, we have to choose an approximative way of the solution of the eq.11.

We have to assess how strongly quantum mechanical the system is. According to the de Broglie wavelength, hydrogen seems to be a good candidate for the strongly quantum part of the system. This is certainly true in the ground state where the energy is small. In the excited state, however, energy of several electronvolts is pumped into the system. Due to this high excess energy the hydrogen atom starts to behave almost classically. For obtaining most of the relevant physical information and insight it is required to describe the initial wavefunction in a fully quantum way, while the subsequent dynamics can be treated classically. Practically, this is performed via the so called *Wigner trajectories* method, which is described in the next section. Finding a connection between quantum and classical mechanics represents one direction of the approximate solution of eq. 11. Wigner trajectories are the crudest example of these techniques. With this method we loose all effects connected with the interferences, e.g., tunneling To account for these phenomena, we can use approximative quantum methods exploiting the separability of the wavefunction or semiclassical methods from the WKB family.

3.1. CONSTRUCTION OF POTENTIAL ENERGY SURFACE

The interaction potential in excited states of the HX-Rg_n clusters has been divided into a non-pairwise $X \cdots Rg_n$ component and the remaining pairwise additive interactions

$$V^\alpha = V_{HX}^\alpha + V(X \cdots Rg) + \sum_{i=1,n} V(Rg \cdots H) + \sum_{i=1,n} \sum_{j=i,n} V_{Rg-Rg}, \qquad (13)$$

where the index α denotes the particular HX excited state ($^1\Pi$, $^3\Sigma$ and $^3\Pi$). The interaction potential of the rare gas dimer has been assumed to be the same as in the case of the ground state. The interaction between the rare gas atom and the hydrogen atom has been calculated by *ab initio* methods (see later in this section).

The interaction between an open shell atom with a closed shell atom or molecule can be modeled with the Diatomics-in-Molecule (DIM) method [11]. This is an approximate approach, however, with a sound chemical motivation. The total interaction energy between an open shell atom and all the remaining closed shell atoms in the cluster can be expressed in a pair additive way as $V_{DIM} = \sum_{i=1,n} U_i^{DIM}(\vec{r_i})$, where $\vec{r_i}$ is the radius vector between the i-th rare gas atom and the p-atom (open shell atom) and U_i^{DIM} is the interaction energy between a single rare gas atom and the open shell atom. The U_i^{DIM} term is expanded in Legendre polynomials, with only two terms contributing $U_i^{DIM}(r_i, \gamma_i) = V_0(r_i) + V_2(r_i)P_2(\cos \gamma_i)$ The potentials are then obtained by a diagonalization of V_{DIM} in a suitable electronic basis (p_x, p_y, p_z functions).

3.2. QUANTUM DYNAMICS OF LARGE CLUSTERS: REDUCED DIMENSIONALITY AND SEMICLASSICAL APPROACH

The time dependent quantum dynamical method based on the assumption of separability is so called TDSCF approach (also called the Time-Dependent Hartree method) [13]. The goal is to find using the time-dependent variational principle the best single particle separable representation of the multidimensional time-dependent wavefunction. Thus, we star with expressing the total wavefunction as $\Psi(q_1, ..., q_N, t) = \prod_{j=1}^{N} \phi_j(q_j, t)$, where the multiplication runs over all modes. For the description of photodissociation process we have widely used an extension of TDSCF method called the Classical Separable Potential method, in which the effective potentials in the one dimension Schrödiger equation are evaluated using classical trajectories [17]. Note that both for the TDSCF and CSP method the configuration interaction extension is possible, although the convergence is very slow. Other approximative methods are based on the use of gaussians or on the path integral formalism of quantum mechanics [18].

3.3. CLASSICAL DYNAMICS: WIGNER TRAJECTORIES APPROACH

The method of Wigner trajectories is essentially a purely classical dynamics with a set of initial conditions given by an initial wavefunction. Thus, the only issue in this method is how to properly map the initial wavefunction onto a classical phase space. The coordinate distribution is in quantum mechanics given by a square of the modulus of the wavefunction $|\Psi((\vec{r}))|^2$, analogically we can get the distribution in the momentum space. Due to the Heisenberg uncertainty relations it is impossible to specify *uniquely* coordinates *and* momenta at the same time. This is a principial issue with no analogue in classical mechanics. There are plenty of quantum phase-space distributions and some of them look *almost* like the classical phase-space distribution functions. This problem is more serious for photodissociation than for the collisional processes: the motion in the excited state begins at short distances, in an area where the interaction between modes is the strongest. A small change in the initial conditions may cause a huge change in the final distribution.

The distribution which is most widely used is the so called Wigner distribution function [15]. It is defined as

$$W(\vec{q}, \vec{p}) = \frac{1}{\pi\hbar} \int d\eta \Psi^*(\vec{q} + \frac{\vec{\eta}}{2}) \Psi(\vec{q} - \frac{\vec{\eta}}{2}) e^{\frac{\vec{\eta} \cdot \vec{p}}{\hbar}}, \tag{14}$$

where $\vec{q}$ and $\vec{p}$ are coordinates and conjugated momenta. The Wigner function has many appealing features which suggest it as a good candidate for a classical phase-space representation of the wavefunction. Most importantly, the time evolution equations for the Wigner function collapse to classical Hamilton equations in the limit $\hbar \to 0$ [15]. The price is that the Wigner distribution function is not necessarily always positive.

We have taken the initial coordinates and momenta for the swarm of trajectories from the Wigner distribution. It can be easily proven that for a separable wavefunction the Wigner function can be written in a product form. As a basis for photodissociation calculations we have used a wavefunction in the form 3, therefore, the corresponding Wigner distribution is given by an expression

$$P(q_1, ..., q_{3N-6}, \rho, \phi, \theta, p_1, ..., p_{3N-6}, p_\rho, J_z, p_z\rho) \propto \qquad (15)$$
$$e^{-\omega_1(q_1{}^2 + p_1{}^2)}...e^{-\omega_{3N-6}(q_{3N-6}{}^2 + p_{3N-6}{}^2)} \frac{P^{HX,vib}(\rho, p_\rho)}{\rho^2} P^{HX,rot}(\phi, \theta, J_z, p_z\rho).$$

Here, p_i is the momentum coordinate of a cage mode i, p_ρ is the momentum in the HX vibrational coordinate, J_z and $p_z\rho$ are conjugated momenta to the polar angles ϕ and θ, respectively. J_z is the projection of the total angular momentum onto the z-axis and $p_z\rho$ is the momentum in the z-axis multiplied by the radius. $P^{HX,vib}$ and $P^{HX,rot}$ are the Wigner quasi-probabilities for the degrees of freedom of the HCl molecule.

Once the initial coordinates, momenta, and weights are generated, a swarm of classical trajectories is propagated by numerically solving the Newton equations of motion [26] in a standard way [2]. Typically, several hundreds trajectories are required for converged results.

If we impose an assumption that the chromophore molecule is excited by an ultrashort laser, then the pulse covers all the frequencies. Consequently, the whole initial wavefunction is promoted to the excited state. In the experiment, however, a cw laser with a fixed wavelength is usually used. Within the Wigner trajectories approach we have, therefore, to filter the Wigner distribution function in such a way that the energetic relation

$$\hbar\omega = E^e_{Rg-HX} - E^g_{Rg-HX} \qquad (16)$$

is fulfilled. Here, $\hbar\omega$ is the energy of the exciting photon, E^g_{Rg-HX} and E^e_{Rg-HX} are the interaction energies between argons and HX in the ground and in the excited states. Note that quantum dynamics simulation of photodissociation process with a cw laser field would require incorporating the laser field into a molecular Hamiltonian. The difference between a simulation with an ultrashort excitation time and that with a fixed wavelength can be rather pronounced, namely when the wavelength excites the blue or the red tail of the ground state wavefunction.

3.4. NON-ADIABATIC DYNAMICS

After the HX molecule is promoted into a specific electronic state, it evolves and can also relax back to the ground electronic state via a non-adiabatic transition. It has been referred [27] that non-adiabatic transitions can play an important role for large HCl-Ar_n systems. Within the DIM approach it is possible to construct not only the potential energy surfaces of the excited states but also non-adiabatic

couplings. Then the dynamics can proceed via a semiclassical surface hopping algorithm as proposed by Tully [42].

4. Analysis

4.1. QUANTITIES IN TIME AND ENERGY DOMAINS

The result of a molecular dynamics simulation is a time dependent wavefunction (quantum dynamics) or a swarm of trajectories in a phase space (classical dynamics). To analyze what are the processes taking the place during photodissociation one can directly look at these. This analysis is, however, impractical for systems with a high dimensionality. We can calculate either quantities in the time domain or in the energy domain. In the time domain survival probabilities can be measured by pump-probe experiments [44], in the energy domain the distribution of the hydrogen kinetic energy can be experimentally obtained [8].

In the case of our systems it is in principal possible to measure the probability of hydrogen to stay in the cluster. In the molecular dynamics simulation the survival probability is calculated by integrating the square of the wavefunction over the cluster region $P(t) = \int_{\text{cluster}} |\Psi_f(\vec{r}, t)|^2 \, d\vec{r}$, where $\Psi_f(\vec{r}, t)$ is the time-dependent hydrogen wavepacket. In classical simulations we simply count at each the number of trajectories localized in the cluster region. The cluster region we define as a sphere to a radius corresponding with the cluster size.

In the energy domain, one can calculate the final distribution $P(E)$ of the kinetic energy of the hydrogen outgoing from the cluster (KED spectrum). While the calculation of this quantity within the classical framework is straightforward (simply we do a histogram of the final kinetic energies), the calculation of this quantity from wavepackets deserves a small remark. The KED spectrum is given as

$$\lim_{t \to \infty} P(E_{\text{kin}}, t) = \lim_{t \to \infty} \frac{1}{|\vec{k}|} \int \left| \left\langle \exp\left(i\vec{k}\vec{r}\right) |\Psi_f(\vec{r}, t)\right\rangle \right|^2 \sin(\theta_k) d\theta_k d\phi_k,$$

$$|\vec{k}|^2 = 2mE_{\text{kin}} \frac{1}{\hbar^2}, \tag{17}$$

where Ψ_f is hydrogen wavefunction moving on the excited surface, $\vec{k}$ is the momentum of hydrogen divided by the Planck constant, $\vec{r}$ is the coordinate of hydrogen, and m is the hydrogen mass. It can be shown that

$$\lim_{t \to \infty} P(E_{\text{kin}}, t) = \int_{-\infty}^{\infty} , \langle \Psi(\vec{r}, t = 0) | \Psi(\vec{r}, t) \rangle \exp\left(\frac{i}{\hbar} E_{\text{kin}} t\right) dt, \tag{18}$$

which is actually nothing else than a Fourier transform of an autocorrelation function. This prescription is (except of the prefactor) identical with that for absorption

or emission spectrum [14]. The recurrences in the time domain correspond to resonances in the energy domain. These phenomena are not apparent in the classical framework.

4.2. SCATTERING OF HYDROGEN ATOMS FROM THE CAGE AND MIXING OF ELECTRONIC STATES

The direct comparison of calculations and experiment is more complicated for systems which are excited into more than one electronically excited state depending on laser polarization, e.g. in the case of HI where the system is excited to three states corresponding either with ground or excited spin orbit state I and I*. We define a branching fraction

$$\Gamma = \frac{[I*]}{[I] + [I*]}. \tag{19}$$

The measured kinetic energy distribution spectrum $P(E)$ is then actually a functional of the two dimensional kinetic energy distributions $P_g(E, \Theta_S)$ and $P_e(E, \Theta_S)$ (where index g denotes ground spin orbit state, e excited spin orbit state and Θ_S is a scattering angle of the photodissociated hydrogen). Without going into details [35], the measured KED spectrum is given as:

$$P(E) = \frac{1}{2}(1 - \Gamma) \int_0^{2\pi} \int_0^{\pi} \sin \Theta_E P_g(\Theta_D, E) \sin^2(\Theta_E) d\Theta_E d\phi_E$$
$$+ \Gamma \int_0^{2\pi} \int_0^{\pi} \sin \Theta_E P_e(\Theta_D, E) \cos^2(\Theta_E) d\Theta_E d\phi_E \tag{20}$$

where the angle Θ_D is related to the Θ_E depending on the laser polarization used.

Thus, we can obtain not only energetic information but by comparing the calculation with the experiment also an information on scattering characteristics of the photodissociated hydrogen atoms. Let us show this on an example of HI-Ar$_{147}$ cluster. Here we assume two dopant positions, either in the second (subsurface) shell, or in the surface shell. The overall KED integrated over all scattering angles are almost identical for these two cases. However, two-dimensional plots of $P_g(E, \Theta_S)$ and $P_e(E, \Theta_S)$ are completely different for these two isomers (see Fig. 6). After processing the two dimensional KEDs according to eq. 20, we can directly compare the calculations with the experiment. In Fig. 6e,f we can see that while we have a very good agreement for a surface isomer for both polarizations measured, this agreement is lost for the sub-surface isomer. This strongly suggests that the true position of the HI is in the surface substitutional position.
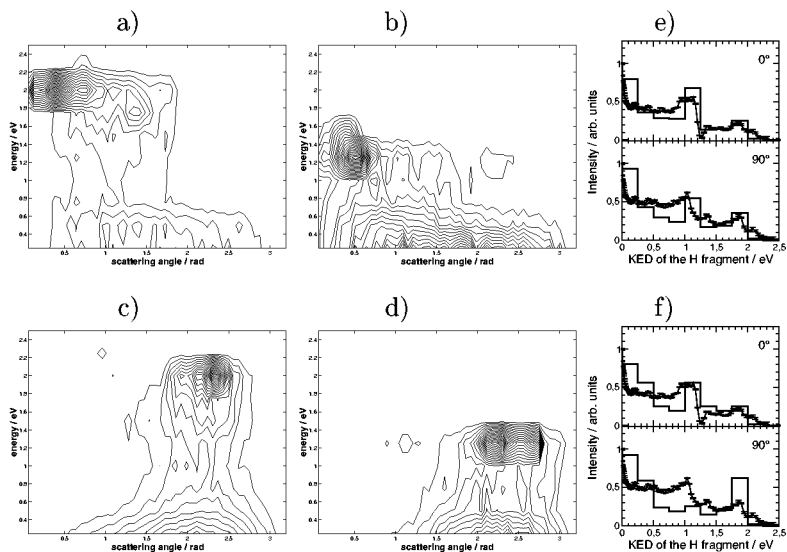
Figure 6.   Angular and kinetic energy distribution of the outgoing hydrogen atoms. Graphs a) and c) corresponds to the H + I exit channel, while b) and d) with the H + I* channel. In the case a) and b) the dopant is placed in the second shell, while in the case c) and d) the dopant is on the surface. e) Simulation of the photodissociation of the dopant on the surface (histogram) compared with a pick-up photodissociation experiment (line with error bars). f) Simulation of the photodissociation of the dopant in the sub-surface shell (histogram) compared with a pick-up photodissociation experiment (line with error bars).

5.   Simulation of experiment and control

5.1. SIZE AND SITE CONTROL

Size of the cluster as well as the position of the dopant can significantly change the character of the photodissociation. We show this effect on the example of the HBr-Ar$_n$ clusters. Fig. 7 depicts these survival probabilities for embedded (surface) isomers of different sizes initially in the ground rotational (librational) state of HBr. There is a dramatic difference in the decay of the hydrogen population in the cage between the two smaller and the larger clusters with embedded HBr. Figure 7a clearly shows that the first two solvation layers are quite inefficient in caging, which only becomes strong after the third argon layer starts to build up. The size dependence is much weaker for surface isomers where we see a continuous increase of the transient survival probabilities upon enlarging the cluster.

KED spectra for HBr(Ar)$_n$ clusters are depicted in Figs. 8. For each cluster size two KED spectra have been evaluated, corresponding to the embedded or surface isomer. The KED spectra for these two isomers differ significantly from each other at each size. Note, that caging is very inefficient for the embedded isomer of HBr(Ar)$_{12}$. As a result, high energy peaks at 1.3 and 0.9 eV, corresponding to

a)   b)
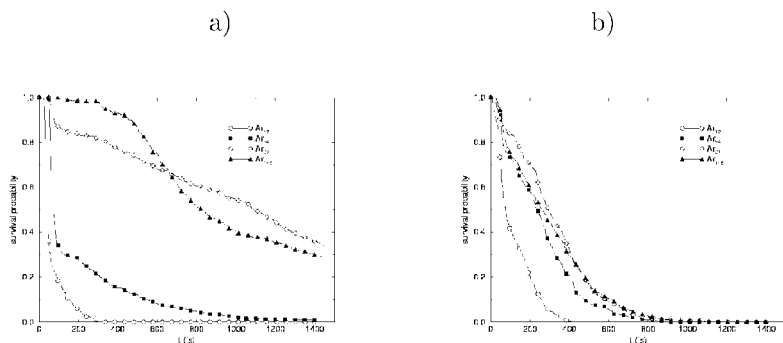
Figure 7. a)Transient probabilities of finding the photodissociating hydrogen inside the cluster for embedded HBr(Ar)$_n$ (n=12-146) isomers. b) Transient probabilities of finding the photodissociating hydrogen inside the cluster for embedded HBr(Ar)$_n$ (n=12-146) isomers.

directly exiting hydrogens for the Br and Br* channels, represent the main features in the KED. Upon adding more argon atoms, a peak at zero hydrogen velocity, which corresponds to efficient caging, starts to grow and finally dominates the spectrum. For large embedded isomers, we observe only a small component of fast hydrogen for the HBr(Ar)$_{97}$ (not shown here) cluster with a half-filled third solvation layer and zero intensity at high kinetic energies for the HBr(Ar)$_{146}$ cluster with three complete solvation layers. In contrast, the KEDs for surface isomers change only slightly upon increasing the cluster size from 12 to 146 argon atoms. Even for the smallest surface isomer under study, the HBr(Ar)$_{12}$ cluster, caging is efficient and, consequently, a significant signal at zero kinetic energy is observed. The results for the three larger surface isomers are very similar. The dominant signal appears at zero velocity, however, the fast hydrogen component does not vanish even for the largest cluster. Effectively, HBr deposited on the argon cluster surface is surrounded by more argon "solvation layers", than for the embedded isomer of the same size. On the other hand, some trajectories corresponding to tails of the librational wavefunctions do not penetrate into the argon cluster.

The experimental results depicted on Fig. 9 can be readily compared with simulations of HBr(Ar)$_{54}$ to HBr(Ar)$_{146}$ clusters depicted at Fig. 8. It is obvious that all the trends both for the embedded an for the surface isomers are well reproduced by the MD simulation. Namely that for a surface isomers, only a weak size dependence of the KED spectra is observed, while strong dependence on the cluster size is recorded for the embedded isomer. Note, that the experiment generates clusters with a certain size distribution and also that for smaller clusters there are rather pronounced error bars in the experiment. This can explain small differences between experiment and simulation in the sharpness of the peaks in the KED spectra, especially for the embedded case. Note also that in the case of

HBr-Ar$_{12}$
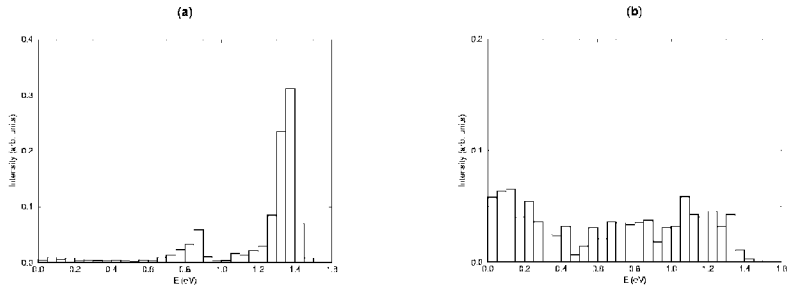
HBr-Ar$_{54}$
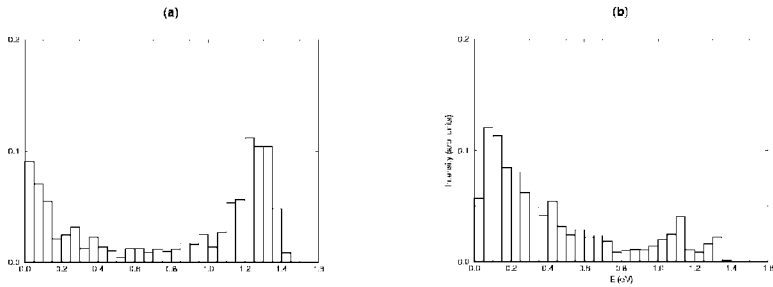
HBr-Ar$_{146}$
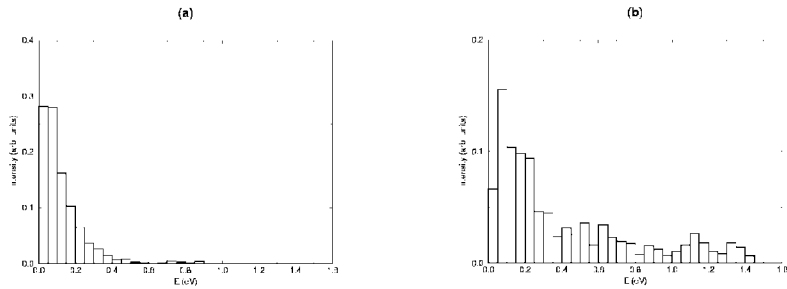
Figure 8.   Final kinetic energy distributions of the photolyzed hydrogen for the a) embedded and b) surface isomers of HBr(Ar)$_n$.

surface isomer also different clusters with different dopant positions can contribute and can enhance the fast component of the KED spectrum [7].
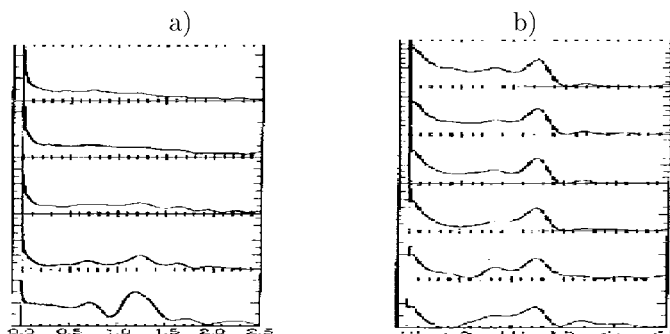
Figure 9. Experimental kinetic energy distributions of the photolyzed hydrogen for the a) embedded and b) surface isomers of HBr(Ar)$_n$ with a mean value of $\overline{n}$ changing gradually from 55 (lower graphs) to 139 (upper graphs).

5.2. LIBRATIONAL CONTROL

The control scheme of librational control [19] relies on the following scheme

$$AB + h\nu(IR) \longrightarrow AB(v > 0) \tag{21}$$
$$AB(v > 0) + h\nu(UV) \longrightarrow AB*$$
$$AB* \longrightarrow A(\alpha) + B(\beta),$$
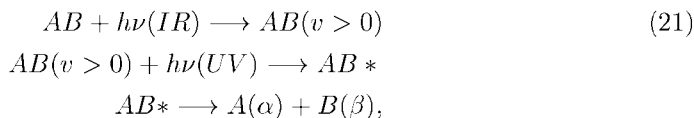
where $AB(v > 0)$ denotes the vibrationally excited AB molecule in its ground state and AB* is the electronically excited AB molecule. The initial wavefunction can have different spatial orientations and by choosing the proper vibrationally excited state we can determine the photodissociation results. This principle is demonstrated on the HCl-Ar$_n$ system [46].

In all clusters there exist low-lying excited librational states, where most of the hydrogen wavefunction is oriented away from the cluster or at least sidewise. This is demonstrated in Fig. 10 for the case of the HCl(Ar)$_{12}$ complex. For these excited librational states caging becomes inefficient since the photodissociating hydrogen minimizes the interaction with the argon cage. In other words, librational preexcitation can be used to "turn off" the cage effect for surface solvated hydrogen halides.

Among of the systems under study, clusters with three, five, six and twelve atoms possess higher symmetries having more than a twofold rotational axis. As a result doubly degenerate librational states occur in these complexes. In Fig. 10 one of the possible representations of these degenerate states in the HCl(Ar)$_{12}$ cluster is displayed, however, any linear combination of these functions is also valid. Three pronounced recurrences shown in Fig. 10 demonstrate repeated collisions of hydrogen with the cluster. The situation becomes dramatically different for photolysis started from the first non-degenerate librationally excited state. In this
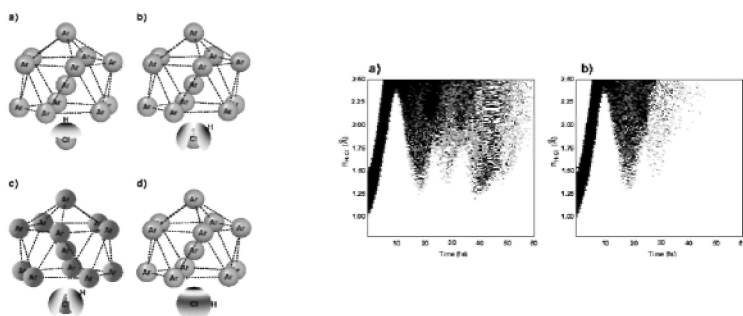
Figure 10.   a) Ground and b)-c) lowest excited librational wavefunctions of the HCl molecule deposited on clusters with twelve argon atoms. The shadowing represents the angular hydrogen probability and the wired spheres correspond to effective radii of the heavy atoms. Note the structures b) and c) corresponding to a degenerate pair of functions. For the sake of clarity, the radius of the hydrogen sphere is artificially expanded. In the right part, the quantum dynamics of the radial hydrogen wavepacket motion for HCl photolysis on the Ar_{12} cluster initiated from the a) ground, b) first non-degenerate excited librational state is represented.

state most of the initial hydrogen density is oriented sidewise with respect to the cage. As a results caging becomes very inefficient and, consequently only a single recurrence occurs during the dynamics.

From the point of view of measurable quantities, this is manifested in a following way. Fig. 11 shows the KED spectra for HCl photolysis on the Ar_{12} cluster, initiated either from the ground or from the first non-degenerate excited librational state. In the former case strong caging results in a well developed vibrational structure in the KED. This means that a significant part of the hydrogen wavefunction lives for nearly 100 fs in the cage and repeatedly returns to the Franck-Condon region. Clearly, the resonant structure is the strongest among the systems under study. It is even stronger than in the case of a rotationally cold photodissociating HCl molecule fully solvated in the Ar_{12} cluster. On the other hand, the structure in the KED disappears upon librational preexcitation, which orients most of the photodissociating hydrogen away from the argon cluster.

For the possible experimental realization of librational control it is important to take into account energy considerations. Our calculations show that the level spacing between the ground and lowest excited librational state amounts to 35-70 cm^{-1}. Thus, for efficient discrimination between the librational states the cluster temperature should not exceed few tens of Kelvins. This is realistic for the cluster sizes investigated here. For larger clusters, where higher temperatures might cause a problem, the technique of embedding in helium droplets, which leads to a very efficient cooling, could in principle be employed. Another point is which
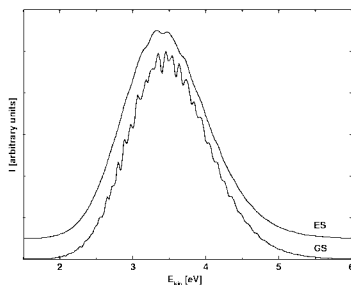
Figure 11. Kinetic energy distributions of hydrogen atoms produced from photolysis of HCl@Ar$_{12}$ started from the ground (GS) or first non-degenerate excited (ES) librational states of the HCl molecule. For clarity, the spectra are arbitrarily vertically shifted with respect to each other.

experimental observable should be used as a fingerprint of the librational control mechanism. Here, we suggest to monitor the disappearance of the resonant structure in the hydrogen KED upon librational preexcitation. The present setup corresponds to an ultrashort (therefore, energetically broad) exciting UV pulse. Another option is to use a longer (nanosecond) pulse with a frequency at the low energy tail of the hydrogen halide absorption band. Such an excitation produces a much less energetic hydrogen, which is more efficiently trapped in the argon cage. An observable consequence of librational preexcitation is then a disappearing low energy part of the KED, corresponding to caged hydrogens.

5.3. EXTERNAL ELECTRIC FIELD

The librational wavefunction delocalization can be efficiently controlled by a direct current electric field [16]. The dipole moment of the HX molecule is coupled to the external electric field by a factor $-\vec{\mu}.\vec{E}$ in the the Hamiltonian. The higher the intensity of the electric field, the more classically the system behaves. The principle is demonstrated for the case of the Ne-HI molecule 12. This molecule has a vibrationally averaged structure corresponding to a secondary minimum (DMC wavefunction in Fig. 12a). If we apply an electric field of the intensity 2.5×10^5 V/cm, the librational wavefunction becomes more classical but still the structure is not covering the global minimum on the potential energy surface. An electric field of the intensity of $2.5.10^6$ V/cm flips the wavefunction, so that the other isomer is formed. Note that unlike for the ground state no cage effect would be observed for this second minimum. For smaller fields applied, the cage effect would be, however, more pronounced. One could observe in this case long living resonances.

a)   b)   c)
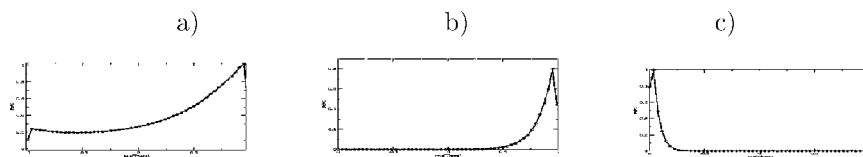
Figure 12.   Structure control of a Ne-HBr cluster by a DC electric filed. x-axis: $\cos\Theta$, y-axis: wavefunction(Θ is the angular part of the Jacobi coordinate system).

6. Conclusions

In this chapter we have described the way how to simulate the photodissociation dynamics in large, cryogenic clusters. We have emphasized the role of the initial conditions for the correct description of the experimental quantities. Preparing the system in different initial states is also a way how to control the photodissociation process. We can tune the cage effect by changing cluster size, the site of the chromophore, by librational preexcitation, by an external electric field, by cluster composition of by changing the temperature of the clusters. All these control exploits the the orientation by weak intermolecular forces. We have shown that for the dynamical description usually the classical mechanics within the Wigner trajectories approach is sufficient.

Acknowledgment

References

1.   Alimi, R. and R. Gerber: 1990, 'Solvation effects on chemical reaction dynamics in clusters: Photodissociation of HI in Xe_nHI'. *Phys. Rev. Lett.* **64**, 1453–1456.
2.   Allen, M. P. and D. J. Tildesley: 1987, *Computer Simulations of Liquids.* Clarendon Press, Oxford.
3.   Anderson, D., S. Davis, and D. Nesbitt: 1997, 'Sequential solvation of HCl in argon: High resolution infrared spectroscopy of Ar_nHCl(n=1,2,3)'. *J. Chem. Phys.* **107**, 1115–1127.
4.   Aques, C., L. Valachovic, S. Iionov, E. Bohmer, Y. Wen, J. Segall, and C. Wittig: 1993, 'Photoinitiated processes in complexes - subpicosecond studies of CO_2-HI and stereospecificity in Ar-HX'. *J. Chem. Soc. Faraday T* **89**, 1419–1425.
5.   Auer, B. M. and A. B. McCoy: 2003, 'Using diffusion Monte Carlo to evaluate the initial conditions for classical studies of the photodissociation dynamics of HCl dimer'. *J. Phys. Chem. A* **107**, 4–12.
6.   Barnett, R. N., P. J. Reynolds, and W. A. Lester: 1991, 'Monte Carlo algorithms for expectation values of coordinate operators'. *J. Comput Phys.* **96**, 258–276.
7.   Baumfalk, R., N. Nahler, U.Buck, M. Niv, and R. Gerber: 2000, 'Photodissociation of HBr adsorbed on the surface and embedded in large Ar_n clusters'. *J. Chem. Phys.* **113**(1), 329–338.
8.   Buck, U.: 2002, 'Photodissociation of hydrogen halide molecules in different cluster

environments'. *J. Phys. Chem.* **106**, 10050 10062.

9.   Castillo-Chara, J., R. R. Lucchese, and J. W. Bevan: 2001, 'Differentiation of the ground vibrational and global minimum structures in the Ar : HBr intermolecular complex'. *J. Chem. Phys.* **115**, 899–911.

10. Dickey, J. M. and A. Paskin: 1969, 'Computer simulation of the lattice dynamics of solids'. *Phys. Rev.* **188**, 1407–1418.

11. Ellison, F. O.: 1996, 'A method of Diatomics in Molecules. I. General theory and applications'. *J. Am. Chem. Soc.* **85**, 3540 3544.

12. Feynman, R. P. and A. R. Hibbs: 1965, *Quantum Mechanics and Path Integrals.* New York: McGraw Hill.

13. Gerber, R. B., R. Kosloff, and M. Ratner: 1986, 'Time dependent wavepacket calculations of molecular scattering from surfaces'. *Comp. Phys. Rep.* **5**, 59 113.

14. Heller, E.: 1981, 'The semiclassical way to molecular spectroscopy'. *Acc. Chem. Res.* **14**, 368–375.

15. Hillery, M., R. F. O'Connel, M. O. Scully, and E. P. Wigner: 1984, 'Distribution functions in physics - fundamentals'. *Phys. Rep.* **106**, 121 167.

16. Hinde, R. J.: 1998, 'Structural control of Ar-HF complexes using dc electric fields: a diffusion quantum Monte Carlo study'. *Chem. Phys. Lett.* **283**, 125–130.

17. Jungwirth, P. and R. B. Gerber: 1995, 'Quantum dynamics of large polyatomic systems using a classically based separable potential method'. *J. Chem. Phys.* **102**, 6046 6056.

18. Jungwirth, P. and R. B. Gerber: 1999, 'Quantum molecular dynamics of ultrafast processes in large polyatomic system's'. *Chem. Rev.* **99**, 1583 1606.

19. Jungwirth, P., P. Žďánská, and B. Schmidt: 1998, 'Librational control of photochemical reactions in small clusters'. *J. Phys. Chem. A* **102**, 7241 7244.

20. Kosloff, R.: 1994, 'Propagation methods for quantum molecular dynamics'. *Annu Rev. Phys. Chem.* **45**, 145–178.

21. Leake, J. A., W. B. Daniels, J. J. Skalyo, B. C. Frazer, and G. Shirane: 1969, 'Lattice dynamics of neon at two densities from coherent inelastic neutron scattering'. *Phys. Rev.* **181**, 1251–1260.

22. Lepetit, B. and D. Lemoine: 2002, 'State-to-state ArHBr photodissociation quantum dynamics'. *J. Chem. Phys.* **117**, 8676–8685.

23. Monnerville, M. and B. Pouilly: 1998, 'First quantum investigation of the photodissociation of the Ar-HBr complex: Three-dimensional time-dependent approach'. *Chem. Phys. Lett.* **294**, 473–479.

24. Nahler, N. H., R. Baumfalk, U. Buck, H. Vach, P. Slavíček, and P. Jungwirth: 2003, 'Photodissociation of HBr in and on Ar_n clusters: the role of the position of the molecule'. *Phys. Chem. Chem. Phys.* **5**, 3394.

25. Narevicius, E. and N. Moiseyev: 1998, 'Structured photo-absorption spectra of ArHCl: fingerprints of overlapping broad resonances'. *Chem. Phys. Lett.* **287**, 250–254.

26. Newton, I.: 1687, *Philosophia Naturalis Principia Mathematica.* London.

27. Niv, M., A. Krylov, and R. Gerber: 1997a, 'Photodissociation, electronic relaxation and recombination of HCl in Ar_n(HCl) clusters: Nonadiabatic molecular dynamics simulations'. *Faraday Discussions* **108**, 243–254.

28. Niv, M., A. I. Krylov, and R. B. Gerber: 1997b, 'Photodissociation, electronic relaxation and recombination of HCl in Ar_n(HCl) clusters'. *Faraday Discuss. Chem. Soc.* **108**, 243.

29. Niv, M. Y., A. I. Krylov, R. B. Gerber, and U. Buck: 1999, 'Photodissociation of HCl adsorbed on the surface of an Ar_12 cluster: Nonadiabatic molecular dynamics simulations'. *J. Chem. Phys.* **110**, 11047.

30. Portwich, G.: 1995. Master's thesis, Universität Göttingen.

31. Schmidt, B.: 1999, 'Quantum dynamics of HF photodissociation in icosahedral Ar_12HF clusters: rotational control of the hydrogen cage exit'. *Chem. Phys. Lett.* **301**, 207.

32. Schröder, T., R. Schinke, S. Liu, Z. Bacic, and J. Moskowitz: 1995, 'Photodissozi-

ation of HF in Ar_nHF (n=1-14,54) van der Waals clusters: Effects of the solvent cluster size on the solute fragmentation dynamics'. *J. Chem. Phys.* **103**, 9228 9241.

33. Segall, J., Y. Wen, R. Singer, C. Wittig, A. García-Vela, and R. Gerber: 1993, 'Evidence for a Cage Effect of HBr in Ar-HBr. Theoretical and Experimental Results'. *Chem. Phys. Lett.* **207**, 504 509.

34. Sese, L. M.: 1994, 'Study of the Feynman-Hibbs effective potential against the path-integral formalism for Monte Carlo simulations of quantum many-body Lennard-Jones systems'. *Mol. Phys.* **81**, 1297 1312.

35. Slavíček, P., P. Jungwirth, M. Lewerenz, N. H. Nahler, M. Farnik, and U. Buck: 2003, 'Photodissociation of HI on the surface of large argon clusters: The orientation of the librational wavefunction and the scattering from the cluster cage'. *J. Chem. Phys.* p. submitted.

36. Slavíček, P., M. Roeselová, P. Jungwirth, and B. Schmidt: 2001, 'Preference of cluster isomers as a result of quantum delocalization: Potential energy surfaces and intermolecular vibrational states of Ne···HBr, Ne···HI, and HI(Ar)$_n$ $(n = 1 - 6)$'. *J. Chem. Phys.* **114**(4), 1539 1548.

37. Slavíček, P., P. Žďánská, P. Jungwirth, R. Baumfalk, and U. Buck: 2000, 'Size effects on photodissociation and caging of hydrogen bromide inside or on the surface of large inert clusters: From one to three icosahedral layers'. *J. Phys. Chem. A* **104**, 7793–7802.

38. Sterling, M., Z. Li, and V. A. Apkarian: 1995, 'Simulations of quantum crystals by classical dynamics'. *J. Chem. Phys.* **103**, 5679 5683.

39. Stratt, R. M.: 1995, 'The instantaneous normal-modes of liquids'. *Accounts Chem. Res* **28**, 201–207.

40. Suhm, M. A. and R. O. Watts: 1991, 'Quantum Monte Carlo studies of vibrational-states in molecules and clusters'. *Phys. Rep* **204**, 293 329.

41. Trin, J., M. Monnerville, B. Pouilly, and H. D. Meyer: 2003, 'Photodissociation of the ArHBr complex investigated with the multiconfiguration time-dependent Hartree approach'. *J. Chem. Phys.* **118**, 600 609.

42. Tully, J. C.: 1990, 'Molecular-dynamics with electronic-transitions'. *J. Chem. Phys.* **93**, 1061–1071.

43. von Pietrowski, R., M. Rutzen, K. von Haeften, S. Kakar, and T. Möller: 1997, 'Fluorescence excitation spectroscopy of xenon doped neon clusters: size and site effects, and cluster melting'. *Z. Phys. D* **40**, 22–24.

44. Willberg, D. M., M. Gutmann, J. J. Breen, and A. H. Zewail: 1992, 'Real time dynamics of clusters 1.: I_2X_n (n=1)'. *J. Chem. Phys.* **96**, 198–212.

45. Žďánská, P., B. Schmidt, and P. Jungwirth: 1999, 'Photolysis of hydrogen chloride embedded in the first argon solvation shell: Rotational control and quantum dynamics of photofragments'. *J. Chem. Phys.* **110**, 6246–6256.

46. Žďánská, P., P. Slavíček, and P. Jungwirth: 2000, 'HCl photodissociation on argon clusters: Effects of sequential solvation and librational preexcitation'. *J. Chem. Phys.* **112**(24), 10761–10766.

List of participants of the Advanced Research Workshop

Alexander M.H.
University of Maryland, College Park, MD, USA
Aquilanti V.
University of Perugia, Italy
Auzinsh M.
University of Latvia, Riga, Latvia
Baer M.
Soreq NRC, Yavne, Israel
Balint-Kurti G.G.
University of Bristol, UK
Basilevsky M.V.
Karpov Institute of Physical Chemistry, Moscow, Russia
Bencsura Á.
Institute of Chemistry, Budapest, Hungary
Bene E.
Institute of Chemistry, Budapest, Hungary
Bosanac S.D.
R. Boskovic Institute, 10001 Zagreb, Croatia
Clary D.C.
University of Oxford, UK
Császár A.
Eötvös University, Budapest, Hungary
Dashevskaya E.
Technion, Haifa, Israel
Drahos L.
Institute of Chemisty, Budapest, Hungary
Faginas Lago N.
University of Perugia, Italy
Guo H.
Department of Chemistry, University of New Mexico, Albuquerque, NM, USA
Harding L.B.
Chemistry Division, Argonne National Laboratory, Argonne, IL, USA
Herman Z.
Heyrovsky Institute, Prague, Czech Republic
Lagana A.
University of Perugia, Italy
Launay J. M.
PALMS/SIMPA - UMR 6627 du CNRS, Universite de Rennes I, Rennes, France
Lendvay G.
Institute of Chemistry, Hungarian Academy of Sciences, Budapest, Hungary
Light J.C.
University of Chicago, IL, USA

Maergoiz A.
>Institute of Chemical Physics, Russian Academy of Science, Moscow, Russia

Manthe U.
>Theoretische Chemie, TU Muenchen, Garching, Germany

Miklavc A.
>National Institute of Chemistry, Ljubljana, Slovenia

Miller W.H.
>University of Berkeley, CA, USA

Nikitin E.E.
>Technion, Haifa, Israel

Nyman G.
>University of Göteborg, Sweden

Oref I.
>Technion, Haifa, Israel

Rozgonyi T.
>Institute of Chemistry, Budapest, Hungary

Schatz G.C.
>Department of Chemistry, Northwestern University, Evanston, IL. USA

Schiller R.
>KFKI Atomic Energy Research Institute, Budapest, Hungary

Schinke R.
>University of Göttingen, Germany

Slavicek P.
>Heyrovsky Institute of Physical Chemistry, Academy of Sciences, Prague, Czech Republic

Smirnov B. M.
>Institute for High Temperatures, Russian Academy of Sciences, Moscow, Russia

Szalay P.
>Department of Theoretical Chemistry, Eötvös University, Budapest, Hungary

Szalay V.
>Research Institute for Solid State Physics and Optics, Budapest, Hungary

Troe J
>Institut für physikalische Chemie, Universität Göttingen, Göttingen, Germany

Troya D.
>University of La Rioja, Logrono, Spain

Ushakov V.
>Institute of Problems of Chemical Physics, Chernogolovka, Russia

Vértesi T.
>Unversity of Debrecen, Hungary

Wagner A.F.
>Chemistry Division, Argonne National Laboratory, Argonne, IL, USA

Werner H.-J.
>Institute for Theoretical Chemistry, University of Stuttgart, Germany

Zhang D. H.
>University of Singapore, Singapore
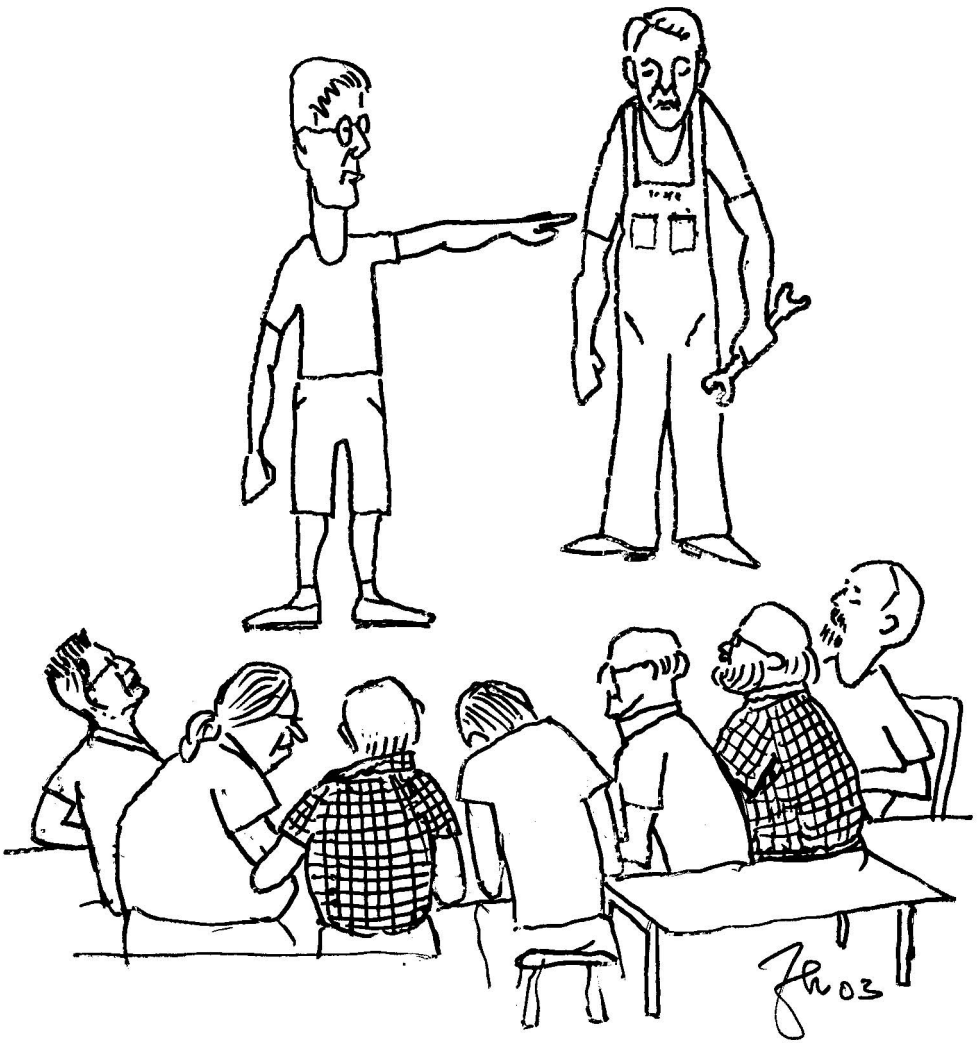
The only experimentalist at the Workshop.

We thank Zdenek Herman for permission to publish his drawing.

List of papers given at the Advanced Research Workshop

Alexander M.H.
Nonadiabatic effects in abstraction reactions of ^2P atoms with H_2

Aquilanti V.
Exact reaction cross sections and rates by the hyperquantization algorithm

Auzinsh M.
Manipulation of atoms and molecules with a laser radiation and external fields

Baer M.
On the Quantization of the Electronic Non-Adiabatic Coupling Terms: The $H+H_2$ system as a case of Study

Balint-Kurti G.G.
Time-Dependent wavepacket calculations for reactive scattering and photodissociation

Basilevsky M.V.
Momentum representation of the solute/bath interaction in the dynamic theory of chemical processes in condensed phase

Bosanac S.D.
Dynamics of atoms and molecules in phase space

Clary D.C.
Quantum reaction dynamics of polyatomic molecules

Császár A.
Chemical reactions at the focal point

Dashevskaya E.
Vibrational relaxation of diatoms in collisions with atoms at low energies

Guo H.
Chebyshev propagation and applications to scattering problems

Harding L.B.
Radical-Radical Reactions

Herman Z.
Dynamics of chemical reactions of molecular dications: Beam scattering studies

Laganà A.
Towards a grid based molecular simulator

Launay J.M.
Quantum dynamics of atom-hydrogen insertion reactions

Lendvay G.
Dynamics of reactions of vibrationally excited molecules

Light J.C.
Energy Selected Bases for Vibrations and Reaction Dynamics

Maergoiz A.
Statistical Adiabatic Channel Model for low-temperature capture in open shell systems. Asymptotic interactions in $H+O_2$ and $O+OH$ systems

Manthe U.
Accurate quantum dynamics calculations for polyatomic reactions

Miklavc A.
>   Strong Acceleration of Chemical Reactions Arising Through the Effects of Rotational Excitation on Collision Geometry

Miller W.H.
>   Using the Semiclassical Initial Value Representation to add Quantum Effects to Classical Molecular Dynamics Simulations

Nikitin E.E.
>   Vibrational Predissociation: quasiclassical tunneling through the classical chaotic sea

Nyman G.
>   Wavepacket calculations in curvilinear coordinates on coupled potential energy surfaces and a Wigner transform of the Boltzmann operator

Oref I.
>   Termolecular collisions between benzene and Ar

Schatz G.C.
>   Intersystem crossing effects in chemical reactions

Schinke R.
>   Isotope effects in ozone: Some answers, more questions

Slavicek P.
>   Exact reaction cross sections and rates by the hyperquantization algorithm

Smirnov B. M.
>   Coupling of electron momenta in ion-atom collosions

Szalay P.
>   Analytic Evaluation of Nonadiabatic Coupling Terms and Efficient Searching Algorithm of Conical Intersections within the COLUMBUS Program System

Szalay V.
>   On one-dimensional discrete variable representations with general basis functions

Troe J.
>   Recent advances in the modeling of ion-molecule reactions in the gas phase

Troya D.
>   Dynamics Studies of $O(^3P)$+Hydrocarbon Reactions

Ushakov V.
>   Wavepacket calculations in curvilinear coordinates on coupled potential energy surfaces and a Wigner transform of the Boltzmann operator

Wagner A.F.
>   Theoretical Studies of the Addition of H or D to Acetylene

Werner H.-J.
>   Non-adiabatic effects in bimolecular reactions

Zhang D. H.
>   Quantum Reaction Dynamics in Tetraatomic Systems and Beyond

INDEX